IAEA TECDOC SERIES

IAEA-TECDOC-2006

Modelling and Simulation of the Source Term for a Sodium Cooled Fast Reactor Under Hypothetical Severe Accident Conditions

Final Report of a Coordinated Research Project

IAEA
International Atomic Energy Agency

MODELLING AND SIMULATION OF THE SOURCE TERM FOR A SODIUM COOLED FAST REACTOR UNDER HYPOTHETICAL SEVERE ACCIDENT CONDITIONS

The following States are Members of the International Atomic Energy Agency:

AFGHANISTAN
ALBANIA
ALGERIA
ANGOLA
ANTIGUA AND BARBUDA
ARGENTINA
ARMENIA
AUSTRALIA
AUSTRIA
AZERBAIJAN
BAHAMAS
BAHRAIN
BANGLADESH
BARBADOS
BELARUS
BELGIUM
BELIZE
BENIN
BOLIVIA, PLURINATIONAL STATE OF
BOSNIA AND HERZEGOVINA
BOTSWANA
BRAZIL
BRUNEI DARUSSALAM
BULGARIA
BURKINA FASO
BURUNDI
CAMBODIA
CAMEROON
CANADA
CENTRAL AFRICAN REPUBLIC
CHAD
CHILE
CHINA
COLOMBIA
COMOROS
CONGO
COSTA RICA
CÔTE D'IVOIRE
CROATIA
CUBA
CYPRUS
CZECH REPUBLIC
DEMOCRATIC REPUBLIC OF THE CONGO
DENMARK
DJIBOUTI
DOMINICA
DOMINICAN REPUBLIC
ECUADOR
EGYPT
EL SALVADOR
ERITREA
ESTONIA
ESWATINI
ETHIOPIA
FIJI
FINLAND
FRANCE
GABON
GEORGIA
GERMANY
GHANA
GREECE
GRENADA
GUATEMALA
GUYANA
HAITI
HOLY SEE
HONDURAS
HUNGARY
ICELAND
INDIA
INDONESIA
IRAN, ISLAMIC REPUBLIC OF
IRAQ
IRELAND
ISRAEL
ITALY
JAMAICA
JAPAN
JORDAN
KAZAKHSTAN
KENYA
KOREA, REPUBLIC OF
KUWAIT
KYRGYZSTAN
LAO PEOPLE'S DEMOCRATIC REPUBLIC
LATVIA
LEBANON
LESOTHO
LIBERIA
LIBYA
LIECHTENSTEIN
LITHUANIA
LUXEMBOURG
MADAGASCAR
MALAWI
MALAYSIA
MALI
MALTA
MARSHALL ISLANDS
MAURITANIA
MAURITIUS
MEXICO
MONACO
MONGOLIA
MONTENEGRO
MOROCCO
MOZAMBIQUE
MYANMAR
NAMIBIA
NEPAL
NETHERLANDS
NEW ZEALAND
NICARAGUA
NIGER
NIGERIA
NORTH MACEDONIA
NORWAY
OMAN
PAKISTAN
PALAU
PANAMA
PAPUA NEW GUINEA
PARAGUAY
PERU
PHILIPPINES
POLAND
PORTUGAL
QATAR
REPUBLIC OF MOLDOVA
ROMANIA
RUSSIAN FEDERATION
RWANDA
SAINT KITTS AND NEVIS
SAINT LUCIA
SAINT VINCENT AND THE GRENADINES
SAMOA
SAN MARINO
SAUDI ARABIA
SENEGAL
SERBIA
SEYCHELLES
SIERRA LEONE
SINGAPORE
SLOVAKIA
SLOVENIA
SOUTH AFRICA
SPAIN
SRI LANKA
SUDAN
SWEDEN
SWITZERLAND
SYRIAN ARAB REPUBLIC
TAJIKISTAN
THAILAND
TOGO
TONGA
TRINIDAD AND TOBAGO
TUNISIA
TÜRKİYE
TURKMENISTAN
UGANDA
UKRAINE
UNITED ARAB EMIRATES
UNITED KINGDOM OF GREAT BRITAIN AND NORTHERN IRELAND
UNITED REPUBLIC OF TANZANIA
UNITED STATES OF AMERICA
URUGUAY
UZBEKISTAN
VANUATU
VENEZUELA, BOLIVARIAN REPUBLIC OF
VIET NAM
YEMEN
ZAMBIA
ZIMBABWE

The Agency's Statute was approved on 23 October 1956 by the Conference on the Statute of the IAEA held at United Nations Headquarters, New York; it entered into force on 29 July 1957. The Headquarters of the Agency are situated in Vienna. Its principal objective is "to accelerate and enlarge the contribution of atomic energy to peace, health and prosperity throughout the world''.

IAEA-TECDOC-2006

MODELLING AND SIMULATION OF THE SOURCE TERM FOR A SODIUM COOLED FAST REACTOR UNDER HYPOTHETICAL SEVERE ACCIDENT CONDITIONS

FINAL REPORT OF A COORDINATED RESEARCH PROJECT

INTERNATIONAL ATOMIC ENERGY AGENCY
VIENNA, 2022

For further information on this publication, please contact:

Nuclear Power Technology Development Section
International Atomic Energy Agency
Vienna International Centre
PO Box 100
1400 Vienna, Austria
Email: Official.Mail@iaea.org

Printed by the IAEA in Austria
August 2022

IAEA Library Cataloguing in Publication Data

Names: International Atomic Energy Agency.
Title: Modelling and simulation of the source term for a sodium cooled fast reactor under hypothetical severe accident conditions / International Atomic Energy Agency.
Description: Vienna : International Atomic Energy Agency, 2022. | Series: IAEA TECDOC series, ISSN 1011–4289 ; no. 2006 | Includes bibliographical references.
Identifiers: IAEAL 22-01526 | ISBN 978–92–0–135322–1 (paperback : alk. paper) | ISBN 978–92–0–135222–4 (pdf) |
Subjects: LCSH: Sodium cooled reactors. | Nuclear facilities — Accidents. | Nuclear facilities — Safety measures.

FOREWORD

The IAEA supports Member States' activities in advanced fast reactor technology development by providing a major forum for information exchange and collaborative research programmes. The IAEA's activities in this field are mainly carried out within the framework of the Technical Working Group on Fast Reactors (TWG-FR), which assists in the implementation of corresponding IAEA activities and the alignment of technical activities with the expressed needs of Member States. In the broad range of activities, the IAEA proposes and establishes coordinated research projects (CRPs). The CRP discussed in this publication aimed at improving Member States' capabilities in fast reactor design and analysis.

To support the development of fast reactor technologies in Member States and to extend the predictive capabilities of the simulation tools for sodium cooled fast reactor design and safety analysis, a CRP was launched in 2015 to perform modelling and simulation of the source term for sodium cooled fast reactors resulting from a hypothetical severe accident. The purpose of the research was to perform a realistic estimation of fission products and fuel particles inventory inside the reference sodium cooled fast reactor volumes under severe accident conditions. At different time scales, the propagation of radioactive isotopes was simulated in the primary vessel, the cover gas system and the containment building. This challenging modelling and simulation problem aimed at improving the understanding of key phenomena involving radioactive material transport was undertaken by nine organizations from seven IAEA Member States.

The CRP was divided into three work packages, with a choice for the participating organizations to contribute to one or all of the work packages. The outputs of the CRP and discussions are vital to understanding these phenomena and reducing the uncertainties in the estimation of potential releases to the environment under severe accident conditions in a sodium cooled fast reactor. The CRP was completed in 2020; the results of the calculations along with their analysis are provided in this publication.

The IAEA expresses its appreciation to all participants in the CRP for their dedicated efforts leading to this publication. The IAEA extends its special thanks to J.A. Arokiaswamy (IGCAR) for providing technical specifications for this CRP. The IAEA officers responsible for this publication were J. Mahanes, C. Batra and V. Kriventsev of the Division of Nuclear Power.

EDITORIAL NOTE

This publication has been prepared from the original material as submitted by the contributors and has not been edited by the editorial staff of the IAEA. The views expressed remain the responsibility of the contributors and do not necessarily represent the views of the IAEA or its Member States.

Neither the IAEA nor its Member States assume any responsibility for consequences which may arise from the use of this publication. This publication does not address questions of responsibility, legal or otherwise, for acts or omissions on the part of any person.

The use of particular designations of countries or territories does not imply any judgement by the publisher, the IAEA, as to the legal status of such countries or territories, of their authorities and institutions or of the delimitation of their boundaries.

The mention of names of specific companies or products (whether or not indicated as registered) does not imply any intention to infringe proprietary rights, nor should it be construed as an endorsement or recommendation on the part of the IAEA.

The authors are responsible for having obtained the necessary permission for the IAEA to reproduce, translate or use material from sources already protected by copyrights.

The IAEA has no responsibility for the persistence or accuracy of URLs for external or third party Internet web sites referred to in this publication and does not guarantee that any content on such web sites is, or will remain, accurate or appropriate.

CONTENTS

FOREWORD

The IAEA supports Member States' activities in advanced fast reactor technology development by providing a major forum for information exchange and collaborative research programmes. The IAEA's activities in this field are mainly carried out within the framework of the Technical Working Group on Fast Reactors (TWG-FR), which assists in the implementation of corresponding IAEA activities and the alignment of technical activities with the expressed needs of Member States. In the broad range of activities, the IAEA proposes and establishes coordinated research projects (CRPs). The CRP discussed in this publication aimed at improving Member States' capabilities in fast reactor design and analysis.

To support the development of fast reactor technologies in Member States and to extend the predictive capabilities of the simulation tools for sodium cooled fast reactor design and safety analysis, a CRP was launched in 2015 to perform modelling and simulation of the source term for sodium cooled fast reactors resulting from a hypothetical severe accident. The purpose of the research was to perform a realistic estimation of fission products and fuel particles inventory inside the reference sodium cooled fast reactor volumes under severe accident conditions. At different time scales, the propagation of radioactive isotopes was simulated in the primary vessel, the cover gas system and the containment building. This challenging modelling and simulation problem aimed at improving the understanding of key phenomena involving radioactive material transport was undertaken by nine organizations from seven IAEA Member States.

The CRP was divided into three work packages, with a choice for the participating organizations to contribute to one or all of the work packages. The outputs of the CRP and discussions are vital to understanding these phenomena and reducing the uncertainties in the estimation of potential releases to the environment under severe accident conditions in a sodium cooled fast reactor. The CRP was completed in 2020; the results of the calculations along with their analysis are provided in this publication.

The IAEA expresses its appreciation to all participants in the CRP for their dedicated efforts leading to this publication. The IAEA extends its special thanks to J.A. Arokiaswamy (IGCAR) for providing technical specifications for this CRP. The IAEA officers responsible for this publication were J. Mahanes, C. Batra and V. Kriventsev of the Division of Nuclear Power.

1. INTRODUCTION

1.1. BACKGROUND

In a typical medium to large sized pool type sodium cooled fast reactor (SFR), severe accident conditions are postulated and studied for evaluating the design adequacy of containment and severe accident management strategies. The most dangerous severe accident is a hypothetical core disruptive accident (CDA) resulting from either the loss of flow or transient overpower events combined with the complete loss of reactor shutdown function: unprotected loss of flow accident (ULOFA) and unprotected transient overpower accident (UTOPA), respectively. These unprotected transients might release large thermal energy in a very short time, wherein very high temperatures and pressures are reached in the reactor core. Since the mechanical work potential is usually much less than one percent of the thermal energy released, the overall structural integrity of the primary system is still ensured although some radioactive material may still get into the RCB through 'leakage paths' (see below). Even though the likelihood of such an accident is classified as a beyond design basis accident (BDBA), or a "design extension condition (DEC)"as per recent safety classification [1], the reactor containment building (RCB) is designed to "prevent or control and limit the release and the dispersion of radioactive substances" [1]. CDA is also possible from another class of events, such as an initiating event combined with the successful operation of the shutdown system but with an accompanied loss of decay heat removal systems, referred to as a protected loss of heat sink (PLOHS) accident. This class of events is not considered within the scope of this study as the time scales involved are longer and the energetics and extent of core damage are expected to be bounded by ULOFA, although the radionuclide transport and release phenomena could be different.

The consequences of the CDA in terms of radioactivity release outside the containment system which may affect the environment and public are of paramount importance from public acceptance. Even though the structural integrity of the primary vessel can be ensured by way of demonstrating its capability to withstand high mechanical energy release, the pressure developed within the vessel during a CDA can lead to sodium and radioactivity release within the RCB through several potential leak paths in the top shield structure of the reactor. The ejected sodium can burn inside the RCB leading to temperature and pressure build up. The sodium release to the RCB can also be accompanied by a certain fraction of radioactive fission products and fuel that are released from the failed fuel pins. Subsequently some of these radionuclides can leak out to the environment through the leak paths in the RCB.

It is part of the licensing criteria that the radioactivity and hence the dose rates at the site boundary (and also habitability of critical areas inside the plant) owing to severe accidents need to be evaluated to assure the public protection against accidental radiation release. The evaluation would also be used to provide necessary design measures to eliminate the possibility of those accidents that would cause unacceptable consequences (requirement of permanent relocation of large populations) and to practically eliminate the possibility of those severe accidents that could require short term or small scale evacuation and thereby ensure that the dose exposure is within the permissible limits.

Realistic quantification of the radioactive source term requires a good understanding of the whole range of phenomena under a severe accident scenario. Towards this, it is essential to model the process of transport of fission products involving core bubble expansion characteristics, heat transfer and mass transfer among core materials, sodium and cover gas, chemical interaction between fission products and sodium etc., and to characterize the parameters influencing the fission product retention and release. There are several simulation

tools and established methodology (methodology considered mature enough by the practitioners and licensing authorities) available for the estimation of the source term for light water reactors (LWRs), which is not the case for SFRs. However, the phenomenon of radiation transport beyond the containment is similar for both SFRs and LWRs. In this context it is appropriate to focus resources on the development of mechanistic models and codes for the in-vessel, vessel-containment interface, and in-containment source term modelling for SFRs.

This coordinated research project (CRP) was implemented as a specific task of the IAEA project 1000154 "Advanced Technology for Fast and Gas-cooled Reactor", with first research coordination meeting conducted in 2016. Among others, the project 1000154 has the objective to enable member states to take informed decisions on the development of advanced fast reactor designs, and to increase cooperation between member states in achieving advances in fast reactor development through international collaborative R&D, in particular in the area of verification, validation and qualification of advanced simulation tools and data for the design and safety analysis of fast reactors. This publication presents the outputs of the CRP as a comprehensive review of the calculations performed and results analysed during the four years of collaborative research.

1.2. OBJECTIVE

The objective of this publication is to share the findings of an IAEA CRP entitled 'Radioactive Release from the Prototype Sodium Cooled Fast Reactor under Severe Accident Conditions'. The purpose of the CRP was to perform realistic estimation of fission product and fuel particle inventory inside reference sodium-cooled fast reactor (SFR) volumes (i.e., in-primary vessel, cover gas system and in-containment building) at different time scales (few seconds for the instantaneous source terms and several days for the long-term source term), under severe accident conditions (i.e. DECs with core melting). The objective was to improve the understanding of the key phenomena involving radioactive material transport inside the reactor vessel and the containment compartments, in order to reduce uncertainties in estimation of the releases to the environment under severe accident conditions in an SFR. Therefore, the CRP intended to extend the predictive capabilities of simulation tools devoted to SFR design and safety analysis in order to make informed decisions on enhancing the safety of the proposed fast reactor designs.

1.3. SCOPE

Towards improving the current state of the art for modelling the in-vessel and in-containment source terms, the IAEA launched the CRP in which participants from nine countries have completed benchmark simulations for the source term estimation with different models and tools. The technical aspects addressed are divided into three main parts. First is the in-vessel source term estimation, consisting of risk important fission product distribution in the fuel pins, their release mechanisms into the coolant and subsequent reaction and transport in the coolant and release to the cover gas. Second is the primary system/containment interface source term estimation consisting of models for the cover gas, sodium ejection, and radionuclide chemical composition and distribution in the containment. The third part is the estimation of the fission product evolution within the containment considering sodium burning scenarios, aerosol behaviour, and physical boundary conditions. The scope of this publication is the publication of the relevant facility and material information, introduction of methods of analysis, simulation results, comparison between methods and assumptions, and evaluation performed by the CRP participants for the benchmark.

1.4. STRUCTURE

The publication is organized in eight major sections, with this being the first section. Section 2 presents the technical specifications used for the benchmarking exercise. Section 3 defines three work packages into which the CRP was divided into and the outputs that were requested to be calculated in each of these work packages. Section 4 describes the work performed and results of WP-1, Section 5 presents the work performed and results obtained in WP-2, and section 6 presents the WP-3 methods and results by all the participants of the work package 3. Section 7 presents the compilation and comparison of the results. The main conclusions are presented in Section 8. In addition, the Appendix describes the participating organizations and the codes and tools used in the CRP.

2. DESCRIPTION OF THE BENCHMARK

2.1. DESCRIPTION OF THE CRP AND ITS SCOPE

Due to the inherent characteristics and robust design of Sodium cooled Fast Reactors (SFR), the core disruptive accident (CDA) is considered a very unlikely event. Nevertheless, to confirm the safety of the reactor, one of the hypothetical scenarios arising from the loss of coolant flow coupled with the complete failure of the shutdown system, referred to as the Unprotected Loss of Flow Accident (ULOFA), is postulated to serve as a basis for containment design and severe accident management measures. Determination of the corresponding radioactive source term released into the containment is an important initial condition for the assessment of the adequacy of the containment and subsequently the radiological impact at the site. Estimation of the source term for the sodium cooled fast reactors requires computational tools similar to those developed for the assessment of thermal reactor source term.

Scope of analysis was divided into three parts, defined as work packages of the CRP:

(1) In-vessel source term estimation;
(2) Primary system/containment system interface source term estimation; and
(3) In-containment phenomenology analysis.

The in-vessel source term consists of the transport of fuel and fission products from the damaged fuel pins to the cover gas volume through the sodium matrix. It can be divided into two components: an instantaneous source term, associated with the energetics of the assumed accident scenario, and a long-term source term associated with the release of fission products (and potentially fuel particles) from the sodium matrix of the primary system. The instantaneous source term is primarily governed by the dynamics of the sodium vapour bubble and the corresponding transport of fission products and fuel particles through the interface of the vapour bubble and the sodium matrix. The long-term source is due to the evaporation of sodium and dissolved radionuclides into the containment, through open leak paths in the top shield.

The primary system/containment system interface source term is also defined by two components: one being the release of fission products from the primary coolant and cover gas directly into the Reactor Containment Building (RCB), and the other one being the long-term leakage into the containment system. The first component also includes the associated mass of primary sodium instantaneously ejected through the leak paths in the vessel head into the RCB.

The in-containment phenomena are essentially defined by the transport of fission products through various containment compartments under the prevailing thermodynamic conditions, basically governed by the SFR specific processes such as sodium spray fire, sodium pool fire and various dynamic aerosol processes.

The benchmark exercise was carried out for a reference mixed oxide fuelled, pool type SFR of 500 MW(e) capacity with assumed initial conditions such as pressure and temperature corresponding to specified energy release estimated by deterministic calculations for a ULOFA.

2.2. DESCRIPTION OF THE REFERENCE SODIUM COOLED FAST REACTOR

The reactor assembly as shown in FIG. 1, consists of core, control, and shield assemblies loaded on to a grid plate which is supported by a core support structure resting on the bottom of the Main Vessel (MV). The MV is closed on the top by the roof slab, which is a box type structure and is supported from the top. The MV houses the primary sodium circuit, consisting of core,

hot pool, four Intermediate Heat Exchangers (IHX), cold pool, and two primary sodium pumps. The decay heat removal condensers of the Safety Grade Decay Heat Removal System (SGDHRS) are dipped into the hot pool. These components are supported by the roof slab. Primary sodium while passing through the fuel subassemblies (FSA) pickup heat and become hot. The hot sodium coming out of the FSA mixes in the hot pool and enters the IHX. The hot sodium flowing through the IHX transfers heat to the secondary sodium and the cold primary sodium coming out of the IHX mixes in the cold pool to be pumped back through the core. The secondary sodium transfers heat from the IHX to the steam generator steam-water system. The control plug houses instrumentation and control assemblies.

The purpose WP-1 of this CRP was to calculate the inventory of radionuclides in the primary system and cover gas space above the coolant free level following a core damage accident. Therefore, this section describes the initial fission product inventory in the core and operating conditions in terms of temperature distribution in the core and flow characteristics of the primary system. The internal structures details are required for knowing the coolant flow path and area of deposition of the radionuclides.

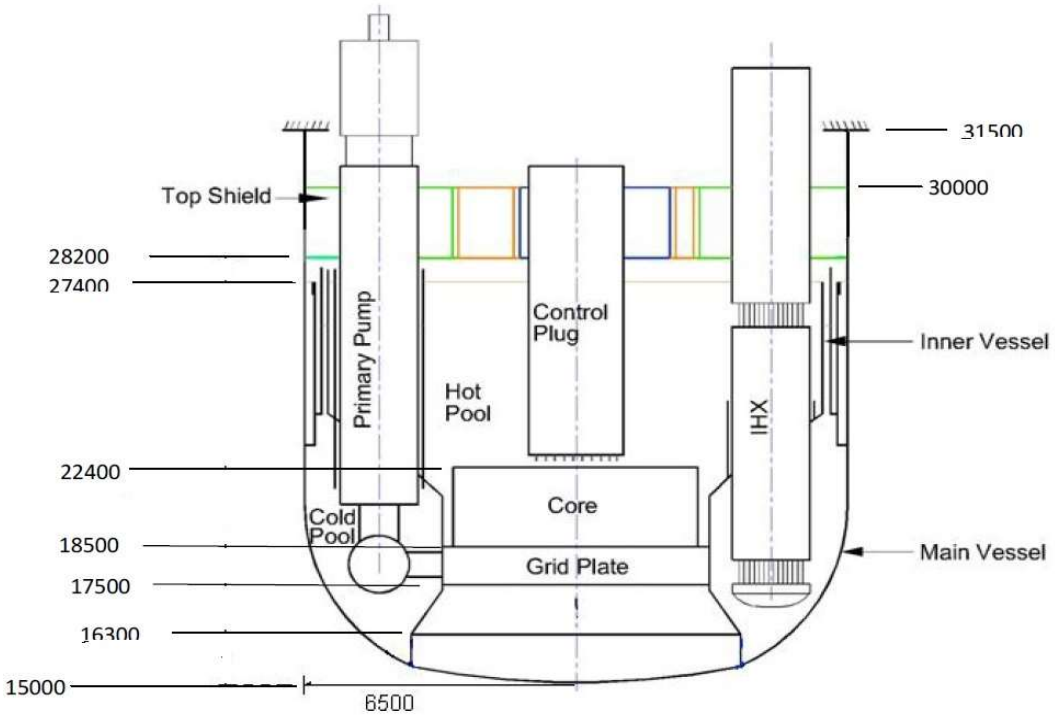

FIG. 1. Elevation Scheme (in mm) of Reactor Assembly Section through IHX and PUMP.

All dimensions are given at room temperature. Core top shown in FIG. 1 is subassembly (SA) top. The dimensions of the important structures in the Main Vessel are given below in TABLE 1.

TABLE 1. IMPORTANT STRUCTURES IN MAIN VESSEL

Sq. No.	Component	Diameter, (m)	Length, (m) (starting from Roof Slab)	Number

1	Pump	2.0	5	2
2	Intermediate heat exchanger (IHX)	2.0	5	4
3	Decay heat exchange (DHX)	0.5	4.0	4
5	Control plug	2.25	5	1

The hot pool and cold pool are separated by a thin vessel known as inner vessel (IV). The IV consists of two cylindrical shells of different diameters joined by a conical shell called the redan. The primary sodium pumps (PSP) and IHX bridge the two pools through penetrations in the redan conical section. The control plug (CP) is located at the centre of the hot pool above the core and is supported on the small rotating plug (SRP) and large rotating plug (LRP) of the top shield. It houses vertical cylindrical canals used as passages for control rod drive mechanisms and thermocouples. The top view of the roof slab is shown in FIG. 2. Pitch circle diameter of IHX and PSP = 9.8 m.

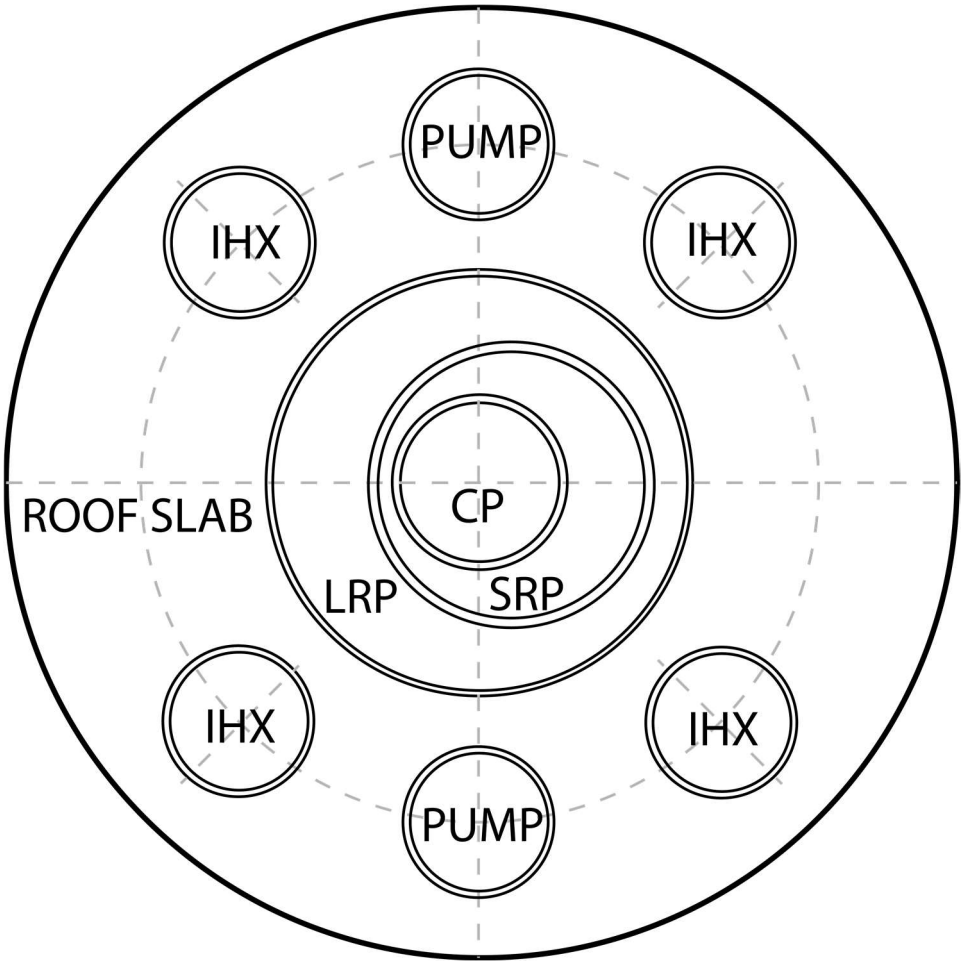

FIG. 2. Schematic of reactor assembly top view.

2.2.1. **Core Configuration**

A simplified diagram without internal structures for simpler radionuclide transport calculations is shown in FIG. 3.

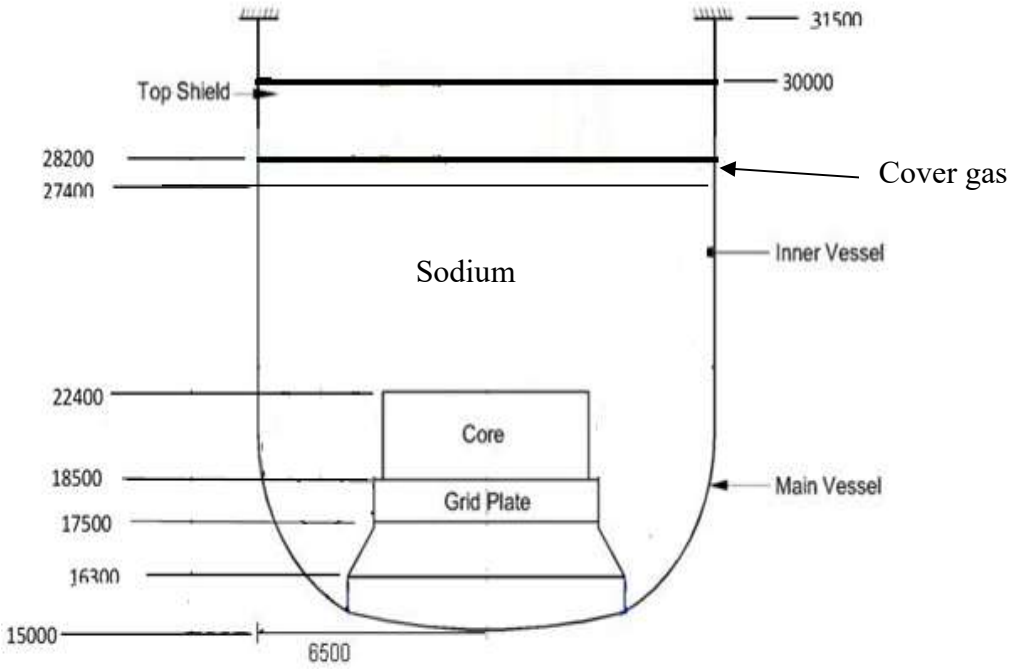

FIG. 3. Elevation (in mm) schematic of reactor assembly section.

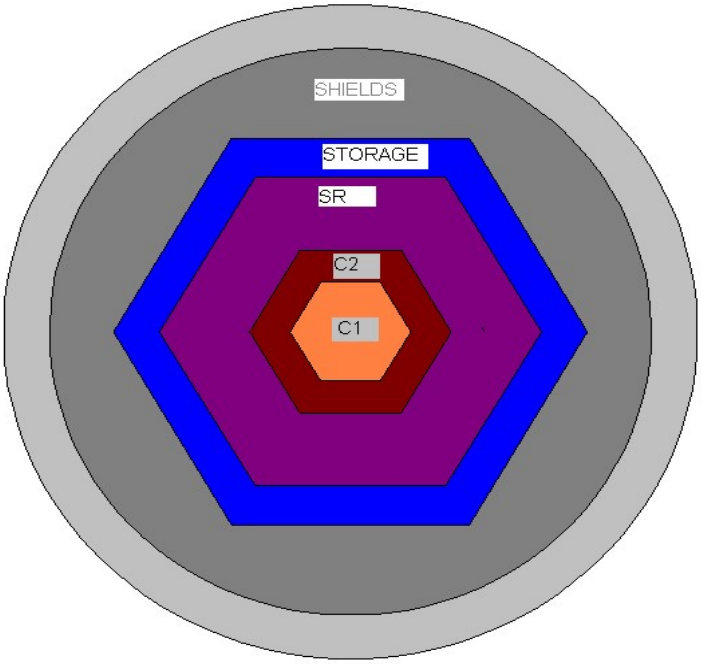

FIG. 4. Core configuration.

C1 and C2– Inner Core 1 and Inner Core 2 (5+3 rows) = 180 FSA

SR – Steel Reflector (4 rows), Radius - 151.5 cm (R-Z model)

STORAGE – (2 rows), Radius - 189.00 cm

SHIELDS – (9 rows), Radius - 300.00 cm

The core parameters are given in TABLE 2.

TABLE 2. CORE PARAMETERS

Reactor power	1250 MW(th)/500 MW(e)
Fuel	PuO_2-UO_2
Coolant	Sodium
Max. fuel burnup	100 GWd/t
No. of fuel subassemblies (FSA)	180
Refuelling interval	180 EFPD
Coolant inlet temperature	670 K
Coolant outlet temperature	820 K

The reactor core SAs are arranged in a hexagonal layout as shown in FIG. 4 and consists of various types of subassemblies such as fuel, shield and reflectors. Schematic of fuel subassemblies (FSA) are shown in FIG. 5. Each FSA consists of 217 helium bonded pins of 6.6 mm diameter with spacer wire of 1.65 mm wound helically at pitch 150 mm and 7 shielding rods of 36 mm diameter. In order to achieve nearly uniform temperature at the outlet of each subassembly, dual enriched fuel zone and flow zoning is considered. The inner core has lesser

fissile content compared to the outer core. The flow zoning in the core is achieved by providing orifices of varying resistances at the inlet of subassembly. The nominal core inventory is given in TABLE 3.

TABLE 3. NOMINAL CORE INVNVENTORIES

Material	Inner core FSA, (kg)	Outer core FSA, (kg)	Nominal Reactor Loading, (kg)
UO_2 (active core)	40.0	36.7	6923
UO_2 (axial blankets)	33.0	33.0	5973
PuO_2	10.5	14.0	2236

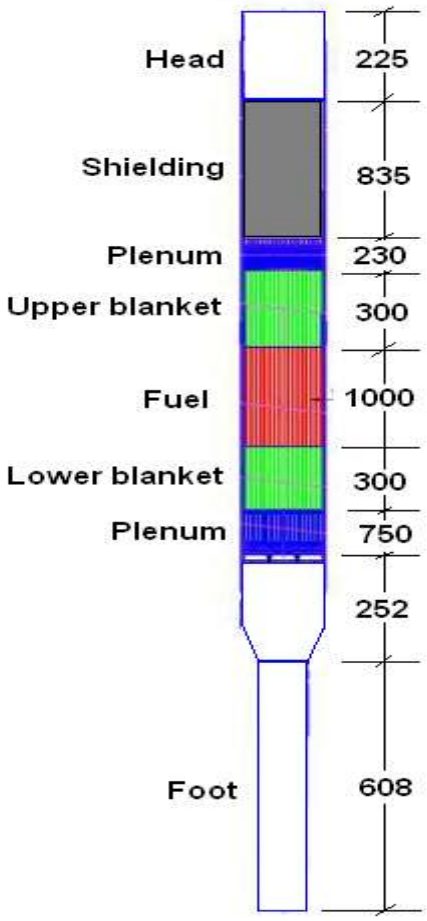

FIG. 5. Scheme (in mm) of fuel subassembly (FSA).

FSA dimensions are given in FIG. 5 for fresh core (before irradiation).

Total height of FSA = 4.5 m

Active core height = 1 m

Width across flats of FSA = 131.6 mm (Max), 131.3 (Nominal)

Triangular pitch of the FSA = 135 mm

Total core volume= 3000 litres (The core-1 and core-2 volumes being 1400 l and 1600 l Respectively, volume as per the pre-disassembly transient model= 2913.7 l).

Inner Core 1 and Inner Core 2 Peak Burn up**:** 100 and 90 MWd/kg

Oxide Fuel – Fissile Fractions 21% and 28%

Sodium Inventory in Main Vessel: 1150 t

Primary Cover Gas Volume: 120 m^3

2.2.2. Nominal core power and temperature data

Steady state core volumes (cm^3), steady state power (kW) and fuel temperature (K) in the meshes are given below in TABLE 4 through TABLE 6. The active core has been divided into 7 radial meshes and 10 axial meshes, without axial blankets. The decay power after reactor shutdown as a function of time is given in TABLE 7 and FIG. 6.

TABLE 4. CORE VOLUMES (CM^3) IN THE MESHES

1610.0	48292.0	38631.0	48296.0	48290.0	67614.0	38631.0
1610.0	48292.0	38631.0	48296.0	48290.0	67614.0	38631.0
1610.0	48292.0	38631.0	48296.0	48290.0	67614.0	38631.0
1610.0	48292.0	38631.0	48296.0	48290.0	67614.0	38631.0
1610.0	48292.0	38631.0	48296.0	48290.0	67614.0	38631.0
1610.0	48292.0	38631.0	48296.0	48290.0	67614.0	38631.0
1610.0	48292.0	38631.0	48296.0	48290.0	67614.0	38631.0
1610.0	48292.0	38631.0	48296.0	48290.0	67614.0	38631.0
1610.0	48292.0	38631.0	48296.0	48290.0	67614.0	38631.0
1610.0	48292.0	38631.0	48296.0	48290.0	67614.0	38631.0

TABLE 5. STEADY STATE POWER (KW) IN THE MESHES

529.0	14589.0	10454.0	12113.0	13483.0	15139.0	6571.0
700.0	19713.0	14251.0	16334.0	18152.0	20257.0	8742.0
851.0	24035.0	17399.0	19898.0	22112.0	24679.0	10643.0
960.0	27159.0	19663.0	22472.0	24976.0	27877.0	12018.0
1020.0	28859.0	20892.0	23873.0	26521.0	29608.0	12760.0
1026.0	29028.0	21011.0	24003.0	26656.0	29743.0	12814.0
977.0	27666.0	20030.0	22858.0	25362.0	28276.0	12176.0
876.0	24870.0	18021.0	20535.0	22740.0	25301.0	10886.0
732.0	20906.0	15186.0	17237.0	19012.0	21048.0	9044.0
565.0	16381.0	11972.0	13479.0	14748.0	16099.0	6903.0

TABLE 6. FUEL TEMPERATURE (K) IN THE MESHES

1575.0	1506.0	1439.0	1393.0	1441.0	1308.0	1188.0
1797.0	1729.0	1645.0	1575.0	1644.0	1466.0	1302.0
1988.0	1912.0	1810.0	1723.0	1812.0	1598.0	1398.0
2120.0	2037.0	1922.0	1823.0	1926.0	1687.0	1462.0
2181.0	2095.0	1972.0	1868.0	1979.0	1727.0	1488.0
2167.0	2082.0	1958.0	1853.0	1966.0	1713.0	1474.0
2077.0	1999.0	1880.0	1780.0	1888.0	1647.0	1419.0
1919.0	1852.0	1746.0	1654.0	1750.0	1533.0	1329.0
1702.0	1653.0	1565.0	1485.0	1563.0	1379.0	1209.0
1458.0	1431.0	1367.0	1299.0	1355.0	1205.0	1074.0

TABLE 7. DECAY POWER FOR MOEC AND EOEC

Cooling period	**Neutronic power (MW(th))**	**MOEC Decay power (MW(th))**	**EOEC Decay power (MW(th))**
1 s	190.61	72.39	72.04
10 s	78.9	58.1	57.87
50 s	25.39	45.61	45.49
100 s	10.81	40.19	40.11
200 s	5.76	35.24	35.22
500 s	4.53	29.47	29.48
1000 s	3.96	25.04	25.11
1 h	2.09	16.91	17.04
2 h	-	13.57	13.73
5 h	-	10.54	10.72
10 h	-	8.83	9.03
1 d	-	6.89	7.1
2 d	-	5.51	5.73
6 d	-	3.49	3.7
10 d	-	2.71	2.91
30 d	-	1.53	1.71
45 d	-	1.2	1.37
60 d	-	1.01	1.16
75 d	-	0.88	1.02
90 d	-	0.78	0.91
180 d	-	0.46	0.55
1 y	-	0.24	0.3

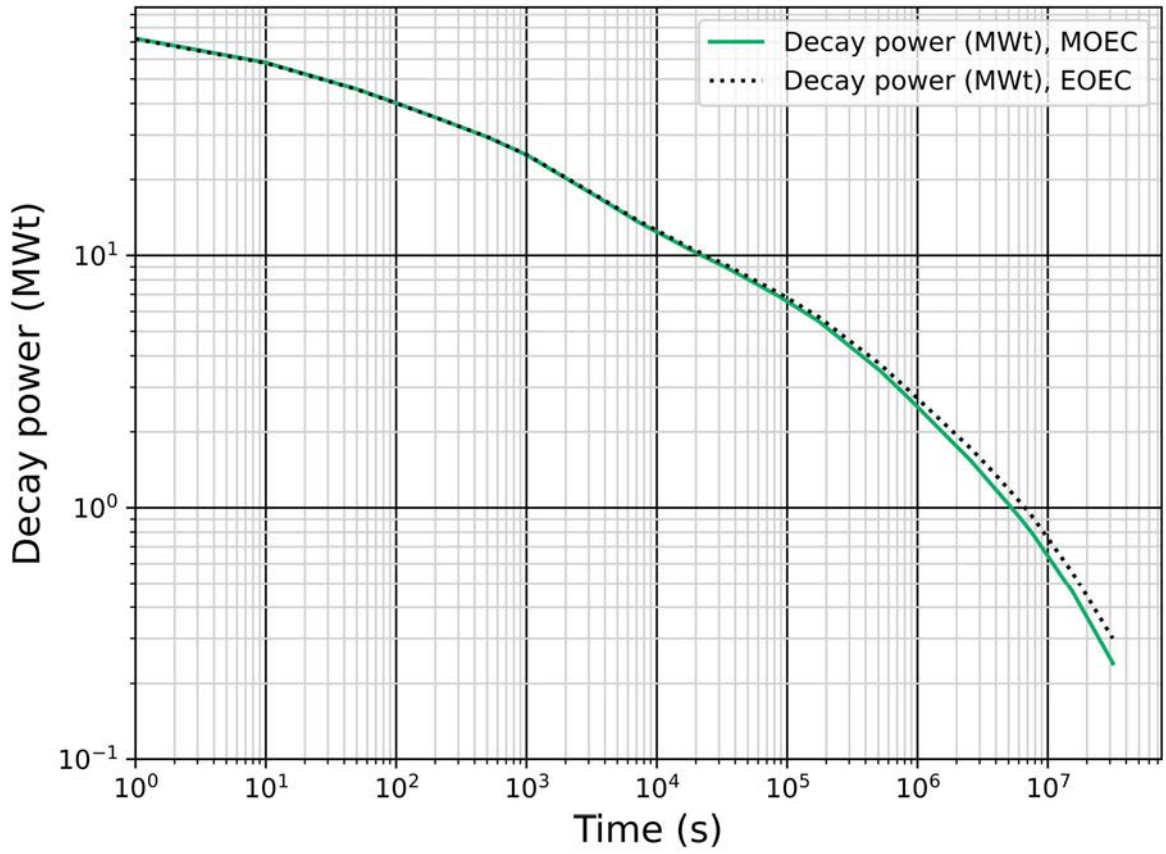

FIG. 6. Core Decay Power – MOEC.

2.2.3. **Fission product inventory**

The radionuclide inventory (in Bq) of important fission product isotopes is given in TABLE 8. Since there are 180 fuel assemblies, and 1/3 of them are discharged and 1/3 fresh FSA loaded during each fuel handling operation, the activities for the Middle of Equilibrium Core (MOEC) is obtained as follows.

$$A_{100GWd/t}\,(Bq) = 180 \times A_{100GWd/t} \quad (1)$$

$$A_{MOEC}\,(Bq) = 60 \times A_{2.5} + 60 \times A_{1.5} + 60 \times A_{0.5} \quad (2)$$

where
A is the activity in Bq
A_x is the activity for 'x' cycles burnt fuel 1(cycle= 180 effective full power days)
BOEC=beginning of equilibrium cycle (1/3rd fresh, 1/3rd 1 cycle, 1/3rd 2 cycles burnt)
MOEC= middle of equilibrium cycle (1/3rd0.5 cycles, 1/3rd1.5 cycles, 1/3rd 2.5 cycles burnt)
EOEC= end of equilibrium cycle (1/3rd 3cycles, 1/3rd 2 cycles, 1/3rd 1 cycles burnt)

TABLE 8. CORE INVENTORY*

Radionuclide	Half life	Activity in Bq for MOEC	Activity in Bq for EOEC (100 MWd/t)
I-131	8.02 d	1.46E+18	1.48E+18
I-132	2.30 h	1.94E+18	1.96E+18
I-133	20.80 h	2.51E+18	2.54E+18
I-134	52.50 m	2.50E+18	2.53E+18
I-135	6.57 h	2.21E+18	2.23E+18
Cs-134	754.50 d	5.19E+16	9.65E+16
Cs-137	30.07 y	4.98E+16	1.00E+17
Rb-88	17.78 m	5.17E+17	5.22E+17
Ru-103	39.26 d	2.22E+18	2.41E+18
Ru-106	373.59 d	6.16E+17	1.06E+18
Sr-89	50.53 d	6.31E+17	7.12E+17
Sr-90	28.79 y	1.43E+16	2.88E+16
Ce-141	32.50 d	1.98E+18	2.11E+18
Ce-144	284.89 d	6.37E+17	1.05E+18
Te-131m	30.00 h	1.61E+17	1.63E+17
Te-132	3.20 d	1.86E+18	1.88E+18
Ba-140	12.75 d	1.91E+18	1.93E+18
Zr-95	64.02 d	1.49E+18	1.76E+18
La-140	1.68 d	1.94E+18	1.96E+18
Kr-83m	1.85 h	2.36E+15	4.69E+15
Kr-85	10.70 y	2.24E+17	2.26E+17
Kr-85m	4.48 h	4.04E+17	4.08E+17
Kr-87	76.30 m	4.89E+17	4.94E+17
Kr-88	2.84 h	2.52E+18	2.55E+18
Kr-89	3.15 m	2.63E+18	2.66E+18
Xe-131m	11.84 d	1.46E+18	1.48E+18
Xe-133	5.24 d	1.94E+18	1.96E+18
Xe-133m	2.2 d	2.51E+18	2.54E+18
Xe-135	9.14 h	2.50E+18	2.53E+18
Xe-135m	15.29 m	2.21E+18	2.23E+18
Xe-137	3.82 m	5.19E+16	9.65E+16
Xe-138	14.08 m	4.98E+16	1.00E+17
U-237	6.75 d	1.37E+17	1.46E+17
U-239	23.45 m	2.34E+19	2.84E+19
Np-239	2.35 d	2.53E+19	2.59E+19
Pu-238	87.7 y	2.51E+14	5.77E+14
Pu-239	2.4E+4 y	2.38E+15	2.17E+15
Pu-240	6564 y	3.68E+15	3.87E+15
Pu-241	14 y	3.08E+17	2.95E+17
Pu-242	3.7E+5 y	4.61E+12	5.79E+12
Cm-242	0.44 y	3.51E+16	8.16E+16
Cm-243	28.5 y	8.74E+12	2.49E+13
Cm-244	18.1 y	9.40E+14	2.70E+15

* Calculations will use MOEC values. 100GW/t is for reference only.

2.2.4. **Primary Systems**

2.2.4.1. *Primary Sodium Pump*

The primary sodium pump circulates sodium through the core and IHX for the transport of heat from the core to the IHX.

Outer casing SS 304 LN
Nominal operating temperature: 670 K (397 °C)
Flow halving time: 50% flow after 8 s
For dimensional details please refer to TABLE 1.

2.2.4.2. *IHX*

The IHX transfers heat from primary sodium to secondary sodium. It provides a leak tight barrier between primary sodium and secondary sodium. There are two identical IHX for each of the two secondary sodium circuits. IHX is a vertical shell and tube counter-flow unit with primary sodium on shell side and secondary sodium on tube side featuring single pass on both shell and tube side.

IHX top level of top window is EL 26000 mm and bottom level is EL 25100 mm.

Material: SS316LN

Heat Removal capacity: 314 MW(th)
Primary inlet temperature: 817 K (544ºC)
Primary outlet temperature: 667 K (394ºC)
Primary sodium flow rate: 1649 kg/s
Secondary inlet temperature: 628 K (355ºC)
Secondary outlet temperature: 798 K (525ºC)
Secondary sodium flow rate: 1450 kg/s
Tube size: 19 mm OD
No. of tubes: 3600
Nominal heat transfer area: 1600 m^2 (based on OD)
Pressure drop on primary side: 1.5 m liquid column of sodium
For dimensional details please refer to TABLE 1.

2.2.4.3. *DHX*

It transfers the decay heat from primary sodium to intermediate sodium. It provides physical barrier between primary sodium on the shell side and intermediate sodium on the tube side.

Material: SS 316 LN
Heat Removal capacity: 8 MW(th)
Primary Sodium inlet temperature: 820 K (547ºC)
Primary sodium outlet temperature: 655 K (382ºC)
Primary sodium flow rate: 38.5 kg/s
Intermediate sodium inlet temperature: 576 K (303ºC)
Intermediate sodium outlet temperature: 767 K (494ºC)
Tube size OD thickness: 24 x 1 mm (DHX – Type ‘A’)
25.4 x 1.2 mm (DHX – Type ‘B’)
Number of tubes: 108 (DHX Type ‘A’)

90 (DHX – Type ‘B’)
Heat transfer area: 27 m^2 (Type ‘A’) for two DHX and 47 m^2 (Type ‘B’) for two DHX.
For dimensional details please refer to TABLE 1.

2.2.4.4. *Top shield leak path*

Schematic of top shield is shown in FIG. 7. The major leak paths in the top shield are the annular gaps between the Roof Slab (RS) and Large Rotating Plug (LRP) and Small Rotating Plug (SRP). The other penetrations in the RS are passages for IHX, Primary Sodium Pumps, DHX, In Vessel Transfer Post cum Periscope access, Hot Pool Level Detector (HPLD), Cold Pool Level Detector (CPLD), Delayed Neutron Detector (DND), Sodium Fill and Drain Lines, Argon Feed and Outlet Lines, Sodium Purification Lines, and Inclined Fuel Transfer Machine (IFTM). The penetrating paths in the SRP are due to the Control Plug, Oval Shield Plug of Transfer Arm, and Guide Tube of Transfer Arm. Control plug has penetrating paths due to Control and Safety Rod Drive Mechanisms (CSRDM), Diverse Safety Rod Drive Mechanisms (DSRDM), Failed Fuel Location Modules (FFLM), Thermocouples penetrations, and Central Canal Plug.

All the components are very large and are secured with adequate number of bolts, with good redundancy. Hence, no ejection of any component is considered. The leak paths are only due to extension of the bolts. Number of bolts is large (~150). Even if 1 or 2 bolts are not secured properly, the effect is negligible on sodium release. Rupture of pipe lines was not postulated as the lines are designed for static equivalent of dynamic pressure under CDA. Accordingly, no leakage was expected through the sodium fill and drain lines, sodium purification lines, and argon feed and outlet lines. However, it may be highlighted that any possible leaks through the sodium purification lines and the argon feed and outlet lines would reach the respective cells and not the RCB. Also, the sodium flow through these lines would be small owing to the short time duration of the phenomenon (~1 s) and longer lengths of these lines. The sodium leaks through thermocouple penetrations and central canal plug are expected to be very small since they are provided with tight fits.

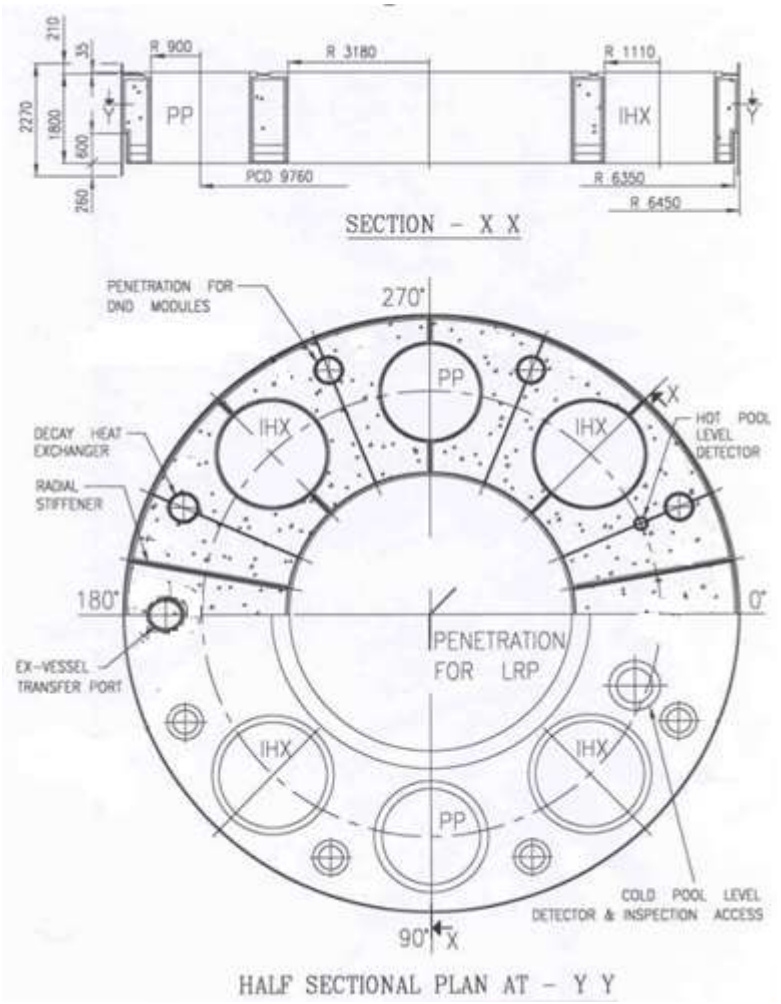

FIG. 7. Schematic (in mm) of reactor top shield

The geometric details of leak area, leak path length, leak path diameter, and sodium mass in the leak path is given in TABLE 9.

TABLE 9. GEOMETRICAL DETAILS OF THE PENETRATIONS USED FOR THE SODIUM LEAK CALCULATIONS (L & D IN M, A IN M^2, M IN KG)

Penetration		**RS-LRP**	**LRP-SRP**	**RS-IHX/PUMP**	**SRP-CP**	**RS-DHX**
Section - 1	A1	0.4995	0.2652	0.1382	0.1426	0.0179
	L1	1.840	1.835	1.800	1.800	1.800
	D1	0.05	0.04	0.040	0.040	0.020
	M1	772.05	408.8	207.00	213.60	26.82
Section - 2	A2	0.1006	0.0667	3.58E-3	7.38E-3	1.0E-3
	L2	0.690	0.580	0.060	0.060	0.060

	D2	0.010	0.010	0.001	0.002	0.001
	M2	71.55	45.23	0.1788	0.3685	0.0502
Section - 3	A3	0.0211	0.0143	-	-	-
	L3	0.165	0.145	-	-	-
	D3	0.002	0.002	-	-	-
	M3	2.92	1.741	-	-	-
Section-4	A4	0.105	-	-	-	-
	L4	0.160	-	-	-	-
	D4	0.010	-	-	-	-
	M4	14.28	-	-	-	-

A is the cross-sectional flow area, L is the path length, D is the hydraulic diameter which is twice the gap width, and M is the mass of sodium in the section.

The geometrical detail of each penetration is given in FIG. 8 to FIG. 12. The major leakage paths RS-LRP and LRP-SRP consist of two branches, as can be seen in FIG. 8 and FIG. 9. The first is below the hold down ring while the second is through the support ring, bearing support ring, and bearing. The schematic of leak paths in other components mounted over the roof slab are shown in FIG. 12.

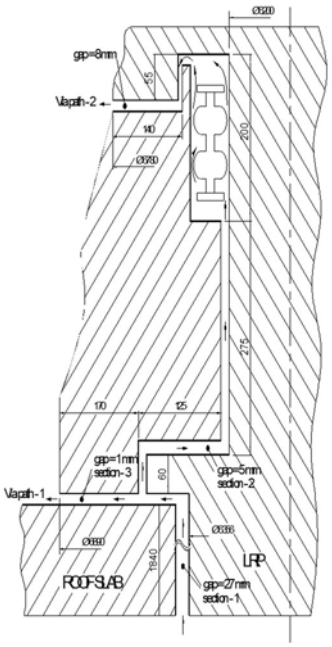

FIG. 8. Schematics of LRP roof slab.

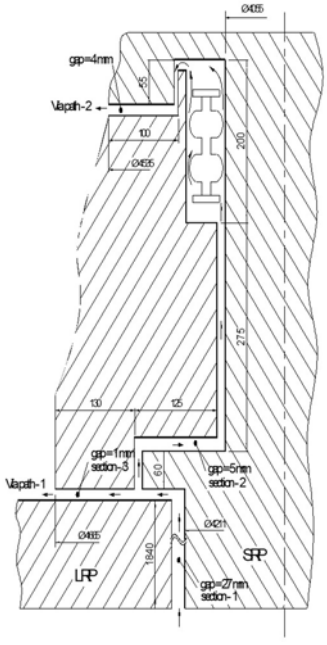

FIG. 9. schematics of the SRP-LRP.

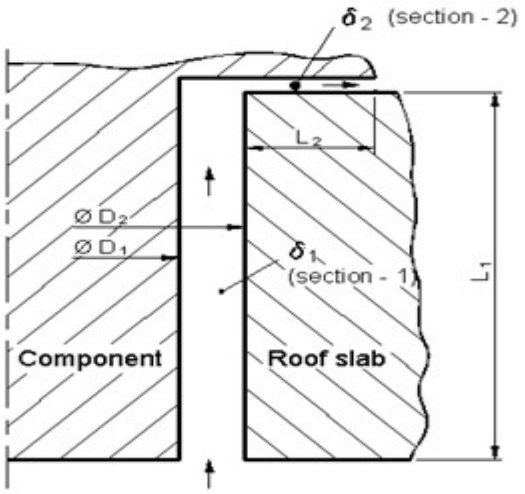

FIG. 10. Schematic of leak paths in other components mounted over roof slab.

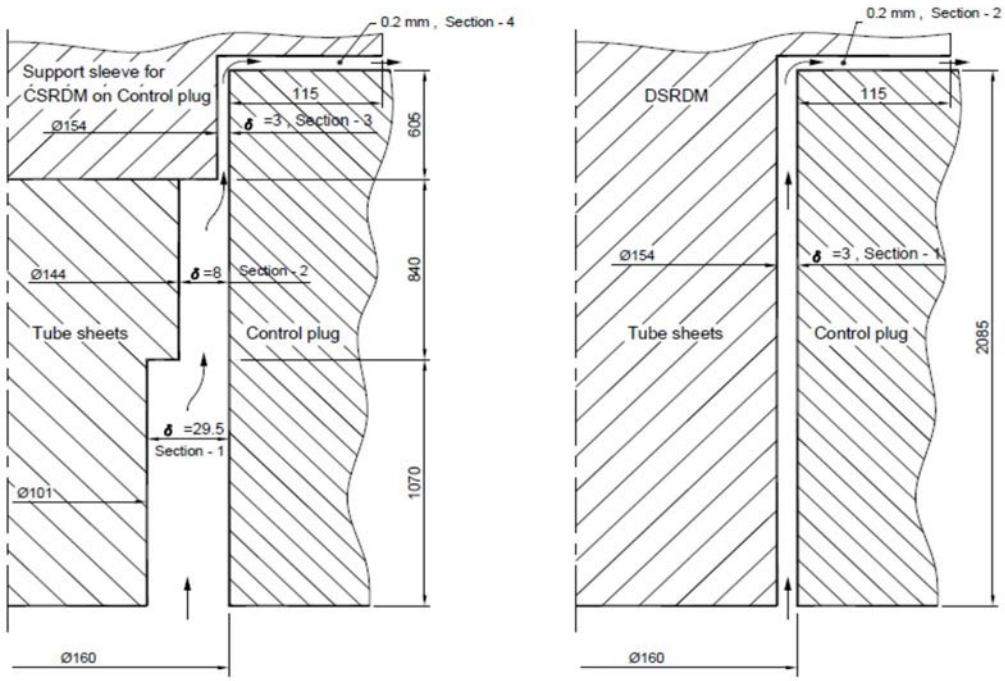

FIG. 11. Schematic of control plug – absorber rod drive path leaks.

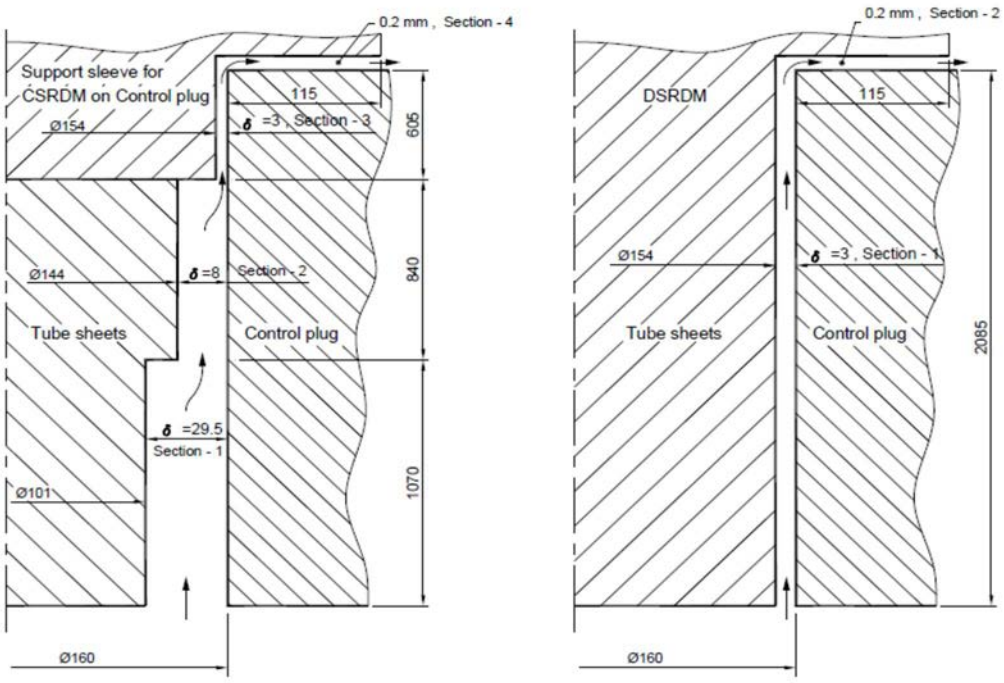

FIG. 12. Schematic of control plug – absorber rod drive path leaks.

TABLE 10. DIMENSION INFORMATION OF THE ANNULAR LEAK PATHS THROUGH THE TOP SHEILD

Annular Path	D_1 (m)	D_2 (m)	δ_1 (m)	L_1 (m)	L_2 (m)	δ_2 (mm)
RS-IHX	2.18	2.2	0.02	1.8	0.06	0.5
RS-PUMP	2.18	2.2	0.02	1.8	0.06	0.5
RS-DHX	0.56	0.58	0.01	1.8	0.06	0.5
RS-Fuel Transfer Port	0.56	0.58	0.01	1.8	0.14	0.5
RS- Hot Pool Level Detector	0.18	0.2	0.01	1.8	0.12	0.5
RS-Cold Pool Level Detector	0.68	0.7	0.01	1.8	0.15	0.5
RS-DND	0.33	0.35	0.01	1.8	0.14	0.5
RS-Fuel Transfer Machine Bottom Flange	0.56	0.58	0.01	1.8	0.14	0.5

2.2.5. Containment

Containment dimension:

- Net free volume = 74 000 m3
- Effective height = 54 m
- RCB wall and ceiling thickness = 1 m
- RCB wall and ceiling material = concrete

Enclosure dimensions:

- Diameter = 14 m

— Height = 4 m
— Side wall or liner thickness = 30 mm
— Side wall or liner material = carbon steel
— Top ceiling or liner thickness = 30 mm
— Top ceiling or liner material = carbon steel
— Floor area =150 m^2 [forming the sodium pool]
— Vent area total = 5 m^2
— Top vent area = 3.5 m^2
— Side vent area = 1.5 m^2
— Elevation of side vent area = 2 m [from the roof slab]

Enclosure (reactor vault) and cells location:

— Enclosure (Reactor Vault) centre distance from ‘left’ wall = 17.5 m
— Enclosure (Reactor Vault) centre distance from 'bottom' wall = 12.5 m
— Cells distance from 'top' wall = 11 m
— Cells distance from 'right' wall = 4 m
— Cells width = 18 m
— Cells depth = 7 m
— Cells height = 22 m [from the 18 m height]

Enclosure/roof slab compositions [from top to bottom]:

— Carbon steel = 30 mm
— Air gap = 100 mm
— Carbon steel = 20 mm
— Concrete = 1200 mm [or 1.2 m]
— Air gap = 400 mm
— Carbon steel = 30 mm

Ventilation conditions:

— Flow rate =100 000 m^3/hr
— Elevation of inlet = 49.5 m
— Elevation of exhaust = 49.5 m (opposite to Inlet)
— Inlet vent area= 1.53 m^2
— Exhaust vent area= 1.53 m^2
— Isolation time = 10 seconds

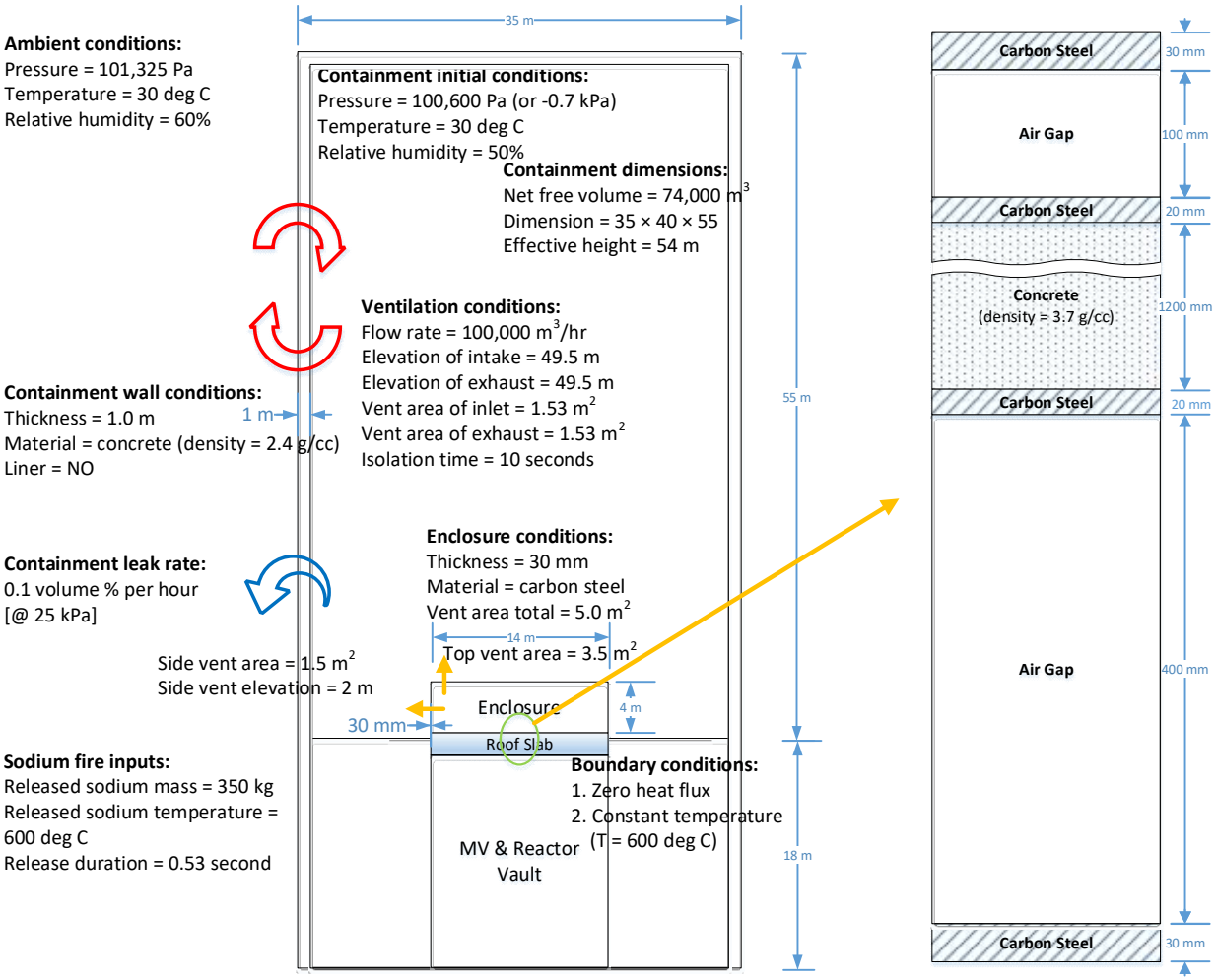

FIG. 13. Side view of the reactor containment building and details of enclosure/ roof slab section.

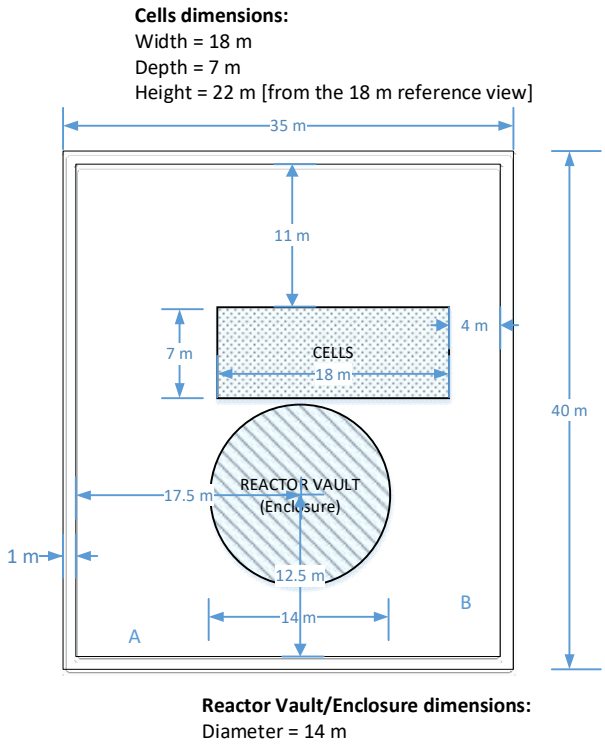

FIG. 14. Top view of reactor containment building at 18m height.

2.3. ACCIDENT SEQUENCE TO BE CONSIDERED

The accident sequence considered was an Unprotected Loss of Flow Accident (ULOFA). This event is assumed to result in a core damage event with release of radionuclides into the primary coolant and cover gas.

An Unprotected Loss of Flow Accident (ULOFA) is the typical scenario to be analysed for determining the bubble fraction, pressure, and temperature evolution. A ULOFA transient is initiated due to loss of primary coolant flow resulting from loss of power to both the primary pumps and the failure to shut down the reactor. This leads to coolant temperature rise but there is an initial decrease in power and fuel temperature due to negative core expansion feedback. However, since the power to flow ratio is high, eventually this event results in coolant temperature rise and voiding in the upper part of the highly rated channel. As a void spreads radially outward and axially inward towards the core centre, large positive reactivity is introduced. It leads to power excursion and finally to clad dry out then rapid increase in clad and fuel temperatures, resulting in clad and fuel melting. At this stage, molten fuel is likely swept out of the core by shearing force of the coolant and clad vapours for fresh fuel and in addition by fission gas pressure for irradiated fuel. Due to inherent uncertainties in modelling this phase, a conservative approach was followed for energy release calculation. Once one third part of the fissile zone is molten, fuel slumping is initiated as follows. The middle one third core slumps and occupies the bottom one third coolant. The top one third slumps and occupies the middle one third. The transient moves to the disassembly phase when the peak fuel temperature reaches boiling point. The analysis is continued in the disassembly phase till reactor becomes subcritical. The CDA parameters are consolidated and given in TABLE 11.

TABLE 11. CDA PARAMETERS

No.	Parameter	Value
1	Reactor Thermal Power	1250 MW
2	Fuel Melting Point	2750 °C
3	Fuel Boiling Point	3387 °C
4	Clad Melting Point	1427 °C
5	Clad Boiling Point	2750 °C
6	Total Core Volume	$3m^3$
7	Transient + Disassembly Phase	80s+11ms
8	Peak Temp.	4945 °C
9	Peak Pressure	9.7 MPa
10	Thermal Energy Released	5000MJ (100MJ, Mech. Work)
11	Liquid Fraction	54 %
12	Vapor Fraction	40 %
13	Peak cover gas pressure	1.6 MPa
14	Quasi static pressure of core bubble	0.2 MPa

2.3.1. Core temperature and pressure distribution after CDA

Core temperatures and pressure distribution values after CDA are given in TABLE 12.

TABLE 12. CORE FUEL TEMPERATURE AND VOLUME FOR MESHES WHICH ARE ABOVE MELTING POINT AT THE END OF DISASSEMBLY PHASE (T IN KELVIN AND V IN CM^3) – 100 MJ CASE

T = 3433 V = 1605	3353 48176	3228 38605	3033 48302	3213 48311	3027 67623	
T = 4693 **V = 1552**	**3661** **46957**	3543 38132	3451 48076	3560 48106	3154 67401	3026 38635
T = 5047 **V = 1619**	**4639** **47416**	**3780** **37656**	**3666** **47495**	**3798** **47930**	3495 66796	3030 38610
T = 5219 **V = 988**	**4892** **38563**	**3946** **38601**	**3821** **47592**	**3968** **49728**	**3666** **67224**	3033 38549
T = 5217 **V = 1572**	**4873** **34913**	**4041** **33070**	**3904** **47926**	**4062** **51423**	**3705** **66937**	3057 38414
T = 4889 **V = 4824**	**4228** **71536**	**4050** **41744**	**3911** **47340**	**4068** **51120**	3604 67141	3032 38243
T = 4232 **V = 6189**	**4132** **75731**	**3973** **38497**	**3727** **47385**	**3975** **50257**	3401 67455	3030 38155

T = 4043 **V = 4392**	**3884** **54746**	3631 34018	3409 47521	3631 49280	3104 67086	3025 38155
T =3488 V =2543	3366 38960	3158 32727	3032 47931	3143 48835	3027 67092	
T =3030 V =1224	3029 38269	3026 38013	3023 47828	3025 48277		

Total Volume =2.74 m^{3i}

TABLE 13. CORE FUEL PRESSURE FOR MESHES AT THE END OF DISASSEMBLY PHASE (IN ATM) – 100 MJ CASE

9.46	**8.04**	0.23	0.05	0.10	0.03	0.00
31.53	**17.95**	**2.33**	0.41	0.64	0.08	0.03
69.58	**27.51**	**4.81**	**1.12**	**1.82**	0.48	0.04
97.47	**50.12**	**5.20**	**2.11**	**3.54**	**1.04**	0.06
97.16	**48.01**	**5.82**	**2.90**	**4.95**	**1.24**	0.07
49.77	**31.51**	**7.17**	**2.89**	**5.05**	0.84	0.05
19.20	**15.30**	**3.64**	**1.51**	**3.61**	0.34	0.03
4.66	**3.32**	**1.08**	0.48	0.89	0.10	0.03
0.57	0.60	0.11	0.05	0.06	0.03	0.00
0.03	0.04	0.03	0.03	0.03	0.00	0.00

2.3.2. Temperature and pressure time history

FIG. 15 gives the pressure in the core bubble and in the cover, gas following the CDA. FIG.16 presents the evolution of hot pool temperature after CDA assuming DHR is functional, with a maximum capacity of 24 MW(th).

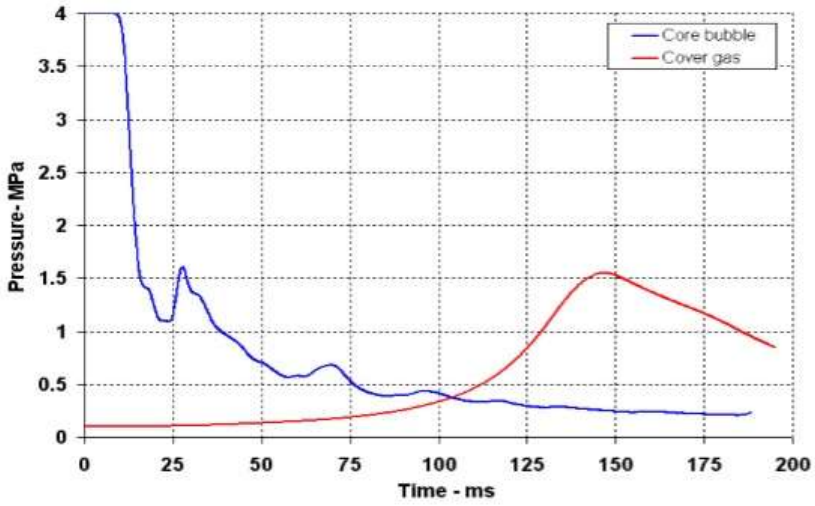

FIG. 15. Evolution of core bubble and cover gas pressure during the disassembly phase.

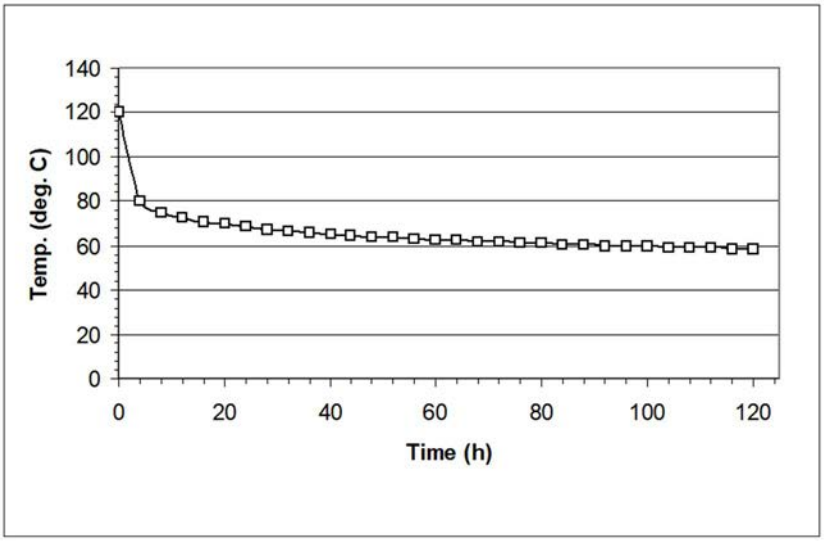

FIG.16. Evolution of hot pool temperature following a CDA.

2.3.3. In-containment release fractions and sodium ejection rates

In-containment release fractions and sodium release fractions for the standalone calculation (decoupled case) are given in TABLE 9 and TABLE 10.

TABLE 14. IN-CONTAINMENT RELEASE FRACTIONS

Group	Elements	Designated release fractions
Noble Gases	Xe, Kr	1
Halogen	I, Br	0.1
Alkali metals	Cs, Rb	0.1
Tellurium group	Te, Sb, Se	1.0E-04
Barium	Ba, Sr	0.1
Noble metals	Ru, Rh, Pd, Mo, Tc, Co	1.0E-04

Lanthanides	La, Zr, Nd, Eu, Nb, Pm, Pr, Sm, Y, Cm, Am	1.0E-04
Cerium	Ce, Pu, Np	1.0E-04

TABLE 15. SODIUM EJECTION RATE (FOR THE INPUT OF WP-3)

Time, (s)	**Mass flow rate, (kg/sec)**	**Released sodium, (kg)**
0.00000E+00	4.07936E+00	4.07936E-02
1.00000E-02	5.74394E+02	5.78473E+00
2.00000E-02	7.05970E+02	1.28444E+01
3.00000E-02	8.05702E+02	2.09015E+01
4.00000E-02	8.84402E+02	2.97455E+01
5.00000E-02	9.44102E+02	3.91865E+01
6.00000E-02	9.87338E+02	4.90599E+01
7.00000E-02	1.01671E+03	5.92270E+01
8.00000E-02	1.03493E+03	6.95763E+01
9.00000E-02	1.04421E+03	8.00184E+01
1.00000E-01	1.04636E+03	9.04820E+01
1.10000E-01	1.04302E+03	1.00912E+02
1.20000E-01	1.03561E+03	1.11268E+02
1.30000E-01	1.02505E+03	1.21519E+02
1.40000E-01	1.01201E+03	1.31639E+02
1.50000E-01	9.97142E+02	1.41610E+02
1.60000E-01	9.80762E+02	1.51418E+02
1.70000E-01	9.63312E+02	1.61051E+02
1.80000E-01	9.44962E+02	1.70501E+02
1.90000E-01	9.25894E+02	1.79760E+02
2.00000E-01	9.06232E+02	1.88822E+02
2.10000E-01	8.86210E+02	1.97684E+02
2.20000E-01	8.65570E+02	2.06340E+02
2.30000E-01	8.44660E+02	2.14786E+02
2.40000E-01	8.23492E+02	2.23021E+02
2.50000E-01	8.01940E+02	2.31041E+02
2.60000E-01	7.80140E+02	2.38842E+02
2.70000E-01	7.58016E+02	2.46422E+02
2.80000E-01	7.35574E+02	2.53778E+02
2.90000E-01	7.12784E+02	2.60906E+02
3.00000E-01	6.89672E+02	2.67802E+02
3.10000E-01	6.66286E+02	2.74465E+02
3.20000E-01	6.42574E+02	2.80891E+02
3.30000E-01	6.18418E+02	2.87075E+02
3.40000E-01	5.93844E+02	2.93014E+02
3.50000E-01	5.68728E+02	2.98701E+02
3.60000E-01	5.43224E+02	3.04133E+02
3.70000E-01	5.17112E+02	3.09304E+02

3.80000E-01	4.90312E+02	3.14207E+02
3.90000E-01	4.62882E+02	3.18836E+02
4.00000E-01	4.34644E+02	3.23183E+02
4.10000E-01	4.05470E+02	3.27237E+02
4.20000E-01	3.75234E+02	3.30990E+02
4.30000E-01	3.43771E+02	3.34427E+02
4.40000E-01	3.10630E+02	3.37534E+02
4.50000E-01	2.75529E+02	3.40289E+02
4.60000E-01	2.37514E+02	3.42664E+02
4.70000E-01	1.95783E+02	3.44622E+02
4.80000E-01	1.71624E+02	3.46338E+02
4.90000E-01	1.45650E+02	3.47795E+02
5.00000E-01	1.14212E+02	3.48937E+02
5.10000E-01	8.09480E+01	3.49746E+02
5.20000E-01	4.54620E+01	3.50201E+02
5.30000E-01	6.75700E+00	3.50269E+02

2.4. WORK PACKAGES

WP-1 of the CRP dealt with the calculations for in-vessel source term in case of the core disruptive accident (CDA). The source term depends on the accident sequences and the accidents considered are different in LWR and SFR.) In SFRs, for design extension conditions (DECs), two major groups of accidents merit special attention: failure to reduce power or shut down the reactor following an off-normal initiating event, and inability to remove heat from the core. Among other, ULOF and UTOP are considered as initiation events that can lead to the CDA. Refuel operates at higher temperature and higher burnups and the chemical forms of fission products are different due to fuel types and coolant.

The primary system/containment system interface source term (WP-2) is also defined by two components: One being the release of fission products and fuel from the primary system directly into the Reactor Containment Building (RCB), and the other one being the long-term leakage from the argon cover gas system into the containment system. The first component should also include the associated mass of primary sodium instantaneously ejected through the leak path of the vessel head into the RCB.

WP-3 dealt with the ‘In-containment phenomena’ after the postulated CDA which included aerosol mass evolution e.g. agglomeration, wall plating, gravitational sedimentation etc. in the containment.

Required inputs for the respective work packages are provided in section 3.

3. DESCRIPTION OF THE CRP WORK PACKAGES

3.1. WORK PACKAGE 1: IN-VESSEL SOURCE TERM ESTIMATION

3.1.1. Description

Participants in this work package calculated the in-vessel source term in case of CDA. Source term depends on the accident sequences and the accidents considered are different in LWR and SFR. Typical LWR source term analysis considers LOCA, while FBR considers ULOF, UTOP accidents. FBR fuel operates at higher temperature and higher burnups than LWR fuels and the chemical forms of fission products are different due to fuel types and coolant.

The in-vessel source term challenge is to determine the partitioning of the radionuclides (RNs) in fuel debris, coolant, and cover gas. The in-vessel source term estimation is a difficult problem as the accident evolution itself can follow many diverse paths. Though advanced code systems can predict the evolution with good degree of confidence, there is still considerable uncertainty imposed by accident initial conditions. The release of RNs from the fuel is controlled by their diffusion characteristics, chemical reactions between RNs, and coolant thermal hydraulic characteristics for aerosol bubble transport in the pool to name a few phenomena. Many of the various possible phenomena and mechanisms are illustrated in FIG. 17.

The mechanistic modelling of in-vessel source term considering all phenomenon is a numerically challenging task. For this analysis, whole melt accident initiated by loss of flow to coolant pumps with failure of both the shutdown systems (ULOFA) is considered.

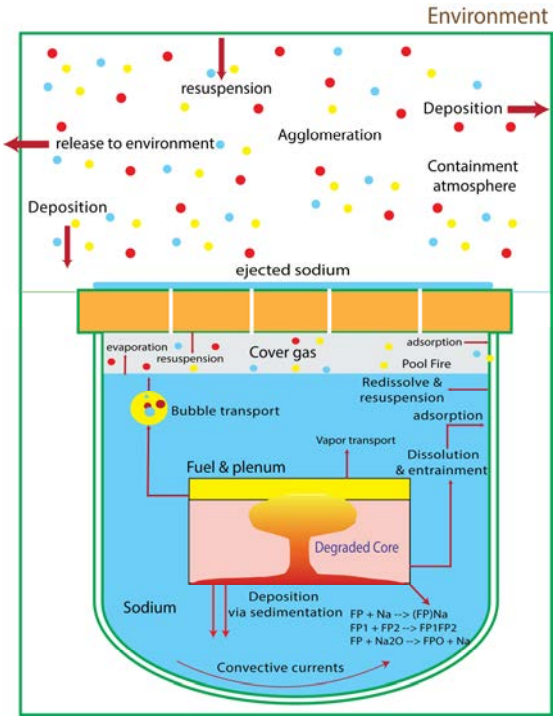

FIG. 17. Various release phenomenon in the reactor vessel (not to scale).

3.1.2. Outputs

For participants who independently simulated the CDA, the following parameters were requested to be reported:

— Onset of sodium boiling, s
— Onset of cladding melting, s
— Time of cladding rupture, s
— Start of fuel melting, s
— Start of clad boiling, s
— Start of fuel boiling, s

It was requested for the data to be represented in table format. In the table the time of the first fuel rod melting, cladding, and fuel boiling should be specified. Also, the corresponding data should be represented in tables for each zone into which the core is subdivided in the nodalization scheme.

The following mass and fraction changes as a function of time should be given (0s – beginning of ULOF):

— Sodium vapor mass, kg
— Fuel vapor mass, kg
— Cladding vapor mass, kg
— Liquid fuel fraction, %
— Vapor fuel fraction, %
— Liquid clad fraction, %
— Vapor clad fraction, %

The total masses and fractions should be specified. The data should be represented in figures.

Radionuclide isotopic fraction (of initial inventory) as a function of time in:

— Debris – molten fuel fragments;
— Coolant;
— Cover gas;
— Surface deposits (with internal components);
— for all isotopes or elements listed in Section 2.

3.2. WORK PACKAGE 2: PRIMARY SYSTEM/CONTAINMENT SYSTEM INTERFACE SOURCE TERM ESTIMATION

3.2.1. Description

Participants in this work package calculated the interface source term. The outputs from the WP-1 on the sodium and cover gas pressure transients are used as input to determine the quantity of sodium and cover gas released into the containment as a function of time. In addition, the partition of the RN in the sodium and cover from WP-1 were utilized to arrive at the source term input to the containment.

The primary system/containment system interface source term is also defined by two components: One being the release of fission products and fuel from the primary system directly into the Reactor Containment Building (RCB), and the other one being the long-term leakage from the argon cover gas system into the containment system. The first component should also include the associated mass of primary sodium instantaneously ejected through the leak path of the vessel head into the RCB.

WP includes two cases:

— Case 2.1: Energetic case instantaneous calculations – short term (24h)
— Case 2.2: Energetic case instantaneous + long term calculations (168h, 720h)

3.2.2. Additional Inputs

— Pressure from core bubble vs time
— Cover gas pressure vs time
— 100% FPNG, 1 % volatile 0.01% other-
— Point of sodium ejection
— FP inventory in Na and CG before sodium ejection
— FP inventory after sodium ejection

3.2.3. Geometry of sodium leak paths in the roof slab

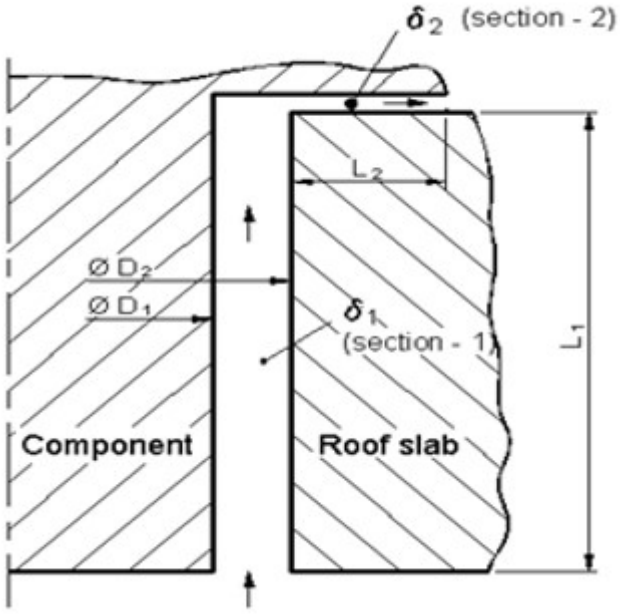

FIG. 18. Dimensions of sodium leak paths in the roof slab.

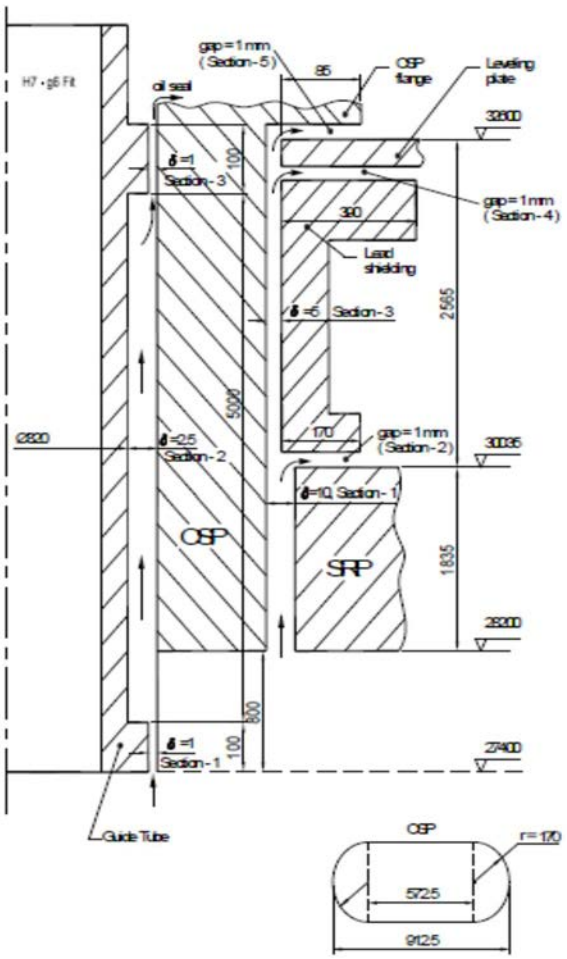

FIG. 19. Schematic of SRP- fuel handling machine leak paths.

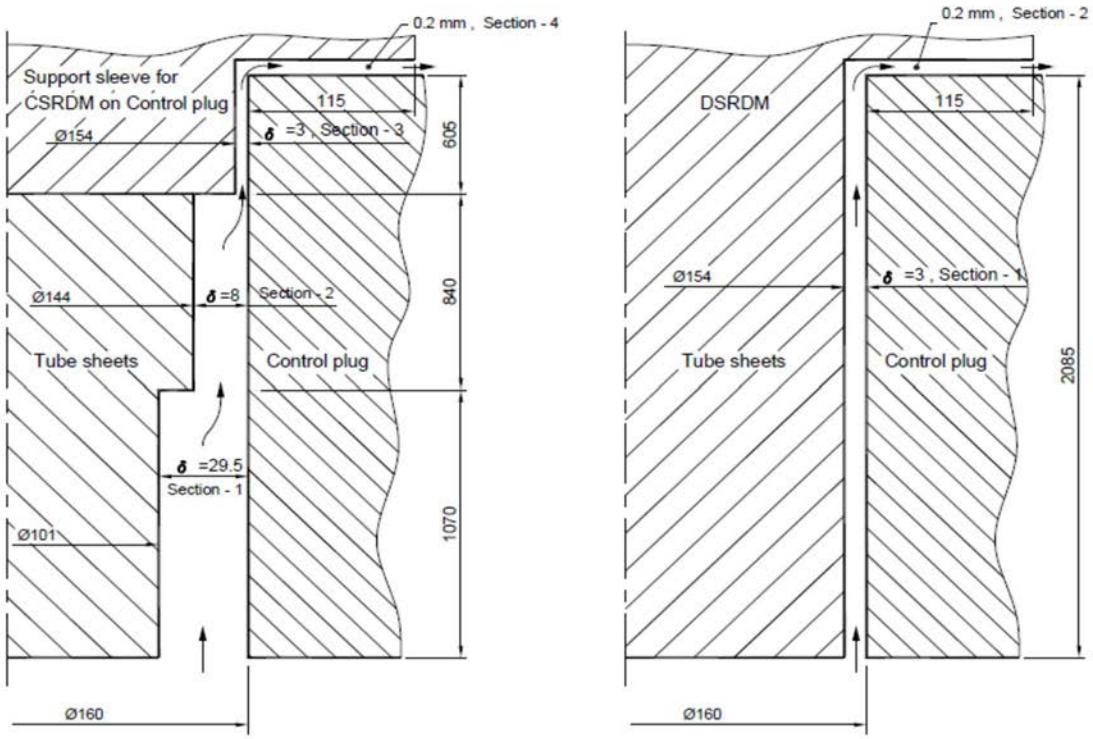

FIG. 20. Schematic of control plug – absorber rod drive path leaks.

The evolution of hot pool temperature following a CDA is depicted in FIG. 21. In FIG. 22 and FIG. 23, the temperature and pressure evolution within RCB is plotted. There are two curves in each of Fig and FIG. 23, which study the sensitivity of RCB air to wall heat transfer coefficient (h_w).

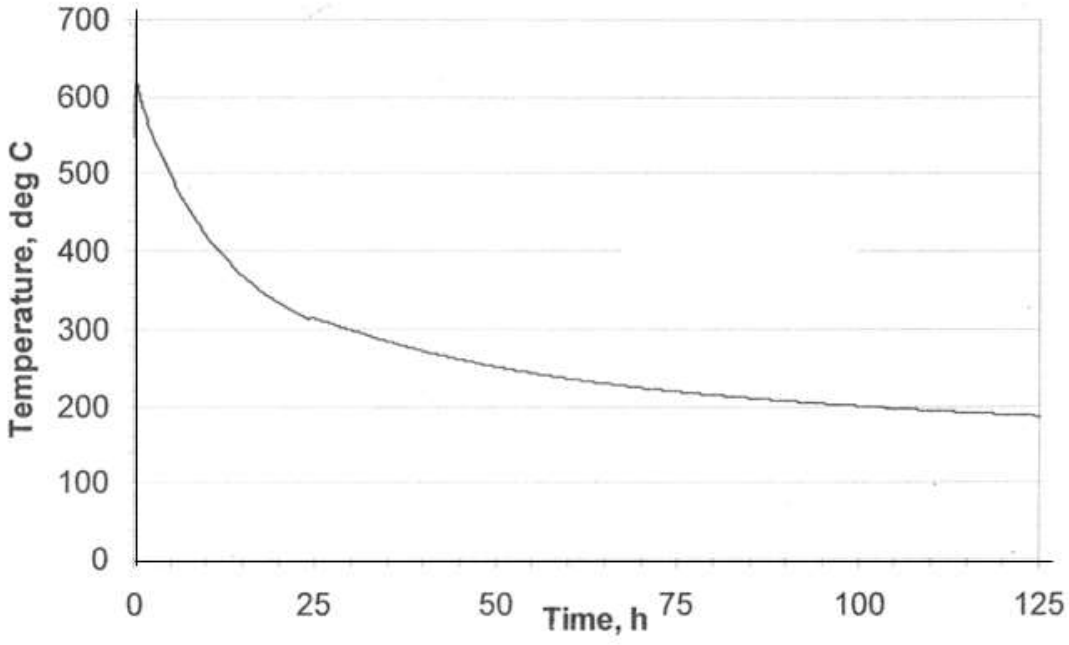

FIG. 21. Evolution of hot pool temperature following a CDA.

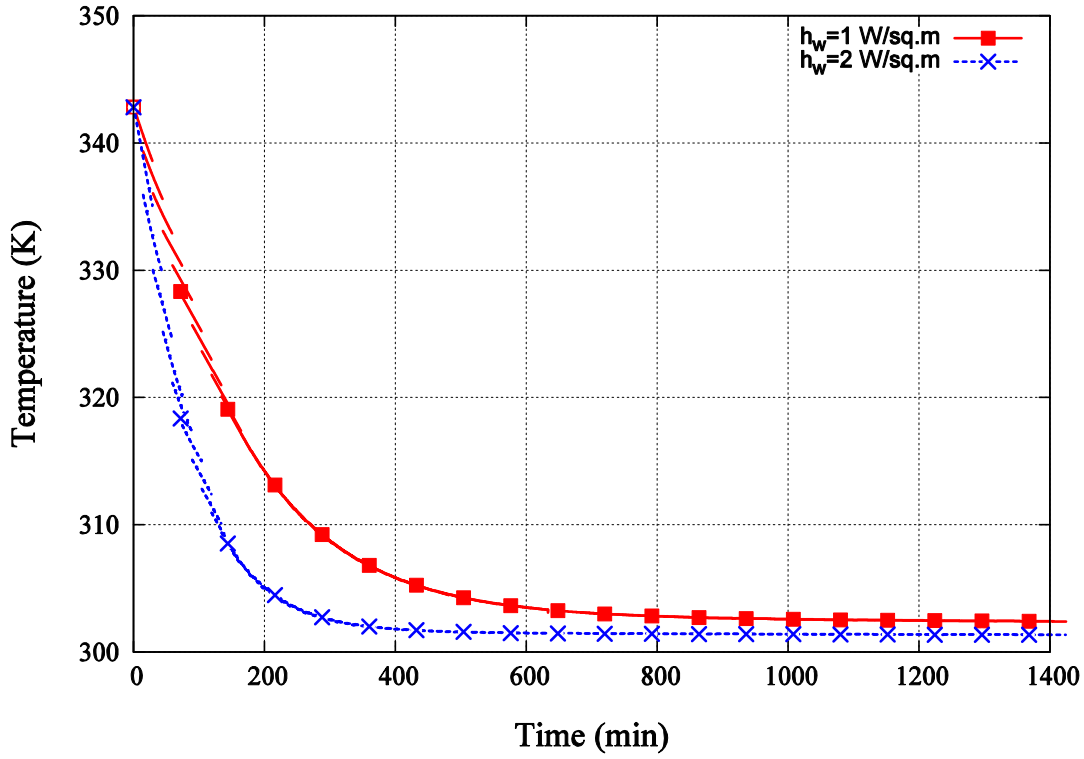

FIG. 22. Evolution of RCB Gas temperature due to instantaneous sodium fire.

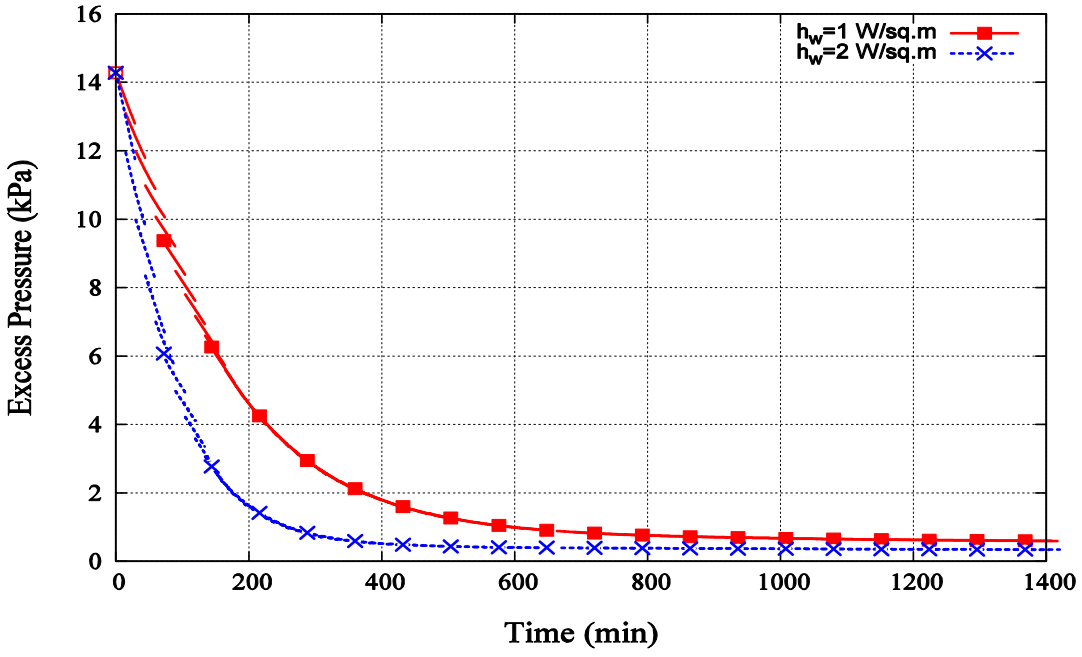

FIG. 23. Evolution of RCB Gas pressure due to instantaneous sodium fire.

3.2.4. **Outputs**

— Na leak mass flow rate and its temperature vs. time – short term due to CDA pressure
— Cover gas leak rate and its temperature vs. time - short term due to CDA pressure
— Concentration of fission products in the ejected Na and cover gas vs. time – short term

— Long term Na aerosol and FP flow rate into RCB - Long term

3.3. WORK PACKAGE 3: IN-CONTAINMENT PHENOMENOLOGY ANALYSIS

3.3.1. Description

WP-3 participants modeled and simulated the 'in-containment phenomena' after the ejection of sodium and radionuclides following the CDA. The phenomena modelled includes sodium chemical reactions, aerosol generation, and aerosol mass evolution (e.g., agglomeration, wall plating, gravitational sedimentation etc.) in the containment. The inputs such as the geometry of containment, boundary conditions, ventilation, and leak rates are given in section 2.2.5 and additional inputs are given below.

3.3.2. Additional Inputs

3.3.2.1. *Initial and Boundary Conditions*

The details on the initial and boundary conditions are described in section 2.

Containment initial conditions:

— Pressure = 100600 Pa (or -0.7kPa)
— Temperature = 30°C
— Relative humidity = 50%

Ambient conditions:

— Pressure = 101325 Pa (or 1 atm)
— Temperature = 30°C
— Relative humidity = 60%

3.3.2.2. *Enclosure/roof slab boundary conditions*

Two boundary conditions are available for participants depending on their preferences.

— Zero heat flux or insulated boundary
— Constant temperature of the cover gas region vapor temperature, i.e., T = 600°C

3.3.2.3. *Sodium fire inputs*

The ejected sodium during the postulated accident is an input to WP-3.

— Released sodium mass = 350 kg
— Released sodium temperature = 600°C
— Release duration = 0.53 second

3.3.3. Outputs

3.3.3.1. *Calculation Options*

The following calculation options used by the CRP participants:

— Case 1: sodium spray fire [no enclosure, no containment leakage]
— Case 2: sodium pool fire [enclosure, containment leakage]

3.3.3.2. *Output parameters and units*

Following outputs were requested to be calculated:

— Containment pressure (Pa)
— Containment temperature (K)
— Enclosure pressure (Pa) [Case 2 only]
— Enclosure temperature (K) [Case 2 only]
— Sodium burn mass rate (kg/s)
— Sodium burn energy release rate (J/s)
— Suspended radionuclide elemental mass in containment (kg)
— Suspended radionuclide isotope mass in containment (kg)
— Suspended radionuclide isotope activity in containment (Bq)
— Suspended total aerosol mass in containment (kg)
— Deposited radionuclide elemental mass in containment (kg)
— Deposited radionuclide isotopic mass in containment (kg)
— Deposited radionuclide isotopic activity in containment (Bq)
— Deposited total aerosol mass in containment (kg)
— Noble gas elemental mass in containment (kg)
— Noble gas isotope mass in containment (kg)
— Noble gas isotope activity in containment (Bq)

4. WP-1 MODELS, SIMULATIONS AND RESULTS

4.1. SIMULATION EXERCISE USING MINICHEM CODE (IGCAR, INDIA)

4.1.1. Description of the Methods and Model

The in-vessel source term was determined using a thermo-chemical approach and the release fractions of RN to the cover gas was estimated from the vapour fractions. This is a step towards mechanistic model development for oxide fuelled SFRs. Chemical equilibrium calculations were performed with no mixture, ideal, and real mixture cases. The estimated equilibrium species mole numbers for the no-mixture assumption would yield the respective vapour pressures at specified temperature. This assumption leads to conservative estimates, whereas ideal mixture case follows Raoult's law. In the real mixture case, mixing excess functions are utilized to obtain the results for the non-ideal behaviour (to account for any deviations from the Raoult's law). With the help of the equilibrium species distribution, partition of RN in the three phases (solid, liquid, and gas) can be determined. From the mass fraction in the gas phase, release fractions of RNs to the cover gas are evaluated. The determination of the species distribution from the chemical equilibrium approach is described in the following sections.

4.1.1.1. *Thermo-chemical equilibrium from free energy minimization*

The problem of determining the equilibrium species concentration for a given set of input elements can be formulated either in terms of entropy, Gibbs or Helmholtz function. For multi-phase system with $(x_1, x_2, \dots, x_{N_g}, \dots, x_{N_g+N_s})$ mole numbers for $(N_g + N_s)$ species with N_e elements, the Helmholtz function to be minimized is as follows:

$$\begin{aligned} A_{system} &= G - PV \\ &= \sum_{i=1}^{N_s+N_g} \mu_i x_i - PV \end{aligned} \tag{3}$$

Where G is the Gibbs function. Dividing the equation by RT,

$$\tilde{A}(T,V) = \frac{A_{system}}{RT} = \sum_{i=1}^{N_s+N_g} \tilde{\mu}_i x_i - \overline{x^g} \tag{4}$$

where,

$\overline{x^g}$ is the total number of the moles of the gas present in the system;

$\tilde{\mu}_i$ can be given in terms of their standard chemical potential function as,

$$\tilde{\mu}_i = \begin{cases} (\tilde{\mu}^o)_i^g + \ln\dfrac{RT}{V} + ln\, x_i^g \;\; for\; i = 1,2,\dots,N_g \\ (\tilde{\mu}^o)_i^c \; for\; i = 1,2\dots,N_s \end{cases} \tag{5}$$

The superscript 'g' and 'c' are used for the gaseous and condensed species. The N_s is the total number of the condensed species and N_g is the total number of the species in the gaseous phase. The above formulation considers one condensed phase (solid + liquid as no-mixture) denoted

by ‘c’ and one gas phase (as ideal mixture). If a condensed phase real or ideal mixture has to be treated one more term similar to gas phase has to be added to Eq. (5). The above cost function is minimised with non-negativity and mass constraint. The mass constraint can be given as follows.

$$\sum_{i=1}^{N_g} a_{ij}^{g} x_i^{g} + \sum_{i=1}^{N_s} a_{ij}^{c}\, x_i^{c} = b_j \quad for\ j = 1,2,3, \ldots N_e \tag{6}$$

where,

a_{ij}^{g} is the number of atoms of j^{th}element in the species ‘i’ in the gas phase;

a_{ij}^{c} is the number of atoms of j^{th} element in the i^{th} species with condensed phase;

b_j is the total number of moles of element j, originally present in system mixture.

The above free energy functions are minimized with the quadratic gradient descent method. The detailed formulation for the Helmholtz free energy minimization using quadratic gradient descent method is given in [2].

The present analysis is performed for the no-mixture and real mixture cases. Excess functions for few species are given in TABLE 16 compiled from Schram et al. [3]. These excess functions are dependent on the temperature and the mole fraction of the component of the element. Since, the compiled solubility database is limited in the literature, the experiments are planned to extend such a database.

TABLE 16. THERMODYNAMIC EXCESS FUNCTIONS FOR VARIOUS SPECIES

Species	**Excess functions (kJ × mol^{-1})**	**Temperature range (K)**
NaI	$59.4 - 0.025T$	930-1230
NaI*	$62 - 0.0024T$	923-1103
NaI*	$64.1 - 0.0298T$	623-1073
NaBr	$57.3 - 0.025T$	1020-1230
Cs	$8.45 - 0.00063T$	>371
Cs (diluted)	$7.84 + 0.00096T$	>371
Rb	7.206-0.00079T	>371
Rb(diluted)	$7.52 + 0.0282 \times 10^{-3}$	>371
Sr	8.352	1002
Ba(diluted)	2.113	1002
Sb	56.2-0.0156T	463-823
Te	$24.5 - 23.92 \times 10^{-3}\, T$	-
UO_2	$115.05 - \frac{0.05071}{T}$	848-1083
PuO_2	$209.63 - \frac{0.02628}{T}$	848-1083
Ce_2O_3	$-12.597 + \frac{186.93}{T}$	-

*Different correlations correspond to different sources of data

4.1.1.2. *Code structure*

The program to calculate the free energy minimisation is developed in Python. The code system consists of modular structure that can be easily integrated into future source term code builds.

The detailed flow chart of the code structure is given in FIG. 24. The code is divided into seven modules. Each module is described as below:

PyMakelib: This module reads the NASA's CEA [4] thermo-chemical database file. The data is further extrapolated for higher temperature. This extrapolated data is saved in a suitable format. The module is a Python translation from original Fortran makelib module (available in CEA code package.)

PyThermoread: This module takes extrapolated thermo-chemical data from PyMakelib and problem specified temperature information as an input. From these inputs, the chemical potentials and stoichiometric information for all species are calculated. These potential for respective species is returned in the form of a dictionary.

Species search: According to the input element inventory specified, this module returns the chemical potential of all combination of input element inventory. This module also has an additional option where species can be defined manually.

Stoichiometric coefficient matrix generator: This module generates the stoichiometric coefficient matrix for given elements, condensed species, and gaseous species.

MINI: This module performs constrained Helmholtz or Gibbs function minimization. The MINI module contains two sub-modules, one can minimize the energy function using 'Sequential Least Squares Programming (SLSQP)' and other uses quadratic gradient based minimiser. The MINI module can solve both (T, P) or (T, V) problems for no mixture, ideal mixture, and real mixture cases. In the module the excess chemical potentials are defined as dictionaries.

Release fraction calculation: From the resultant equilibrium species distributed in the condensed and gas phases, the species which are in the gaseous phase are considered to be released in the cover gas. The release fractions are calculated as follows,

$$\text{Elemental release fraction,} \phi_j = \frac{\sum_i Number\ of\ moles\ of\ j^{th}\ element\ in\ i^{th} gaseous\ species}{Total\ mole\ inventory\ of\ j^{th} element} \quad (7)$$

$$\text{Isotopic release fraction } \psi_k = \phi_j \text{ x isotopic fraction of } k^{th} \text{ isotope.} \quad (8)$$

Plotting: The plotting module can plot the Sankey chart for the selected chemical species for better visualisation of chemical interaction between different species. The module can also plot as list of species with given element of interest.

Validation: The code has been validated by intercomparison with other codes such as CEA [4] and published data available in the literature on chemical reactions [3] [4] [5].

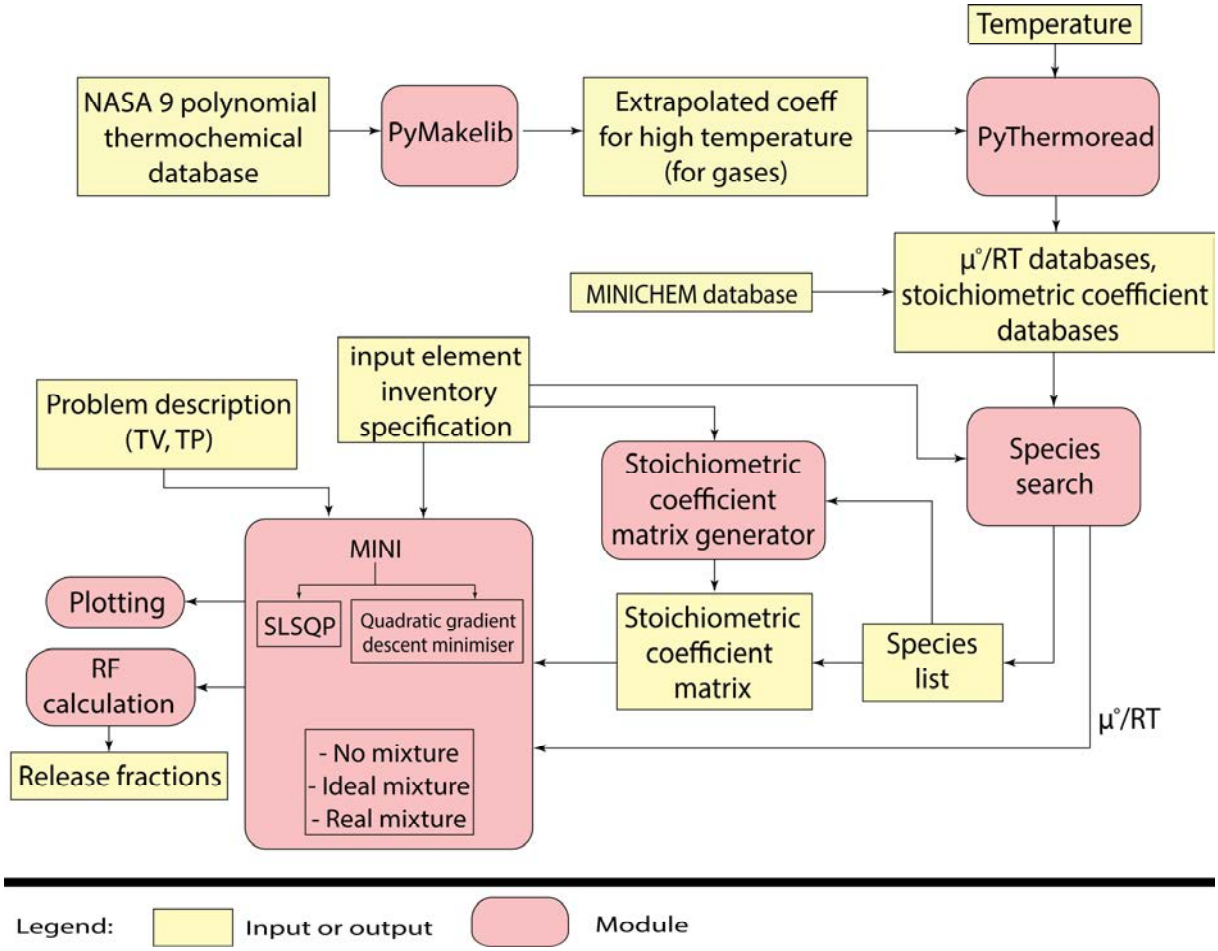

FIG. 24. The structure of MINICHEM code.

Assumption and inputs for the calculation:

For the application of the thermo-chemical equilibrium method to derive the RN partition to the different phases of the in-vessel material, it is assumed that all the fuel and RNs are homogeneously mixed in the sodium pool at uniform temperature. Further, it is assumed that the considered species have reached thermal and chemical equilibrium. For the calculation, among several possible burnups at which the accident may take place, middle of equilibrium core (MOEC) burn up is chosen as discussed and agreed in the RCMs.

The thermo-chemical equilibrium assumption would be valid for the chemical species, if during the whole core melt accident, the fuel temperature would remain more than 873 K for few hours and if the typical time constants of important reactions are much shorter. The uniform temperature assumption is not valid during the energy release and disassembly phases of the accident. However, after the termination of the nuclear excursion thermal equilibrium is reached with a time constant of 0.72 seconds. The homogenous mixing assumption for fuel and radionuclides is justified since, as per deterministic severe accident calculations almost the entire core is in molten phase (>90%). Besides most of the volatile RNs like ‘Cs, I’ are soluble in the sodium. To address the uncertainty in the calculations, the calculations have been repeated at various temperatures of the thermodynamic system.

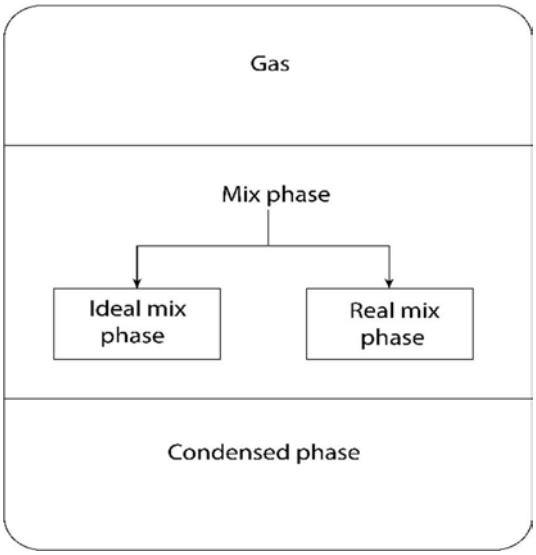

FIG. 25. General thermo-chemical model used in the simulations.

TABLE 17. RADIONUCLIDE INVENTORY IN THE CORE FOR THE MOEC BURN UP AND PEAK BURN UP

Radionuclide	**Half life**	**Activity in Bq for MOEC**	**Activity (Bq) Peak Burnup (100 MWd/t)**
I-131	8.02 d	1.46E+18	1.48E+18
I-132	2.30 h	1.94E+18	1.96E+18
I-133	20.80 h	2.51E+18	2.54E+18
I-134	52.50 m	2.50E+18	2.53E+18
I-135	6.57 h	2.21E+18	2.23E+18
Cs-134	754.50 d	5.19E+16	9.65E+16
Cs-137	30.07 y	4.98E+16	1.00E+17
Rb-88	17.78 m	5.17E+17	5.22E+17
Ru-103	39.26 d	2.22E+18	2.41E+18
Ru-106	373.59 d	6.16E+17	1.06E+18
Sr-89	50.53 d	6.31E+17	7.12E+17
Sr-90	28.79 y	1.43E+16	2.88E+16
Ce-141	32.50 d	1.98E+18	2.11E+18
Ce-144	284.89 d	6.37E+17	1.05E+18
Te-131m	30.00 h	1.61E+17	1.63E+17
Te-132	3.20 d	1.86E+18	1.88E+18
Ba-140	12.75 d	1.91E+18	1.93E+18
Zr-95	64.02 d	1.49E+18	1.76E+18
La-140	1.68 d	1.94E+18	1.96E+18
Kr-83m	1.85 h	2.36E+15	4.69E+15
Kr-85	10.70 y	2.24E+17	2.26E+17
Kr-85m	4.48 h	4.04E+17	4.08E+17
Kr-87	76.30 m	4.89E+17	4.94E+17
Kr-88	2.84 h	2.52E+18	2.55E+18
Kr-89	3.15 m	2.63E+18	2.66E+18

Xe-131m	11.84 d	1.46E+18	1.48E+18
Xe-133	5.24 d	1.94E+18	1.96E+18
Xe-133m	2.2 d	2.51E+18	2.54E+18
Xe-135	9.14 h	2.50E+18	2.53E+18
Xe-135m	15.29 m	2.21E+18	2.23E+18
Xe-137	3.82 m	5.19E+16	9.65E+16
Xe-138	14.08 m	4.98E+16	1.00E+17
U-237	6.75 d	1.37E+17	1.46E+17
U-239	23.45 m	2.34E+19	2.84E+19
Np-239	2.35 d	2.53E+19	2.59E+19
Pu-238	87.7 y	2.51E+14	5.77E+14
Pu-239	2.4E+4 y	2.38E+15	2.17E+15
Pu-240	6564 y	3.68E+15	3.87E+15
Pu-241	14 y	3.08E+17	2.95E+17
Pu-242	3.7E+5 y	4.61E+12	5.79E+12
Cm-242	0.44 y	3.51E+16	8.16E+16
Cm-243	28.5 y	8.74E+12	2.49E+13
Cm-244	18.1 y	9.40E+14	2.70E+15

TABLE 18. TOTAL FISSION YIELD PER FISSION FOR EACH ELEMENT

No	Name	Stable yield (abs)	Unstable yield (abs)
1	Xe	0.233	0.00104
2	Bk	0	3.63E-12
3	Tm	1.43E-09	2.22E-10
4	Sm	0.0417	0.00537
5	Zr	0.159	0.00837
6	H	0	0.000502
7	Te	0.022	0.000766
8	Ra	5.89E-14	3.78E-12
9	Dy	0.000122	1.57E-09
10	Fr	0	2.41E-20
11	Be	1.12E-07	0
12	Ho	1.13E-06	1.57E-09
13	Tb	0.000187	1.46E-05
14	I	0.0161	0.000945
15	Pd	0.161	2.05E-05
16	Ru	0.164	0.0349
17	Tl	0	8.08E-16
18	He	0.00329	0
19	Br	0.00158	1.71E-06
20	Po	0	2.97E-18
21	Co	0	6.06E-18
22	Ba	0.0804	0.00185
23	Pm	0	0.013
24	Ni	0	3.28E-14
25	Ga	1.18E-09	3.11E-09
26	Cu	0	3.95E-13

27	Se	0.00356	1.9E-07
28	Ag	0.00945	0.000146
29	Li	4.32E-07	0
30	Cs	0.138	0.0685
31	Pr	0.0501	0.00157
32	Pb	1.43E-09	4.73E-13
33	Pa	1.13E-10	7.9E-11
34	Kr	0.0155	0.00127
35	Y	0.0175	0.00407
36	Nb	2.92E-07	0.0044
37	Zn	1.36E-08	5.84E-09
38	Gd	0.00448	6.91E-07
39	In	0.000238	3.33E-07
40	At	0	2.73E-24
41	Tc	0.0564	4.07E-05
42	Mo	0.198	0.000469
43	Sn	0.00408	6.03E-05
44	Sr	0.0137	0.0239
45	Yb	2.97E-10	0
46	Rn	0	6.65E-16
47	C	1.48E-08	0
48	La	0.0555	0.000279
49	Eu	0.00345	0.00248
50	Nd	0.156	0.000618
51	Sb	0.000633	0.000857
52	Ce	0.104	0.0261
53	Rh	0.0624	0.000231
54	Es	0	2.14E-20
55	Rb	0.0153	1.55E-05
56	Bi	1.18E-15	4.45E-14
57	As	1.11E-05	3.2E-07
58	Ge	3.09E-05	6.73E-08
59	Cd	0.00705	2.17E-05
60	Er	7.18E-07	1.17E-10

4.1.2. **Results**

The problem is formulated as a constant (T, V) problem with no mix assumption. The cover gas volume in the main vessel can be considered constant till the opening of the seals by sodium slug impact. The current report deals with this phase of the accident and determination of in-vessel source term [2]. The interpretation of the calculated release fractions is discussed in terms of the approximate chemical group to which the RN belong (as per NUREG-1465 grouping).

The equilibrium model for the calculation is shown in the FIG. 25. The following elements were considered in the simulation: Ag, Am, Ar, Ba, Br, Cd, Ce, Cm, Cs, Eu, Gd, Ge, H, He, I, Kr, La, Mo, Na, Nb, Nd, Np, O, Pm, Pr, Pu, Rb, Ru, Sb, Sm, Sn, Sr, Tb, Te, U, Xe, Zr. The

oxygen inventory (apart from the fuel oxygen inventory) includes the oxygen impurity in the sodium (3ppm). The criteria for the selection of RN considered those with high radiological importance and with core inventory above 0.1 moles. Since the activity of the actinides and fission products will be dominant, the structural material activation products were not considered in the analysis. The core inventory considered for the calculation is given in TABLE 17. Additionally, the elemental stable and unstable fission yield is given in TABLE 18. The results are given in terms of the release fraction, released activity and released mass in FIG. 28 through FIG. 45. The release fractions refer to the fraction released to the cover gas. The complement is retained in Na and fuel debris.

Noble gases:

Since the noble gasses are chemically inert in nature, most of He, Xe, Kr gets released from the fuel as the solubility of the noble gases is negligible in the sodium. Although complete inventory will be released eventually, the initial release will be from the gap inventory. The gap inventory is mainly from the diffusional release during the steady-state operation. The remaining noble gas RNs are expected to be released during the melt phase of the accident.

Halogens:

Iodine has strong chemical affinity to both caesium and iodine. The core inventory of iodine is several times less than the caesium and sodium inventory. It is found that the chemical form and release behaviour of the sodium iodide or caesium iodide is dependent on the mixing property and excess functions. For no mix assumption, most of the iodine reacts with the available caesium. The formation of sodium iodide is in trace amount. For calculation with real mixture, it is found that NaI(L) is the predominant chemical species in the primary sodium with a fraction of I reacting with Cs and Rb. This confirms the observation by Castleman et al. [6], while the results are different for the no mixture case.

The real mix case does result in one order higher release compared to the ideal mix case; This is due to the contribution of the excess function to the Gibbs potentials. By comparing all the release fractions, the release from the no mix assumption is highest compared to real mix and ideal mix cases as expected.

The lower release of the iodine at this temperature is due to the limited volume available for the release. Additionally, it is found that unlike uranium halide compounds observed for the metal fuelled reactor by Schram et al. [3] for the oxide fuelled fast reactor, the uranium halide compounds are not found either in the coolant or cover gas. This might be due to the stronger affinity of uranium towards oxygen.

The chemical affinity of caesium to bromine is similar to the affinity of caesium to iodine. For no mixture, it is found that the release behaviour for the iodine and the bromine remains similar as iodine and most of bromine gets bound with caesium. At 950 K it is observed that about 50% of bromine inventory is released to cover gas in the form of CsBr, remaining 50% is retained. Near sodium boiling point, the complete inventory of bromine gets released into the cover gas. With consideration of the mixture properties, most of bromine reacts with sodium.

Alkali metals:

This group consists of Cs, Rb, and Na. For no-mixture case, a smaller fraction of caesium binds with iodine, rubidium, bromine, and sodium as CsI, CsRb, CsBr and CsNa respectively. The remaining 90% of caesium inventory was released to the cover gas. It should be noted that one of the reasons for the higher release of caesium is due to ignoring the mixing property of

caesium in the sodium. The caesium interaction with RNs is shown in FIG. 26. The Cs_2 dissociates as the temperature increases. The CsI(cr) to CsI(L) occurs at 950 K. With mixture properties, the caesium is found mostly in the solute form in the sodium as in elemental form. This behavior contrasts that seen in no mixture, where 10% of Cs was bound with iodine.

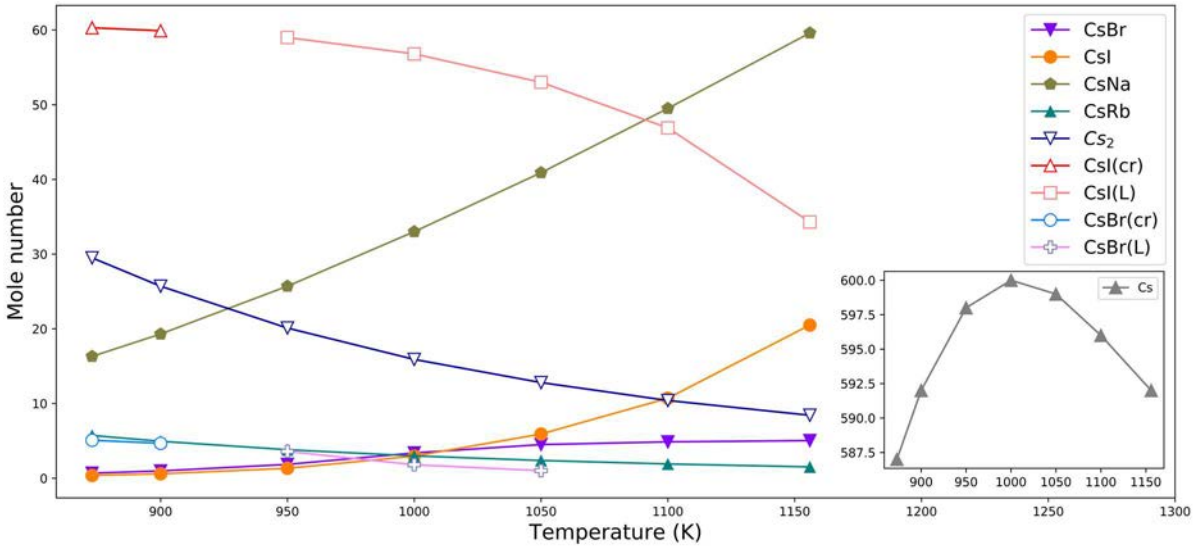

FIG. 26. Caesium interactions with various species as a function of temperature.

For the no mixture assumption, complete rubidium inventory is released at 873 K and above temperatures. Almost 90% of rubidium inventory is in elemental gaseous form (Rb). 8-9% of rubidium binds with caesium and forms CsRb(g). A small amount of rubidium will also form RbNa(g). The higher release of rubidium is due to the no-mix assumption. The rubidium is soluble in sodium. In the real mix assumption, most of the rubidium is retained in liquid sodium in the elemental form, unlike no mixture case where 9% of total Rb is in cover gas as CsRb.

The most dominant species in sodium is sodium oxide. The second most dominant sodium species in condensed form is trisodium uranium(V) oxide (Na3UO4). Due to less oxygen available for reaction, in metal reactors, the formation of trisodium uranium(V) oxide is not reported. In the cover gas, the is sodium mostly present as sodium vapour with a trace amount of the CsNa. As shown in FIG. 26, the release of CsNa increases with temperature. The formation of Cs with temperature is shown as an inset image. The initial increase in Cs formation is due to Cs vaporisation, later after 1000 K, a small decrease is seen. This decrease might be due to the formation of other sable species (i.e., CsI, CsRb) [2]. In the real mixture case, sodium mostly binds with uranium, iodine, and rubidium. The rest of sodium remains in Na(L) form.

Tellurium group:

The tellurium group consists of Te, Sb, and Se. For no mixture case, all of the tellurium binds with the barium and makes condensates of the barium telluride in the sodium. This leads to trace release of Te. With consideration of the mixture property, most tellurium reacts with sodium and forms Na2Te (L). Antimony is found to be released 100% at all temperatures. Since, the excess functions are not considered in this calculation, the higher release fractions are reported. However, with (real or ideal) mixture assumption, only trace amounts of antimony are expected to be released [3].

Barium, Strontium group:

For the no mix assumption, most of the barium and strontium is in sodium in condensed form. Almost 70% of the barium is in the oxide form, and rest of barium binds with the tellurium. With (real or ideal) mixture assumption, about 60% of the barium is retained as Ba(L) in the sodium and rest of the barium forms oxide condensates (BaO(cr)).

For no mixture, Schram et al. [3] observed higher release fraction of the strontium (0.077) since, for the metal reactor, the available oxygen for the reaction is less compared to the oxide fuelled fast reactor and metallic strontium is more volatile compared to its oxide forms. For mixture assumption also formation of strontium oxide condensate in the sodium is observed.

Noble Metals:

The noble metal group consists of Ru, Rh, Pd, Mo, Tc, Co. For no mixture assumption, ruthenium is in solid form in the sodium, and only trace amounts of the ruthenium is released to the cover gas. It should be noted that higher volatile oxide forms of ruthenium are not considered in this analysis. Molybdenum is found in condensed form in the sodium, and trace amounts of the oxides of noble metals are found in the cover gas. For mixture assumption, all ruthenium stays in condensed form. Molybdenum is found in Mo(L) form in the sodium.

Lanthanides:

The lanthanide group consists of La, Zr, Y, Cm, Am, Nd, Eu, Nb, Pm, Pr, Sm. With no mixture, lanthanides mostly form M2O3 oxides. The volatility of these elements is dependent on the availability of the oxygen [7]. For example, for metal reactors [3], It is observed that Eu has volatile behaviour (RF: 0.133); this is due to the less available oxygen for reaction in the metal fuelled fast reactor. In oxide core, Eu is in stable condensate form (Eu2O3). Hence, it is concluded that the availability of oxygen for reactions is an important parameter to the release fractions. Ideal and real mixture cases also follow the same trend as the no mixture case.

Cerium group:

The cerium group mainly consist of Ce, Pu and Np. For mixture and no mix assumptions, all three elements form stable oxide condensates in the sodium with negligible release fractions.

The release behaviour of various RNs at 1156 K for no mixture is shown in FIG. 27. The release behaviour of Noble gases, Alkali metals, Halogens, Barium group, Noble metals, and Cerium groups agree with their release grouping according to NUREG-1465. Though Te and Sb are in the same group, their release fraction is very different (RF at 1156 K: Te: 1.87E-13, Sb: 1.00). This is mainly due to the difference in the inventory, where small RN inventory in elemental form of the antimony (5 moles) can lead to complete evaporation. The tellurium (inventory: ~80 moles) has 16 times more inventory which mostly formed stable tellurides with barium and oxides with the oxygen. This lead to only trace release of the tellurium to the cover gas [2].

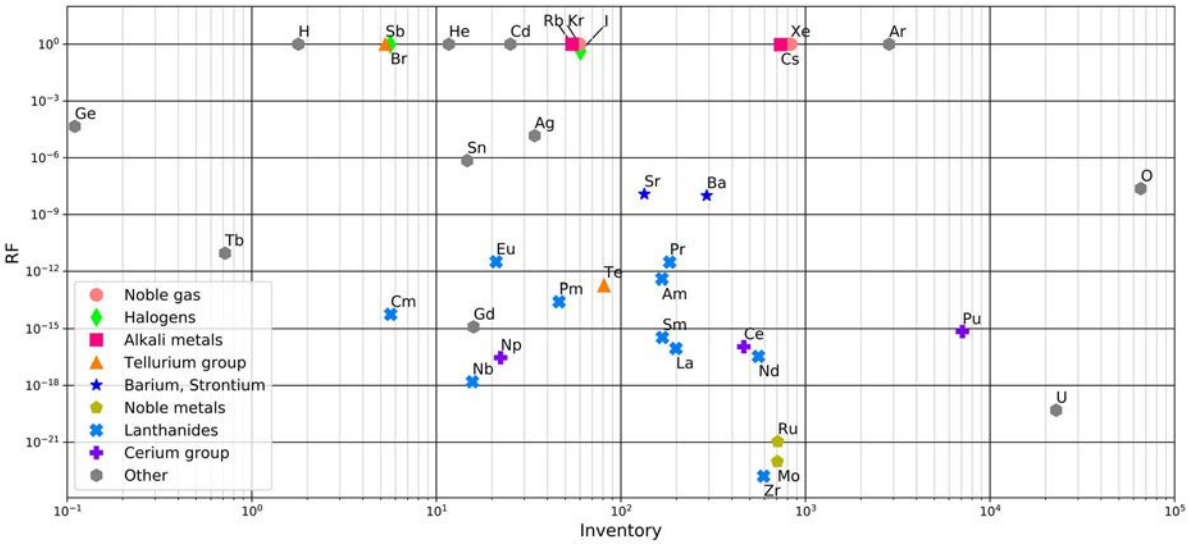

FIG. 27. Release fraction of various RN (by inventory in mole) at 1156 K with no mixture assumption.

No mix release fraction, released activity and released mass:

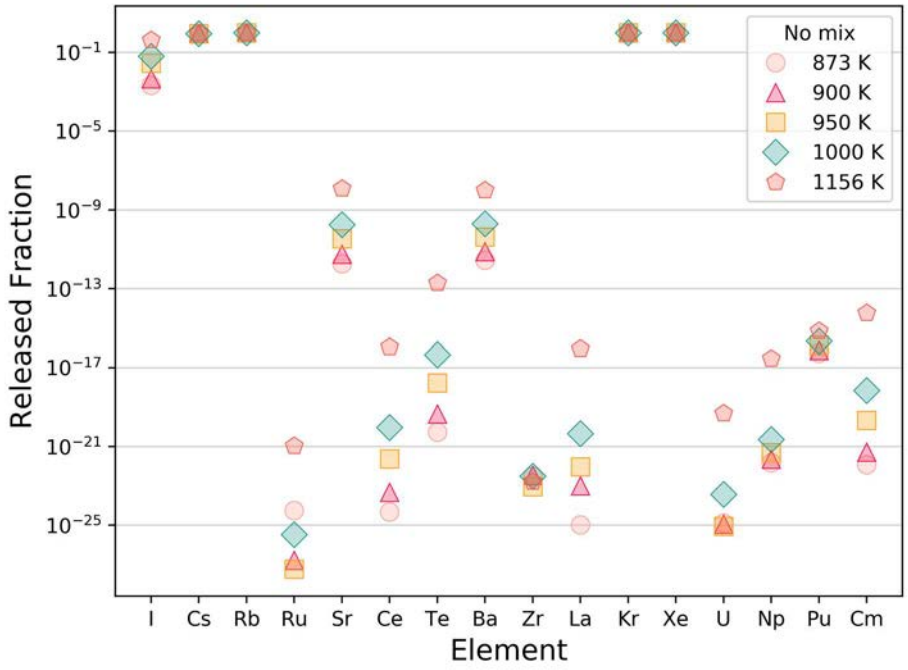

FIG. 28. Variation of release fraction to cover gas with temperature (for no mix assumption).

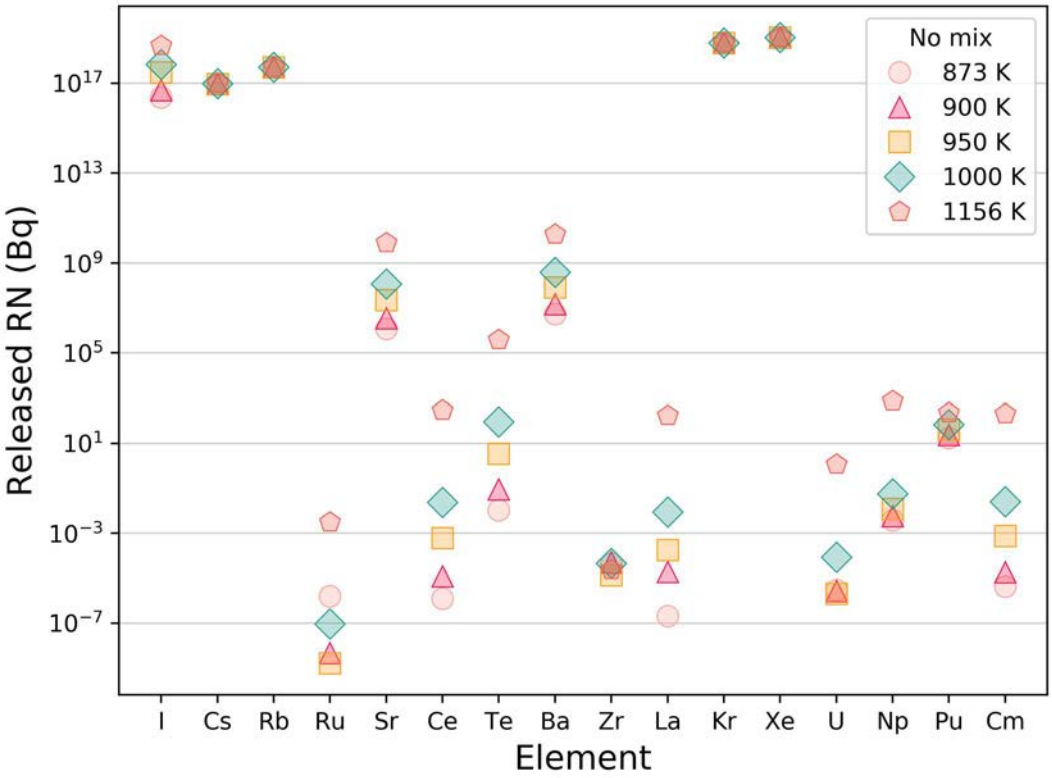

FIG. 29. Variation of released RN activity (Bq) with temperature, for no mix assumption.

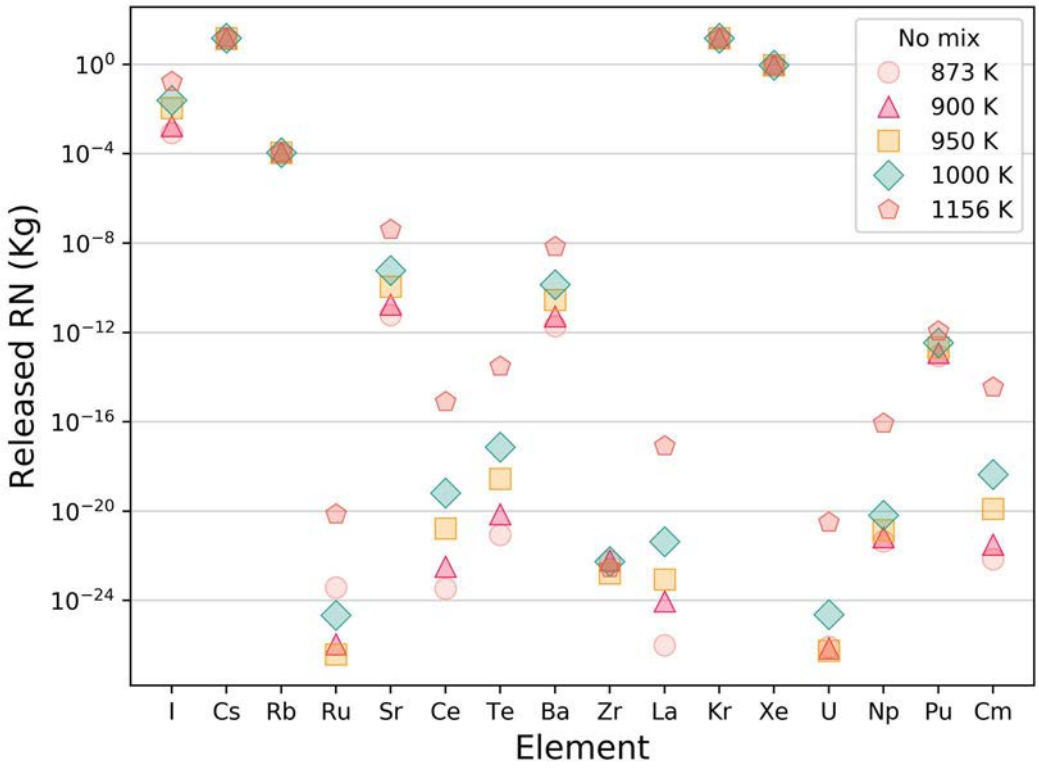

FIG. 30. Variation of released RN mass (kg) with temperature for no mix assumption.

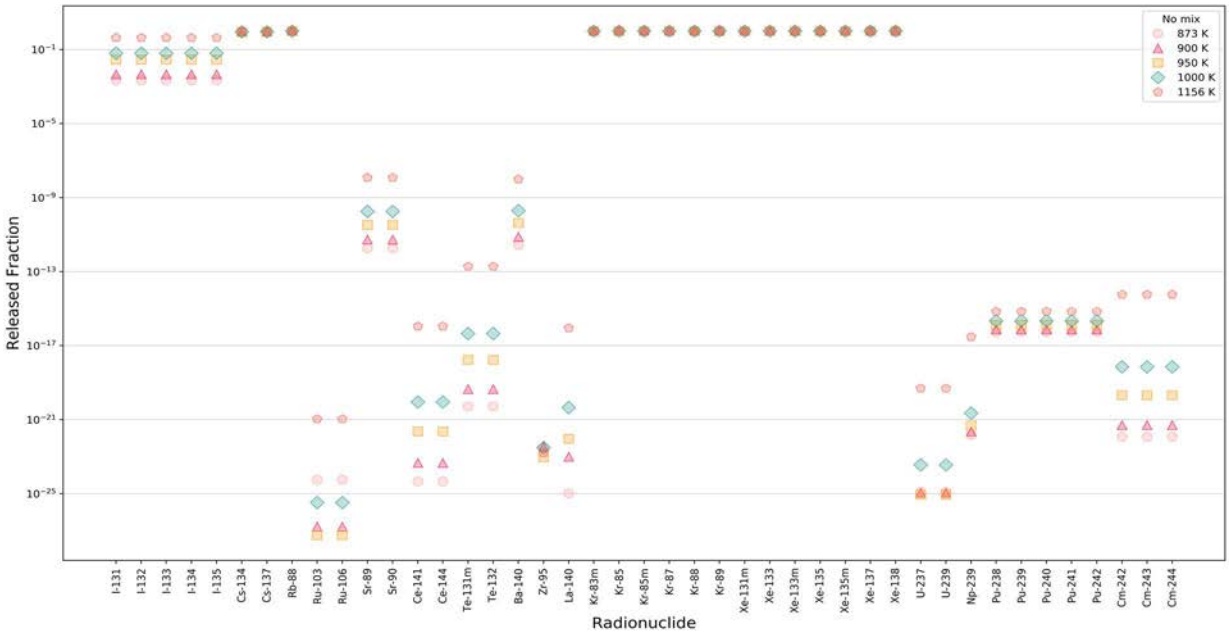

FIG. 31. Variation of release fraction to cover gas as a function of temperature, for no mix assumption.

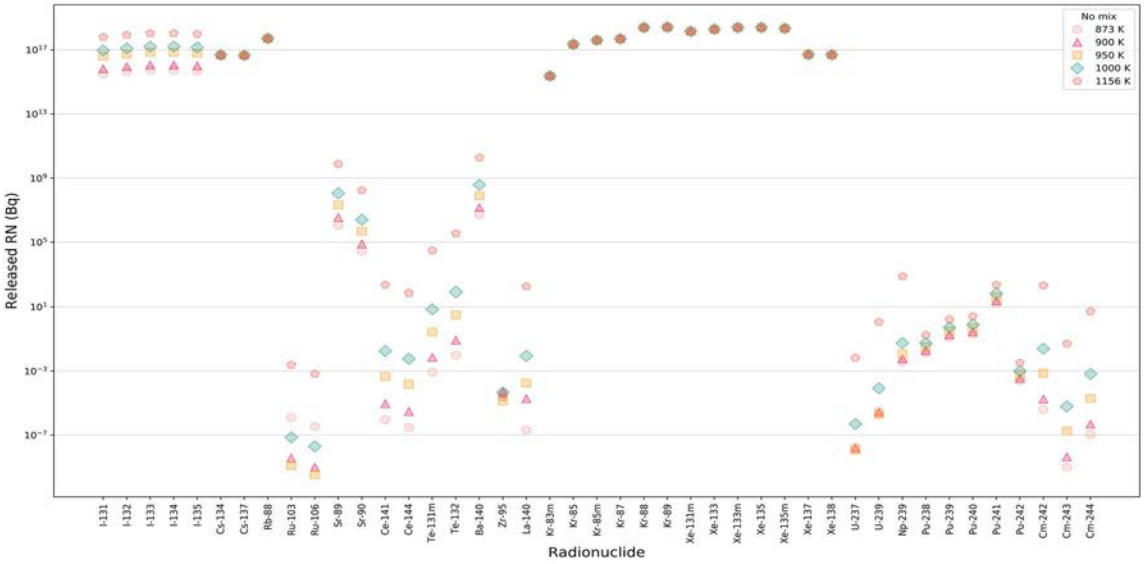

FIG. 32. Variation of released RN activity (Bq) with temperature for no mix assumption.

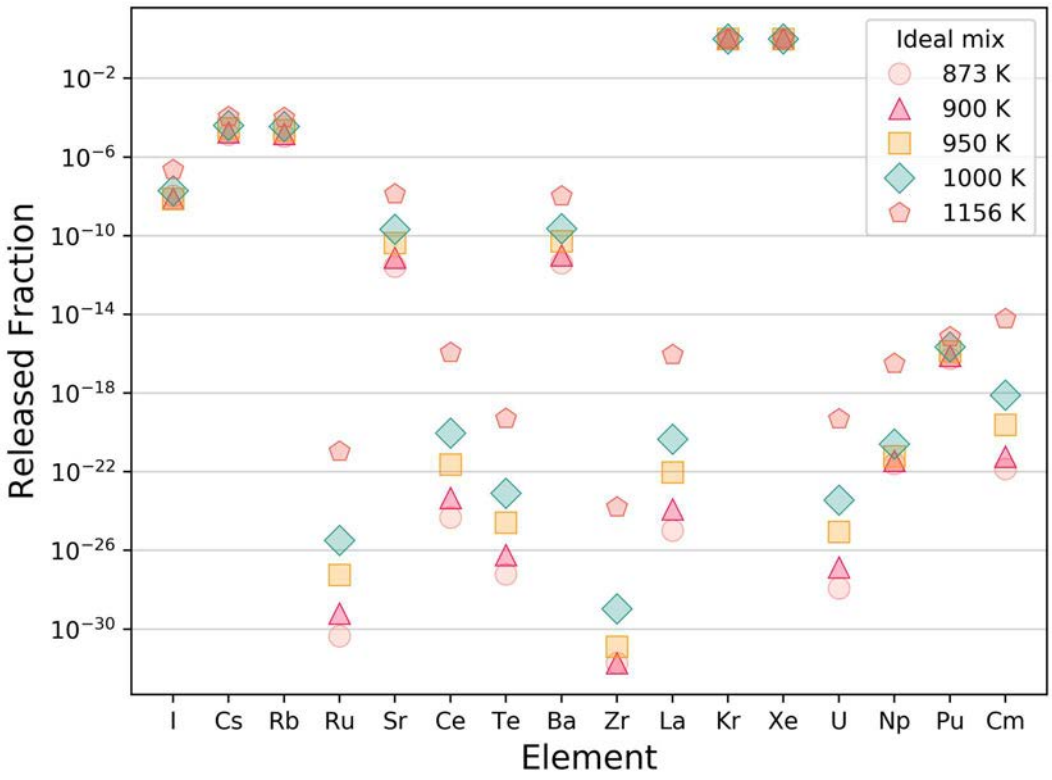

FIG. 33. Variation of released RN mass (kg) with temperature for no mixture assumption.

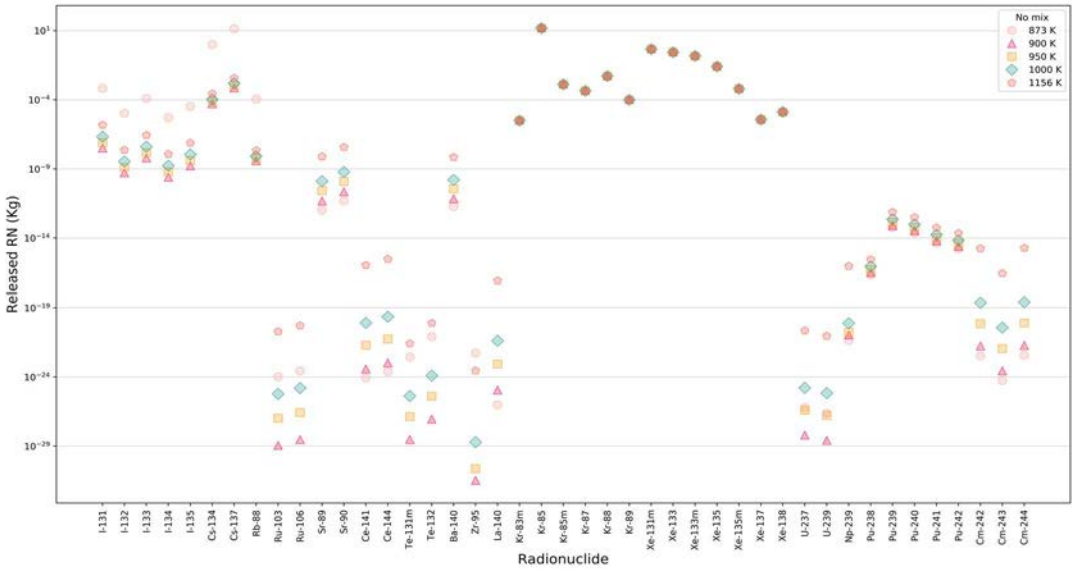

FIG. 34. Variation of element release fraction with temperature, for ideal mix assumption.

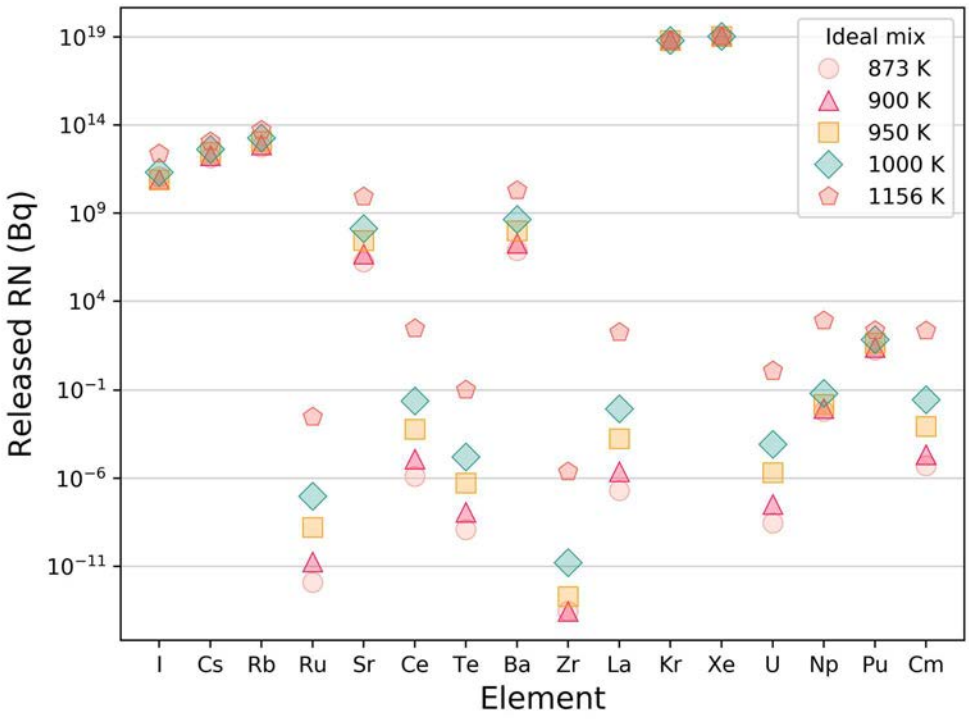

FIG. 35. Variation of released RN activity with temperature, for ideal mix assumption.

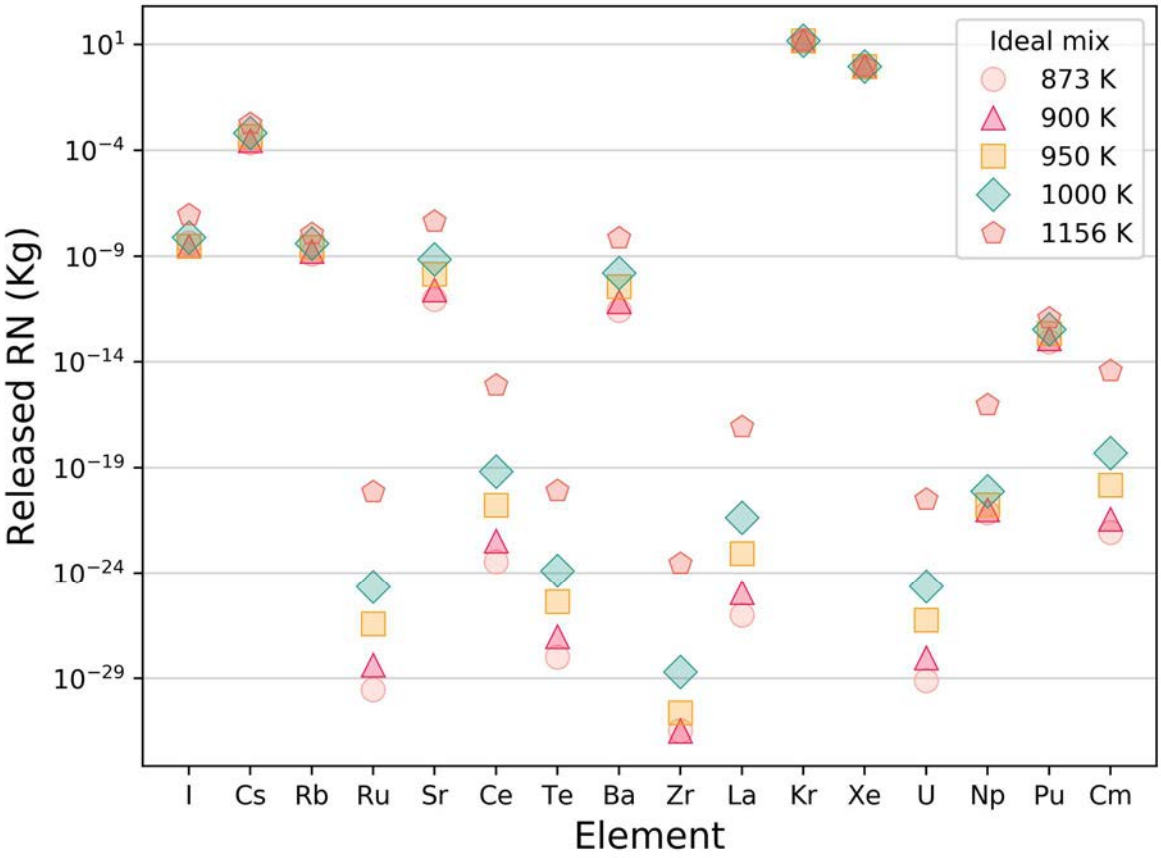

FIG. 36. Variation of released RN mass with temperature, for ideal mix assumption.

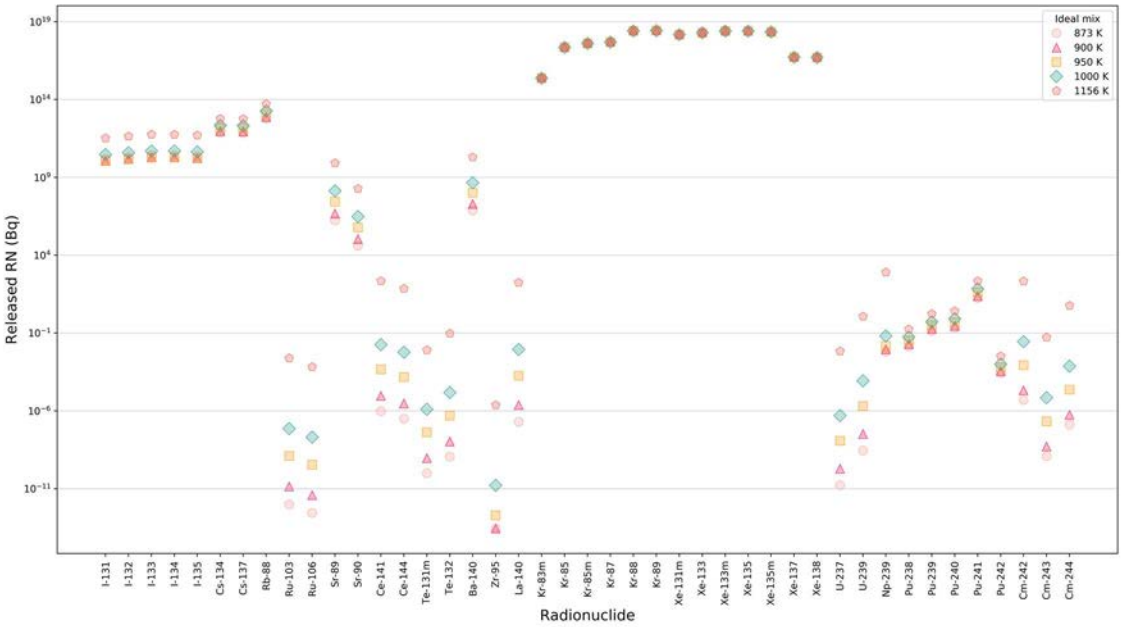

FIG. 37. Variation of RN release fraction with temperature, for ideal mix assumption.

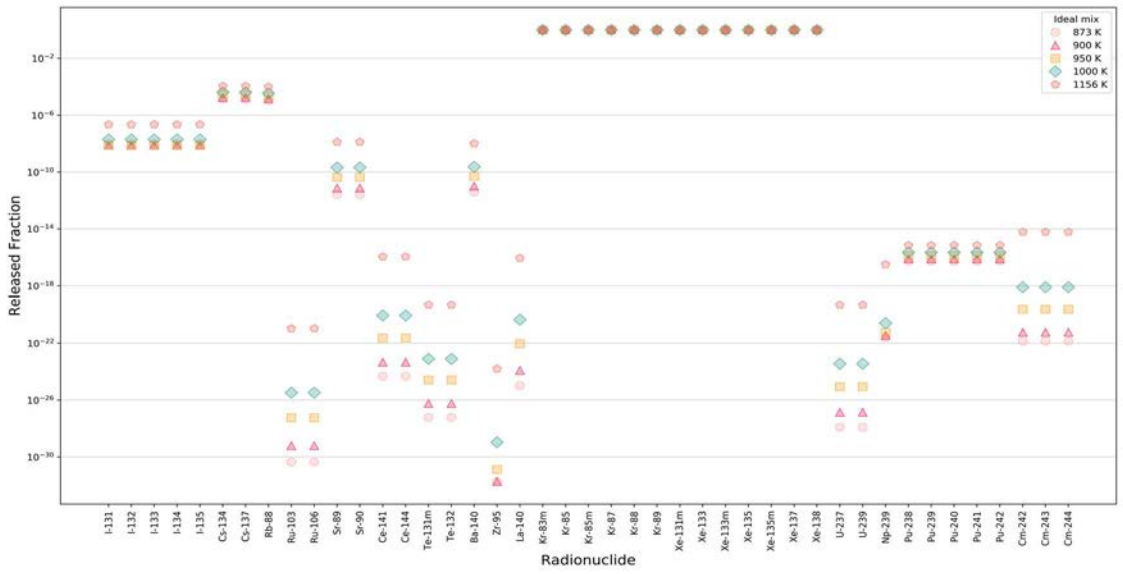

FIG. 38. Released activity (Bq), with ideal mix assumption.

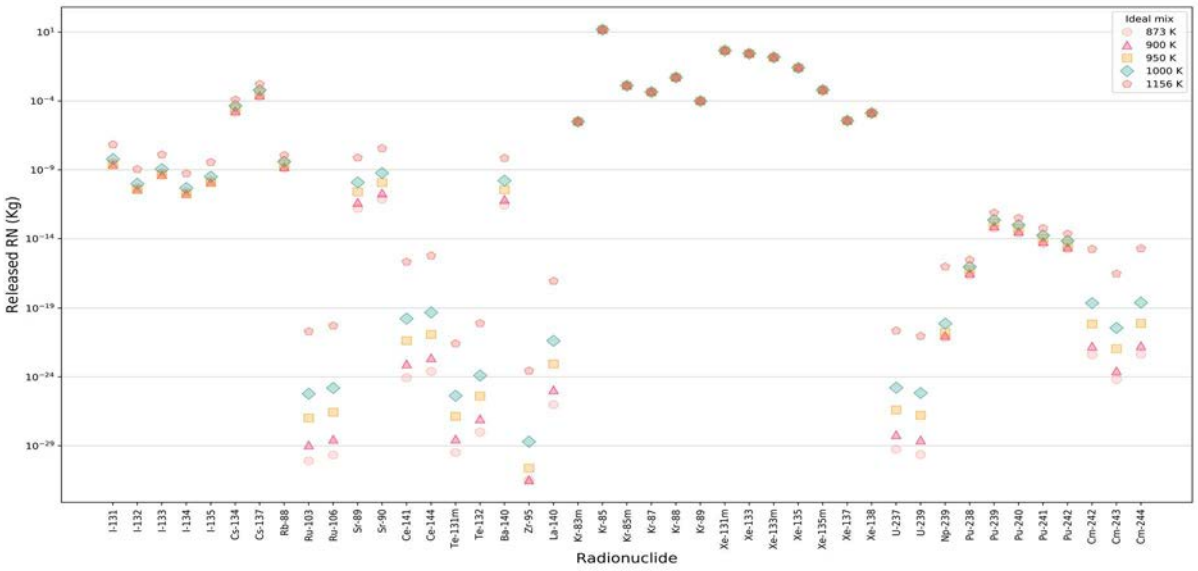

FIG. 39. Released RN (kg), with ideal mix.

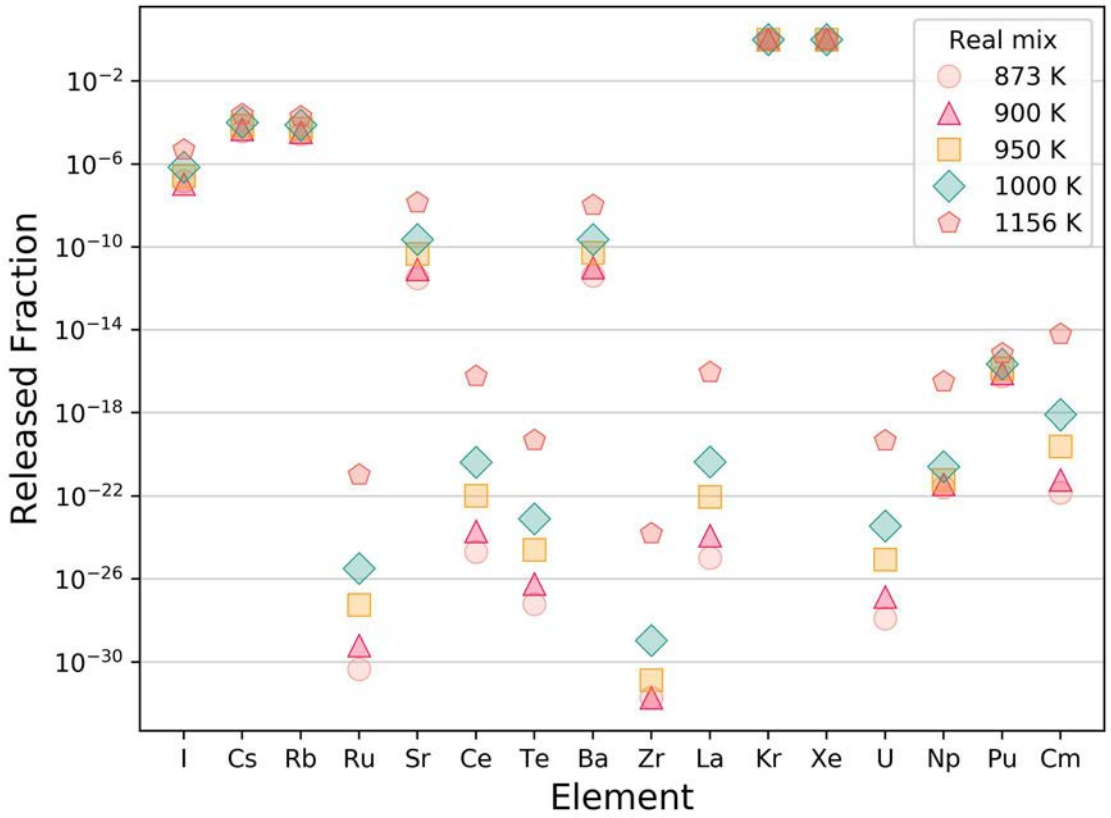

FIG. 40. Variation of element release fraction with temperature for real mix assumption.

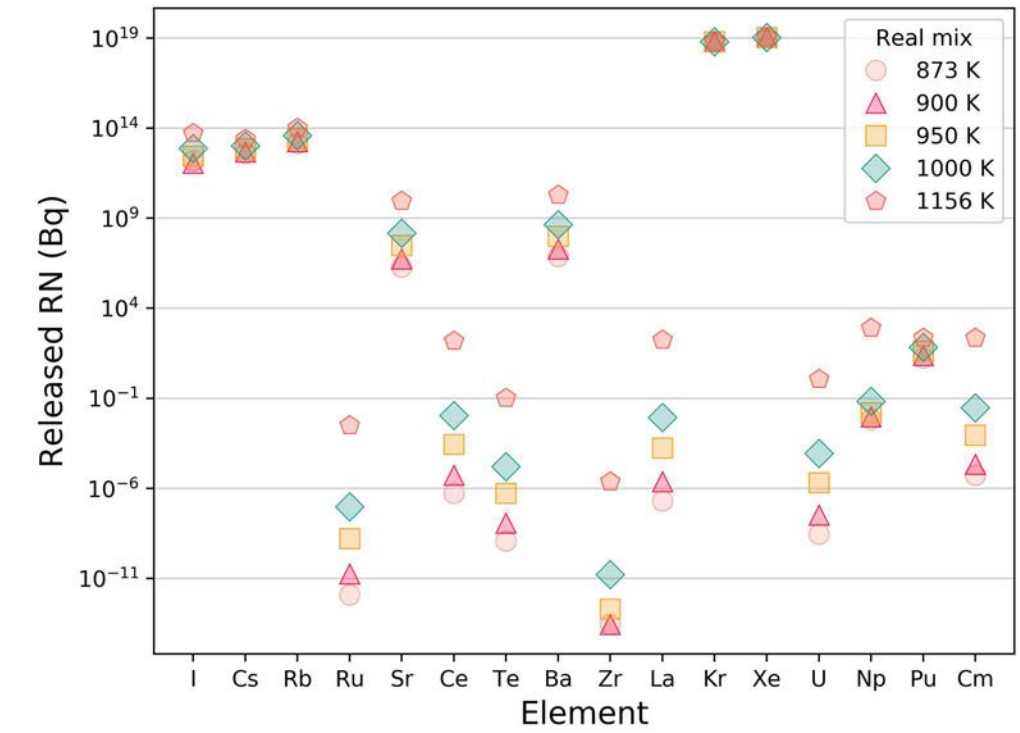

FIG. 41. Variation of RN activity released with temperature for real mix assumption.

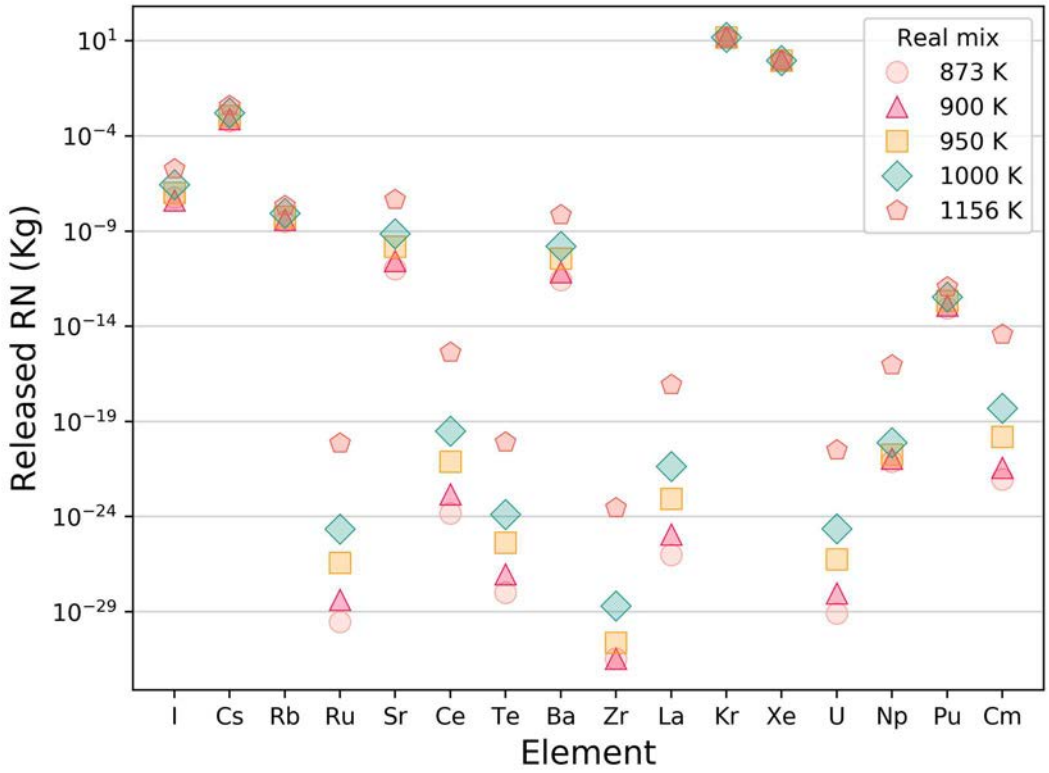

FIG. 42. Variation of released RN mass (kg) with temperature for real mix.

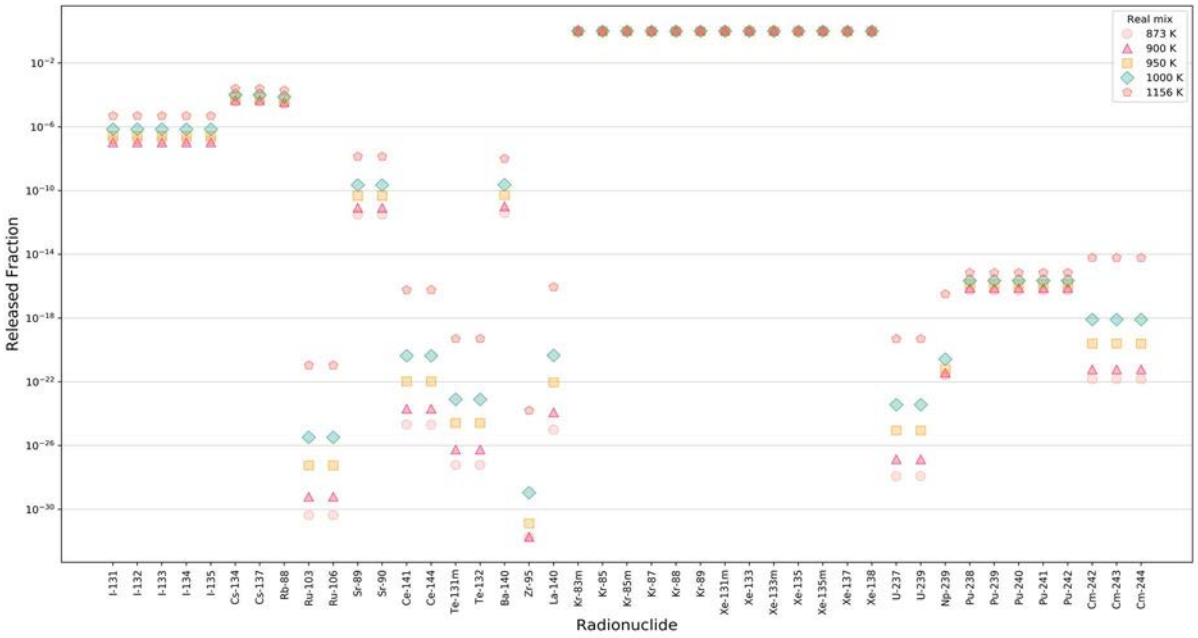

FIG. 43. Variation of release fraction with temperature for real mix assumption.

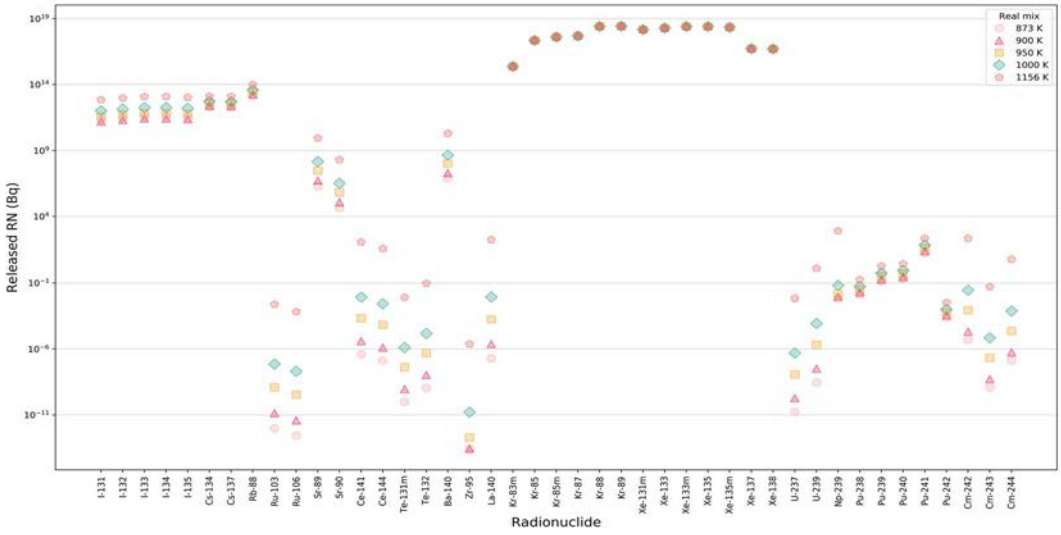

FIG. 44. Variation of released RN activity with temperature for real mixture assumption.

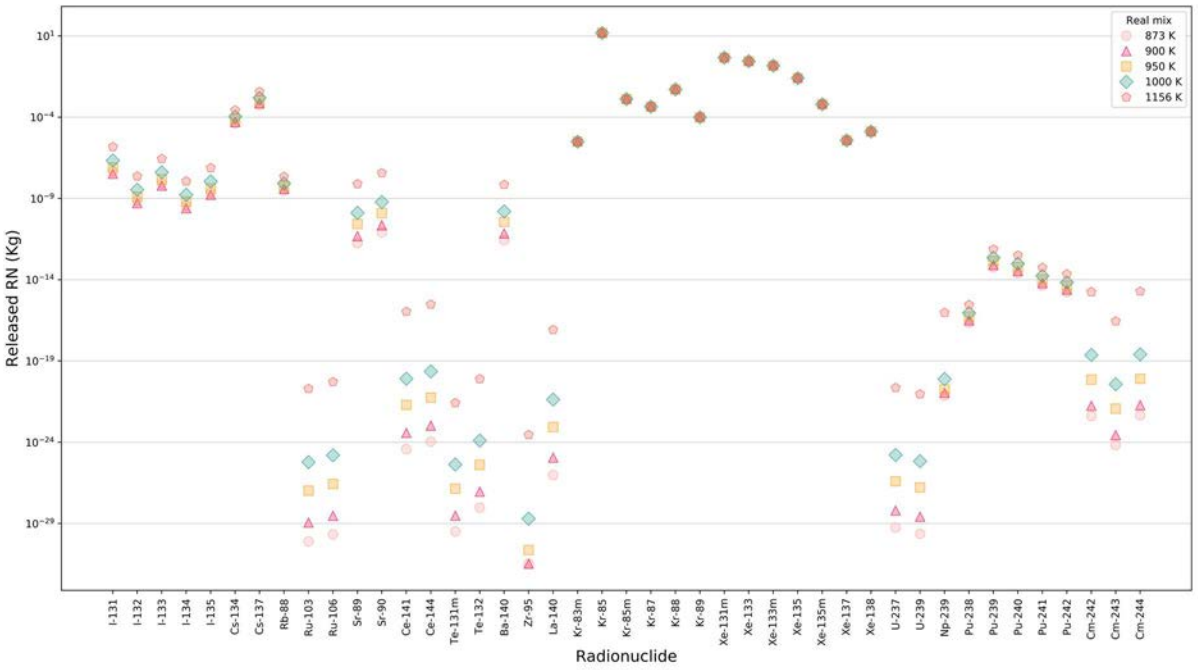

FIG. 45. Variation of released RN mass (kg) with temperature for real mix assumption.

TABLE 19. RELEASE FRACTION TO COVER GAS FOR NO MIXTURE ASSUMPTIONAT TWO DIFFERENT TEMPERATURES

Element	Activity (Bq) (MOEC)	Fraction in cover gas	
		873 K	1156 K
I	1.06E+19	2.17E-03	4.35E-01
Cs	1.02E+17	9.10E-01	9.53E-01
Rb	5.17E+17	1.00E+00	1.00E+00
Ru	2.84E+18	5.65E-25	1.08E-21
Sr	6.45E+17	1.83E-12	1.20E-08
Ce	2.62E+18	4.72E-25	1.11E-16
Te	2.02E+18	5.29E-21	1.87E-13
Ba	1.91E+18	2.77E-12	9.97E-09
Zr	1.49E+18	3.01E-23	1.60E-23
La	1.94E+18	1.05E-25	8.86E-17
Kr	6.27E+18	1.00E+00	1.00E+00
Xe	1.07E+19	1.00E+00	1.00E+00
U	2.35E+19	1.27E-25	4.89E-20
Np	2.53E+19	1.51E-22	2.92E-17
Pu	3.14E+17	5.46E-17	7.02E-16
Cm	3.60E+16	1.17E-22	5.70E-15

TABLE 20. RELEASE FRACTION TO THE COVER GAS FOR THE REAL MIXTURE ASSUMPTION FOR TWO DIFFERENT TEMPERATURES

Element	Activity (Bq) (MOEC)	Fraction in cover gas	
		873 K	1156 K
I	1.06E+19	1.48E-07	4.82E-06
Cs	1.02E+17	3.81E-05	2.46E-04
Rb	5.17E+17	2.72E-05	1.92E-04
Ru	2.84E+18	4.42E-31	1.08E-21
Sr	6.45E+17	3.06E-12	1.36E-08
Ce	2.62E+18	2.06E-25	5.81E-17
Te	2.02E+18	6.12E-28	4.99E-20
Ba	1.91E+18	3.98E-12	1.02E-08
Zr	1.49E+18	1.85E-32	1.58E-24
La	1.94E+18	1.03E-25	8.86E-17
Kr	6.27E+18	1.00E+00	1.00E+00
Xe	1.07E+19	1.00E+00	1.00E+00
U	2.35E+19	1.23E-28	4.89E-20
Np	2.53E+19	2.65E-22	3.19E-17
Pu	3.14E+17	5.63E-17	7.02E-16
Cm	3.60E+16	1.45E-22	6.08E-15

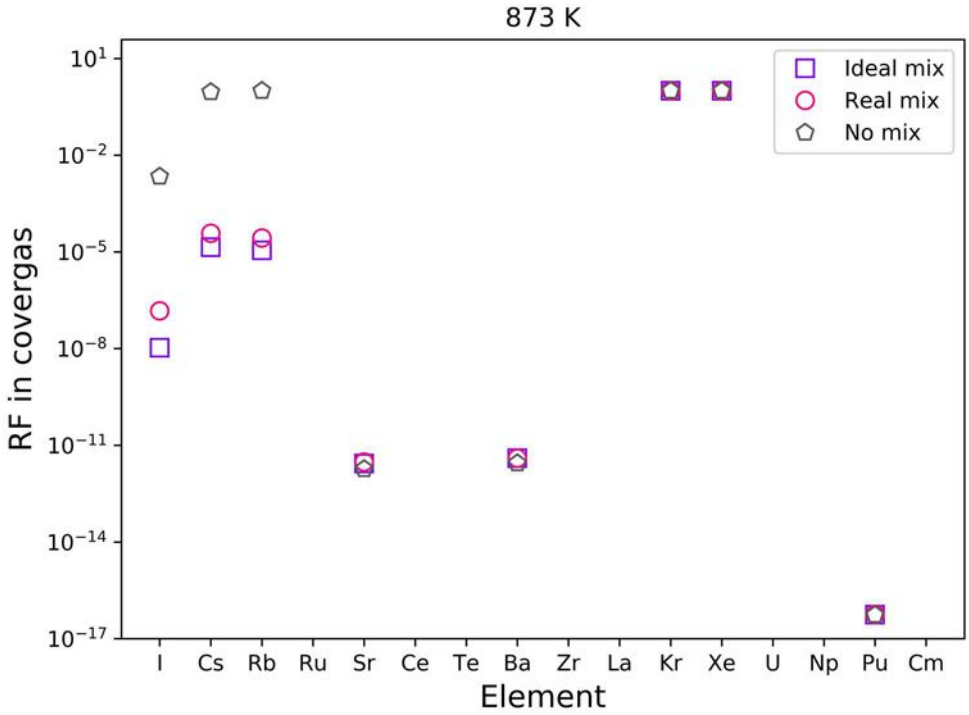

FIG. 46. Comparison of RN release fraction to cover gas for different mixture assumptions at 873 K, Here the no mixture case represents the conservative bound.

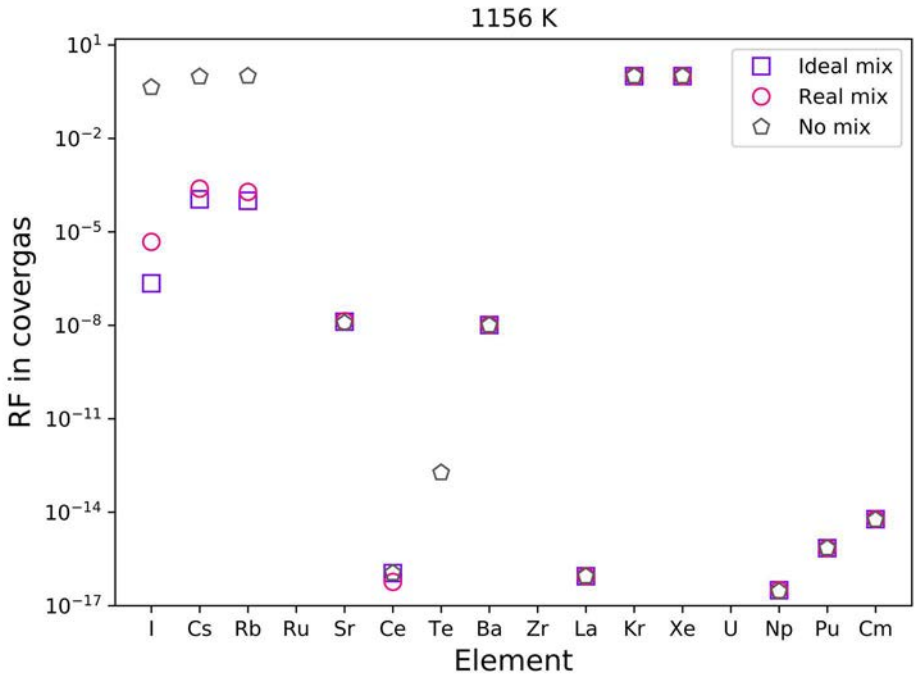

FIG. 47. Comparison of RN release fraction to cover gas for various mixture assumptions at 1156 K.

For the calculation of the in-vessel source term, a thermo-chemical equilibrium-based approach was followed. For this, in-house developed code MINICHEM is used, which is validated with many standard problems. The equilibrium calculation was performed at various temperatures with different mixing assumptions. It was found that, the amount of the oxygen available for the reaction strongly determines the release behaviour of lanthanides and barium-strontium

group. For example, Eu and Sr are more volatile in metal reactors, whereas in oxide fuelled reactors, they form stable oxides which eventually lead to lower release fractions of Eu and Sr. Further, it was observed that different mixture assumptions do affect the estimates of chemical reactions between various RNs. For example, with no mix assumption iodine had more affinity toward Cs, where in the real mixture assumption case, almost all iodine reacts with Na. It was found that the solubility of the RN has greater impact on the release. In the no mixture case, the release fraction for Cs is about 0.9, but when mixing is considered, the release fractions are of the order of between 1E-04 and1E-05. This is due to higher actual solubility of Cs in the sodium. It should be noted that the analysis was performed with single volume homogenous mixture of fuel and RN with available sodium in the reactor vessel. A multi-zone model with realistic sodium mixing volumes and a series of quasi equilibrium calculations would help to improve the prediction.

4.2. SIMULATION EXERCISE USING EUCLID/V2 CODE (IBRAE RAN, RUSSIAN FEDERATION)

4.2.1. Description of the Methods and Models

HYDRA-IBRAE/LM is a system thermal-hydraulic code module of EUCLID/V2. It allows calculation of non-stationary thermohydraulics applied to reactor loops and experimental facilities with liquid metal coolants, including the capability to describe the behavior of the water circuit and heat exchange equipment important for the safety of the NPP [8] [9]. Computation of the thermal-hydraulic processes in HYDRA-IBRAE/LM is based on the non-equilibrium nonhomogeneous two- or three-fluid model.

The equations for conservation of the mass of phases are given by

$$\frac{\partial}{\partial t}\left(\varphi_g \rho_g\right) + \frac{1}{A}\frac{\partial}{\partial z}\left(A\varphi_g \rho_g V_g\right) = \Gamma_v + \sum_{n=1}^{N_n} S_n + S_v \qquad (9)$$

$$\frac{\partial}{\partial t}\left(\varphi_f \rho_f\right) + \frac{1}{A}\frac{\partial}{\partial z}\left(A(1 - E_{dv})\varphi_f \rho_f V_f\right) + \frac{1}{A}\frac{\partial}{\partial z}\left(A \cdot E_{dv}\varphi_f \rho_f V_g\right) = \Gamma_f + S_f \qquad (10)$$

where

φ_k is the phase k volume fraction;
ρ_k is the phase k density, kg/m3 ;
A is the channel flow crosssection area, m^2 ;
V_k is the phase k velocity, m/s;
z is the coordinate along the channel, m;
N_n is the number of non-condensable gases;
Γ_v is the vapor generation rate at the phase interface boundary, kg/(m3 s);
Γ_k is the phase k mass transfer rate at the phase interface boundary, kg/(m3 s);
S_v is the generation rate of vapor due to ingress from the external source;
S_n is the generation rate of the non-conedensable gas due to ingress from the external source;
S_f is the generation rate of liquid due to ingress from the external source;
E_{dv} is the volume fraction of droplets in the liquid phase;
k is the phase identifier (f for fluid and g for gas).

The gas (gas–droplet core) momentum conservation equation is given by

$$\frac{\partial(\varphi_c \rho_c V_g)}{\partial t} + \frac{1}{A}\frac{\partial(A\,\varphi_c\,\rho_c V_g V_g)}{\partial z} + \varphi_c \frac{\partial}{\partial z} P = \Gamma_v V_i + \tau_{ig} + \tau_{wg} - \varphi_c \rho_c g \cdot \sin\vartheta - V_g S_D + V_f S_E + F_m + I_{ge} + \varphi_c H_{pump} \quad (11)$$

where, in addition to the notation used above,

P is pressure, Pa;
S_D is the specific droplet deposition rate in the dispersed–annular flow regime;
S_E is the specific droplet entrainment rate in the dispersed–annular flow regime;
I_{ge} is the momentum introduced by external sources of non-condensable gases and vapor;
ϑ is the channel slope angle to a horizontal plane;
H_{pump} is the pump head, Pa/m;
τ_{ik} is the friction force between the phase and interface boundary per unit volume, N/m3 ;
τ_{wk} is the friction force between the phase and channel wall per unit volume, N/m3 ;
φ_c is the gas– droplet core volume fraction;
ρ_c is the gas–droplet core density;
F_{st} is the force that differs from zero only for stratified flow in horizontal channels;
F_m is the connected mass force.

The phase energy conservation equations are given by

$$\frac{\partial[(1-\varphi_c)\rho_f V_f]}{\partial t} + \frac{1}{A}\frac{\partial[A(1-\varphi_c)\rho_f V_f V_f]}{\partial z} + (1-\varphi_c)\frac{\partial}{\partial z} P = \Gamma_f V_i + \tau_{if} + \tau_{wf} - (1-\varphi_c)\rho_f g \cdot \sin\vartheta + V_g S_D - V_f S_E - F_m - F_{st} + I_{fe} + (1-\varphi_c) H_{pump} \quad (12)$$

The velocities of phases at the phase interface surface are determined from the following correlation:

$$V_{ik} = \begin{cases} V_f, \Gamma_{iv} > 0, \\ V_g, \Gamma_{iv} < 0; \end{cases} \quad (13)$$

i.e., it is assumed that the generated vapor has the same velocity as that of the liquid phase, and that the condensed liquid has the same velocity as that of the gaseous phase.

The phase energy conservation equations are given by

$$\frac{\partial(\varphi_g \rho_g h_g)}{\partial t} + \frac{1}{A}\frac{\partial}{\partial z}(A\varphi_g \rho_g h_g V_g) - \varphi_g \frac{dP}{dt} = Q_{g,ext} + Q_{wg} + \Gamma_{iv} h_{iv} + \Gamma_w h_{iv}^w + Q_{g,diss} + Q_{iv} + \sum_{n=1}^{N_n} S_n h_{*n} + S_v h_{*v}, \quad (14)$$

$$\frac{\partial(\varphi_f \rho_f h_f)}{\partial t} + \frac{1}{A}\frac{\partial}{\partial z}(A\varphi_f \rho_f h_f V_f) - \varphi_f \frac{dP}{dt} = Q_{f,ext} + Q_{wf} - \Gamma_{iv} h_{if} - \Gamma_w h_{if}^w + Q_{f,diss} + Q_{if} + S_f h_{*f} + \frac{1}{A}\frac{\partial}{\partial z}\left(A\varphi_f \lambda_f \frac{\partial T_f}{\partial z}\right). \quad (15)$$

where
h_k is the specific enthalpy of the source/sink of phase *k*, J/kg;
h_n is the specific enthalpy of the source/sink of non-condensable gases, J/kg;
λ_f is the liquid phase heat conductivity, W/(m K);
T_f is the liquid phase temperature, K.

Q_{ig}, Q_{if}, and Q_{gf} are determined, as follows:

$$Q_{ig} = \frac{P_v}{P}\alpha_i\alpha_{ig}(T_s - T_g) \tag{16}$$

$$Q_{if} = \alpha_i\alpha_{if}(T_s - T_f) \tag{17}$$

$$Q_{gf} = \frac{P - P_v}{P}\alpha_i\alpha_{gf}(T_g - T_f) \tag{18}$$

where
α_i is the phase interface surface density, 1/m;
T_g is the gaseous phase temperature, K;
T_s is the saturation temperature, K;
α_{gf} is the coefficient of heat transfer from the gaseous phase to the liquid phase, W/(m^2 K);
α_{ik} is the coefficient of heat transfer from phase *k* to the phase interface surface, W/(m^2 K).

If there are no non-condensable gases, Q_{gf} is equal to zero. The last term in the two equations above is the heat flux transferred due to longitudinal heat conductance, and is only used for liquid metal coolants. The terms $Q_{g,diss}$ and $Q_{f,diss}$ stand for heat release due to energy dissipation. The term Q_{wk} consists of two parts, one of which describes convective heat transfer with the phase, and the other one describes the vapor generation process. The whole heat flux from the wall is spent for vaporization during the boiling of saturated liquid. During the boiling of subcooled liquid, part of the heat flux is spent for vaporization and its remaining part is spent for increasing the liquid's enthalpy.

The following conditions must be satisfied for preserving the balance of energy and mass of the phases:

$$\Gamma_v + \Gamma_f = 0 \tag{19}$$

$$Q_{ig} + Q_{if} += \Gamma\left(h_{ig} - h_{if}\right) + Q_{wfi} + Q_{wgi} = 0 \tag{20}$$

in which the variables h_{ig} and h_{if} are determined as follows:

$$h_{ig} = \frac{1}{2}\left[\left(h_{gs} + h_g\right) + \eta\left(h_{gs} - h_g\right)\right] \tag{21}$$

$$h_{if} = \frac{1}{2}\left[\left(h_{fs} + h_f\right) - \eta\left(h_{fs} - h_f\right)\right] \tag{22}$$

$$\eta = \begin{cases} 1 \ with \ \Gamma_v \geq 0 \\ -1 \ with \ \Gamma_v < 0 \end{cases} \quad (23)$$

where h_{gs}, h_{fs} are the specific enthalpies of the phases at the saturation curve. For sodium coolant, the terms Q_{wfi} and W_{wgi} are equal to zero. The continuity equations for non-condensable gases are given by

$$\frac{\partial}{\partial t}(\varphi_g \rho_g X_n) + \frac{1}{A}\frac{\partial}{\partial z}(A\varphi_g \rho_g X_n V_g) = S_n \quad (24)$$

In Eq. (24), it is assumed that non-condensable gas enters the gaseous phase with the velocity equal to that of the gaseous phase.

For closing the system of equations, the following relations are written:

$$\rho_k = \rho_k(P, h_k) \quad (25)$$

$$\varphi_g + \varphi_f = 1 \quad (26)$$

In the previous equation, it is assumed that the density of liquid does not depend on the mass concentrations of non-condensable gases. The list of factors that are of key importance in two-fluid thermal–hydraulic models includes, in particular, the choice and validation of the used flow and heat transfer regime map and also the block of closing equations describing the two-phase flow friction, interphase friction, heat transfer from the fluid to the wall, and interphase heat transfer intensity. It should be noted that the main difference between liquid metals and water is that the liquid phase has high heat conductivity and, consequently, is characterized by a low Prandtl number. Thus, the differences between the hydrodynamics and heat transfer processes during the flow of liquid metals and water should manifest themselves in phenomena accompanied by heat transfer. Hence, the description of hydrodynamic processes in liquid metal should be close to that for processes in water coolant. In view of this circumstance, a decision was made to orient with the correlations obtained for water and written in terms of dimensionless complexes in the selection of the closing equations.

The code includes an additional set of specialized modules (AEROSOL/LM) allowing to simulate the transport of fission, corrosion and activation products over the loops of the reactor facility and also the behavior of multicomponent polydisperse aerosols inside the reactor containment building (RCB) of NPP with fast reactors [10]. Heat transfer in structure elements is described in a two-dimensional approximation.

The code can simulate both the flow of coolant with fission products in reactor loops and the dynamics of the containment atmosphere gas with hydrogen, oxygen, and fission products in the RCB. During the sodium fire the amount of O_2 decreases which allows to describe oxygen starvation.

The aerosol module AEROSOL/LM allows simulating the following processes:

— The nucleation of different vapors;
— The coagulation of multicomponent polydisperse aerosol particles;
— The condensation of various (multicomponent) vapors on particles;
— The condensation and sorption of vapors on surfaces;

— The deposition of aerosols on surfaces due to different mechanisms;
— The formation of multicomponent deposits on surfaces;
— The absorption of water vapor by hygroscopic aerosol (equilibrium and kinetic approach);
— The transfer of aerosols and various vapors through the compartments.

The more detailed description of models is presented in [11] [12]. In the calculations the influence of ionizing radiation and ions on aerosol behavior in containment rooms was not considered since these processes would not likely play a significant role in aerosol behavior during severe accident in SFRs [13].

The behavior of multicomponent particles with time t is simulated by a system of differential equations for the mass $M_{i,p}(t)$ of the p-th product in particles of the i-th size-fraction with bounds m_{i-1}, m_i per unit volume of a spatial cell. The mass (M_i) and concentration (N_i) of particles of the given i-th size-fraction are determined by the following relations (here the particle 'size' is defined as the particle mass x_i)

$$M_i = \sum_{p=1}^{N_{FP}} M_{i,p}\,, N_i = M_i/x_i, x_i = (m_{i-1} + m_i)/2 \tag{27}$$

where
$i = 1,2,\ldots,N_B$;
N_B is the number of size fractions;
N_{FP} is the number of components contained in particles.

The fixed volume of particles in i-mode is defined as $v_i = m_i/\rho_p^0$, where ρ_p^0 – an aerosol bulk density, which is constant and identical for all particles of all fractions. The assumption, that $\rho_p^0 = const$ independently on the composition of the particle, is the weakest point in this approach, in particularly, for mixed particles composed of components with the bulk density that is essentially different on the water density.

The behavior of components in vapor and deposit phases is simulated by a system of differential equations for the mass $M_p^{vap}(t)$ of the p-th vapor per unit volume and the mass $M_{s,p}^{dep}(t)$ of the p-th component per unit of the s-th surface ($s = 1,2,\ldots,N_s$) respectively for each spatial cell. As a result, the total number of differential equations N_{eq} for each spatial cell is defined as

$$N_{eq} = \overbrace{N_B \times N_{FP}}^{\substack{particle\\phase}} + \overbrace{N_{FP}}^{\substack{vapor\\phase}} + \overbrace{N_S \times N_{FP}}^{\substack{deposition\\phase}} \tag{28}$$

where N_S is the number of different structure surfaces for the given spatial cell, for example, $N_S = 3$ in the case of the cylindrical compartment (floor, walls and ceiling).

The module enables the modelling of aerosol formation kinetics for the wide particle size spectrum and any multimode function of the aerosol particle size distribution. The multicomponent composition of deposits is also simulated in the module. The module database is based on following factors: firstly, radionuclide composition of gases, aerosols and depositions on surfaces, which determines the level of radioactivity inside the reactor rooms; secondly, the components which affect the mass content and hence the particle size and mass

and therefore the velocity of aerosol deposition on surfaces. The consideration of these factors allows to adequately simulate dynamic properties, composition and radioactivity of aerosols and deposits and when necessary to calculate an amount of residual heat release on surfaces.

The size distribution of aerosols is influenced by condensation of water vapor and fission products. The growth of aerosols by condensation of water vapor occurs in most cases on a faster timescale than other processes, e.g. coagulation or deposition of aerosols. In the module, to simulate the absorption of water vapor by hygroscopic particles two methods are considered. In the case of humidity $RH < 100\ \%$, an equilibrium approach for given temperature and composition of the dry aerosol is used, following the equation:

$$RH(T) \times\ 100 = A_w(n_i, n_w) \tag{29}$$

where A_w is the water activity in the solution, depend on the composition of dry aerosol in terms of the number of moles of hygroscopic components (n_i) and water (n_w). In this approach the hygroscopic aerosol is always being at equilibrium with water vapor for given temperature.

In the case of supersaturated water vapor ($RH > 100\ \%$) the kinetic approach is used to simulate the condensation and evaporation of water vapor on aerosol particles and deposits on walls. The condensation on aerosol is treated as the collision between the water molecular and aerosol particle. The rate of evaporation is determined with accounting for the Kelvin effect. The equilibrium vapor concentration above the surface of the multicomponent particle is determined taking account of the molar content of components in a particle in the ideal solution approximation [14]. Vapor condensation on the surface of structures is modelled separately for each vapor component based on analogy between the heat and mass transfer and accounting for its thermal and diffusion properties. The condensation rate on thermal structures is modelled similarly to the model used in the SOPHAEROS module [15].

The BERKUT fuel rod module of the EUCLID/V2 integrated code is used to model the processes occurring in fuel rods of fast reactors with mixed nitride and mixed oxide uranium–plutonium fuels, uranium mononitride and uranium dioxide fuels and claddings made of austenitic or ferrite-martensite steels under normal operating conditions, normal operation failure and emergency conditions.

The BERKUT fuel rod module allows to simulate the following processes:

— Temperature distribution in a fuel rod;
— Stress-strain state of a fuel rod with the open gap and in the case of the pellet-cladding mechanical interaction (PCMI);
— Cladding integrity analysis according to the performance criteria (margins for melting, ultimate strength, long-term strength, etc.);
— Fission gas release (FGR) under the cladding;
— Degradation of the gas gap conductivity due to FGR.

The simulation is performed taking into account dependencies of thermophysical and mechanical material properties on fuel rod fabrication parameters and irradiation conditions.

The module SAFR/V1 allows simulating the following processes:

— The melting of a fuel rod and solidification of the formed melt;
— The movement of the melt along the surface of the fuel element under the influence of gravitational force and friction of the melt with fuel pin surface and coolant flow;
— The blockage of the cross sectional area of the fuel pin bundle due to solidification of the melt on the surface of fuel pins;
— The entrainment of the melt into the coolant flow and deposition of the melt on fuel pin surface;
— The formation of melting pool;
— The fission products release from melting pool;
The more detailed description of models is presented in [16] [17] [18].

To calculate fuel rod melting and melt solidification the thermal problem solves, the energy equation is written in the enthalpy formulation in the cylindrical geometry r-z:

$$\frac{\partial \rho_m h}{\partial t} = \nabla \cdot (k \nabla T) + Q \tag{30}$$

where
h is the specific enthalpy (J/kg);
Q is the volumetric energy release (W/m3);
K is the thermal conductivity (W/(m K));
t is the time (s);
ρ_m is the density (kg);
T is the temperature (K).
The finite volume method is used for the numerical solution of the equation.

The equations of momentum, energy and mass are solved in solving the problem of film flowing:

$$\begin{cases} \frac{\partial \rho S}{\partial t} + \frac{\partial \rho U S}{\partial z} = \Gamma_m, \\ \frac{\partial \rho h S}{\partial t} + \frac{\partial \rho h U S}{\partial z} = q_w \Pi_w + q_c \Pi_c + \Gamma_m h, \\ \frac{\partial \rho S U}{\partial t} + \frac{\partial \chi \rho S U^2}{\partial z} = \Gamma_m U_m + \rho g S \sin\theta \\ + \tau_c \Pi_c - \tau_w \Pi_w + \sigma \Pi_w \cos\theta_w \, \delta(z - z_i), \end{cases} \tag{31}$$

where
ρ is the density;
S is the cross-area of film;
h is the film enthalpy;
U is the average velocity.

The right-hand of the equations includes different source terms:
Γ_m is the mass source due melting/solidification of materials;
U_m is the mass source rate;
q_w,q_c is the heat, entering into the cell from the wall and the gas flow respectively;
Π_c, Π_w is the wetting perimeter;

τ_c is the friction stress of the melt at the boundary with the gas flow;
τ_w is the friction stress of the melt with the surface of the wall;
σ is the surface tension;
θ_w is the contact angle between the melt and the wall;
$\delta(z - z_i)$ is the delta function, which determines that the force of surface tension at the point of contact is applied to the melt-solid interface;
z_i is the melt boundary coordinate.

The coefficient χ takes into account the presence of the velocity profile along the thickness of the melt. The model of the melt movement is one-dimensional, and it assumes two melt flow regimes. In the basic mode, it is assumed that the melt moves in the form of a film. In the additional mode, the so-called 'continuous' mode, it is possible to simulate the movement of the melt as an incompressible fluid in a circular pipe at a given pressure drop.

Fission products module SAFR/V1 includes a model of gaseous and volatile fission products release from melted pool. The list of fission products calculated by this model is presented in TABLE 21.

TABLE 21. LIST OF FISSION PRODUCTS

Volatility	**Element**
Volatile	Am, Cs, Cr, Kr, Te, Xe, I
Semi-volatile / Non-volatile	Ba, Co, Ce, Cm, Co, Fe, Mn, Mo, Np, Nd, Ni, Sr, La, Pu, Ru, U, Zr

The masse of volatile fission product release is determined by the equation:

$$\frac{dm_i}{dt} = -\frac{\frac{C_\infty}{M}}{\frac{\rho_m}{M_m}} C_{si}(T) \sum_{k=1}^{N} \frac{1}{6} \pi D_{bk}^3 \cdot n_k v_k S \tag{32}$$

where
C_∞ is the fission product concentration in melt pool;
C_{si} is the fission product mass concentration on melt pool surface;
M, M_m is the molecular mass of melt and fission product.

The rate of bubble floating-up v_k is determined by friction coefficient ζ_{bk} of bubble with fluid and by bubble diameter. Concentration of fission product in the pool n_k is determined by the equation:

$$\begin{cases} \frac{dn_1}{dt} = f \cdot s_n - \frac{n_1}{\tau_{21}} - \sum_{i=1} B_{i1} n_i \cdot n_1 - \frac{v_k n_k}{H} \\ \dots \\ \frac{dn_k}{dt} = \frac{n_{k-1}}{\tau_{kk-1}} - \frac{n_k}{\tau_{k+1k}} + \frac{1}{2} \sum_{i+j=k} B_{ij} n_i \cdot n_j - \sum_{i=1} B_{ik} n_i \cdot n_k - \frac{v_k n_k}{H} \end{cases} \tag{33}$$

with initial conditions: $n_1 = 0..n_N = 0$, where
H is the height of the pool;
$\tau_{k,l}$ is the grow time from bubble diameter D_{bk-1} to D_k;
B_{ij} is the coagulation velocity given by Eq. (34)

$$B_{ij} = \pi \left(\frac{D_{bi} + D_{bj}}{2} \right)^2 |v_i - v_j| \tag{34}$$

The masse of semi-volatile or non-volatile fission product release is determined by the equation following:

$$\frac{dm_i}{dt} = S \left(\frac{1}{\alpha_{cm}} + \frac{\frac{\rho_m M}{M_m}}{2\sqrt{\frac{RT}{2\pi M}} C_s(T)} + \frac{\frac{\rho_m M}{M_m}}{\alpha_{cg} C_s(T)} \right)^{-1} \left(C_\infty - C_g \frac{\frac{\rho_m M}{M_m}}{C_s(T)} \right) \tag{35}$$

where
C_g is the fission product mass concentration over melt pool;
C_∞ is the fission product mass concentration in melt pool;
α_{cm} is the mass transfer coefficient to melt surface;
α_{cg} is the mass transfer coefficient from melt surface;
ρ_m is the melt pool density;
M is the fission product molecular mass;
M_m is the melt pool molecular mass;
$C_s(T)$ is the fission product saturation concentration.

4.2.1.1. *Nodalization Scheme General Case*

The general purpose is to calculate the inventory of radionuclides in the primary system and cover gas space above the coolant free level following a core damage accident.

The calculation of the general case is divided into 2 parts:

— Fission product release from melted fuel
— Fission product release from sodium to cover gas

For case with fission products release from melted fuel nodalization scheme consists of one cell, FIG. 48.

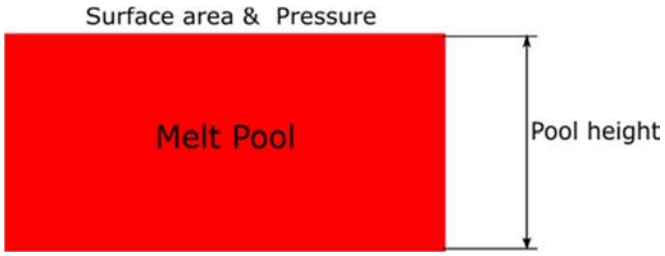

FIG. 48. Nodalization scheme for FP release from melted fuel.

The assumption is made that all melted fuel with RN have flowed down and formed a pool. The mass of fuel in the pool is 13305.5 kg with temperature 3205 K. The height of the pool assumes

to be 0.6 m, surface area 2.55 m^2 and surface pressure corresponds to core bubble pressure 0.2 MPa.

All fission products are injected as gases. Initial activity corresponding to MOEC case for each fission product is presented in TABLE 22.

TABLE 22. FISSION PRODUCTS ACTIVITY IN MELTED POOL

No.	Radionuclide	Activity (Bq)
1	Cs-134	5.19E+16
2	Cs-137	4.98E+16
3	Te-131m	1.61E+17
4	Te-132	1.86E+18
5	I-131	1.46E+18
6	I-132	1.94E+18
7	I-133	2.51E+18
8	I-134	2.50E+18
9	I-135	2.21E+18
10	Kr-83m	2.36E+15
11	Kr-85	2.24E+17
12	Kr-85m	4.04E+17
13	Kr-87	4.89E+17
14	Kr-88	2.52E+18
15	Kr-89	2.63E+18
16	Xe-131m	1.46E+18
17	Xe-133	1.94E+18
18	Xe-133m	2.51E+18
19	Xe-135	2.50E+18
20	Xe-135m	2.21E+18
21	Xe-137	5.19E+16
22	Xe-138	4.98E+16
23	Sr-89	6.31E+17
24	Sr-90	1.43E+16
25	Ce-141	1.98E+18
26	Ce-144	6.37E+17
27	Ba-140	1.91E+18
28	La-140	1.96E+18
29	Ru-103	2.22E+18
30	Ru-106	6.16E+17

For case with fission products release from sodium into cover gas nodalization scheme consists of 2 cells, one for sodium volume and one for cover gas, FIG. 49.

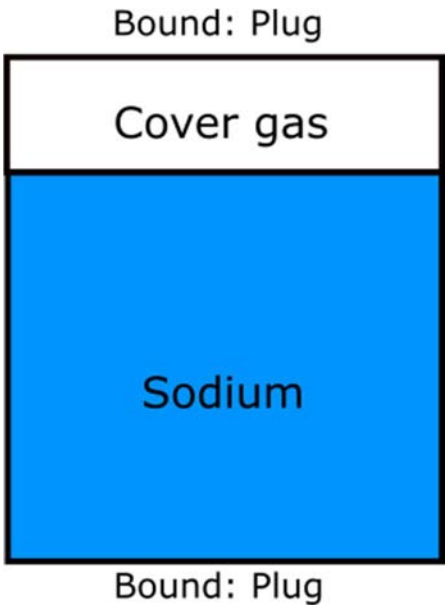

FIG. 49. Nodalization scheme for FP release from sodium into cover gas.

Sodium volume is 1437 m^3 and temperature is 900 K. Cover gas volume is 100 m^3 and temperature is 303 K. Interphase area between sodium and cover gas is 130 m^2.

All fission products are injected in atomic form, no chemistry is modelled. No decay chains are taken into consideration. Hence the masse of nuclides exponentially decreases due to decay. Initial activity for each fission product is result of fission product release from melted fuel.

4.2.1.2. *Nodalization Scheme of Additional Case*

For additional case the ULOF accident for PSFR is considered. Only part of PSFR core is modelled. The reactor core consists of various types of subassemblies such as fuel, blanket, and control rods, all SAs are arranged in a hexagonal layout at pitch 135 mm, with 131.3 mm wrench size and 3.2 mm wall thickness. Each FSA consists of 217 helium bonded pins of 6.6 mm diameter with spacer wire of 1.65 mm wound helically at pitch 150 mm and 7 shielding rods of 36 mm diameter. Each pin has 1000 mm column of MOX, 300 mm each of upper and lower depleted UO2, blanket columns and fission gas plena.

For calculation simple scheme of main vessel was chosen which includes only fuel (Zone 1 – Zone 7), blanket (Zone B) and CR (Zone CR, control rods) subassemblies (SA). SA distribution by zones is shown in FIG. 50, core nodalization scheme is shown in FIG. 51 and core thermohydraulic parameters in TABLE 23. Inlet sodium temperature is assumed to be constant and equal to 670 K. Pressure drop in each zone is 0.53 MPa. Outlet pressure boundary – 0.1 MPa.

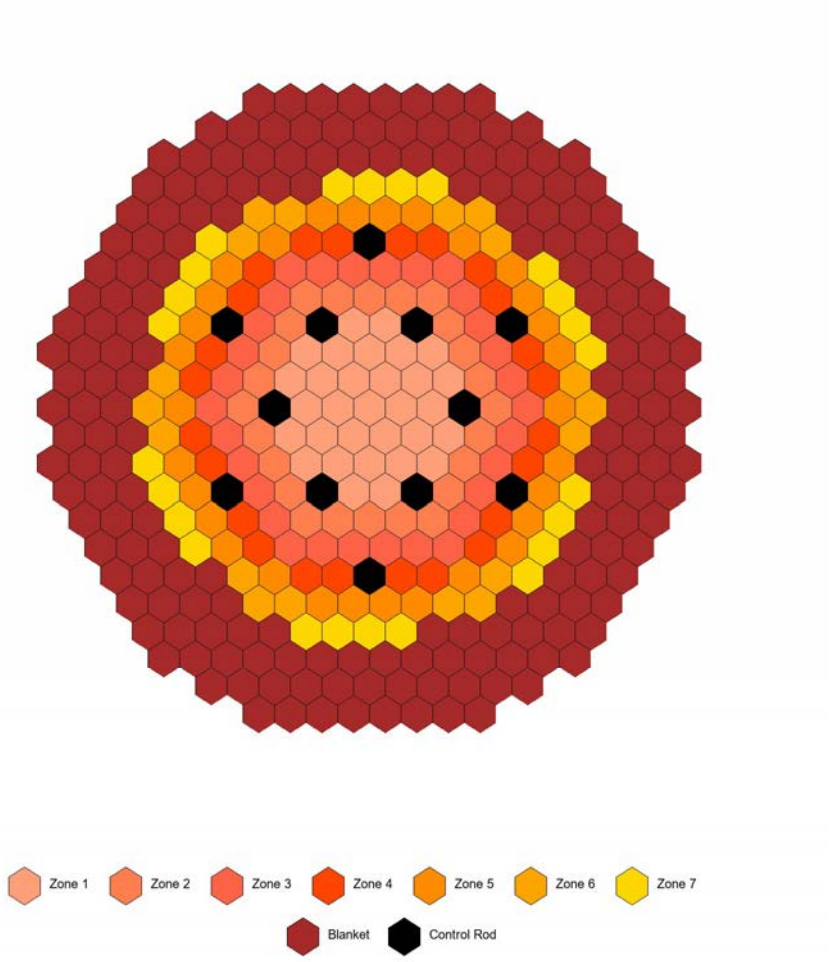

FIG. 50. PSFR core

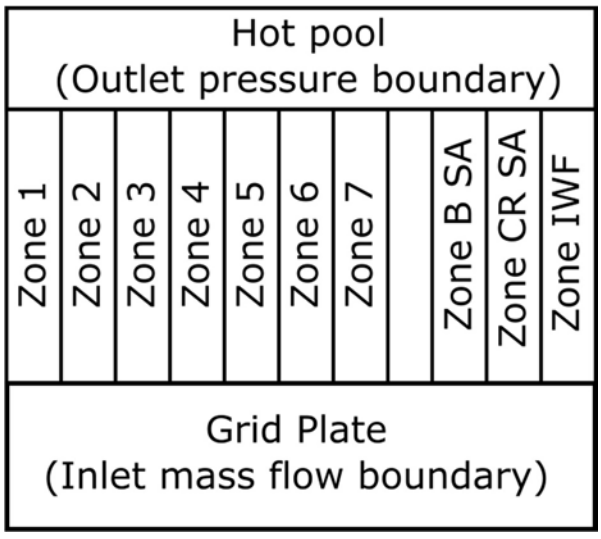

FIG. 51. Core nodalization scheme

Nodalization scheme for all subassemblies with geometry parameters is presented in TABLE 24. Inter-wrapper flow (IWF) is modelled as a single zone with total mass flowrate 30 kg/s.

TABLE 23. CORE THERMOHYDRAULIC PARAMETERS

Region	SA Type	Mass flow per SA (kg/s)	Total no. of SA in the zone	Power per pin (kWt)
Zone 1	Fuel	35.83	31	36.23309
Zone 2		31.4	24	32.81106
Zone 3		28.72	30	29.95392
Zone 4		34.07	24	33.89401
Zone 5		28.8	30	28.60829
Zone 6		25.3	18	23.30261
Zone 7		20.82	24	20.27649
Zone BLANKET	Blanket	3.39	186	1.534364
Zone CR	CSR&DS	2.55	12	0
Zone IWF	-	30.0 (for Zone)	-	0

TABLE 24. SUBASSEMBLY NODALIZATION SCHEME

Cell	Region	Cell height (m)	Area (m^2)	Hydraulic diameter, (m) or Rod diameter, (m) / Pitch, (m)
Channels: Zone 1 – Zone 7, Zone BLANKET, Zone CR,				
1	Coolant entry tube	0.2	7.853982 · 10-3	0.1
2		0.2	7.853982 · 10-3	0.1
3		0.2	7.853982 · 10-3	0.1
4		0.1	9.93136 · 10-3	0.11245
5		0.16	9.93136 · 10-3	0.11245
6	Bottom gas volume	0.15	5.615129 · 10-3	6.6·10-3/8.25·10-3
7		0.1	5.615129 · 10-3	6.6·10-3/8.25·10-3
8		0.1	5.615129 · 10-3	6.6·10-3/8.25·10-3
9		0.1	5.615129 · 10-3	6.6·10-3/8.25·10-3
10		0.1	5.615129 · 10-3	6.6·10-3/8.25·10-3
11		0.1	5.615129 · 10-3	6.6·10-3/8.25·10-3
12		0.1	5.615129 · 10-3	6.6·10-3/8.25·10-3
13	Bottom blanket	0.05	5.615129 · 10-3	6.6·10-3/8.25·10-3
14		0.05	5.615129 · 10-3	6.6·10-3/8.25·10-3
15		0.05	5.615129 · 10-3	6.6·10-3/8.25·10-3
16		0.05	5.615129 · 10-3	6.6·10-3/8.25·10-3
17		0.05	5.615129 · 10-3	6.6·10-3/8.25·10-3
18		0.05	5.615129 · 10-3	6.6·10-3/8.25·10-3
19	Fuel	0.05	5.615129 · 10-3	6.6·10-3/8.25·10-3
20		0.05	5.615129 · 10-3	6.6·10-3/8,25·10-3
21		0.05	5.615129 · 10-3	6.6·10-3/8.25·10-3
22		0.05	5.615129E-3	6.6·10-3/8.25E-3
23		0.05	5.615129E-3	6.6·10-3/8.25E-3
24		0.05	5.615129E-3	6.6·10-3/8.25E-3
25		0.05	5.615129E-3	6.6·10-3/8.25E-3
26		0.05	5.615129E-3	6.6·10-3/8.25E-3

Cell	Region	Cell height (m)	Area (m^2)	Hydraulic diameter, (m) or Rod diameter, (m) / Pitch, (m)
27		0.05	5.615129E-3	6.6·10-3/8.25E-3
28		0.05	5.615129E-3	6.6·10-3/8.25E-3
29		0.05	5.615129E-3	6.6·10-3/8.25E-3
30		0.05	5.615129E-3	6.6·10-3/8.25E-3
31		0.05	5.615129E-3	6.6·10-3/8.25E-3
32		0.05	5.615129E-3	6.6·10-3/8.25E-3
33		0.05	5.615129E-3	6.6·10-3/8.25E-3
34		0.05	5.615129E-3	6.6·10-3/8.25E-3
35		0.05	5.615129E-3	6.6·10-3/8.25E-3
36		0.05	5.615129E-3	6.6·10-3/8.25E-3
37		0.05	5.615129E-3	6.6·10-3/8.25E-3
38		0.05	5.615129E-3	6.6·10-3/8.25E-3
39	Top blanket	0.05	5.615129E-3	6.6·10-3/8.25E-3
40		0.05	5.615129E-3	6.6·10-3/8.25E-3
41		0.05	5.615129E-3	6.6·10-3/8.25E-3
42		0.05	5.615129E-3	6.6·10-3/8.25E-3
43		0.05	5.615129E-3	6.6·10-3/8.25E-3
44		0.05	5.615129E-3	6.6·10-3/8.25E-3
45	Top gas volume	0.1	5.615129E-3	6.6·10-3/8.25E-3
46		0.065	5.615129E-3	6.6·10-3/8.25E-3
47		0.065	5.615129E-3	6.6·10-3/8.25E-3
48	Subassembly	0.045	6.384871E-3	0.0208597
49	Absorbing rod	0.16	6.384871E-3	36E-3/37.65E-3
50		0.2	6.384871E-3	36E-3/37.65E-3
51		0.2	6.384871E-3	36E-3/37.65E-3
52		0.2	6.384871E-3	36E-3/37.65E-3
53		0.1	6.384871E-3	36E-3/37.65E-3
54	Head	0.0775	11.594244E-3	0.1215
55		0.0775	11.594244E-3	0.1215

Fuel pin and absorbing rod are modelled in r-z geometry. Nodalization schemes for fuel pin and for absorbing rod are shown in FIG. 52b.

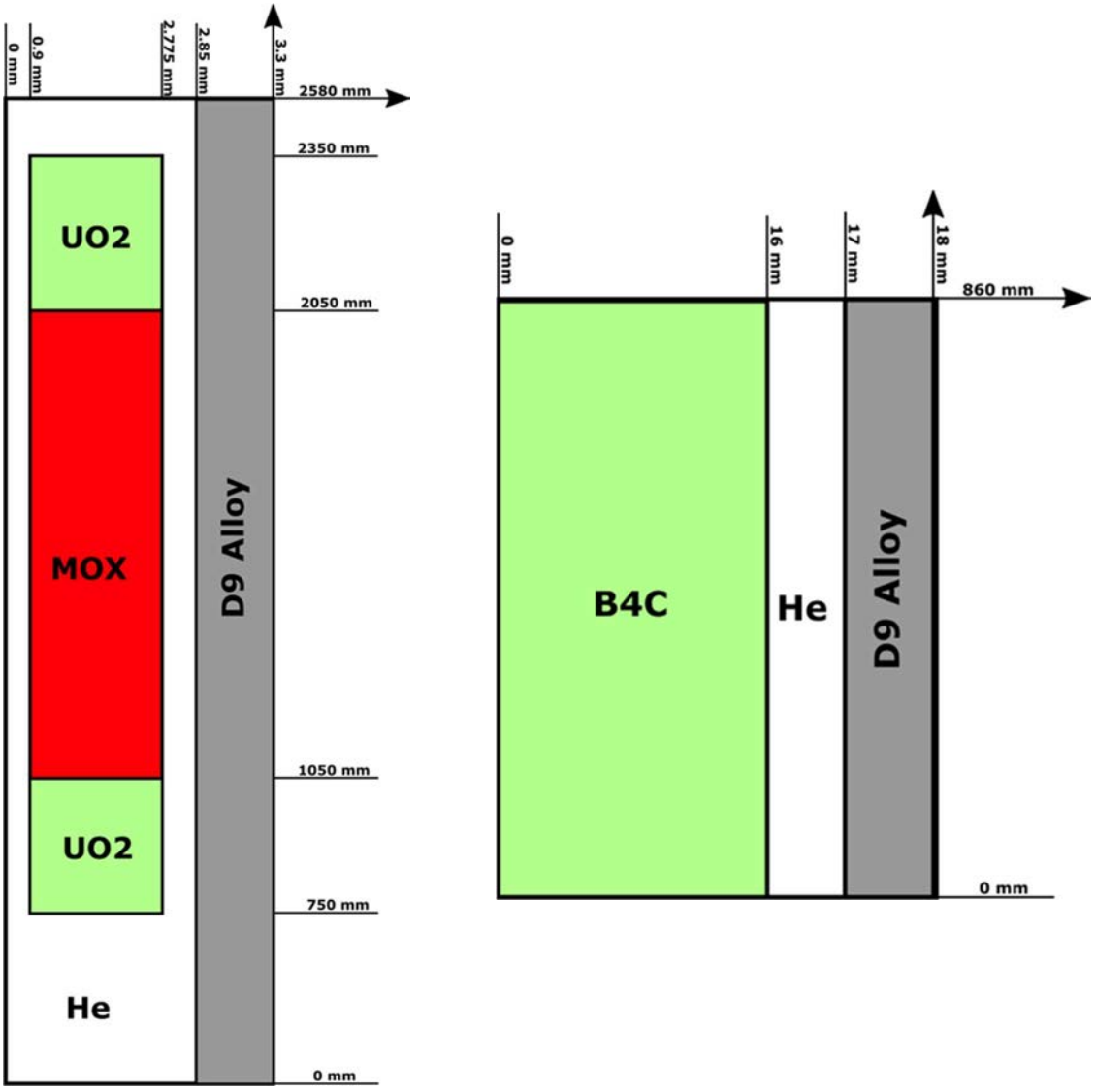

a) Fuel pin nodalization scheme. b) Absorbing rod nodalization scheme.

FIG. 52. Fuel pin and absorbing rod nodalization schemes.

The linear power distribution for fuel pin along its length is shown in FIG. 53.

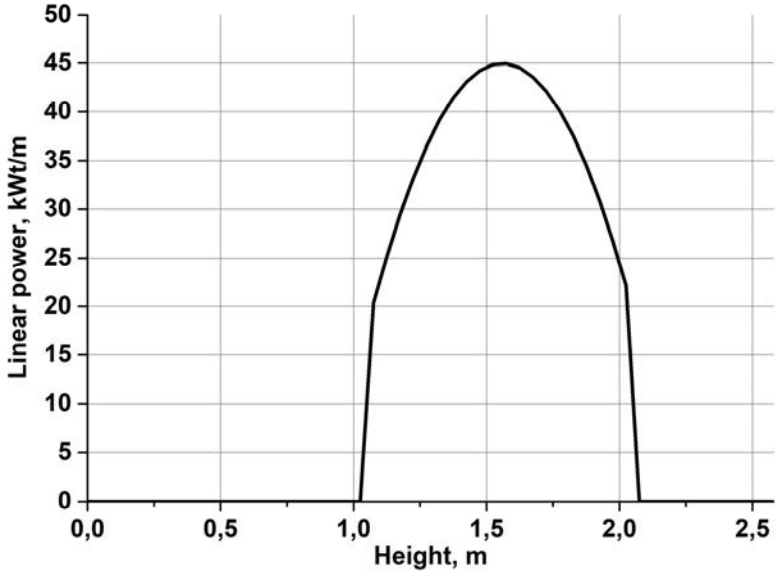

FIG. 53. Linear power distribution.

4.2.2. **Results**

4.2.2.1. *General case*

Results for volatile fission products release from melted fuel are presented in FIG. 54. It can be concluded that release lasts less than one minute for volatile fission products.

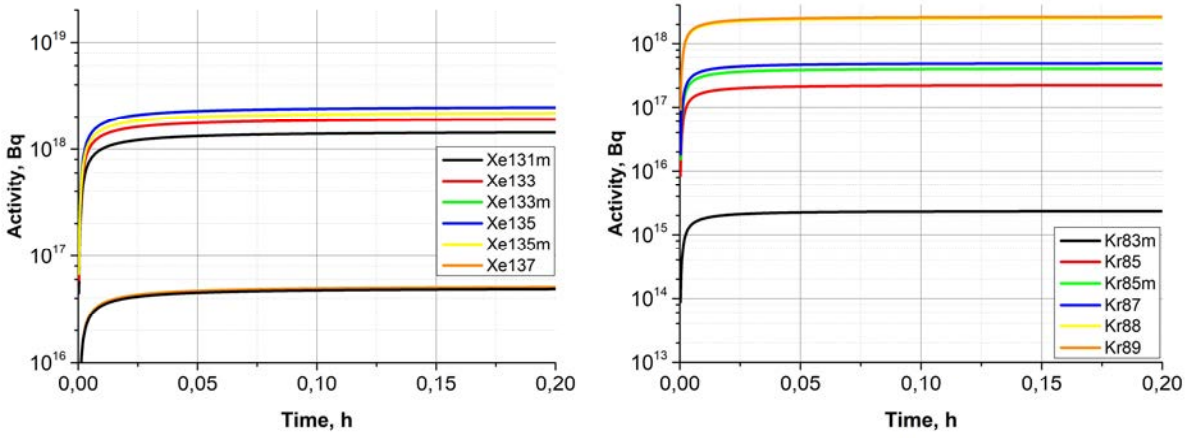

a) Xenon b) Krypton

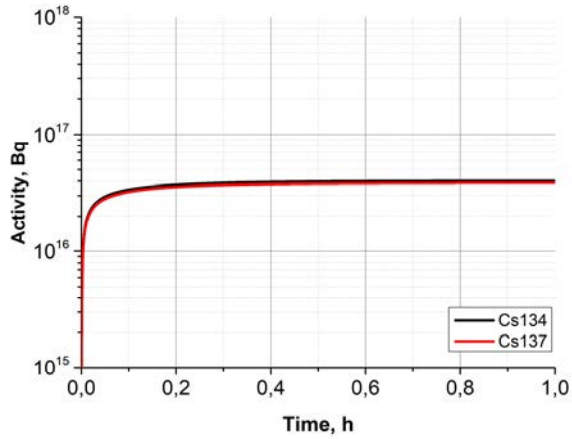

c) Caesium

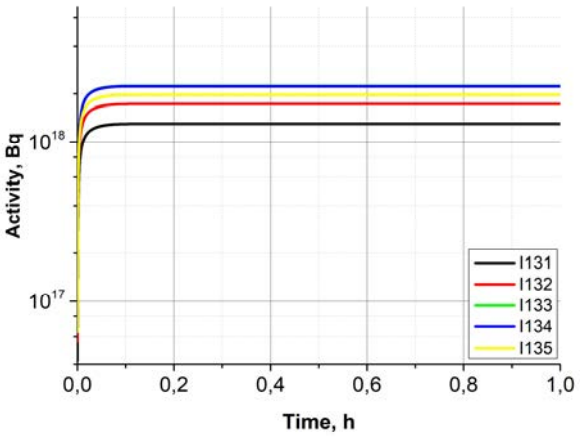

d) Iodine

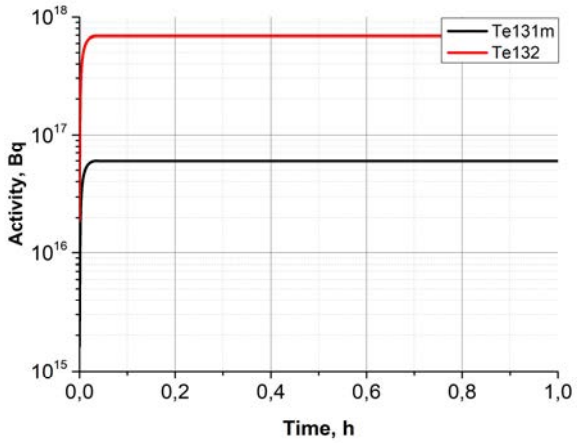

e) Tellurium

FIG. 54. Volatile FP activity released from melted fuel.

Results for non-volatile fission products release are presented in FIG. 55. It can be concluded that release lasts for about 10 minutes for no-volatile fission products, except strontium which lasts 20 hours.

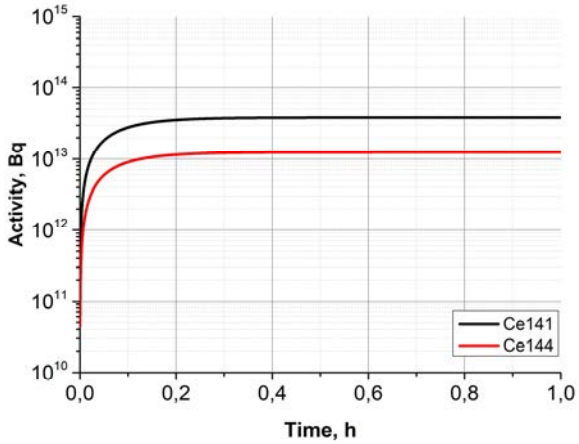

a) Cerium

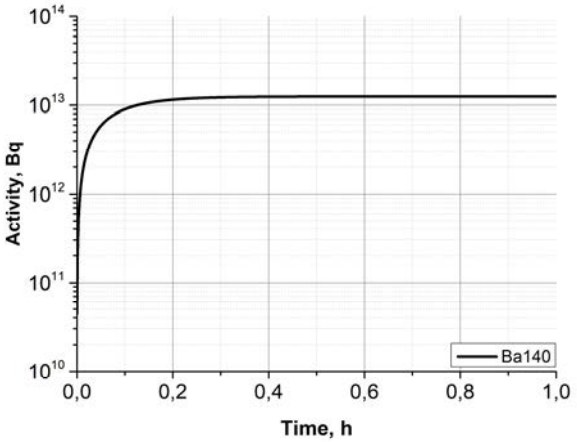

b) Barium

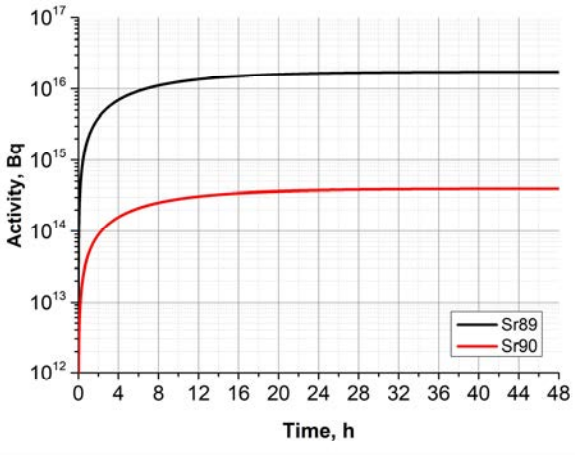

c) Strontium

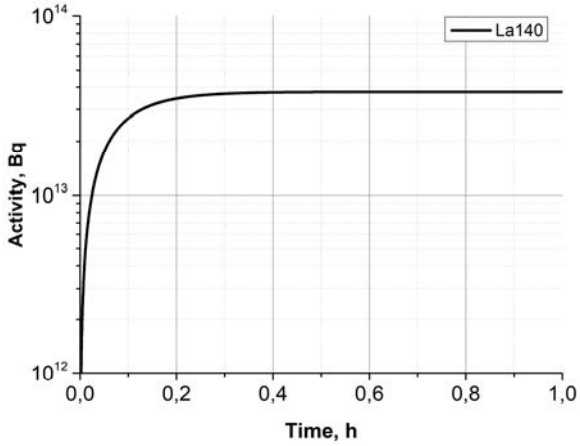

d) Lanthanum

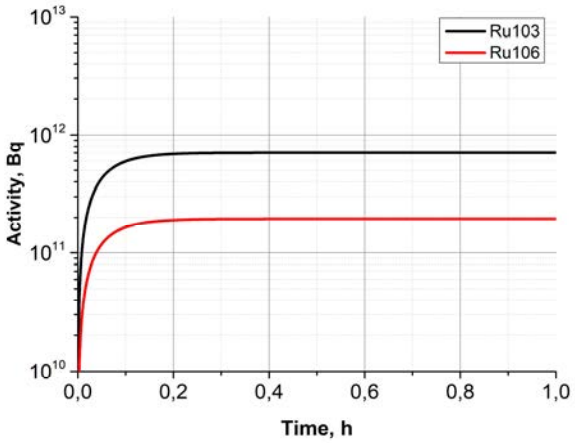

e) Ruthenium

FIG. 55. Non-volatile FP activity released from melted fuel.

The initial FP activity in sodium is presented in TABLE 25 for calculation of RN release from coolant into cover gas.

TABLE 25. FISSION PRODUCTS ACTIVITY IN SODIUM

No.	Radionuclide	Activity in sodium (Bq)
1	Cs-134	4.02282E+16
2	Cs-137	3.86011E+16
3	Te-131m	1.66060E+16
4	Te-132	1.91894E+17
5	I-131	1.14714E+18
6	I-132	1.52429E+18
7	I-133	1.97216E+18
8	I-134	1.96431E+18
9	I-135	1.73646E+18
10	Kr-83m	2.35959E+15
11	Kr-85	2.23961E+17

12	Kr-85m	4.0393E+17
13	Kr-87	4.88915E+17
14	Kr-88	2.51956E+18
15	Kr-89	2.62954E+18
16	Xe-131m	1.45983E+18
17	Xe-133	1.93977E+18
18	Xe-133m	2.50971E+18
19	Xe-135	2.49971E+18
20	Xe-135m	2.20971E+18
21	Xe-137	5.18939E+16
22	Xe-138	4.97942E+16
23	Sr-89	1.73881E+16
24	Sr-90	3.94056E+14
25	Ce-141	3.87485E+13
26	Ce-144	1.24661E+13
27	Ba-140	2.9297E+14
28	La-140	3.76048E+13
29	Ru-103	7.03476E+11
30	Ru-106	1.952E+11

Calculation results of RN activity for the case with fission products released from sodium into cover gas are presented in FIG. 56.

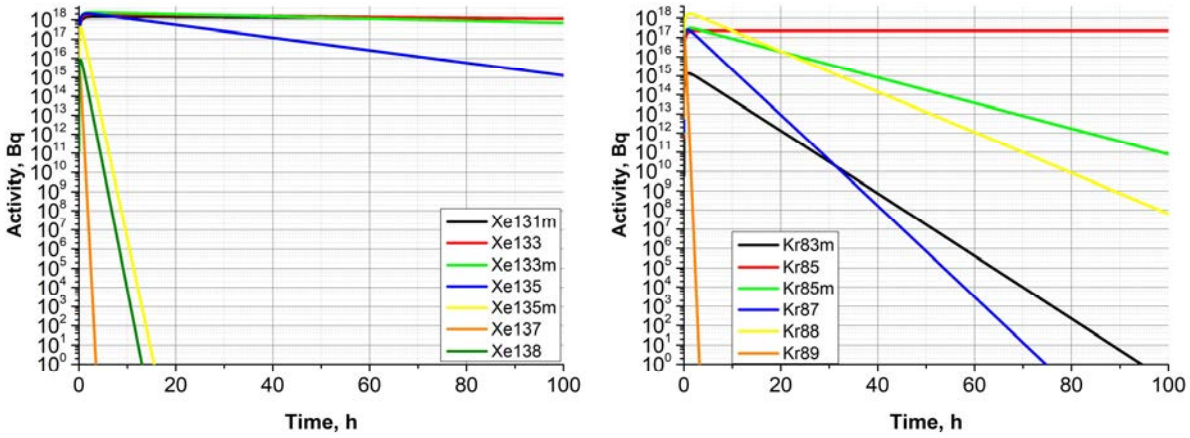

a) Xenon

b) Krypton

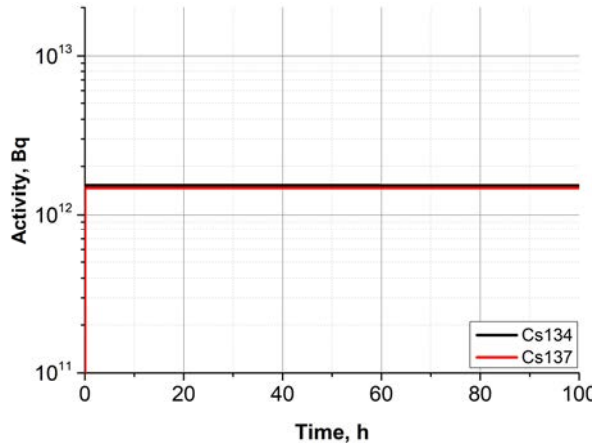

c) Caesium

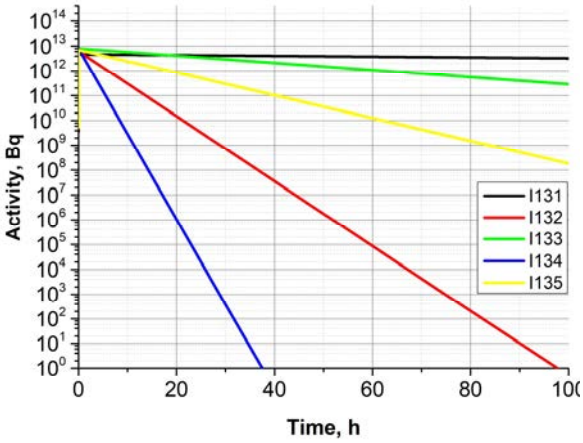

d) Iodine

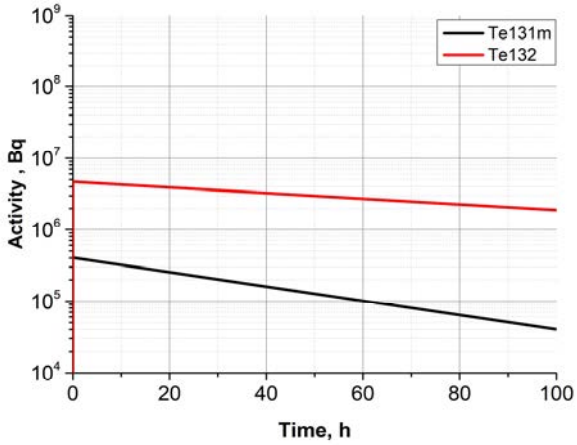

e) Tellurium

FIG. 56. FP activity in cover gas.

The fraction of fission products in melted fuel, sodium and cover gas are presented in TABLE 26.

TABLE 26. FISSION PRODUCTS FRACTION RELATED TO INITIAL CORE INVENTORY

Radionuclide	Melted fuel	Sodium	Cover gas containment
Cs-134	2.248902E-01	7.750804E-01	2.937727E-05
Cs-137	2.248775E-01	7.750931E-01	2.937898E-05
Te-131m	8.968571E-01	1.031429E-01	2.517406E-12
Te-132	8.968312E-01	1.031688E-01	2.518048E-12
I-131	2.142877E-01	7.857092E-01	3.173615E-06
I-132	2.142835E-01	7.857133E-01	3.173681E-06
I-133	2.142789E-01	7.857179E-01	3.173635E-06
I-134	2.142760E-01	7.857208E-01	3.173696E-06
I-135	2.142715E-01	7.857253E-01	3.173758E-06
Kr-83m	1.737288E-04	0.000000E+00	9.998263E-01
Kr-85	1.741071E-04	0.000000E+00	9.998259E-01

Kr-85m	1.732673E-04	0.000000E+00	9.998267E-01
Kr-87	1.738241E-04	0.000000E+00	9.998262E-01
Kr-88	1.746032E-04	0.000000E+00	9.998254E-01
Kr-89	1.749049E-04	0.000000E+00	9.998251E-01
Xe-131m	1.164384E-04	0.000000E+00	9.998836E-01
Xe-133	1.185567E-04	0.000000E+00	9.998814E-01
Xe-133m	1.155378E-04	0.000000E+00	9.998845E-01
Xe-135	1.160000E-04	0.000000E+00	9.998840E-01
Xe-135m	1.176471E-04	0.000000E+00	9.998824E-01
Xe-137	1.175337E-04	0.000000E+00	9.998825E-01
Xe-138	1.164659E-04	0.000000E+00	9.998835E-01
Sr-89	9.724436E-01	2.755642E-02	9.974309E-10
Sr-90	9.724436E-01	2.755636E-02	9.974782E-10
Ce-141	9.999804E-01	1.956995E-05	-
Ce-144	9.999804E-01	1.957002E-05	-
Ba-140	9.998466E-01	1.533874E-04	-
La-140	9.999808E-01	1.918612E-05	-
Ru-103	9.999997E-01	3.168811E-07	-
Ru-106	9.999997E-01	3.168831E-07	-

4.2.2.2. *Additional case*

The temperature rise in each Zone was chosen as the main parameter for comparison of calculation results in the steady state, and is presented in TABLE 27. Zones 1-7 are fissile subassemblies while 'Total' includes all fissile, blanket and CR subassemblies, as well as inter-wrapper flow (IWF).

TABLE 27. CORE PARAMETERS

Region	**Designed temperature rise (K)**	**EUCLID/V2**
Zone 1	173.4	170.4
Zone 2	179.1	175.6
Zone 3	179.1	174.7
Zone 4	170.6	167.4
Zone 5	179.3	167.2
Zone 6	157.9	155.2
Zone 7	167.0	163.3
Total:	150	151.7

Sodium boiling started in channel "Zone 1" 23.65 seconds after flow coast down. 5 seconds later boiling started in other zones. TABLE 28 describes the CDA main event timings.

TABLE 28. TIMING OF MAIN EVENTS THROUGH CDA

Event	**Time (s)**
Start of stable sodium boiling in Zone 1	23.65
Start of stable sodium boiling in Zone 2	28.08
Start of stable sodium boiling in Zone 3	28.25
Start of stable sodium boiling in Zone 5	28.75

Start of stable sodium boiling in Zone 6	28.78
Start of stable sodium boiling in Zone 7	28.41
Start of clad melting in Zone 1	26.5
Cladding melting and FP release in Zone 1	27.75

After cladding melting began in Zone 1 at 27.75s, it can be concluded that all FP from the fuel pin gas gap in this zone were released into coolant.

Calculation results for sodium mass flow rate and temperature and cladding temperature are shown in from FIG. 57 to FIG. 61.

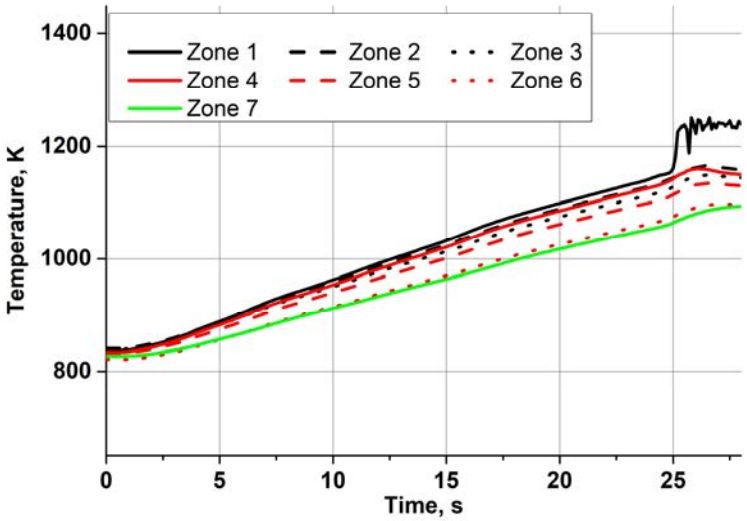

FIG. 57. Outlet sodium temperature per zone.

The onset of sodium boiling was first detected in Zone 1. Shortly after, local boiling started in Zone 2 and Zone 4 but stopped after increasing in flow rate, due flow reverse in Zone 1.

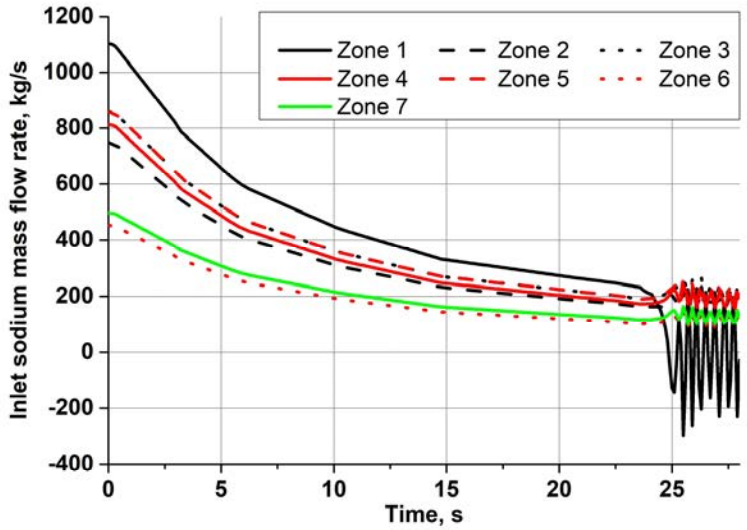

FIG. 58. Inlet sodium mass flow rate per zone.

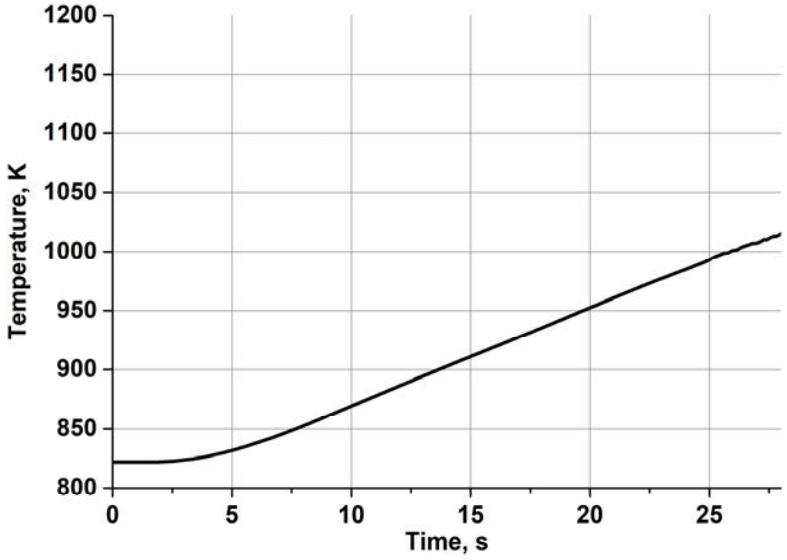

FIG. 59. Core outlet sodium temperature.

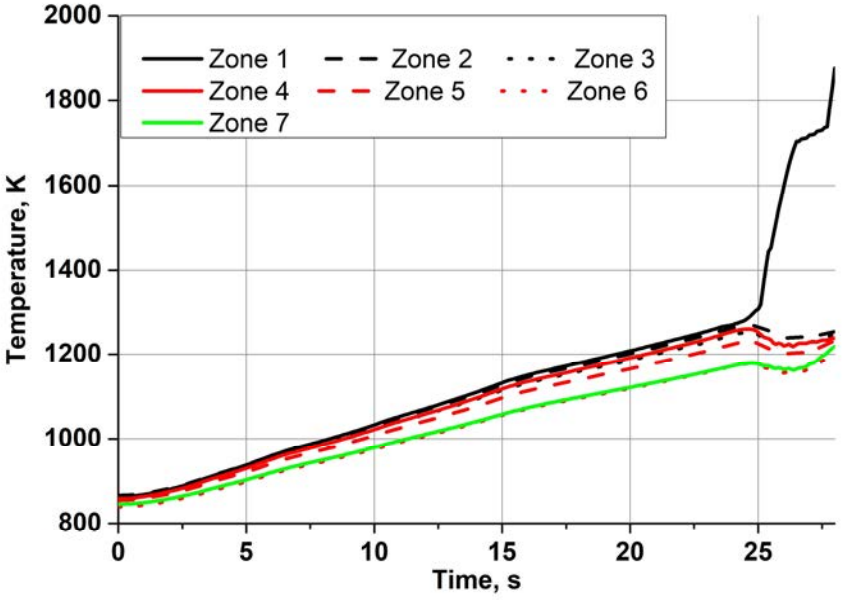

FIG. 60. Maximum clad temperature per zone.

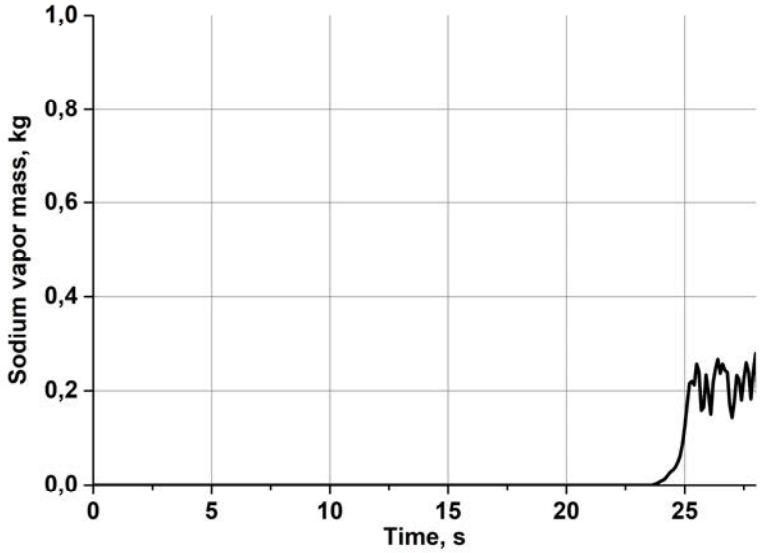

FIG. 61. Sodium vapor mass.

Clad melting and relocation in Zone 1 after the start of melting are shown in FIG. 62. Rectangles with color from yellow to pink define clad cells with liquid fraction from more than 0.0 to 1.0, respectively.

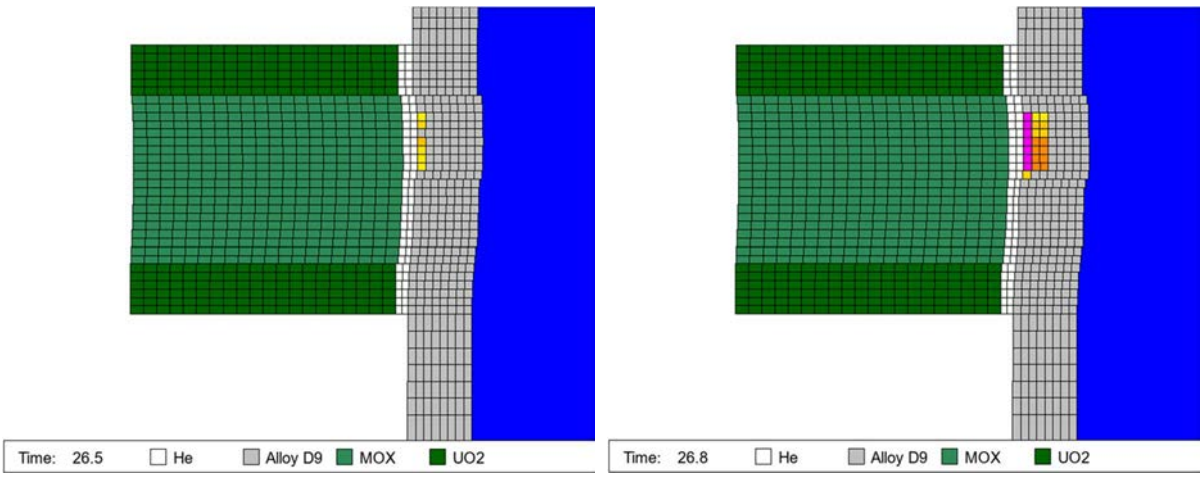

a) 26.5 second

b) 26.8 second

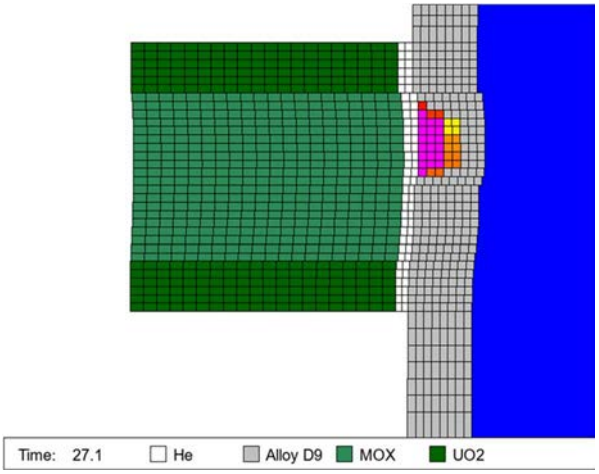

c) 27.1 second

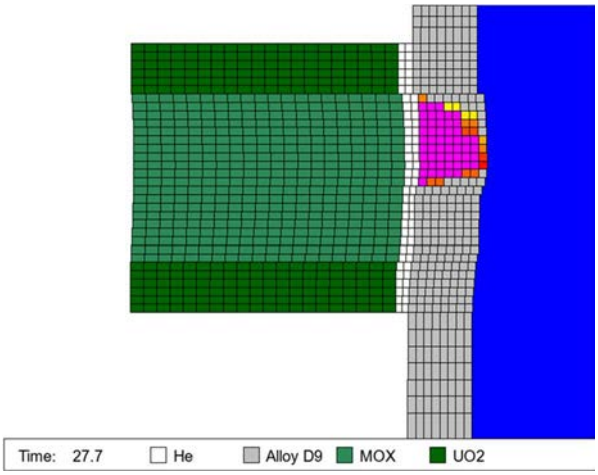

d) 27.7 second

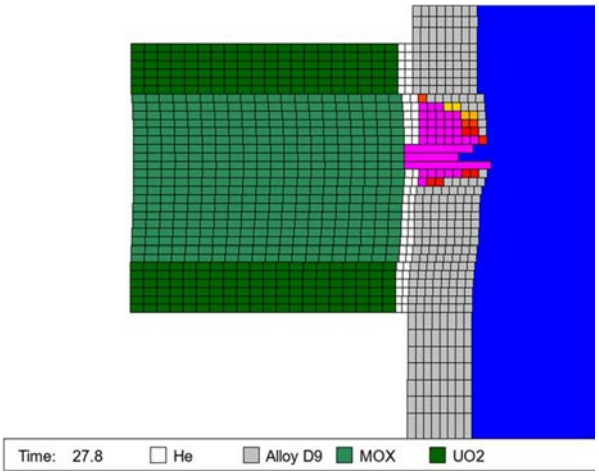

e) 27.8

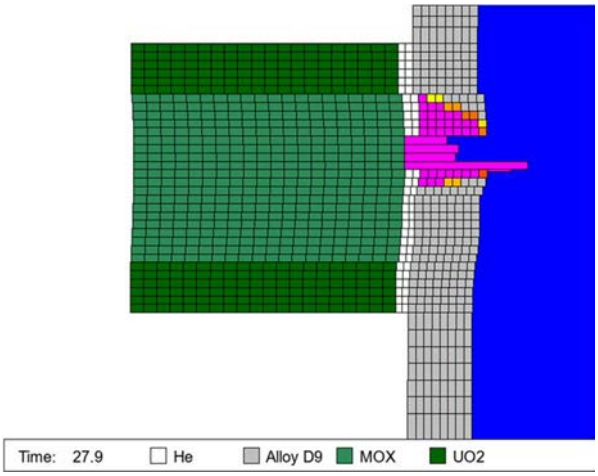

f) 27.9

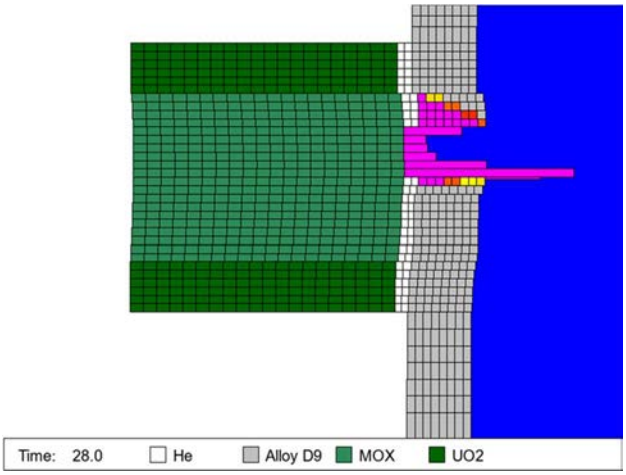

g) 28.0 second

FIG. 62. Fuel pin map in Zone 1.

4.2.3. Summary

Calculation results of FP release show that 100% of xenon and krypton, about 3.2E-4% of iodine, 2.9E-3% of caesium, 2.5E-10% of tellurium, about 1.E-8% of strontium are released into cover gas. FP release from melted fuel into sodium lasted about one minute for volatile fission products and about 10 minutes for non-volatile, except strontium which lasted 20 hours.

4.3. SIMULATION EXERCIE USING SIMMER-IV CODE (JAEA, JAPAN)

4.3.1. Description of the Methods and Models

In this analysis, material distribution within the reactor vessel and mechanical energy released during Post Disassembly Expansion (PDE) phase after power excursion due to energetics are calculated using SIMMER-IV [19]. These results provide basic information for in-vessel source term evaluation. Initial conditions of this calculation are described in Section 2.3.1.

A conceptual overall framework of SIMMER-IV is shown in FIG. 63 and FIG. 64. The SIMMER-IV code models the five basic LMFR core materials: fuel, steel, sodium, control material and fission gas. A material can exist as different physical states, for example fuel needs to be represented by fabricated pin fuel, molten liquid fuel, a crust refrozen on structure, solid particles, and fuel vapor. Thus, the material mass distributions are modelled by 38 density components in the current version of SIMMER-IV. The energy distributions are modelled by only 23 energy components since some density components are assigned to the same energy component. For example, a mixture of different vapor components is defined by a single energy. The structure field components, which consist of fuel pins and can walls, are immobile. Both simple and detailed fuel-pin model is provided, where the fuel pellet is represented by two or several radial temperature nodes, respectively. The mobile components, which include liquids, solid particles, and vapours, are assigned to one of six velocity fields, such that the relative motions of different fluid components can be simulated. Although SIMMER-IV is tailored to LMFR materials, the thermophysical properties and equation-of-state (EOS) functions are sufficiently flexible for non-LMFR materials to be modelled as well.

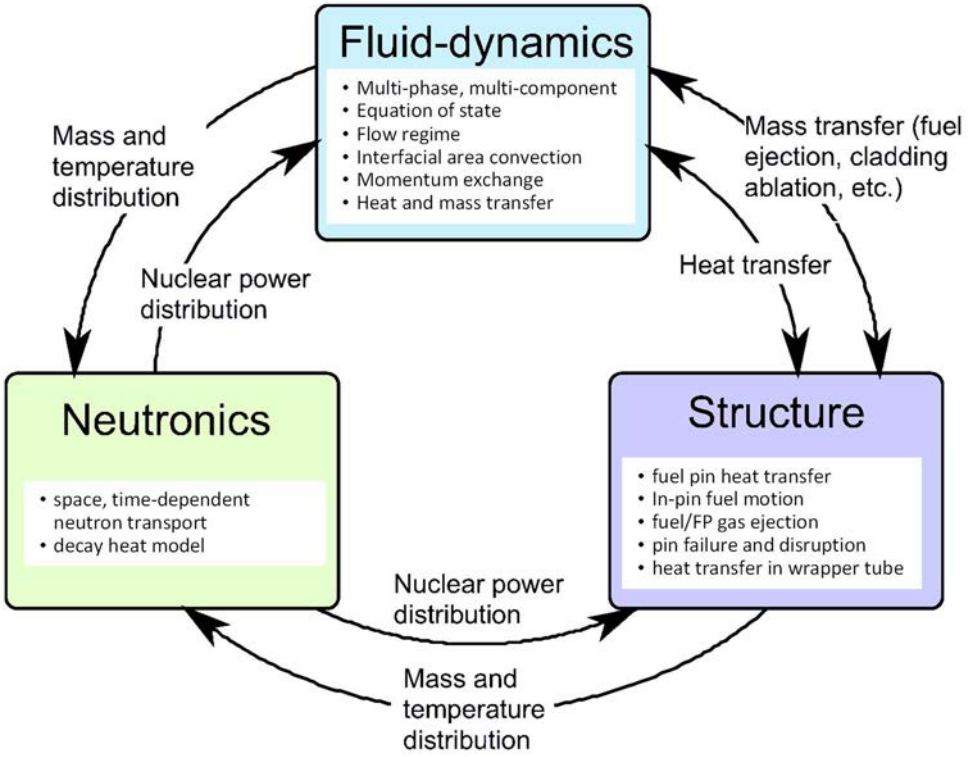

FIG. 63. Overall framework of SIMMER-IV code.

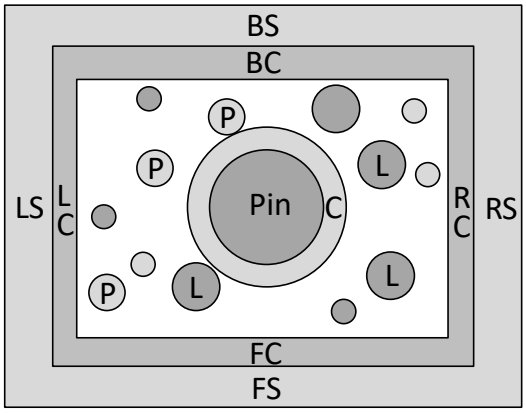

Pin : fuel pin
C : cladding
RS : right can wall
RC : fuel crust on RS
LS : left can wall
LC : fuel crust on LS
BS : back can wall
BC : fuel crust on BS
FS : front can wall
FC : fuel crust on FS
P : solid particles
L : liquids

Material distribution in a subassembly

- 3-dimensional (x-y-z or r-θ-z)
- 6-velocity fields
- Flow regime map for multi-phase flow
- Multi-components
  - 5 material components (fuel, steel, sodium, control and FP gas)
  - 38 density components (20 structures, 13 liquids, and 5 for vapor)
  - 23 energy components (15 structures, 7 liquids, and vapor mixture)

FIG. 64. Multi-phase, multi-component fluid-dynamics model in SIMMER-IV.

Fluid-Dynamics Model

Momentum and energy conservation equations use six velocity fields at the maximum. The six-velocity-field formulation and the fluid convection solution algorithm are based on the time-factorization approach [20] which has also been applied and tested for the former AFDM code [21]. In this approach, intra-cell interfacial area source terms, momentum exchange functions and heat and mass transfer are determined separately from inter-cell fluid convection. A semi-implicit procedure is used to solve inter-cell convection on a Eulerian staggered mesh. Fluid-convection is treated in an explicit scheme, pressure propagation within an implicit one. A higher-order differencing scheme [20] is also implemented to improve the precision by minimizing numerical diffusion, for example at fluid interfaces. Higher order differencing proved to be necessary especially in treating interaction type phenomena as fuel coolant interactions. This solution procedure of separating intra-cell transfers from fluid convection is believed to be the most practical for complex multi-component systems like SIMMER-IV. This approach had far-reaching implications for the code development. Firstly, new models could be easily implemented and added, secondly, computer running times could be kept at a very low level. This fluid mechanics numerical method has been successfully evaluated in the general context of multi-D multiphase flows simulation, using defined criteria [22].

The constitutive models describe intra-cell transfer of mass, momentum, and energy at the fluid interfaces. In SIMMER-IV, seven fluid energy components (liquid fuel, steel, sodium; fuel, steel and control particles; and vapor mixture) can yield 21 binary-contact modes, and each fluid component can interact with five kinds of structure surfaces (a fuel pin and four can walls). In total, there are 56 contact interfaces among the fluid energy components and structure surfaces [19]. SIMMER-IV also has a model for convecting interfacial areas (IFAs) to take better account of highly transient flow [23]. The calculations of intra-cell heat and mass transfers include: structure configuration and heat and mass transfer due to structure breakup, multiple flow regime treatment and IFAs with source terms, momentum exchange functions for each flow regime, inter-cell heat transfer due to conduction, melting and freezing, vaporization and condensation, etc. In addition to the constitutive models, an EOS model is required to close and complete the fluid-dynamic conservation equations. The analytic EOS model in SIMMER-IV employs flexible thermodynamic functions [24] [25] [26] which can be readily adapted to non-LMFR materials.

Structure Model

The structure model represents the configuration, and time-dependent disintegration, of the fuel pins and subassembly can walls. Four can walls can be modelled, at the left, right, front, and back mesh-cell boundaries, each of which contains two temperature nodes. The presence of a can wall at a cell boundary prevents radial fluid convection and provides a surface where fuel can freeze or vapor can condense. The breakup of structure components is currently based on thermal conditions and simple temperature and wall thickness threshold for mechanical breakup. Both a simple fuel-pin model, where the fuel pellet is represented by two temperature nodes and a sophisticated model to calculate pin failure, fuel-pin radial heat conduction, fission-gas plena modelling, molten central cavity description.

Neutronics Model

The space-time-dependent neutron kinetics model in SIMMER-IV is based on an improved quasi-static method with a diffusion acceleration technique where the flux shape is calculated by a standard Sn neutron transport theory based on THREEDANT [27]. Since the changes in material number densities and temperatures are crucial, a cross-section model is included in the code to perform self-shielding operations to determine effective macroscopic cross sections

whenever the reactivity is updated. SIMMER can treat not only neutronic systems with but also without external source [28].

Analysis Condition

FIG. 65 shows the overview of the calculation geometry developed for SIMMER-IV analysis. Major structures in the reactor vessel were modelled in x-y-z three-dimensional meshing from the bottom of active fuel to the bottom of top shield in vertical direction. Each calculation mesh has approximately10 cm edge for x-y-z direction. Green part shown in FIG. 65, which includes radial blanket assemblies, radial shied assemblies, control plug, IHXs, pumps, is treated as rigid structure and is excluded from thermal-hydraulic calculation. The boundary of the calculation geometry as well as inner vessel is also treated as rigid structure.

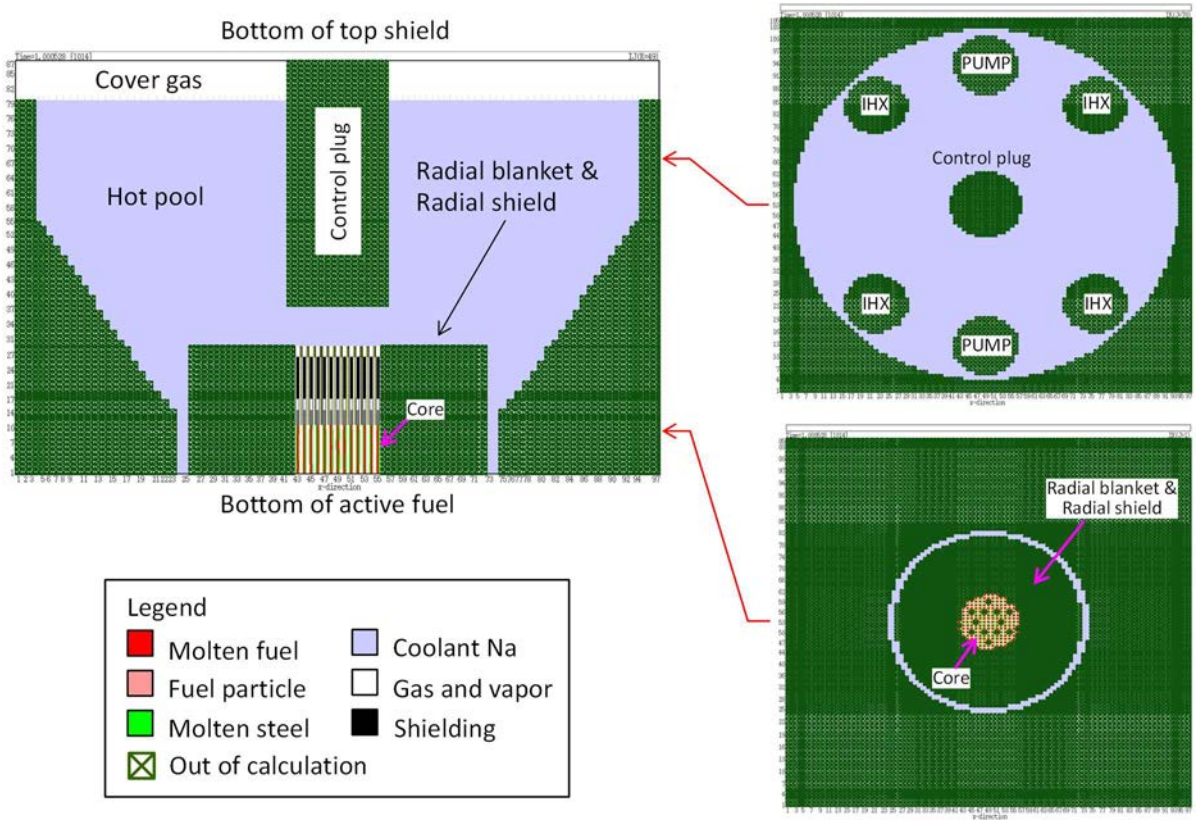

FIG. 65. Overview of the calculation geometry developed for SIMMER-IV analysis.

FIG. 66 shows the calculation geometry of core region. Basically, one mesh is allocated for one fuel sub-assembly. Mass of fuel, steel and fission gas is homogeneously distributed in the core region, assuming all the fuel, cladding, and sub-assembly tubes are completely molten. In the above core region, sub-assembly tube, pin structure including upper axial blanket, Na plenum and upper axial shielding are modelled, and only FP gas is filled in the coolant channel. Radial blanket sub-assemblies, radial shield sub-assemblies and control rods are excluded from thermal-hydraulic calculation.

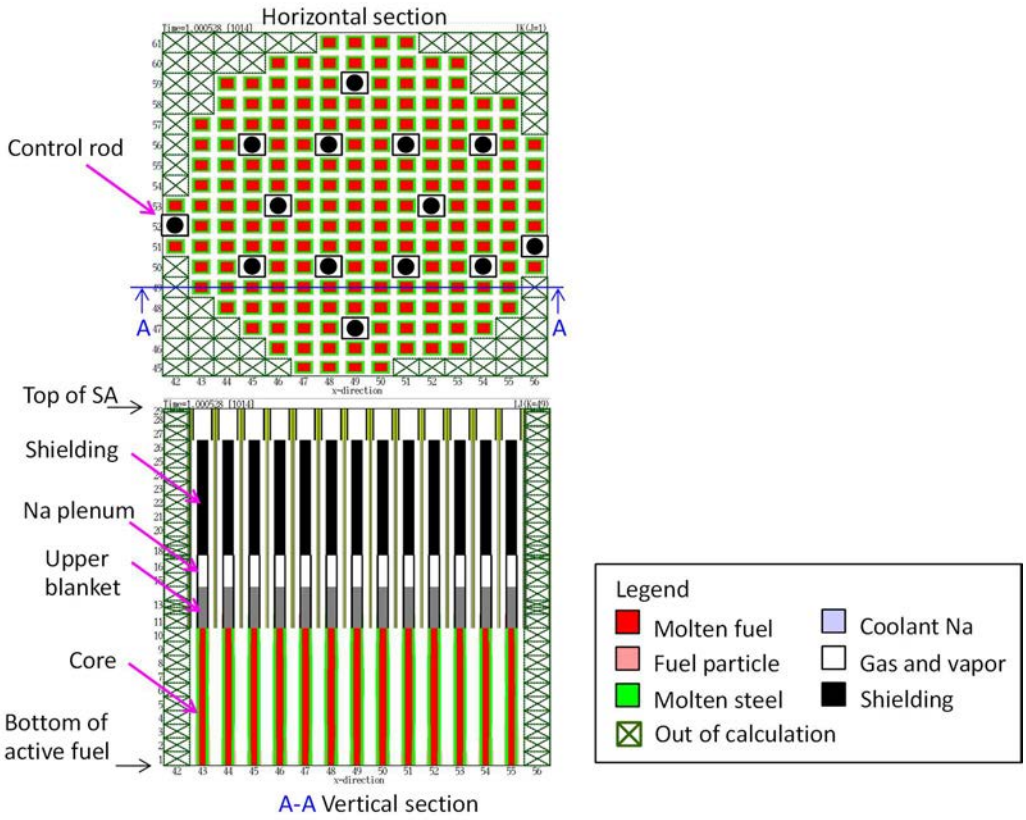

FIG. 66. Calculation geometry of core region.

Initial conditions are provided in Section 2.2.2 and re-arranged in TABLE 29 to TABLE 31. These values are reallocated to each fuel sub-assembly in SIMMER-IV geometry. Red values in TABLE 29 are assumed to be melting point of fuel although they are missing in Section 2.2.2. With these temperature distribution, core averaged fuel temperature becomes 3526 K. Pressure distribution listed in Section 2.2.2 was converted to fit the mesh size used in SIMMER-IV by using adiabatic transition equation, $PV^{\gamma} = \text{constant}$, and shown in TABLE 30. Coolant temperature as well as cover gas temperature is set to 820 K. Cover gas pressure of 1.01325 Pa is given. Temperature of structures in the above core region is given 820 K, and the pressure of the FP gas in that region is set to 102,000 Pa considering the gravity head of hot pool sodium.

TABLE 29. FUEL TEMPERATURE DISTRIBUTION IN PROVIDED MESH AT THE START OF THE PDE PHASE

		Radial mesh number						
		1	2	3	4	5	6	7
Axial mesh number	10	3433	3353	3228	3033	3213	3027	3023
	9	4693	3661	3543	3451	3560	3154	3026
	8	5047	4639	3780	3666	3798	3495	3030
	7	5219	4892	3946	3821	3968	3666	3033
	6	5217	4873	4041	3904	4062	3705	3057
	5	4889	4228	4050	3911	4068	3604	3032
	4	4232	4132	3973	3727	3975	3401	3030
	3	4043	3884	3631	3409	3631	3104	3025
	2	3488	3366	3158	3032	3143	3027	3023
	1	3030	3029	3026	3023	3025	3023	3023

Fuel temperature: K

TABLE 30. FUEL VAPOR PRESSURE DISTRIBUTION IN PROVIDED MESHAT THE START OF THE PDE PHASE

		Radial mesh number						
		1	2	3	4	5	6	7
Axial mesh number	10	0.96	0.81	0.02	0.01	0.01	0	0
	9	3.08	1.77	0.23	0.04	0.06	0.01	0
	8	7.09	2.74	0.48	0.11	0.18	0.05	0
	7	6.06	4.06	0.53	0.21	0.37	0.10	0.01
	6	9.61	3.52	0.50	0.29	0.53	0.12	0.01
	5	15.11	4.73	0.79	0.29	0.54	0.08	0.01
	4	7.48	2.43	0.37	0.15	0.38	0.03	0
	3	1.29	0.38	0.10	0.05	0.09	0.01	0
	2	0.09	0.05	0.01	0.01	0.01	0	0
	1	0	0	0	0	0	0	0

Fuel vapor pressure: MPa

TABLE 31. NUMBER OF SUB-ASSEMBLIES ALLOCATED IN PROVIDED MESH

Radial mesh number							Total
1	2	3	4	5	6	7	
1	30	24	30	30	42	24	181

Two parameters were selected for the sensitivity study which are considered to have relatively high importance in the evaluation of mechanical energy release: molten steel temperature, and FP gas inventory allocated in the active core region. The former, molten steel temperature at the beginning of PDE phase, varies due to power transient history during preceding (transition) phase: the longer the transient duration in transition phase, the higher is the steel temperature. The latter, FP gas inventory in the active core region, varies depending on the time interval when the first pin failure occurs (with FP gas release from gas plenum in the pin) and when power excursion occurs: the longer the time interval, the less is the FP gas inventory in the active core region. TABLE 32 shows the calculation cases considering above mentioned parameters. In this context, in SIMMER-IV analysis, FP gas means noble gas produced by fission, Xe and Kr, and the molecular weight of it is represented by Xe.

TABLE 32. CALCULATION CASES CONSIDERING INITIAL STEEL TEMPERATURE AND FP GAS INVENTORY

Case name	**Initial steel temperature (K)**	**FP gas inventory (kg)**
Case 1	1800	61
Case 2	2200	61
Case 3	3000	61
Case 4	3000	10

Initial steel temperatures listed in TABLE 32 are determined from SIMMER-IV calculations in transition phase. FP gas inventory of 61 kg corresponds to the total amount of fission gas produced at the end of equilibrium cycle. This inventory includes both fission gas retained in the fuel matrix and released to the fission gas plenum within the pin. Within these cases, Case 3 is most pessimistic where higher steel temperature and greater FP gas inventory were

simultaneously assumed. Case 4 is more realistic but still has certain conservativeness regarding steel temperature.

FP gas inventory of 61 kg was calculated from Eq. (36) from [29]:

$$w_{fp} = N_{fis} f_{FP} \frac{1}{N_A} M_{FP} \frac{1}{1000} \tag{36}$$

where
w_{fp} is the Generated FP gas mass (kg);
N_{fis} is the Number of fission (-);
f_{FP} is the Molecular fraction of FP gas per fission (-);
N_A is the Avogadro number (-);
M_{FP} is the Molecular weight of FP gas (amu).

N_{fis} is obtained from power and operation time:

$$N_{fis} = \frac{Pt}{C_{eV} E_{fis}} \tag{37}$$

where
P is the Power (W);
t is the Operation time (s);
C_{eV} is the Unit conversion coefficient (J/eV);
E_{fis} is the Energy generated per fission (eV).

Here t is rewritten as t_{ave} for taking into account that the fuels with different burn up state at the End Of Equilibrium Cycle (EOEC) are mixed, and Eq (36) is re-written as follows:

$$w_{fp} = \frac{P t_{ave}}{C_{eV} E_{fis}} f_{FP} \frac{1}{N_A} M_{FP} \frac{1}{1000} \tag{38}$$

Where t_{ave} is the operation duration assuming that the burn-up states of all the core fuel are the same (s) and calculated using Eq. (39):

$$t_{ave} = \frac{1}{3} \cdot 3 \cdot t_{cycle} + \frac{1}{3} \cdot 2 \cdot t_{cycle} + \frac{1}{3} \cdot 1 \cdot t_{cycle} \tag{39}$$

Where t_{cycle} is the operation duration per cycle (s).

Values used in the calculation of FP gas mass are listed in TABLE 33.

TABLE 33. VALUES USED IN THE CALCULATION OF FP GAS MASS

ID	Value	Unit	Note
P	1.157E+9	W	Total power calculated from TABLE 2
t_{cycle}	1.56E+7	s	=180 x 24 x 60 x 60
C_{eV}	1.60E-19	J/eV	[29]
E_{fis}	1.97E+8	eV	[29]

f_{FP}	0.246	-	[29]
N_A	6.022E+23	-	
M_{FP}	131	Amu	[29]

Note that the material 'FP gas' in SIMMER-IV is treated as noble gas and noncondensing gas without vaporization and condensation: only fuel, steel, and sodium vapor are treated as condensable gas.

For this calculation, only fluid-dynamics and structure models of SIMMER-IV are utilized, because neutronics model is no more necessary for the material relocation calculation in PDE phase: it is necessary in transition phase of the CDA.

4.3.2. **Results**

Material distribution during the first 580 ms in case 4 is shown in FIG. 67. Typical calculation results of SIMMER-IV analysis in case 4 are plotted in FIG. 68 and FIG. 69, and listed below:

(1) Cover gas temperature (averaged in the cover gas region)
(2) Cover gas pressure (averaged in the cover gas region)
(3) Na temperature in hot pool (averaged in the hot pool)
(4) Na pressure in hot pool (averaged in the hot pool)
(5) Na vapor mass in cover gas
(6) Core averaged pressure
(7) Pressure at the lower surface of roof slab (averaged in the meshes along with a radius)
(8) CDA bubble and cover gas volume
(9) Surface pressure of CDA bubble (averaged at the surface of the CDA bubble)
(10) P-V relation of CDA bubble (plotted CDA bubble pressure (9) against volume (8) until at the end of the first two expansion of the CDA bubble)

Molten fuel and steel together with FP gas were ejected from core region to the hot pool through Upper Core Structure (UCS, which includes upper blanket and upper shielding). Then hot molten core materials come into mixing with the sodium at the lower surface of the control plug and this results in sodium vapor generation due to Fuel-Coolant Interaction (FCI). The pressure increase of the CDA bubble from 90 to 110 ms (FIG. 69) is caused by this sodium vapor generation. After 110 ms the pressure of the CDA bubble decreases with the increase of its volume. In this case (Case 4), CDA bubble expands until 270 ms when the maximum volume of it is attained, and sodium slug impacts on the lower surface of the shield plug (but it is relatively weak).

After the first slug impact, CDA bubble volume started to decrease, and at 430 ms it increased again due to subsequent FCI starting from around 380 ms and the second slug impact occurred at around 580 ms. This kind of volume expansion and contraction continued in a repetitive manner.

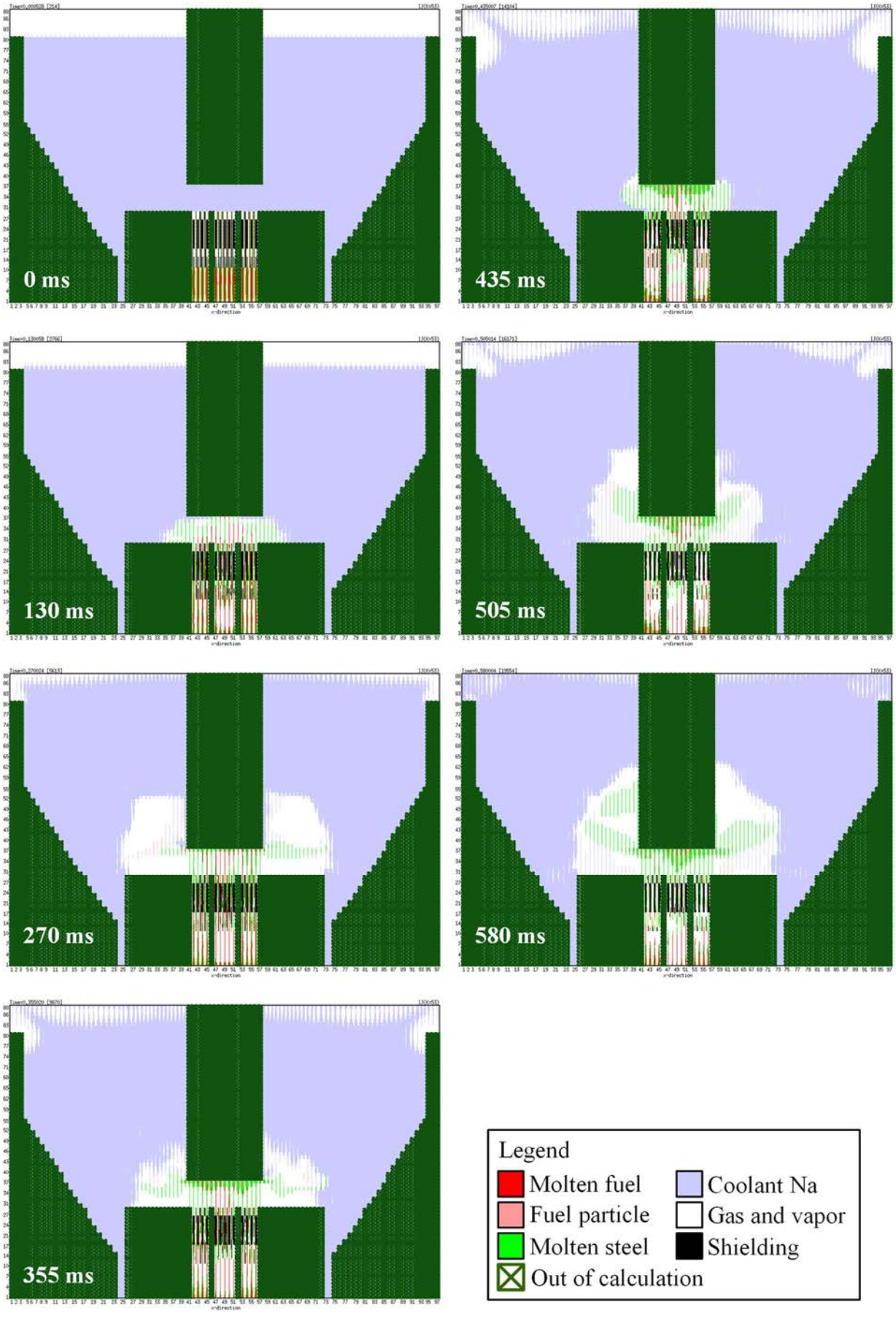

FIG. 67. Material distribution during first 1 s in case 4.

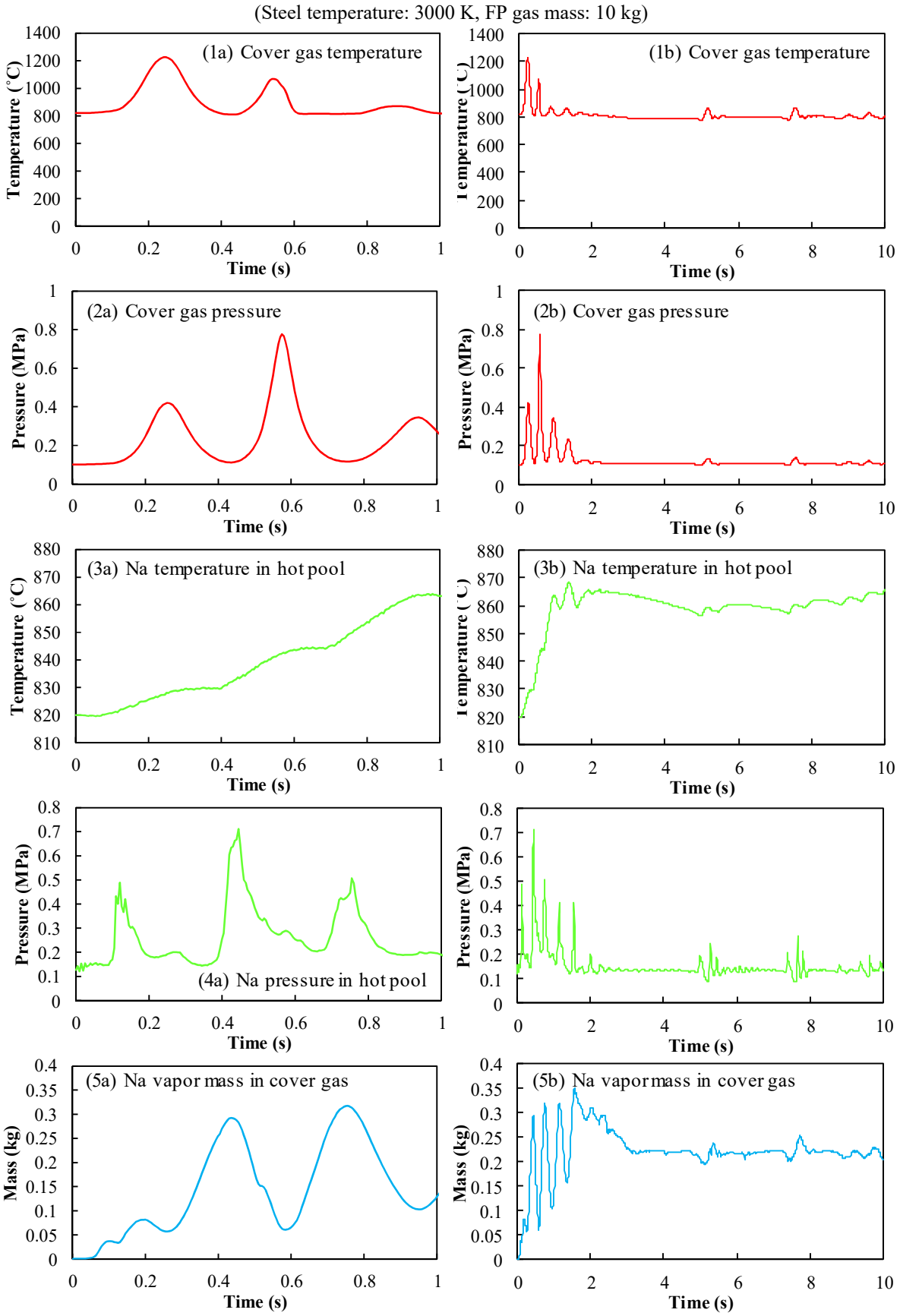

FIG. 68. Typical calculation results of SIMME-IV analysis in case 4.

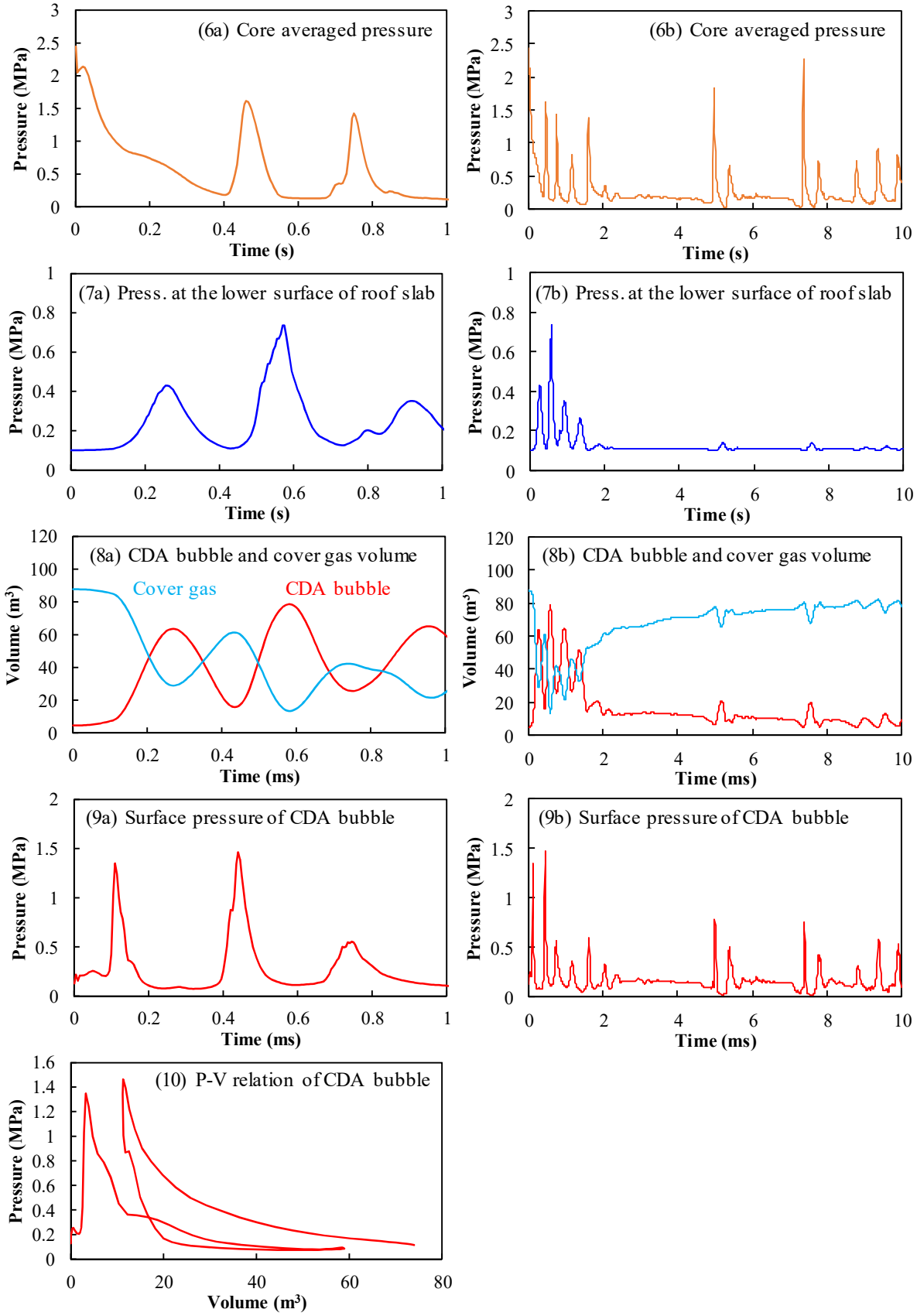

FIG. 69. Typical calculation results of SIMME-IV analysis in case 4 (cont'd).

(Steel temperature: 3000 K, FP gas mass: 10 kg)

Conversion ratio

FIG. 70 shows calculated mechanical energy in case 4. Total mechanical energy was obtained by summing up the cover gas compression energy, liquid sodium kinetic energy and liquid sodium potential energy [30]. Maximum mechanical energy is about 26 MJ at 540 ms. It is 40 ms earlier when cover gas is most significantly compressed and sodium slug impact under the shield plug occurrs.

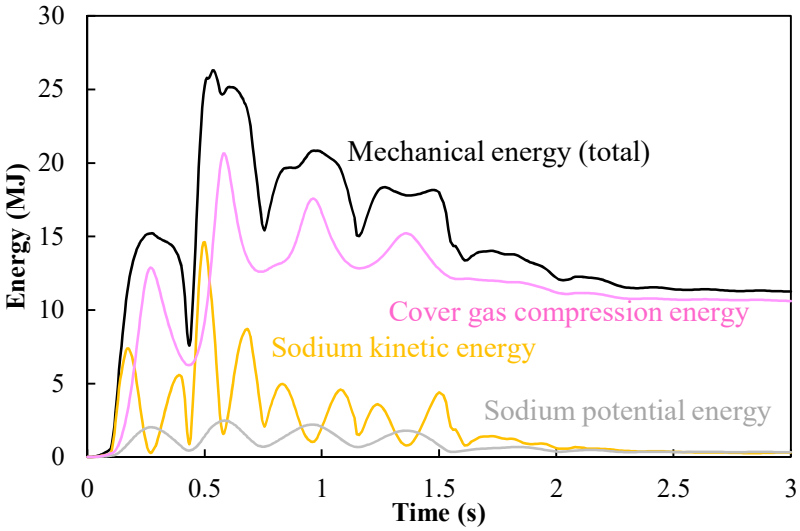

FIG. 70. Calculated mechanical energy in case 4.

In order to calculate conversion ratio from thermal energy mechanical energy, thermal energy which can be released from fuel is defined as ΔE_f. FIG. 71 illustrates the concept of the ΔE_f. This value corresponds to the difference between E_{f1}, averaged fuel energy at the maximum temperature at the beginning of PDE phase, and E_{f2}, averaged fuel energy at the boiling point of the sodium.

$$\Delta E_f = E_{f1} - E_{f2} \tag{40}$$

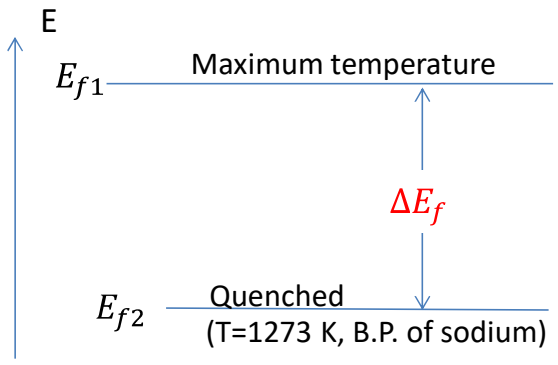

FIG. 71. The concept of the thermal energy which can be released from fuel, ΔE_f.

This definition of ΔE_f is based on the consideration if the temperature of fuel is higher than the saturation temperature of sodium, the fuel has certain potential to release mechanical work through sodium vapor generation. In the same manner, thermal energy which can be released from steel is also defined as ΔE_s.

$$\Delta E_s = E_{s1} - E_{s2} \tag{41}$$

Then, the total thermal energy which can be released from fuel and steel, ΔE_{therm}, is obtained by summing up ΔE_f and ΔE_s.

$$\Delta E_{therm} = \Delta E_f + \Delta E_s \tag{42}$$

The conversion ratio, R_{conv}, is obtained dividing mechanical energy, ΔE_{mec} , by thermal energy ΔE_{the} .

$$R_{conv} = \Delta E_{mech} / \Delta E_{therm} \tag{43}$$

E_{f1}, E_{f2}, E_{s1} and E_{s2} are obtained from averaged temperature using equation of state model implemented in SIMMER-IV [6] [7]. ΔE_{mech} is obtained from the result of SIMMER-IV calculation.

TABLE 34 shows comparison of the obtained conversion ratio for each parametric case. The contribution ratio of steel thermal energy to the total thermal energy amounts to about 35 % in case 4. Comparing Case 1 through Case 3, it is shown that the initial steel temperature affects to the mechanical energy. Comparing Case 3 and Case 4, it is clear that the FP gas inventory has also affected to the mechanical energy.

TABLE 34. COMPARISON OF THERMAL AND MECHANICAL ENERGY AND CONVERSION RATIO

	Case 1	**Case 2**	**Case 3**	**Case 4**
Steel Temperature (K)	1800	2200	3000	3000
FP gas mass (kg)	61	61	61	10
ΔE_f (MJ)	11,700	11,700	11,700	11,700
ΔE_s (MJ)	2760	3920	6350	6350
ΔE_{therm} (MJ)	14500	15600	18050	18050
ΔE_{mech} (MJ)	25.0	28.3	33.7	26.3
R_{conv}	0.0017	0.0018	0.0019	0.0015

Relocation of materials

FIG. 72 and FIG. 73 explain the relocation of materials. FIG. 72 shows the axial distribution of FP gas mass at 0, 1, 4, 7 and 10 sec. The FP gas mass at an axial position j, $M_{fp}(j)$, is obtained by the sum of the FP gas mass at the axial position j in SIMMER-IV geometry, as follows:

$$M_{fp}(j) = \sum_{i,k} \left[m_{fp}(i,k,j) / \Delta z(j) \right] \tag{44}$$

where

$m_{fp}(i,k,j)$ is the FP gas mass in a mesh located at $(x,y,z) = (i,k,j)$ (kg)

$\Delta z(j)$ is the height of a mesh located at $(x,y,z) = (i,k,j)$ (m)

FIG. 72 indicates that it takes about 10 s to have fission gas arrived at the cover gas region.

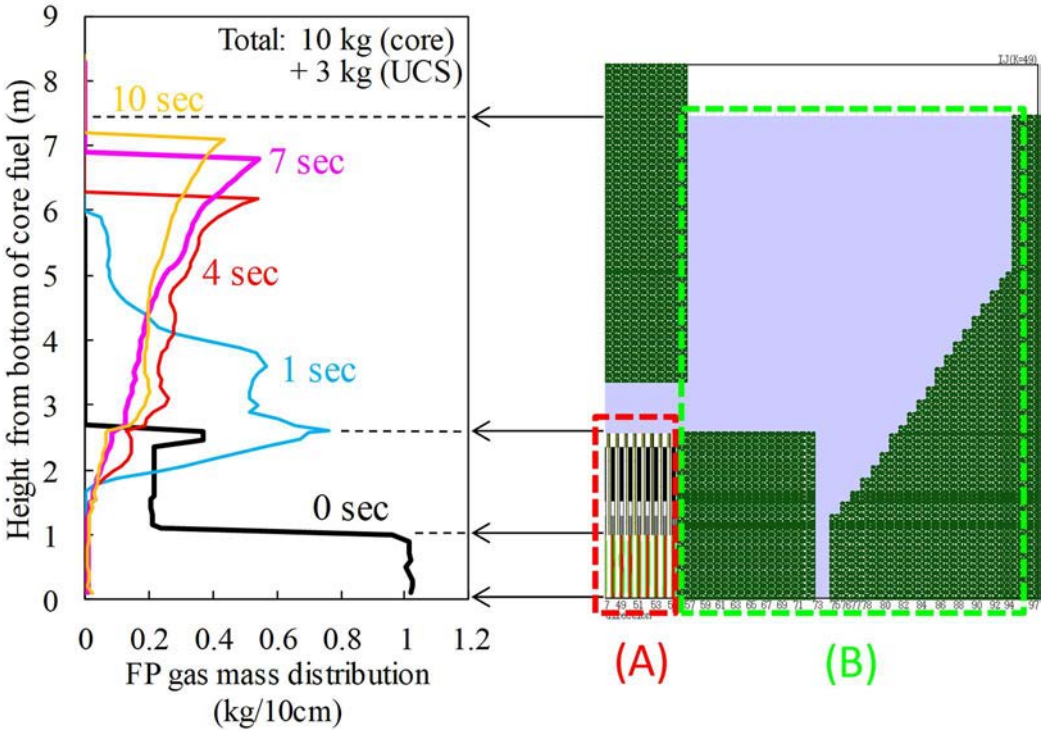

FIG. 72. Axial FP gas mass distribution at selected time, 0, 1, 4 and 9 s.

FIG. 73 shows the history of fuel and steel mass relocation: red line is the mass in the region (A) in FIG. 72, and the green one is that of region (B). From this figure, it is confirmed that about half of fuel is discharged from core region during first 2 s. On the other hand, almost an equivalent initial inventory of mobile steel is maintained around core region during first 5 s as a result of balancing of molten steel ejection and generation due to steel ablation within UCS region. Remaining molten fuel and steel in core region provided heat source for succeeding FCI.

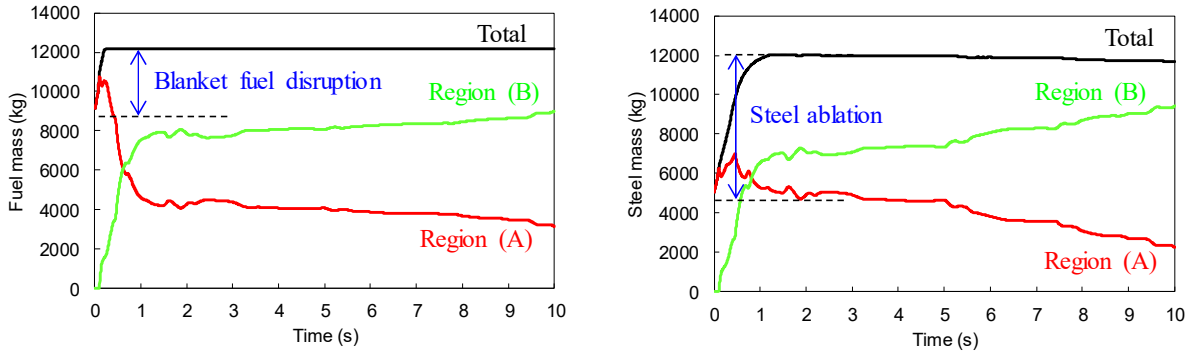

Fuel mass distribution

Steel mass distribution

FIG. 73. History of fuel and steel mass relocation during the transient.

Note that during the first 100 ms, fuel mass in region (A) increased. This is due to the disruption or melting of upper axial blanket fuel which became mobile during this interval. Once blanket fuel became mobile, it did not return to the immobile component in SIMMER-IV, so that the total amount of mobile fuel stays constant after blanket fuel mobilization.

To the contrary, ablated steel can return to an immobile component depending on the contact surface: if the contact surface is assigned for the thermal-hydraulic calculation, molten steel can solidify on the contact surface and hence the mobile steel amount (total) shown in FIG. 73 decreased a little after 1.7s.

Driving force of the sodium slug impact

The transition of mole fraction of the gas phase, steel vapor, sodium vapor and FP gas, at the selected time is shown in Fig. 74. Left images express material distribution. Times are selected referring to the CDA bubble expansion behaviour plotted on FIG. 69: the beginning of expansion (10 ms), about half the way to the peak (130 ms), the first peak (270 ms) and the first shrink (435 ms). From this figure, following can be derived:

1) The major constituents of the CDA bubble expanded into hot pool are sodium vapor and FP gas. FP gas occupies the outer surface of the CDA bubble because it is filled in the UCS region at the beginning and hence released prior to the molten material.

2) Steel vapor is scarcely ejected into the hot pool. It can exist in the hot pool only when certain amount of molten steel exits in the hot pool.

Note that mole fraction of FP gas in cover gas region is unity in Fig. 74 because FP gas, Xe, is allocated there instead of Argon due to the limitation of the number of materials in SIMMER-IV.

Pressure distribution is shown in FIG. 75, in vertical direction along the center line of the core (i=49, k=53) from bottom of the active fuel to the bottom of Control Plug ($1 \leq j \leq 36$) with breakdown of partial pressure contribution. Fuel vapor abundantly existed within the core region at the beginning of the calculation (0.5 ms), but the contribution ratio of fuel vapor pressure to the total pressure rapidly decreased to about 10% until 10 ms due to condensation and pressure flattening by convection. After that, steel vapor and FP gas dominated pressure in the core region and the contribution ratio of fuel vapor pressure became and was maintained around 6% at the maximum. Although fuel vapor can exist in the hot pool during 250 – 380 ms, when steel vapor outflowed into the hot pool, it existed only in the core region after 380 ms.

The following can be concluded from above mentioned analysis:

1) The driving force of CDA bubble expansion during first 270 ms is the combination of the fuel and steel vapor pressure which maintain core pressure and the sodium vapor pressure generated in the hot pool due to FCI.

2) The driving force of second and succeeding expansion (after 435 ms) is dominated by sodium vapor due to FCI.

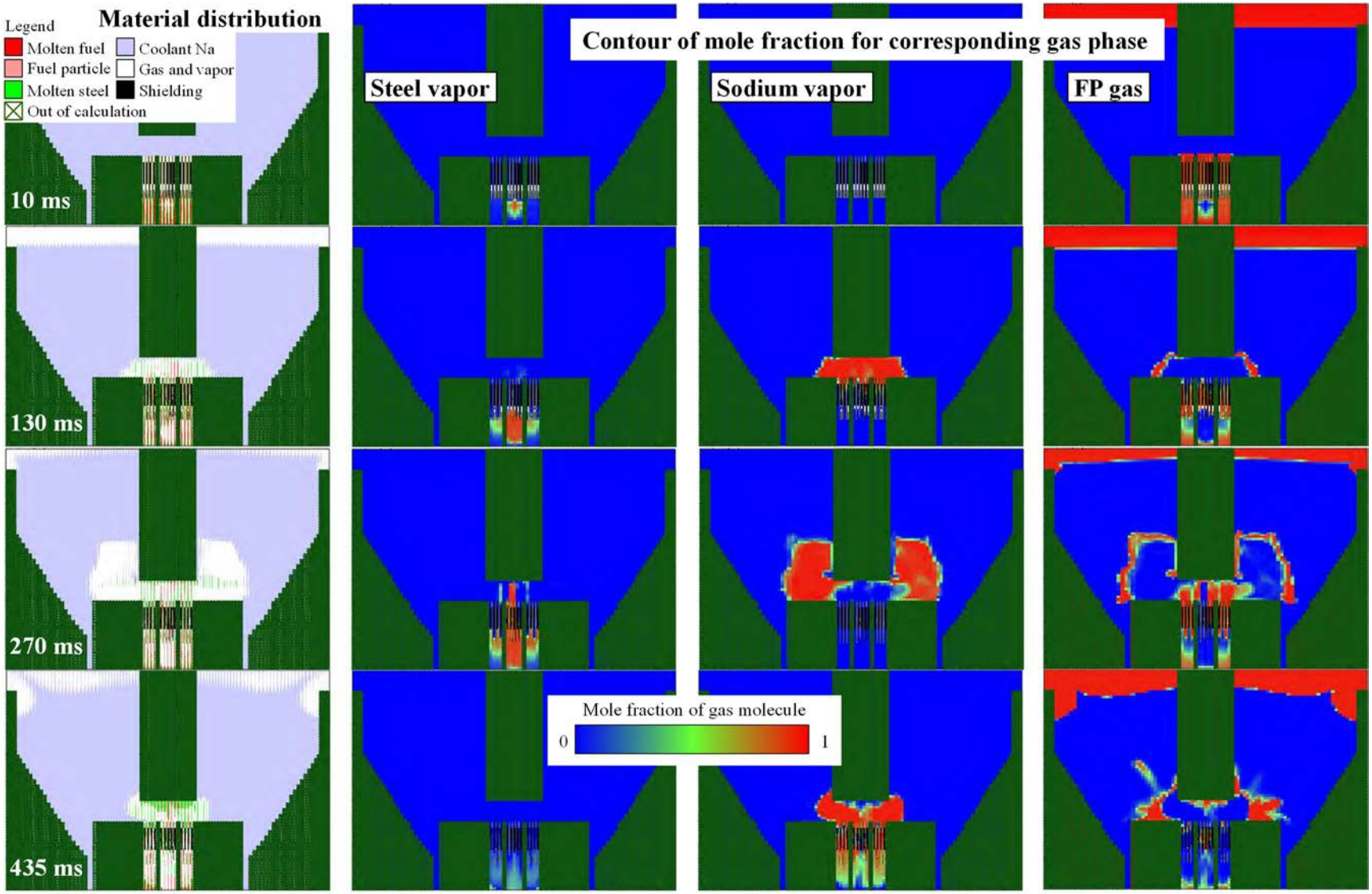

Fig. 74. History of fuel and steel mass relocation during the transient

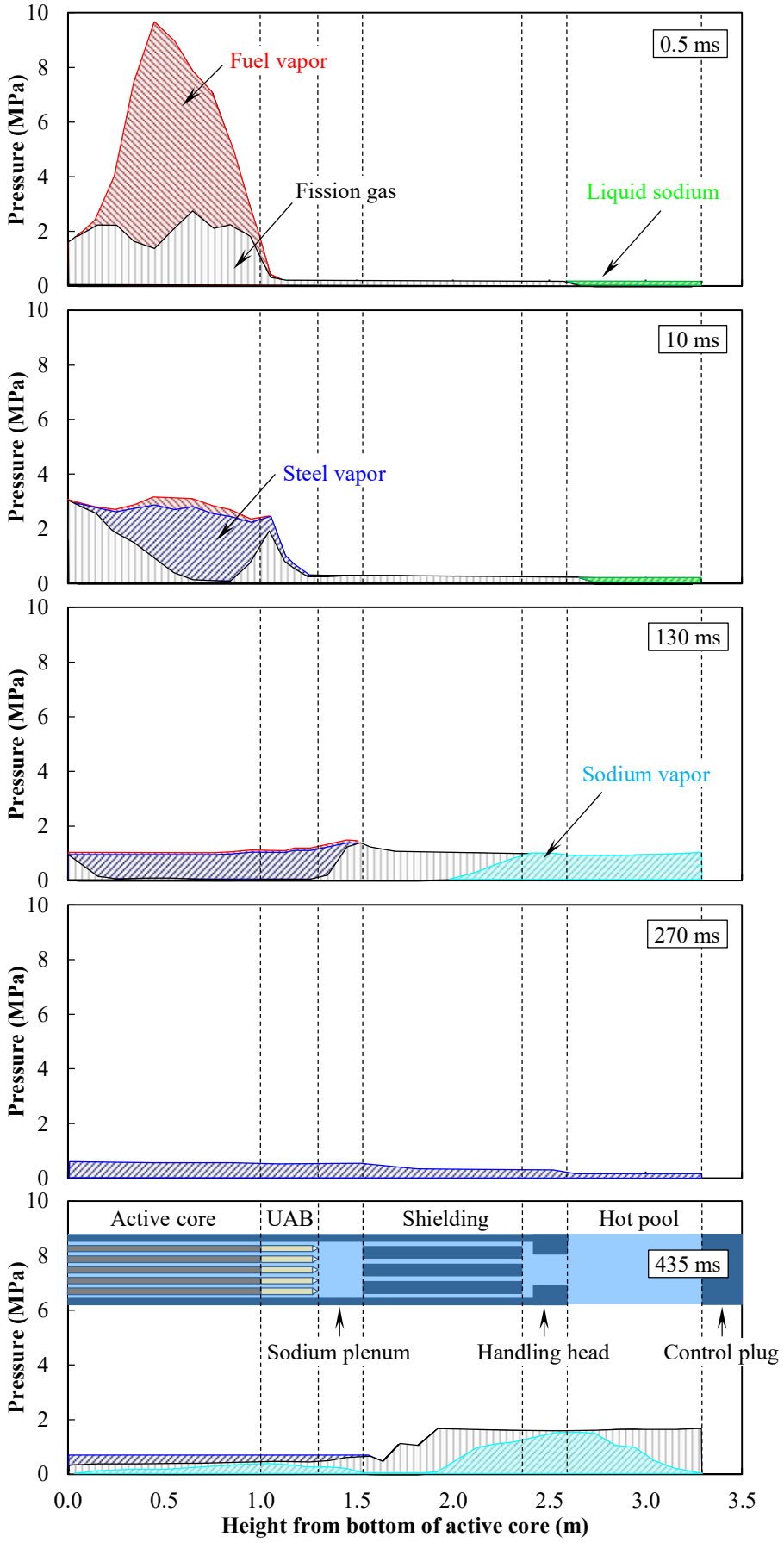

FIG. 75. Pressure distribution in vertical direction at the center of the core

4.3.3. Summary

Four calculation cases of Post-Disruption Expansion phase of prototype sodium cooled fast reactor severe accident condition using SIMMER-IV code were conducted.

The main outcomes of these calculations are as follows:

- Material relocation behaviour as well as pressure and temperature transient during molten material ejection from the disrupted core region to the hot pool were reasonably simulated by SIMMER-IV code.
- Conversion ratio from thermal energy to mechanical energy amounted only to 0.19 % even in a conservative case
- Sensitivity of mechanical energy to steel temperature and FP gas inventory was revealed. These effects should properly be considered in the evaluation.
- It takes ~10s to have fission gas arrived at the cover gas region after the initiation of core expansion.
- About half of the fuel was released from the core region within 2s, although initial inventory of molten steel is maintained within the core region due mainly to the ablation of UCS.
- The driving force of CDA bubble expansion at the beginning is the combination of the fuel and steel vapor pressure and the sodium vapor pressure, but it is dominated only by sodium vapor pressure after the first expansion.

Mechanical energy was reasonably calculated by the method developed and the results, pressure history and P-V relation, can be used for the calculation of sodium ejection and reactor vessel response.

5. WP-2 MODELS, RESULTS AND DISCUSSIONS

5.1. SIMULATION EXERCISE USING ANSYS (FLUENT) CODE (NCEPU, CHINA)

5.1.1. Description of Methods and Model

ICEM CFD (The Integrated Computer Engineering and Manufacturing code for Computational Fluid Dynamics) is a professional pre-processing software for CAE, with powerful capabilities of CAD model repair, automatic mid-face extraction, unique grid 'sculpture' technology, grid editing technology and extensive solver support capabilities. At the same time, as a professional analysis environment of ANSYS family, it can also be integrated into the ANSYS Workbench platform to obtain all the advantages of Workbench. ICEM replaces GAMBIT as the standard grid-generation software for FLUENT and CFX.

ANSYS FLUENT uses computational fluid dynamics (CFD) numerical simulation technology to provide solutions to fluid problems for engineers in various industries worldwide. The rich physical models of FLUENT make it useful in everything from aircraft pneumatics to boiler combustion, bubble towers to glass manufacturing, and so on. In addition, the software's powerful simulation capabilities expand the application of rotating machinery, aerodynamic noise, internal combustion engines and multiphase flow systems.

FLUENT has a wide range of model systems to provide leading turbulence simulation capabilities which include several popular versions of k-epsilon and k-omega models, as well as Reynolds stress models for highly anisotropic flows. It also provides advanced scale-solving turbulence models, including large eddy simulation (LES), separated eddy simulation (DES), and adaptive eddy simulation (SAS). In this CRP, the standard k-e was established by NCEPU.

The commercial software ICEM CFD was used to build the models needed for WP2. Except for the two main leakage channels, the other channels have similar geometric characteristics. They all have similar geometric features, with an 'inverted L' shape. The geometric model of the fluid domain is established based on known parameters, and the model is meshed with ICEM CFD to calculate the leakage of liquid sodium using FLUENT.

In this section, the movement of fission products in the RS-FTP gap channel under severe reactor accidents was analysed. The dimensions of the channel and the top shield are given in TABLE 10 and FIG. 76.

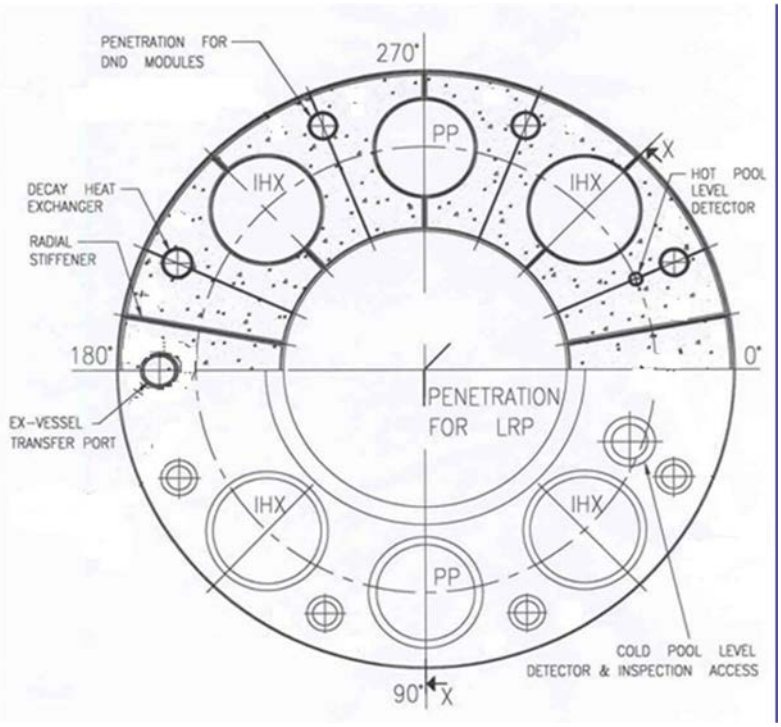

FIG. 76. Top view of the core top plate.

The ratio of the length of the ascending channel to the width of the outlet is 3,600:1, which makes it impossible to build a computational grid model through unstructured grids. The drawn geometric model was imported into ICEM for meshing, and the lower part of the slit channel was named as the flow field inlet face. The upper part was named the flow field outlet face. Then, the other faces were named WALL faces, etc., and the vacant area in the middle of each face is the area where the fluid flows. Meshing used a structured mesh, and the boundaries did not consider friction and stickiness.

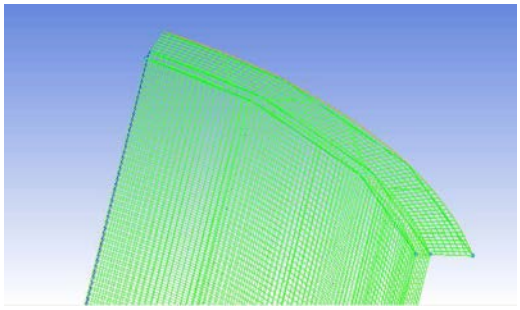

FIG. 77. Grid diagram of 1/6 leakage.

The total number of grids after division is about 1.5 million, including some 4-sided grids and some 6-sided grids. The mesh quality was checked to see if it met the design requirements. The grid quality is shown in FIG. 78. The quality is greater than 0.85, which meets the engineering requirements of the design.

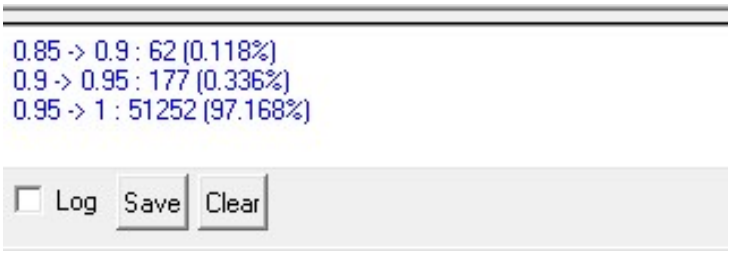

FIG. 78. Grid quality detection

In addition to the 1/6 model, NCEPU also attempted to create a 360° 'inverted L' leaky channel model. The unstructured mesh of the geometric model was divided. Good grid quality was applied, as shown in FIG. 79. The pressure boundary conditions were compiled into a user-defined function (UDF), and the change in leakage at the outlet over time was calculated in FLUENT.

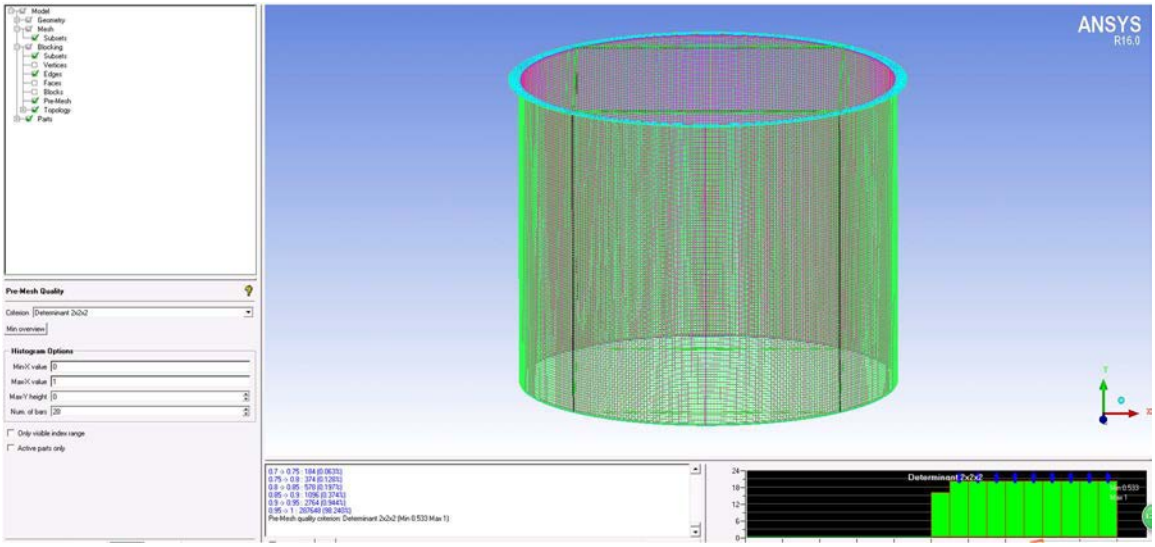

FIG. 79. The model of RS-DHX.

Other leak paths were also modelled based on the above methods. It is worth noting that different 'inverted L' leak paths are modelled and calculated separately according to the corresponding dimensions.

5.1.2. Results

The steps of simulation calculation and setting of boundary conditions are the same for all models in FLUENT. First, the meshed model is imported into FLUENT. The unit of the grid is specified as millimetre, and then the grid parameters are checked. The model is checked to ensure there is no negative grid, that is, the volume of the grid must be a positive number. Next, the process selects an algorithm with pressure as a parameter. The flow field is a constant flow. The turbulence model selects the Standard k-e model in k-epsilon (2 epn). The wall uses an algorithm to select the Standard function. The core melt in the sodium cooled fast reactor is liquid metal sodium, and the outlet surface pressure is atmospheric pressure. The number of iteration steps is selected to get the residual curve as shown below in FIG. 80, indicating that it is convergent.

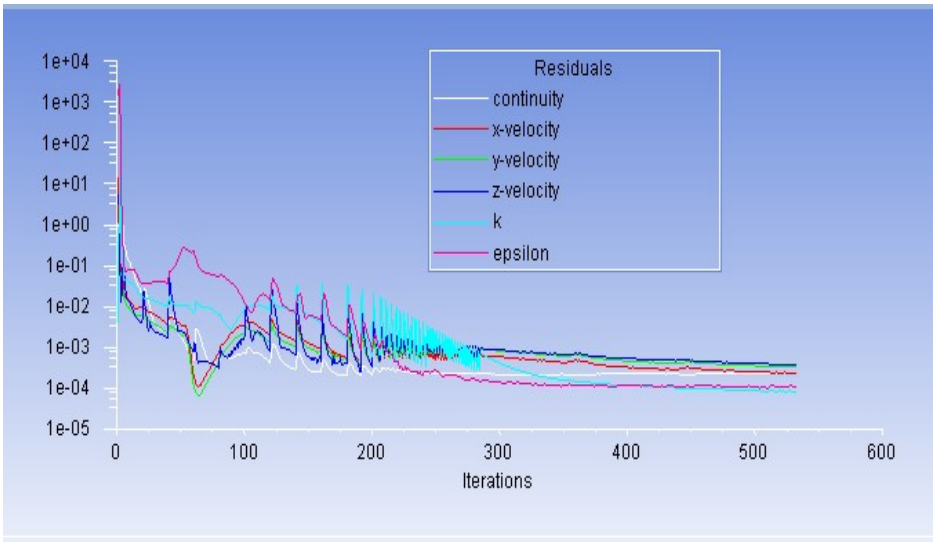

FIG. 80. Residual plot of continuous phase flow field iteration.

The mass flow and velocity changes at the exit were monitored. While monitoring the changes in these parameters during the flow, as many transient changes have stabilized during this time, the calculations were more scientifically optimized.

According to the calculation results of FLUENT, the sodium leakage in each subchannel is determined, as shown in FIG. 81 to FIG. 84.

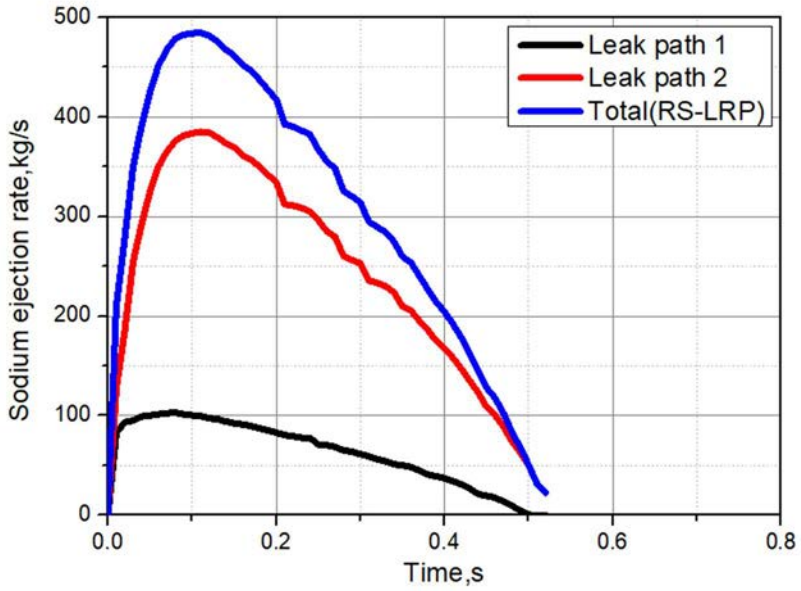

FIG. 81. Sodium ejection rate for RS-LRP.

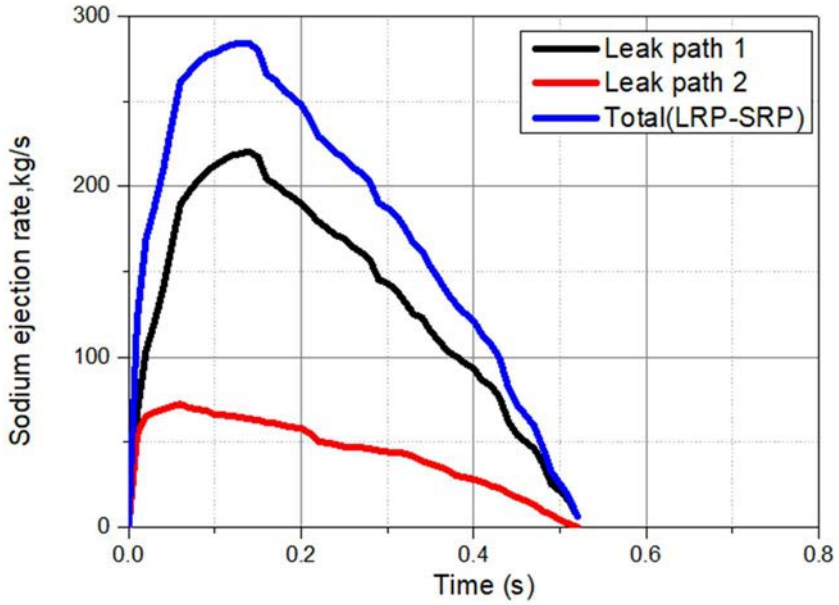

FIG. 82. Sodium ejection rate for LRP-SRP.

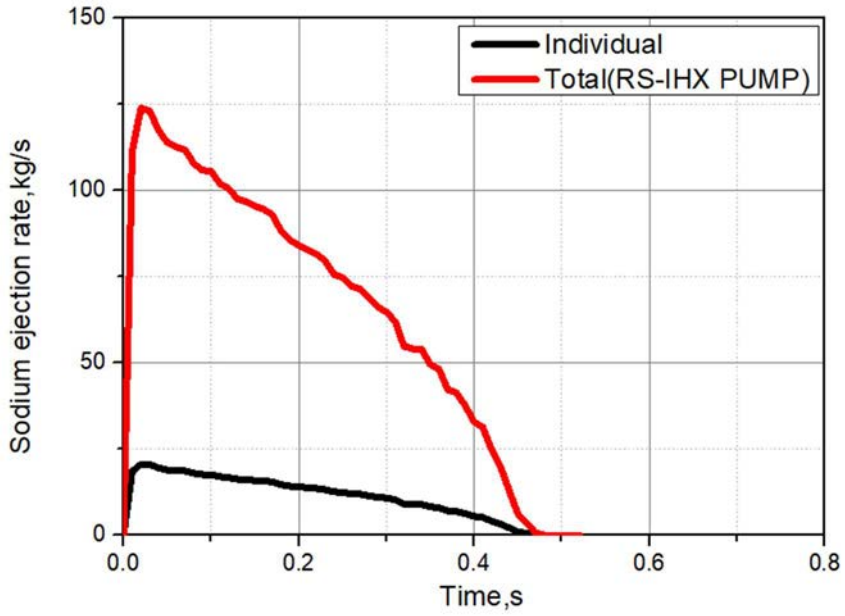

FIG. 83. Sodium ejection rate for RS-IHX PUMP.

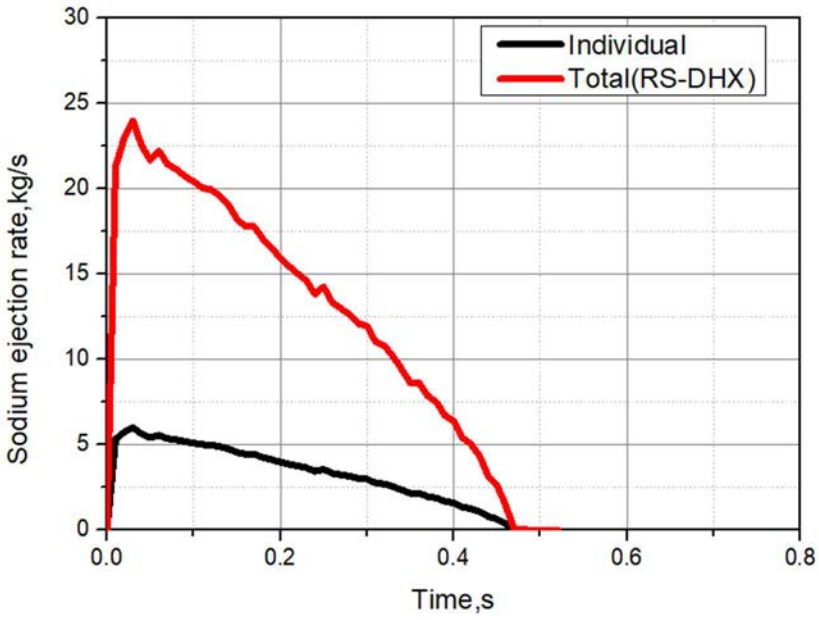

FIG. 84. Sodium ejection rate for RS-DHX.

In the two main leakage channels (RS-LRP & LRP-SRP), the leakage rate of Na peaked at about 0.13 s and then decreased to 0. In other narrower leakage channels, the leakage rate reached its peak in less time, less than 0.05s. In all channels, the sodium leakage rate tends to 0 after 0.55 s.

One challenge encountered was the structure of the two main channels (RS-LRP & LRP-SRP). Due to the relatively complicated models, there may be deviations in the numerical simulation results of the fluid characteristics at the corners of the leakage channels.

5.1.3. Experiment

Based on the experimental facility, the migration and deposition experiments of large-size melt fragments in the pipeline were carried out, but unpredictable results occurred. During the process of increasing the coolant flow rate, the test section pipeline was broken due to the inability to withstand the internal pressure. The large amount of water from the coolant flowed out of the pipeline, as shown in the following figure, which caused the gantry to analyze only the influence of the density of the particulate matter on the migration and deposition phenomenon, and it is impossible to predict the influence of the coolant flow rate on the migration and deposition phenomenon.

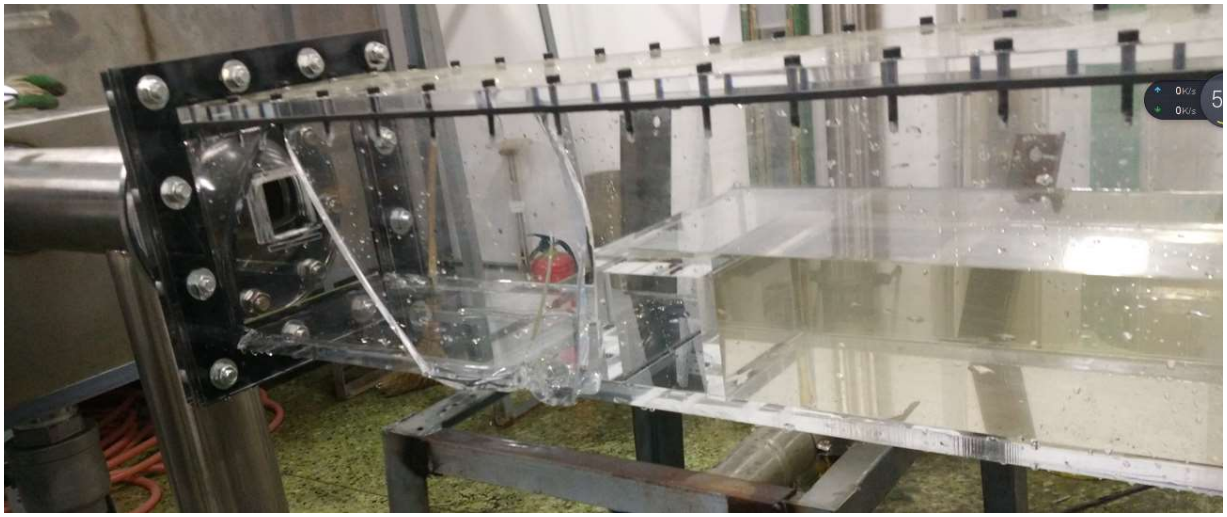

FIG. 85. Pipe rupture in the experimental section caused by unexpected experimental conditions

5.2. SIMULATION EXERCISE USING EUCLID/V2 CODE (IBRAE RAN) RUSSIAN FEDERATION)

5.2.1. Description of Methods and Models

The EUCLID/V2 module for system thermal-hydraulic analysis, HYDRA-IBRAE/LM was utilized in WP-2. A description of this module is available in Section 4.2.1. The list of factors that are of key importance in two-fluid thermal–hydraulic models includes, in particular, the choice and validation of the utilized flow and heat transfer regime map and also the block of closing equations describing the two-phase flow friction, interphase friction, heat transfer from the fluid to the wall, and interphase heat transfer intensity. It should be noted that the main difference between liquid metals and water is that the liquid phase has high heat conductivity and, consequently, is characterized by a low Prandtl number. Thus, the differences between the hydrodynamics and heat transfer processes during the flow of liquid metals and water should manifest themselves in phenomena accompanied by heat transfer. Hence, the description of hydrodynamic processes in liquid metal should be close to that for processes in water coolant. In view of this circumstance, a decision was made to orient with the correlations obtained for water and written in terms of dimensionless complexes in the selection of the closing equations. The map of sodium flow regimes used in the EUCLID/V2 integrated code thermal–hydraulic module is given in [31], [32] and the closing equations used for sodium coolant are published in [31].

The correlations for the calculations of friction pressure losses, heat exchange with wall and interphase interactions used in the thermohydraulic module were obtained mainly in FSUE "SSC RF – IPPE" based on analysis of experimental data.

Local pressure loss coefficients Δp are determined as follows:

$$\Delta p = \zeta \frac{\rho u^2}{2} \tag{45}$$

where

ζ is the coefficient of local resistance;

u is the average coolant velocity, m/s;

ρ is the coolant density.

Schematic of abrupt contraction and extension of channel is shown in FIG. 86.

FIG. 86. Schematic of abrupt contraction, extension of channel.

Coefficient of local resistance for abrupt extension of channel at Re > 3300 is determined as:

$$\zeta = \left(1 - \frac{F_0}{F_1}\right)^2 \tag{46}$$

where F_0 и F_1 – area of narrow and wide flow section, m^2.

Coefficient of local resistance for abrupt contraction of channel at Re > 10000 is determined as:

$$\zeta = 0,5\left(1 - \frac{F_1}{F_0}\right)^{3/4} \tag{47}$$

where F_0 и F_1 – area of wide and narrow flow section, m^2.

Schematic of pipeline rotation to angle δ with sharp elbows is shown in FIG. 87.

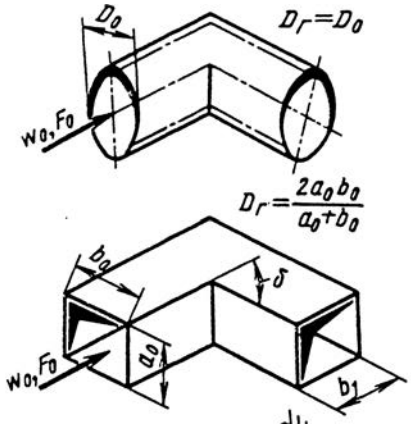

FIG. 87. Pipeline rotation.

Coefficient of local resistance is determined as [33]:

Smooth walls:

$$\zeta = C_1 A \zeta_m \tag{48}$$

Rough walls:

$$\zeta = k_\Delta k 1_{m_{Re}} \tag{49}$$

where δ - bend angle, ζ_m - is determined from:

$$\zeta_m = 0.95\, sin^2\left(\frac{\delta}{2}\right) + 2.05\, sin^4\left(\frac{\delta}{2}\right), \tag{50}$$

where
A, C_1, k_{Re} and k_Δ are coefficients;
$\overline{\Delta} = \frac{\Delta}{D_Г}$ is the relative roughness;
Δ is the roughness;
$D_Г$ is hydraulic diameter before bend;
Re is the Reynolds number;
And a_0 and b_0 are shown in FIG. 87.

A schematic of T-branch local resistance is shown in FIG. 88.

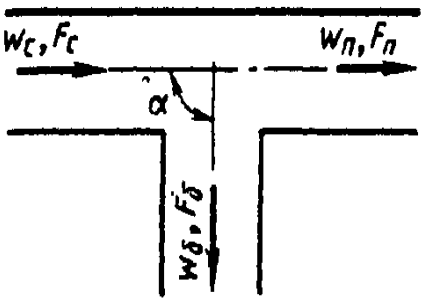

FIG. 88. T-branch local resistance Fδ+Fc> Fc; Fn = Fc.

The value of local resistance coefficient on outflow is determined as:

$$\zeta_{б} = \zeta_{c-б} / \left(\frac{Q_{б}}{Q_{c}} \frac{F_{c}}{F_{б}} \right)^{2} \tag{51}$$

where Q_i is the flux through cross-section *i*.

5.2.1.1. *Nodalization Scheme, Scenario, Boundary, and Initial Conditions*

The pressure developed within the vessel during a Core Disruptive Accident can lead to sodium release to Reactor Containment Building (RCB) though several potential leak paths in the top shield structure of the reactor. The object is to find the mass of ejected sodium to the RCB.

The major leak paths and its number in top shield are given below in TABLE 35.

TABLE 35. MAJOR LEAK PATHS IN THE TOP SHIELD

Penetration	**Number**
RS-LRP	1
LRP-SRP	1
RS-IHX	4
RS-Pump	2
RS-IVTP	1
RS-HPLD	1
RS-CPLD	1
RS-DND	1
RS-IFTM	1
RS-DHX	4

CP-CSRDM	9
CP-DSRDM	3
CP-FFIM	3
SRP-OSP	1
OSP-Guide Tube	1

Nodalization scheme for penetrations with simple leak path consists of vertical and horizontal annular channel - FIG. 89a. Nodalization schemes of RS-LRP, LRP-SRP, SRP-OSP and OSP-Guide Tube penetrations are shown in FIG. 89b, c, d.

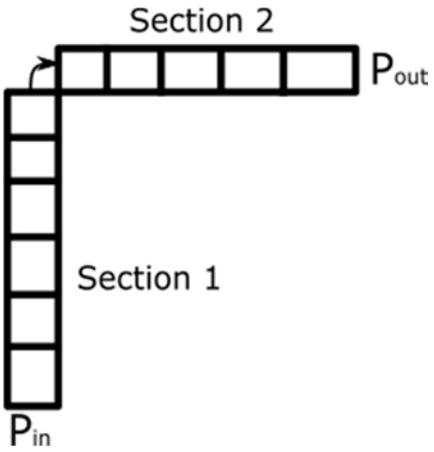

a) Simple leak path

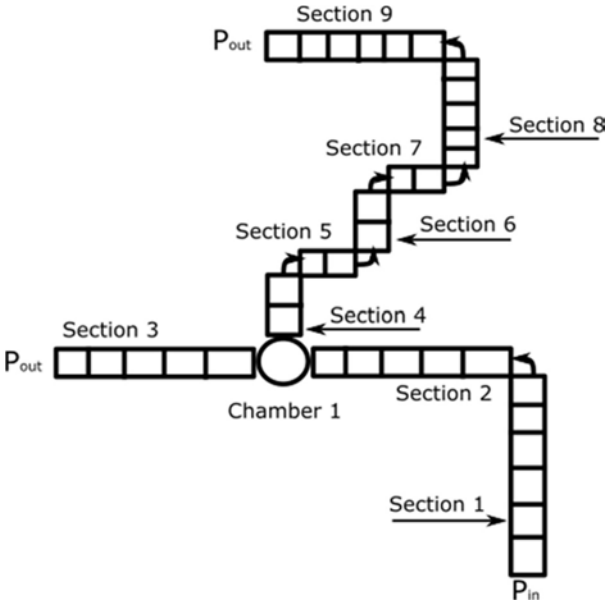

b) RS-LRP and LRP-SRP

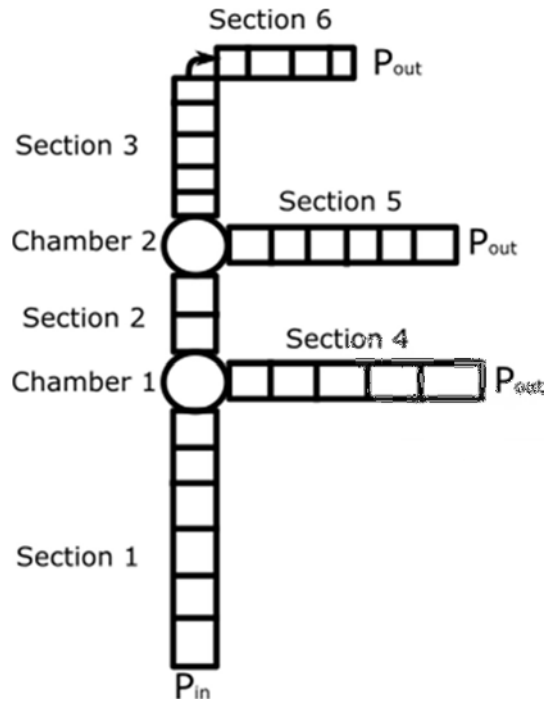

c) SRP-OSP

d) OSP-GUIDE

FIG. 89. Nodalization scheme for RS-LRP and LRP-SRP penetrations.

Dimensions of nodalization scheme for each penetration are given in TABLE 36.

TABLE 36. DIMENSIONS OF NODALIZATION SCHEME FOR EACH PENETRATION

Section number	Length (m)	Orientation	Area (m^2)	Hydraulic diameter (m)
Penetration	**RS-IHX**			
1	1.8005	Vertical	0.0688	0.02
2	0.06	Horizontal	0.0035 – 0.0036	0.001
Penetration	**RS-PUMP**			
1	1.8005	Vertical	0.0688	0.02
2	0.06	Horizontal	0.0035 – 0.0036	0.001
Penetration	**RS-DHX**			
1	1.8005	Vertical	0.0179	0.02
2	0.06	Horizontal	0.00093 – 0.00108	0.001
Penetration	**RS-IVTP**			
1	1.8005	Vertical	0.0179	0.02
2	0.14	Horizontal	0.00093 – 0.00134	0.001
Penetration	**RS-HPLD**			
1	1.8005	Vertical	0.0060	0.02
2	0.12	Horizontal	0.00033 – 0.00068	0.001
Penetration	**RS-CPLD**			
1	1.8005	Vertical	0.0217	0.02
2	0.15	Horizontal	0.00112 – 0.00156	0.001
Penetration	**RS-DND**			
1	1.8005	Vertical	0.0107	0.02
2	0.14	Horizontal	0.00057 – 0.00097	0.001

Penetration	**RS-IFTM**			
1	1.8005	Vertical	0.0179	0.02
2	0.14	Horizontal	0.00093 – 0.00134	0.001
Penetration	**CP-FFIM**			
1	2.3103	Vertical	0.0029	0.006
2	0.052	Horizontal	0.00031 – 0,00039	0.0006
Penetration	**CP-DSRDM**			
1	2.085	Vertical	0.0015	0.006
2	0.115	Horizontal	0.00011 – 0.00024	0.0004
Penetration	**CP-CSRDM**			
1	1.07	Vertical	0.0121	0.059
2	0.84	Vertical	0.0038	0.016
3	0.6052	Vertical	0.0015	0.006
4	0.115	Horizontal	0.00011 – 0.00024	0.0004
Penetration	**RS-LRP**			
1	1.85	Vertical	0.50148	0.05
2	0.09	Horizontal	0.20169 – 0.20672	0.02
3	0.165	Horizontal	0.02075 – 0.02174	0.002
4	0.06	Vertical	0.10359	0.01
5	0.045	Horizontal	0.10316 – 0.10246	0.01
6	0.065	Vertical	0.10202	0.01
7	0.0475	Horizontal	0.10157 – 0.10083	0.01
8	0.34	Vertical	0.10037	0.01
9	0.14	Horizontal	0.10265 – 0.10595	0.01
Chamber 1	0.005	Horizontal	0.207188036	0.02
Penetration	**LRP-SRP**			
1	1.845	Vertical	0.26647	0.04
2	0.062	Horizontal	0.13419 – 0.13743	0.02
3	0.145	Horizontal	0.01384 – 0.01469	0.002
4	0.06	Vertical	0.06896	0.01
5	0.045	Horizontal	0.06853 – 0.06782	0.01
6	0.065	Vertical	0.06739	0.01
7	0.022	Horizontal	0.06696	0.01
8	0.3	Vertical	0.066538932	0.01
9	0.096	Horizontal	0.05498 – 0.05659	0.008
Chamber 1	0.005	Horizontal	0.137915917	0.02
Penetration	**SRP-OSP**			
1	1.835	Vertical	0.02245	0.02
2	2.515	Vertical	0.01114	0.01
3	0.49	Vertical	0.01114	0.01
4	0.165	Horizontal	0.00234 – 0.00325	0.002
5	0.39	Horizontal	0.00231 – 0.00463	0.002
6	0.085	Horizontal	0.00231 – 0.00271	0.002
Chamber 1	0.001	Vertical	0.02245	0.02
Chamber 2	0.001	Vertical	0.01114	0.01
Penetration	**OSP-Guide Tube**			
1	0.1	Vertical	0.00102	0.002
2	5.0	Vertical	0.00253	0.005
3	0.1	Vertical	0.00102	0.002

Inlet sodium pressure is obtained from the following equation:

$$P(t) = P_0 \left(\frac{V_0}{V_0 + Q(t)} \right) e^{-t/\tau} \tag{52}$$

where
P_0 is 0.21 MPa at t = 0, is the quasi-static pressure at the instant of starting of sodium release;
τ is 0.8 s;
V_0 is 80 m^3;
$Q(t)$ is the volume of sodium released up to time t.

Outlet pressure is assumed to be atmospheric pressure. Sodium temperature is 900 K.
For initial conditions inside leak paths next situation was explored: Initially leak path volumes are filled with sodium.

5.2.2. **Results**

5.2.2.1. *Sodium ejection*

Sodium ejection rate to the reactor containment building for each penetration is shown in FIG. 90. Most of the sodium mass was released through following leak paths: RS-LRP (150.55), LRP-SRP (108.02 kg), RS-IHX (27.32 kg), RS-Pump (13.66 kg), RS-DHX (7.6 kg), SRP-OSP (11.46 kg). Total injected sodium mass to the reactor containment is 329.55 kg.

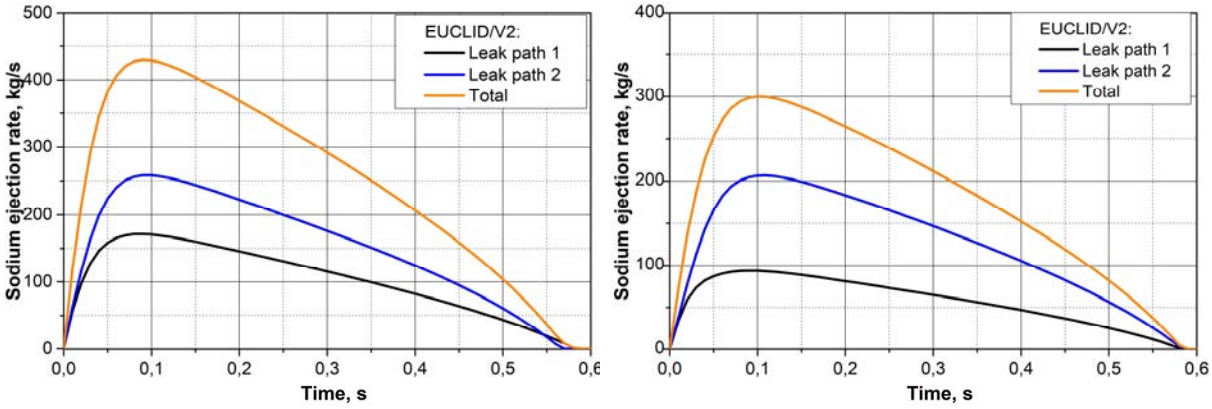

a) RS-LRP b) LRP-SRP

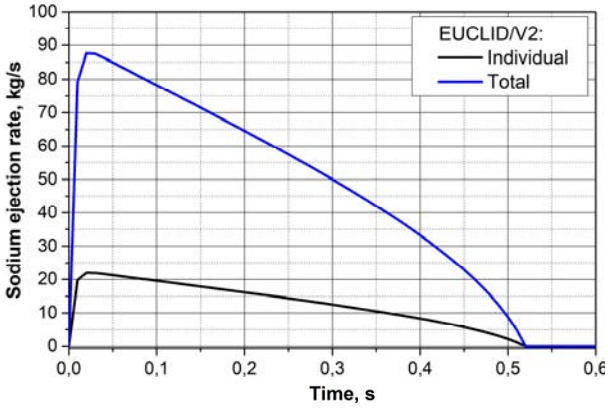

c) RS-IHX

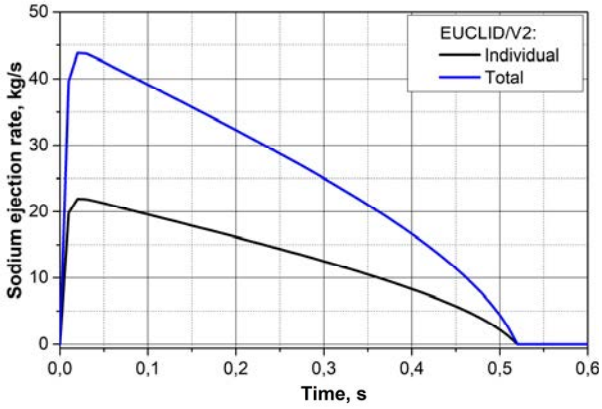

d) RS-PUMP

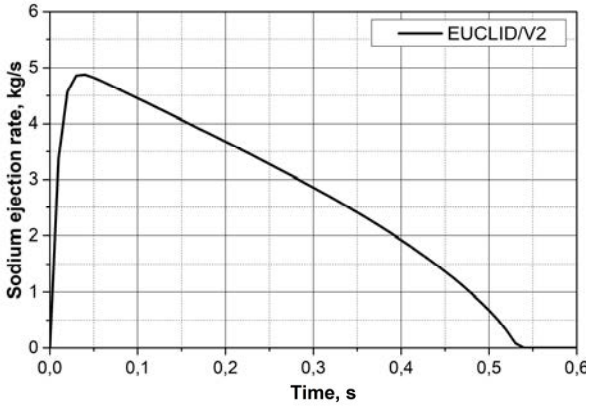

e) RS-IVTP

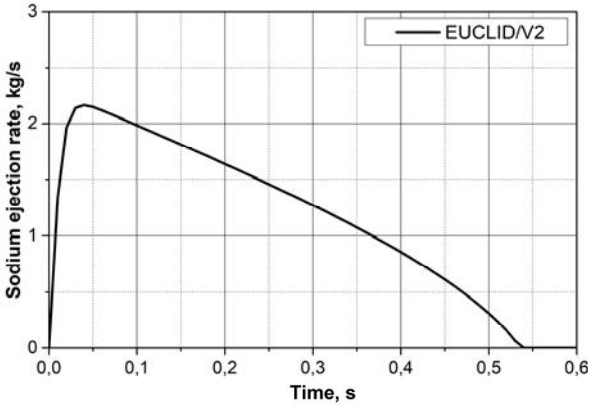

f) RS-HPLD

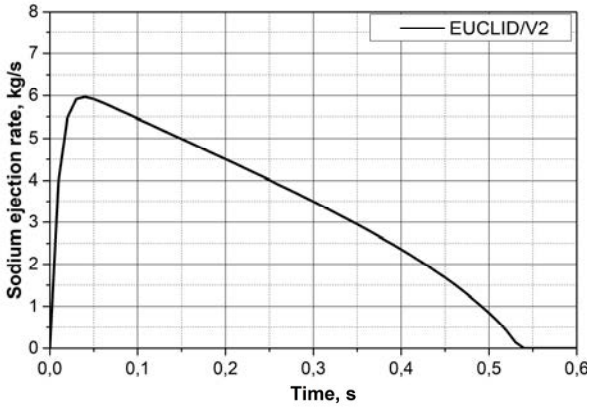

g) RS-CPLD

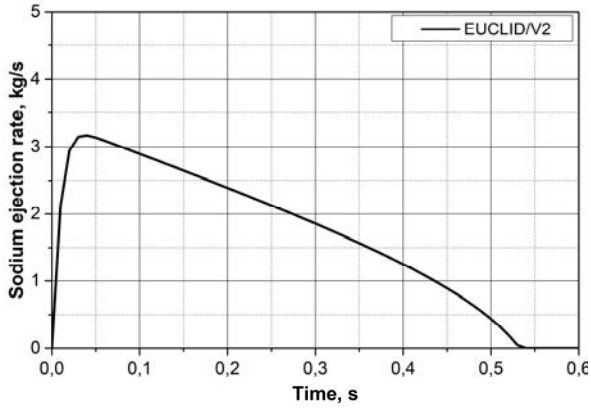

h) RS-DND

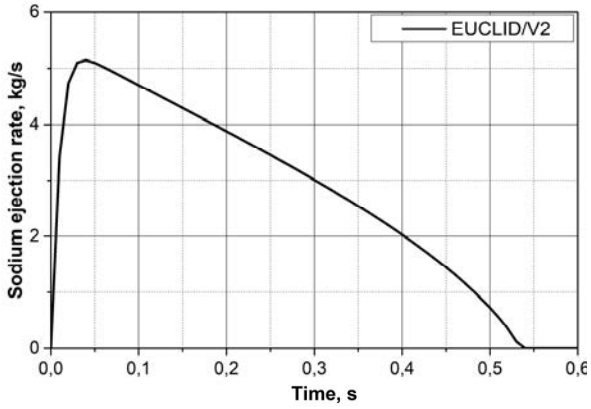

i) RS-IFTM

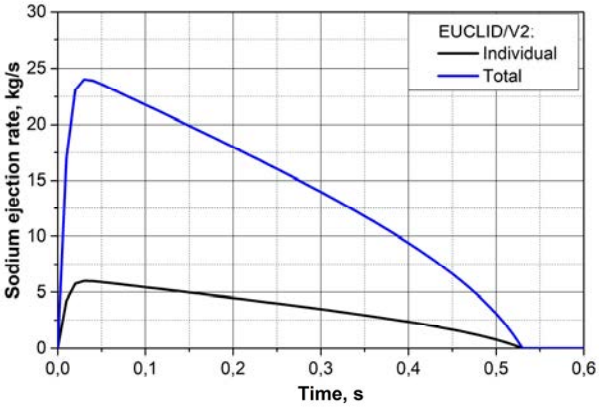

j) RS-DHX

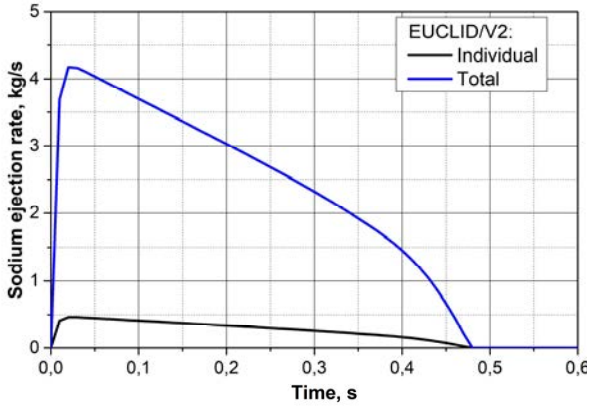

k) RS-CSRDM

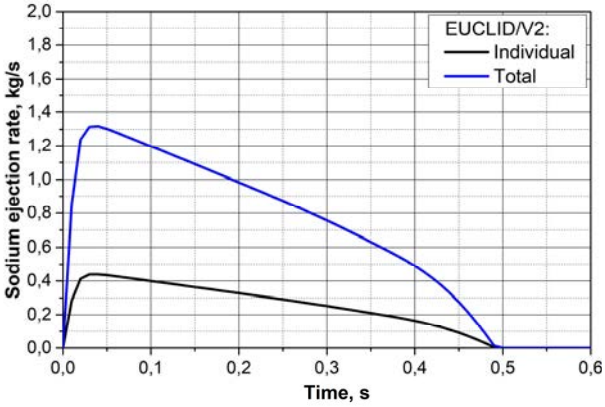

l) RS-DSRDM

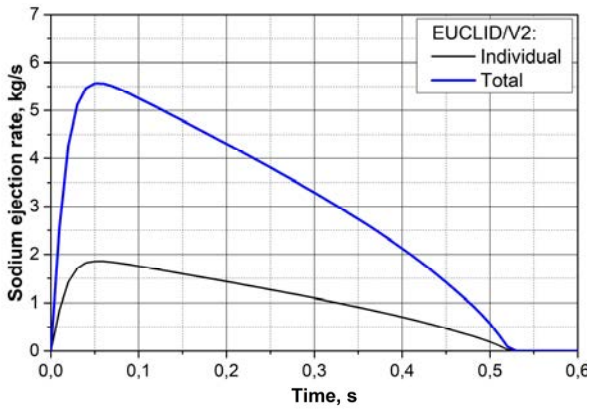

m) RS-FFIM

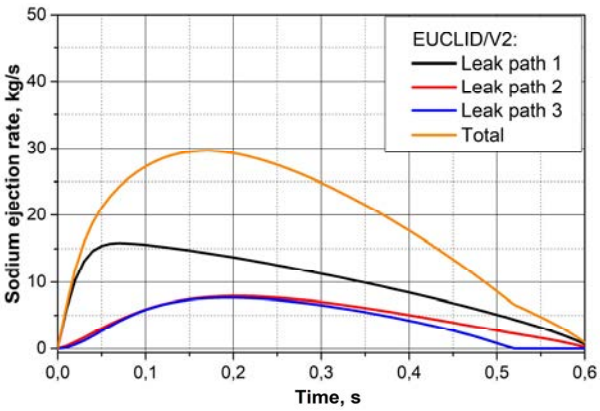

n) SRP-OSP

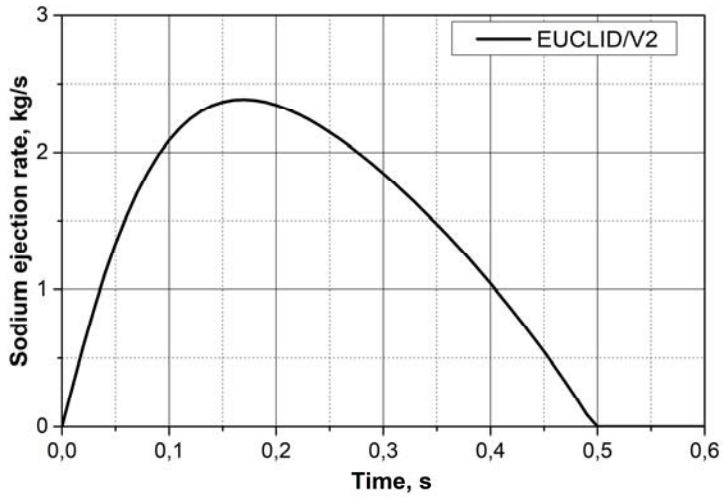

o) OSP-GT

FIG. 90. Sodium ejection rate for leak paths.

Ejected sodium mass for each leak path is presented in TABLE 37.

TABLE 37. EJECTED SODIUM MASS

Penetration	**EUCLID/V2 (IBRAE RAN)**
	Ejected sodium mass (kg)
RS-LRP	150.55
LRP-SRP	108.02
RS-IHX	27.32
RS-Pump	13.66
RS-IVTP	1.55
RS-HPLD	0.69
RS-CPLD	1.90
RS-DND	1.01
RS-IFTM	1.64
RS-DHX	7.60
CP-CSRDM	1.24
CP-DSRDM	0.40
CP-FFIM	1.75
SRP-OSP	11.46
OSP-Guide Tube	0.77

Total	**329.55**

5.2.2.2. *Sensitivity study*

The results of sodium mass release rate and injected mass were studied on different grids 0.5*N, N, and 2*N, where N is cell number for nominal case. The results are shown in FIG. 91. The minimum size for most cells for nominal case with N cells is about 1 cm, maximum – 10 cm. The sensitivity study for grids with different size was performed. It shows that by reduction the cell size the sodium mass injected to RCB converges to 330 kg.

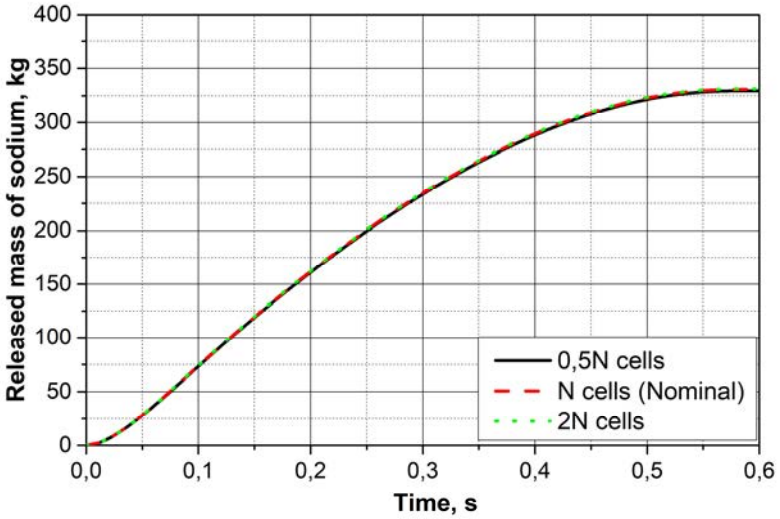

FIG. 91. Injected sodium mass depending on grid size.

The study of the influence of input parameters on the calculation results was performed. In a series of calculations, the input parameters: sodium temperature, inlet and outlet pressure, and cross-section area were changed by a small value. The range of change for the parameters is presented in TABLE 38.

TABLE 38. PARAMETERS OF VARIATION RANGE FOR SENSITIVITY STUDY

Parameter	Range
Sodium Temperature, K	±50
Inlet pressure, %	±5
Outlet pressure, kPa	0 - 10
Cross-section area, %	±3

Results of the sensitivity study of sodium injection rate for each penetration leak paths are presented in FIG. 92. The input and output pressure have the greatest influence on the calculation results. Injected sodium mass varies from 284 to 353 kg (FIG. 93).

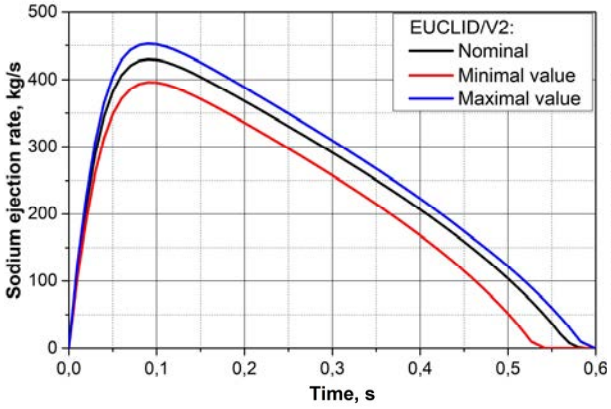

a) RS-LRP

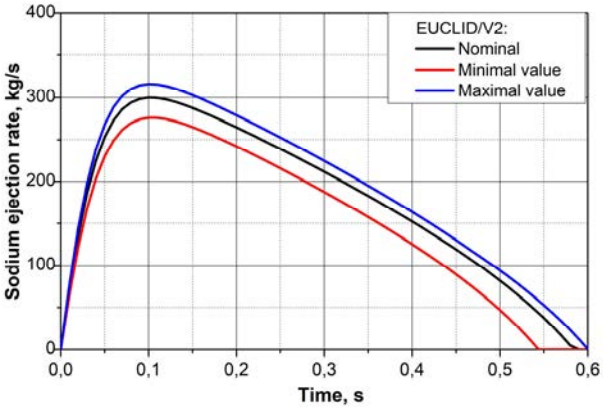

b) LRP-SRP

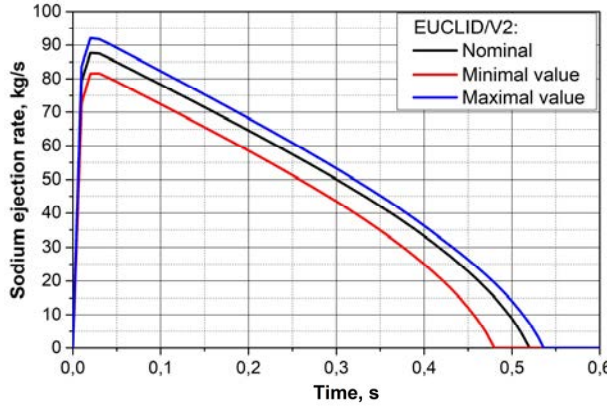

c) RS-IHX

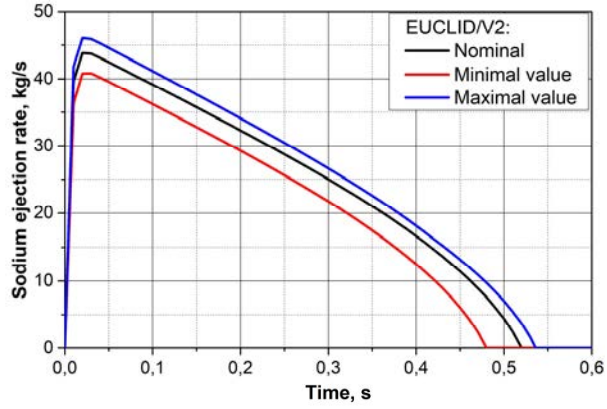

d) RS-PUMP

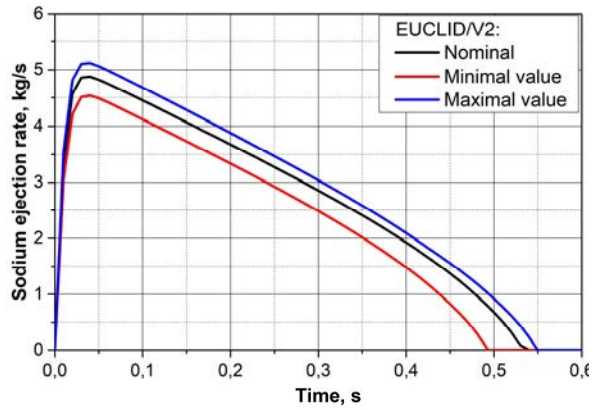

e) RS-IVTP

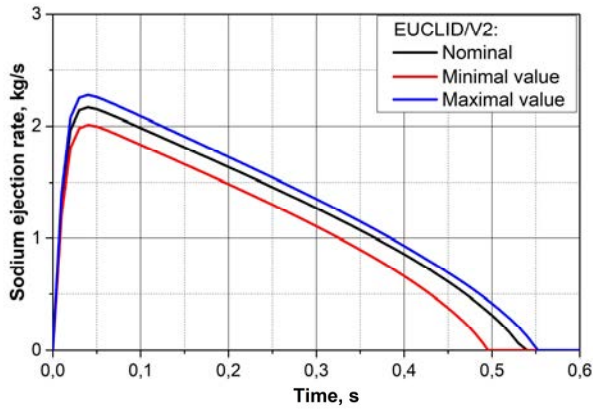

f) RS-HPLD

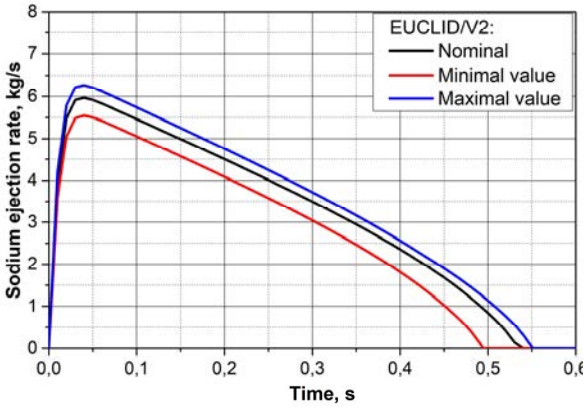

g) RS-CPLD

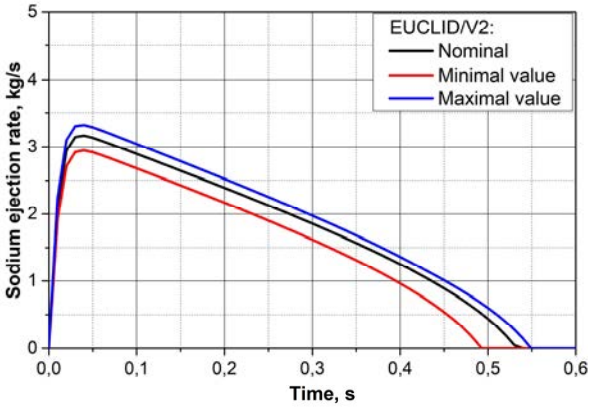

h) RS-DND

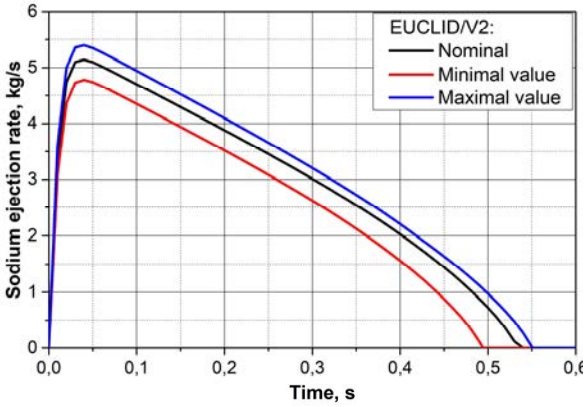

i) RS-IFTM

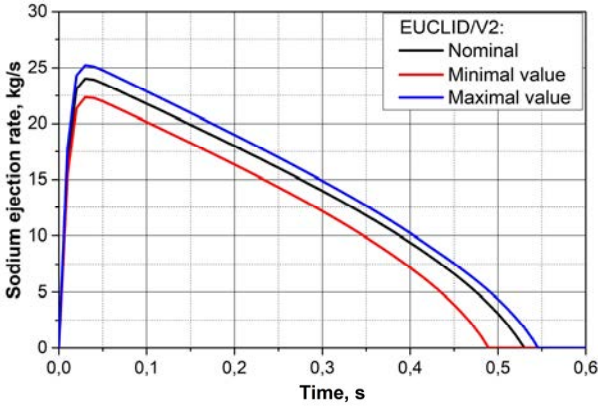

j) RS-DHX

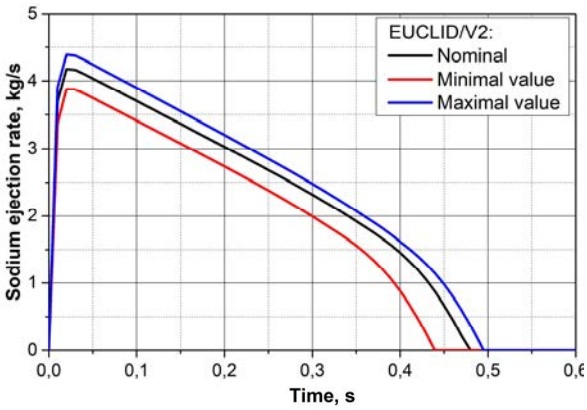

k) RS-CSRDM

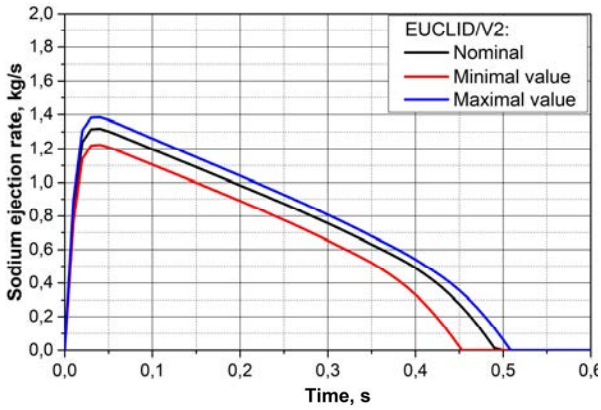

l) RS-DSRDM

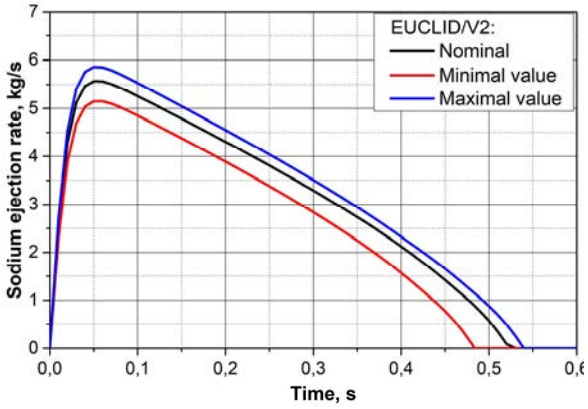

m) RS-FFIM

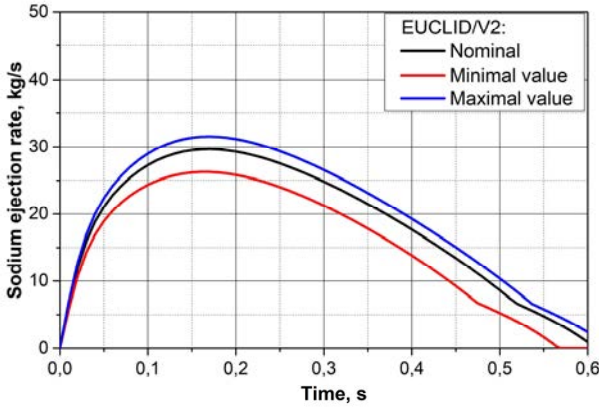

n) SRP-OSP

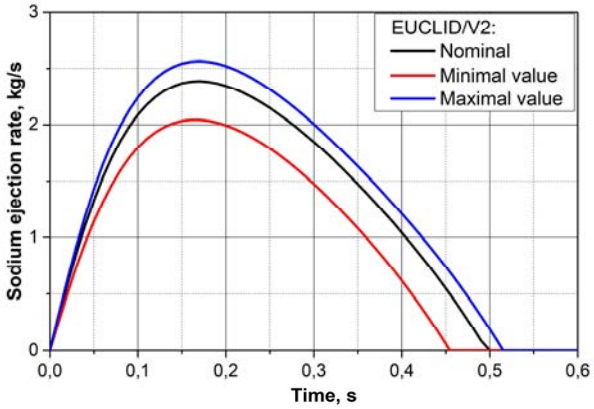

o) OSP-GT

FIG. 92. Sensitivity study of sodium ejection rate for leak paths.

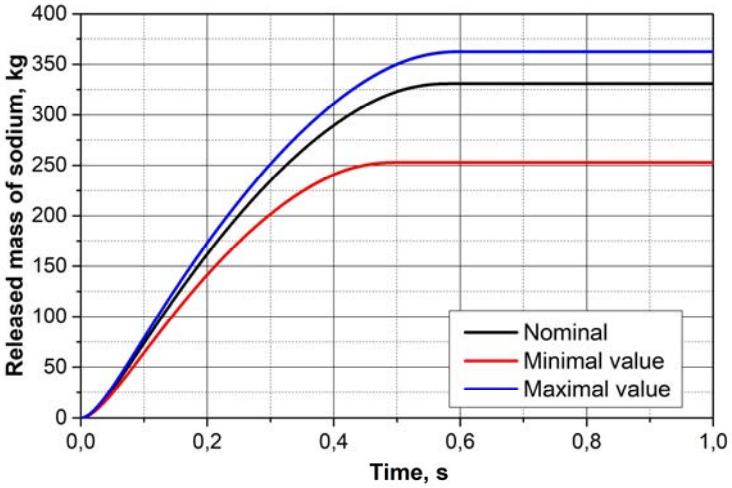

FIG. 93. Sensitivity study of injected sodium mass to the RCB.

5.2.3. **Summary**

The integral EUCLID/V2 code with module HYDRA-IBRAE/LM was used to calculate sodium ejection rate through top shield leak paths. The simulation predicted that about 330 kg of sodium is ejected during 0.6 sec. The RN release to the containment is apportioned from the WP-1 calculations. Sensitivity analysis shows that the largest contribution to calculation results is made by inlet and outlet pressure and where the value of injected sodium varied from 284.3 kg to 353.8 kg

5.3. SIMULATION EXERCISE USING NETFLOW CODE (IGCAR, INDIA)

5.3.1. **Description of Methods and Models**

A general-purpose hydraulic network model was developed to determine the leak rate of sodium mass through various sections of the leak paths in the top shield. The numerical model was implemented in Python and named NETFLOW. The network model is useful for modelling arbitrary leak paths. The equations that govern the leak rate are based on force balance between flow resistance, inertia of sodium mass in various sections of leak paths, gravitational force, and upward force acting due to the quasi-static core bubble pressure [34] [8]. For example, the governing equations for the five-node network with four branches FIG. 94 are as follows:

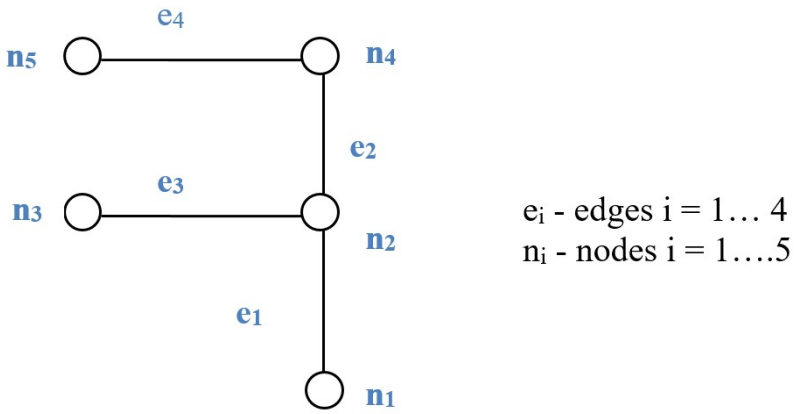

FIG. 94. Flow network model of a typical sodium leak path in top shield. Nodes n1, n3 and n5 are boundary nodes.

For edge-1 the force balance equation is,

$$m_1 \frac{dv_1}{dt} = \mathrm{A_1}(\mathrm{p_1} - \mathrm{p_2}) - \mathrm{k_{i1}}(v_1)v_1 + \ f_{g1}\ (\theta_1)$$
$$\frac{dv_1}{dt} = \frac{A_1}{m_1}(\mathrm{p_1} - \mathrm{p_2}) - \frac{k_{l1}(v_1)}{m_1}v_1 + \ \frac{f_{g1}(\theta_1)}{m_1} \quad (53)$$

Where, $f_g = {}^{A}/_{m}\, PLg\cos\theta$

For edge-2 the force balance equation is,

$$\frac{dv_2}{dt} = \frac{A_2}{m_2}(\mathrm{p_2} - \mathrm{p_4}) - \frac{k_{l2}(v_2)}{m_2}v_2 + \ \frac{f_{g2}(\theta_2)}{m_2} \quad (54)$$

For edge-3 the force balance equation is,

$$\frac{dv_3}{dt} = \frac{A_3}{m_3}(\mathrm{p_2} - \mathrm{p_3}) - \frac{k_{l3}(v_3)}{m_3}v_3 + \ \frac{f_{g3}(\theta_3)}{m_3} \quad (55)$$

For edge-4 the force balance equation is,

$$\frac{dv_4}{dt} = \frac{A_4}{m_4}(\mathrm{p_4} - \mathrm{p_5}) - \frac{k_{l4}(v_4)}{m_4}v_4 + \ \frac{f_{g4}(\theta_4)}{m_4} \quad (56)$$

For mass conservation at node i,

$$\sum_{\mathrm{i}} \mathrm{A}_i\, \mathrm{v}_i = 0 \text{ at any node i} \quad (57)$$

The above equations can be summarised below in matrix form as:

$$\frac{d}{dt}\begin{bmatrix} v_1 \\ v_2 \\ v_3 \\ v_4 \end{bmatrix} = -\begin{bmatrix} \frac{k_{l1}}{m_1} & & 0 & \\ & \frac{k_{l2}}{m_2} & & \\ & & & \frac{k_{l4}}{m_4} \\ 0 & & & \end{bmatrix}\begin{bmatrix} v_1 \\ v_2 \\ v_3 \\ v_4 \end{bmatrix} + D\left(\frac{A}{M}\right)\begin{bmatrix} -1 & 0 \\ 1 & -1 \\ 1 & 0 \\ 0 & 1 \end{bmatrix}\begin{bmatrix} p_2 \\ p_4 \end{bmatrix} + D\left(\frac{A}{M}\right)\begin{bmatrix} p_1 \\ 0 \\ -p_3 \\ -p_5 \end{bmatrix} + D\left(\frac{1}{M}\right)\begin{bmatrix} f_{g1}(\theta_1) \\ f_{g2}(\theta_2) \\ f_{g4}(\theta_4) \end{bmatrix} f_g\, g\cos(\theta) \tag{58}$$

Mass conservation in matrix form:

$$0 = \begin{bmatrix} 1 & -1 & -1 & 0 \\ 0 & 1 & 0 & -1 \end{bmatrix} D(A)\begin{bmatrix} v_1 \\ v_2 \\ v_3 \\ v_4 \end{bmatrix} \tag{59}$$

The equations can be written compactly as follows,

$$\frac{d}{dt}\begin{bmatrix} 0 \\ 0 \\ v_1 \\ v_2 \\ v_3 \\ v_4 \end{bmatrix} = \left[\begin{array}{c|c} O & A^{mw} \\ \hline A^{wp} & A^{ww} \end{array}\right]\begin{bmatrix} p_2 \\ p_4 \\ v_1 \\ \vdots \\ v_4 \end{bmatrix} + \begin{bmatrix} o \\ \\ bc \end{bmatrix} \tag{60}$$

Where A^{ww} and A^{wp} are the first two matrices in Eq. (58), connecting flow with flow and flow with pressure respectively. A^{mw} is the matrix in Eq. (59) connecting flow with mass. The boundary condition (b.c.-vector) at inlet is the core bubble quasi-static bubble pressure, and at the edge exit is the containment air pressure. The quasistatic core bubble pressure decay can be given as below,

$$\mathrm{Pr} = P_o e^{-\frac{t}{\tau}} \frac{V_o}{V_o + Q} \tag{61}$$

where

P_o is the starting pressure of the quasistatic pressure value, 0.21 MPa;
V_o is the starting volume of the core bubble corresponding to pressure, P_o;
Q is the quantity of sodium (volume) released from the reactor assembly.

Based on experimental data reported in open literature [35], the cool-down time constant of the core bubble is given by,

$$\tau = \frac{100}{3} R \tag{62}$$

where
τ is in milliseconds;
R is inside radius of main vessel in ft.

The time constant estimated from this relation is 0.72 s (τ).
The semi-implicit discretised form for the force balance equation can be given as,

$$\begin{pmatrix} o \\ v^{n+1} \end{pmatrix} = A^n \begin{bmatrix} p^{n+1} \\ v^{n+1} \end{bmatrix} \Delta t + \begin{bmatrix} o \\ bc \end{bmatrix} \Delta t$$
$$(I' - A^n \Delta t) \begin{bmatrix} p^{n+1} \\ v^{n+1} \end{bmatrix} = \left[\begin{pmatrix} o \\ v^n \end{pmatrix} + \begin{bmatrix} o \\ bc \end{bmatrix} \Delta t \right] \tag{63}$$

Where,

$$I' = \begin{bmatrix} 0 & 0 \\ 0 & 1 \end{bmatrix}$$

$$\begin{bmatrix} p^{n+1} \\ v^{n+1} \end{bmatrix} = (I' - A^n \Delta t)^{-1} \left[\begin{pmatrix} o \\ v^n \end{pmatrix} + \begin{bmatrix} o \\ bc \end{bmatrix} \Delta t \right] \tag{64}$$

Eq. (63) and Eq. (64) are solved numerically to find pressure and velocities in the edges. Once the velocities are calculated from the above equations, the quantity of sodium released through path 'i' is calculated from,

$$Q_i = \int_0^{\Delta\tau} \rho A_i v_i \, dt \tag{65}$$

Where, A_i is the cross-sectional area for leak flow,

Friction factors:

The friction factors used are as follows

$$\begin{aligned} f &= \frac{64}{Re} \qquad if \quad Re < 2000 \\ &= 0.0032 + \frac{0.221}{Re^{0.237}} \quad if \quad 2000 \le Re < 10^5 \end{aligned} \tag{66}$$

$$K_i = (K_L + f \frac{L}{D_h}) \frac{\rho v}{2} \tag{67}$$

where,

D_h is hydraulic diameter (which is twice the gap width);
K_L is the local loss coefficient which is the sum of exit, entry, and bend coefficients.

$$K_L = K_{exit} + K_{entry} + K_{bend} \quad (68)$$

The geometric details of leak area, leak path length, leak path diameter and sodium mass in the leak path are given in TABLE 39. The loss coefficients for the entry bends and exit are given in TABLE 41-TABLE 45 [36].

TABLE 39. GEOMETRICAL DETAILS OF THE PENETRATIONS USED FOR THE SODIUM LEAK CALCULATIONS (L & D IN M, A IN M^2, M IN KG)

Penetration		**RS-LRP**	**LRP-SRP**	**RS-IHX/PUMP**	**SRP-CP**	**RS-DHX**
Section - 1	A1	0.4995	0.2652	0.1382	0.1426	0.0179
	L1	1.840	1.835	1.800	1.800	1.800
	D1	0.05	0.04	0.040	0.040	0.020
	M1	772.05	408.8	207.00	213.60	26.82
Section - 2	A2	0.1006	0.0667	3.58×10^{-3}	7.38×10^{-3}	1.0×10^{-3}
	L2	0.690	0.580	0.060	0.060	0.060
	D2	0.010	0.010	0.001	0.002	0.001
	M2	71.55	45.23	0.1788	0.3685	0.0502
Section - 3	A3	0.0211	0.0143	-	-	-
	L3	0.165	0.145	-	-	-
	D3	0.002	0.002	-	-	-
	M3	2.92	1.741	-	-	-
Section-4	A4	0.105	-	-	-	-
	L4	0.160	-	-	-	-
	D4	0.010	-	-	-	-
	M4	14.28	-	-	-	-

A is the cross-sectional flow area, L is the path length, D is the hydraulic diameter which is twice the gap width and M is the mass of sodium in the section.

5.3.2. Results

The numerical procedures for solving the conservation equations Eq. (63) and Eq. (64) were written in Python. The initial quasi static pressure of core bubble is 0.21 MPa. The transient variation of core bubble pressure after start of quasi static phase is given in the FIG. 95. The core bubble reaches the atmospheric pressure in 0.52 seconds, from Eq (61).

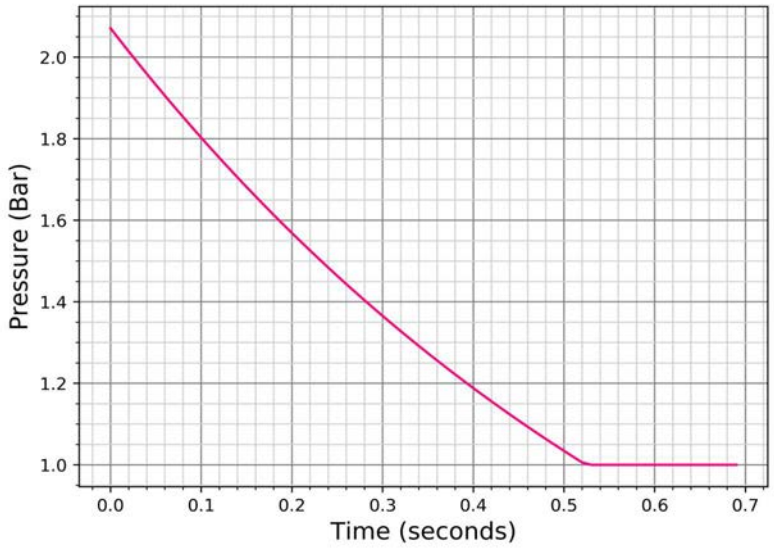

FIG. 95. Transient variation of core bubble after start of quasi static phase.

5.3.2.1. *Total leaked mass from major leak paths*

The calculated total mass leaked through major leak paths are given in the TABLE 40. As shown in TABLE 40, 83% (~312 kg) of total sodium released comes from the RS-LRP and LRP-SRP leak paths. The leak from other leak paths is less than ~20 kg. The total released sodium is about ~330 Kg. The details of the loss coefficients used in the calculation are given in TABLE 41 to TABLE 45. For exit nodes, the loss coefficient is assigned as 1. The mass flow rates through different leak paths are shown in FIG. 96 to FIG. 100. The total leak mass flow rate is given in FIG. 101.

TABLE 40. TOTAL LEAKED MASS FROM EACH LEAK PATHS

Leak Paths	**Leaked mass (kg)**
RS-LRP	150.54
LRP-SRP	103.73
IHX/Pump-RS	36.15 (4 * 6.02 + 2 * 6.02)
CP-SRP	14.47
DHX-RS	6.84 (1.71 * 4)
Total:	**311.73 (Kg)**

Loss coefficient data:

TABLE 41. RS-LRP

Branch	**K_{entry}**	**K_{bend}**	**K_{exit}**
1	0.5	0	0
2	0.5	5	0
3	0.5	1	1
4	0.5	1	1

TABLE 42. LRP-SRP

Branch	**K_{entry}**	**K_{bend}**	**K_{exit}**
1	0.5	0	0
2	0.5	5	1
3	0.5	1	1

TABLE 43. PUMP/IHX-RS

Branch	**K_{entry}**	**K_{bend}**	**K_{exit}**
1	0.5	0	0
2	0.5	1	1

TABLE 44. CP-SRP

Branch	**K_{entry}**	**K_{bend}**	**K_{exit}**
1	0.5	0	0
2	0.5	1	1

TABLE 45. DHX-RS

Branch	**K_{entry}**	**K_{bend}**	**K_{exit}**
1	0.5	0	0
2	0.5	1	1

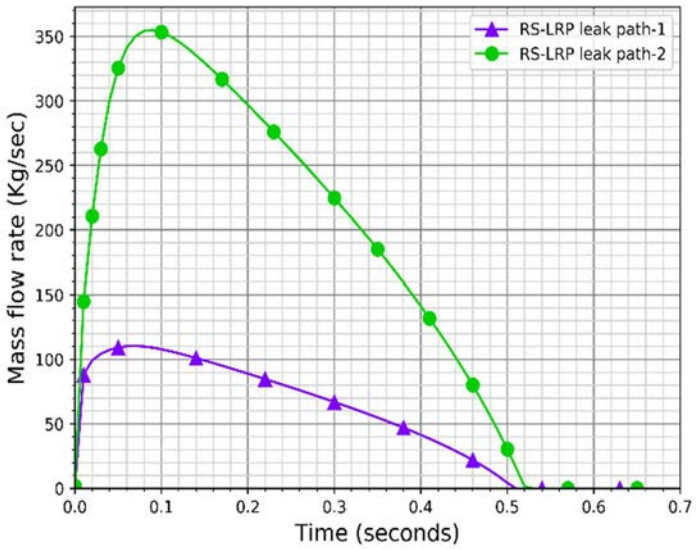

FIG. 96. Mass flow rate from leak rate paths of RS-LRP.

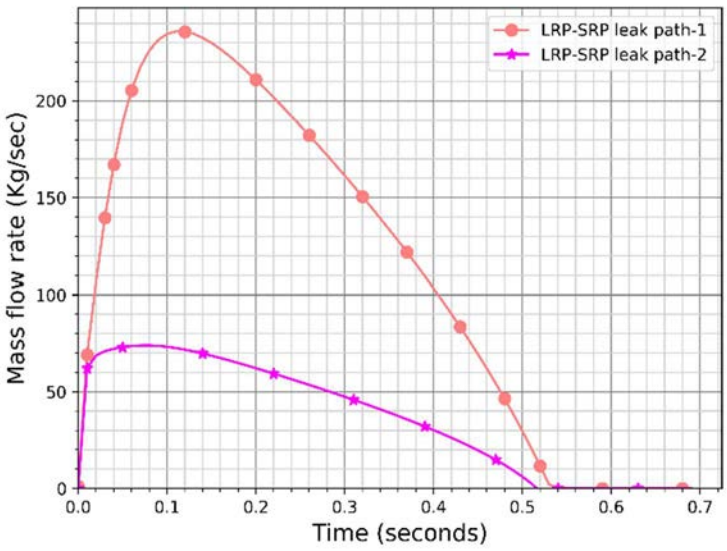

FIG. 97. Mass flow rate from leak rate paths of LRP-SRP.

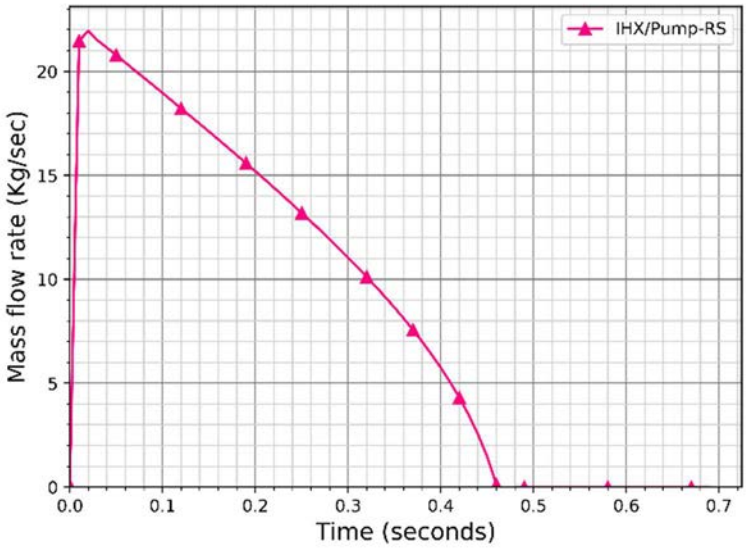

FIG. 98. Mass flow rate from leak path of IHX/Pump-RS.

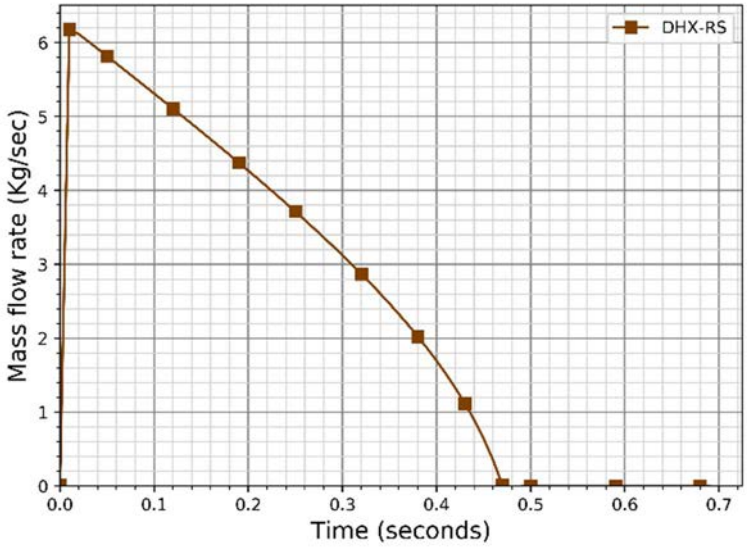

FIG. 99. Mass flow rate from leak path of DHX-RS.

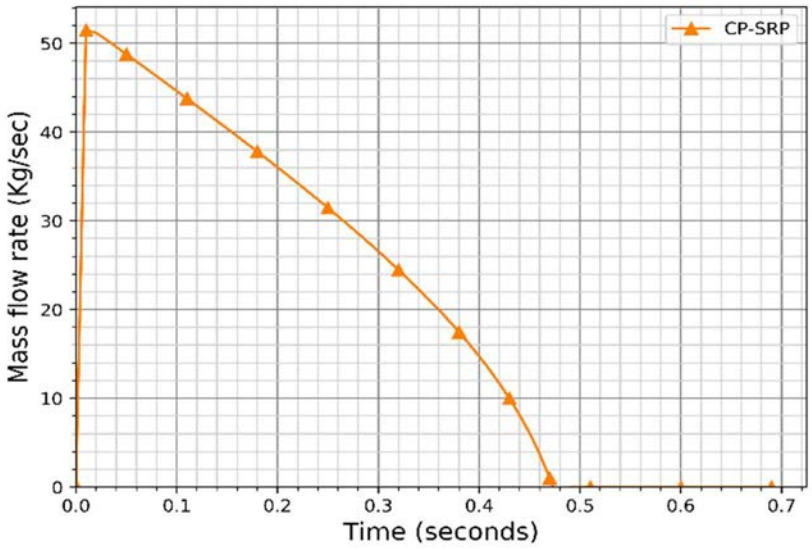

FIG. 100. Mass flow rate from leak path of CP-SRP.

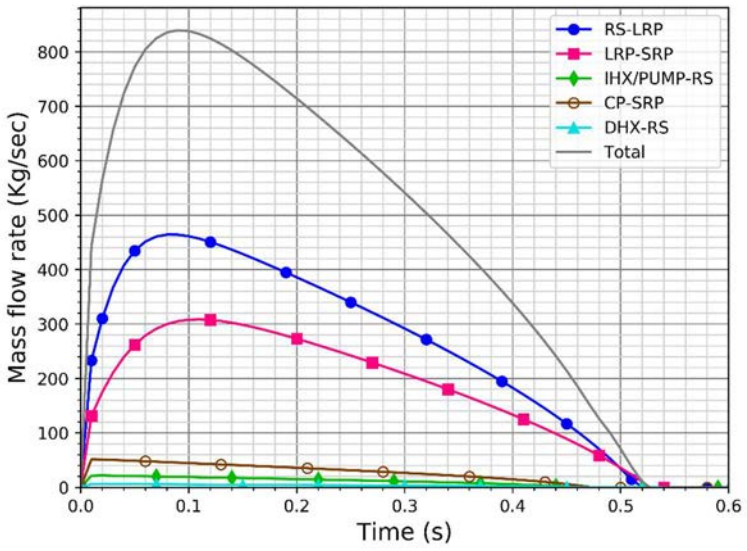

FIG. 101. Mass flow rate for different penetrations.

5.3.2.2. *Sensitivity study*

The flow resistance in the leak paths depends on type of the flow, geometrical features of the flow channels, flow area etc. For this calculation, the loss coefficients were adapted from the open literature [36]. A sensitivity study was performed to study effect of loss coefficients on the leaked sodium amounts. Two cases were considered: 1) The entry coefficients were neglected 2) The loss coefficient for bend was varied from 0.3-1.0. As shown in FIG. 102, when entry coefficients were neglected, the peak mass flow rates increased by ~25 Kg/sec, which leads to 10 Kg increase in leaked sodium from the reference case. When the bend coefficients

were varied from 1 to 0.3, the peak mass flow rate increased by 120 Kg/sec. This leads to ~47 Kg increase in the leaked sodium from the reference case. These results indicate that the mass flow rates are sensitive to the loss coefficients; The accurate estimation of the loss coefficient is crucial.

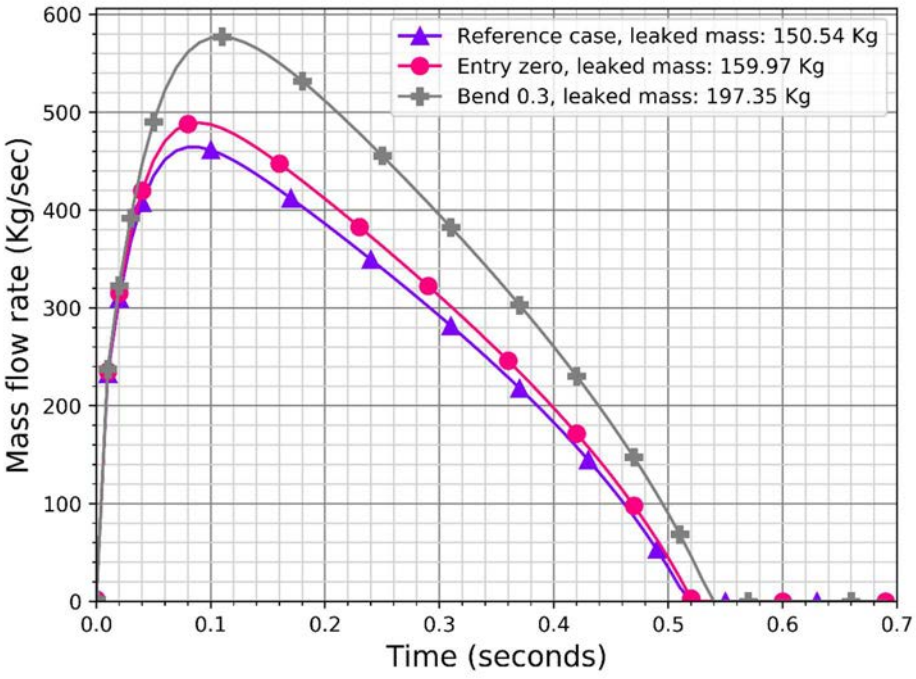

FIG. 102. Sensitivity study of loss coefficient on sodium leak.

5.3.3. Experimental validation

5.3.3.1. *Description of experiment*

The quantity of sodium released is important data for RCB design. Considering the fact that sodium release is a fast-transient process and the annular flow paths are complex with multiple bends, experiments [37] have been conducted to verify the numerically predicted quantity of sodium release. A 1:13 scale experimental top-shield set-up was designed. In the experimental top-shield, RS-LRP, RS-IHX, RS-PSP, RS-DHX and SRP-CP penetrations were simulated. The LRP-SRP penetration was not simulated as it is geometrically similar to that of RS-LRP penetration and the quantity of water leak through it can be calculated from the measured leak through the RS-LRP penetration. The leaks through these simulated penetrations constitute 95% of the total leak. Since, the other minor penetrations constitute only 5% of total leak, they were not simulated to simplify the experimental model. The controlling hydraulic diameters of the leak paths in the experiments were maintained same as or larger than that in the reactor, to simulate the resistance characteristics accurately. The leak paths of all 12 simulated penetrations are combined into three groups. They are: (i) two leak paths of RS-LRP penetration, (ii) leak path of SRP-CP penetration and (iii) leak paths of IHX, PSP and DHX. These groups were physically partitioned using aluminium sheets. This enabled collection of water leakage through each of this group separately. Wet cotton was used to absorb the water leakage through each of these groups. The difference in mass of wet cotton before and after the experiments directly gives the mass of water leak. The nuclear excursion and the subsequent pressure rise / decay in the primary system are simulated using a special chemical explosive. Primary sodium is represented by water as the hydraulic properties of sodium (density and

viscosity) are very close to that of water. Four experiments were conducted for energy release equivalent to 100 MJ.

5.3.3.2. *Sodium Leak Extrapolated for Reactor*

The value of initial quasi-static pressure predicted using Eq. (61) for the reactor is 0.21 MPa , while the measured peak pressure below the roof slab in the experiment is 8.668 MPa. The density of sodium is 840 kg/m^3 and that of water is 1000 kg/m^3. The duration of the quasi static stage in the reactor was 0.6 s while the duration of loading in the experiments was 0.009s. The sodium leak in the reactor through various penetrations were extrapolated from the measured water leak and are presented in TABLE 46. From TABLE 46, the maximum value of sodium leak expected through the LRP penetrations is 104.2 kg and hence, the same through the SRP penetration is 69.5 kg (104.2 x 2/3 kg). The maximum sodium leak through the CP, IHX, PSP and DHX penetrations is 87.8 kg. Thus, the sum of sodium leakage through all penetrations is 261.5 kg. Since the smaller penetrations, which are not simulated in the experiment, contribute 5% of total leak, the sodium leak through them is estimated 13 kg. Thus, the maximum value of total sodium leak expected in the reactor is 275 kg. This value is 54 kg less than that calculated for the reactor, suggesting that adequate margin is available in the numerical calculations. Hence, a sodium leak of 350 kg has been used for the RCB fire calculations and the eventual pressure seen by the RCB.

TABLE 46. WATER LEAK MEASURED IN EXPERIMENTS AND SODIUM LEAK EXTRAPOLATED FOR REACTOR

Penetration	**No. of the run**	**Water leak measured (kg)**	**Expected Sodium leak in the reactor (Kg)**
LRP	Run-1	0.920	104.2
	Run-2	0.100	11.326
	Run-3	0.600	67.957
	Mean	**0.540**	**61.162**
Control plug	Run-1	0.275	30.950
	Run-2	0.150	16.881
	Run-3	0.170	19.133
	Mean	**0.198**	**22.284**
IHX-PSP-DHX	Run-1	1.220	56.860
	Run-2	1.120	52.200
	Run-3	1.100	51.268
	Mean	**1.147**	**53.458**
Sodium leak expected in the reactor based on the maximum value of water leak			**275 (kg)**

Discussion:

From the experimental evaluation, maximum value of total sodium leak expected in the reactor is 275 kg. This value is 55 kg less than that calculated for the reactor (as in section 5.3.3.2.),

suggesting that adequate margin is available in the numerical calculations. Hence, a sodium leak of 350 kg has been used for further RCB fire and aerosol evolution analysis.

5.3.4. Calculation of radionuclide release fractions

Radioactive release:

In a typical accident scenario as informed by the deterministic calculations, fuel clad is expected to melt first leading to the release of plenum inventory to the cover gas. Following the power excursion, when the top layer of sodium is expelled during the quasi-static stage of bubble pressure transient, the RN from the core bubble would not have enough time to reach the top layer of sodium. The RN ejected along with sodium will only be due to the gap inventory. Subsequently the RN inventory in the coolant could be released through the leak paths by vaporisation.

In a bubble expansion model, the Release Fraction for WP-2 (RFWP-2) can be written as,

RFWP-2 = RFgap-release + RFmelt-release + RFevaporation

Where RFgap-release is the release fraction due to the release of gap inventory to the cover gas and sodium which is expelled to the RCB during the quasi static stage of core bubble expansion and condensation. Similarly, RFmelt-release is the fraction distributed in sodium and in the cover gas following the whole core melt which would be released to the RCB in later stages. RFevaporation is the release fraction due to evaporative release from the primary sodium pool.

RFgap-release = RFgr-gas +RFgr-na

RFmelt-release = RFmr-gas +RFmr-na

Here, the subscripts mr - refers to melt release, gr – refers to gap release, gas –refers to RN in the cover gas and na – refers to RN in the sodium.

However, in the thermo-chemical equilibrium model such time sequencing of the RN release behaviour could not be modelled. In the thermo-chemical equilibrium release model, the RN from the core is mixed uniformly in the sodium during the core melt and the RN in vapour phase are assumed to be released to the cover gas. This RN inventory in the cover gas is assumed to be ejected completely during the sodium release phase. The release fractions estimated for coupled calculation is given in TABLE 47 and TABLE 48 (same as WP-1 release fractions). That is the current calculation assumes that the release fraction for WP-2 will be, RFWP-2 = RFgr-gas + RFmr-gas for performing coupled WP-3 calculations. To facilitate independent calculations of WP-3 and for comparing WP-3 calculation aspects a set of reference release fractions based on open literature is also given in TABLE 49.

TABLE 47. RELEASE FRACTION TO COVER GAS FOR NO MIXTURE ASSUMPTION

Element	**Activity (Bq) (MOEC)**	Fraction in cover gas	
		873 K	**1156 K**
I	1.06E+19	2.17E-03	4.35E-01
Cs	1.02E+17	9.10E-01	9.53E-01
Rb	5.17E+17	1.00E+00	1.00E+00
Ru	2.84E+18	5.65E-25	1.08E-21

Sr	6.45E+17	1.83E-12	1.20E-08
Ce	2.62E+18	4.72E-25	1.11E-16
Te	2.02E+18	5.29E-21	1.87E-13
Ba	1.91E+18	2.77E-12	9.97E-09
Zr	1.49E+18	3.01E-23	1.60E-23
La	1.94E+18	1.05E-25	8.86E-17
Kr	6.27E+18	1.00E+00	1.00E+00
Xe	1.07E+19	1.00E+00	1.00E+00
U	2.35E+19	1.27E-25	4.89E-20
Np	2.53E+19	1.51E-22	2.92E-17
Pu	3.14E+17	5.46E-17	7.02E-16
Cm	3.60E+16	1.17E-22	5.70E-15

TABLE 48. RELEASE FRACTION TO THE COVER GAS FOR THE REAL MIXTURE ASSUMPTION

Element	**Activity (Bq) (MOEC)**	Fraction in cover gas	
		873 K	**1156 K**
I	1.06E+19	1.48E-07	4.82E-06
Cs	1.02E+17	3.81E-05	2.46E-04
Rb	5.17E+17	2.72E-05	1.92E-04
Ru	2.84E+18	4.42E-31	1.08E-21
Sr	6.45E+17	3.06E-12	1.36E-08
Ce	2.62E+18	2.06E-25	5.81E-17
Te	2.02E+18	6.12E-28	4.99E-20
Ba	1.91E+18	3.98E-12	1.02E-08
Zr	1.49E+18	1.85E-32	1.58E-24
La	1.94E+18	1.03E-25	8.86E-17
Kr	6.27E+18	1.00E+00	1.00E+00
Xe	1.07E+19	1.00E+00	1.00E+00
U	2.35E+19	1.23E-28	4.89E-20
Np	2.53E+19	2.65E-22	3.19E-17
Pu	3.14E+17	5.63E-17	7.02E-16
Cm	3.60E+16	1.45E-22	6.08E-15

TABLE 49. RELEASE FRACTIONS FOR INPUT TO THE STANDALONE WP-3 CASE

Group	**Elements**	**Designated release fractions**
Noble Gases	Xe, Kr	1
Halogen	I, Br	0.1

Alkali metals	Cs, Rb	0.1
Tellurium group	Te, Sb, Se	1.0E-04
Barium	Ba, Sr	0.1
Noble metals	Ru, Rh, Pd, Mo, Tc, Co	1.0E-04
Lanthanides	La, Zr, Nd, Eu, Nb, Pm, Pr, Sm, Y, Cm, Am	1.0E-04
Cerium	Ce, Pu, Np	1.0E-04

5.3.5. Summary

A numerical code was developed for the estimation of leaked sodium mass to the containment. The results were checked against experimental data. The RN release to the containment is apportioned from the WP-1 calculations. As of now it is assumed that only the RN in the cover gas as estimated by the thermo-chemical equilibrium model is expelled. The fraction of RN released from sodium pool by evaporation would be included in future work.

5.4. SIMULATION EXERCISE USING PLUG CODE (JAEA, JAPAN)

5.4.1. Description of Methods and Models

The PLUG code was developed to model the dynamic movement of shielding plugs and the bolts that fix them, and to evaluate the amount of sodium ejected onto the top shield through the gaps between the plugs using the pressure difference above and below the shielding plug as inputs. In this project, the amount of sodium ejected onto the top shield was calculated without determining the dynamic movement of the plugs, assuming that there are gaps between the plugs as an initial condition.

5.4.1.1. *Basic equation for the calculation of sodium ejection*

In the PLUG code, the amount of sodium ejected onto the top shield is calculated based on the modified Bernoulli's equation:

$$P_1 + \rho g H_1 + \frac{1}{2}\rho V_1^2 = \sum \Delta p + P_0 + \rho g H_0 + \frac{1}{2}\rho V_0^2 \quad (69)$$

where,

P is pressure;
ρ is density;
g is gravity acceleration;
H is height from reference level;
V is velocity;
0 is subscript indicating position 0 (outlet);
1 is subscript indicating position 1 (inlet);
$\sum \Delta p$ is sum of all the friction and singular loss.

If position 1 is set to the level where its diameter corresponds to reactor vessel, V_1 becomes nearly zero, and Eq. (79) can be re-written as follows:

$$P_1 - P_0 = \sum \Delta p + \rho g \Delta H + \frac{1}{2}\rho V_0^2 \quad (70)$$

$$\Delta H = H_0 - H_1$$

Equations Eq. (69) and Eq. (70) are steady-state equations which don't include the time derivative term. PLUG code calculates the amount of sodium ejected in each time step by solving equation Eq. (70) with the pressure difference between above and below the roof slab, assuming that the gaps between plugs are filled with liquid sodium and the flow there is in steady-state.

5.4.1.2. *Criterion for sodium flow*

Judging whether sodium flows into the gaps between plugs was done by evaluating whenPressure difference between above and below top shield exceeds the value which corresponds to potential head of liquid sodium in the gap. FIG. 103 shows the flow paths with one exit and three exits. The criterion is explained as follows:

In the case of flow path with one exit, FIG. 103 (a), liquid sodium starts to flow into the gap if the pressure difference between inlet and outlet exceeds the potential head of liquid sodium between Z and A (Eq. (71)).

$$\rho g \Delta H_A < P_1 - P_0 \quad (71)$$

where,

ΔH_A is height from position Z to A.

In the case of flow path with three exits, FIG. 103 (b), liquid sodium starts to flow into the gap if the pressure difference between inlet and outlet exceeds the potential head of liquid sodium between Z and A, although it does not flow into the gap between A and B on the following condition:

$$\rho g \Delta H_A < P_1 - P_0 < \rho g \Delta H_B \quad (72)$$

where,

ΔH_A is height from position Z to A,
ΔH_B is height from position Z to B.

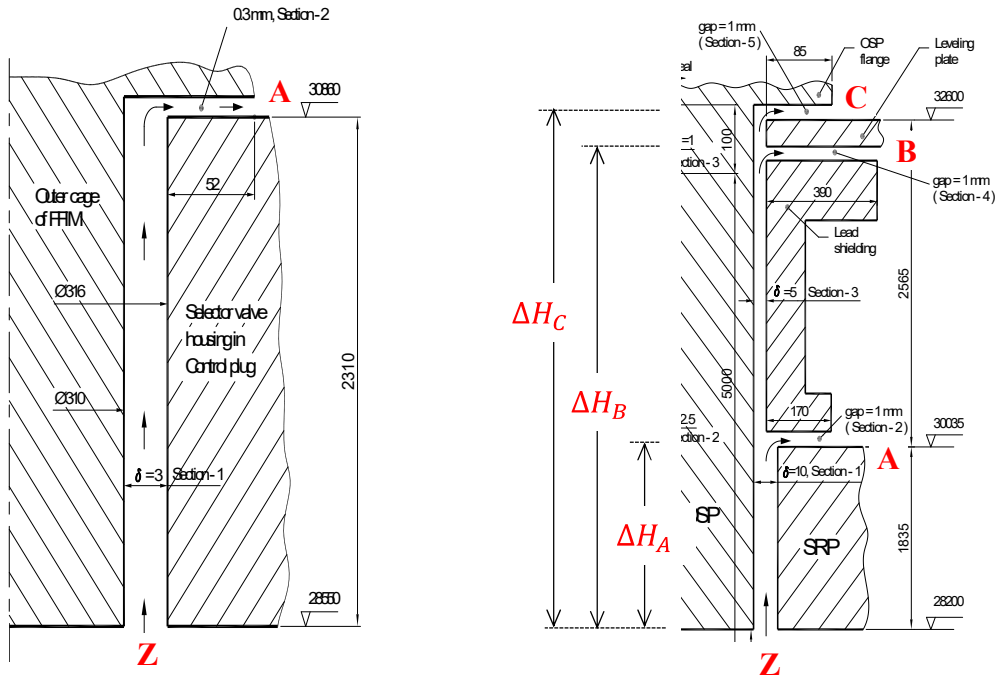

(a) Path with one exit

(b) Path with three exit

FIG. 103. Flow paths with one exit and three exits.

5.4.1.3. *Modelling of flow parts and friction loss*

Vertical flow part:

Friction loss in the vertical flow part is calculated using Darcy-Weisbach equation:

$$\Delta P = \lambda \frac{L}{D_h} \frac{\rho V^2}{2} \tag{73}$$

where,

ΔP is friction loss,
λ is friction coefficient,
L is length of flow segment,
D_h is hydraulic diameter,
ρ is liquid density,
V is liquid velocity.

Vertical flow is modelled as a concentric ring as shown in FIG. 104. Friction coefficient of this flow part is calculated using following equations [38]:

For $Re \leq Re_{crit-l}$

$$\lambda = \frac{64}{Re} \frac{(D_o - D_i)^2}{{D_o}^2 + {D_i}^2 - (D_o - D_i)/[ln\,(D_o/D_i)]} \tag{74}$$

For $Re_{crit-} \leq Re$

$$\lambda = 0.3051 \cdot Re^{-\frac{1}{4}} \cdot f(\varepsilon) \tag{75}$$

$$f(\varepsilon) = 1.056 + 0.02 \log_{10}(\varepsilon - 0.0015)$$

$$\varepsilon = \frac{D_i}{D_o}$$

where,

Re	is Reynolds number;
Re_{crit-l}	is upper bound Reynolds number for laminar flow (=2000);
Re_{crit-l}	is lower bound Reynolds number for turbulent flow (=4000);
D_o	is outer diameter of flow path;
D_i	is inner diameter of flow path.

For $Re_{crit-l} \leq Re \leq Re_{crit-}$

λ is linearly interpolated between $\lambda|_{Re=R\ crit-}$ and $\lambda|_{Re=Re_{crit-t}}$.

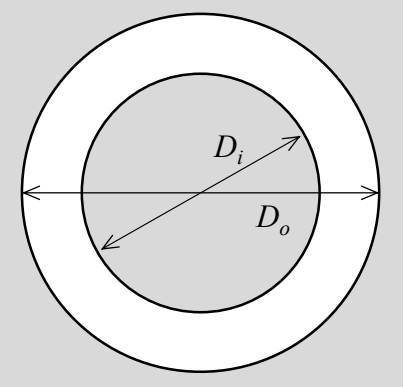

FIG. 104. Cross section of vertical flow channel.

Horizontal flow part:

Friction loss in the horizontal flow part is also calculated using the Darcy-Weisbach equation. Horizontal flow part is modelled as a path with rectangular cross section as shown in FIG. 105, which width, height and depth are respectively perimeter of large concentric ring, height of concentric ring and difference of radii between large and small ring. Friction coefficient of this flow part is calculated using following equations [39]:

For $Re \leq Re_{crit-}$

$$\lambda = \frac{64}{Re} \cdot k \tag{76}$$

$$k = \frac{3/2}{(1+\varepsilon)^2} \cdot \left[1 - \frac{192\varepsilon}{\pi^5}\left\{tanh\left(\frac{\pi}{2\varepsilon}\right) + \frac{1}{3^5} tanh\left(\frac{3\pi}{2\varepsilon}\right)\right\}\right]^{-1}$$

$$\varepsilon = \frac{b}{a}$$

For $Re_{crit-} \leq Re$

$$\lambda = 0.3164 \cdot Re^{-\frac{1}{4}} \tag{77}$$

For $Re_{crit-} \leq Re \leq Re_{crit-}$

λ is linearly interpolated between $\lambda|_{Re=R\ crit-}$ and $\lambda|_{Re=Re_{crit-}}$.

Eq. (76) (correlation for circular tube) was selected for use because this equation gives smaller friction loss at given Reynolds number (and hence this treatment gives conservative results regarding the amount of ejected sodium) than others, although there are several correlations of friction coefficient for turbulent flow in a tube with rectangular flow cross section.

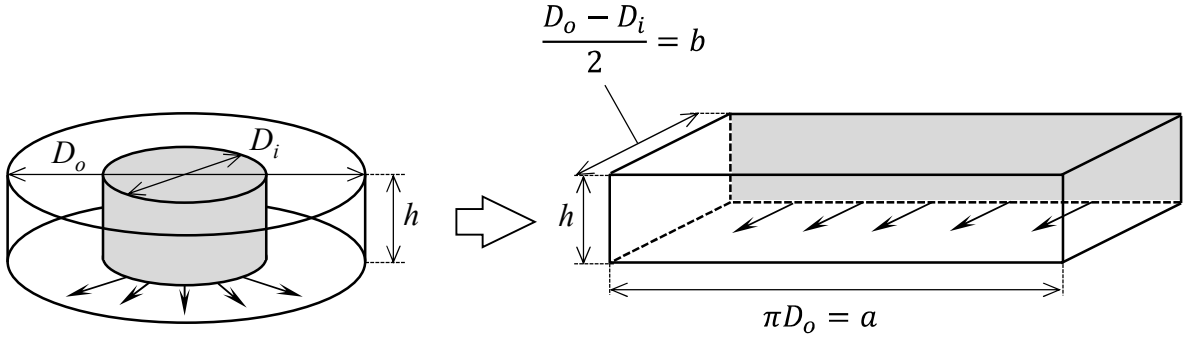

FIG. 105. Cross section of horizontal flow channel.

Bend and inlet section:

The resistance coefficient of the bend and inlet sections is also calculated using Darcy-Weisbach equation:

$$\Delta P = \zeta \frac{\rho V^2}{2} \tag{78}$$

where,

ζ: is resistance coefficient.

Cross sectional area of the inlet side of the bend and the narrow side of the inlet section is used for velocity calculation in Eq. (78). Resistance coefficient of 1.0 is given for all bends (except the first entrance).

5.4.1.4. *Analysis conditions*

The outline of all flow paths modelled in the PLUG code is listed on TABLE 50. There are 16 paths modelled. The image of flow paths of RS-LRP, SRP-OSP and CP-FFIM is shown in FIG. 106. Specifications of flow parts in each flow path are described in TABLE 51 and TABLE 52 where Do is outer diameter, Di is inner diameter, δ is gap width, H is height, L is length, Dh is hydraulic diameter, S is cross sectional area, ΔV is volume and Rc is resistance coefficient.

Two calculation cases were performed: one was the basic case which pressure history is calculated using Eq. (61) with the starting pressure of the quasistatic pressure value, 0.21 MPa and the other was the parametric case where pressure history was calculated by SIMMER code, as described in Section 4.3.2 (case 4). The pressure histories used in these calculations are plotted on FIG. 107. Pressure at the outlet (upper surface of the top shield) was set to 1.013E+5 Pa as initial and boundary condition.

TABLE 50. LIST OF FLOW PATHS MODELLED IN PLUG CODE

Path No.	**Path ID*1**	**Qty**	**Di*2 (m)**	**Do*2 (m)**
1	RS-LRP	1	6.360	6.410
2	LRP-SRP	1	4.221	4.261
3	SRP-OSP	1	0.340	0.360
4	SRP-CP	1	2.250	2.290
5	RS-IHX	4	2.160	2.200
6	RS-PUMP	2	2.160	2.200
7	RS-CPLD	1	0.680	0.700
8	RS-DHX	4	0.560	0.580
9	RS-FTP	1	0.560	0.580
10	RS-IFTM	1	0.560	0.580
11	RS-DND	1	0.330	0.350
12	OSP-GT	1	0.323	0.325
13	CP-FFIM	3	0.310	0.316
14	RS-HPLD	1	0.180	0.200
15	CP-CSRDM	9	0.101	0.160
16	CP-DSRDM	3	0.154	0.160

*1 Abbreviations

RS	Roof Slab	IFTM	Inclined Fuel Transfer Machine
LRP	Large Rotating Plug	DND	Delayed Neutron Detector
SRP	Small Rotating Plug	OSP	Oval Shield Plug of Transfer Arm
CP	Control Plug	GT	Guide Tube
IHX	Intermediate Heat Exchanger	FFIM	Failed Fuel Identification Module
PSP	Primary Sodium Pump	HPLD	Hot Pool Level Detector
CPLD	Cold Pool Level Detector	CSRDM	Control and Safety Rod Drive Mechanisms
DHX	Decay Heat Exchanger	DSRDM	Diverse Safety Rod Drive Mechanisms
FTP	Fuel Transfer Port		

*2 Diameter at the lower surface of roof slab

TABLE 51. SPECIFICATIONS OF FLOW PARTS IN EACH FLOW PATH (1/2)

No.	ID	PIPE/BEND	Do(m)	Di(m)	H(m)	δ(m)	L(m)	Dh(m)	S(m^2)	ΔV(m^3)	Rc
1	RS-LRP	PIPE_A1	6.4100	6.3600	1.84	0.025	1.84	0.0500	0.5014767	0.9227172	-
		PIPE_A2	6.6000	6.5900	0.055	0.005	0.055	0.0100	0.1035940	0.0056977	-
		PIPE_A3	6.5000	6.4900	0.055	0.005	0.055	0.0100	0.1020232	0.0056113	-
		PIPE_A4	6.3950	6.3850	0.215	0.005	0.215	0.0100	0.1003739	0.0215804	-
		PIPE_A5	6.5285	6.3248	0.1025	0.101849	0.102457	0.2037	2.0563212	0.2106845	-
		PIPE_R1	6.5900	6.4100	0.01	0.01	0.09	0.0200	0.2070310	0.0183783	-
		PIPE_R2	6.9300	6.6000	0.001	0.001	0.165	0.0020	0.0217712	0.0035067	-
		PIPE_R3	6.5900	6.5000	0.005	0.005	0.045	0.0100	0.1035155	0.0046264	-
		PIPE_R4	6.4900	6.3950	0.005	0.005	0.0475	0.0100	0.1019447	0.0048069	-
		PIPE_R5	6.8085	6.5285	0.005	0.005	0.14	0.0100	0.1069481	0.0146649	-
		BEND_AB1	6.4100	6.3600	-	-	-	-	-	-	0.01
		BEND_AB2	6.4100	6.3600	-	-	-	-	-	-	1.0
		BEND_AB3	6.6000	6.5900	-	-	-	-	-	-	1.0
		BEND_AB4	6.5000	6.4900	-	-	-	-	-	-	1.0
		BEND_AB5	6.5285	6.3248	-	-	-	-	-	-	1.0
		BEND_RB1	6.6000	-	0.01	-	-	-	-	-	1.0
		BEND_RB2	6.9300	-	0.001	-	-	-	-	-	0
		BEND_RB3	6.5000	-	0.005	-	-	-	-	-	1.0
		BEND_RB4	6.3950	-	0.005	-	-	-	-	-	1.0
		BEND_RB5	6.8085	-	0.005	-	-	-	-	-	0
2	LRP-SRP	PIPE_A1	4.2610	4.2210	1.835	0.02	1.835	0.0400	0.2664699	0.4889722	-
		PIPE_A2	4.3950	4.3850	0.055	0.005	0.055	0.0100	0.0689580	0.0037927	-
		PIPE_A3	4.2950	4.2850	0.055	0.005	0.055	0.0100	0.0673872	0.0037063	-
		PIPE_A4	4.2410	4.2310	0.215	0.005	0.215	0.0100	0.0665389	0.0143059	-
		PIPE_A5	4.3228	4.1935	0.0645	0.064664	0.064536	0.1293	0.8650300	0.0558256	-
		PIPE_R1	4.3850	4.2610	0.01	0.01	0.062	0.0200	0.1377588	0.0084203	-
		PIPE_R2	4.6850	4.3950	0.001	0.001	0.145	0.0020	0.0147184	0.0020681	-
		PIPE_R3	4.3850	4.2950	0.005	0.005	0.045	0.0100	0.0688794	0.0030678	-
		PIPE_R4	4.2850	4.2410	0.005	0.005	0.022	0.0100	0.0673086	0.0014732	-
		PIPE_R5	4.5148	4.3228	0.005	0.005	0.096	0.0100	0.0709182	0.0066634	-
		BEND_AB1	4.2610	4.2210	-	-	-	-	-	-	0.01
		BEND_AB2	4.2610	4.2210	-	-	-	-	-	-	1.0
		BEND_AB3	4.3950	4.3850	-	-	-	-	-	-	1.0
		BEND_AB4	4.2950	4.2850	-	-	-	-	-	-	1.0
		BEND_AB5	4.3228	4.1935	-	-	-	-	-	-	1.0
		BEND_RB1	4.3950	-	0.01	-	-	-	-	-	1.0
		BEND_RB2	4.6850	-	0.001	-	-	-	-	-	0
		BEND_RB3	4.2950	-	0.005	-	-	-	-	-	1.0
		BEND_RB4	4.2410	-	0.005	-	-	-	-	-	1.0
		BEND_RB5	4.5148	-	0.005	-	-	-	-	-	0
3	SRP-OSP	PIPE_A1	0.3600	0.3400	1.835	0.01	1.835	0.0200	0.0224456	0.0411876	-
		PIPE_A2	0.3500	0.3400	2.513	0.005	2.513	0.0100	0.0111442	0.0280055	-
		PIPE_A3	0.3500	0.3400	0.05	0.005	0.05	0.0100	0.0111442	0.0005572	-
		PIPE_R1	0.6900	0.3600	0.001	0.001	0.165	0.0020	0.0033127	0.0004611	-
		PIPE_R2	1.1300	0.3500	0.001	0.001	0.39	0.0020	0.0046950	0.0013532	-
		PIPE_R3	0.5200	0.3500	0.001	0.001	0.085	0.0020	0.0027786	0.0002135	-
		BEND_AB1	0.3600	0.3400	-	-	-	-	-	-	0.01
		BEND_AB2	0.3600	0.3400	-	-	-	-	-	-	1.0
		BEND_AB3	0.3500	0.3400	-	-	-	-	-	-	1.0
		BEND_AB4	0.3500	0.3400	-	-	-	-	-	-	1.0
		BEND_RB1	0.6900	-	0.001	-	-	-	-	-	0
		BEND_RB2	1.1300	-	0.001	-	-	-	-	-	0
		BEND_RB3	0.5200	-	0.001	-	-	-	-	-	0
4	SRP-CP	PIPE_A1	2.2900	2.2500	1.800	0.02	1.8	0.0400	0.1426283	0.2567310	-
		PIPE_R1	2.3900	2.2900	0.001	0.001	0.05	0.0020	0.0075084	0.0003676	-
		BEND_AB1	2.2900	2.2500	-	-	-	-	-	-	0.01
		BEND_AB2	2.2900	2.2500	-	-	-	-	-	-	1.0
		BEND_RB1	2.3900	-	0.001	-	-	-	-	-	0
5	RS-IHX	PIPE_A1	2.2000	2.1600	1.800	0.02	1.8	0.0400	0.1369734	0.2465522	-
		PIPE_R1	2.3200	2.2000	0.0005	0.0005	0.06	0.0010	0.0036442	0.0002130	-
		BEND_AB1	2.2000	2.1600	-	-	-	-	-	-	0.01
		BEND_AB2	2.2000	2.1600	-	-	-	-	-	-	1.0
		BEND_RB1	2.3200	-	0.0005	-	-	-	-	-	0

TABLE 52. SPECIFICATIONS OF FLOW PARTS IN EACH FLOW PATH (2/2)

No.	ID	PIPE/BEND	Do(m)	Di(m)	H(m)	δ(m)	L(m)	Dh(m)	S(m^2)	ΔV(m^3)	Rc
6	RS-PUMP	PIPE_A1	2.2000	2.1600	1.800	0.02	1.8	0.0400	0.1369734	0.2465522	-
		PIPE_R1	2.3200	2.2000	0.0005	0.0005	0.06	0.0010	0.0036442	0.0002130	-
		BEND_AB1	2.2000	2.1600	-	-	-	-	-	-	0.01
		BEND_AB2	2.2000	2.1600	-	-	-	-	-	-	1.0
		BEND_RB1	2.3200	-	0.0005	-	-	-	-	-	0
7	RS-CPLD	PIPE_A1	0.7000	0.6800	1.800	0.01	1.8	0.0200	0.0216770	0.0390186	-
		PIPE_R1	1.0000	0.7000	0.0005	0.0005	0.15	0.0010	0.0015708	0.0002003	-
		BEND_AB1	0.7000	0.6800	-	-	-	-	-	-	0.01
		BEND_AB2	0.7000	0.6800	-	-	-	-	-	-	1.0
		BEND_RB1	1.0000	-	0.0005	-	-	-	-	-	0
8	RS-DHX	PIPE_A1	0.5800	0.5600	1.800	0.01	1.8	0.0200	0.0179071	0.0322327	-
		PIPE_R1	0.7000	0.5800	0.0005	0.0005	0.06	0.0010	0.0010996	0.0000603	-
		BEND_AB1	0.5800	0.5600	-	-	-	-	-	-	0.01
		BEND_AB2	0.5800	0.5600	-	-	-	-	-	-	1.0
		BEND_RB1	0.7000	-	0.0005	-	-	-	-	-	0
9	RS-Fuel Transfer Port	PIPE_A1	0.5800	0.5600	1.800	0.01	1.8	0.0200	0.0179071	0.0322327	-
		PIPE_R1	0.8600	0.5800	0.0005	0.0005	0.14	0.0010	0.0013509	0.0001583	-
		BEND_AB1	0.5800	0.5600	-	-	-	-	-	-	0.01
		BEND_AB2	0.5800	0.5600	-	-	-	-	-	-	1.0
		BEND_RB1	0.8600	-	0.0005	-	-	-	-	-	0
10	RS-IFTM	PIPE_A1	0.5800	0.5600	1.800	0.01	1.8	0.0200	0.0179071	0.0322327	-
		PIPE_R1	0.8600	0.5800	0.0005	0.0005	0.14	0.0010	0.0013509	0.0001583	-
		BEND_AB1	0.5800	0.5600	-	-	-	-	-	-	0.01
		BEND_AB2	0.5800	0.5600	-	-	-	-	-	-	1.0
		BEND_RB1	0.8600	-	0.0005	-	-	-	-	-	0
11	RS-DND	PIPE_A1	0.3500	0.3300	1.800	0.01	1.8	0.0200	0.0106814	0.0192265	-
		PIPE_R1	0.6300	0.3500	0.0005	0.0005	0.14	0.0010	0.0009896	0.0001078	-
		BEND_AB1	0.3500	0.3300	-	-	-	-	-	-	0.01
		BEND_AB2	0.3500	0.3300	-	-	-	-	-	-	1.0
		BEND_RB1	0.6300	-	0.0005	-	-	-	-	-	0
12	OSP-Guide Tube	PIPE_A1	0.3250	0.3230	0.1	0.001	0.1	0.0020	0.0010179	0.0001018	-
		PIPE_A2	0.3250	0.3200	5	0.0025	5	0.0050	0.0025329	0.0126645	-
		PIPE_A3	0.3250	0.3230	0.1	0.001	0.1	0.0020	0.0010179	0.0001018	-
		BEND_AB1	0.3250	0.3230	-	-	-	-	-	-	0.01
		BEND_AB2	0.3250	0.3200	-	-	-	-	-	-	1.0
		BEND_AB3	0.3250	0.3230	-	-	-	-	-	-	0
13	CP-FFIM	PIPE_A1	0.3160	0.3100	2.3100	0.003	2.31	0.0060	0.0029500	0.0068144	-
		PIPE_R1	0.4200	0.3160	0.0003	0.0003	0.052	0.0006	0.0003958	0.0000180	-
		BEND_AB1	0.3160	0.3100	-	-	-	-	-	-	0.01
		BEND_AB2	0.3160	0.3100	-	-	-	-	-	-	1.0
		BEND_RB1	0.4200	-	0.0003	-	-	-	-	-	0
14	RS-HPLD	PIPE_A1	0.2000	0.1800	1.8000	0.01	1.8	0.0200	0.0059690	0.0107442	-
		PIPE_R1	0.4400	0.2000	0.0005	0.0005	0.12	0.0010	0.0006912	0.0000603	-
		BEND_AB1	0.2000	0.1800	-	-	-	-	-	-	0.01
		BEND_AB2	0.2000	0.1800	-	-	-	-	-	-	1.0
		BEND_RB1	0.4400	-	0.0005	-	-	-	-	-	0
15	CP-CSRDM	PIPE_A1	0.1600	0.1010	1.07	0.0295	1.07	0.0590	0.0120943	0.0129410	-
		PIPE_A2	0.1600	0.1440	0.84	0.008	0.84	0.0160	0.0038202	0.0032089	-
		PIPE_A3	0.1600	0.1540	0.605	0.003	0.605	0.0060	0.0014797	0.0008952	-
		PIPE_R1	0.3900	0.1600	0.0002	0.0002	0.115	0.0004	0.0002450	0.0000199	-
		BEND_AB1	0.1600	0.1010	-	-	-	-	-	-	0.01
		BEND_AB2	0.1600	0.1010	-	-	-	-	-	-	1.0
		BEND_AB3	0.1600	0.1440	-	-	-	-	-	-	1.0
		BEND_AB4	0.1600	0.1540	-	-	-	-	-	-	1.0
		BEND_RB1	0.3900	-	0.0002	-	-	-	-	-	0
16	CP-DSRDM	PIPE_A1	0.1600	0.1540	2.0850	0.003	2.085	0.0060	0.0014797	0.0030852	-
		PIPE_R1	0.3900	0.1600	0.0002	0.0002	0.115	0.0004	0.0002450	0.0000199	-
		BEND_AB1	0.1600	0.1540	-	-	-	-	-	-	0.01
		BEND_AB2	0.1600	0.1540	-	-	-	-	-	-	1.0
		BEND_RB1	0.3900	-	0.0002	-	-	-	-	-	0

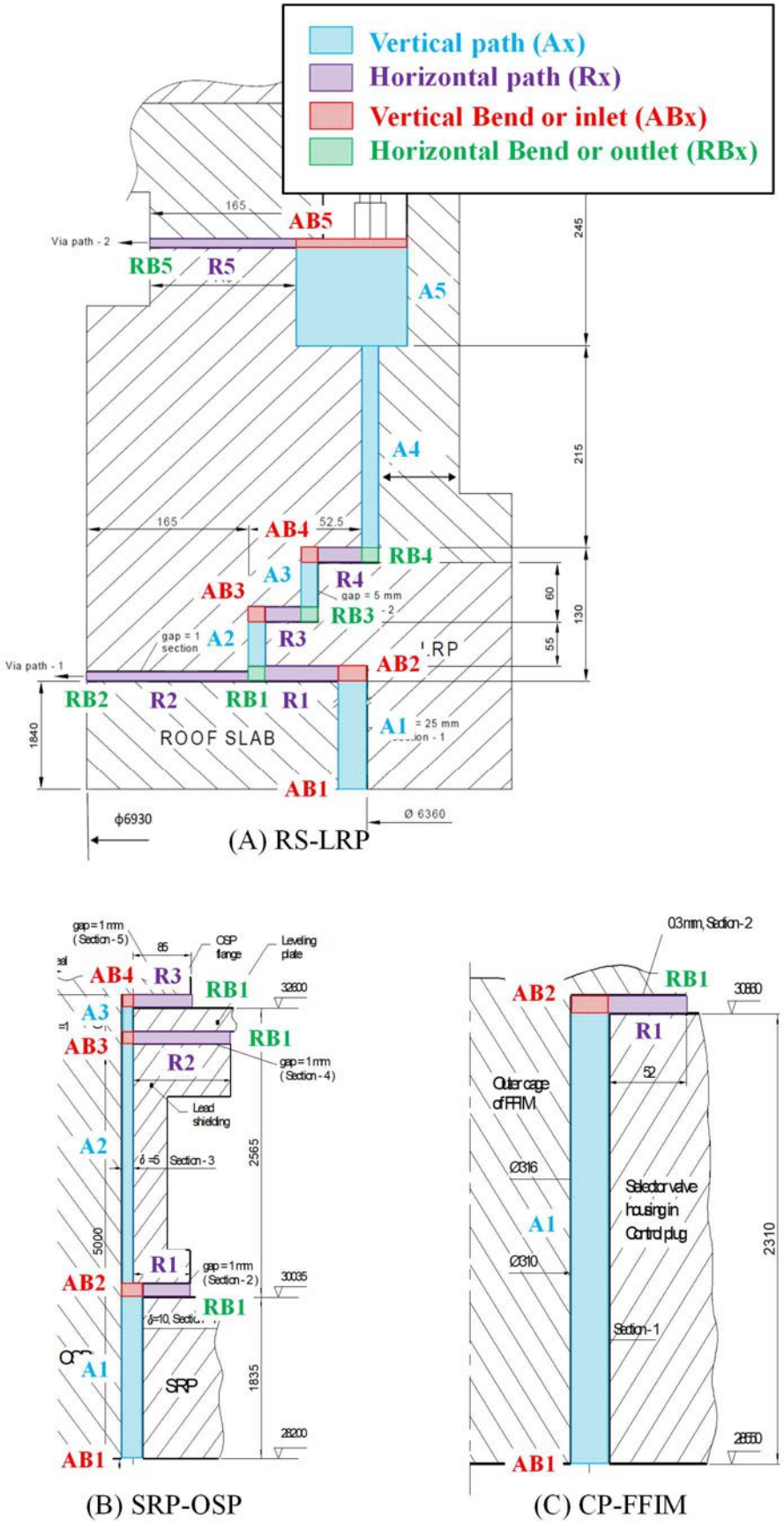

FIG. 106. Flow path model of RS-LRP, SRP-OSP and CP-FFIM.

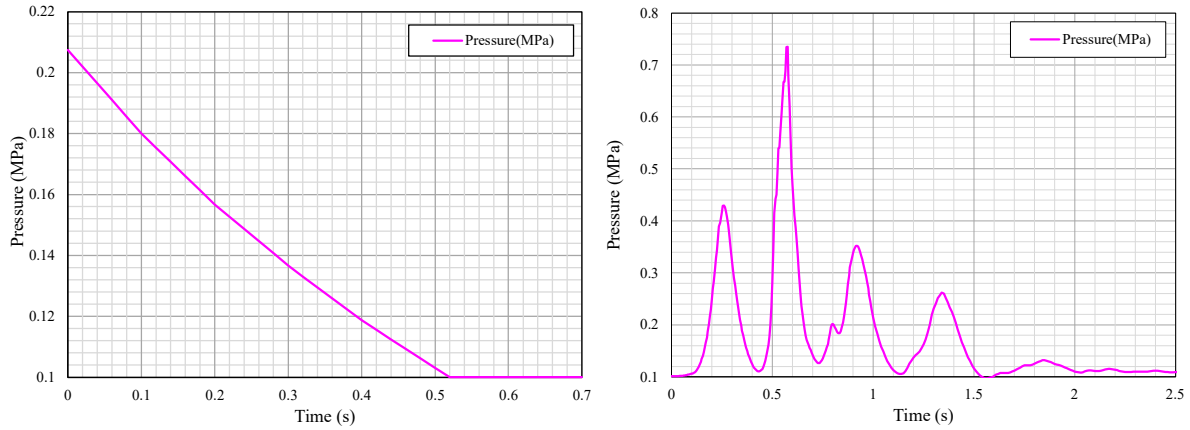

(a) Basic case (b) Parametric case

FIG. 107. Pressure histories used in these calculations.

5.4.1. Results

FIG. 108 to FIG. 113 shows the results of the basic case calculation. The dominant flow path is RS-LRP, and it is followd by LRP-SRP, RS-IHX, and SRP-CP. The maximum sodium flowrate amounts to 560 kg/s at RS-LRP path. TABLE 53 shows the total leaked mass from each flow path, and the total leaked mass calculated in basic case is 335 kg.

The results of the basic case can be compared with those evaluated in Section 5.3. In the calculation carried out in Section 5.3, time derivative was considered in the basic equation so that the inertia of the fluid is appropriately taken into account, although it is not in the calculation using PLUG code. Because input pressure is the same, and friction and singular loss of the flow paths are not so far in each calcunlation, the effect of the inertia of the fluid can be highlighted by comparison.

The amount of sodium ejected is 335 kg in the PLUG code calculation, similar to that calculated in the basic case in Section 5.3, 312 kg. This result can be explained by the fact that at the beginning of the leak, mass flow rate is greater in the PLUG code calculation, whereas at the end of the leak, mass flow rate decreases rapidly in the PLUG code calculation due to no inertia effect and as a result, the total leaked mass become comparable in both calculations.

FIG. 114 to FIG. 117 show the results of parametric case. The maximum sodium flowrate amounts to 1500 kg/s at RS-LRP path. The total leaked mass is also listed in TABLE 53, and this amounts to 1840 kg. In parametric case, not only peak pressure increased relative to the basic case from 0.2 MPa to 0.7 MPa but also duration of the pressure loading increased from 0.5 s to 1.5 s. This is the reason for the increase of the amount of sodium leaked.

In the PLUG code calculation, it is assumed that the flow path is filled with sodium as an initial condition. This ignores the transient where sodium is filling into the flow path. In reality, the sodium enters into the gaps between the plugs after the sodium slug impacts on the lower surface of the top shield, and after the gap capacity is filled with the sodium, it outflows onto the top shield. The approximate capacity of the gaps between the plugs is listed in TABLE 53. If the gap capacity is taken into account, the sodium does not outflow onto the top shield in the

basic case, and the amount of sodium outflowed onto the top shield amounts to 75 kg in the parametric case (from paths LRP-SRP and SRP-OSP).

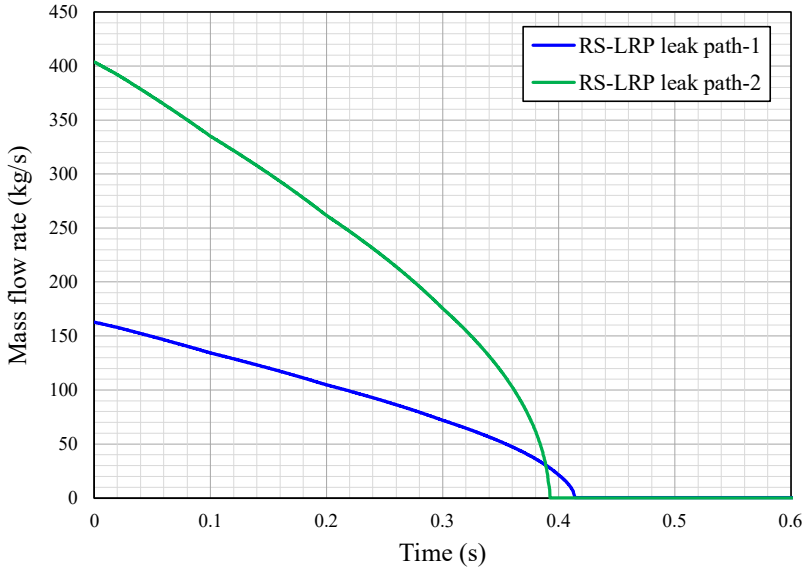

FIG. 108. Calculated sodium mass flow rate leaked from path RS-LRP (basic case).

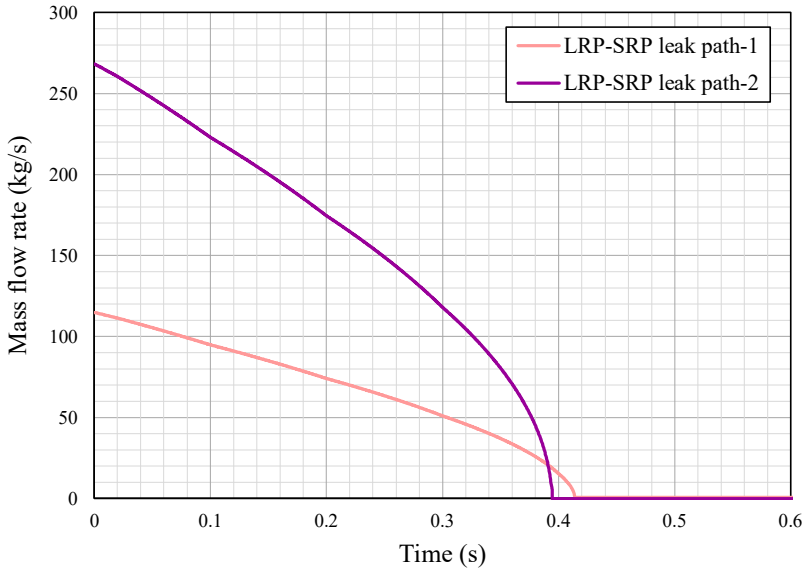

FIG. 109. Calculated sodium mass flow rate leaked from path LRP-SRP (basic case).

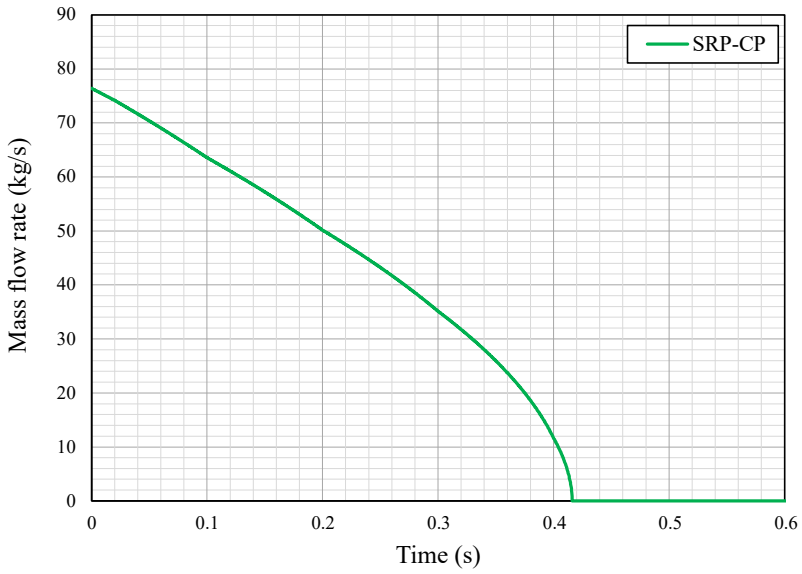

FIG. 110. Calculated sodium mass flow rate leaked from path SRP-CP (basic case).

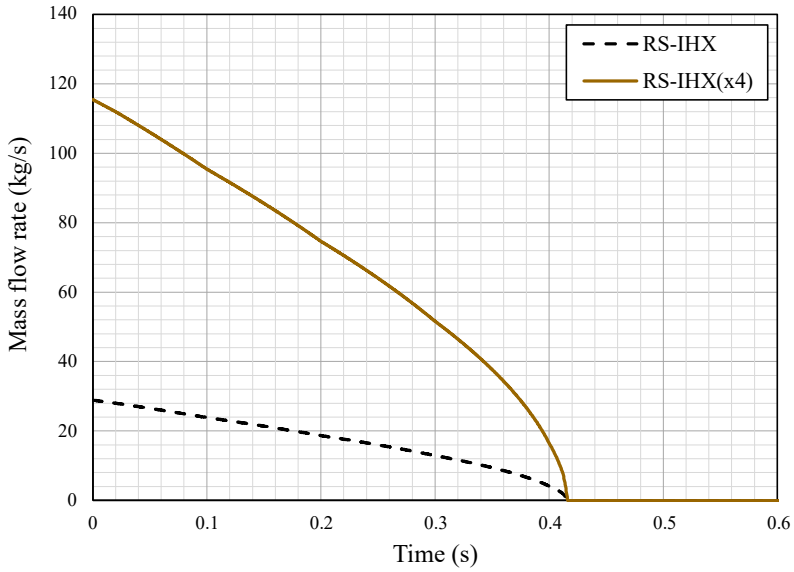

FIG. 111. Calculated sodium mass flow rate leaked from path RS-IHX (basic case).

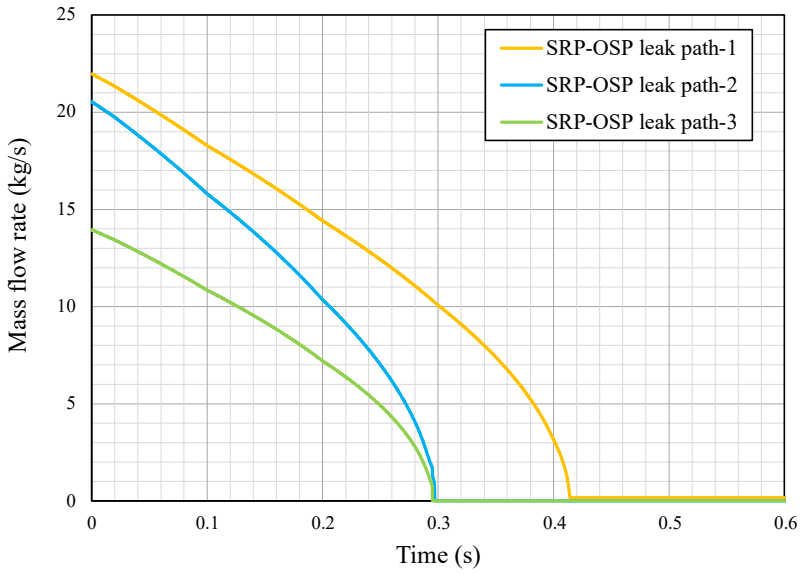

FIG. 112. Calculated sodium mass flow rate leaked from path SRP-OSP (basic case).

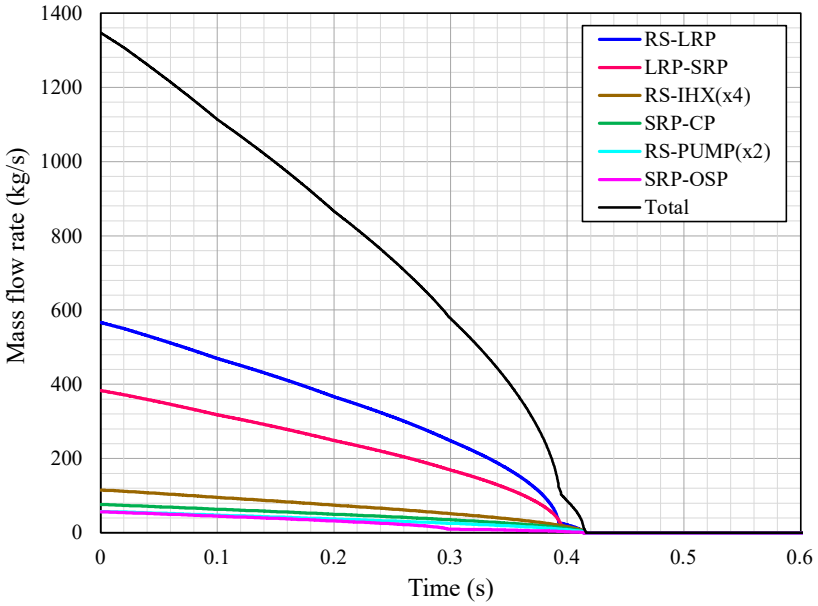

FIG. 113. Calculated sodium mass flow rate for different penetrations (basic case).

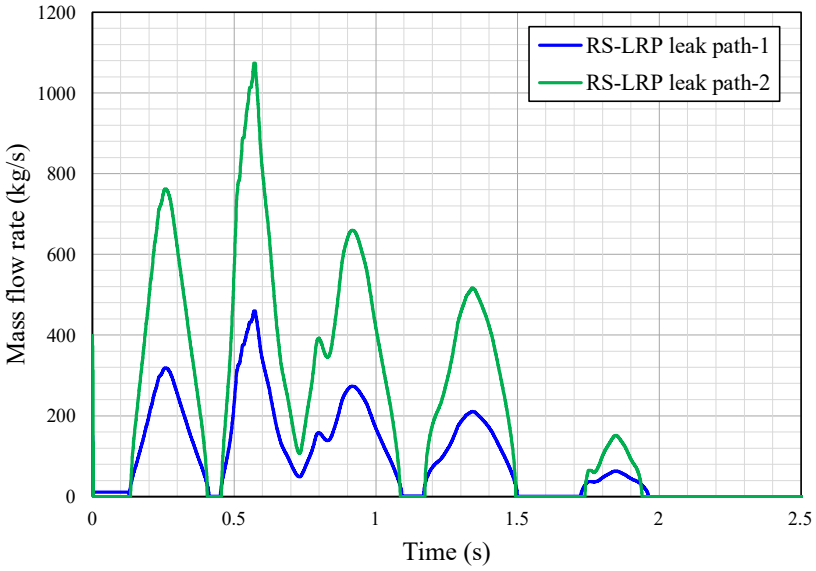

FIG. 114. Calculated sodium mass flow rate leaked from path RS-LRP (parametric case).

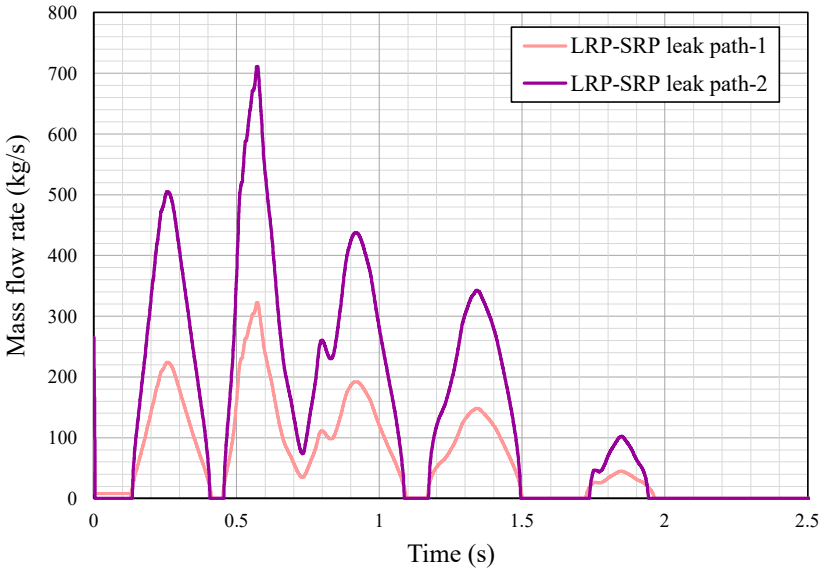

FIG. 115. Calculated sodium mass flow rate leaked from path LRP-SRP (parametric case).

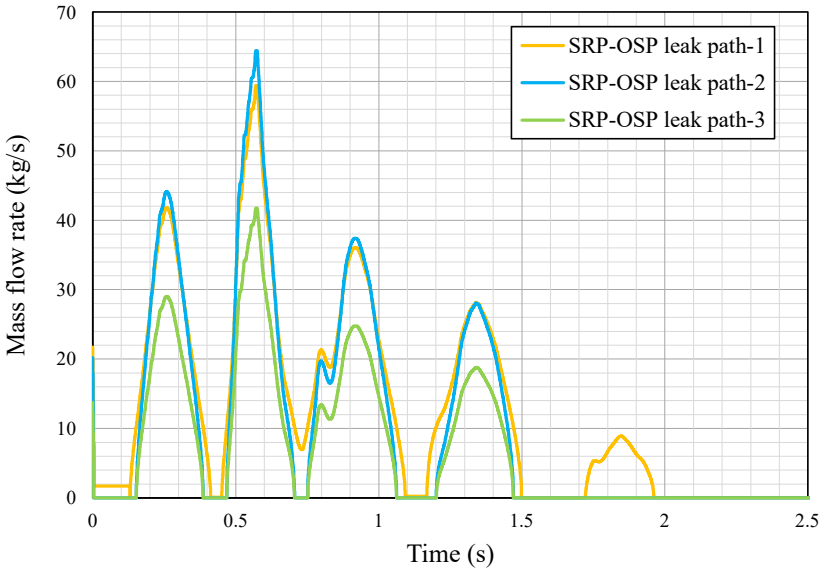

FIG. 116. Calculated sodium mass flow rate leaked from path SRP-OSP (parametric case).

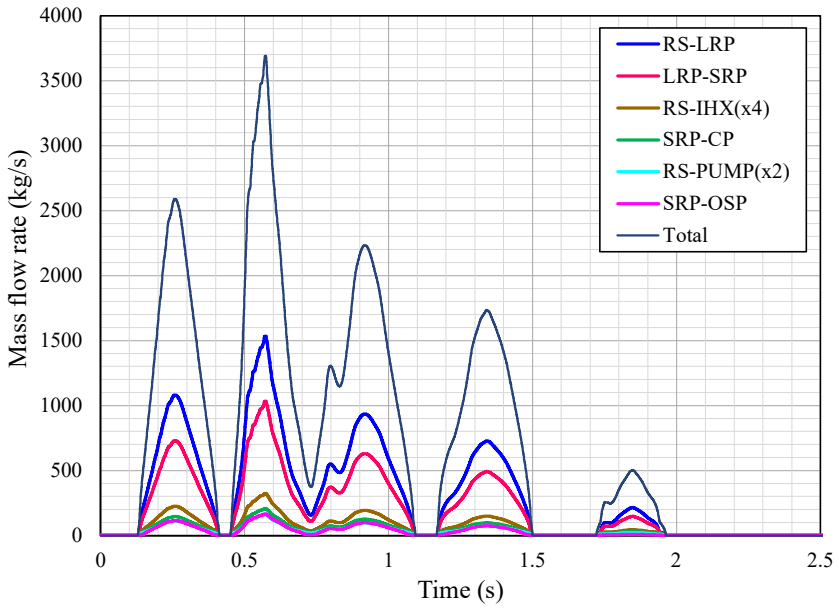

FIG. 117. Calculated sodium mass flow rate for different penetrations (parametric case).

TABLE 53. TOTAL LEAKED MASS FROM EACH LEAK PATHS (IN KG)

Path ID	**Basic case**	**Parametric case**	**Gap Capacity[*2]**
RS-LRP	141.1	771.0	908
LRP-SRP	95.9	522.0	460
RS-IHX(4)[*1]/Pump(2)[*1]	44.0	241.2	1212
SRP-CP	19.7	106.0	211

SRP-OSP	12.1	74.5	34
RS-DHX(4)*1	8.8	48.4	104
Other	13.8	77.23	275
Total:	334.9	1840.3	3204

*1 Value in the bracket corresponds to the number of the component.
*2 Gap Capacity = Volume of the gap x Sodium density. Liquid sodium density is assumed here to 820 kg/m^3 (~550°C). Only the volume of vertical and horizontal part of the leak path is considered (volume of the bends is excluded).

5.4.1. Summary

In the basic case calculation using the PLUG code, the maximum sodium flow rate amounts to 560 kg/s at RS-LRP path, whereas it amounts to 1500 kg/s in parametric case, depending on the pressure loaded under the shield plugs. The amount sodium leaked from all the leak paths is 335 kg in the basic case, whereas it is 1840 kg in the parametric case.

If the gap capacity, the capacity of the gaps between plugs which can retain the flowing sodium, is taken into account, the sodium does not outflow onto the top shield in the basic case and the amount of sodium outflowed onto the top shield amounts to 75 kg in the parametric case (from paths LRP-SRP and SRP-OSP).

6. WP-3 MODELS, RESULTS AND DISCUSSIONS

6.1. SIMULATION EXERCISE USING CONTAIN-LMR CODE (CIAE, CHINA)

6.1.1. Description of Methods and Model

In WP3 Case 1, 350 kg sodium was ejected directly into the containment building, along with fission products from the reactor core. The following assumptions were made: the enclosure and ventilation of the containment were not considered, the containment leak rate was 0.1% Δv/v/h@ 25 kPa. Sodium pool fire was not considered, the sodium combustion form was spray fire.

The objective of this simulation was to obtain a better understanding of the in-containment phenomena following the core disruptive accident. Sodium fire occurs immediately following the sodium ejected into the containment, the fission products and fuel from the primary sodium decay and transport in the containment building. As the containment is not sealed, the fission products and sodium aerosols may leak to the environment. The CONTAIN-LMR models used in the calculation includes sodium spray fire, aerosol transport, fission product, and intercell flow.

6.1.1.1. *Sodium spray fire*

The sodium spray fire is patterned after the phenomenological model used in NACOM, a code developed and tested at Brookhaven National Laboratory. In the model, an initial size distribution is determined from a correlation using a specified mean droplet diameter. The trajectory of the drops is downward, with a velocity equal to the terminal velocity. The combustion rate (a function of droplet size, fall velocity and atmospheric conditions) is integrated over the droplet's fall to obtain the total mass of sodium burned. Two chemical reactions of sodium droplets and oxygen in the air are simulated:

$$\text{Monoxide:} \quad 2Na+0.5O_2 \rightarrow Na_2O$$
$$\text{Peroxide:} \quad 2Na+O_2 \rightarrow Na_2O_2$$

If a droplet of a given size is not predicted to burn completely, a temporal, numerical integration of the droplet is performed. The time increment for the integration is taken as one-eighth of the fall time initially determined. The appropriate combustion equation is integrated over each timestep using a Runge-Kutta scheme. Following each integration step, the resulting droplet diameter is determined, from which a new terminal velocity is found. The heat of reaction is transferred to the atmosphere. A heat balance results in a new value for the droplet temperature. This process continues until the droplet is either consumed or reaches the cell bottom.

Parameters of the sodium spray fire model specified by the user are as follows:

- HITE: fall height of sodium spray.
- DME: mean sodium droplet diameter.
- FNA2O2: mole fraction of sodium peroxide produced by the fire.
- Spray Source: sodium spray source of the leak.

It is assumed as an input parameter setting that the fall height of the spray is twice the height of the enclosure and all the oxygen consumed goes into the formation of peroxide. The value for

mean sodium droplet diameter is 1mm which is the default value in the code. TABLE 54 shows the input parameters of sodium spray fire model used in the calculation.

TABLE 54. THE INPUT PARAMETERS OF SODIUM SPRAY FIRE MODEL

Parameter	**unit**	**Value**
Sodium temperature	K	873
Fall height of spray	m	8
Mean sodium droplet diameter	mm	1
Combustion product	—	Na_2O_2
Spray source	—	Table input*

*350 kg total sodium is ejected in 0.53s. According to the mass flow rate for sodium ejection table, the mass flow rates are scaled to 3 points using liner interpolation in the calculation. Three time points are 0s, 0.1s, 0.53s. The corresponding flow rates are 700 kg/s, 1050 kg/s, 170 kg/s.

6.1.1.2. *Aerosol behavior*

The MAEROS aerosol model, a state-of the-art code for modelling aerosol behavior in either wet or dry environments, forms the basis for the aerosol behavior model in CONTAIN. MAEROS uses a number “nsectn” of size classes, or sections, to represent the particle size distribution for the suspended aerosols. In addition, the code is designed to cope with the fact that certain aerosols, particularly the radiologically significant ones, may behave quite differently from the other aerosols. Therefore, one may specify a number “nac” of aerosol species, or components, which are tracked individually, and which can have independent source size distributions and source rates. Up to eight aerosol components can be specified. Thus, MAEROS is said to be a multisectional, multicomponent aerosol model.

The initial airborne size distribution and the distribution of sizes in a source of new particles are taken to be lognormal. The lognormal distribution of mass m(D) in particles with a spherical equivalent diameter between D and D+dD is given by the standard expression

$$m(D)dD \propto exp\left\{-\frac{1}{2}\left[\frac{ln^2(D/"amean")}{"avar"^2}\right]\right\}\frac{dD}{D} \tag{79}$$

In aerosol terminology, “amean” is the volume-equivalent mass median diameter, and “avar” is the natural logarithm of the geometric standard deviation with respect to diameter.

The physical phenomena included in the MAEROS model are: 1) coagulation, 2) deposition, 3) particle growth due to condensation or what is often called gas-to-particle conversion and 4) time varying sources of particles with different sizes and chemical compositions.

Coagulation

Any mechanism which results in the collision and subsequent coalescence of particles may be classified as coagulation process. The three mechanisms of primary interest are 1) Brownian motion, 2) turbulence and 3) gravity.

Deposition

The three mechanisms considered for aerosol removal are 1) gravitational settling, 2) diffusive wall deposition and 3) thermophoretic wall deposition.

Condensation

Condensation of a vapor on to a particle results in particle growth. For isothermal condensation, the growth rate given by Fuchs and Sutugin is often used to calculate particle growth.

In the case calculated, the aerosol material density is 1000 kg/m^3, the volume-equivalent mass median diameter is 1um, the geometric standard deviation is 0.693, turbulent dissipation rate is 0.1 m^2/s^3. Some other main parameters, such as dynamic shape factor and agglomeration shape factor, are default values in the code.

6.1.1.3. *Fission product behavior*

The code follows the birth and decay of each fission product specified, and accounts for the associated decay heating. It tracks the movement of fission products throughout the containment system, and, if a breach of containment occurs to a cell that represents the outside environment, the code will predict the extent of fission product releases.

Fission products are associated with various 'hosts', or repositories. Some hosts, such as the upper cell atmosphere gas or aerosol, are mobile, while others such as the wall surfaces, are fixed. In general, the initial introduction of fission products onto various hosts is specified by the user. Fission products are assigned to various hosts. The user should assign fission products to a host based primarily on the chemical affinity and physical characteristics of the fission product.

Fission product modelling is coupled to the thermal-hydraulics models in CONTAIN through the effects of fission product decay heating. The decay heat of fission products hosted to the gas and to aerosols is assumed to be deposited in the atmosphere. The decay heat of fission products on structure surfaces is assumed to heat the structure node immediately below the surface. The decay heat of fission products in the lower cell layers is assumed to be distributed uniformly in the layer.

Airborne fission products flow with the atmosphere gas as it passes from one cell to another. Released fission products are most effectively transported within containment and into the environment as gases and aerosols.

43 isotopes were considered in the problem. TABLE 55 shows the main input of fission products. Noble gases in-containment release fraction is 100%, Halogen, Alkali metals and Barium group release fraction is 10%, the other fission products release fraction is 0.01%. The host of noble gases is gas, the host of Halogen, Alkali metals and Barium group is aerosol Na_2O, host of the other fission products is aerosol UO_2.

TABLE 55. THE MAIN INPUT OF FISSION PRODUCTS

Radionuclide	MOEC Activity (Bq)	Core mass inventory (kg)	Percentage entering containment	Form in containment	Host Material
I-131	1.46E+18	3.18E-01	0.1	aerosol	AEROSOL NA2O2
I-132	1.94E+18	5.08E-03	0.1	aerosol	AEROSOL NA2O2
I-133	2.51E+18	5.99E-02	0.1	aerosol	AEROSOL NA2O2
I-134	2.50E+18	2.53E-03	0.1	aerosol	AEROSOL NA2O2
I-135	2.21E+18	1.69E-02	0.1	aerosol	AEROSOL NA2O2
Cs-134	5.19E+16	1.09E+00	0.1	aerosol	AEROSOL NA2O2
Cs-137	4.98E+16	1.55E+01	0.1	aerosol	AEROSOL NA2O2

Rb-88	5.17E+17	1.16E-04	0.1	aerosol	AEROSOL NA2O2
Ru-103	2.22E+18	1.86E+00	0.0001	aerosol	AEROSOL UO2
Ru-106	6.16E+17	5.05E+00	0.0001	aerosol	AEROSOL UO2
Sr-89	6.31E+17	5.87E-01	0.1	aerosol	AEROSOL NA2O2
Sr-90	1.43E+16	2.80E+00	0.1	aerosol	AEROSOL NA2O2
Ce-141	1.98E+18	1.88E+00	0.0001	aerosol	AEROSOL UO2
Ce-144	6.37E+17	5.41E+00	0.0001	aerosol	AEROSOL UO2
Te-131m	1.61E+17	5.46E-03	0.0001	aerosol	AEROSOL UO2
Te-132	1.86E+18	1.63E-01	0.0001	aerosol	AEROSOL UO2
Ba-140	1.91E+18	7.06E-01	0.1	aerosol	AEROSOL NA2O2
Zr-95	1.49E+18	1.88E+00	0.0001	aerosol	AEROSOL UO2
La-140	1.94E+18	9.44E-02	0.0001	aerosol	AEROSOL UO2
Kr-83m	2.36E+15	3.13E-06	1	gas	GAS
Kr-85	2.24E+17	1.54E+01	1	gas	GAS
Kr-85m	4.04E+17	1.33E-03	1	gas	GAS
Kr-87	4.89E+17	4.67E-04	1	gas	GAS
Kr-88	2.52E+18	5.43E-03	1	gas	GAS
Kr-89	2.63E+18	1.06E-04	1	gas	GAS
Xe-131m	1.46E+18	4.69E-01	1	gas	GAS
Xe-133	1.94E+18	2.80E-01	1	gas	GAS
Xe-133m	2.51E+18	1.52E-01	1	gas	GAS
Xe-135	2.50E+18	2.66E-02	1	gas	GAS
Xe-135m	2.21E+18	6.56E-04	1	gas	GAS
Xe-137	5.19E+16	3.90E-06	1	gas	GAS
Xe-138	4.98E+16	1.39E-05	1	gas	GAS
U-237	1.37E+17	4.54E-02	0.0001	aerosol	AEROSOL UO2
U-239	2.34E+19	1.89E-02	0.0001	aerosol	AEROSOL UO2
Np-239	2.53E+19	2.94E+00	0.0001	aerosol	AEROSOL UO2
Pu-238	2.51E+14	3.96E-01	0.0001	aerosol	AEROSOL UO2
Pu-239	2.38E+15	1.05E+03	0.0001	aerosol	AEROSOL UO2
Pu-240	3.68E+15	4.38E+02	0.0001	aerosol	AEROSOL UO2
Pu-241	3.08E+17	7.85E+01	0.0001	aerosol	AEROSOL UO2
Pu-242	4.61E+12	3.12E+01	0.0001	aerosol	AEROSOL UO2
Cm-242	3.51E+16	2.82E-01	0.0001	aerosol	AEROSOL UO2
Cm-243	8.74E+12	4.57E-03	0.0001	aerosol	AEROSOL UO2
Cm-244	9.40E+14	3.14E-01	0.0001	aerosol	AEROSOL UO2

6.1.1.4. *Intercell flow and cell modelling*

Three different ways are available in CONTAIN to calculate the flow in a flow path: the inertial flow model, the quasi-steady flow model and user-specified flow rates model. The inertial flow model with the implicit method, introduced below, was selected in the problem.

The inertial flow model considers the inertia of the gas in the flow path, as well as the lumped parameter frictional resistance. If a flow path is opened suddenly at a fixed pressure difference, the inertia delays the build-up of the flow rate to the steady-state value. If two cells are close to pressure equilibrium, the inertia manifests itself in a different manner. At the point at which the pressure difference becomes zero, the flow rate is generally finite because of the inertia of the flowing material. A finite flow rate will tend to reverse the direction of the pressure difference across the flow path. The reversal in the pressure difference will eventually reverse the direction of the flow. Under these conditions, damped oscillatory flow will occur.

For the inertial flow model, the flow equation is a simple acceleration equation:

$$\frac{dW_{ij}}{dt} = \left(\Delta P_{ij} - C_{FC}|W_{ij}|W_{ij}/(\rho_{ij}A_{ij}^2)\right)A_{ij}/L_{ij} \quad (80)$$

where

W_{ij} is the total noncondensable gas and condensable material mass flow rate from cell i to j;
A_{ij} is the flow path area;
L_{ij} is its effective length;
C_{FC} is the turbulent flow coefficient;
ρ_{ij} is the gas flow density;
ΔP_{ij} is the driving pressure difference.

In the CONTAIN-LMR input card, leakage area, not the leakage rate, is needed to calculate containment leakage, so it was necessary to change the leakage rate 0.1%△V/V/h @25 kPa overpressure to equivalent leakage area. Two connected cells were modelled to solve the problem in CONTAIN-LMR program, cell1 is containment cell, cell 2 is environment cell, the pressure difference is 25 kPa. As one leakage area corresponds to one leakage rate, the containment leakage area was 1.65E-4 m^2 based on the leakage rate 0.1%△V/V/h @25 kPa overpressure.

The cell modelling of case 1 is sketched in FIG. 118. As the ventilation of containment was not considered, two cells were modelled. Cell 1 is the containment cell, and cell 2 simulates the environment cell. The radioactive materials leakage of containment to environment is through the connected channel whose area is 1.65E-4 m^2 described above.

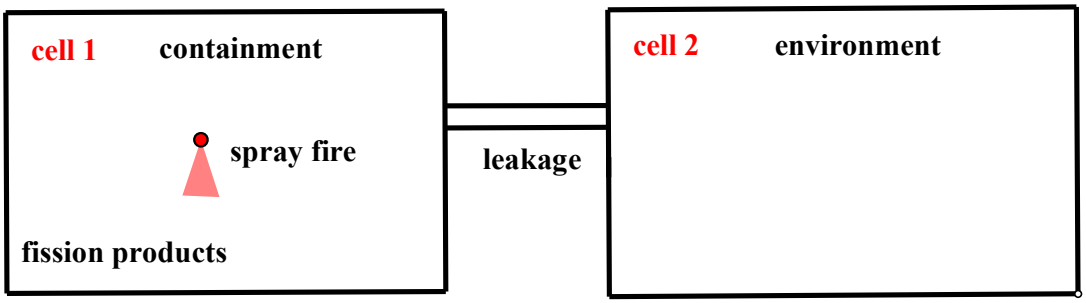

FIG. 118. Cell modelling of case 1.

6.1.2. Results

In the WP3 calculations, the important containment results concerned include containment thermal-hydraulic conditions, aerosol dynamics, sodium fire and radionuclide transport to containment.

Containment thermal-hydraulic conditions

FIG. 119 and FIG. 120 present the average pressure and gas temperature of the reactor containment building. The maximal pressure rise of the containment building was 12.5 kPa at 480 s, and at the same time gas temperature reached the maximal value 341.4 K. As the decay heat of the fission products ejected into the containment, the pressure and temperature of the containment still rose for a short time after the spray stops.

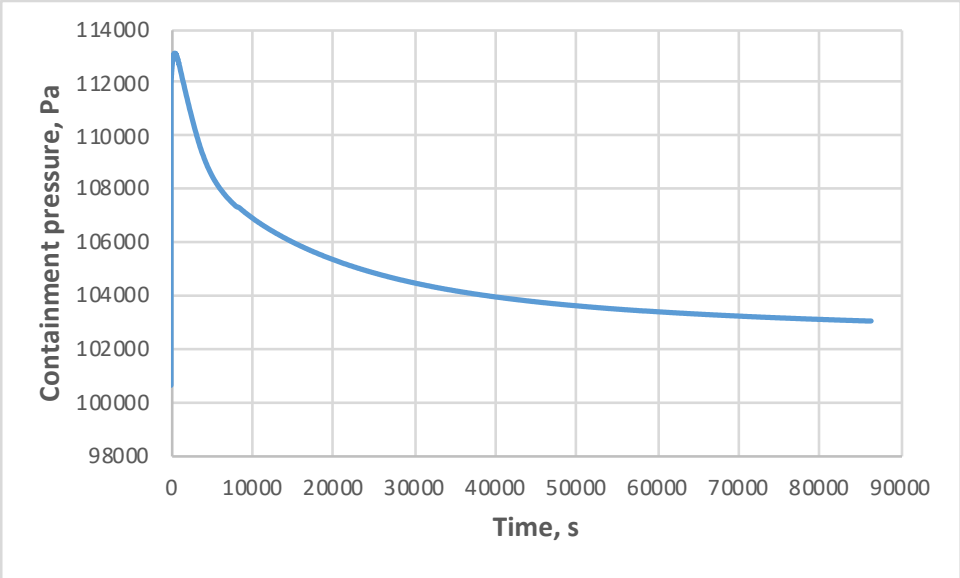

FIG. 119. Average pressure of the reactor containment building.

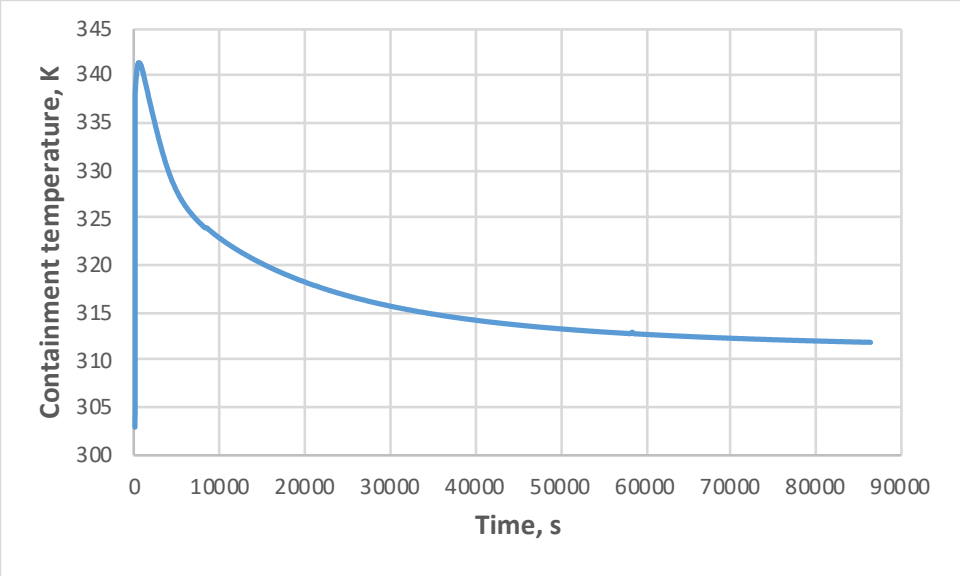

FIG. 120. Average gas temperature of the reactor containment building.

Aerosol dynamics

FIG. 121 depicts the total suspended aerosol mass in the reactor containment building.

FIG. 122 and FIG. 123 show the suspended aerosol elements mass in the reactor containment building. The peak value of total suspended aerosol mass in the reactor containment building was 503.7 kg. Most of the aerosol was the product of sodium spray fire, and the rest was the fission product ejected from the core. Due to the decay and deposition of the fission products, the suspended aerosol mass decreased with time.

FIG. 124 depicts the total deposited aerosol mass in the reactor containment building. FIG. 125 and FIG. 126 show the deposited aerosol elements mass in the reactor containment building. Almost all the suspended aerosol is deposited within 84000s, the total deposited mass is 499.6 kg.

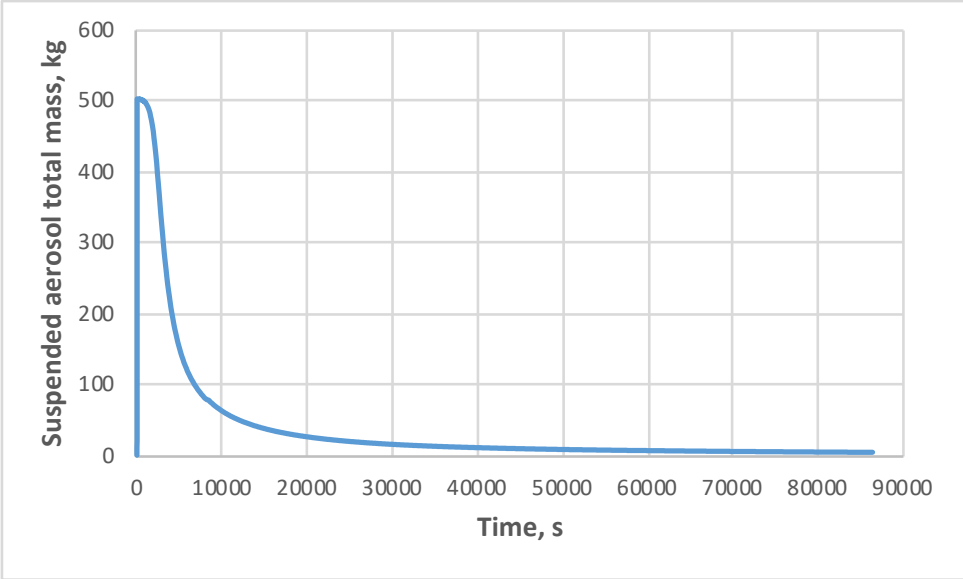

FIG. 121. Total suspended aerosol mass in the reactor containment building.

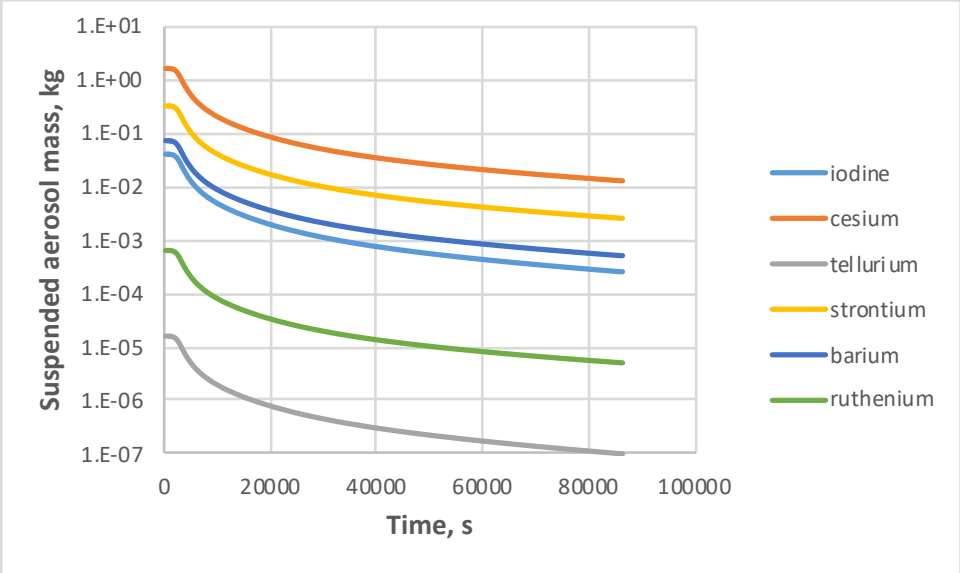

FIG. 122. Suspended aerosol elements mass in the reactor containment building(1).

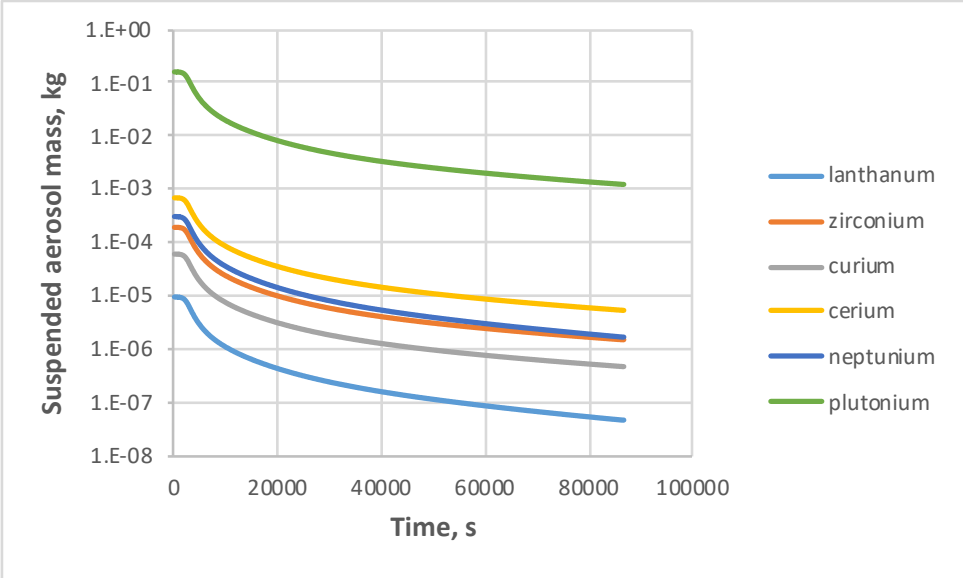

FIG. 123. Suspended aerosol elements mass in the reactor containment building(2).

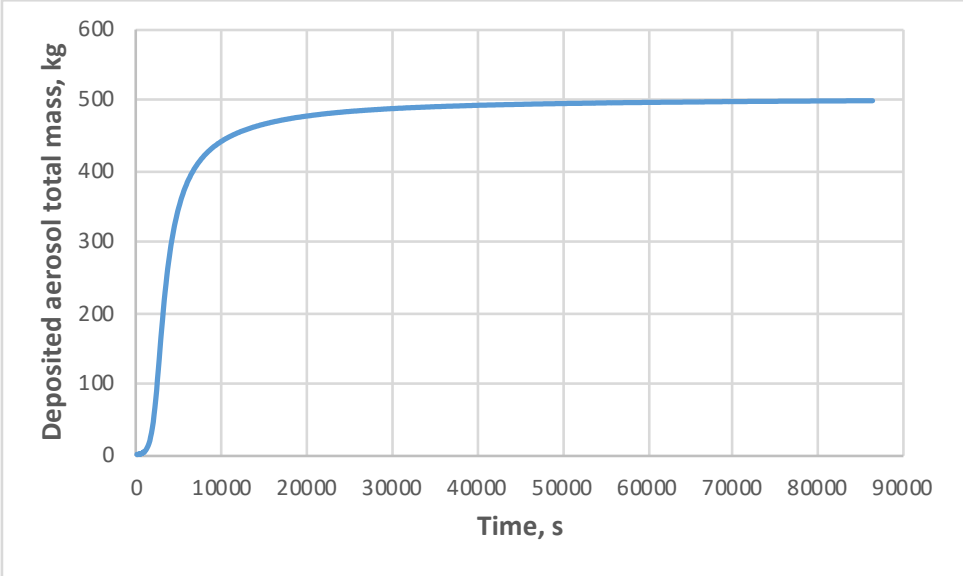

FIG. 124. Total deposited aerosol mass in the reactor containment building.

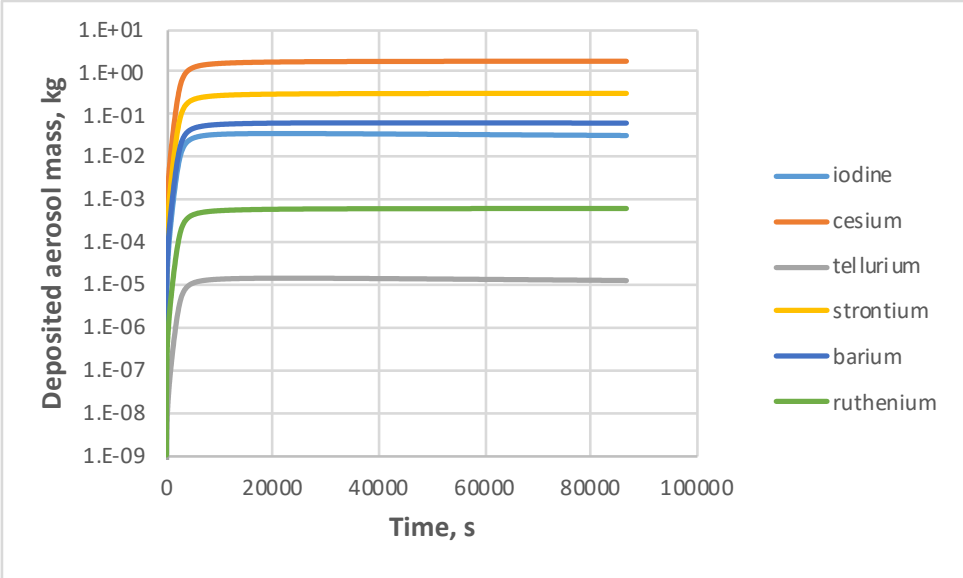

FIG. 125. Deposited aerosol elements mass in the reactor containment building(1).

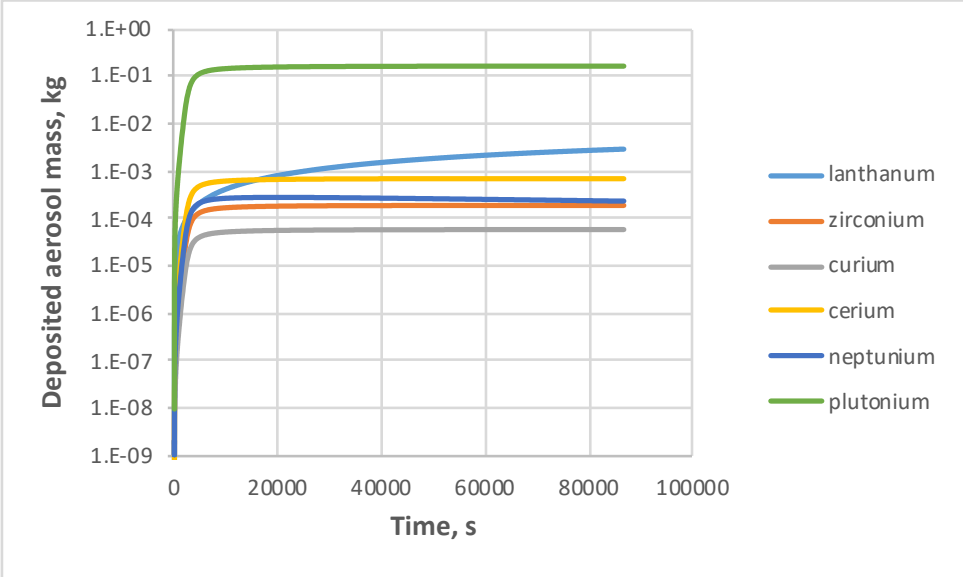

FIG. 126. Deposited aerosol elements mass in the reactor containment building(2).

Sodium fire

The sodium spray fire burn rate is shown in FIG. 127. The total energy released due to the sodium spray fire is shown in FIG. 128. The sodium spray burn rate is closely related to the sodium ejection flow rate. The maximal sodium flow rate value was 1050 kg/s, the max sodium spray burn rate was 900 kg/s. When the sodium flow stops, the sodium burn rate becomes zero. The sodium burn energy release rate is proportional to the sodium burn rate. The maximal energy release rate was 6.64E+9 J/s.

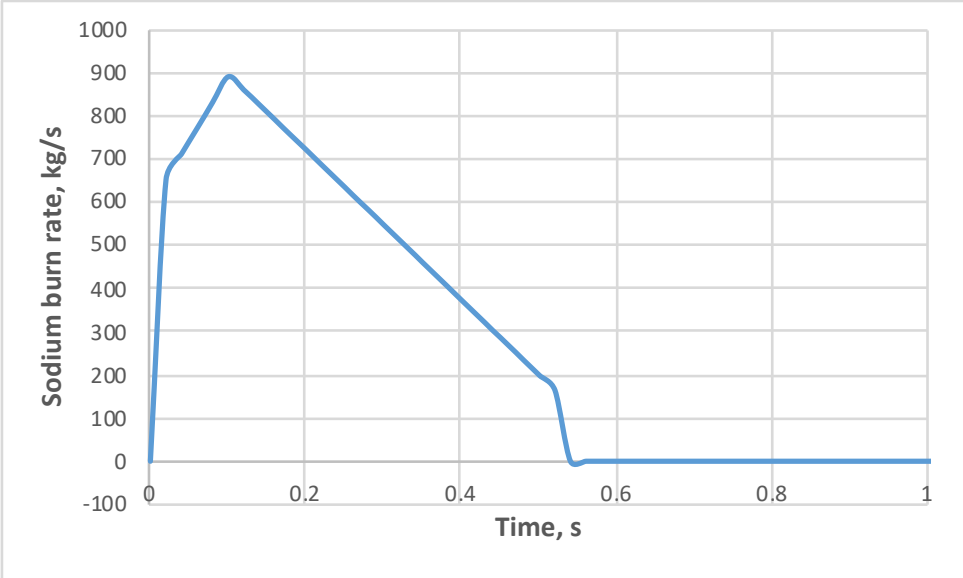

FIG. 127. Sodium spray fire burn rate.

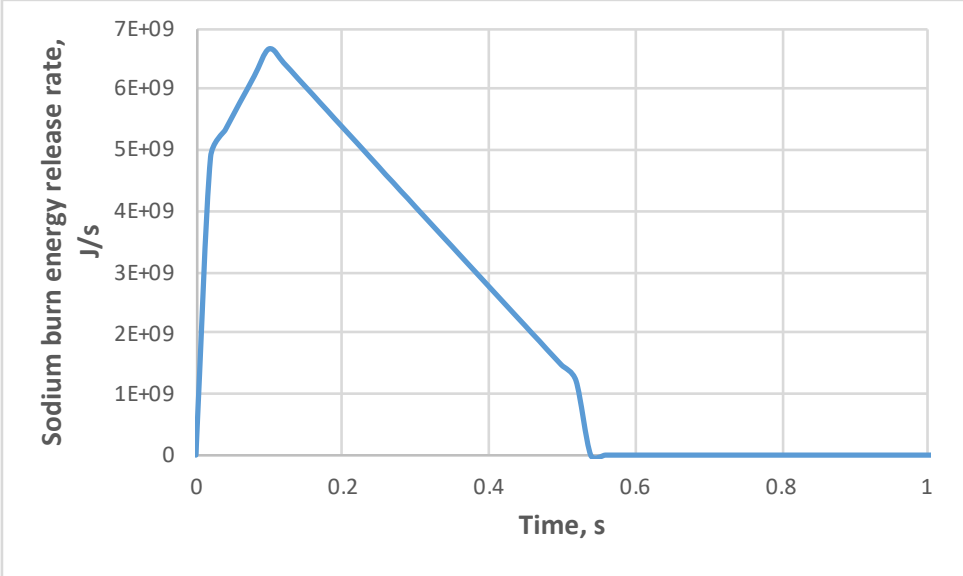

FIG. 128. Total energy release due to the sodium spray fire.

Radionuclide transport to containment

FIG. 129 and FIG. 130 present the elemental mass of fission products in the reactor containment building. FIG. 131 to FIG. 136 show the radionuclide activity in the reactor containment building.

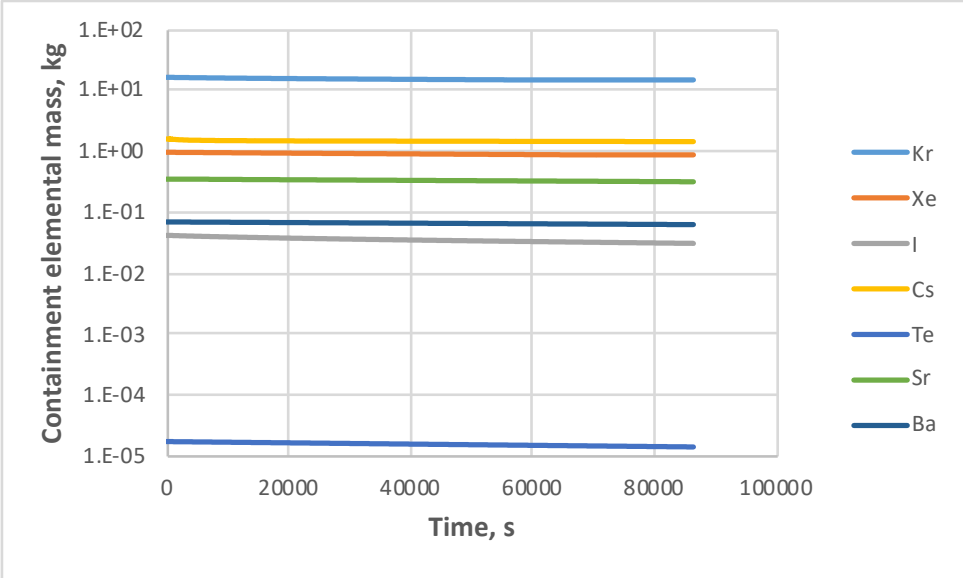

FIG. 129. Elemental mass in the reactor containment building(1).

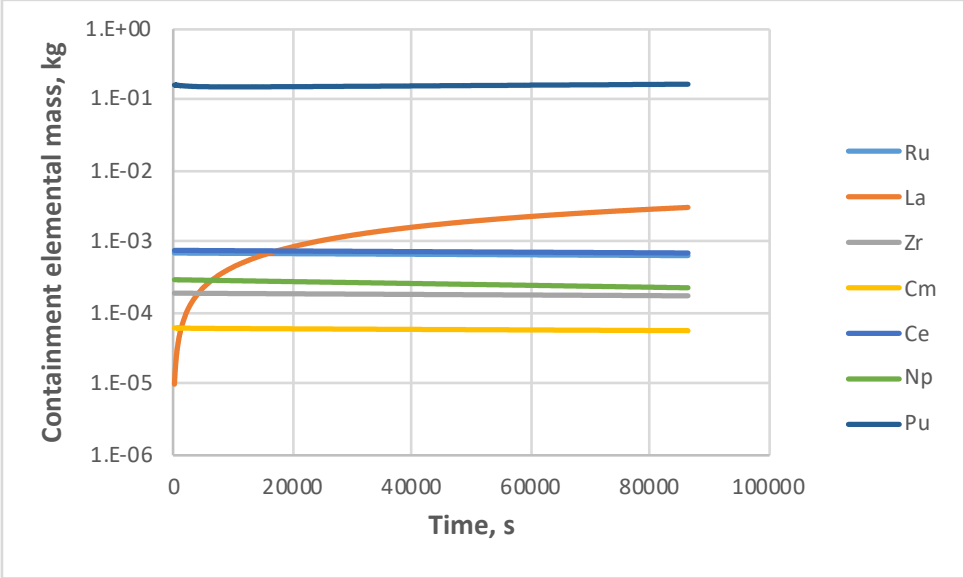

FIG. 130. Elemental mass in the reactor containment building(2).

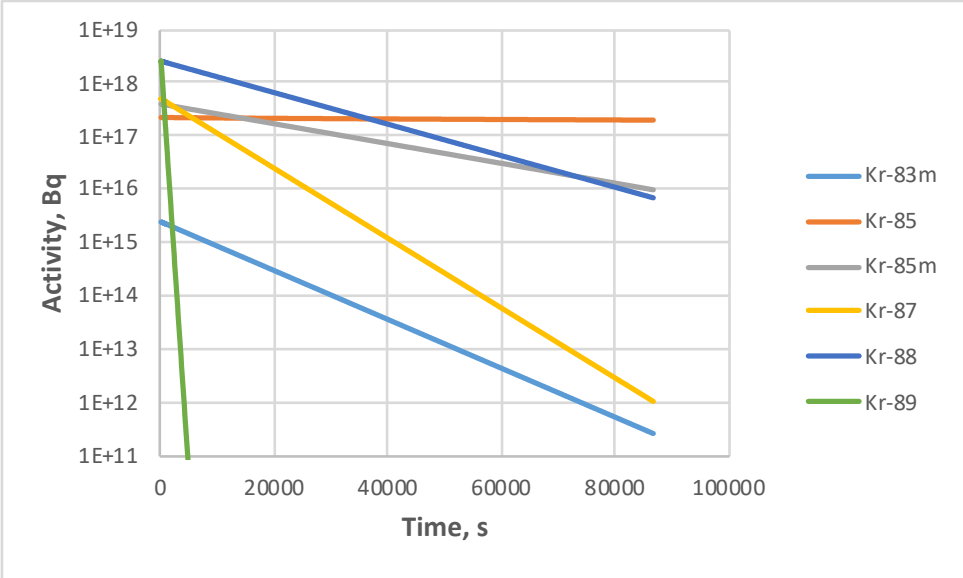

FIG. 131. Krypton activity in the reactor containment building.

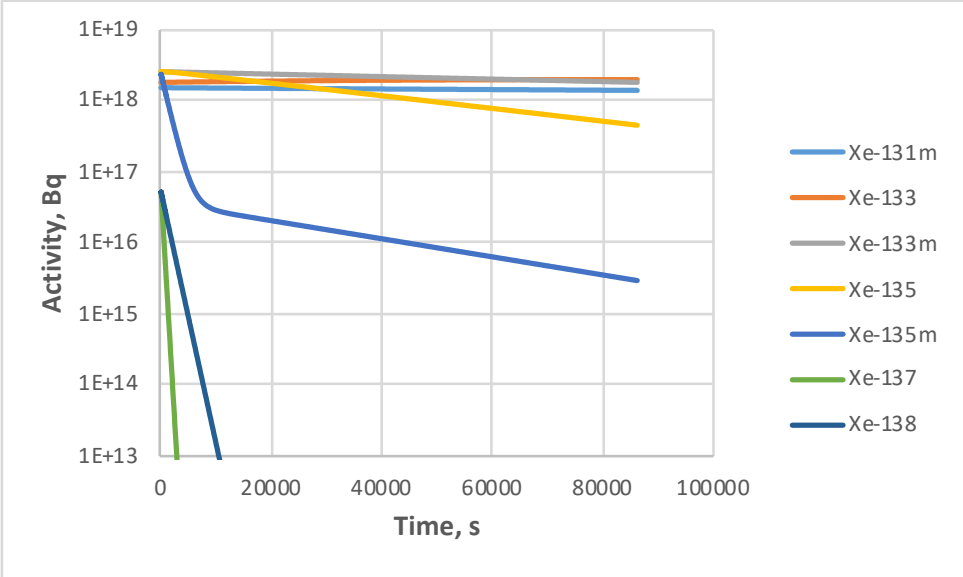

FIG. 132. Xenon activity in the reactor containment building.

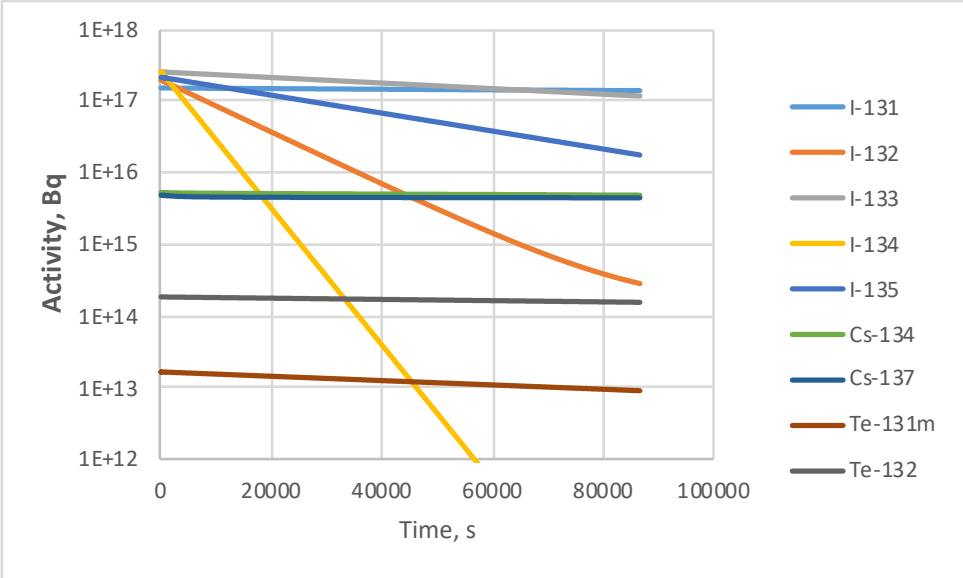

FIG. 133. Iodine, caesium, and tellurium activity in the reactor containment building.

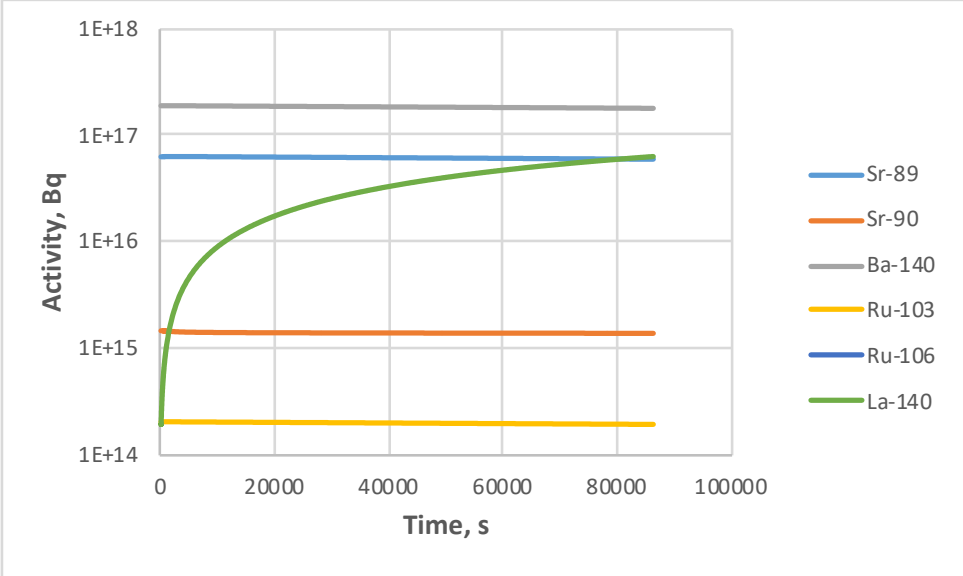

FIG. 134. Strontium, barium, ruthenium, and lanthanum activity in the reactor containment building.

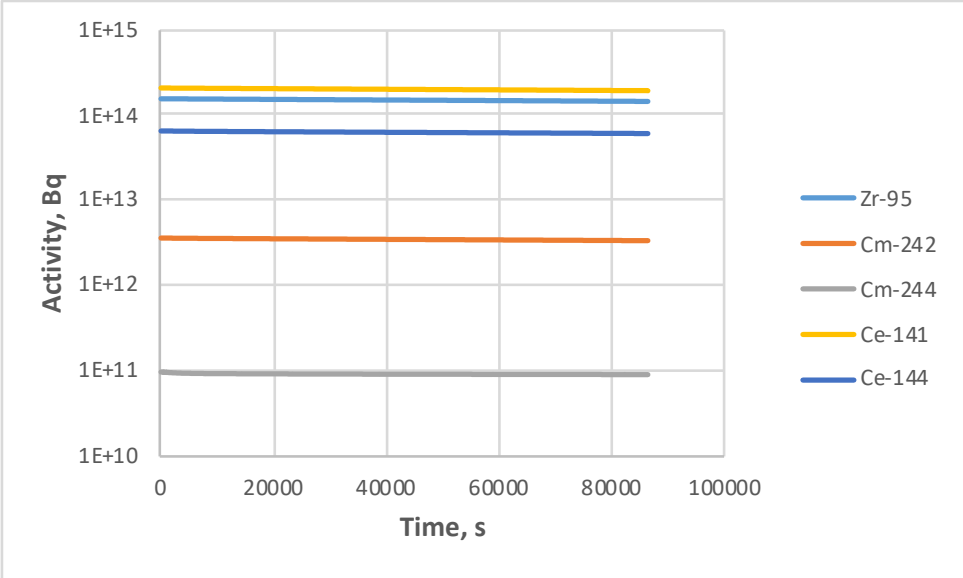

FIG. 135. Zirconium, curium, and cerium activity in the reactor containment building.

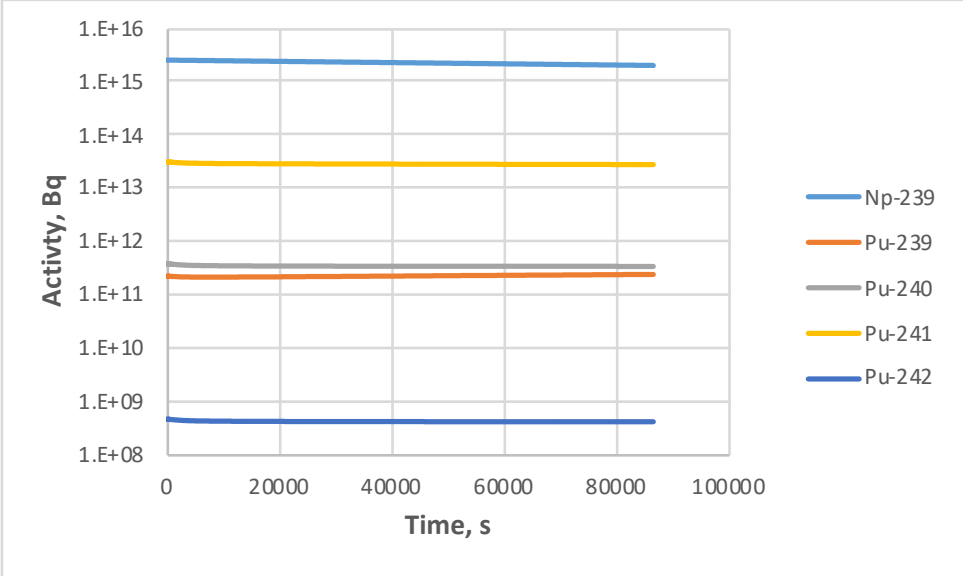

FIG. 136. Neptunium and plutonium activity in the reactor containment building.

6.2. SIMULATION EXERCISE USING REBAC-SFR CODE (XI'AN JIAOTONG UNIVERSITY, CHINA)

6.2.1. Description of Methods and Model

REBAC-SFR is a universal code for fission product analysis of sodium-cooled fast reactor developed at XJTU. The code can simulate pool sodium pool fire, spray fire and fission product aerosol distribution in multiple compartments. In the calculation of aerosol distribution of fission products, the agglomeration between particles and the deposition mechanism of aerosol particles are mainly considered. The sectional method used in REBAC-SFR treats four agglomeration processes: Brownian diffusion, differential gravitational settling, and turbulent

agglomeration by shear and inertial forces. The REBAC-SFR deposition kernel for each type of surface is made up of four contributions: gravitational deposition, Brownian diffusion to surfaces, thermophoresis, and diffusiophoresis. The code has been validated by international experimental tests. The thermal-hydraulic response and fission products of PFSR containment in transient process are calculated by modelling, initial and boundary conditions. In this work package, the code is used to simulate two kinds of accident conditions in the containment. The first is the calculation of the fission products behavior during sodium spray fire without the enclosure. The second case is calculation of fission product behavior during sodium pool fire in the enclosure. The influence of a sodium fire accident on thermal-hydraulic behavior in containment was studied to determine whether a sodium fire accident will cause overpressure failure of containment. The radioactivity of various nuclides in the containment was analysed by calculating the diffusion and migration behavior of aerosols in the containment under sodium fire accident.

6.2.1.1. *Nodalization of containment*

The containment of PFSR plant was simulated by using 3 cells for case 2. There are 2 cells inside the containment pressure boundary and 1 cell outside. The containment air dome and enclosure dome were modelled separately using one control volume. The environment outside the containment pressure boundary was simulated using one control volume. The reactor pressure vessel and the core of the plant were simulated by using a high temperature heat sink. These control volumes are also connected to each other by 3 flow paths. The 3 flow paths are respectively upper opening, left opening and containment leak flow path. The containment floor, wall, ceiling, and environment floor are simulated in the form of a heat sink. The source terms are released to the containment with sodium after the severe accident concluded. For case 1, the enclosure was not modelled, thus there are only 2 cells, the containment and the environment. FIG. 137 and FIG. 138 show the schematic diagram of containment models in case 1 and case 2, respectively.

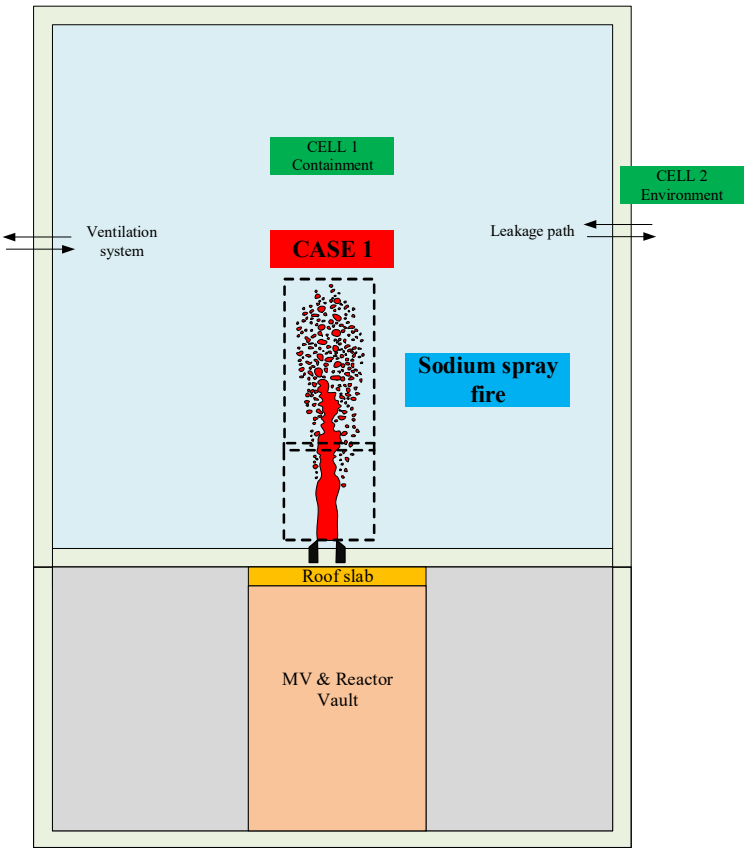

FIG. 137. Case 1: Schematic diagram of containment model.

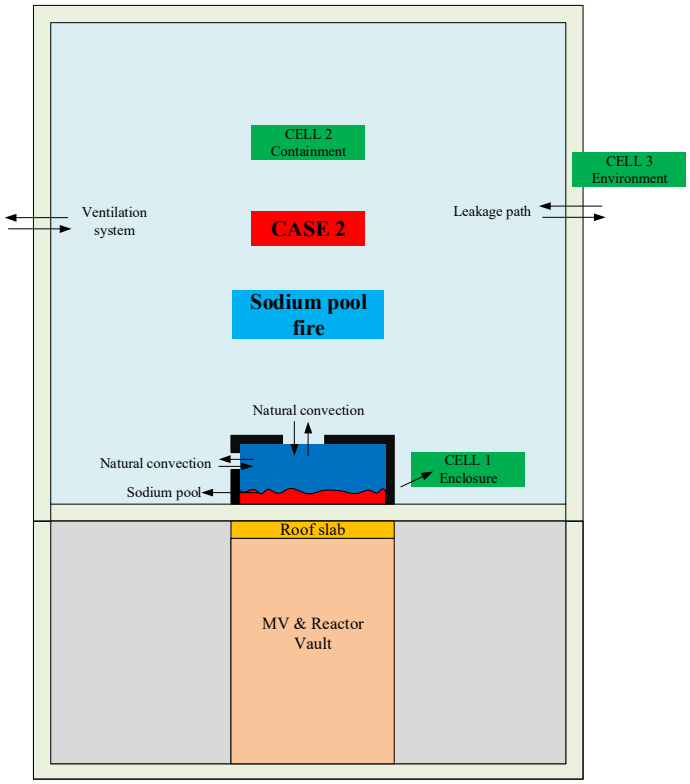

FIG. 138. Case 2: Schematic diagram of containment model.

6.2.1.2. *Physical properties of materials*

Three kinds of materials are considered in the model: carbon steel, liquid sodium metal, and concrete. The density of concrete is 2.4 g/cc and the density of carbon steel is 7.8 g/cc. Of course, other physical parameters, including thermal conductivity, specific heat capacity, enthalpy and others were also considered in the calculation process. These representative physical parameters can be searched according to the material.

6.2.1.3. *Initial conditions*

1. Containment:
   - V_{free}=74,000 m^3, T = 30 °C; P = 100600 Pa; Rel. humidity = 60%
2. Enclosure:
   - Enclosure diameter/height: 14m/4m
   - Enclosure opening (top vent area): 3.5m^2
   - Enclosure opening (side vent area/height): 1.5 m^2/2m
   - Enclosure wall thickness: 30mm
   - Enclosure free volume: 615.44m^3
3. Environment:
   - T = 35 °C; P = 101325 Pa; Rel. humidity = 60%
4. Aerosol:
   - The initial value of particle Geometric Standard Deviation (GSD) for is 2.0 and the Aerodynamic Mass Median Diameter (AMMD) is 0.50 μm. In addition, the settling of aerosol model parameters (agglomeration shape factor, dynamic shape factor, sticking coefficient, etc.) is mainly based on the relevant literature.

6.2.1.4. *Boundary conditions*

The boundary conditions mainly described the roof slab at the bottom of the sodium pool and the walls between the containment and the environment.

1. Roof slab:
   - T_{top}=100°C, T_{bottom}=120°C
2. Containment walls
   - For the calculation of convective heat transfer, the ambient temperature is used as the boundary condition of convective heat transfer on the outer surface of the containment wall.
3. Containment design leak rate
   - 0.1% per hour at 25kPa overpressure (P1= 1.25 bar, where P1 is pressure at CDA, P0= 0.7kPa under pressure, where P0 is initial pressure)
   - Because of the unsealed nature of the building, the room where sodium fire occurs will exchange gas with the surrounding room, known as the room gas leakage. When a pool type sodium fire is in a ventilated room, the pressure difference of the gas medium is generally small, and the gas velocity is much smaller than the sound velocity in the still gas. Assuming that the gas conforms to the ideal gas state equation, the following gas leakage formula can be derived from the Bernoulli equation:

$$Q = C_d A \sqrt{\frac{2\Delta P}{\rho}} \tag{81}$$

where
Q is the gas leakage volume flow;
C_d is the leakage coefficient, (for round opening 1, triangle 0.95, rectangle 0.90);
A is leakage area;
ΔP is the leakage pressure difference;
ρ is the leakage gas density.

The leakage area of the room can be obtained by the known leakage rate of the room and the leakage medium, and it is set as the leakage outlet in the model.
According to $Q = 74 m^3/h$, $\Delta P = 25 kPa$, $\rho = 1.146 kg/m^3$, gives a leakage area 9.841e^{-5}m^2.

4. Containment ventilation system
   - Flow rate=100,000 m^3/hr, elevation of intake = 49.5 m, elevation of exhaust = 49.5 m, vent area of inlet = 1.53 m^2, Vent area of exhaust = 1.53 m^2, isolation time = 10 s, Temp of injected air = 28 °C

6.2.1.5. *Sodium release conditions*

1. Sodium spray fire (case1)
   - Sodium release mass: 350 kg, release time: 0.53 s, T=600°C, spray drop diameter=0.5-2mm(in this work, the diameter is 1 mm), no ventilation.
2. Sodium pool fire (case2)
   - Enclosure volume model included, the burning area equal to 153.938m^2 (diameter is 14m), the depth of sodium pool is about 0.003 m (according the density is 760 kg/m^3, thus the volume of sodium pool is 0.4605 m^3).
3. Hypothetical condition
   - Sodium combustion products are all sodium monoxide.

6.2.1.6. *Fission products inventory*

Fission products aerosol calculations used MOEC values. According to relationship between decay constant and half-life and the relationship between radioactive activity and decay constant, the quality of each nuclide is calculated.

$$T_{1/2} = \frac{\ln(2)}{\lambda}, \qquad A = \lambda N, \qquad m = \frac{N}{N_A} M \tag{82}$$

where
$T_{1/2}$ is radionuclide half-life;
λ is decay constant;
N is number of decay nuclide;
m is nuclide mass;
N_A is number of atoms per mole, 6.02×10^{23};
M is nuclide molar mass.

Finally, the quality of the stored nuclides in the core was calculated as follows. Preliminary calculation assumptions: 100% Noble gas, 10% semi-volatiles, 10% volatiles, and 0.01% lanthanides are released under the condition of the accident. Specific nuclide release fractions are shown in the TABLE 56 and the nuclides inventory in the core is shown in TABLE 57.

TABLE 56. IN-CONTAINMENT RELEASE FRACTIONS

Group	Elements	Designated release fractions
Noble Gases	Xe, Kr	1
Halogen	I, Br	0.1
Alkali metals	Cs, Rb	0.1
Tellurium group	Te, Sb, Se	1.0E-04
Barium	Ba, Sr	0.1
Noble metals	Ru, Rh, Pd, Mo, Tc, Co	1.0E-04
Lanthanides	La, Zr, Nd, Eu, Nb, Pm, Pr, Sm, Y, Cm, Am	1.0E-04
Cerium	Ce, Pu, Np	1.0E-04

TABLE 57. CORE INVENTORY

Radionuclide	Half life	Activity in Bq for MOEC	Nuclide mass(kg)	Release mass(kg)
I-131	8.02 d	1.46E+18	0.317607	0.031760718
I-132	2.30 h	1.94E+18	0.005081	0.000508141
I-133	20.80 h	2.51E+18	0.059906	0.005990585
I-134	52.50 m	2.50E+18	0.002529	0.000252891
I-135	6.57 h	2.21E+18	0.016911	0.00169111
Cs-134	754.50 d	5.19E+16	1.086484	0.108648364
Cs-137	30.07 y	4.98E+16	15.50487	1.550486512
Rb-88	17.78 m	5.17E+17	0.000116	1.16315E-05
Ru-103	39.26 d	2.22E+18	1.858798	0.00018588
Ru-106	373.59 d	6.16E+17	5.050956	0.000505096
Sr-89	50.53 d	6.31E+17	0.587571	0.058757114
Sr-90	28.79 y	1.43E+16	2.800302	0.280030197
Ce-141	32.50 d	1.98E+18	1.878709	0.000187871
Ce-144	284.89 d	6.37E+17	5.410918	0.000541092
Te-131m	30.00 h	1.61E+17	0.005459	5.45882E-07
Te-132	3.20 d	1.86E+18	0.162678	1.62678E-05
Ba-140	12.75 d	1.91E+18	0.705933	0.070593283
Zr-95	64.02 d	1.49E+18	1.876365	0.000187637
La-140	1.68 d	1.94E+18	0.094478	9.4478E-06
Kr-83m	1.85 h	2.36E+15	3.13E-06	3.12638E-06
Kr-85	10.70 y	2.24E+17	15.39697	15.396974
Kr-85m	4.48 h	4.04E+17	0.001327	0.001327269
Kr-87	76.30 m	4.89E+17	0.000467	0.000466747
Kr-88	2.84 h	2.52E+18	0.005434	0.00543353
Kr-89	3.15 m	2.63E+18	0.000106	0.000106019
Xe-131m	11.84 d	1.46E+18	0.468886	0.468886408

Xe-133	5.24 d	1.94E+18	0.279947	0.279947406
Xe-133m	2.2 d	2.51E+18	0.152069	0.1520687
Xe-135	9.14 h	2.50E+18	0.026613	0.02661341
Xe-135m	15.29 m	2.21E+18	0.000656	0.000655938
Xe-137	3.82 m	5.19E+16	3.91E-06	3.90554E-06
Xe-138	14.08 m	4.98E+16	1.39E-05	1.39136E-05
U-237	6.75 d	1.37E+17	0.04538	4.538E-06
U-239	23.45 m	2.34E+19	0.018858	1.88576E-06
Np-239	2.35 d	2.53E+19	2.94224	0.000294224
Pu-238	87.7 y	2.51E+14	0.395945	3.95945E-05
Pu-239	2.4×10^4 y	2.38E+15	1031.741	0.103174115
Pu-240	6564 y	3.68E+15	438.1394	0.043813938
Pu-241	14 y	3.08E+17	78.53811	0.007853811
Pu-242	3.7×10^5 y	4.61E+12	31.19627	0.003119627
Cm-242	0.44 y	3.51E+16	0.282462	2.82462E-05
Cm-243	28.5 y	8.74E+12	0.004575	4.57454E-07
Cm-244	18.1 y	9.40E+14	0.313748	3.13748E-05

6.2.2. Results

CASE 1: Sodium spray fire

Sodium combustion analysis

FIG. 139 shows the sodium burning and energy release rate during spray fire in containment. The rate of sodium droplet combustion is mainly related to the spray rate. The overall trend of spray rate is first increased and then decreased. The simulation shows that the simulation value is consistent with the spray rate. FIG. 140 shows the sodium combustion mass during the spray fire in containment. The total mass of sodium combustion in the containment is about 350 kg.

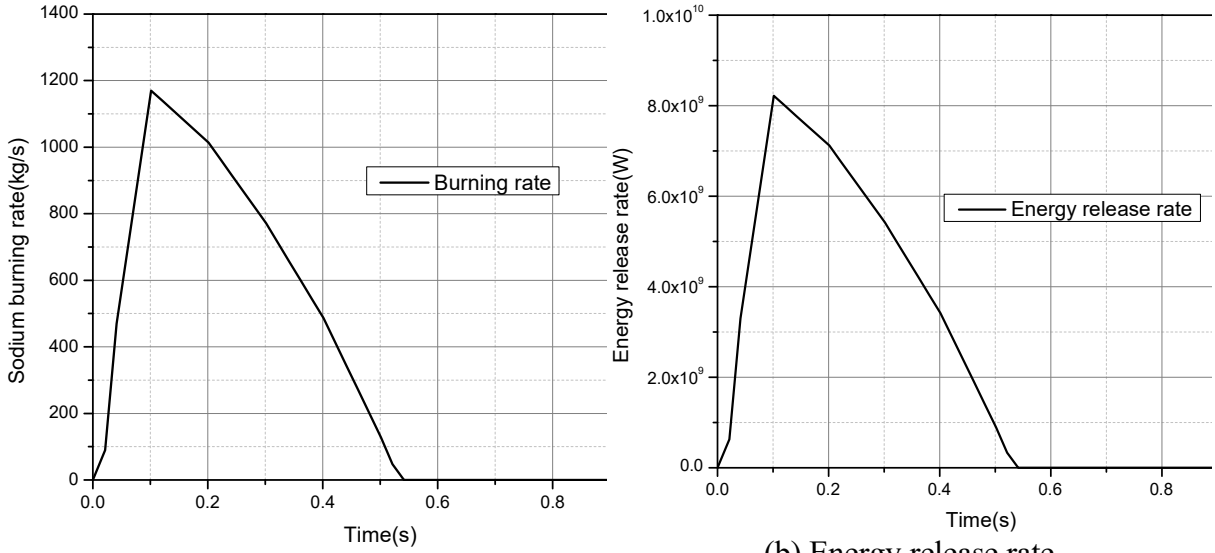

(a) Sodium burning rate (b) Energy release rate

FIG. 139. Sodium burning and energy release rate.

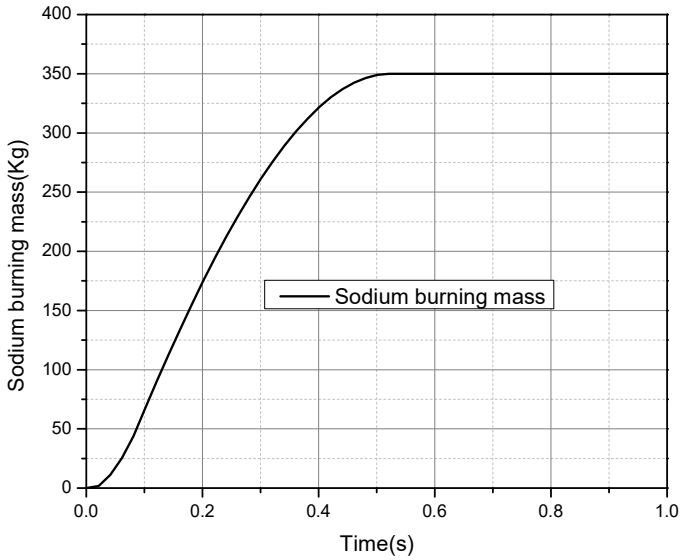

FIG. 140. Sodium combustion mass.

Thermal hydraulic analysis

FIG. 141 shows the pressure and gas temperature during sodium spray fire. The duration of the spray is very short, only 0.53 seconds. Therefore, a large amount of energy released by combustion is transferred to the containment in a short time, which results in the rapid increase of pressure and temperature in the containment. Subsequently, the containment is naturally cooled by heat transfer to the environment, which gradually reduced the pressure and temperature in the containment. During the whole combustion process, the peak pressure of the containment is 114,000 Pa and the peak temperature of the gas was 343 K.

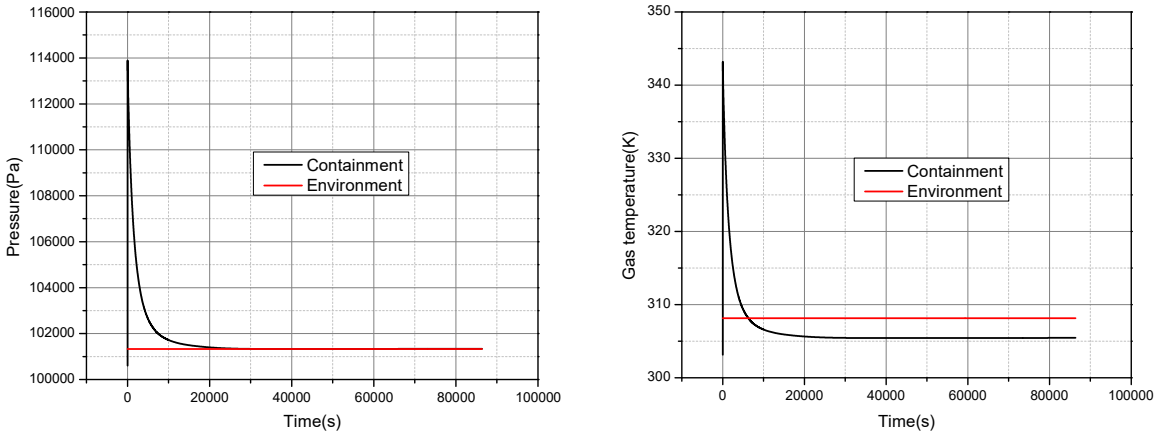

(a) Pressure (b) Gas temperature

FIG. 141. Pressure and gas temperature in containment.

Aerosol and Nobel gas analysis

FIG. 142 shows the total aerosol and noble gas mass in containment. The rapid combustion process of sodium spray fire makes the aerosols of combustion products and fission products release rapidly into the atmosphere of the containment. In a short time, the aerosols suspended in the containment reached 470 kg. Then, due to the natural removal mechanism of aerosols, aerosols gradually deposited on the floor, walls, and ceiling of the containment. In the mechanism of natural removal of aerosols, gravity is the main removal mode, thus most aerosols deposited on the floor of the containment. For noble gases, there was a small reduction

subsequently due to leakage into the environment. FIG. 143 and FIG. 144 show the suspended and deposited mass of fission products in containment. Among them, the Rb element decreased rapidly in a short time due to its very short half-life.

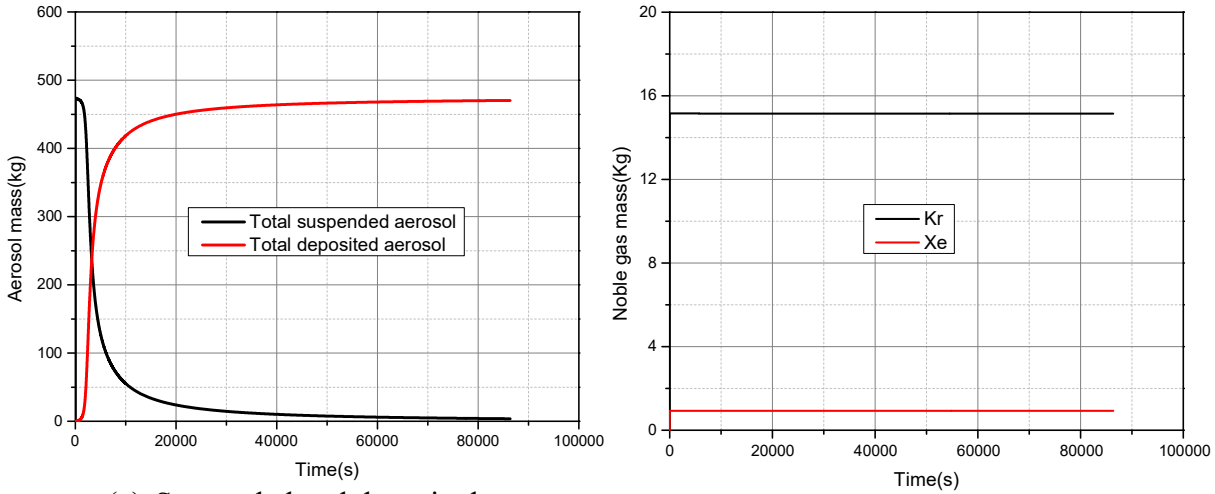

(a) Suspended and deposited mass (b) Noble gas

FIG. 142. Total aerosol and noble gas mass in containment.

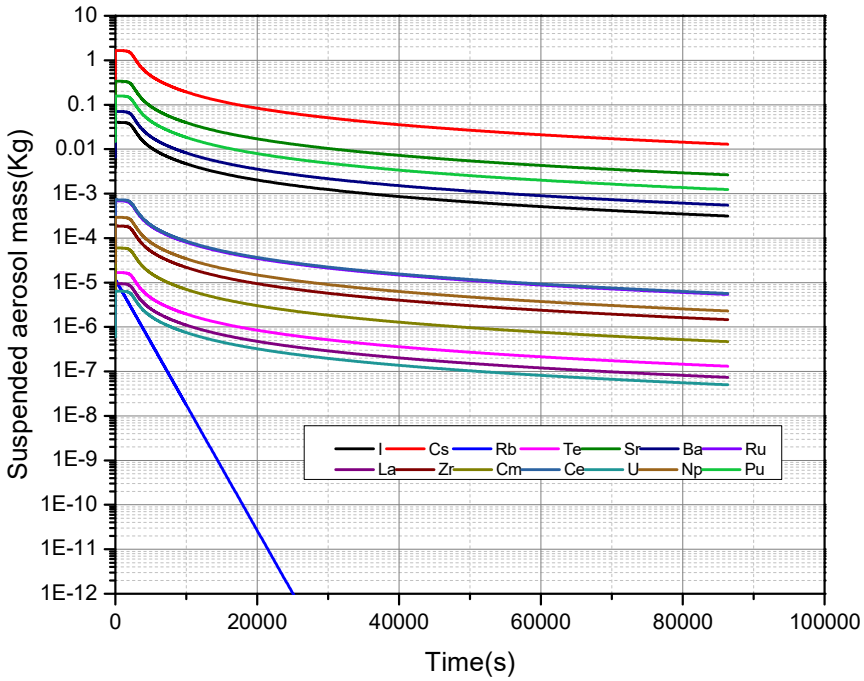

FIG. 143. Suspended mass of fission products in containment.

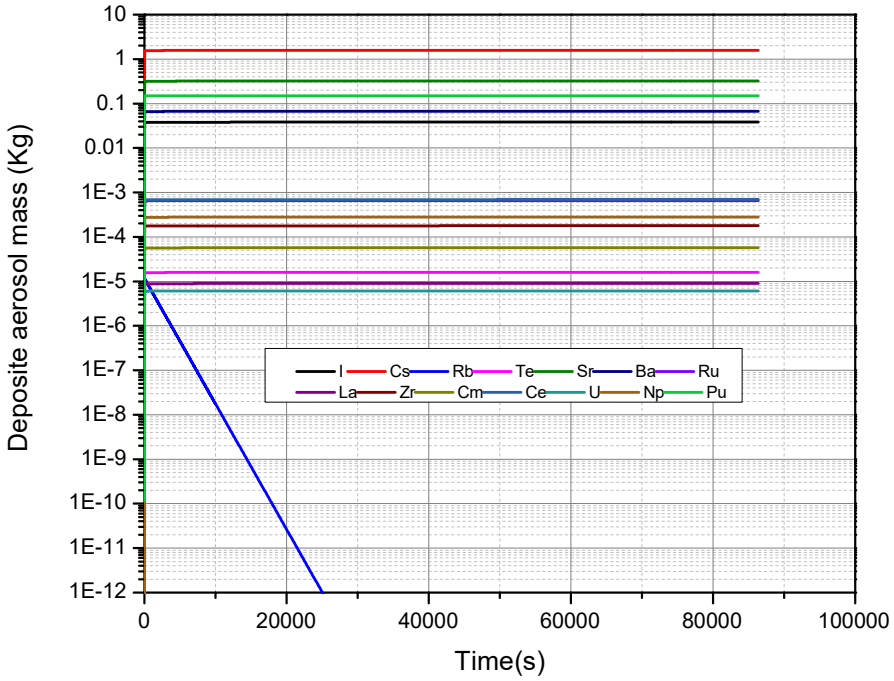

FIG. 144. Deposited Mass of Fission products in containment

Radioactivity analysis

The radioactivity of all fission products elements is shown FIG. 145 through FIG. 154. Radioactivity in containment is mainly related to half-life of fission product nuclides. As shown in the figure, the activity of short half-life nuclides decreased gradually in a short time, while that of long half-life nuclides remained almost constant in 24 hours.

Because the output parameters of radioactivity in the environment are not provided in the output parameter table, the leakage of fission products to the environment was simulated in the actual modelling process. The results show that the mass of noble gas leaking into the environment was 5.06E-3 kg, the mass of fission product aerosol leaking into the environment was 3.18E-4 kg, and the mass of sodium combustion product leaking into the environment was 0.0659 kg. Therefore, the aerosol leak fraction is 1.4E-4, and the noble gas leak fraction is 3.1E-4.

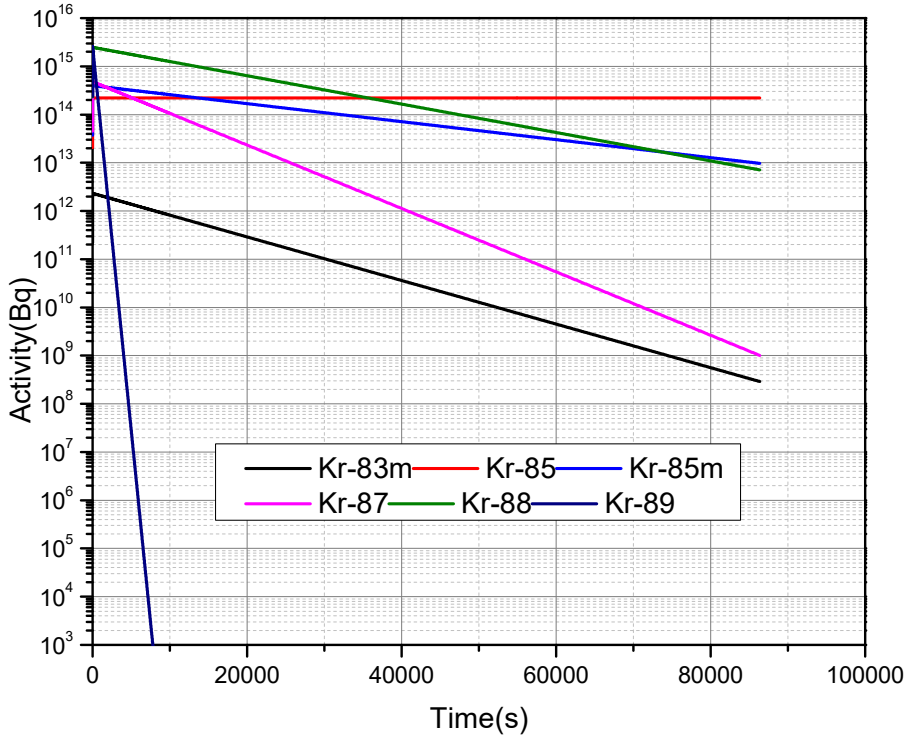

FIG. 145. Total radioactivity over time of krypton.

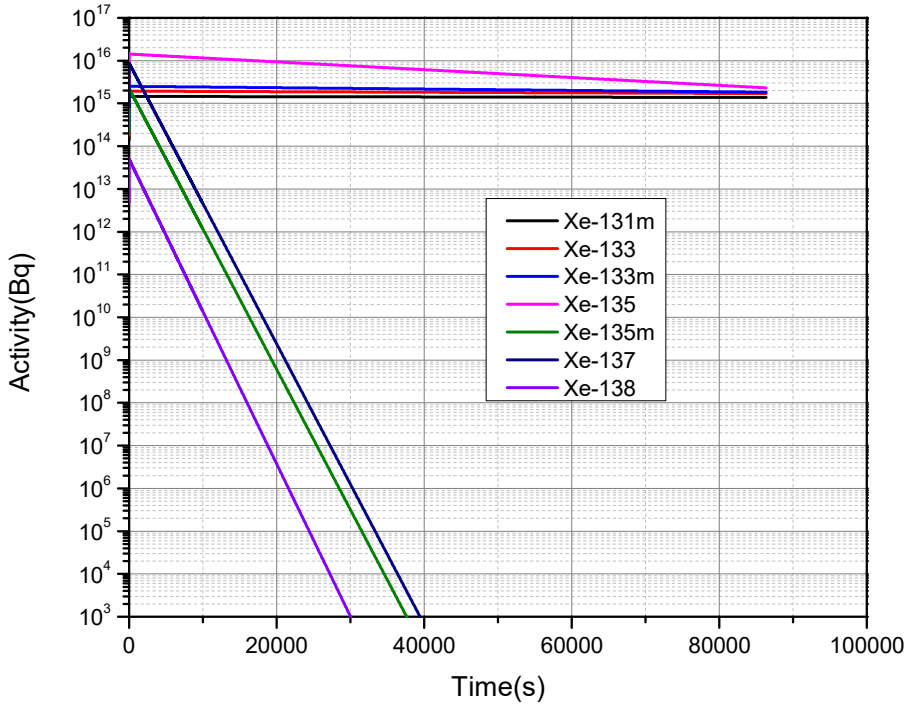

FIG. 146. Total radioactivity over time of xenon.

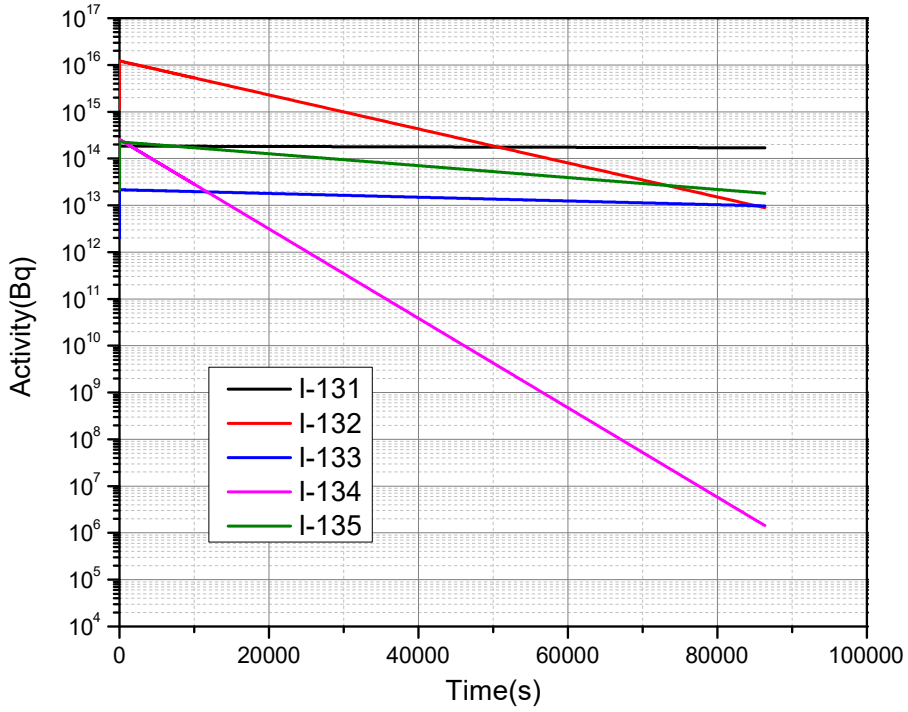

FIG. 147. Total radioactivity over time of halogen.

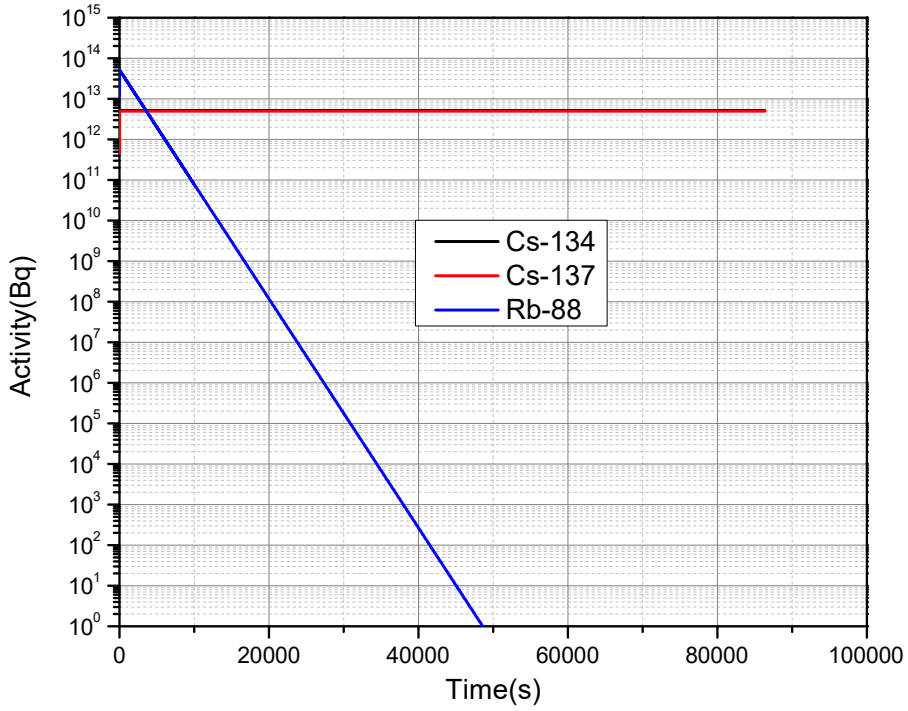

FIG. 148. Total radioactivity over time of alkali metals.

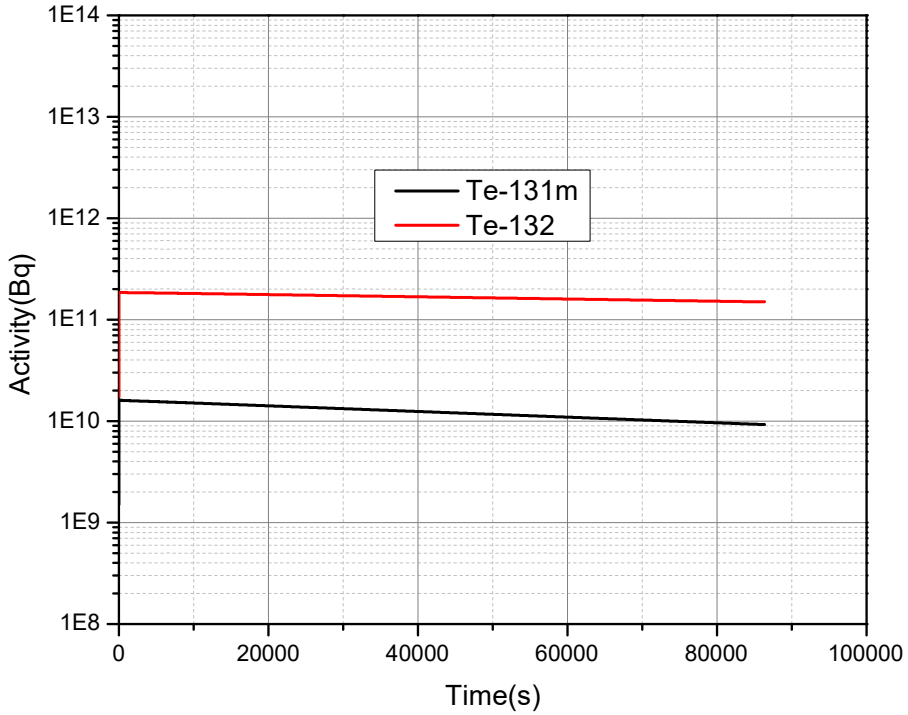

FIG. 149. Total radioactivity over time of tellurium.

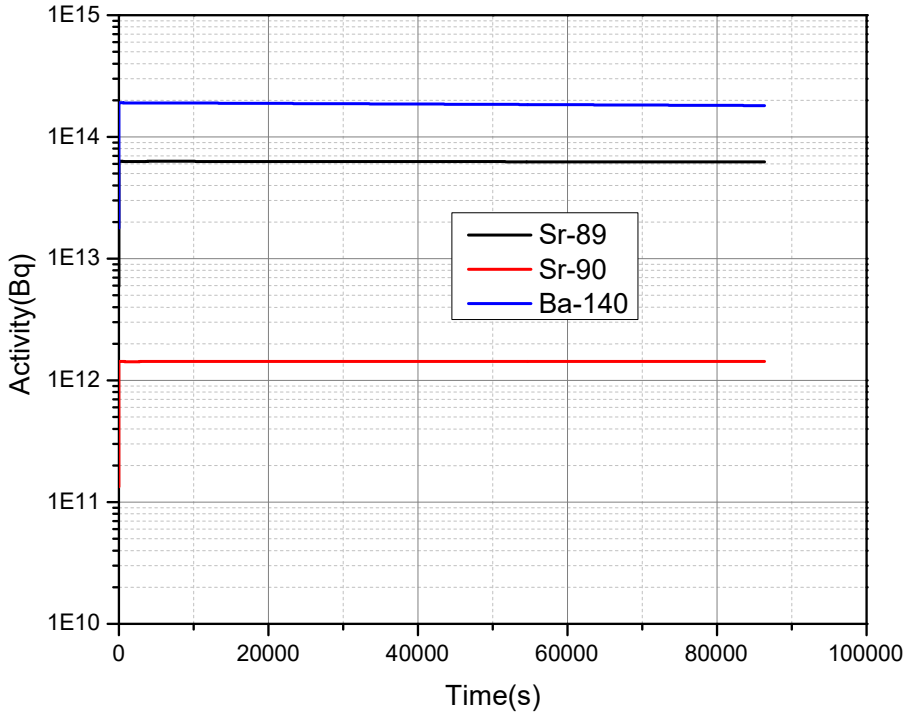

FIG. 150. Total radioactivity over time of barium

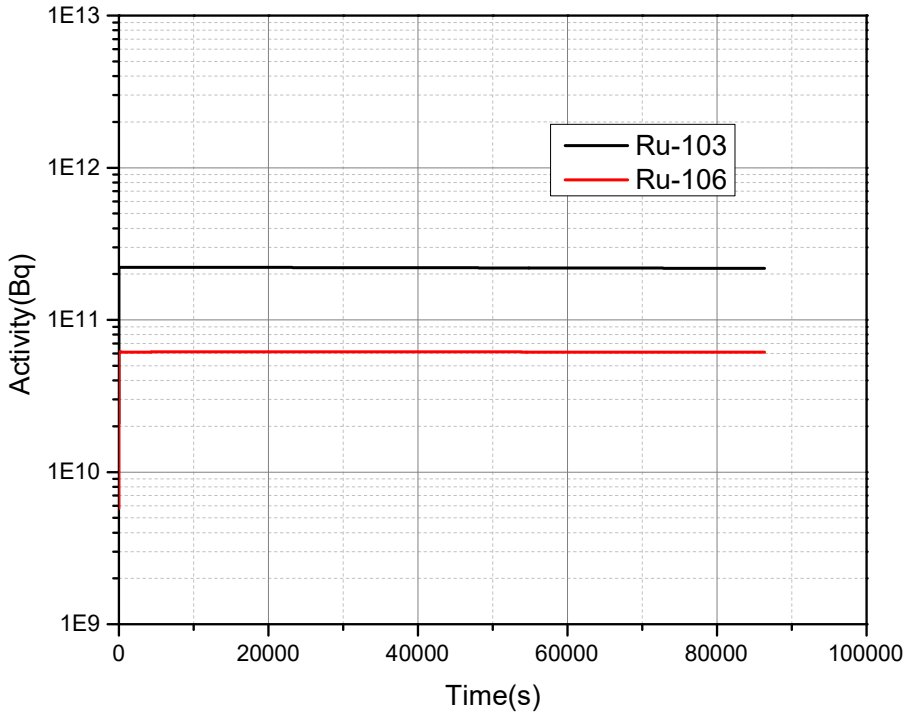

FIG. 151. Total radioactivity over time of noble metals

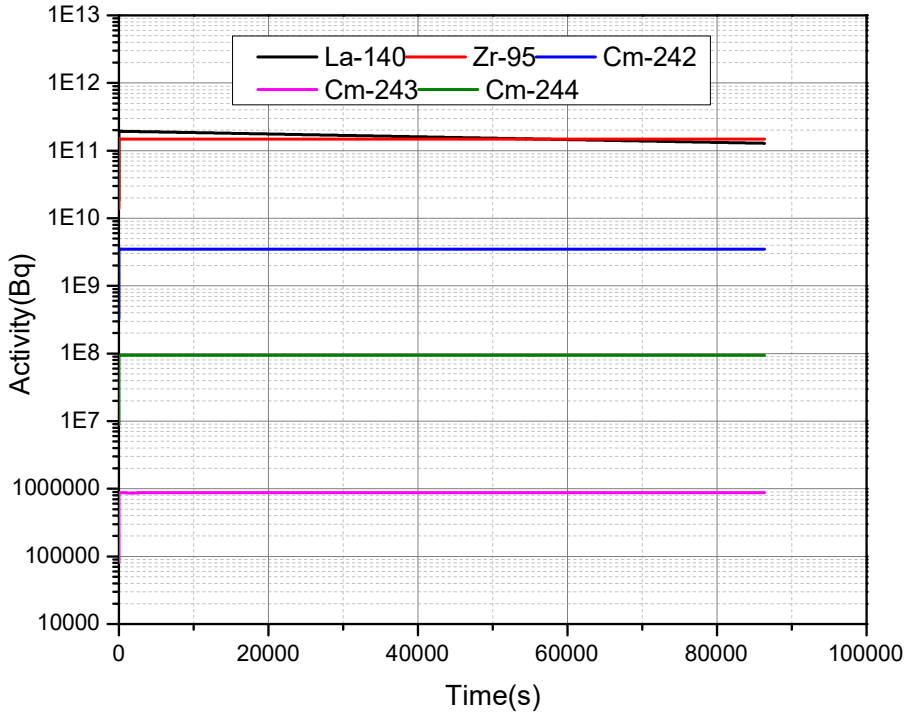

FIG. 152. Total radioactivity over time of lanthanides

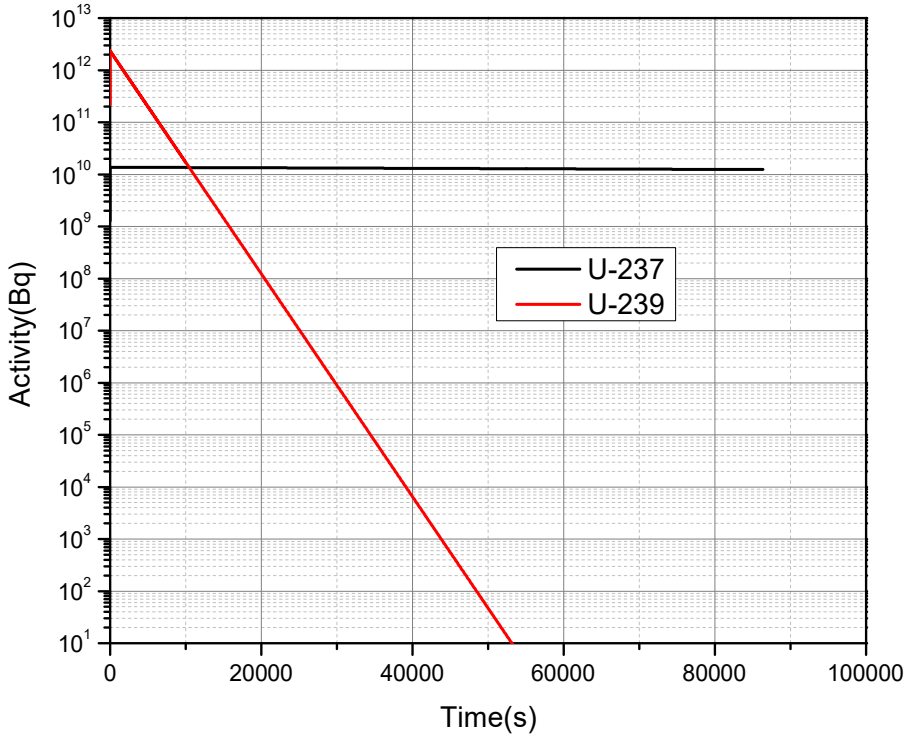

FIG. 153. Total radioactivity over time of uranium

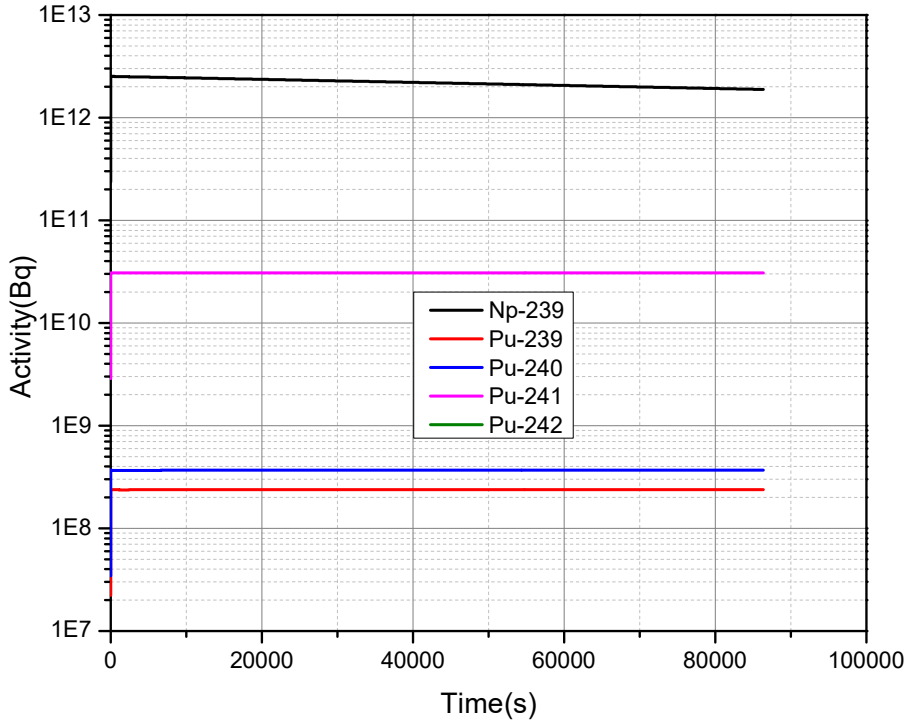

FIG. 154. Total radioactivity over time of cerium

CASE 2: Sodium pool fire

Sodium combustion analysis

FIG. 155 shows the sodium burning and energy release rate during pool fire in enclosure. The combustion rate of sodium pool rises rapidly to a higher value, and then decreases gradually due to the decrease of oxygen concentration in the enclosure. Then, due to the strong natural convection between the enclosure and containment, oxygen in the containment enters the enclosure, thus the combustion rate keeps a relatively balanced value. The relatively stable process stops when the sodium in the pool burns out. The whole combustion process lasted for about 537 s. The energy release rate is consistent with the combustion rate of sodium pool. FIG. 156 shows the sodium combustion mass during the pool fire in enclosure. The total mass of sodium combustion in the containment was 350 kg.

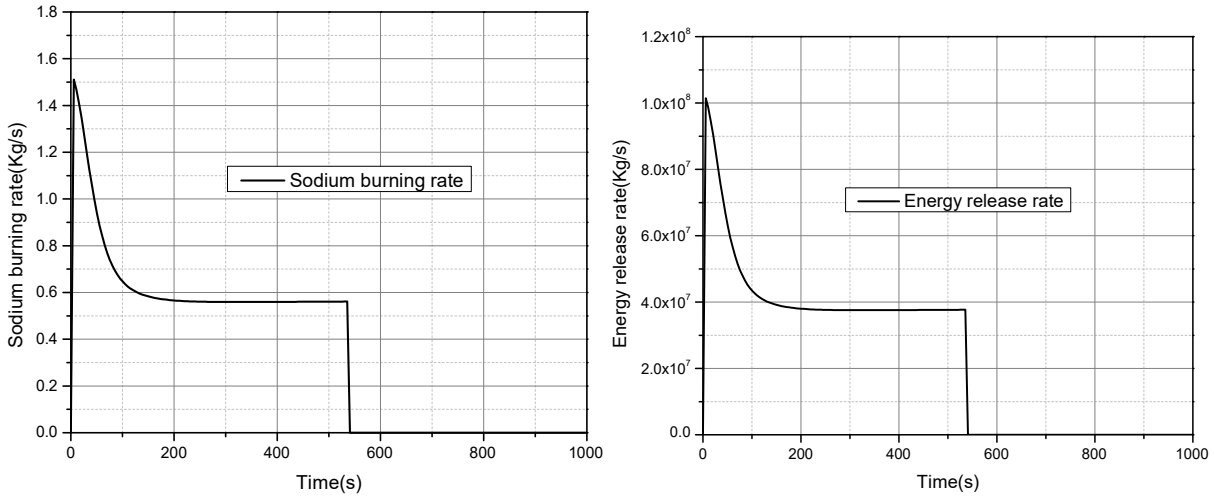

(a) Sodium burning rate (b) Energy release rate

FIG. 155. Sodium burning and energy release rate

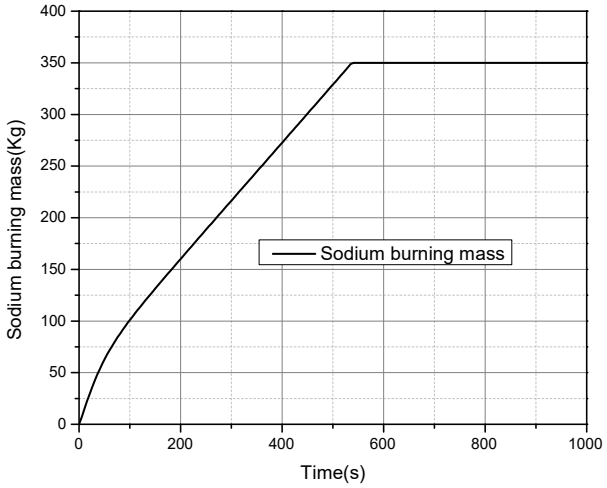

FIG. 156. Sodium combustion mass

Thermal hydraulic analysis

FIG. 157 shows the pressure and gas temperature during sodium pool fire. During the process of combustion, the pressure in the containment increased by about 3 kPa, which is far less than the pressure rise during sodium spray fire in containment. Because combustion occurs in the enclosure and the volume of the enclosure is small, the gas temperature in the enclosure rose to

about 650 K during the combustion of sodium pool, then decreased gradually due to strong natural convection and heat exchange with the gas in the containment. The gas temperature in the containment increased by 7 K during the whole heat transfer process and then decreased due to natural cooling.

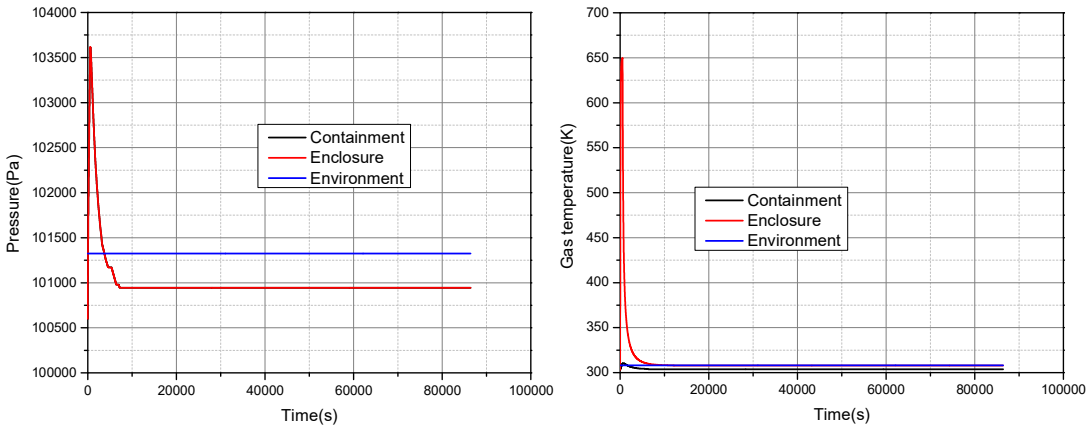

(a) Pressure (b) Gas temperature

FIG. 157. Pressure and gas temperature.

Aerosol and Nobel gas analysis

FIG. 158 and FIG. 159 shows total aerosol and noble gas in containment during the sodium pool fire. Initially, noble gases, combustion products and fission products aerosols are released into the enclosure during the sodium pool fire, and then migrate to the containment through strong natural circulation. Compared with case 1, the total aerosol peak suspension mass in case 2 containment was significantly lower than that in case 1, because some aerosols are suspended in the enclosure. The results show that due to the natural removal of aerosols, about 9.274 kg of aerosols were deposited on floor of enclosure, so the retention fraction of aerosols in the enclosure is about 0.0196. The mass of noble gas remained in the enclosure is 0.141 kg, thus the retention fraction of noble gases is 8.88E-3. FIG. 161 and FIG. 180 shows the suspended and deposited mass of fission products in containment.

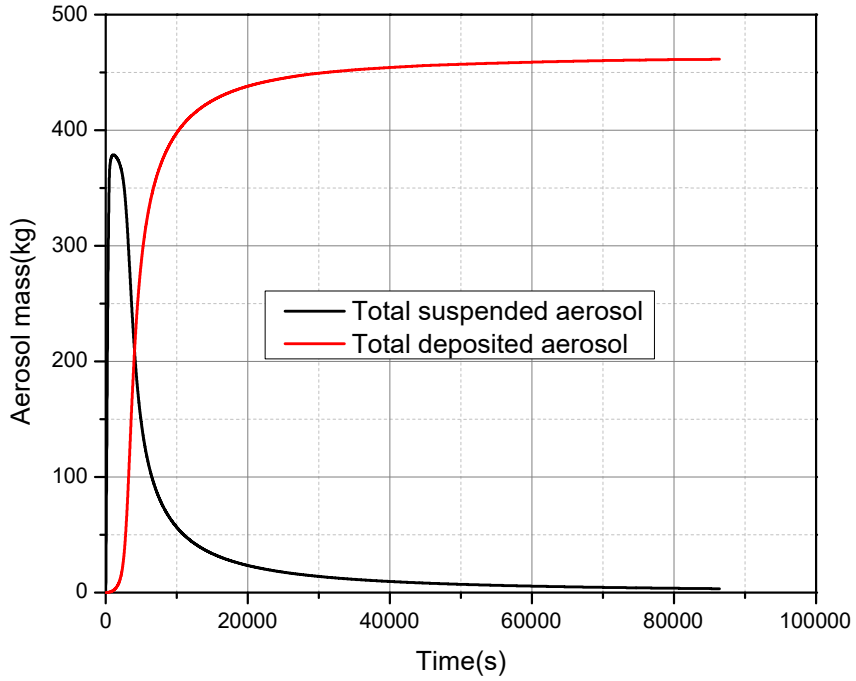

FIG. 158. Total aerosol suspended and deposited mass in containment

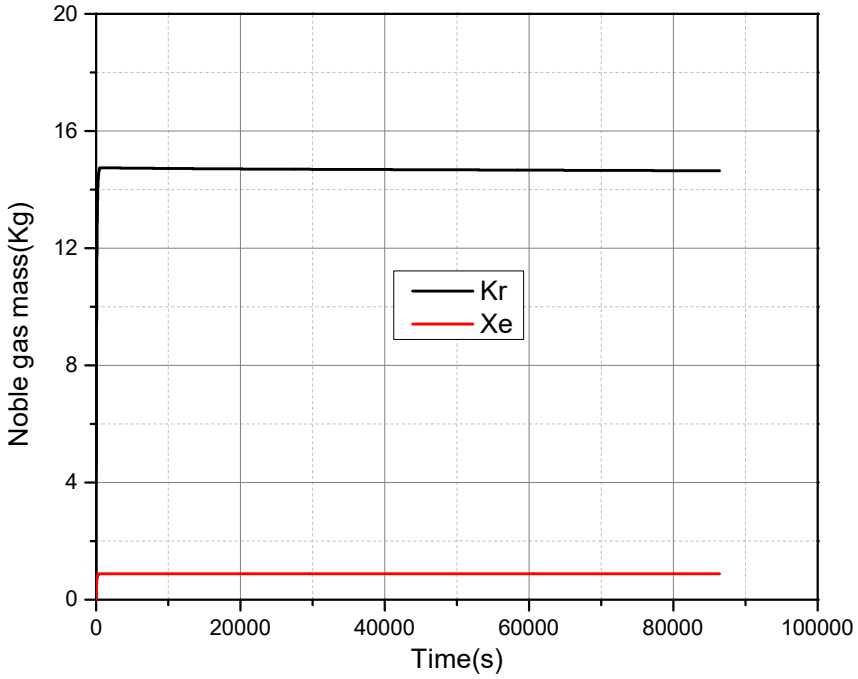

FIG. 159. Total noble gas mass in containment.

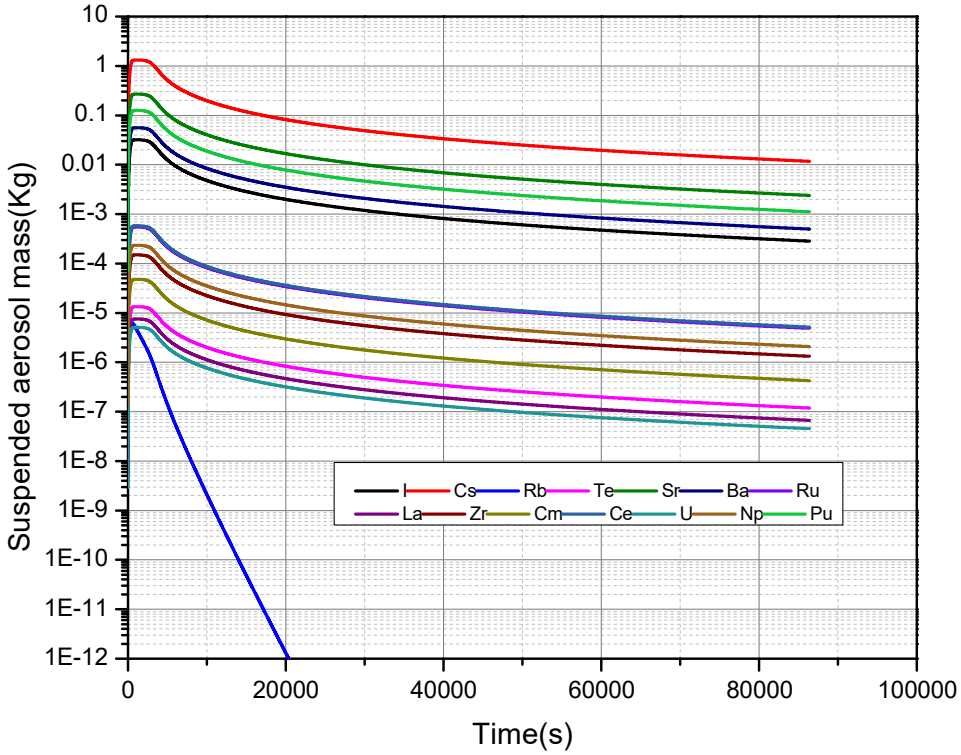

FIG. 160. Fission products suspended mass in containment.

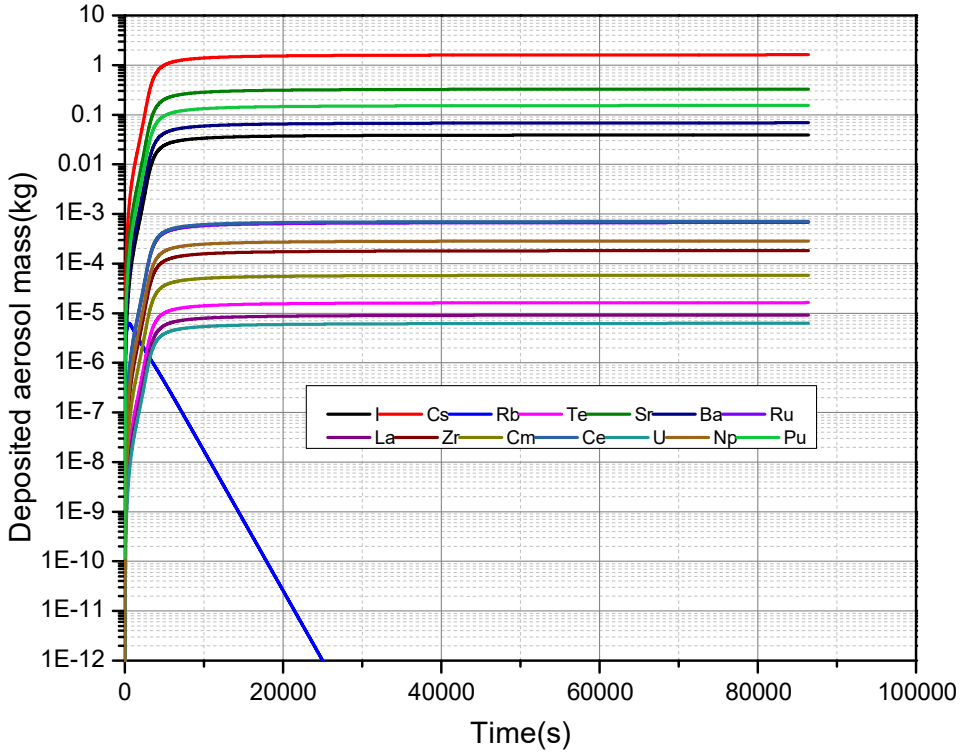

FIG. 161. Fission products deposited mass in containment.

Radioactivity analysis

FIG. 162 through FIG. 171 shows the radioactivity of all fission products elements. Radioactivity has been described in Case 1, which is mainly related to the half-life of nuclides. In case 2 calculation, noble gases and aerosols leaked into the environment were also calculated. The results show that the mass of aerosols released to the environment was 0.0306 kg and the mass of noble gases leaked to the environment was 1.57E-3 kg, thus the leakage fraction of aerosols and noble gases is 9.91E-5 and 6.46E-5, respectively.

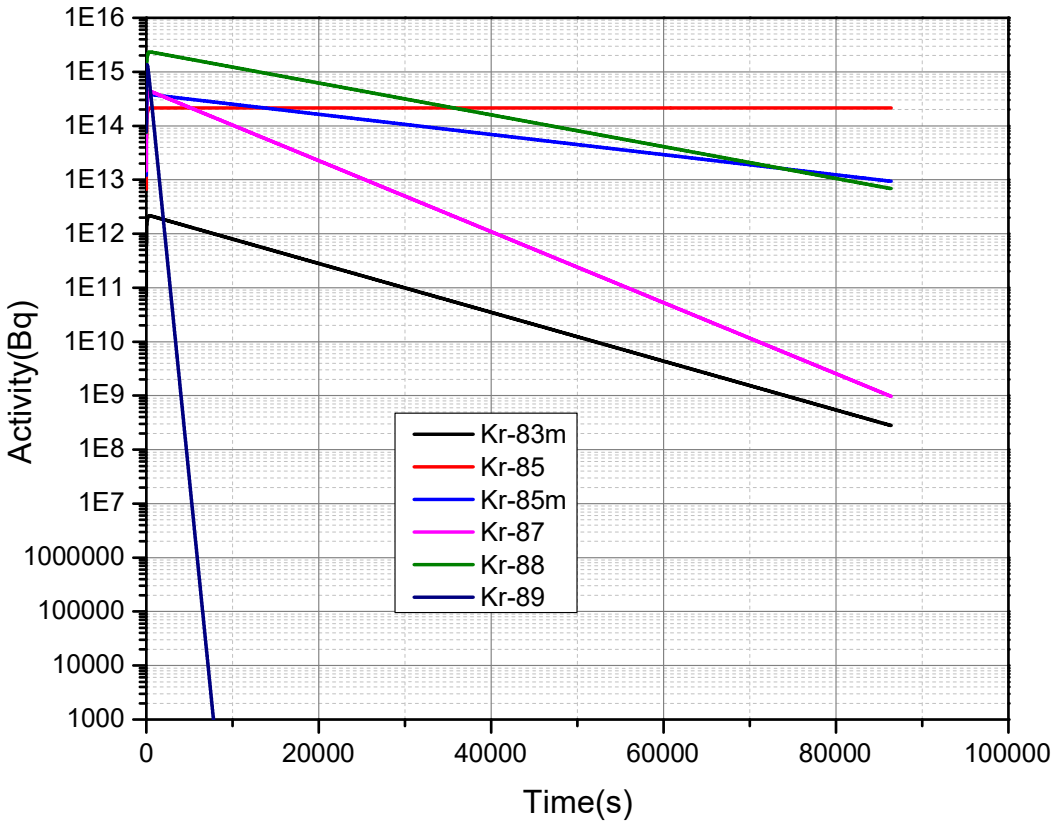

FIG. 162 Total radioactivity over time of krypton.

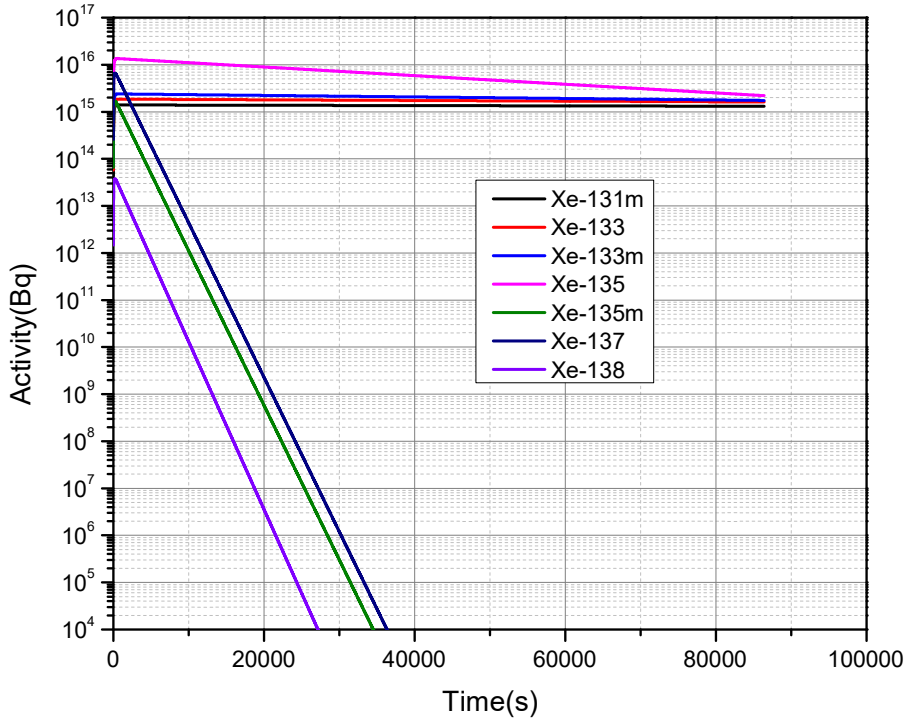

FIG. 163. Total radioactivity over time of xenon.

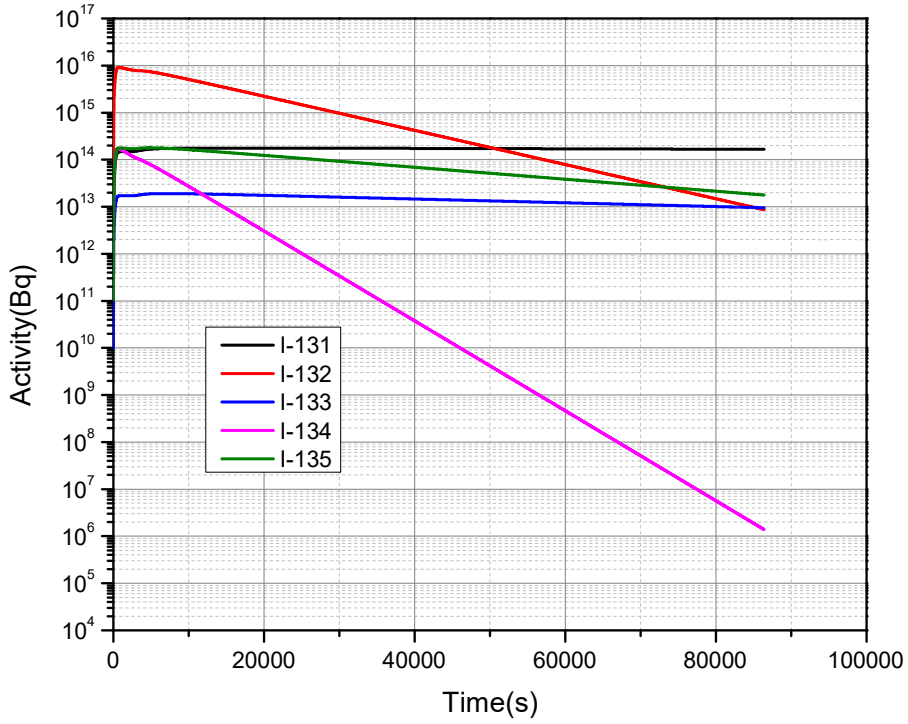

FIG. 164. Total radioactivity over time of halogen.

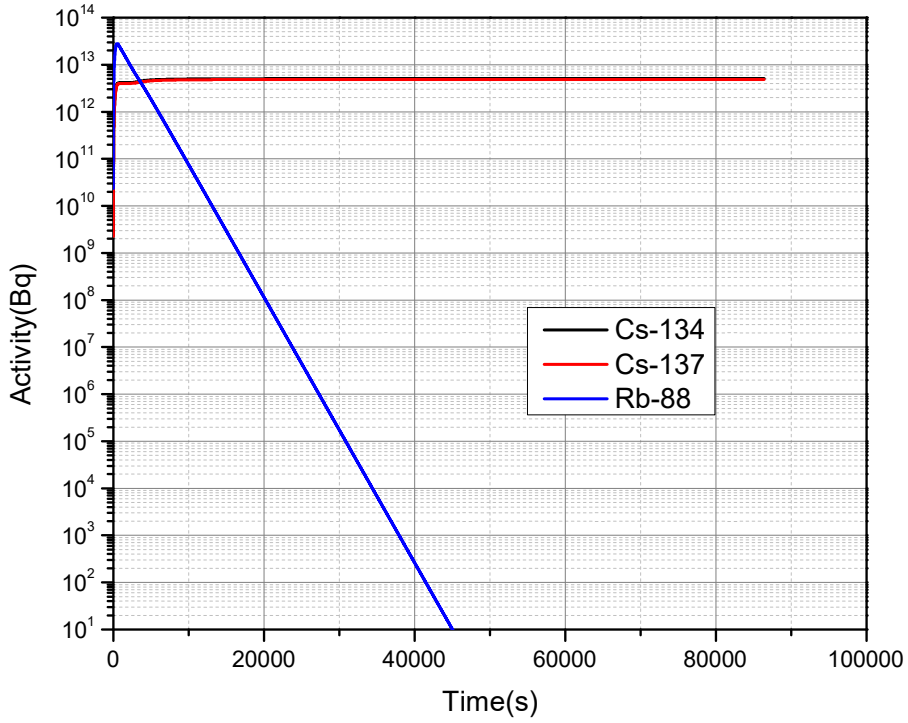

FIG. 165. Total radioactivity over time of alkali metals.

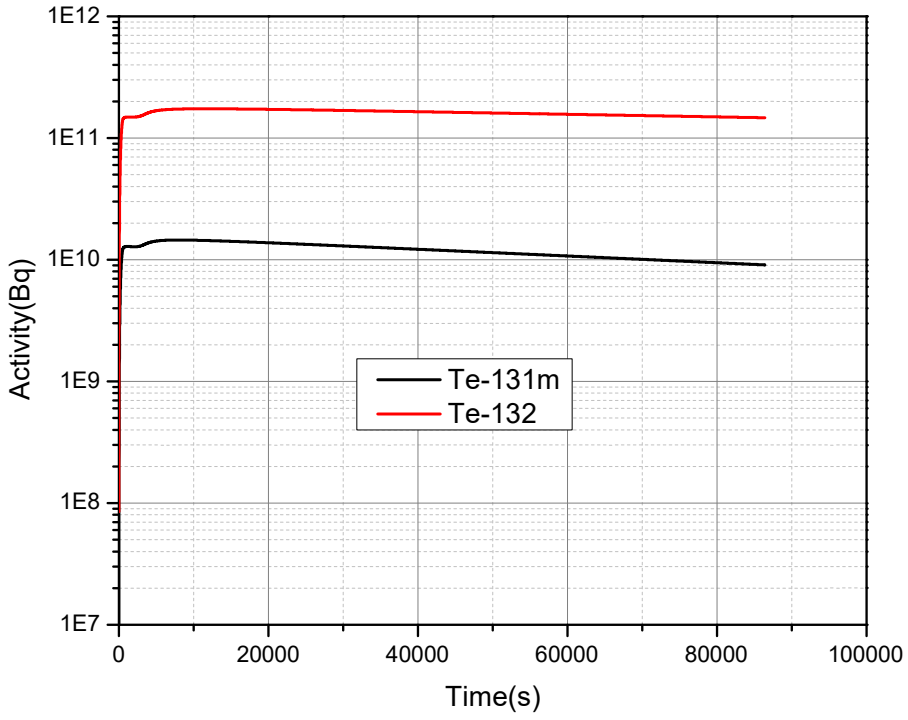

FIG. 166. Total radioactivity over time of tellurium.

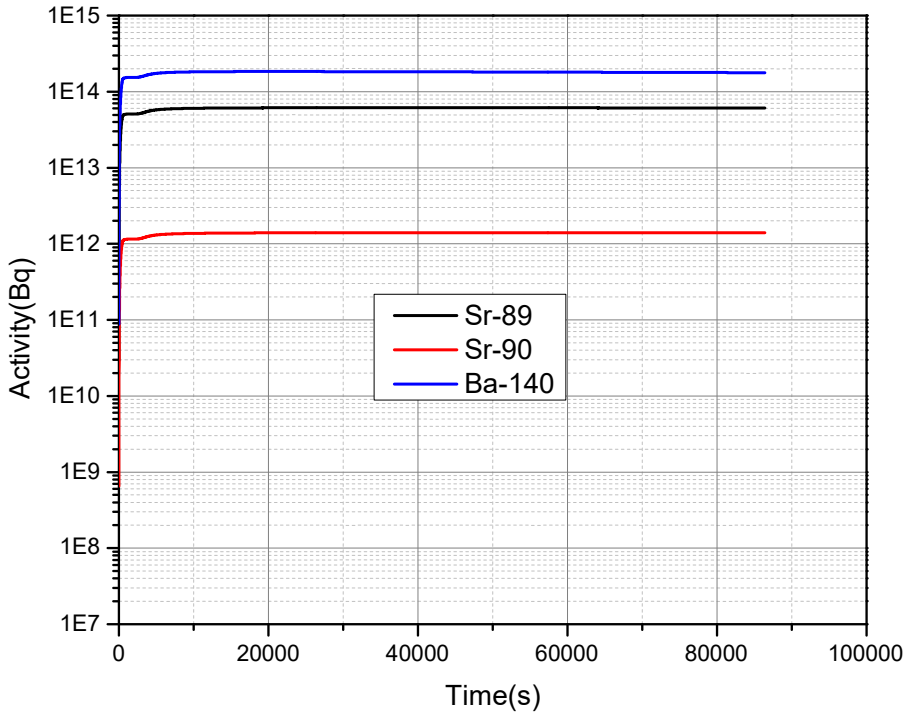

FIG. 167. Total radioactivity over time of barium.

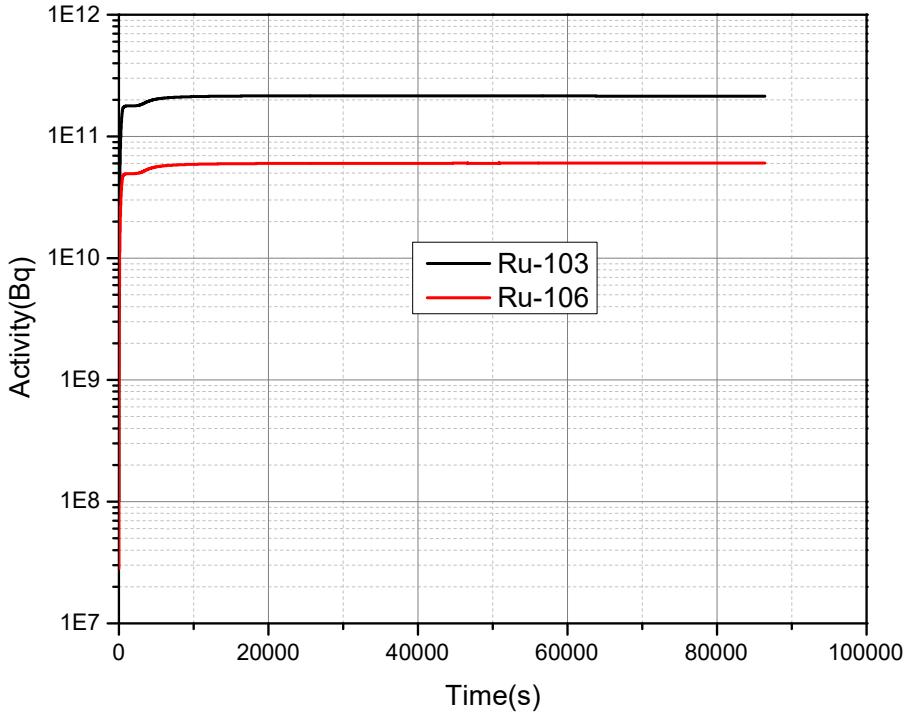

FIG. 168. Total radioactivity over time of noble metals.

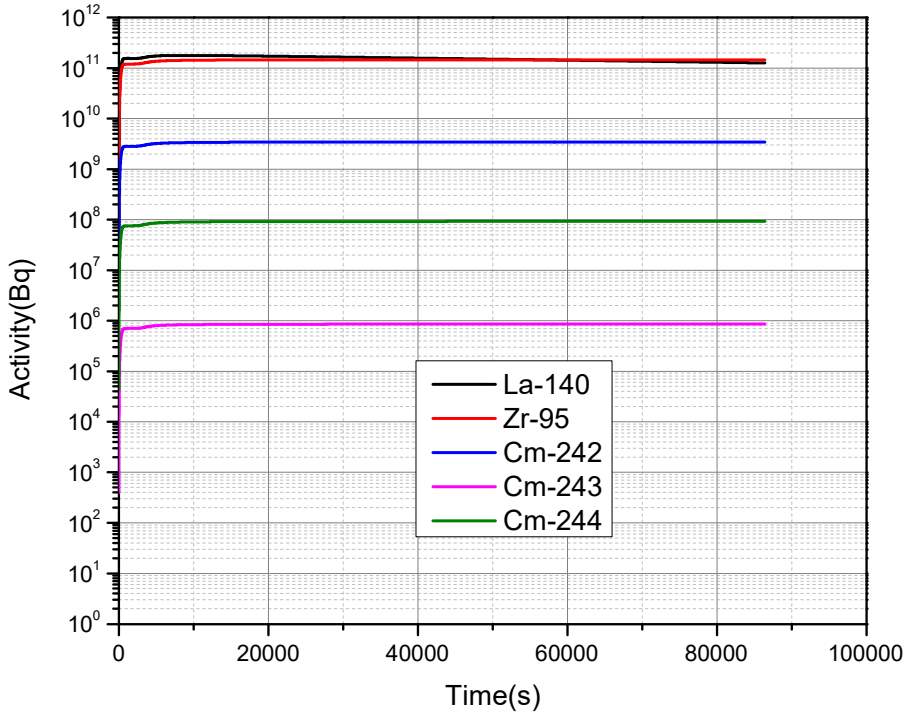

FIG. 169. Total radioactivity over time of lanthanides

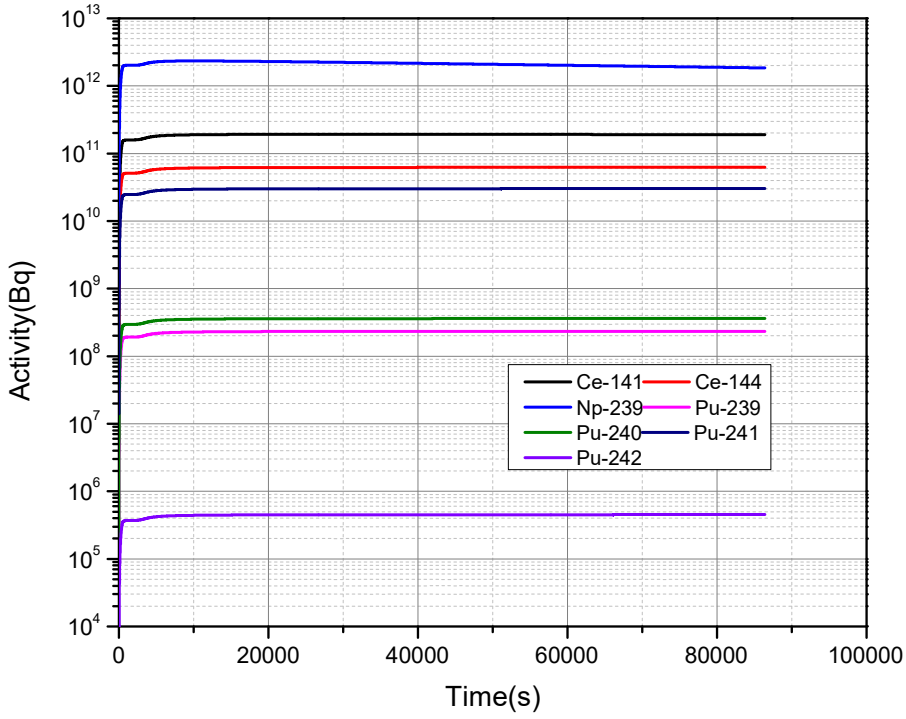

FIG. 170. Total radioactivity over time of cerium.

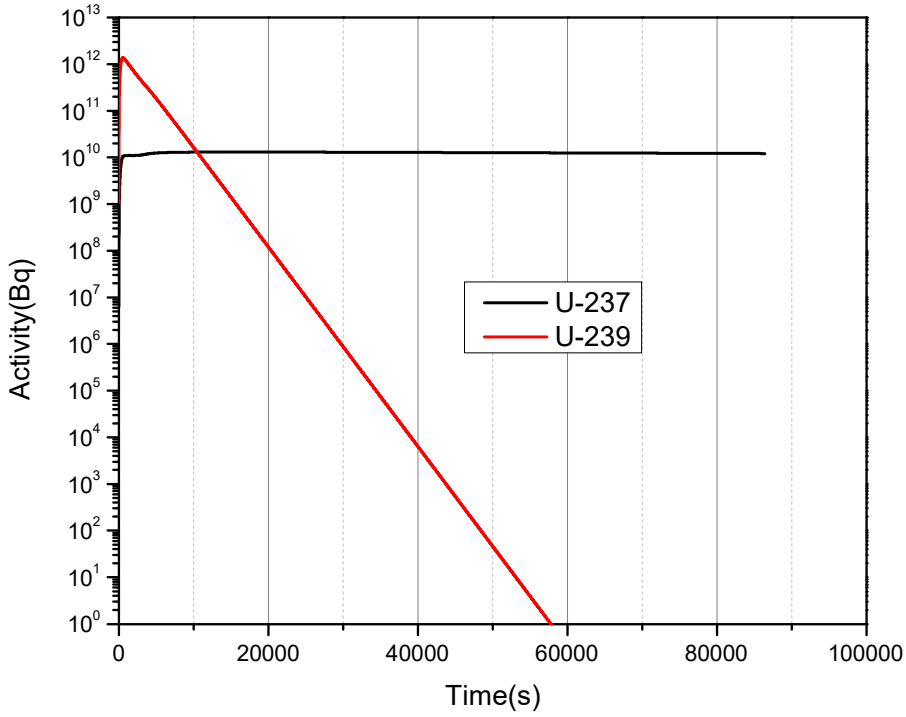

FIG. 171. Total radioactivity over time of uranium.

6.2.3. **Summary**

In case 1, a spray sodium fire releases a large amount of energy in a short time, resulting in a rapid increase in containment pressure and temperature, and then the pressure and gas temperature decrease due to natural cooling. The total pressure increased by about 13.2 kPa in the spray. The results show that a large number of aerosols are deposited on the floor of the containment, and gravity deposition is one of the main removal methods. The share of aerosols and noble gases released into the environment is 1.4E-4 and 3.1E-4, respectively.

In case 2, a sodium pool fire occurs in the enclosure, and the gas temperature in the enclosed chamber compartment rises to about 650K. Subsequently, strong natural convection occurs between the enclosure and the containment. In the process of natural convection, aerosols and noble gases in the enclosed chamber migrated into the containment. The calculation results show that the pressure in the containment increased by about 3 kPa. The retention fraction of aerosols and noble gases in enclosure was about 0.0196 and 8.88E-3, respectively. The leakage fraction of aerosols and noble gases was 9.91E-5 and 6.46E-5, respectively.

From the calculation results, it can be seen that the pressure rise caused by sodium pool fire is much smaller than that caused by sodium spray fire. Similarly, the leakage fraction of aerosols and noble gases in case 2 is lower than that in case 1. The enclosure has a retention effect on the diffusion of fission products; however, the results show that the retention fraction of the enclosure is much lower than that of migration to containment.

In the actual process, the fission product elements will react with sodium, which cannot be simulated in the current program. Especially iodine elements, there are many chemical reactions in the containment. In addition, the reaction between liquid sodium metal and concrete is not considered in the program. It is also identified the lack of explicit modelling in REBAC-SFR for chemical reactions between deposited fission products and structures in the primary system as one of the most important missing models. Similarly, some physical properties of aerosols,

such as moisture absorption on the surface of aerosol particles, are also missing. Aerosol particles that are soluble in water exhibit hygroscopic properties such that they can absorb moisture from an atmosphere with relative humidity less than 100%. This effect will lead to a growth of the particle size as water vapor condenses onto the soluble particle. These challenges should be addressed in the future.

6.3. SIMULATION EXERCISE USING CONTAIN-LMR CODE (CEA FRANCE)

6.3.1. Description of the Methods and Model

A preliminary study was carried-out by modelling the reactor vault, the containment, and the environment. For the CONTAIN-LMR model, 3 cells are used: one for the reactor vault, one for the reactor building and a large cell for the outside-building environment. The cells are connected as shown in FIG. 172. The mass transfers between the vault and the containment is calculated using the surfaces and pressure drops available for WP2. When using the reactor vault as a cell, a 350 kg sodium source was initially introduced in the containment, while the Fission Product (FP) source was chosen to be in the vault. The structures located inside the reactor vault were the vessel, the primary pumps, the heat exchangers, and the roof slab. These structures were involved in the heat exchanges and particularly aerosol deposition from the gases of the reactor vault. In the reactor vault, the low cell represents the sodium pool.

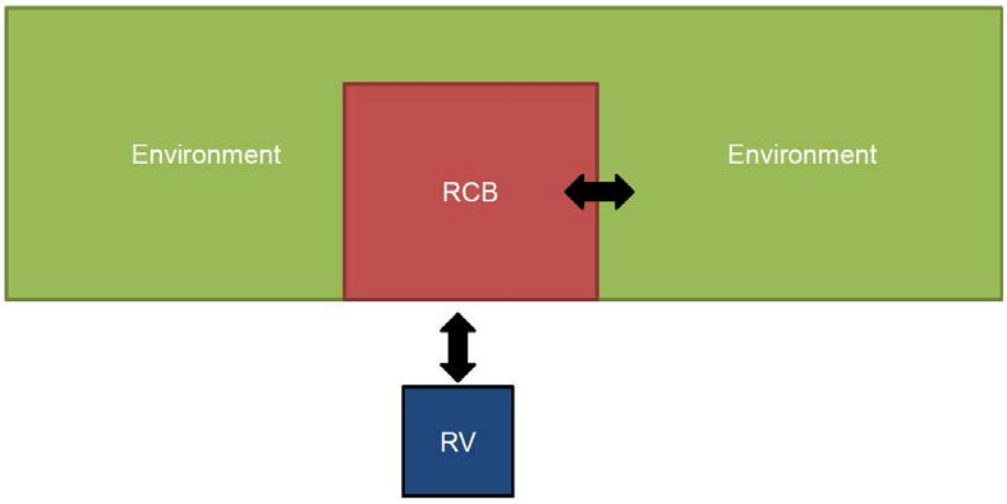

FIG. 172. Description of the interactions of the 3 cells, including the reactor vault (RV).

To comply with agreed assumptions of the WP3, only the Reactor Containment Building (RCB) and the environment were finally represented. The final calculations were performed with only 2 cells (RCB and environment).

The first part of the dataset describes the numerical calculation options. Then, the user-defined materials are described. In the framework of this project, tests were performed with the modelling of the reactor vault that used a concrete material defined by the code user. However, user-defined materials are not used in the final results of this CRP.

The transfer of fission products between hosts (aerosols, structures, etc.) is governed by equations that are dependent on the type of hosts[1] and the PF type. Moreover, a high host temperature increases the velocity of the transfers. The equations used by the CONTAIN-LMR models are summarized in FIG. 173.

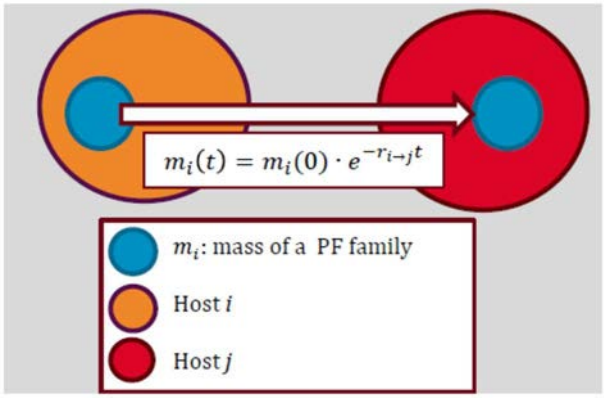

- Governed by the following equation:

$$\frac{dm_i}{dt} = -r_{i\to j}\, m_i.$$

- $ri\to j$ depending on the temperature:

$$r_{i\to j} = \begin{cases} a\, e^{-\frac{b}{T_i}} & T_i \geq T_{seuil} \\ 0 & T_i < T_{seuil} \end{cases}$$

T_i : temperature of the initial host
T_{seuil} : Threshold temperature for enabling host changing
a: Release coefficient
b : Release coefficient

FIG. 173. Fission products transfer between aerosols.

The transfer area between the RCB and the environment was chosen to be variable as a function of the pressure difference, according to the following equation:

$$leakrate = 6.0 \times 10^{-7} \times \Delta P^{0.74} \quad (83)$$

For sodium fire and sodium chemistry, the proportional amount of Na2O and Na2O2 (equation 3 of the FIG. 174) created by oxidation of the sodium is assumed to be 0.5.

[1] In CONTAIN-LMR, the fission products transport models use « hosts » such as the atmosphere, the structures or sodium aerosols. The fission products are located in and carried by those hosts.

1) $Na + H_2O \rightarrow NaOH + \frac{1}{2}H_2$

2) $2Na + H_2O \rightarrow Na_2O + H_2$

3) $\begin{cases} 2Na + \frac{1}{2}O_2 \rightarrow Na_2O \\ 2Na + O_2 \rightarrow Na_2O_2 \end{cases}$

4) $Na_2O_2 + 2Na \rightarrow 2Na_2O$

5) $Na_2O + H_2O \rightarrow 2NaOH$

6) $Na_2O_2 + H_2O \rightarrow 2NaOH + \frac{1}{2}O_2$

FIG. 174. Reactions of the sodium taken into account by the sodium chemistry model of CONTAIN-LMR.

Finally, the sodium initial ingress in the containment was chosen to be performed entirely as a spray, with a mean droplet diameter equal to 0.05mm, thus meaning an almost instantaneous combustion. The low cell of the containment (the sodium pool) is empty at the beginning of the simulation. Thus, the sodium combustion energy was totally released during the first second of the transient.

6.3.2. **Results**

6.3.2.1. *Results of the preliminary calculation with 3 cells*

As noted earlier in previous work packages, this simulation was performed using 3 cells: the reactor vault, the containment, and the environment. The initial large amount of hot sodium in the reactor vault, as well as the mass transfers between the reactor vault and the containment showed large impact on the temperature and pressure evolutions in these volumes. Particularly, the pressure along with the temperature decreased during the first 10 seconds of the transient. Then the temperature in the reactor vault increases due to the temperature of the sodium pool. The pressure difference between the reactor vault and the containment is fast balanced, as shown in FIG. 175. Around 200 seconds, some oxygen from the containment enters the reactor vault where sodium combustion takes place leading to a fast temperature increase in the reactor vault, as shown in FIG. 176.

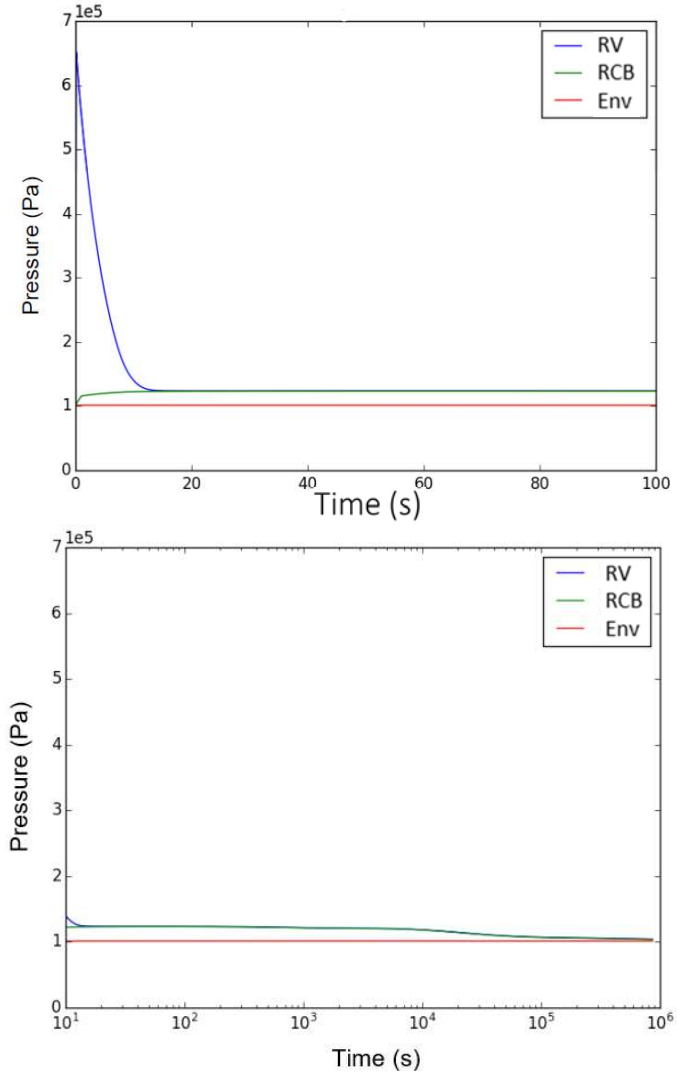

FIG. 175. Short-term (top figure) and long-term (bottom figure) evolution of the pressure in the reactor vault (blue), containment (green) and the environment (red).

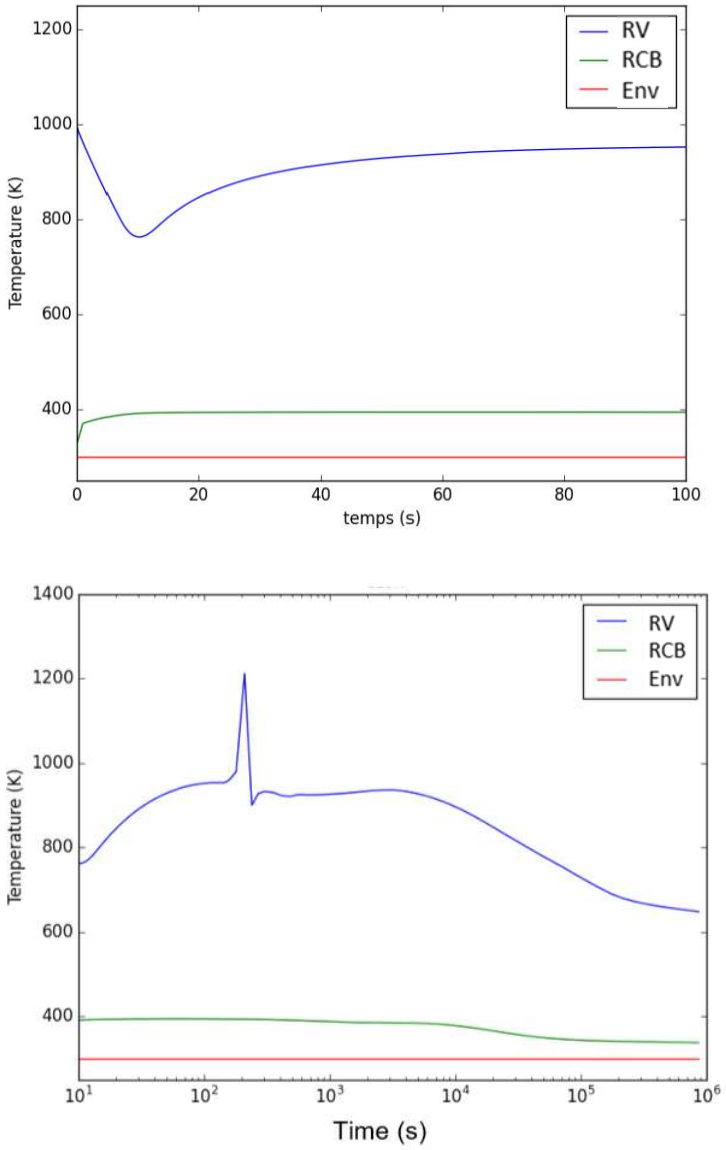

FIG. 176. Short-term (top figure) and long-term (bottom figure) evolution of the temperature in the reactor vault (blue), containment (green) and the environment (red).

The temperature peak was caused by the entrance of oxygen and the sodium chemical reactions in the reactor vault. The different sodium reactions are at the origin of the Na2O and Na2O2 appearance in the reactor vault, shown in FIG. 177. The sodium reactions stops fast due to the aerosol deposition on the various structures of the reactor vault: the deposition rate increased substantially around the temperature peak, shown in see FIG. 178.

The confirmation of the sodium reactions is highlighted by a simulation test without the ATMCHEM2 module, shown in see FIG. 179.

[2] The ATMCHEM module allows the modelling of the different sodium chemical reactions in CONTAIN-LMR

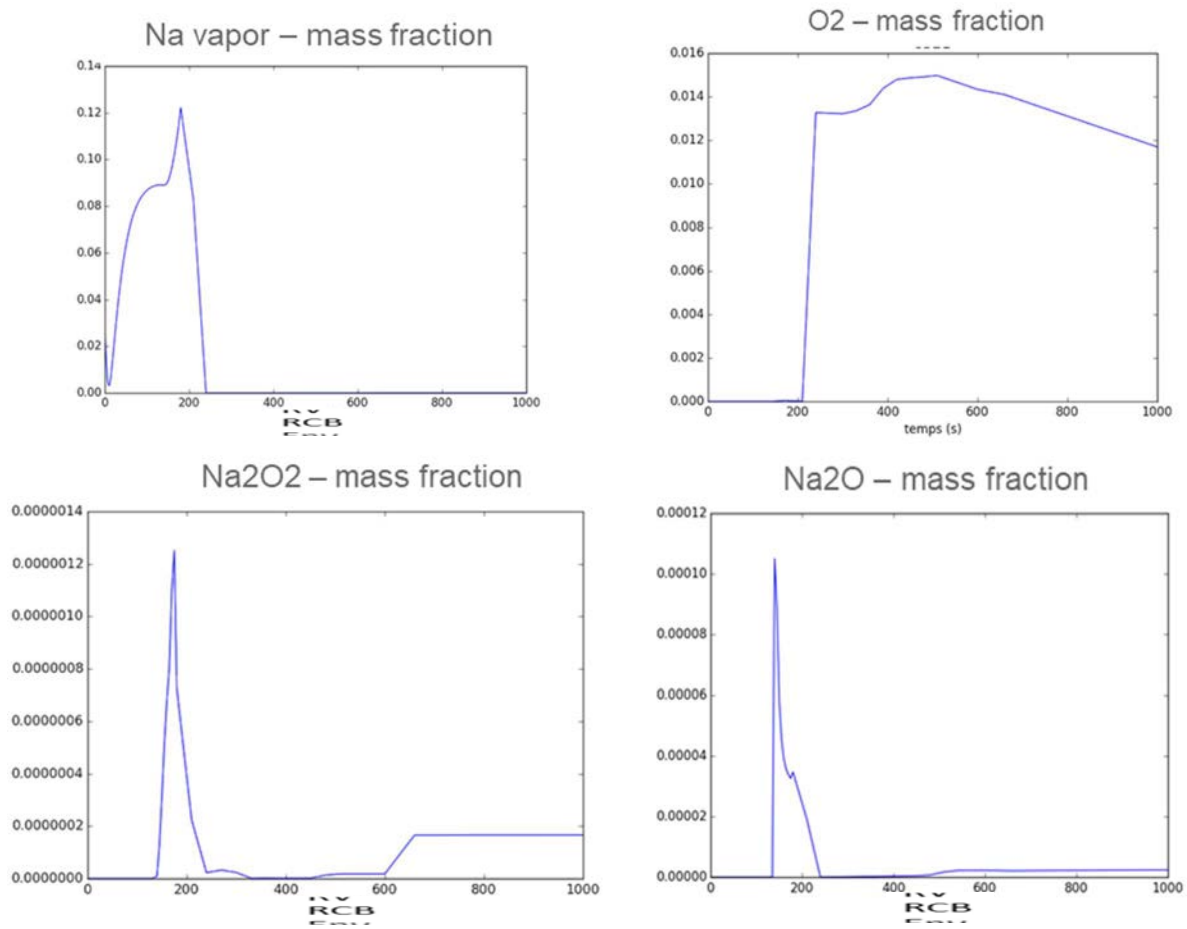

FIG. 177. Na vapor (top left), oxygen (top right), Na2O2 (bottom left), Na2O (bottom right) mass fractions in the reactor vault as a function of the time (s).

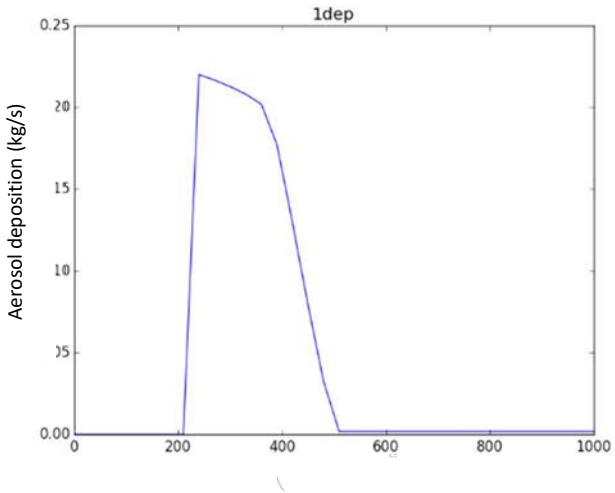

FIG. 178. Evolution of the total aerosol deposition on the structures in the reactor vault.

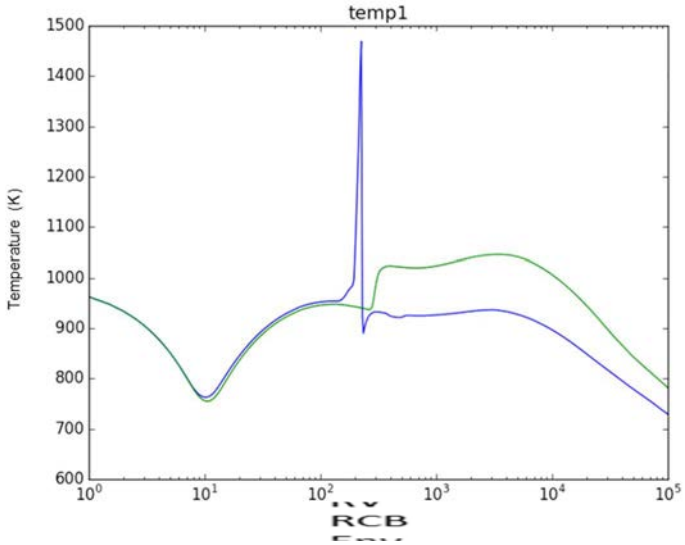

FIG. 179. Evolution of the temperature in the reactor vault with (blue) and without (green) the CONTAIN-LMR chemistry.

It was pointed out that the temperature peak was very sensitive to the initial conditions. For example, during the construction of the dataset, the impact of the $Kr^{83}{}_m$ on the simulation was highlighted. To investigate further, simulations were performed with and without the $Kr^{83}{}_m$ and, even when it is present in very small quantities compared to other isotopes, the simulations behaves as if it carries a significant part of the decay power, shown in FIG. 180, while it should not be physically true as $Kr^{83}{}_m$ is present in very small quantities and has no particular behaviour compared to the other krypton isotopes. Thus, some phenomena were totally different with and without $Kr^{83}{}_m$. For example, the observed temperature peak in the reactor vault was not observed anymore when $Kr^{83}{}_m$was removed, shown in FIG. 181.

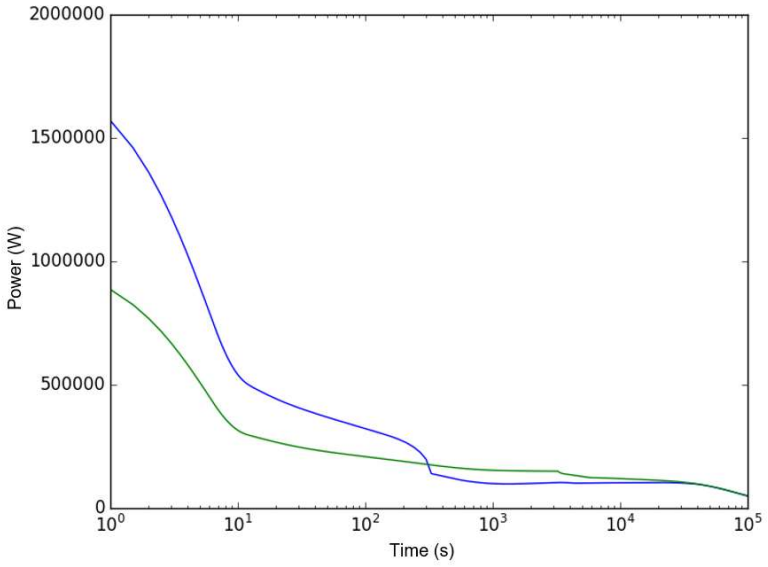

FIG. 180. Evolution of the power carried by aerosols and gaseous FPs in the reactor vault with (blue) and without $Kr^{83}{}_m$ (green).

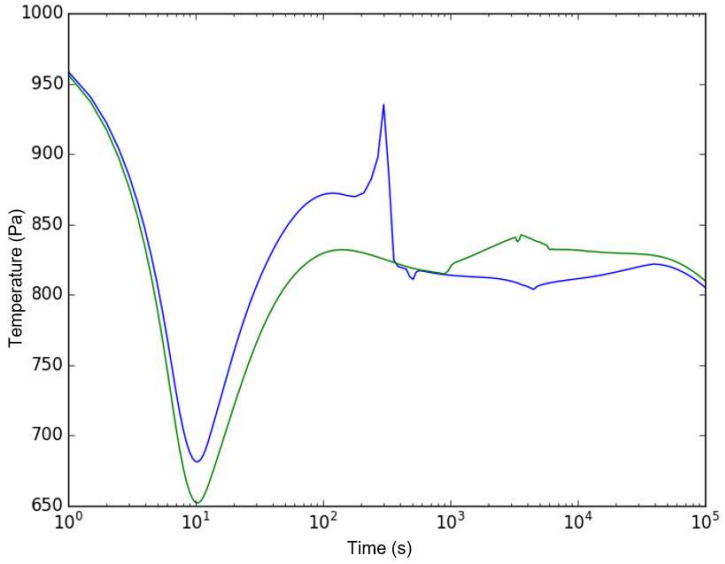

FIG. 181. Evolution of the temperature in the reactor vault with (blue) and without $Kr^{83}{}_m$ (green).

When calculating the reactor vault, both steel and concrete were considered for the roof slab material. The material selection mainly impacts the heat transfer between the reactor vault and the containment. As the conduction is higher in steel, the temperature decreases faster in the reactor vault (see FIG. 182) and increases faster in the containment when using steel. However, the material of the slab only has a minor impact on the phenomena happening in the containment and consequently on the radiological releases.

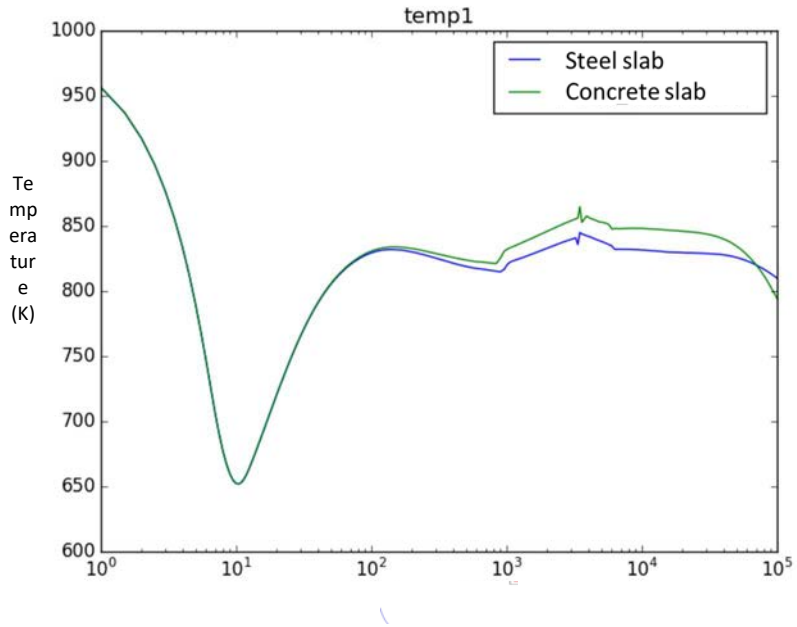

FIG. 182. Evolution of the reactor vault temperature with a steel slab (blue) and a concrete slab (green).

The addition of the enclosure was investigated and the calculations performed with the enclosure showed pressure and temperature oscillations between the enclosure and the containment (see for example FIG. 183). The simulations were not converging for each time step as the surface transfer area between the enclosure and the containment was important. By adding artificial pressure drops between the 2 cells it was possible to stabilize the simulations, but the results were far from what was expected, as there were some abrupt pressure falls. These simulations showed the limitations of the 0-D models used.

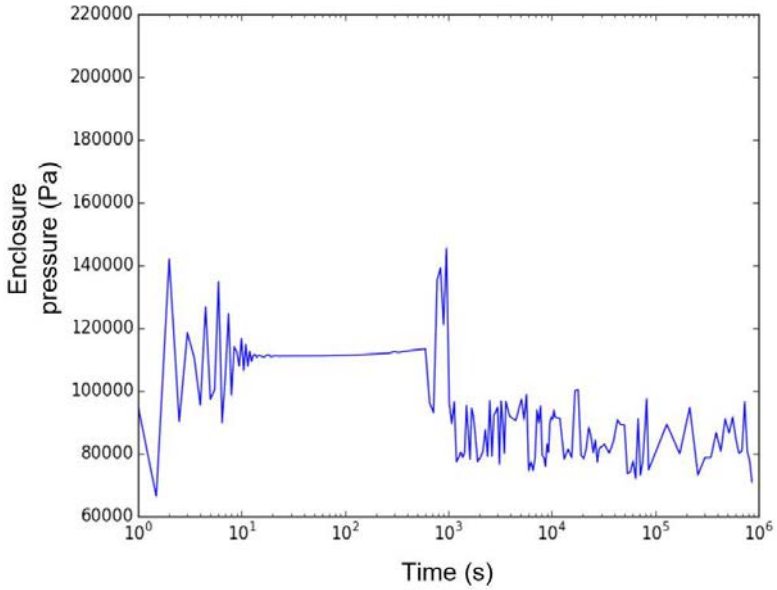

FIG. 183. Example of oscillations of the enclosure pressure obtained with a 3-cell calculation.

6.3.2.2. *Results in the short-term for a 2-cell simulation*

The results described in this section come from the final simulations using only 2 cells: one for the containment and one for the environment.

During the first second of the transient, the temperature quickly increased due to the sodium spray fire. After, the temperature stabilized around 363K (FIG. 184). Due to the low transfers between the containment and the environment, the temperature slowly decreased after the initial increase. The simulations still show a problem at the beginning of the transient: there is an initial steep increase not due to the sodium fire. At the date of the publication writing, this issue in the dataset has not been solved and explains the higher pressure and temperature gotten compared to the other simulations performed in this CRP.

As decided in the simulation parameters, the temperature of the environment is considered constant.

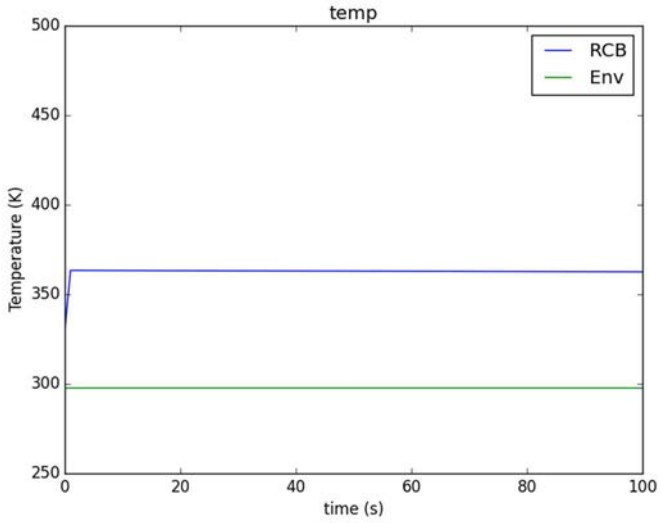

FIG. 184. Short-term evolution of the temperature in the containment (blue) and in the environment (green).

The pressure shows the same evolution as the temperature: the initial sodium spray fire quickly increases the pressure in the containment and, then, as the mass transfers to the environment are low, the pressure stabilizes around 1.22 atm (FIG. 185).

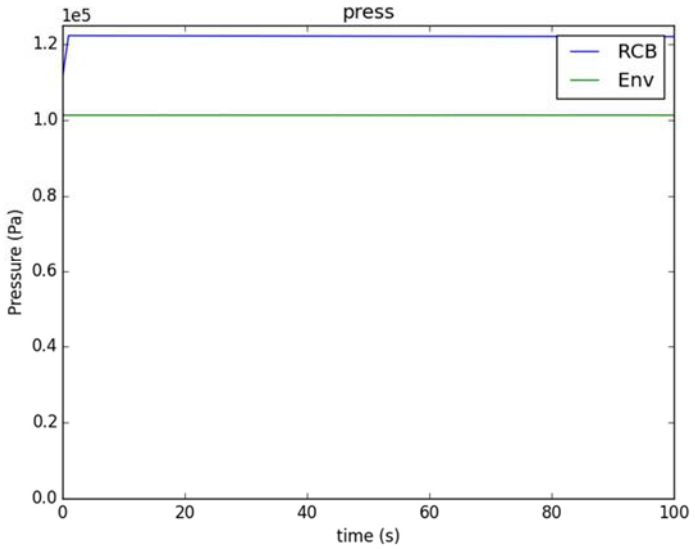

FIG. 185. Short-term evolution of the pressure in the containment (blue) and in the environment (green).

The global mass transfer, shown in FIG. 186, is driven by the pressure difference between the RCB and the environment. Thus, it quickly increases during the first second of the transient before stabilizing.

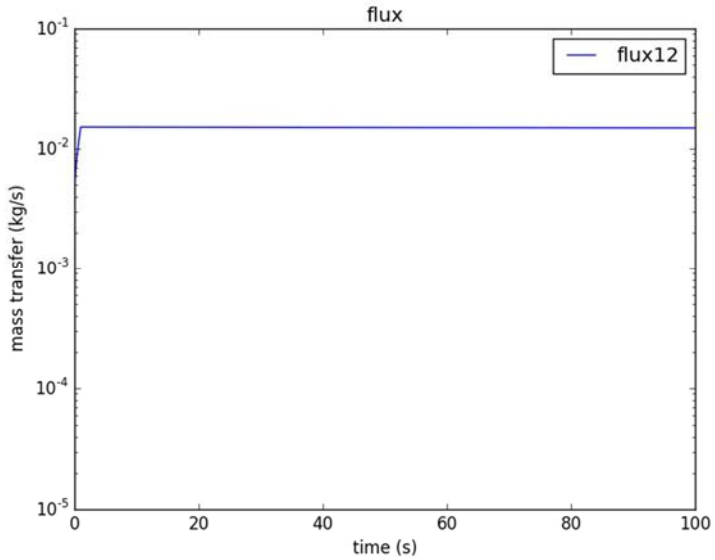

FIG. 186. Short-term mass transfer between the RCB and the environment.

6.3.2.3. *Results in the long-term for a 2-cell calculation*

During longer periods, the heat and mass transfers between the RCB and the environment decreased the temperature and the pressure in the RCB (FIG. 187 and FIG. 188).

The global mass transfer from the RCB to the environment decreased with the RCB pressure (FIG. 189).

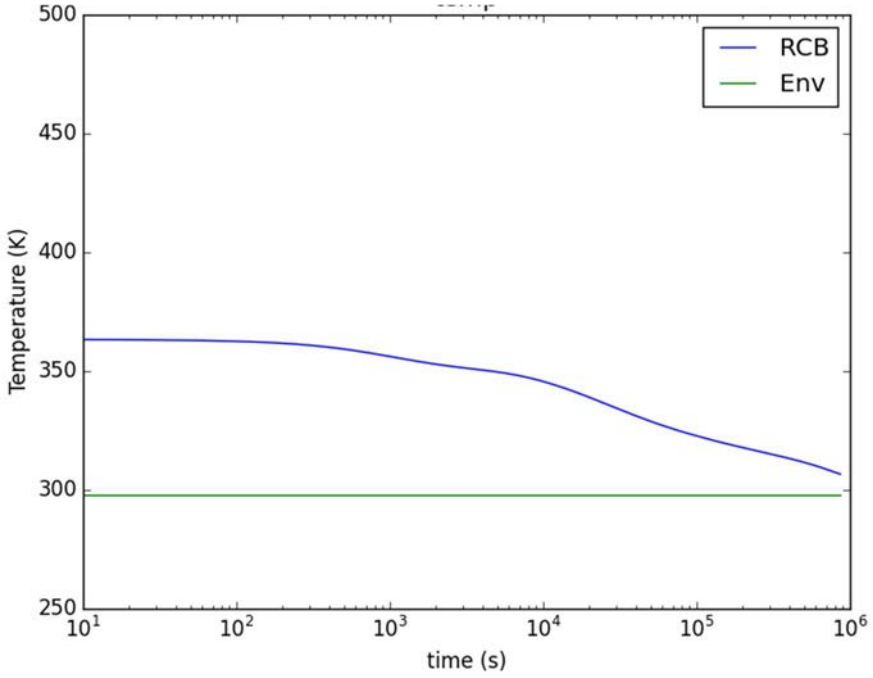

FIG. 187. Long-term evolution of the temperature (lin-log plot) in the containment (blue) and in the environment (green).

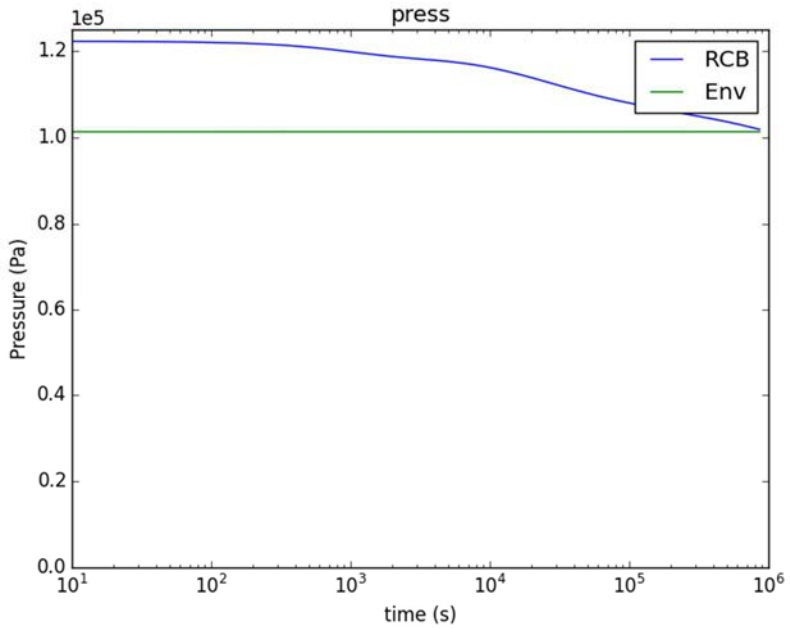

FIG. 188. Long-term evolution of the pressure (lin-log plot) in the containment (blue) and in the environment (green).

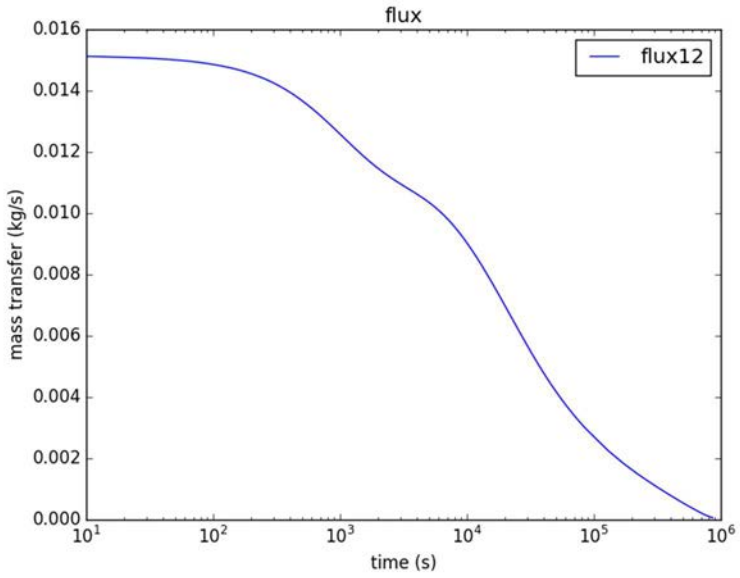

FIG. 189. Long-term evolution of the total mass transfer from the RCB to the environment (lin-log plot).

6.3.3. Summary

In the CONTAIN-LMR studies performed by the CEA, the pressure and the temperature of the containment increased quickly due to the selection of a sodium spray fire and no pool fire at the beginning of the transient. The heat and mass exchanges between the containment and the environment made the pressure and temperature decrease in the containment. As the releases are pressure driven, the total mass release rate followed the pressure decrease. Several simulations were performed with 3 cells, including the reactor vault, and showed that some models are very sensitive to the input parameters chosen by the user. Few models do not behave as expected, particularly the decay power carried by the fission products. These models have yet to be fully understood and corrected if needed to validate the CONTAIN-LMR simulations.

6.4. SIMULATION EXERCISE USING PFIRE AND PANDICA CODES (IGCAR, INDIA)

6.4.1. Description of the Methods and Model

In order to model the sodium combustion and aerosol evolution in the containment, two codes, PFIRE and PANDICA were developed. These codes will be integrated into the SFR source term assessment code system in the future. The detailed models used in these codes are described in the subsequent sections.

6.4.1.1. *Determination of pressure and temperature in the containment:*

The temperature and pressure evolution in the containment is a function of various heat sources present in the containment during accident. The heat sources in the containment are as follows:

(a) Sodium fire.
(b) Decay heat from the RN released to the containment.
(c) Heat dissipation from the sodium pipes and reactor roof slab.

(d) Heat addition from secondary fires due to other flammable material in the containment if any.
(e) Solar radiation.

The heat dissipation from the sodium pipes and conductive and convective heat transport from the roof slab is negligible [40]. Since the released sodium is confined to the roof slab, the possibility of the secondary fires due to other flammable material is remote. In this study the heat addition due to sodium pool fire, released decay heat in the containment, and solar radiations were considered. PFIRE code was developed for calculation of the temperature and pressure evolution in the containment and is based on modified SOFIRE-II one cell code. The detailed flow chart for the temperature and pressure evolution calculation in the containment is given in FIG. 190.

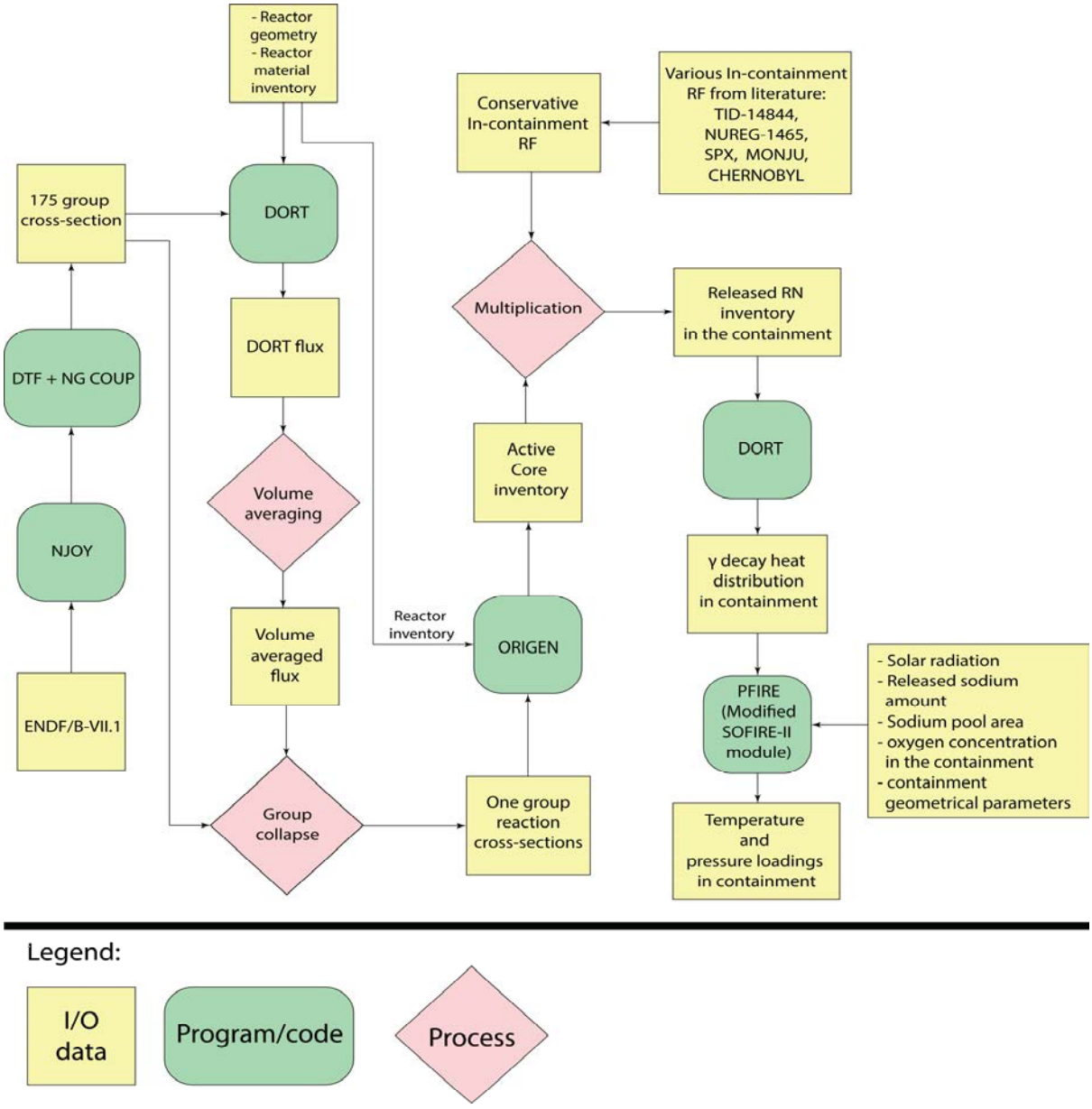

FIG. 190. General calculation flowchart for PFIRE.

The generalized model for the temperature and pressure evolution due to various heat sources in the containment can be given by following energy conservation equations. The equation governing containment air temperature is:

$$m_g(C_v)_g \frac{dT_g}{dt} = Q_{source} - A_w \sigma \epsilon_w \left(T_g^4 - T_w^4\right) - A_w h_{cw}\left(T_g - T_w\right) \quad (84)$$

The heat balance equation for the containment wall is:

$$m_w\left(C_p\right)_w \frac{dT_w}{dt} = h_{cw} A_w \left(T_g - T_w\right) + A_w \sigma \epsilon_g \left(T_g^4 - T_w^4\right) - h_{cw} A_w (T_w - T_a) \quad (85)$$

Where, Q_{source} is the heat source in the containment due to sodium fire and released decay heat. The solar radiation effect is considered through heating of the containment wall. However, it is neglected here. The pressure evolution in the containment is given by following equation derived from the ideal gas law,

$$\frac{1}{P_g}\frac{dP_g}{dt} = \frac{1}{T_g}\frac{dT_g}{dt} - \frac{1}{V}\frac{dV}{dt} \quad (86)$$

where
P_g is the pressure in the containment;
T_g is the temperature ofcontainment air;
T_a is the ambient temperature;
T_w is the wall temperature;
h_{cw} is the convective heat transfer coefficient;
A_w is the wall area of the containment;
σ is the Stephan Boltzmann constant;
ϵ_g is the emissivity coefficient;
m_g is the mass of the containment air;
m_w is the mass of the containment wall;
$(C_v)_g$ is the specific heat capacity of containment air;
$\left(C_p\right)_w$ is the specific heat capacity of containment wall;
$\frac{1}{V}\frac{dV}{dt}$ is the containment fractional leakage term.

The model implemented in the code has multiple nodes for the wall temperature.

Sodium fire

The release of sodium in the containment can result in vigorous reaction with containment air (oxygen, carbon dioxide), vapor content in the containment atmosphere, or concrete surfaces. Since these reactions are exothermic in nature, the heat released due to these reactions will heat up the containment air and structures. The nature and rate of sodium fire is dependent on the release rate, spray or pool formation, available oxygen, and humidity. Since, sodium will be released through mostly horizontal leak paths, formation of the sodium pool on the roof slab

with brief sodium spray is expected. Due to uncertainty in the modelling parameters such as, sodium spray droplet sizes, pool area, amount of the ejected sodium contributing in the sodium spray fire or pool fire, the following three cases are studied:

(1) Instantaneous combustion: Temperature and pressure rise in the containment due to instantaneous combustion of all ejected sodium.
(2) Pool fire: Temperature and pressure rise in the containment owing to pool fire, combustion rate as per the oxygen availability.
(3) Spray fire: Temperature and pressure rise in the containment as per spray fire.

For sodium-oxygen reaction, two main reaction products can be formed: sodium mono-oxide and sodium peroxide. The reactions are as follows:

$$2Na + \frac{1}{2}O_2 \rightarrow Na_2O + 9460\frac{kJ}{kg} of\ Na\ \left(i.e., 27196\frac{kJ}{kg}O_2\right)$$

$$2Na + O_2 \rightarrow Na_2O_2 + 11280\frac{kJ}{kg}\ of\ Na\ \left(i.e., 16123\frac{kJ}{kg}O_2\right)$$

The oxides are subsequently converted to hydroxide and carbonates. These further reactions are not considered here. For these calculations it is assumed that 100% sodium monoxide Na_2O is formed as a combustion product. In order to limit the effect of uncertainty from containment leakage parameter on this study it is assumed that the containment is leak tight.

Instantaneous combustion

In this case it is assumed that all the ejected sodium burns instantaneously. The calculation for the temperature and pressure evolution in the containment is shown in the *FIG. 191* and FIG. 192. For this case, peak temperature rise in the containment is 345 K and the peak pressure rise in the containment is 14 kPa (FIG. 192), which is well below the design pressure of 25 kPa. The temperatures reach room temperature after the 2-3 hours.

Pool fire

For the pool fire case, it is assumed that the ejected sodium forms a pool instantaneously (within 0.5s). The rate of sodium combustion depends on the oxygen concentration in the containment and the rate at which oxygen gets transported to the surface of the sodium pool through natural convection. An approach similar to SOFIRE II [41] has been adopted for the present calculation. The rate of the sodium combustion can be given as,

$$\frac{1}{A_s}\frac{dm_s}{dt} = H_{ngc}X_{O_2}\rho_g S \tag{87}$$

where
A_p is the surface area of sodium pool;
H_{ngc} is the gas transport due to natural convection, given by Eq. (88);
X_{O_2} is the mass fraction of free oxygen in containment air;
S is the stoichiometric combustion ratio;

ρ_g is the density of containment air.

$$H_{ngc} = 0.14 \frac{D}{d_p} (GrSc)^{\frac{1}{8}} \tag{88}$$

The above heat source due to sodium fire is incorporated in the heat conservation equations and solved using the finite difference method in Python. The model for sodium pool fire has been validated with the FAUNA 5, 6 and LTV test 4 experiments. The peak temperatures occur within 5 minutes of start of fire. The peak temperature is 335 K, as shown in FIG. 191. The containment temperature comes near the room temperature within an hour. The peak pressure rise in the containment is approximately 12 kPa, as shown in FIG. 192.

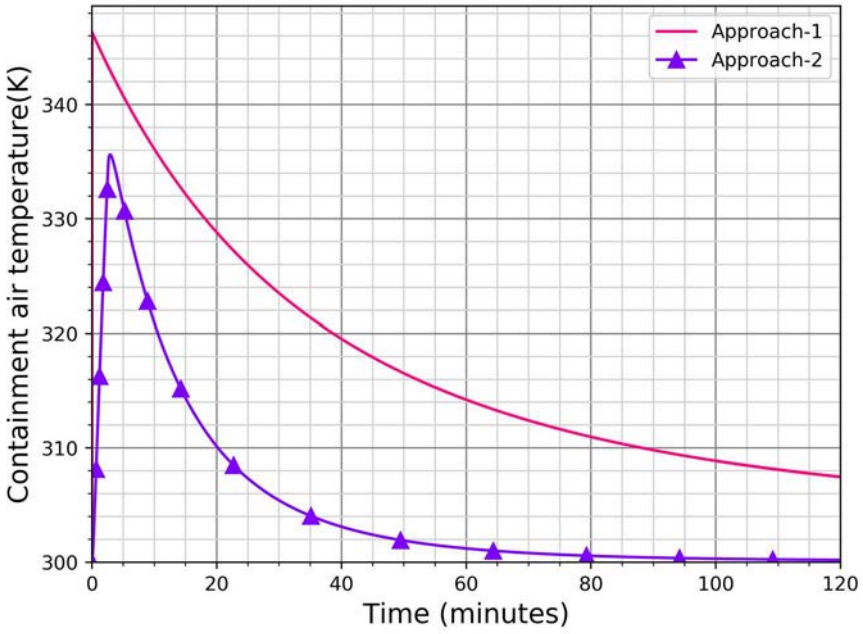

FIG. 191. Temperature evolution in the containment.

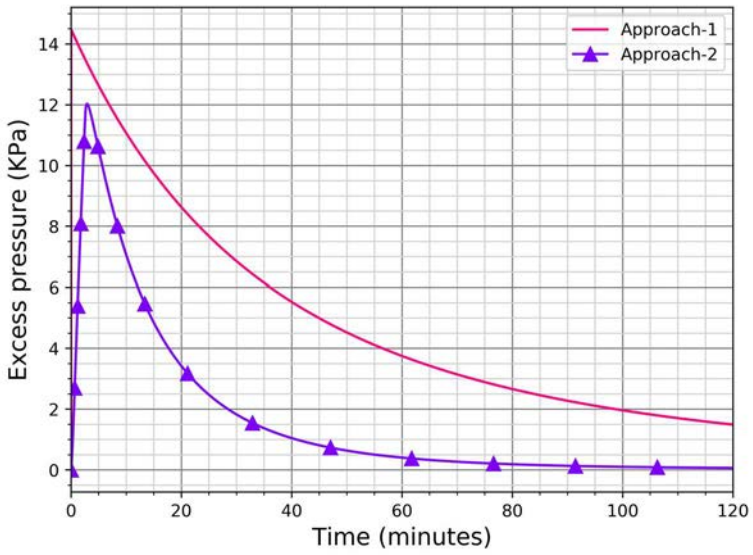

FIG. 192. Pressure evolution in the containment atmosphere.

Spray Fire [42]

The sodium spray may be formed via impaction of sodium jet against the top shield enclosure wall. If the sodium spray fire consists of smaller droplets, burn rate would be higher compared to sodium pool fire. Hence, it was agreed by participants to consider a standalone case 1 as spray fire. Generally, the spray fire is modelled as the combustion of the single droplet and then according to the sodium droplet distribution, the effective combustion rate is summed.

Model for the combustion of the single stationary sodium droplet:

The sodium droplet consists of the burning zone or the flame zone. Sodium gets vaporised from the sodium droplet zone and diffuses towards the flame zone. As the vaporised sodium comes into contact with the oxygen, it instantaneously ignites the combustion. The heat is again fed to the sodium droplet. The mass burning rate, $\dot{m}$ of a droplet can be given as a function of the sodium droplet diameter,

$$\dot{m} = -\frac{d}{dt}\frac{\pi}{6}d^3\rho \tag{89}$$

Here it is assumed that the combustion of the formed droplets is instantaneous. The sodium ejection rate (as specified in the Section 2) into the containment, temperature and pressure evolution for this case are shown in FIG. 193 to FIG. 195.

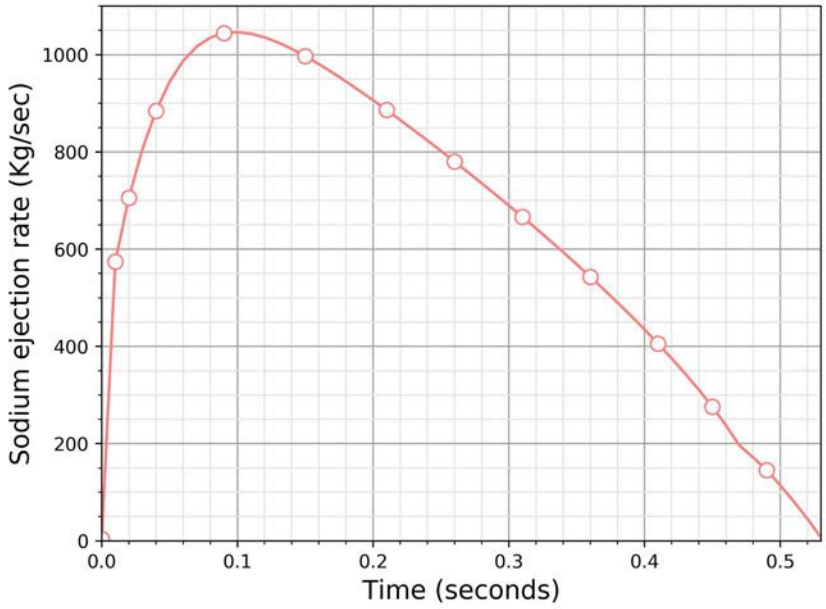

FIG. 193. Sodium ejection rate (kg/sec).

For the temperature and pressure evolution in the containment, 100% formation of Na_2O was assumed. The temperature and pressure evolution in the containment is given in FIG. 194 and FIG. 195. As show in the figure, the peak temperature in the containment is about 340 K, whereas the peak pressure in the containment is about 12 kPa.

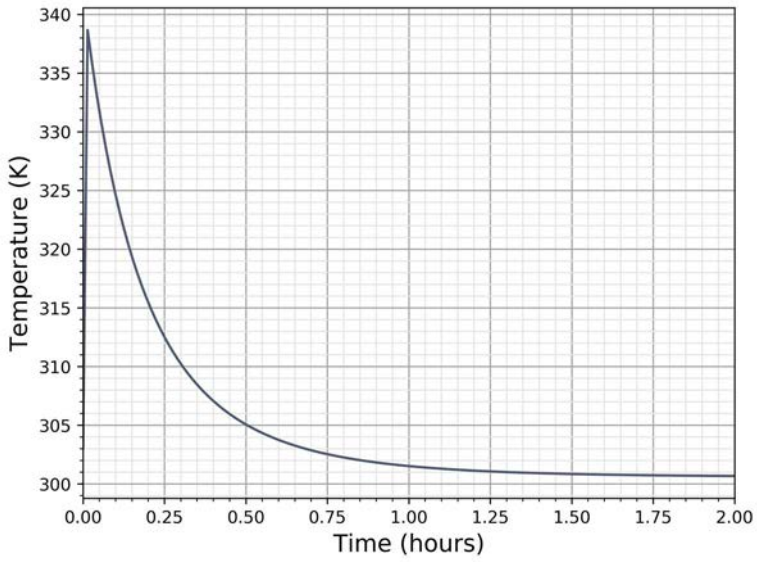

FIG. 194. Temperature evolution in the containment following sodium spray fire.

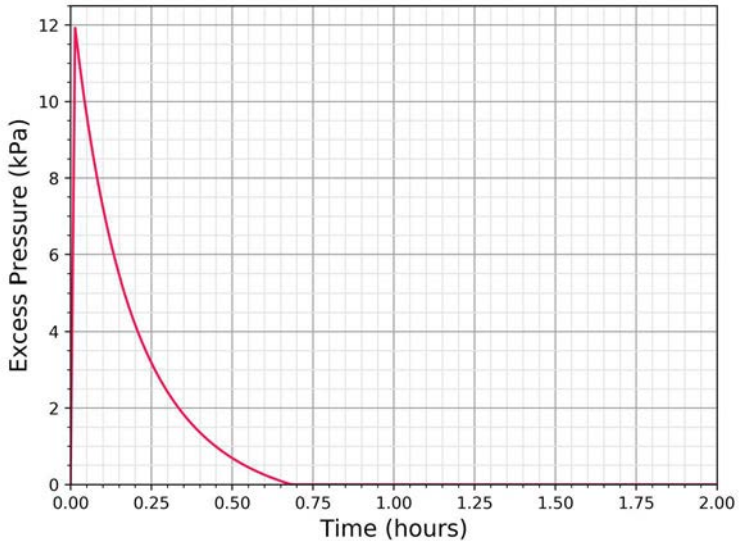

FIG. 195. Pressure evolution following sodium spray fire.

6.4.1.2. *Evolution of the containment activity post-accident*

The radionuclides that are ejected into the containment (that are not in gas) during the bubble expansion phase form aerosols in the containment atmosphere and encounter sodium aerosols. The subsequent rate of removal of these aerosols depends on the condensation rate, size distribution, ambient conditions, agglomeration and removal mechanisms and the surface area available for settling. The following sections address the aerosol agglomeration and removal process. The initial condensation and chemistry are not modelled. The aerosol size distribution is assumed from experiments and it is assumed that RN aerosols would be bound to Na aerosols uniformly.

Aerosol evolution

The following integro-differential equation (Smoluchowski Equation) [43] [44] describes the aerosol number density evolution owing to binary collisions between particles.

$$\frac{\partial n(v)}{\partial t} = \frac{1}{2}\int_0^v \beta(u, v-u)\, n(v-u) n(u) du - \int_0^\infty \beta(u, v) n(v) n(u) du - R(v) n(v) + S(v) \tag{90}$$

where

u and v are the volumes of coagulating particles,
$n(v)$ is the time-dependent number concentration (particles / unit medium volume / particle volume,
n dv is the number of particles per unit medium volume with size between v and v+dv),
$\beta(u, v)$ is the coagulation kernel (including collision efficiency) of the two colliding particles (unit medium volume per particle per unit time).

Eq. (90) is a statement of particle number concentration balance in a unit volume. First term on the r.h.s is for the formation rate of particles of volume v from particles of volume *(v-u)* and particles of volume *u*. The second term on the r.h.s is the removal rate of particles volume v owing to coagulation with particles of all sizes. The first integral in (1) is multiplied by 0.5 to eliminate double counting of production terms. R(v) is the particle removal rate (per unit time) due to various removal mechanisms such as gravitational sedimentation, diffusion and thermophoretic removal. S(v) dv is the source term, i.e., aerosol generation rate per unit volume of particle size between v and v+dv.

Numerical solution

The discretized form of Eq. (90), is

$$\frac{dn_k}{dt} = \sum_{j=1}^{k-1} \beta_{k-j,j} n_{k-j,t} n_{j,t} - \sum_{j=1}^{\infty} \beta_{k,j} n_{k,t} n_{j,t} - R_k n_{k,t} + S_{k,t} \tag{91}$$

Eq. (91) can be solved by any of the numerical methods for solving coupled system of first order differential equations.

A fully implicit discretization of Eq. (91) is,

$$n_{k,t} = n_{k,t-h} + \frac{1}{2} h \sum_{j=1}^{k-1} \beta_{k-j,j}\, n_{k-j,t} n_{j,t} - h \sum_{j=1}^{\infty} \beta_{k,j}\, n_{k,t} n_{j,t} \tag{92}$$

This equation requires an iterative solution. A semi-implicit iterative scheme introduced by Jacobson et. al. [44], which is called the semi-implicit coagulation solution was utilized.

$$n_{k,t} = n_{k,t-h} + \frac{1}{2} h \sum_{j=1}^{k-1} \beta_{k-j,j}\, n_{k-j,t} n_{j,t-h} - h \sum_{j=1}^{\infty} \beta_{k,j}\, n_{k,t} n_{j,t-h} \tag{93}$$

Where, h=Δt . Rearranging the above equation,

$$n_{k,t} = \frac{n_{k,t-h} + \frac{1}{2} h \sum_{j=1}^{k-1} \beta_{k-j,j}\; n_{k-j,t}\, n_{j,t-h}}{1 + h \sum_{j=1}^{\infty} \beta_{k,}\, n_{j,t-h}} \tag{94}$$

The above Eq. (94) allows a non-iterative solution to coagulation. However, it is not aerosol mass conserving. Eq. (92) correctly accounts for number and volume, but it is fully implicit and hence requires iterations.

In order to conserve volume and volume concentration (which coagulation physically does) while giving up some accuracy in number concentration, equation can be rederived in terms of volume concentrations of monomer particles and rewritten as [44],

$$\nu_{k,t} = \frac{\nu_{k,t-h} + h\sum_{j=1}^{k-1}\beta_{k-j,j}\nu_{k-j,t}n_{j,t-h}}{1 + h\sum_{j=1}^{\infty}\beta_{k,j}\,n_{j,t-h}} \tag{95}$$

Where, $\nu_k = v_k n_{k,t}$ Eq. (95) satisfies the volume-conservation requirement, $v_{k-j}P_{k,j} = v_{k-j}L_{k-j,j}$for any k and j.

The solution just presented is applicable to a monomer size distribution. It is usually desirable to solve coagulation over an arbitrary size distribution, such as the volume-ratio distribution. A volume-ratio size distribution is defined so that the volume of a particle in one size bin equals the volume of a particle in the next smallest size bin multiplied by a constant, V_r.

For the volume ratio or any other type of discretized size distribution, the semi-implicit solution can be modified to treat coagulation. The solution is found by first defining the volume of an intermediate particle that results when a particle in size bin 'i' collides and sticks to a particle in size bin 'j' as

$$V_{i,j} = v_i + v_j \tag{96}$$

The intermediate particle has volume between those of two arbitrary model size bins, k, and k + 1, and needs to be partitioned between the two bins. This is done by defining the volume fraction of $V_{i,j}$ that is partitioned to each model bin k as,

$$f_{i,j,k} = \begin{cases} \left(\dfrac{v_{k+1} - V_{i,j}}{v_{k+1} - v_k}\right) & ; v_k \le V_{ij} < v_{k+1} \; and \;\; k < N_B \\ 1 - f_{i,j,k-1} & ; \; v_{k-1} < V_{ij} < v_k \; and \;\; k > 1 \\ 1 & ; \; V_{ij} \ge v_k and \; k = N_B \\ 0 & ; for \; all \; other \; cases \end{cases} \tag{97}$$

When volume fractions are used, the semi-implicit, aerosol volume conserving solution for total particle volume concentration becomes [44],

$$\nu_{k,t} = \frac{\nu_{k,t-h} + h\sum_{j=1}^{k}\left(\sum_{i=1}^{k-1} f_{i,j,k}\beta_{i,j}\nu_{i,t}n_{j,t-h}\right)}{1 + h\sum_{j=1}^{N_B}\left(1 - f_{k,j,k}\right)\beta_{k.j}n_{j,t-h}} \tag{98}$$

The number concentrations are obtained from the equation relating the total particle volume in a bin to the number of particles in that bin as,

$$n_{k,t} = \nu_{k,t} \; / v_k \tag{99}$$

The above Eq. (98) is implemented in Python and named PANDICA (Particle Agglomeration and Deposition In Containment Analysis) for solving the aerosol evolution in the containment with time. The binning scheme is shown in FIG. 196

FIG. 196. The volume ratio bin structure considered in the simulation.

$$V_i = V_1 V_r^{\,i-1}\ ;\ i = 1\ to\ N$$

$$dv_i = \frac{v_i + v_{i+1}}{2} - \frac{v_i + v_{i-1}}{2}$$

$$= v_1 v_r^{i-1}\left(r - \frac{1}{r}\right) \tag{100}$$

The agglomeration mechanisms and the corresponding kernels used in the Smoluchowsky's equation are as follows [44] [45] [46]:

(a) Gravitational agglomeration (β_G)
(b) Brownian diffusion (β_B)
(c) Turbulent diffusion (β_{TD})
(d) Turbulent inertia (β_{TI})

Gravitational – large particles sweep out smaller particles as they fall under the force of gravity

$$\beta_G(u,v) = \frac{2\pi}{9}\left(\frac{3}{4\pi}\right)^{\frac{4}{3}}\frac{\gamma^2}{X}\frac{g\rho_m}{\mu}\in_0 (u,v)\left(v^{\frac{1}{3}} + u^{\frac{1}{3}}\right)^2\left|C\,(v)v^{\frac{2}{3}} - C(u)u^{\frac{2}{3}}\right| \tag{101}$$

where
γ is the collision shape factor;
χ is the dynamic shape factor;
g is the gravitational acceleration;
ρ_m is the material density of the particle;
μ_g is the gas viscosity;
$\in_0$ is given by Eq. (102)

$$\in_0 = \frac{\beta_e v^{2/3}}{(u^{1/3} + v^{1/3})^2} \tag{102}$$

β_e = 0.5 or 1.5

C(v) = Cunningham slip correction factor for a particle of volume v, given by Eq. (103)

$$C(v) = 1 + Kn\left(1.142 + 0.588\ exp(-0.999/Kn)\right) \tag{103}$$

Knudsen number, $K_n = \frac{2\lambda}{d}$, where λ is the mean free path of gas molecules, d is the aerosol particle diameter.

Brownian diffusion – fluctuations in molecular bombardment drive particles across streamlines of flow to contact other particles.

$$\beta_B(u,v) = \frac{2kT}{3\mu_g}\left(v^{\frac{1}{3}} + u^{\frac{1}{3}}\right)\left(\frac{C(v)}{v^{1/3}} + \frac{C(u)}{u^{1/3}}\right) \tag{104}$$

where
K is the Boltzmann constant (1.38065 x 10^{-23} J/K);
T is the Absolute temperature (K).

Turbulent diffusion – Turbulent eddies carry particles across streamlines to contact other particles. Where,

$$\beta_{TD}(u,v) = \frac{3Z}{4\pi}\left(v^{\frac{1}{3}} + u^{\frac{1}{3}}\right)^3 \left(\frac{\in_T \rho_g}{\mu_g}\right)^{1/2} \tag{105}$$

Where $\in_T$ Turbulent energy dissipation rate and $1.29 \leq Z \leq 5.65$.

Turbulent inertia – Particles expelled from turbulent eddies impact other particles

$$\beta_{TI}(u,v) = Z'\left(v^{\frac{1}{3}} + u^{\frac{1}{3}}\right)^2 \left|\left(v^{\frac{2}{3}} - u^{\frac{2}{3}}\right)\right| \frac{\rho_m}{\mu_g}\left(\frac{\in_T^3 \rho_g}{\mu_g}\right)^{1/4} \tag{106}$$

Where $0.188 \leq Z' \leq 0.204$.

Of the many forms suggested for the total coagulation kernel, it is taken either as

$$\beta_{total}(u,v) = \beta_B(u,v) + \beta_g(u,v) + \sqrt{\beta_{TD}^2(u,v) + \beta_{TI}^2(u,v)} \tag{107}$$

or

$$\beta_{total}(u,v) = \beta_B(u,v) + \beta_g(u,v) + \beta_{TD}(u,v) + \beta_{TI}(u,v) \tag{108}$$

Aerosol Removal Phenomena

The aerosol removal rate constants for the dominant process such as gravitational settling, diffusional wall plating and thermophoretic plating are given by the following expressions.

Gravitational settling rate [45]:

$$G_R(v) = \frac{g\rho_m C(v)\left(\frac{6v}{\pi}\right)^{2/3}}{18\,\mu_g \chi}\frac{A_f}{V} \tag{109}$$

where
A_f is the available floor area;
V is the containment volume.

Diffusion deposition rate [46]:

The diffusion coefficient *D(v)* is given by Eq. (110)

$$D(v) = \frac{C(v)kT}{3\pi\mu_g\left(\frac{6v}{\pi}\right)^{1/3}\chi} \tag{110}$$

$$P_R = 0.22D^{0.735}\frac{A_w}{V} \tag{111}$$

Where A_w = the wall or deposition surface area.

Thermophoretic deposition rate [45]:

$$T_R = \frac{3\mu_g A_w \nabla T\, k_T}{2\rho_m V\, T} \tag{112}$$

Where,
k_T is a constant that depends on particle and gas properties;
T is absolute temperature;
∇T is the temperature gradient usually taken as $(T_{gas} - T_{wall})/\Delta_T$ with Δ_T being a boundary layer or deposition distance parameter for thermophoresis.

The total removal rate R(v) can be written as,

$$R(v)=P_R(v) + G_R(v) + T_R(v) \tag{113}$$

where
G_R is the gravitational settling rate;
P_R is the diffusion wall plating rate;
T_R is the thermophoretic removal rate.

TABLE 58. INPUT PARAMETERS FOR THE CALCULATION*

Parameters	Values
Gravitational constant (g)	9.8m/s^2
Floor Area (A_f)	1400m^2
Deposition wall area (A_w)	5600 m^2
RCB volume (V)	74000 m^3
Viscosity of RCB air (μ_g)	20.71E-06 Pa.s
Dynamic shape factor (χ)	1.2-1.3
Collision shape factor (γ)	1.0
Density correction factor (α)	0.5 (calculated)
Temperature (T)	Variable
Deposition distance parameter (Δ)	0.118E-06 m
Temperature Gradient	10000 K/m
k_T	0.1
RCB air density (ρ_g)	1.2kg/m^3
Sodium aerosol material density (Na_2O)/ (Na_2O_2)	2270/2800 kg/m^3
Aerosol median diameter	1 micrometer
Thermal boundary layer thickness	1 E-4 meter
Turbulent energy dissipation rate	0.1 m^2/s^3

* many of the parameters are from SOAR [46]

To study the aerosol evolution, the containment is considered as leak tight.

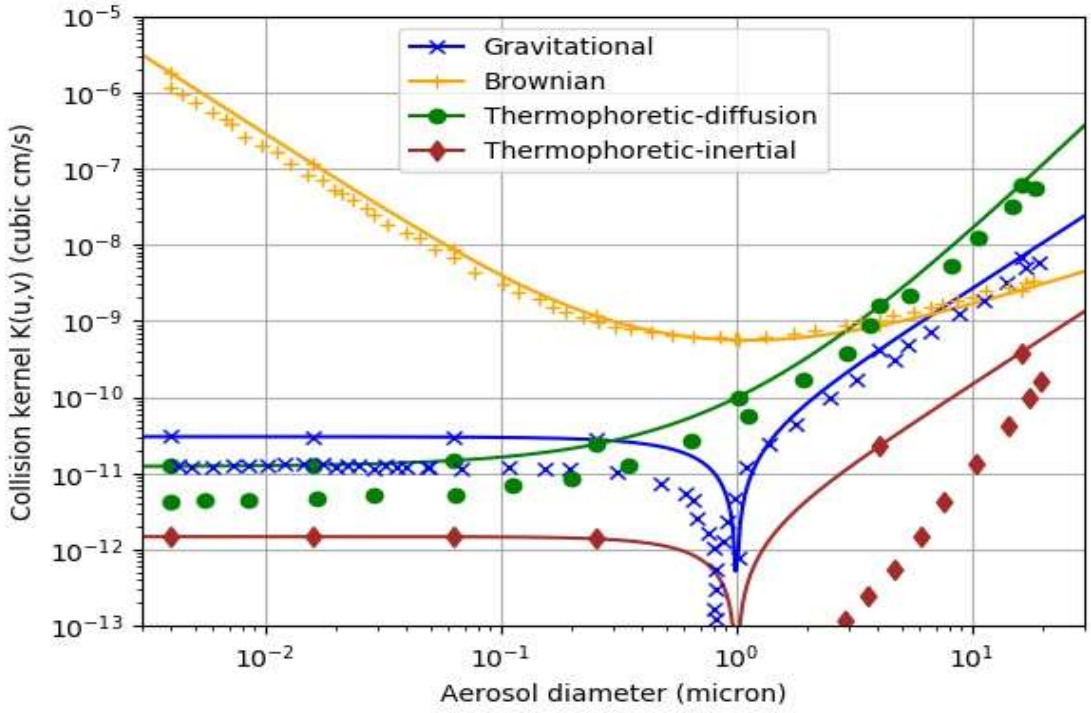

FIG. 197. Different aerosol collision kernels as a function of aerosol size.

The scatter plots with corresponding legends show the values from NEA/CSNI report for comparison. One particle diameter is fixed as 1 micron.

Assuming an initial log-normal distribution, the aerosol time evolution including agglomeration and removal are simulated using Eq. (90), with the above defined agglomeration kernels and removal rates. To validate the kernels used they have been plotted in FIG. 197 against the kernel values reported in SOAR [46] for aerosol diameters ranging from 3E-3 micron to 30 microns. There is some difference noticed especially for the thermophoretic phenomena perhaps due to the parameters used.

The plot of various removal rates for the aerosols in the range of 0.01 micron to 10 micron is depicted in FIG. 198. The Brownian diffusion is dominant for small aerosol sizes. The removal due to turbulent diffusion and the inertial impact is dominant in the size range greater than $5\mu m$. The removal rate due to gravity is negligible (FIG. 198) for smaller diameter aerosol particles.

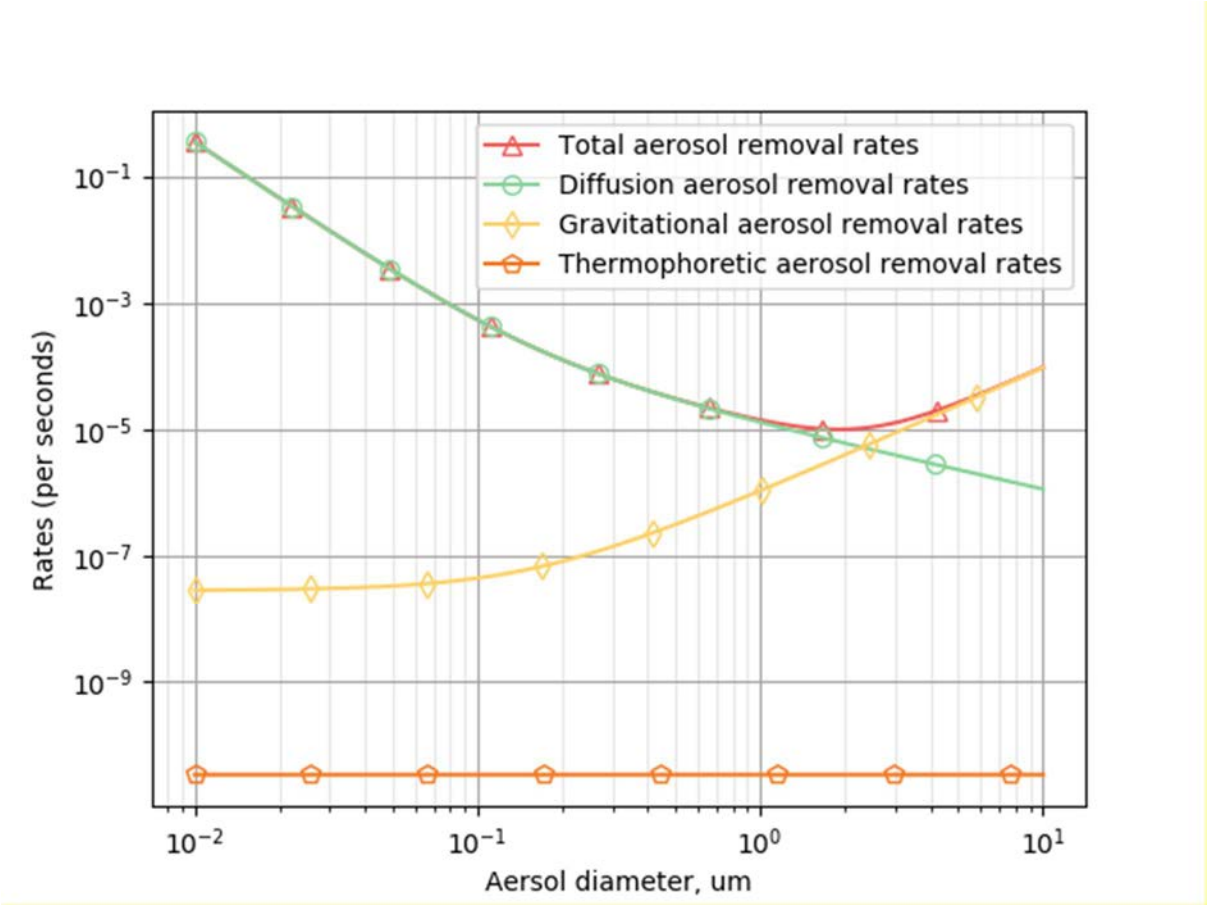

FIG. 198. Aerosol removal rates.

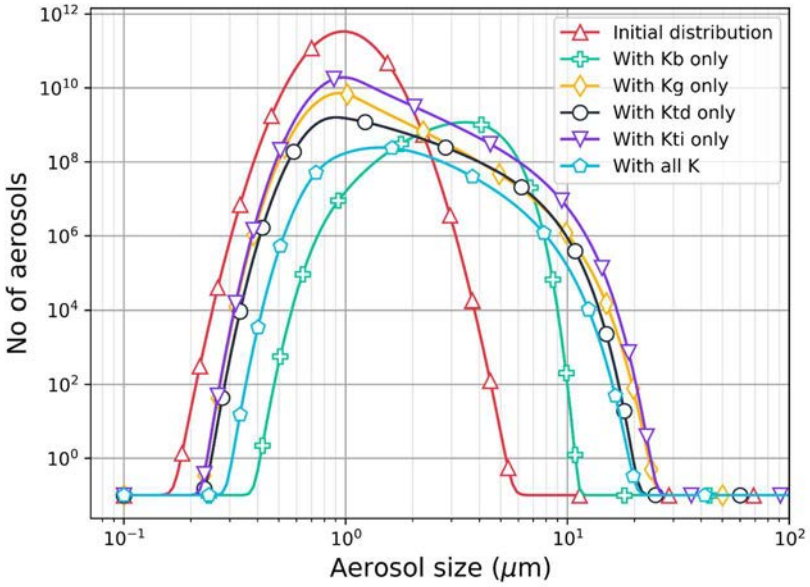

FIG. 199. Aerosol distribution at 24 hours; comparison of different kernel effects.

FIG. 199 depicts the effect of different kernels on the evolution of aerosol size distribution after 24 hours compared to the initial distribution. In the plots, all the removal mechanisms are active and the respective coagulation mechanisms are observed one by one. With only removal by gravity considered, the effect is seen for larger particle sizes.For smaller particle sizes Brownian agglomeration is dominant.

6.4.2. **Results**

As some CRP participants participated in only WP-3, IGCAR results are divided in to two cases:

(1) Standalone case: The participants who simulated only WP-3 were provided in-containment source term release fractions as specified in the Section 2. With this input, the aerosol evolution in the containment was simulated.
(2) Integral case: In this case, the participants who are simulated all work packages, performed a separate coupled calculation with source term input from the WP-1 & 2.

IGCAR performed both standalone case (case 1) and integral case (case 2).

6.4.2.1. *Standalone cases for WP-3:*

The standalone case has two sub cases, where case 1 represents instantaneous spray fire without consideration of roof slab enclosure. This gave conservative estimates for the temperatures and pressure estimates in the containment. In case 2, the pool fire was simulated with consideration of the roof slab enclosure. IGCAR simulated case 1 only for radioactivity and aerosol evolution in containment.

For the simulation, the in-containment source term release fractions are used as shown below (which are specified in Section 2)

TABLE 59. IN-CONTAINMENT RELEASE FRACTIONS

Group	Elements	Designated release fractions
Noble Gases	Xe, Kr	1
Halogen	I, Br	0.1
Alkali metals	Cs, Rb	0.1
Tellurium group	Te, Sb, Se	1.0E-04
Barium	Ba, Sr	0.1
Noble metals	Ru, Rh, Pd, Mo, Tc, Co	1.0E-04
Lanthanides	La, Zr, Nd, Eu, Nb, Pm, Pr, Sm, Y, Cm, Am	1.0E-04
Cerium	Ce, Pu, Np	1.0E-04

Initial aerosol size distribution:

Based on experiments reported in Allelein et al. [46], the initial aerosol size distribution was assumed to be log-normal distribution with d_{median} = 1 micrometer and standard deviation (σ=) 3. The total mass of aerosols is from complete combustion and condensation of 350 kg of sodium released during the accident. Formation of 100% Na_2O is used in the calculations. However, sensitivity studies were done with formation of 100% Na_2O_2.

Though there is a difference in the initial aerosol mass, the suspended mass as a function of time is relatively insensitive to this assumption (FIG. 200). The highest contribution to the suspended aerosol mass in the containment is from sodium monoxide or sodium peroxide (~470/~600 kg respectively). However, the mass of sodium monoxide/peroxide reduces to 60 kg (< 10%) in the containment after about 5h. The second highest contribution is from xenon (16 kg, FIG. 204). Here, since the containment is assumed leak-tight, the concentration of the Xe and Kr is constant in the containment. After Xe and Kr, the Cs is found to be present in the containment at higher concentrations. At t=0 hours, about ~3.5 kg of Cs is in the suspended form (FIG. 201). After 5h it is less than 0.5 kg of Cs is suspended in the containment. This implies that an effective containment would be helpful to reduce the radioactivity available for release.

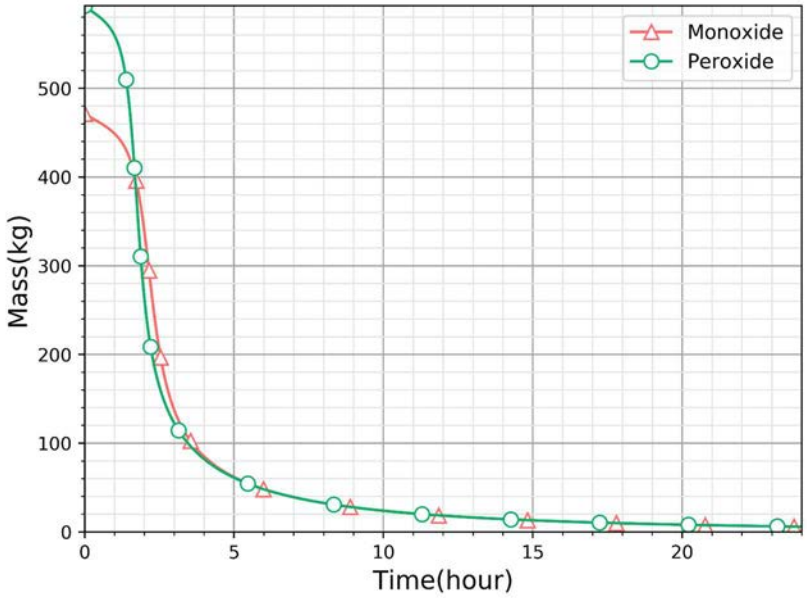

FIG. 200. Aerosol evolution for monoxide and peroxide.

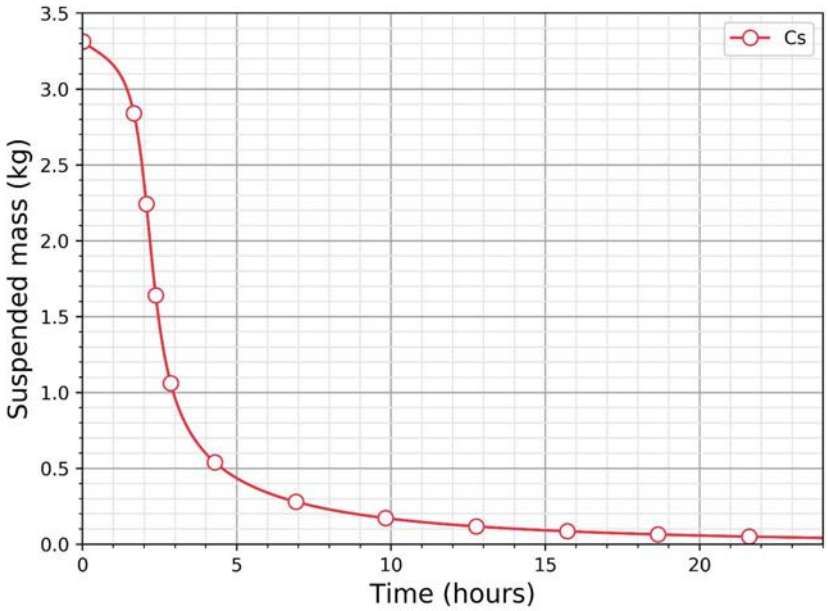

FIG. 201. Suspended Cs mass in the containment.

Since, Rb-88 has a half-life of ~18 minutes, all Rb decays away within one or two hours. The released amount for the Sr and Pu is of the same order (0.2 kg). The higher release for the Sr and Ba is due to assumed conservative release fraction. In realistic calculations, the probability to release Sr and Ba in the containment is less since most of Sr and Ba will be in the condensed oxide form in the reactor vessel. The higher released mass of the Pu is due to high Pu inventory in the core (about 2 tonnes). The conservative release fraction of 1E-4 lead to release of ~0.2 kg in the containment. After 24 hours, the suspended mass in the containment was about 1 gram. However, Pu is a non-volatile RN, and from the chemical equilibrium calculation it is found that most of the Pu is retained in the sodium pool. Since past experiments support that, during the core bubble expansion and oscillation, higher retention of the fragmented material is expected [47]. Hence, the released amount of Pu is expected to be much less than 0.2 kgs.

The evolution of deposited RN in the containment is shown in the FIG. 202 to FIG. 207. Most of RN is deposited within 5 hours. Resuspension was not modelled.

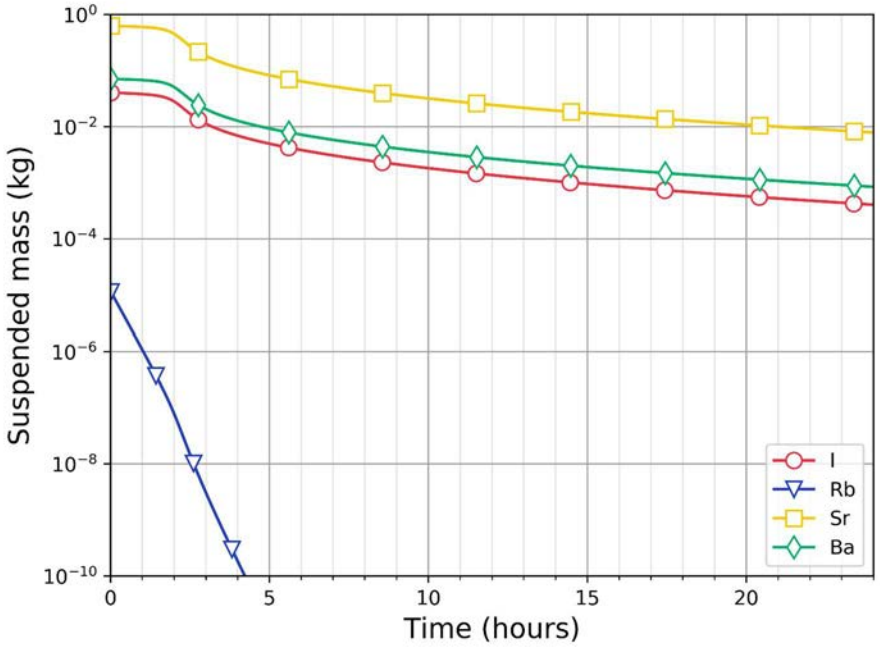

FIG. 202. Suspended mass of volatile species.

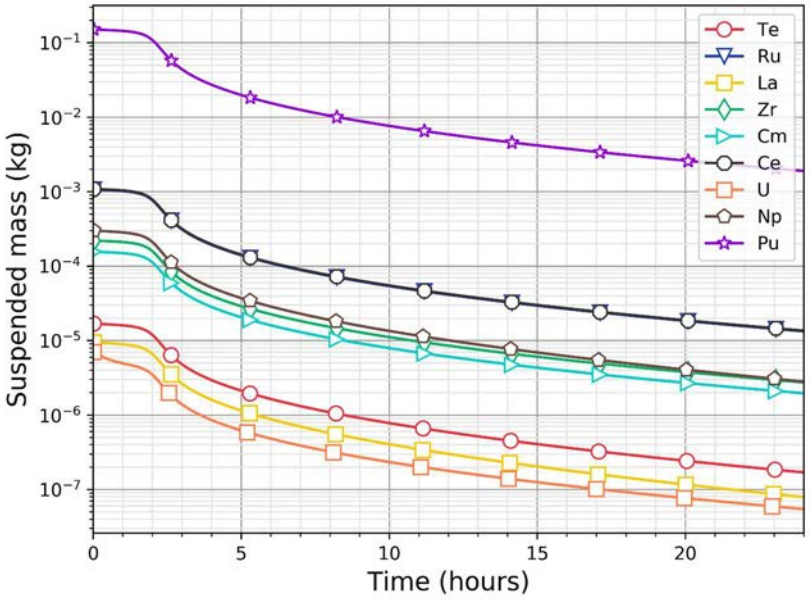

FIG. 203. Suspended mass in the containment.

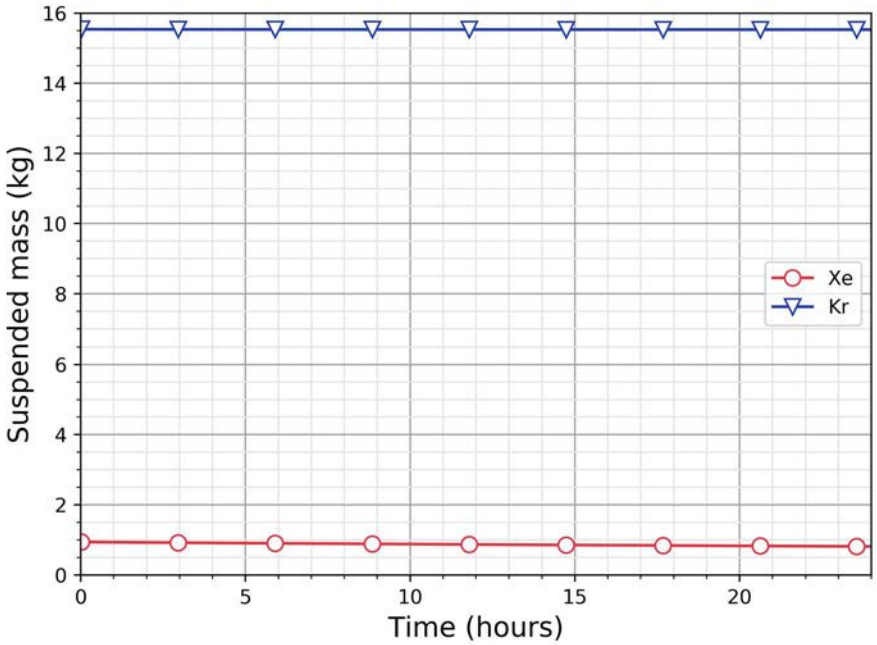

FIG. 204. Containment Xe and Kr (Kg).

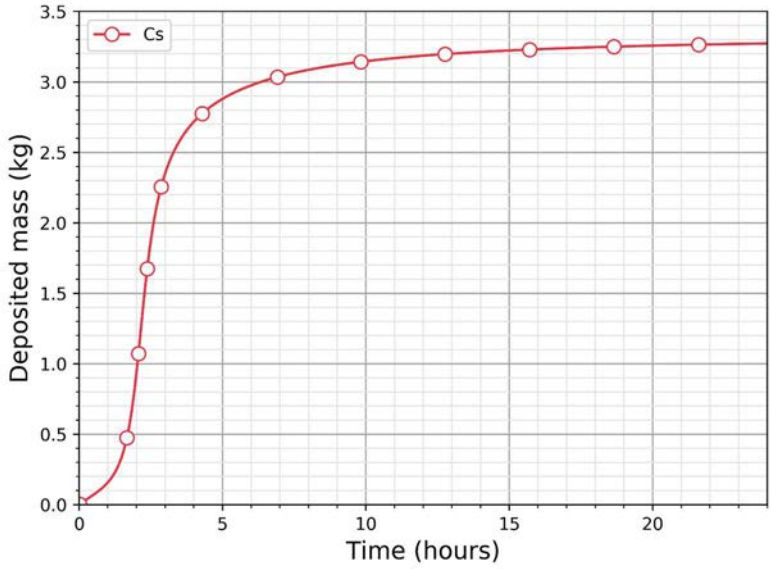

FIG. 205. Deposited Cs mass in the containment.

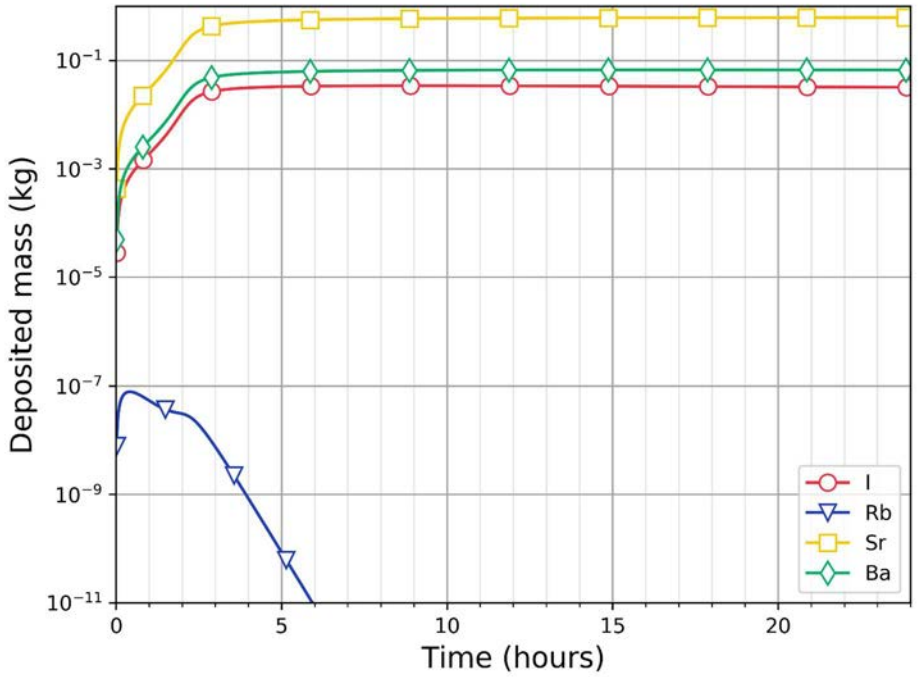

FIG. 206. Deposited volatile RN in the containment.

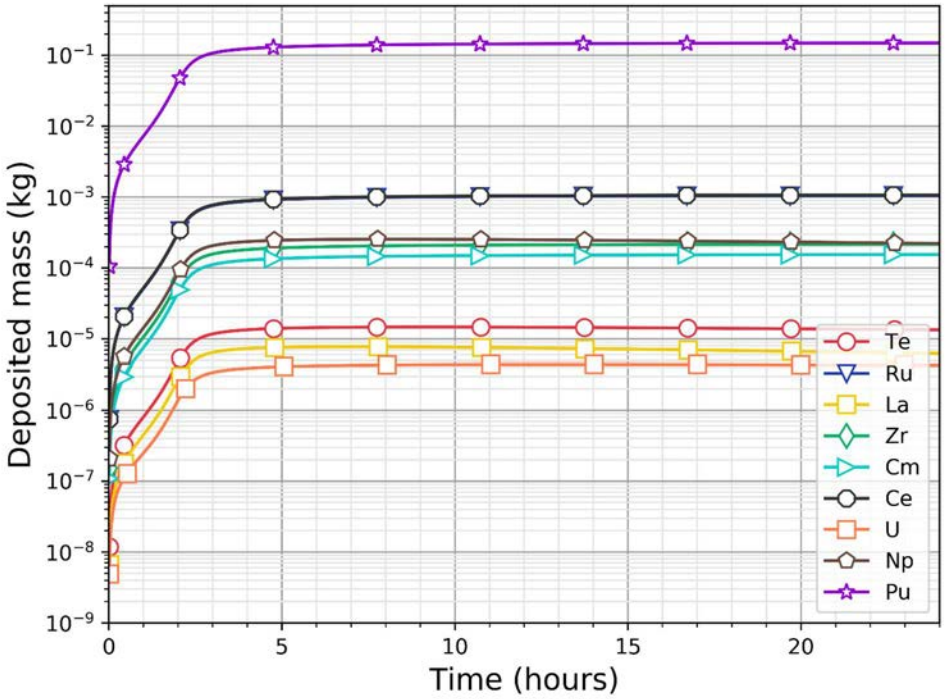

FIG. 207. Deposited various RN in the containment.

The suspended activity by isotope is given in FIG. 208 to FIG. 211. The suspended mass by isotope is given in FIG. 212 to FIG. 215.

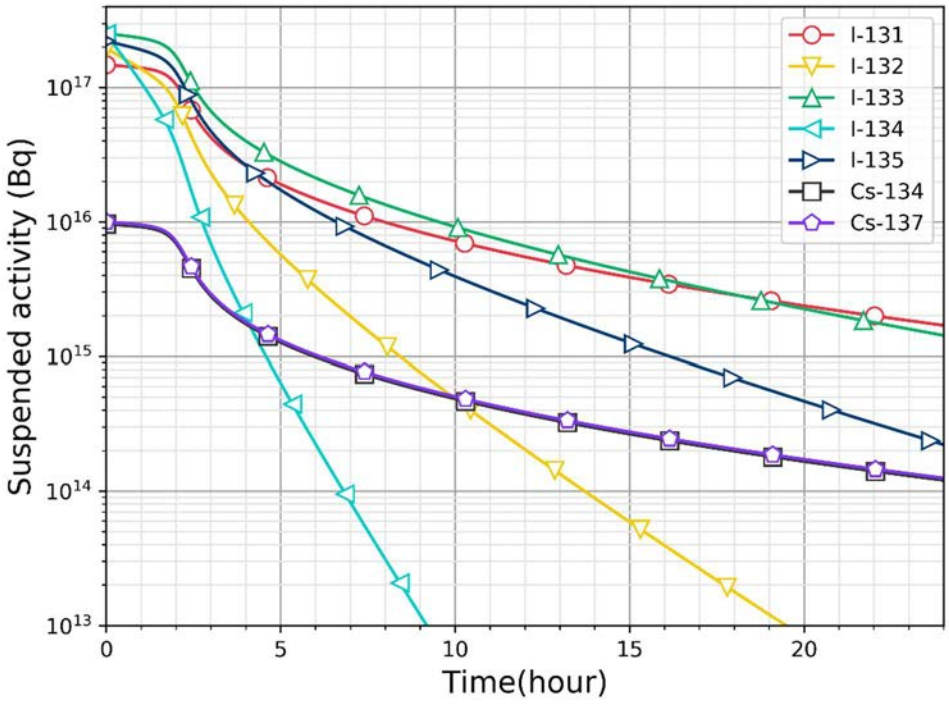

FIG. 208. Suspended activity for I and Cs isotopes in the containment.

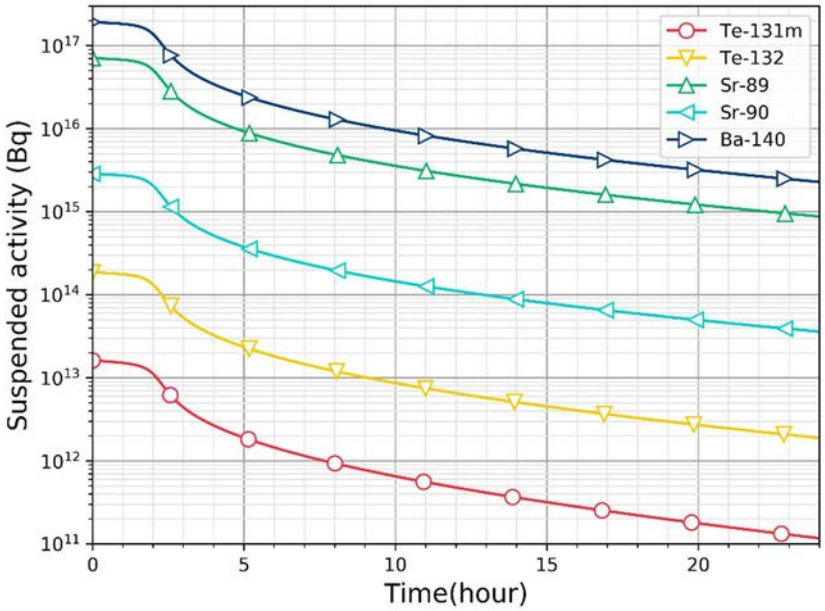

FIG. 209. *Suspended activity for Ba, Sr, and Te isotopes in the containment.*

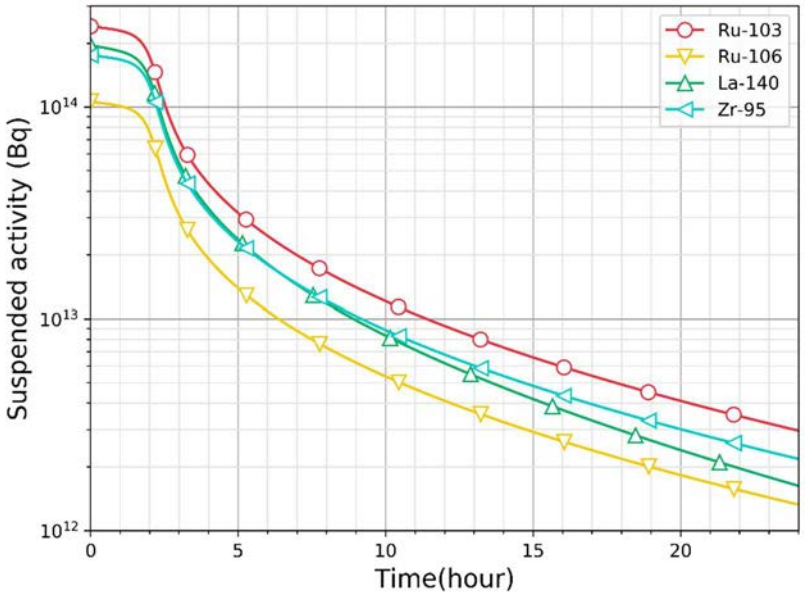

FIG. 210. Suspended activity in the containment for Ru, La and Zr isotopes.

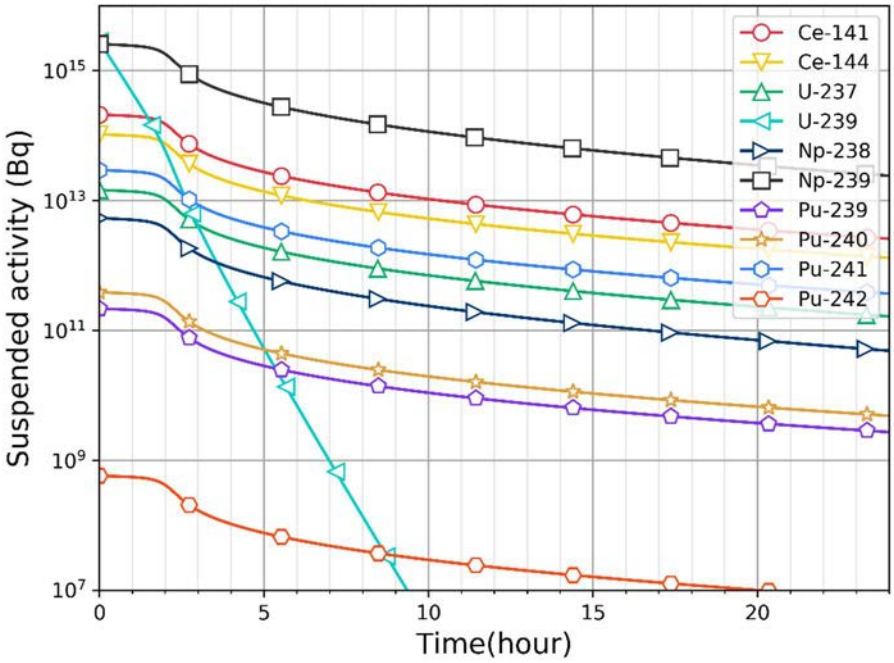

FIG. 211. Suspended activity in the containment for Ce, U, Np, and Pu isotopes.

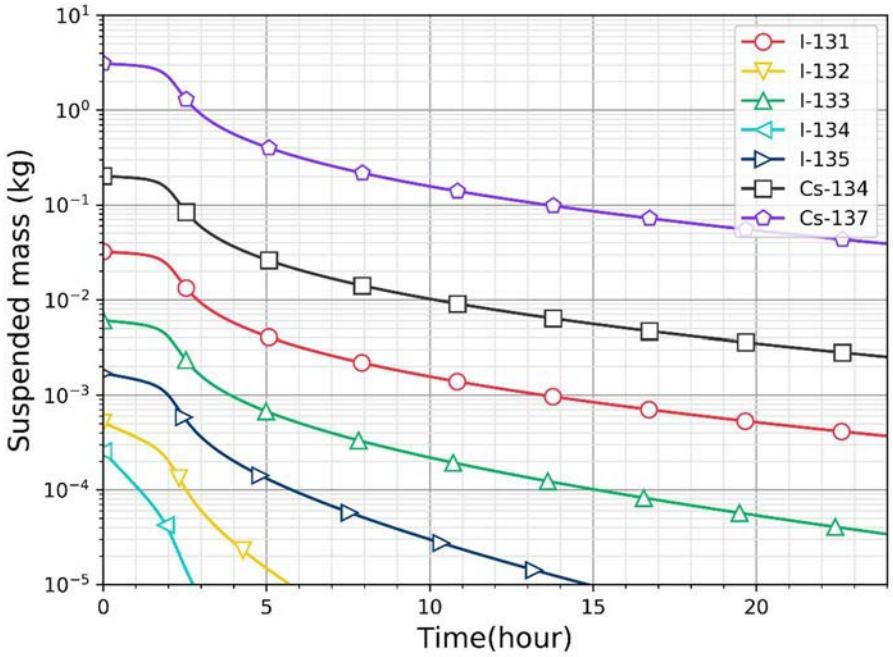

FIG. 212. Suspended mass of Cs and I isotopes in the containment.

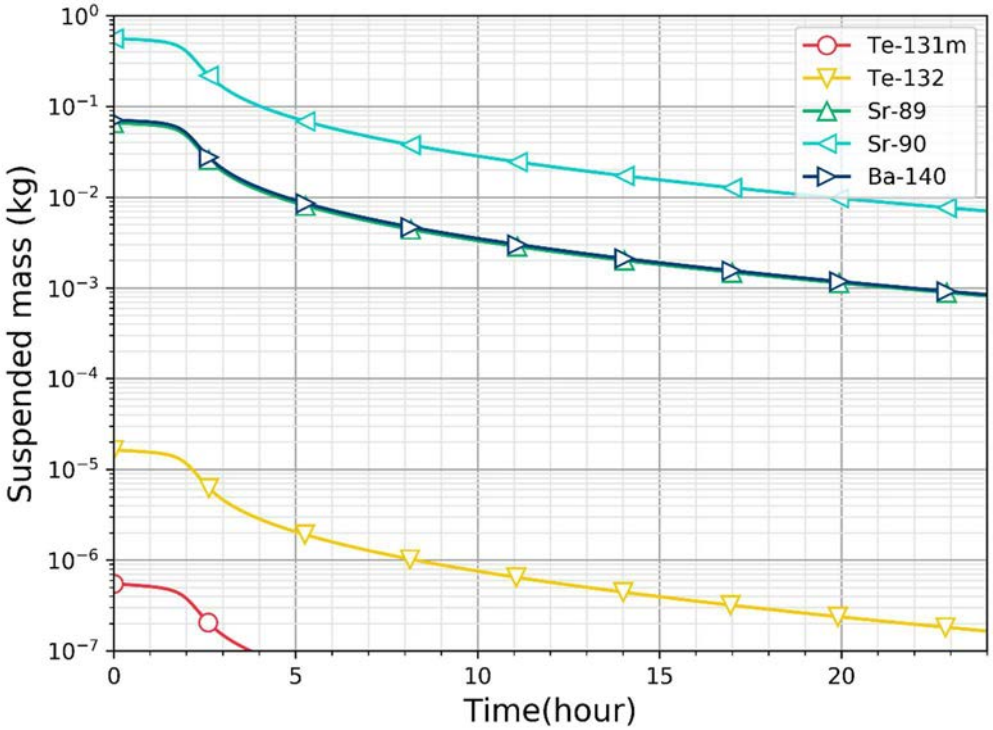

FIG. 213. Suspended mass of Ba, Sr and Te isotopes in the containment.

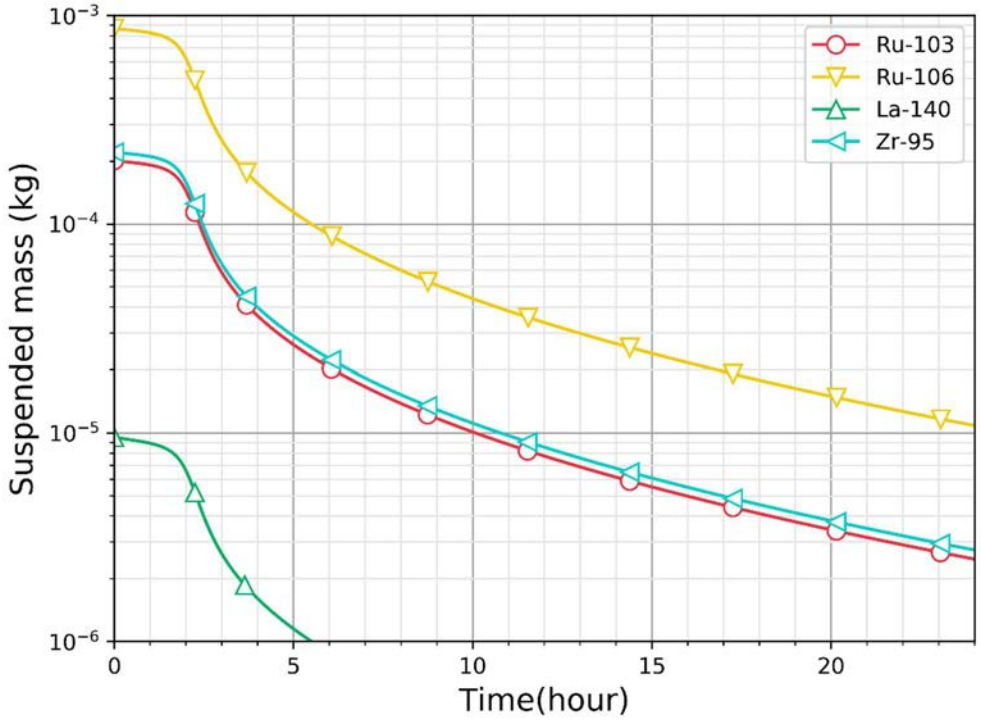

FIG. 214. Suspended mass of Ru, La and Zr isotopes in the containment.

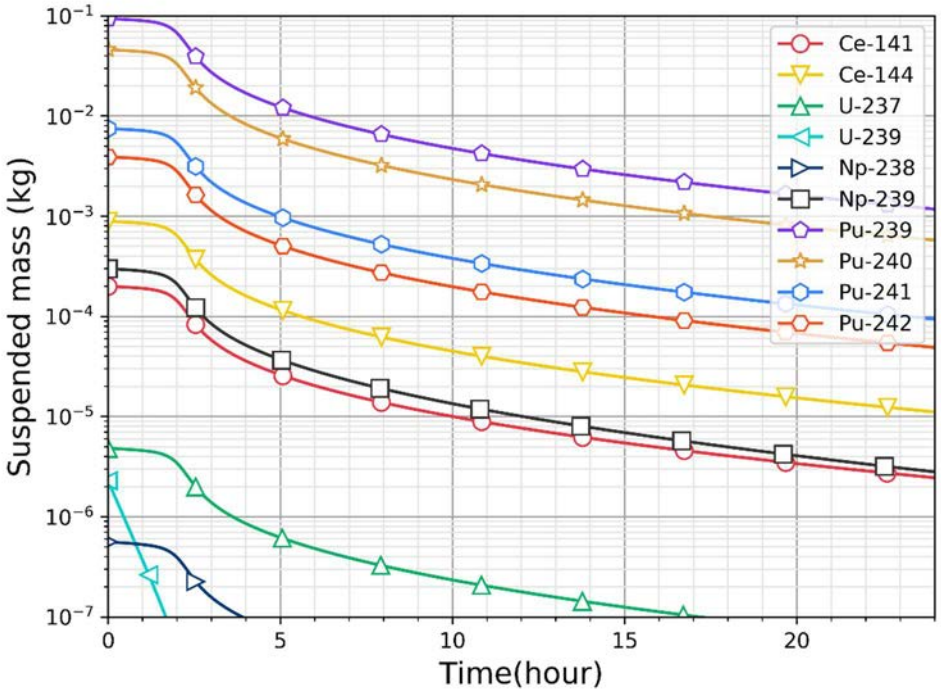

FIG. 215. Suspended mass of Ce, Np, Pu and U isotopes in the containment.

6.4.2.2. *Integral case for the WP-3 (case 1):*

The integral case considers the release fractions from WP-1 & 2 calculations. Similar to the standalone case, this case also consists of two sub case. i.e., spray fire and pool fire with enclosure for the CRP. Only one case was considered, case 1 i.e., spray fire w/o enclosure. The input inventory and the release fraction for the calculation is given in the TABLE 60. The calculations are performed for the two cases of activity evolution in the containment using release fraction calculated from the WP-1 i) with no mixture assumption ii) with real mixture assumption. For the calculation following in-containment release fractions were considered (TABLE 60):

TABLE 60. RELEASE FRACTION CONSIDERED FOR THE INTEGRAL CASE, THE RELEASE FRACTION LESS THAN 1E-18 ARE TRUNCATED TO 1E-18 TO AVOID UNREALISTIC RELEASED VALUES

Representative element	Element group	No mix (873K)	Real mix (873 K)
Xe	He,Ne,Ar,Kr,Xe,H,N	1	1
Cs	Li,Na,K,Rb,Cs,Fr,Cu	0.91	3.18E-5
Ba	Be,Mg,Ca,Sr,Ba,Ra,Es,Fm	2.77E-12	1.48E-7
I	F,Cl,I,Br,At	2.17E-03	1E-18
Te	Os,Se,Te,Po	1E-18	1E-18
Ru	Ru,Rh,Pd,Re,Os,Ir,Pt,Au,Ni	1E-18	1E-18
Mo	V,Cr,Fe,Co,Mn,Nb,Mo,Tc,Ta,W	1E-18	1E-18
Ce	Ti,Zr,Hf,Ce,Th,Pa,Np,Pu,C	5E-17	1E-18
La	Al,Sc,Y,La,Ac,Pr,Nd,Pm, Sm,Eu,Gd,Tb,Dy,Ho,Er,Tm,Yb, Lu,Am,Cm,Bk,Cf	1E-18	1E-18
U	U	1E-18	1E-18

Cd	Cd,Hg,Zn,As,Sb,Pb,Tl,Bi	1E-18	1E-18
Sn	Sn,Ga,Ge,In,Ag	1E-18	1E-18
B	B,Si,P	1E-18	1E-18

Real mix assumption:

The real mixture assumption considered the excess mixing function in the chemical equilibrium calculations. Therefore, the release fractions would be less compared to the no mixture case. However, the excess function is available for limited species. To support a complete realistic calculation, excess functions need to be generated for a number of important species. The suspended masses of major RN for this assumption are given in the FIG. 216 to FIG. 218. The deposited masses of major RN for this assumption are given in the FIG. 219 to FIG. 221.

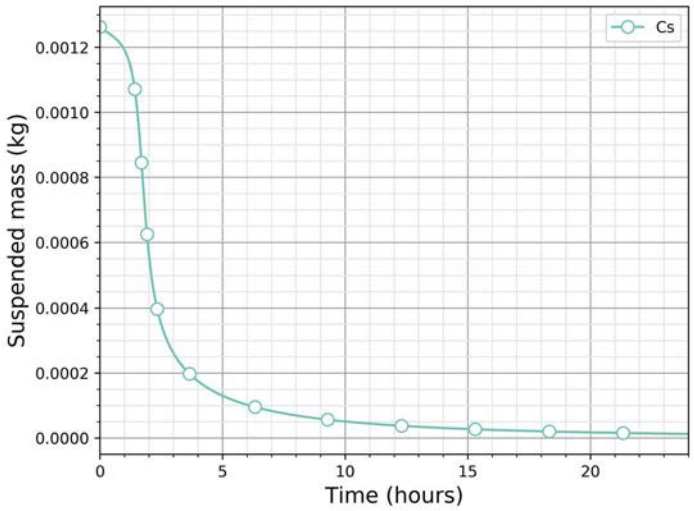

FIG. 216. Suspended Cs in the containment.

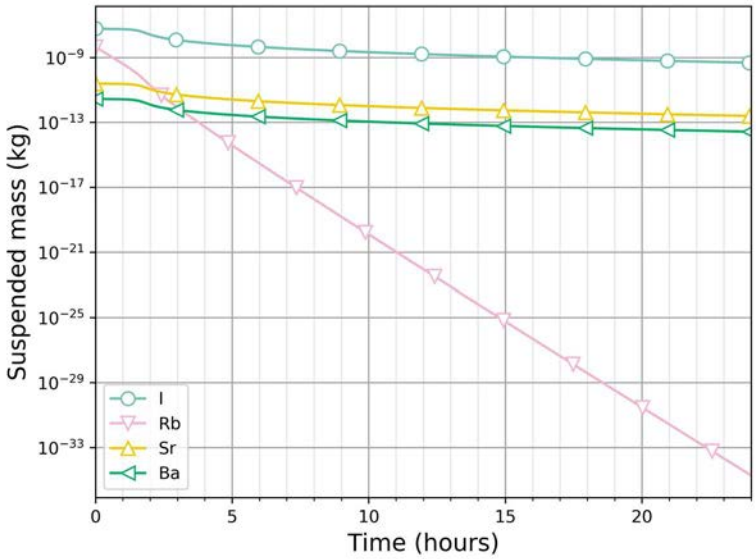

FIG. 217. Volatile RN suspended mass in the containment.

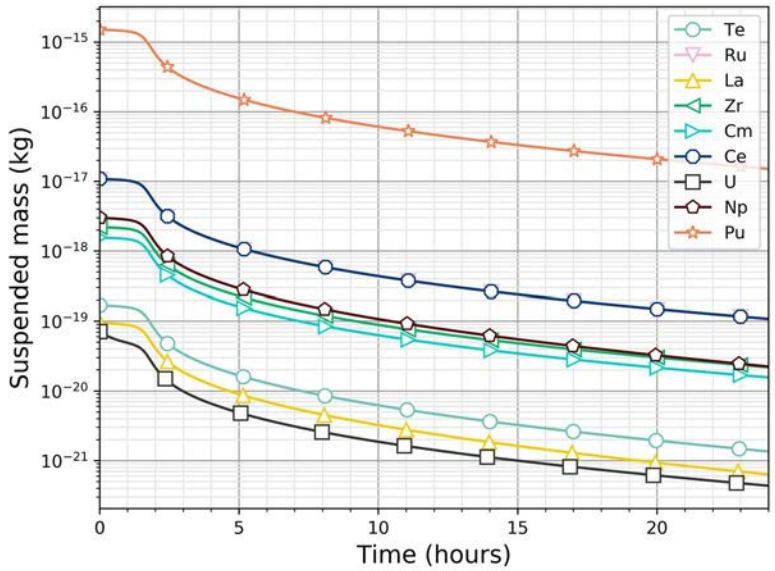

FIG. 218. Suspended RN mass in the containment.

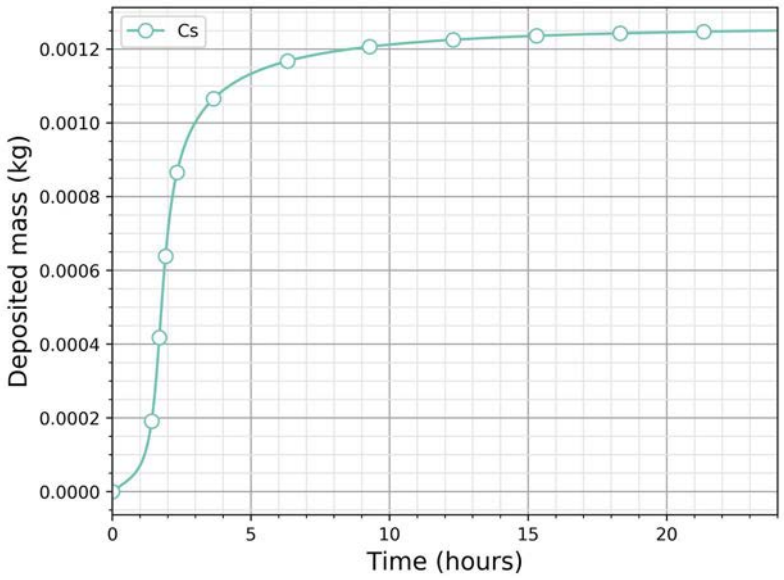

FIG. 219. Evolution of the Cs deposition in the containment.

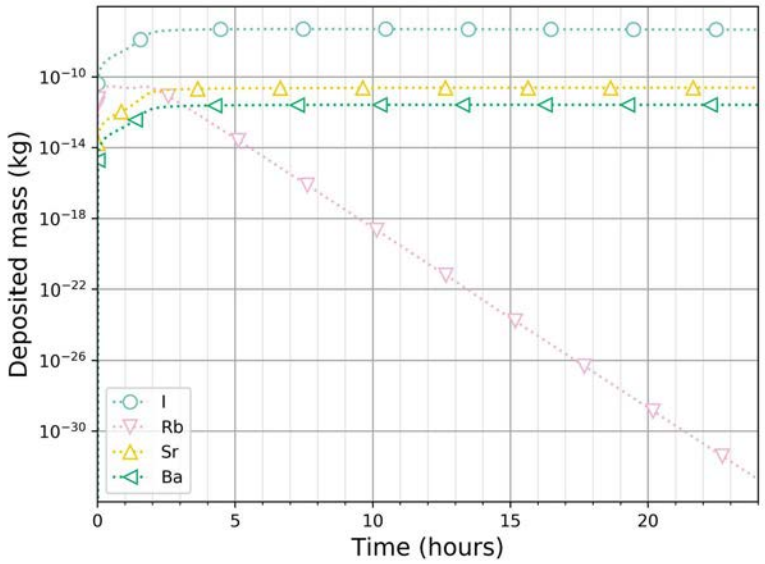

FIG. 220. Deposition of volatile RN in the containment with time.

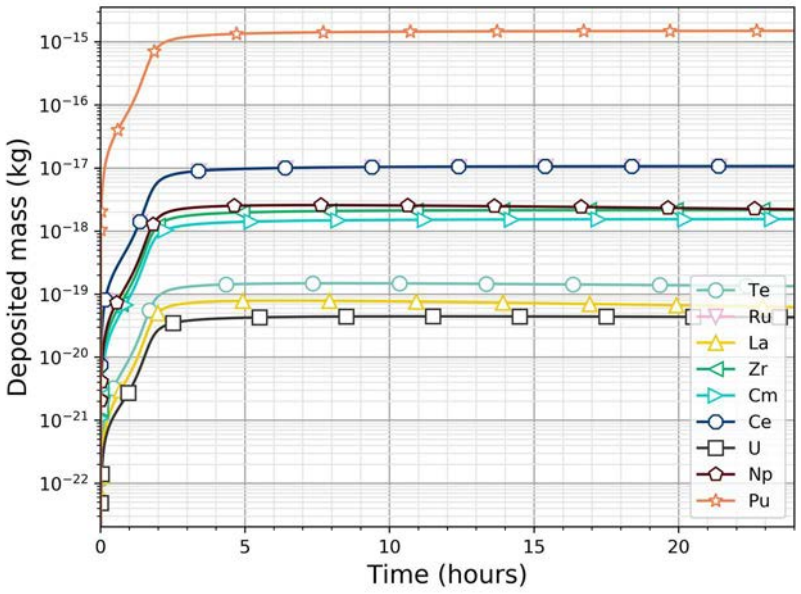

FIG. 221. Deposition of RN in the containment with time.

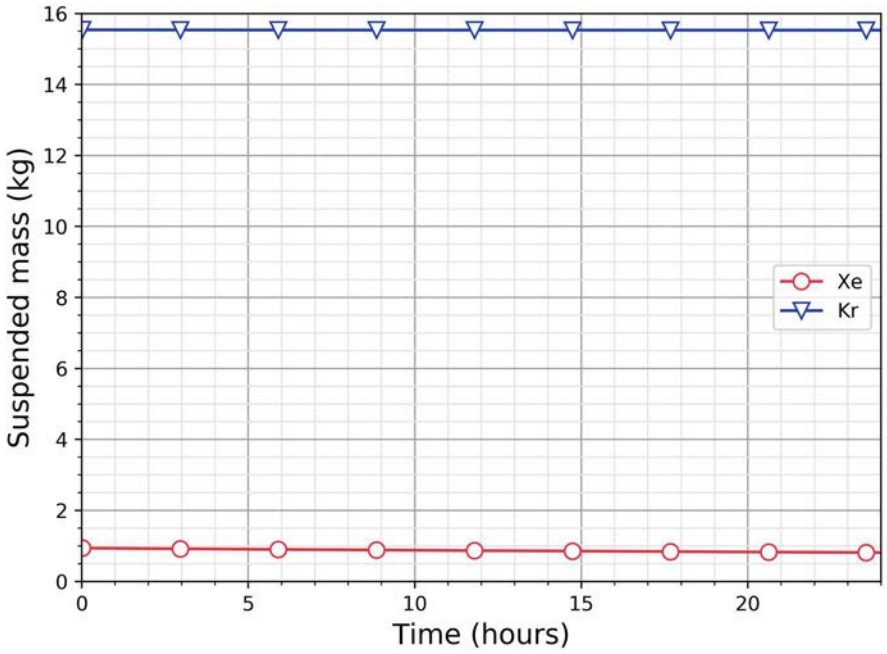

FIG. 222. Noble gases in the containment.

No-mixture case:

In the no mixture assumption case, the species chemical equilibrium calculations are performed without considering the mixing properties of the species. This leads to conservative estimates of release fractions. The suspended masses of major RN for this assumption are given in the FIG. 223 to FIG. 225. The deposited masses of major RN for this assumption are given in the FIG. 226 to FIG. 228. For the no mixture case, the release fractions are close to one for Cs, Xe, Kr, I Rb and Sb.

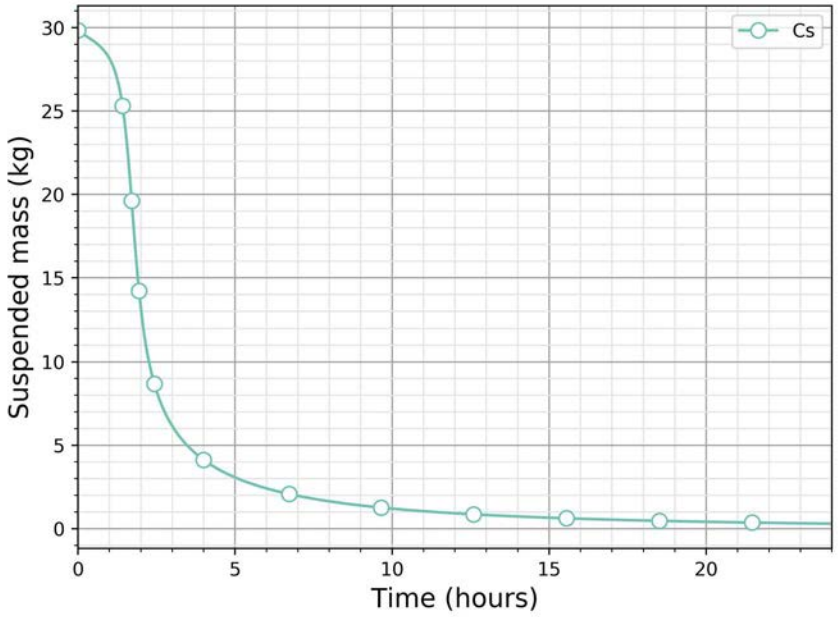

FIG. 223. Suspended total Cs in the containment.

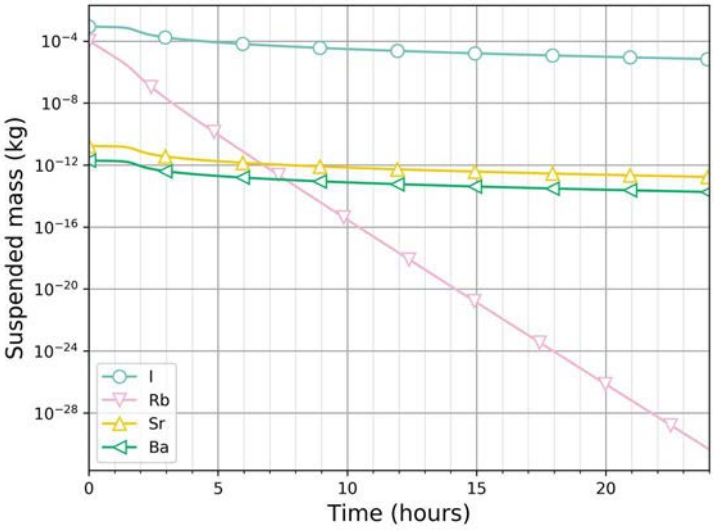

FIG. 224. Suspended volatile RN in the containment.

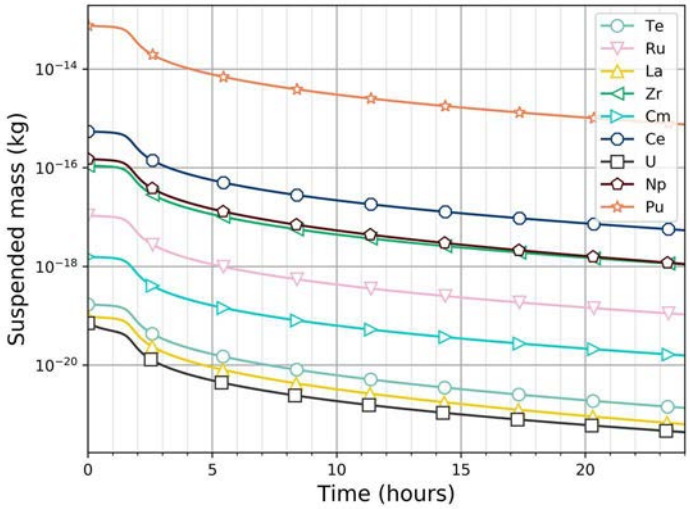

FIG. 225. Suspended RN in the containment.

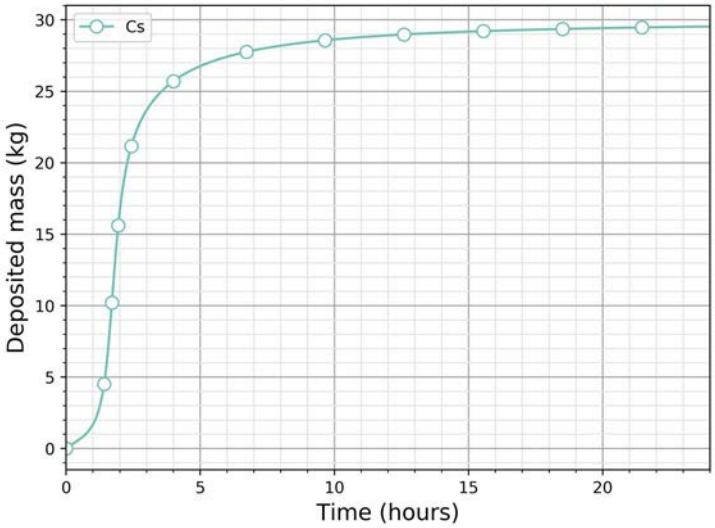

FIG. 226. Deposited total Cs in the containment.

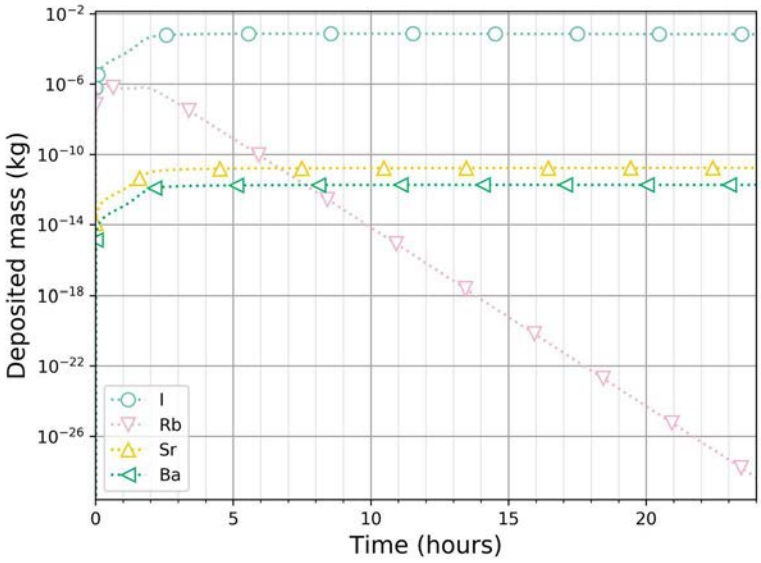

FIG. 227. Deposited volatile RN in the containment.

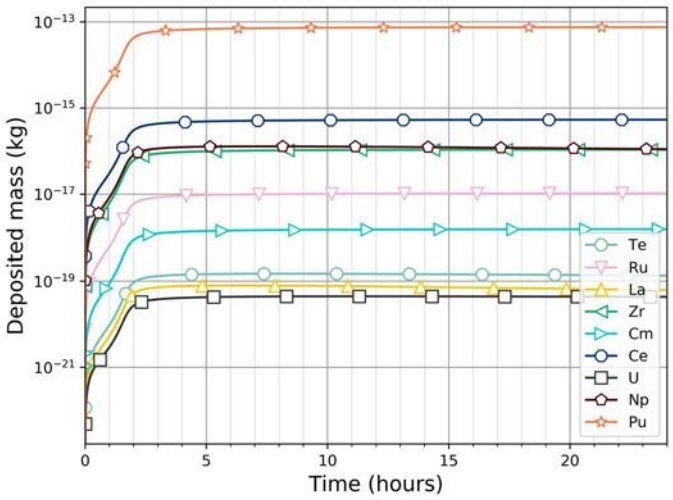

FIG. 228. Deposited RN mass in the containment.

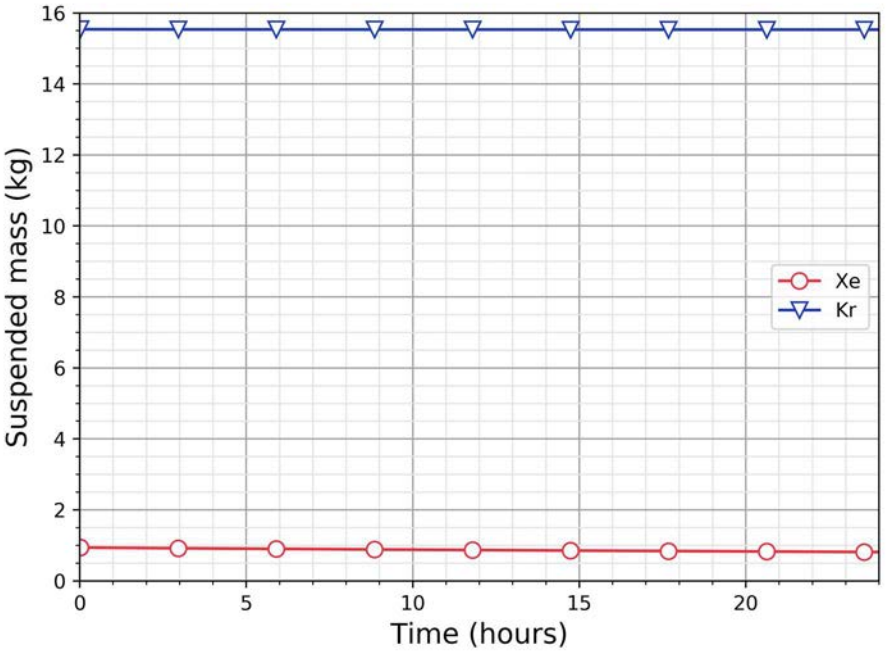

FIG. 229. Total noble gas mass in the containment.

6.4.3. **Summary**

The sodium aerosol evolution was studied using PANDICA and the suspended and deposited RN aerosol masses in the containment were calculated and plotted. The chemical evolution of RN in the containment and aerosol formation by condensation are not modelled in the present study. Though vast literature exists in the form of reports and technical papers on characterizing aerosol evolution with time, the models have several parameters that needs to be evaluated for SFR containment and accident specific conditions. It would be desirable to develop a Monte-Carlo code so that it can easily model multi component aerosols evolution and serve as an

independent tool for validation of calculations. Further experiments or experimental validation of sodium fire aerosol generation and evolution is required to increase the confidence in the code predictions.

6.5. SIMULATION EXERCISE USING EUCLID/V2 CODE (IBRAE RAN, RUSSIAN FEDERATION)

6.5.1. Description of the Methods and Model

EUCLID/V2 includes a specialized module AEROSOL/LM allowing simulation of the transport of fission products over the loops of the reactor facility and also the behavior of multicomponent polydisperse aerosols inside the reactor containment building (RCB) of fast reactor NPPs [10]. Heat transfer in structural elements is described in a two-dimensional approximation.

The code can simulate both the flow of coolant with fission products in reactor loops and the dynamics of the containment atmosphere gas with hydrogen, oxygen, and fission products in the RCB, such as oxygen reduction and starvation during a sodium fire.

The aerosol module AEROSOL/LM allows simulation of the the following processes:

— The nucleation of different vapours.
— The coagulation of multicomponent polydisperse aerosol particles;
— The condensation of various (multicomponent) vapours on particles;
— The condensation and sorption of vapours on surfaces;
— The deposition of aerosols on surfaces due to different mechanisms;
— The formation of multicomponent deposits on surfaces;
— The absorption of water vapor by hygroscopic aerosol (equilibrium and kinetic approach);
— The transfer of aerosols and various vapours through the compartments.

A more detailed description of models is presented in [11] [12] [10]. In these calculations, the influence of ionizing radiation and ions on aerosol behavior in containment rooms was not considered as these processes would not likely play a significant role in aerosol behavior during severe accident in SFRs [48] [13].

The behavior of multicomponent particles with time t is simulated by a system of differential equations for the mass $M_{i,p}(t)$of the p-th product in particles of the i-th size-fraction with bounds m_{i-1}, m_i per unit volume of a spatial cell. The mass (M_i) and concentration (N_i) of particles of the given i-th size-fraction are determined by the following relations (here the particle ‘size’ is defined as the particle mass x_i)

$$M_i = \sum_{p=1}^{N_{FP}} M_{i,p},\ N_i = M_i / x_i,\ x_i = \left(m_{i-1} + m_i\right)/2 \tag{114}$$

For i=1,2,… N_B, where N_B is the number of size fractions and N_{FP} is the number of components contained in particles. The fixed volume of particles in i-mode is defined by

$$v_i = \frac{m_i}{\rho_p^0} \tag{115}$$

where ρ_p^0 is the aerosol bulk density, which is constant and identical for all particles of all fractions. The assumption that ρ_p^0 is constant independent on the composition of the particle, is the weakest point in this approach. This is particularly visible for mixed particles composed of components with a bulk density that is much different from that of water density. However, due to the simplicity and ensuring reasonable calculation times, the given approach is still used widely in aerosol codes.

The behavior of components in vapor and deposit phases is simulated by a system of differential equations for the mass $M_p^{vap}(t)$ of the *p*-th vapor per unit volume and the mass $M_{s,p}^{dep}(t)$ of the *p*-th component per unit of the s-th surface (s=1,2,…N_s) respectively for each spatial cell. As a result, the total number of differential equations N_{eq} for each spatial cell is defined as

$$N_{eq} = \overbrace{N_B \times N_{FP}}^{\substack{particle\\phase}} + \overbrace{N_{FP}}^{\substack{vapor\\phase}} + \overbrace{N_S \times N_{FP}}^{\substack{deposition\\phase}} \tag{116}$$

where N_s is the number of different structure surfaces for the given spatial cell, for example, $N_s=3$ in the case of the cylindrical compartment (floor, walls and ceiling).

The module enables the modelling of aerosol formation kinetics for the wide particle size spectrum and any multimode function of the aerosol particle size distribution. The multicomponent composition of deposits is also simulated in the module. The module database is based on following factors: firstly, radionuclide composition of gases, aerosols and depositions on surfaces, which determines the level of radioactivity inside the reactor rooms; secondly, the components which affect the mass content and hence the particle size and mass and therefore the velocity of aerosol deposition on surfaces. The consideration of these factors allows to adequately simulate dynamic properties, composition and radioactivity of aerosols and deposits and when necessary to calculate an amount of residual heat release on surfaces.

The size distribution of aerosols is influenced by condensation of water vapor and fission products. The growth of aerosols by condensation of water vapor occurs in most cases on a faster timescale than other processes, e.g. coagulation or deposition of aerosols. In the module, to simulate the absorption of water vapor by hygroscopic particles two methods are considered. In the case of humidity $RH < 100\ \%$, an equilibrium approach for given temperature and composition of the dry aerosol is used, following the equation below [9]

$$RH(T) * 100 = A_w(n_i, n_w) \tag{117}$$

where A_w is the water activity in the solution, dependendent on the composition of dry aerosol in terms of the number of moles of hygroscopic components n_i and water n_w. In this approach the hygroscopic aerosol is always being at equilibrium with water vapor for given temperature.

In the case of supersaturated water vapor (RH > 100%) the kinetic approach is used to simulate the condensation and evaporation of water vapor on aerosol particles and deposits on walls. The condensation on aerosol is treated as the collision between the water molecular and aerosol

particle. The rate of evaporation is determined with accounting for the Kelvin effect. The equilibrium vapor concentration above the surface of the multicomponent particle is determined taking account of the molar content of components in a particle in the ideal solution approximation [14]. Vapor condensation on the surface of heat structures is modelled separately for each vapor component based on analogy between the heat and mass transfer and accounting for its thermal and diffusion properties. The condensation rate on thermal structures is modelled similarly to the model used in the SOPHAEROS module [15].

Sodium pool fire is modelled based on the approach given in [48] [13]. The key parameter in this conservative approach is the fraction fE of the burning energy, Q, that is transferred directly to sodium pool and then by heat exchange to walls. In calculations its value was varied.

The calculations were performed for case 2 according to [49]: with Enclosure; with zero heat flux or insulated boundary wit initial temperature of 120°C; pool fire; containment leak rate= 0.1% v/h @ 25kPa.

6.5.1.1. *Nodalization Scheme*

The nodalization scheme for WP-3 modelling using EUCLID/V2 code (HYDRA-IBRAE/LM and AEROSOL/LM modules) is shown in FIG. 230 and FIG. 231.

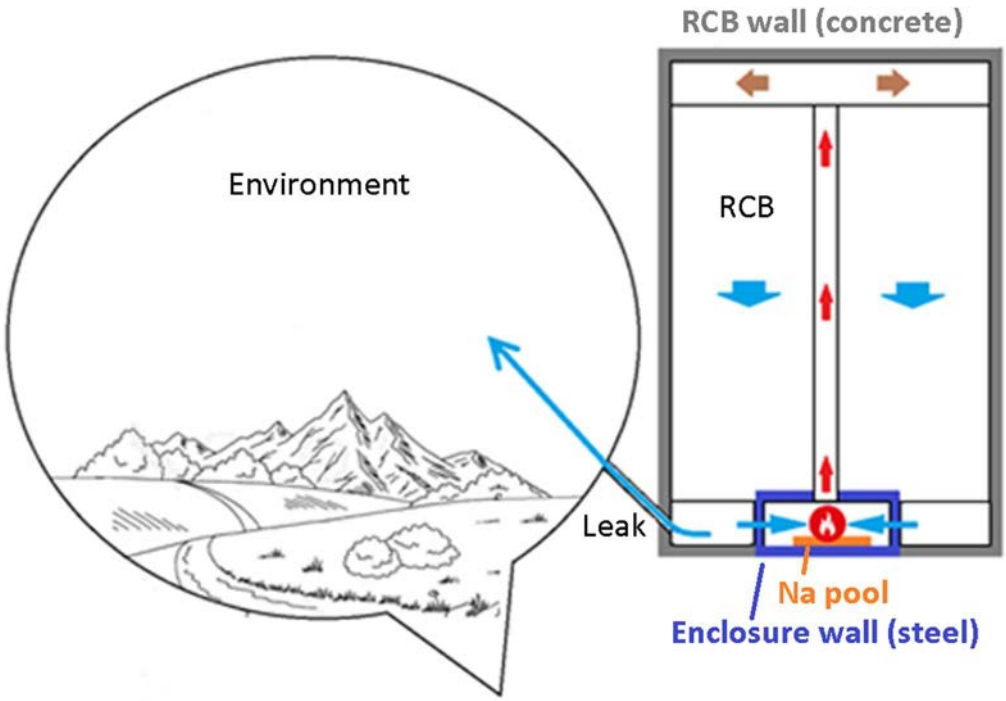

FIG. 230. EUCLID/V2 Nodalization for WP-3: geometry.

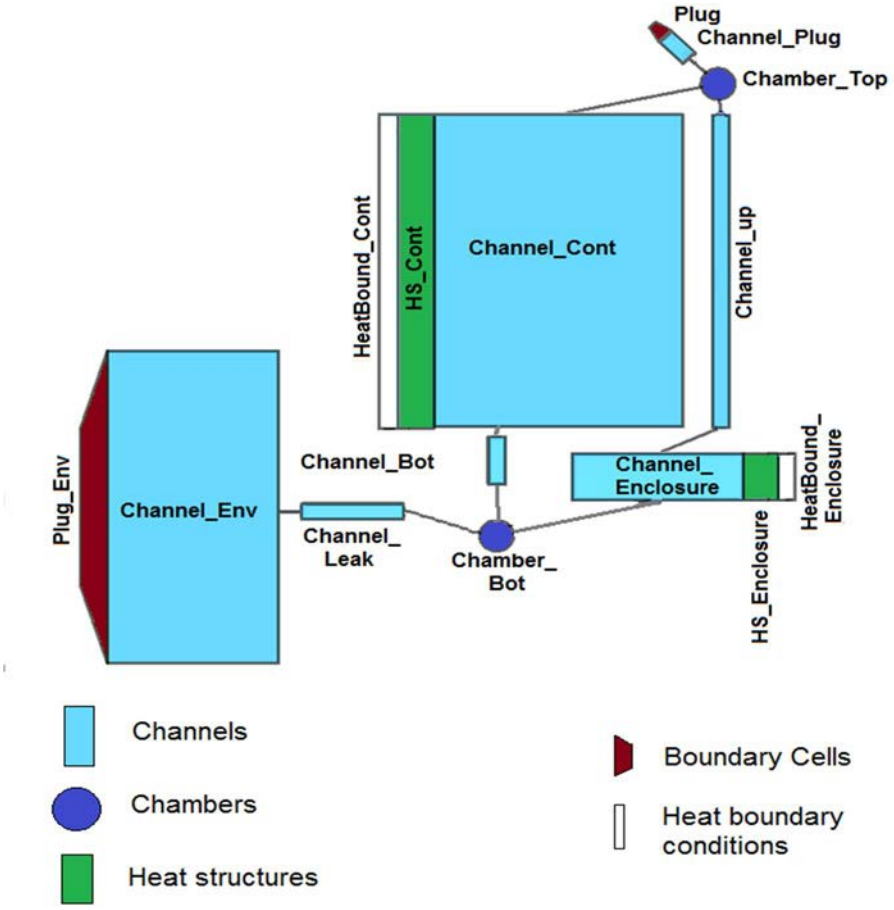

FIG. 231. Simplified Nodalization for WP-3: build by pre-processor.

There are four main channels in the scheme:

(1) Channel_Enclosure (616 m^3) represents gas in enclosure with sodium pool,
(2) Channel_Cont (73386 m^3) represents gas in RCB (temperature 35°C, pressure 99.3 kPa)
(3) Channel_Env (5E+6 m^3) represents gas in environment (temperature 35°C, pressure 100 kPa),
(4) Channel_Leak: guarantees leak rate in accordance with the formula 0.1% per hour 25 kPa.

Several auxiliary channels and chambers are necessary to model natural convection during the sodium fire.

6.5.1.2. *Boundary conditions*

For case 1 (without enclosure) there is one heat structure: wall_RCB (concrete, d = 1 m, external boundary condition is T = 35°C). For case 2 (with enclosure) there is second heat structure wall_Enclosure (steel, d=30 cm, adiabatic external boundary condition). These walls are boundaries for channels RCB and Enclosure respectively.

Heat exchange between gas in channels and walls is usually described by standard HYDRA correlations. However, these correlations are intended for simple flows in channels. For containment problems they usually underestimate heat exchange because of complicated gas flow. In conservative calculations this is not taken into account, which increases overpressure

and gives greater FP release into environment. In realistic calculations heat exchange coefficient is multiplied by user parameter InternalHeatConvFactor = 3.

6.5.1.3. *Sodium fire*

As discussed above, two possibilities are considered: pool fire and spray fire. In both cases sodium burn energy is distributed between gas (1-fE) and wall (fE) according to dimensionless user parameter $0 < fE < 1$. For conservative calculations $fE = 0.1$, for realistic calculations $fE = 0.6$.

6.5.1.4. *Initial conditions*

Initial amount of FP was taken from TABLE 61

TABLE 61. FISSION PRODUCT INSTANTANEOUS INJECTION INTO RCB

Radio nuclide	**Half life**	**Vapor or aerosol**	**Activity in reactor**	**Release factor, stand-alone**	**Release, stand-alone**	**Release, integral**
I-131	8.02 d	Aerosol	1.48E+18	0.1	1.48E+17	5.72E+15
I-132	2.30 h	Aerosol	1.96E+18	0.1	1.96E+17	7.60E+15
I-133	20.80 h	Aerosol	2.54E+18	0.1	2.54E+18	9.83E+15
I-134	52.50 m	Aerosol	2.53E+18	0.1	2.53E+17	9.79E+15
I-135	6.57 h	Aerosol	2.23E+18	0.1	2.33E+17	8.66E+15
Cs-134	754.50 d	Aerosol	9.65E+16	0.1	9.65E+15	2.02E+14
Cs-137	30.07 y	Aerosol	1.00E+17	0.1	1.00E+16	1.94E+14
Rb-88	17.78 m	Aerosol	5.22E+17	0.1	5.22E+16	
Ru-103	39.26 d	Aerosol	2.41E+18	0.0001	2.41E+14	3.50E+09
Ru-106	373.59 d	Aerosol	1.06E+18	0.0001	1.06E+14	9.72E+08
Sr-89	50.53 d	Aerosol	7.12E+17	0.1	7.12E+16	8.66E+13
Sr-90	28.79 y	Aerosol	2.88E+16	0.1	2.88E+15	1.96E+12
Te-131m	30.00 h	Aerosol	1.63E+17	0.0001	1.63E+13	8.27E+13
Te-132	3.2d	Aerosol	1.88E+18	0.0001	1.88E+14	9.56E+14
Ce141	32.50d	Aerosol	2.11E+18	0.0001	2.11E+14	1.93E+11
Ce144	284.89d	Aerosol	1.05E+18	0.0001	1.05E+14	6.21E+10
Ba-140	12.75 d	Aerosol	1.93E+18	0.1	1.93E+17	1.46E+12
La-140	1.68 d	Aerosol	1.96E+18	0.0001	1.96E+14	1.87E+11
Kr-83m	1.85 h	Vapor	4.69E+15	1	4.69E+15	2.36E+15
Kr-85	10.70 y	Vapor	2.26E+17	1	2.26E+17	2.24E+17
Kr-85m	4.48 h	Vapor	4.08E+17	1	4.08E+17	4.04E+17

Kr-87	76.30 m	Vapor	4.94E+17	1	4.94E+17	4.89E+17
Kr-88	2.84 h	Vapor	2.55E+18	1	2.55E+18	2.52E+18
Kr-89	3.15 m	Vapor	2.66E+18	1	2.66E+18	2.63E+18
Xe-131m	11.84 d	Vapor	1.48E+18	1	1.48E+18	1.46E+18
Xe-133	5.24 d	Vapor	1.96E+18	1	1.96E+18	1.94E+18
Xe-133m	2.2 d	Vapor	2.54E+18	1	2.54E+18	2.51E+18
Xe-135	9.14 h	Vapor	2.53E+18	1	2.53E+18	2.50E+18
Xe-135m	15.29 m	Vapor	2.23E+18	1	2.23E+18	2.21E+18
Xe-137	3.82 m	Vapor	9.65E+16	1	9.65E+16	5.19E+16
Xe-138	14.08 m	Vapor	1.00E+17	1	1.00E+17	4.98E+16

6.5.2. **Results**

6.5.2.1. *Stand-alone WP3: variant calculations*

In the case of a spray fire, all sodium is assumed to burn quickly (in 100 seconds). In the case of a pool fire, the rate of sodium burning is calculated by the code. In FIG. 232 pool temperature is shown; the curves end when all sodium is burnt.

In ‘realistic’ calculations a large amount of burning energy is transferred to the walls and to the pool. The pool becomes hot (its temperature is limited by Na evaporation) and the fire lasts about 20-25 minutes.

In ‘conservative’ calculations 90% of burning energy is transferred to the gas. The pool temperature is lower, the fire lasts 60-75 minutes.

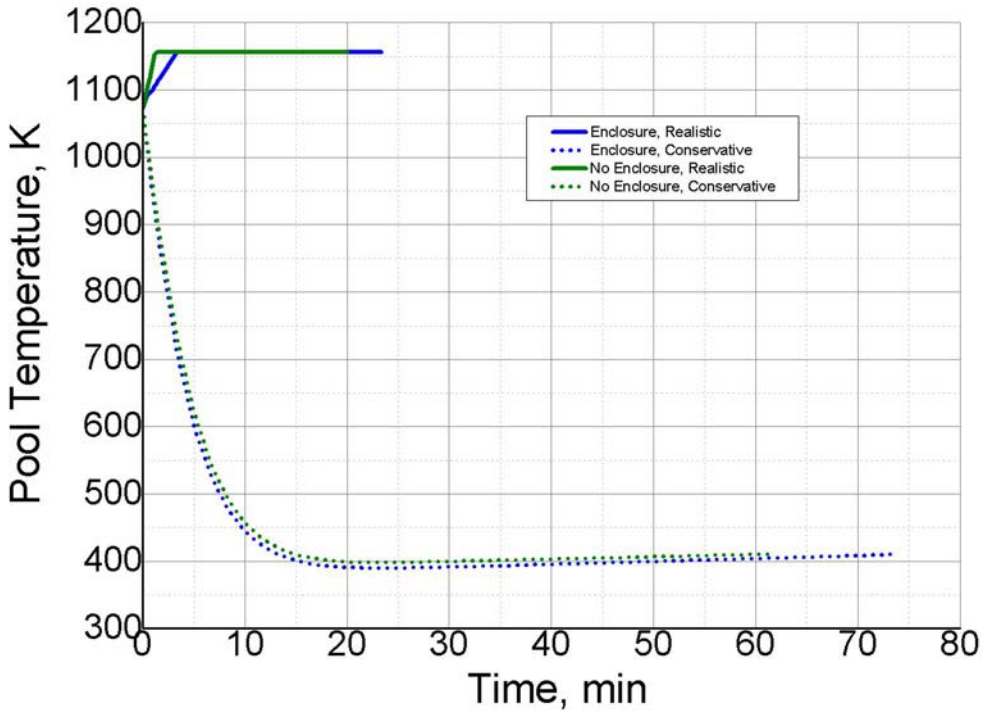

FIG. 232. Sodium pool temperature.

In FIG. 233 RCB overpressure evolution is shown. It can be seen that it reached its peak when the fire ends; then it falls due to heat exchange with walls. In both cases total amount of burning energy was the same. However, in conservative calculations a greater fraction of this energy is transferred to gas.

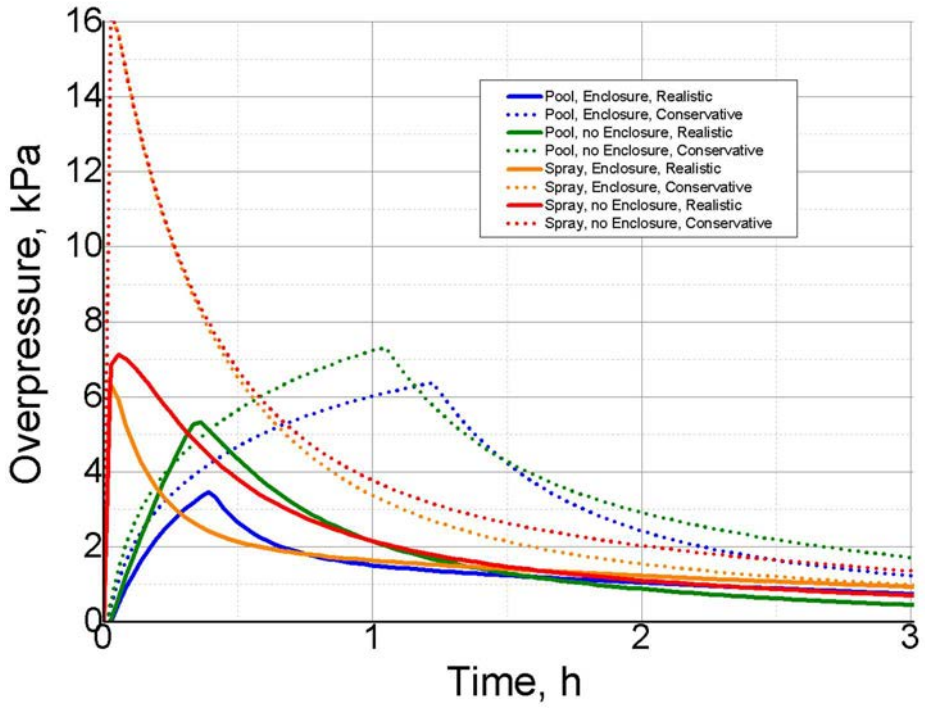

FIG. 233. Overpressure evolution, stand-alone calculations.

To compare results of FP behavior in various calculations, Sr-89 is chosen as its half-life is much longer than calculation time (1 day) and it forms aerosols.

In FIG. 234 to FIG. 236 amount of SR-89 in the RCB atmosphere, on RCB walls, and in environment is shown. The amount of the nuclide in the RCB atmosphere depends strongly on aerosol sizes as the greater the particles, the faster the deposition. In conservative calculations particle diameters are 1.3 μm while in realistic ones it is 3-4 μm. In the case of a spray fire, aerosol particles are larger than in the case of pool fire because sodium burns faster and coagulation begins earlier.

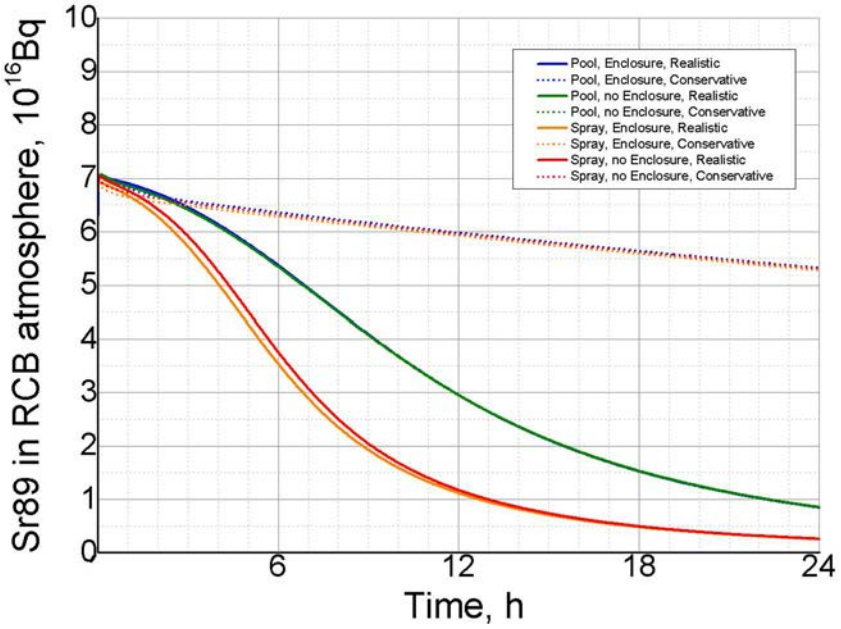

FIG. 234. Sr-89 in RCB atmosphere, stand-alone calculations.

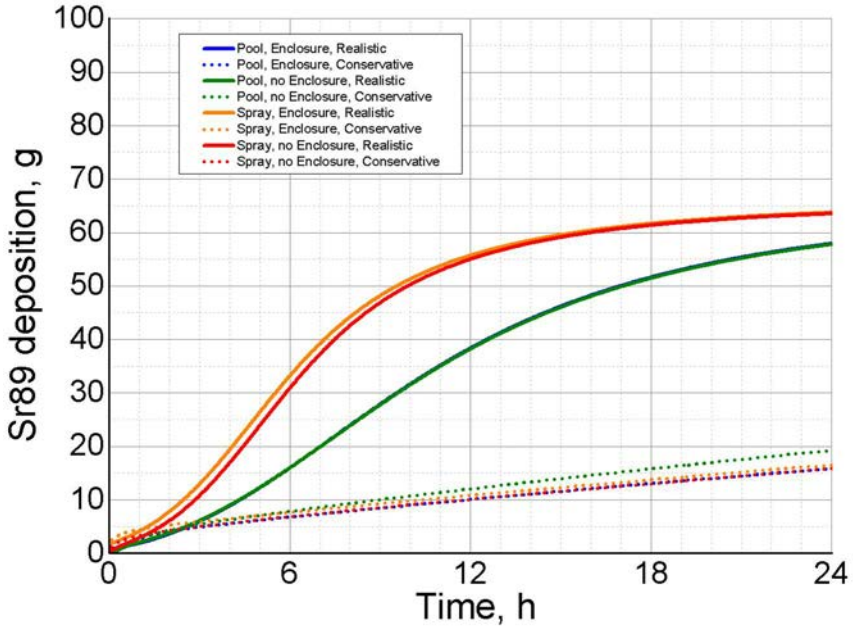

FIG. 235. Sr-89 depositions on the floor, stand-alone calculations.

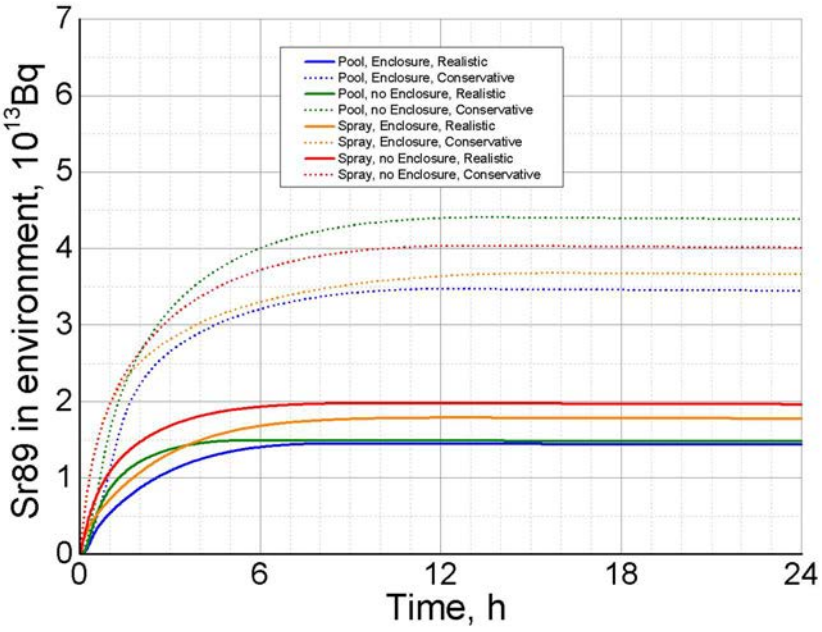

FIG. 236. Sr-89 in environment, stand-alone calculations.

6.5.2.2. *Integral tests: variant calculations of WP3*

In the integral calculation, the amount of Na in the RCB is 330 kg (instead of 350 kg in stand-alone calculation). Gas dynamics are quite similar to that in stand-alone calculation but overpressure is lower and, hence, the release to environment is lower too, FIG. 237.

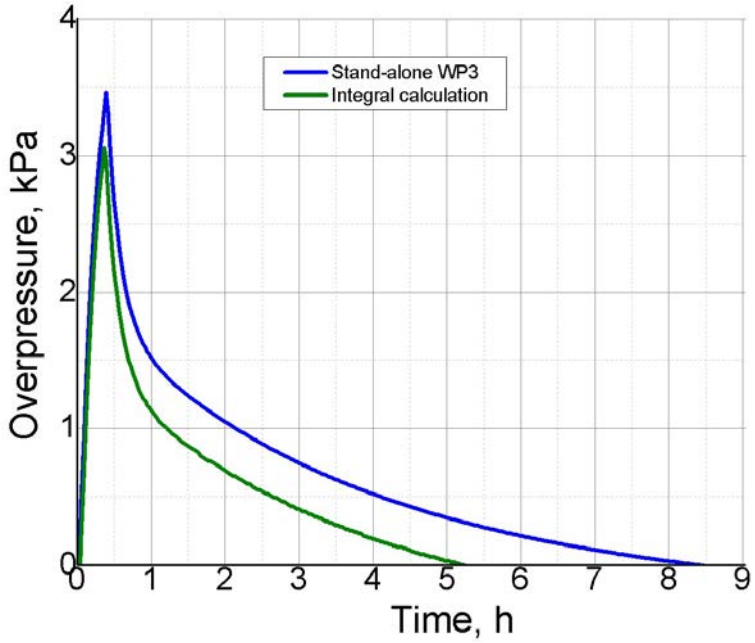

FIG. 237. Overpressure in RCB, stand-alone (350 kg Na) vs integral (330 kg Na).

In FIG. 238 to FIG. 240 aerosol dynamics of Sr-89 is shown.

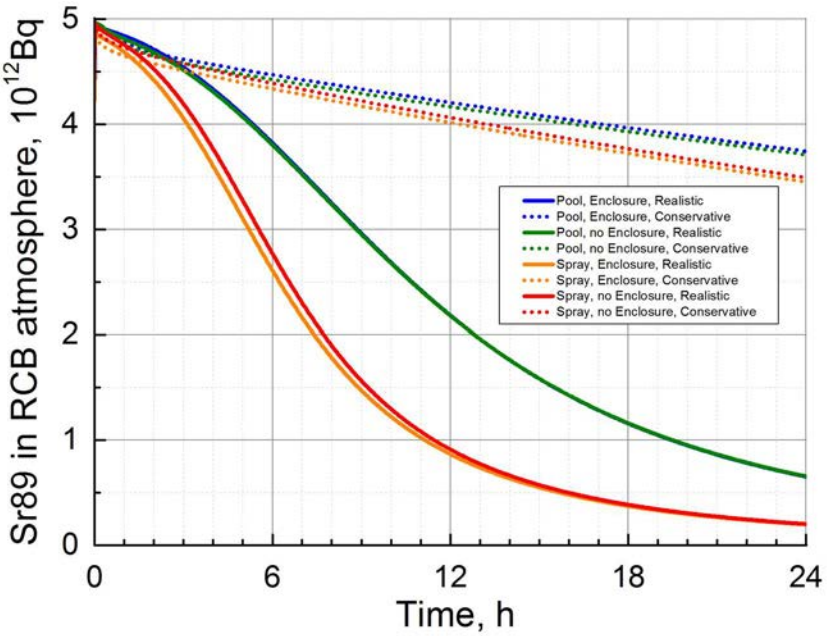

FIG. 238. Sr-89 in RCB atmosphere, integral calculations.

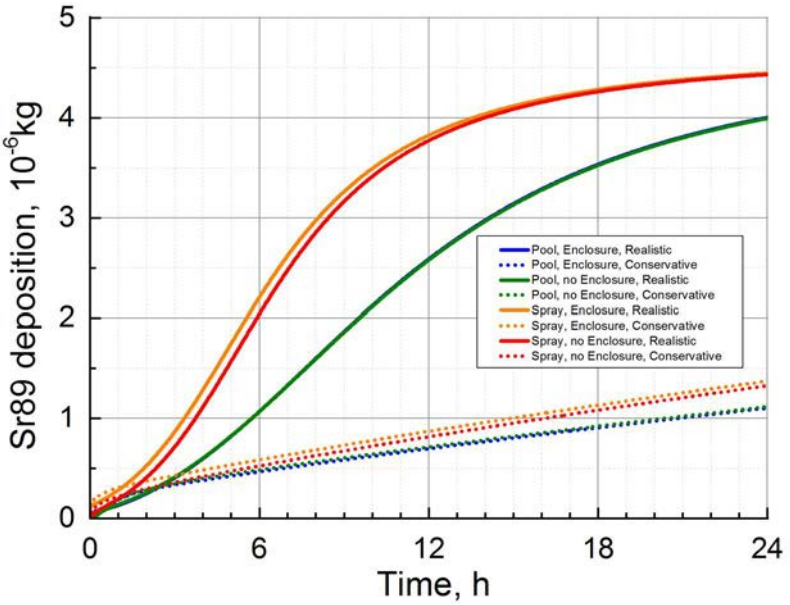

FIG. 239. Sr-89 deposited on floor, integral calculations.

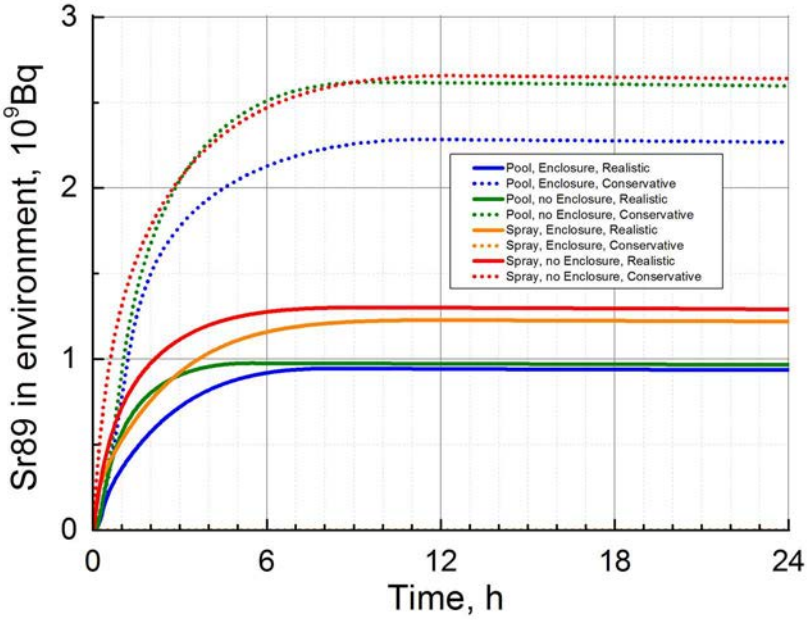

FIG. 240. Sr-89 in environment, integral calculations.

6.5.2.3. *Stand-alone WP3 calculation: all fission products*

The calculation with pool fire, enclosure (case 2), realistic parameters is chosen to show information about all other FPs. FIG. 241 to FIG. 243 represent amount of each FP in RCB. In FIG. 244 and FIG. 245 masses of their depositions are shown. FIG. 246 to FIG. 248 represent FP amount in environment. For depositions radioactive decay is not modelled, there masses do not decrease on graphs.

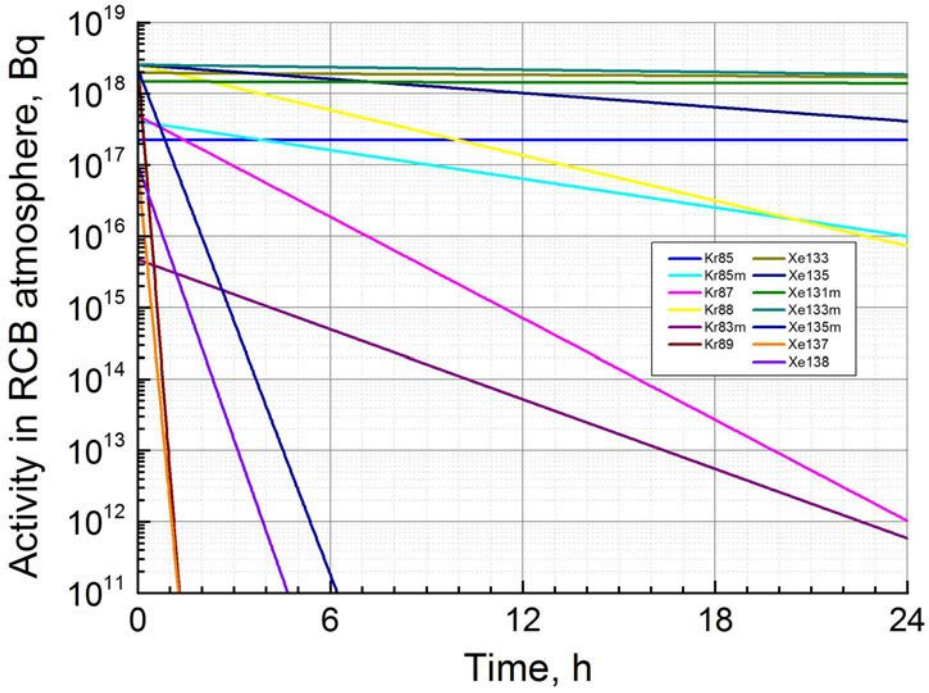

FIG. 241. FP in RCB atmosphere. Stand-alone calculation, case 2, pool fire, realistic

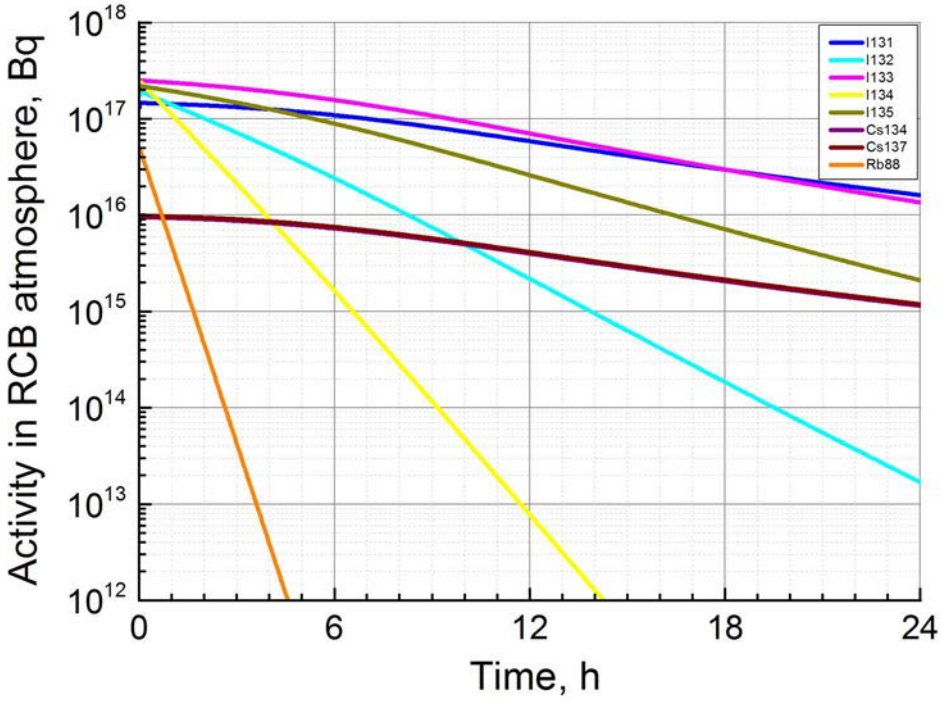

FIG. 242. FP in RCB atmosphere. Stand-alone calculation, case 2, pool fire, realistic.

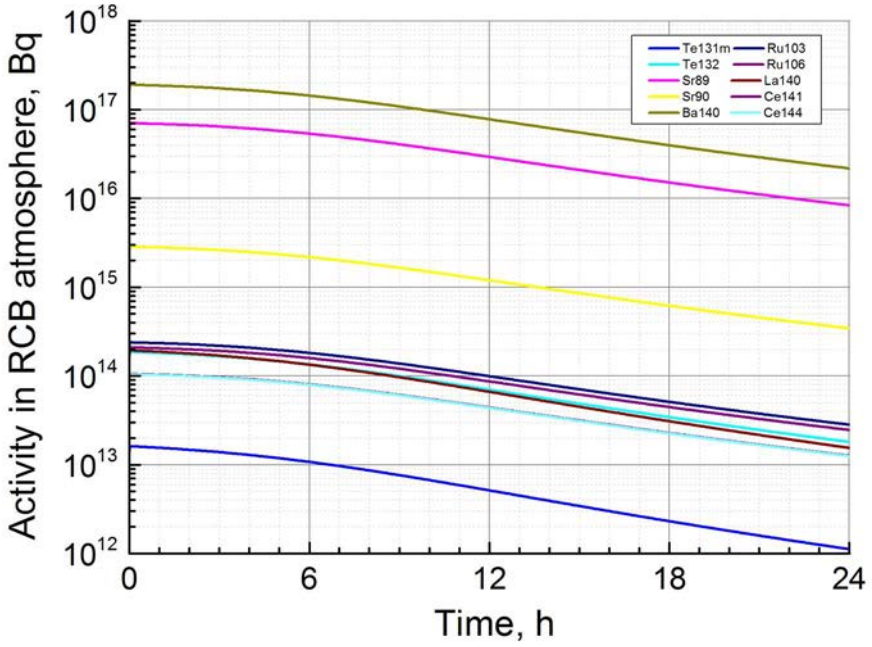

FIG. 243. FP in RCB atmosphere. Stand-alone calculation, case 2, pool fire, realistic.

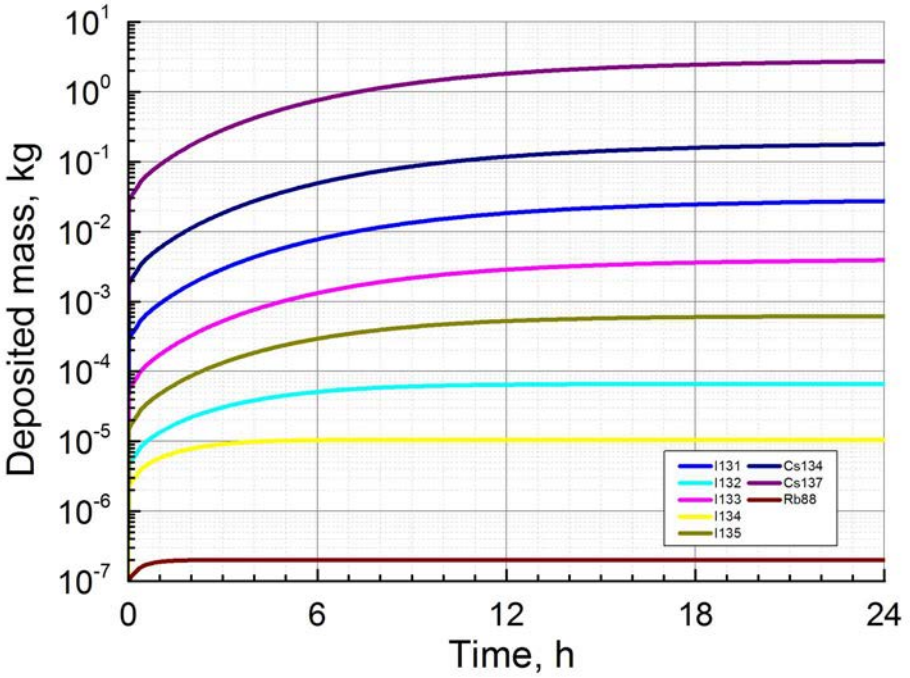

FIG. 244. FP depositions. Stand-alone calculation, case 2, pool fire, realistic.

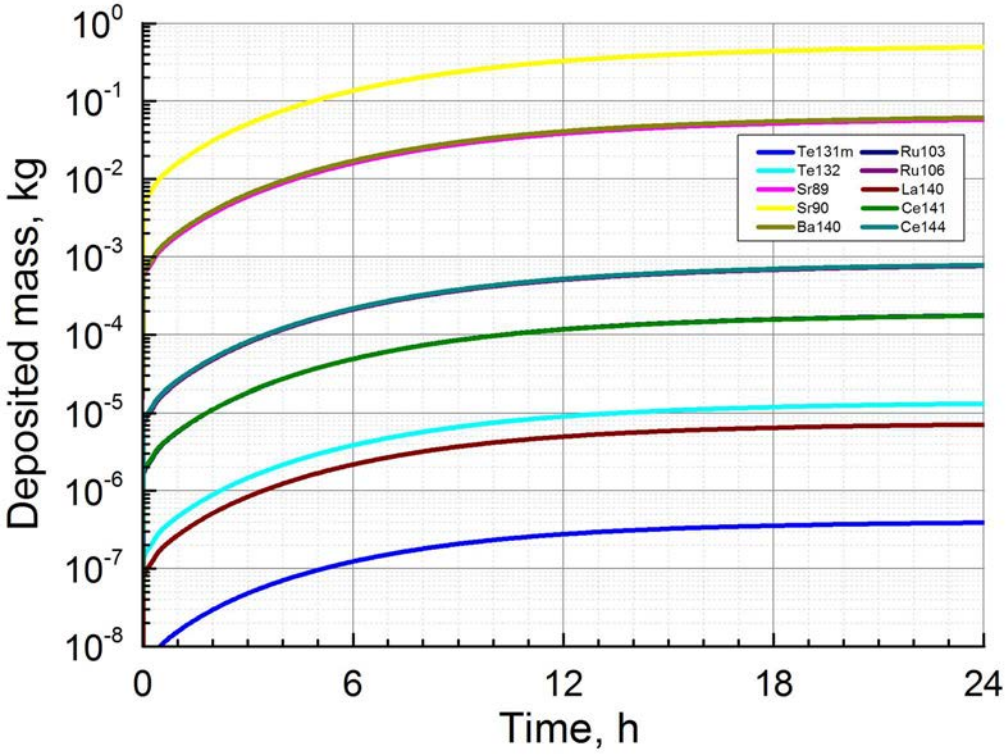

FIG. 245. FP depositions. Stand-alone calculation, case 2, pool fire, realistic.

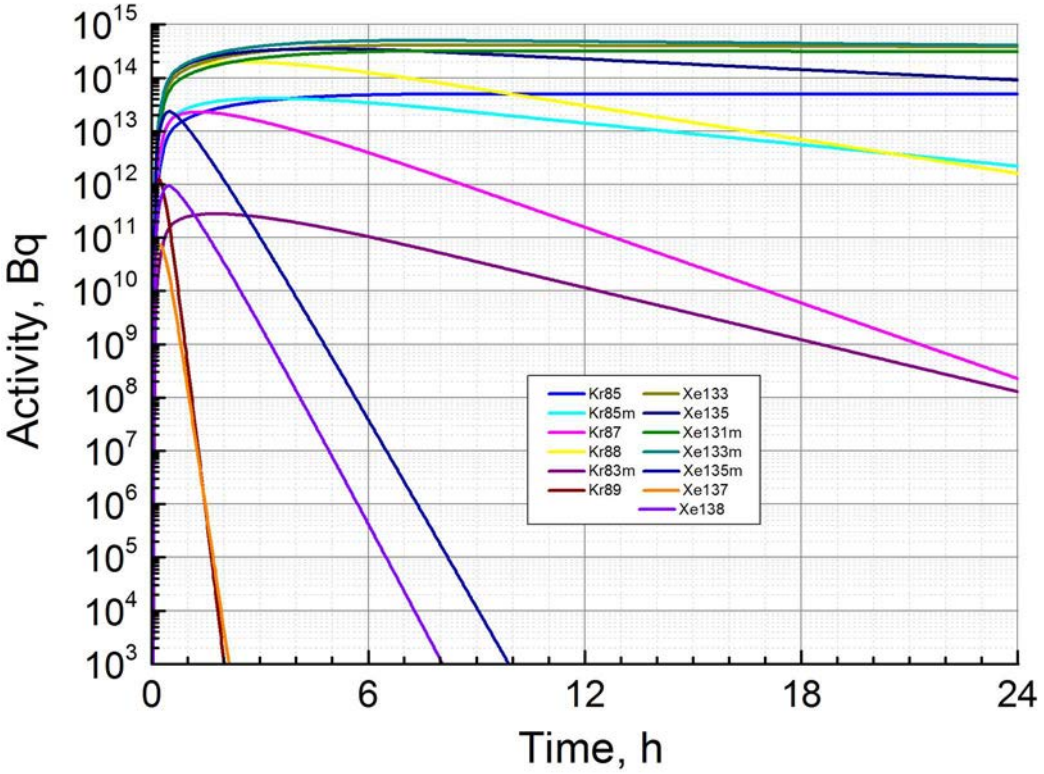

FIG. 246. FP in environment. Stand-alone calculation, case 2, pool fire, realistic.

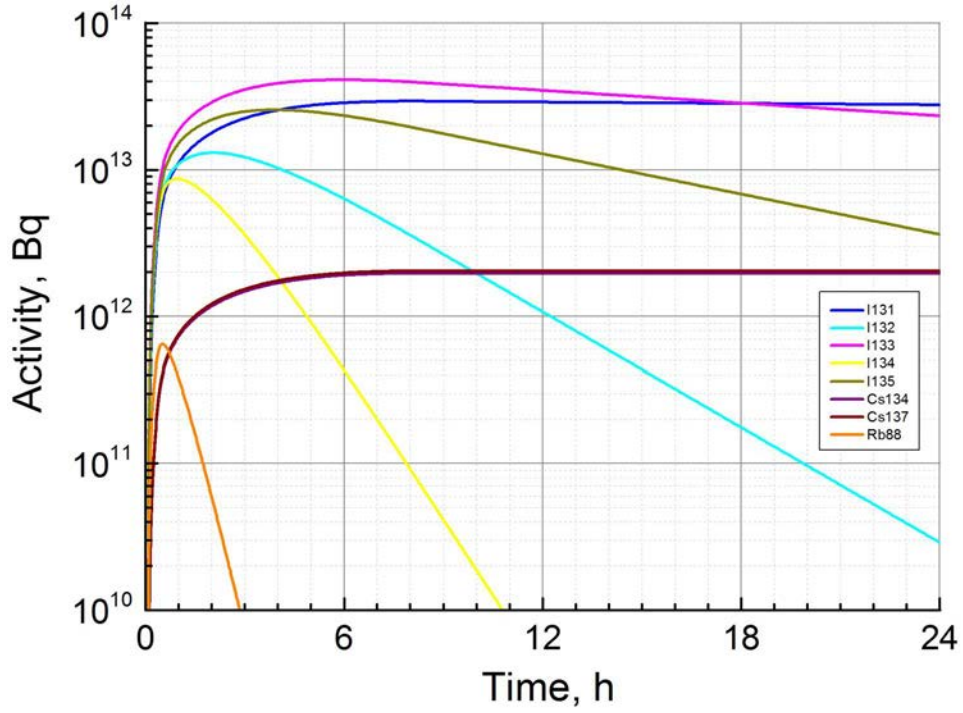

FIG. 247. FP in environment. Stand-alone calculation, case 2, pool fire, realistic.

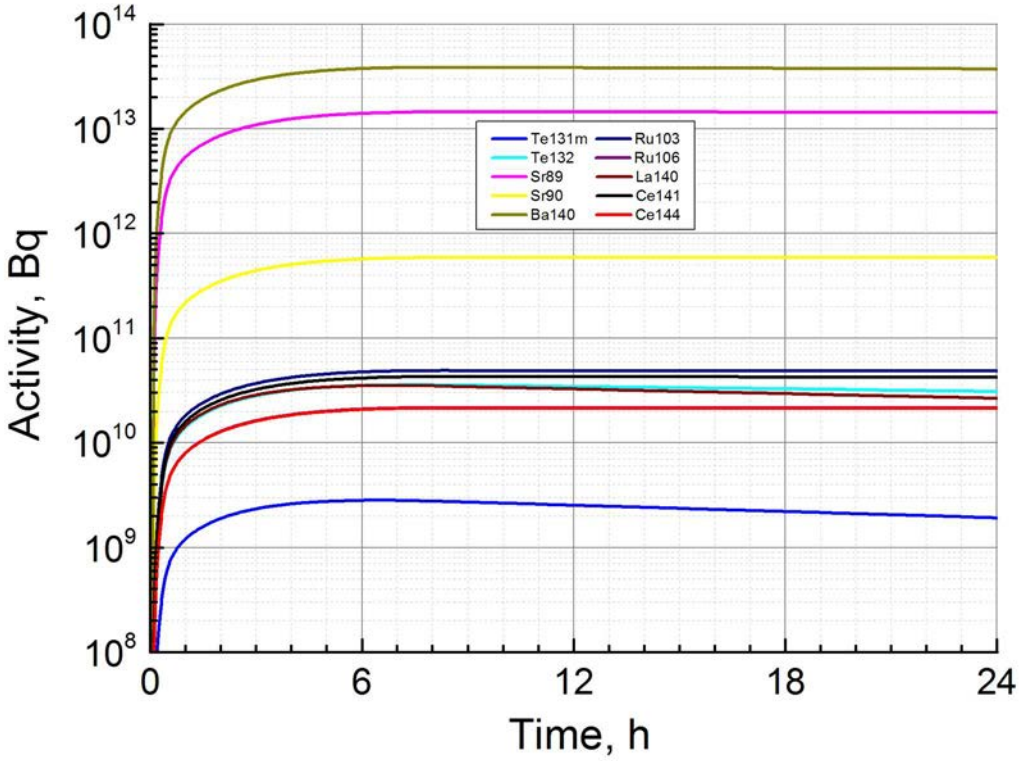

FIG. 248. FP in environment. Stand-alone calculation, case 2, pool fire, realistic.

6.5.2.4. *Calculation of WP3 in integral test: all fission products*

The amount of each FP in the RCB is shown in FIG. 249 through FIG. 251. In FIG. 252 and FIG. 253, masses of their depositions are shown. The FP amount in the environment is shown in FIG. 254 through FIG. 256.

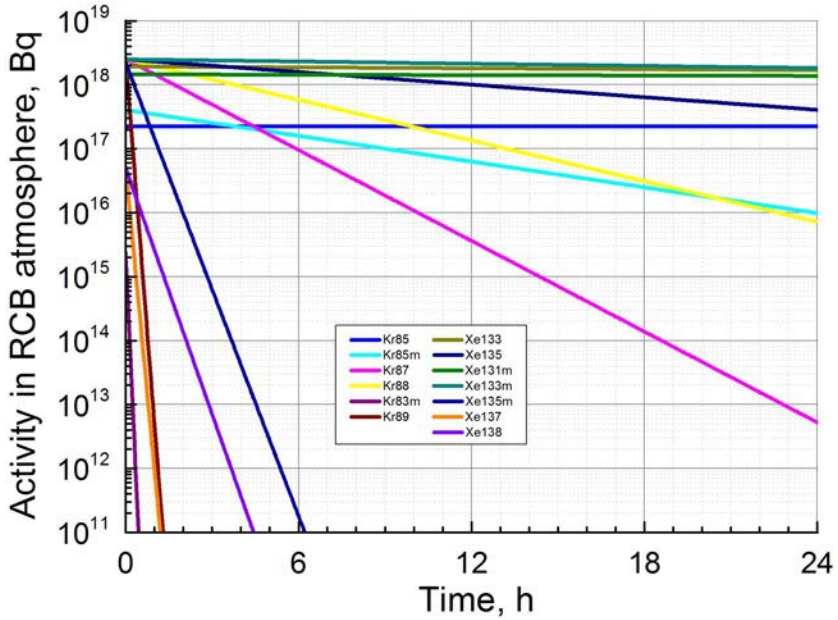

FIG. 249. FP in RCB atmosphere. Integral calculation, case 2, pool fire, realistic.

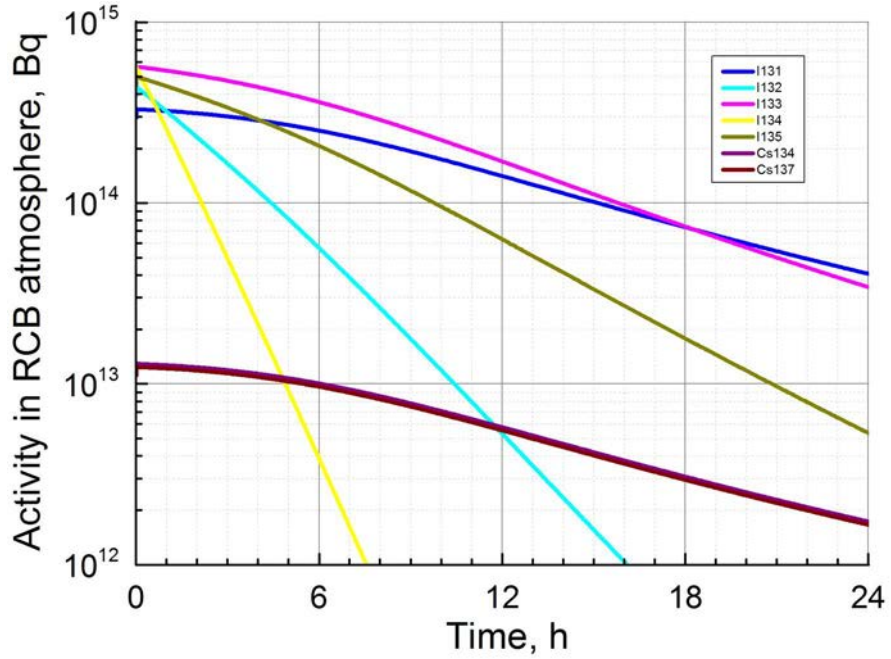

FIG. 250. FP in RCB atmosphere. Integral calculation, case 2, pool fire, realistic.

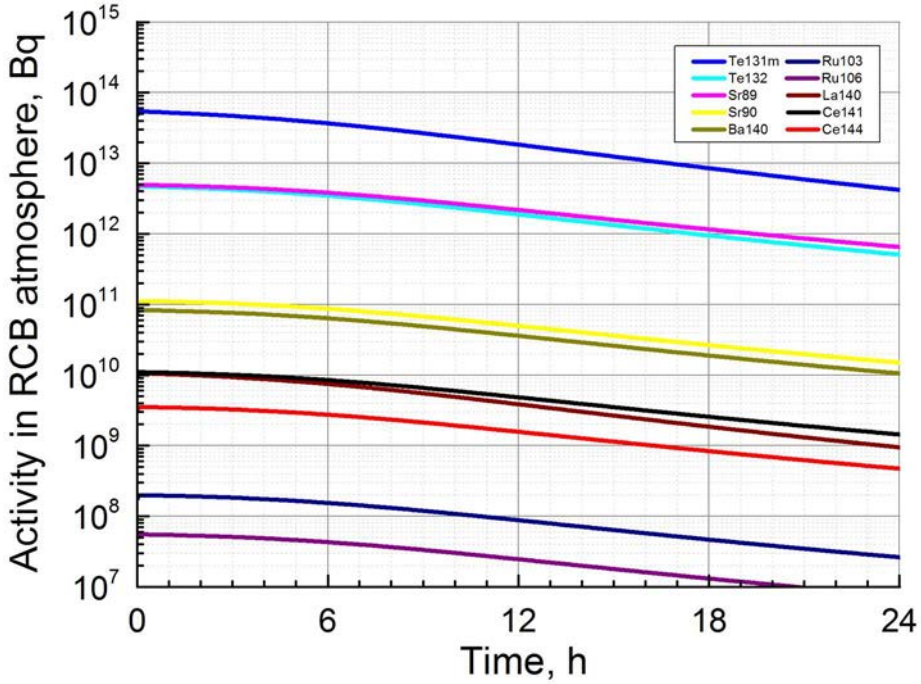

FIG. 251. FP in RCB atmosphere. Integral calculation, case 2, pool fire, realistic.

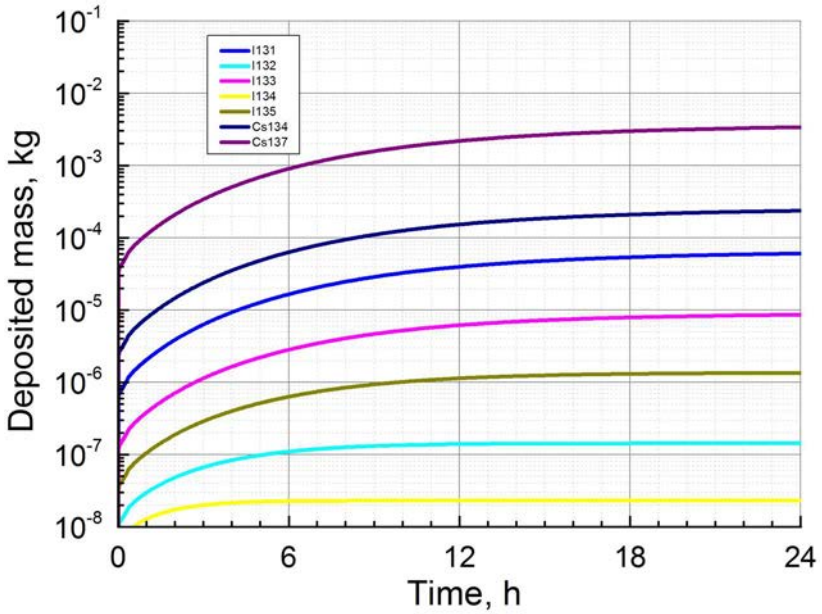

FIG. 252. FP depositions. Integral calculation, case 2, pool fire, realistic.

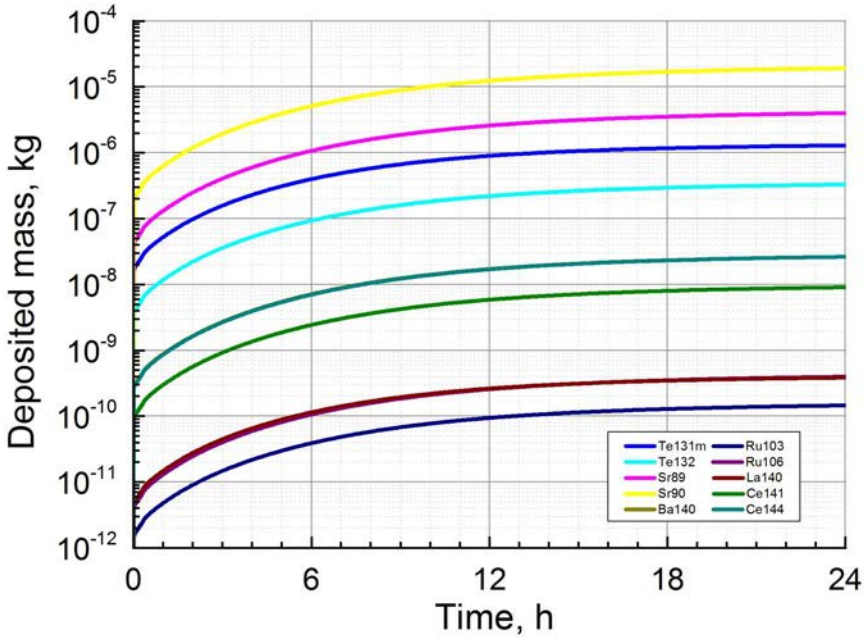

FIG. 253. FP depositions. Integral calculation, case 2, pool fire, realistic.

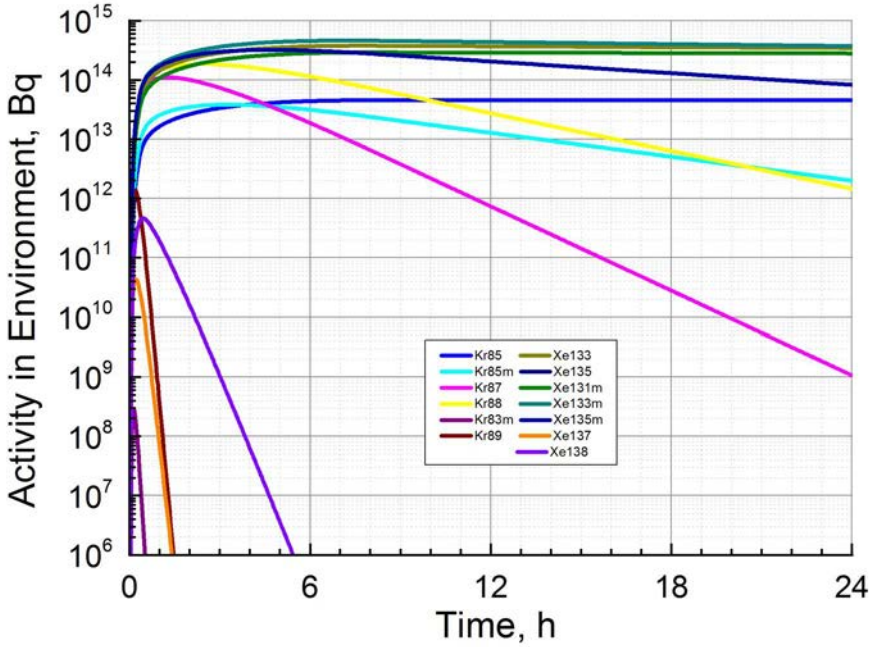

FIG. 254. FP in environment. Integral calculation, case 2, pool fire, realistic.

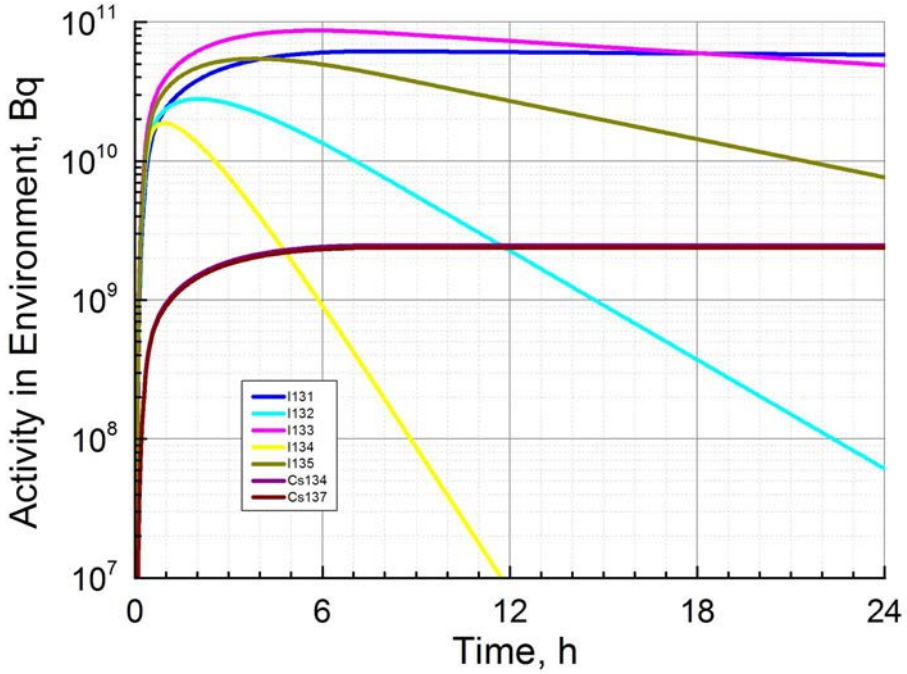

FIG. 255. FP in environment. Integral calculation, case 2, pool fire, realistic.

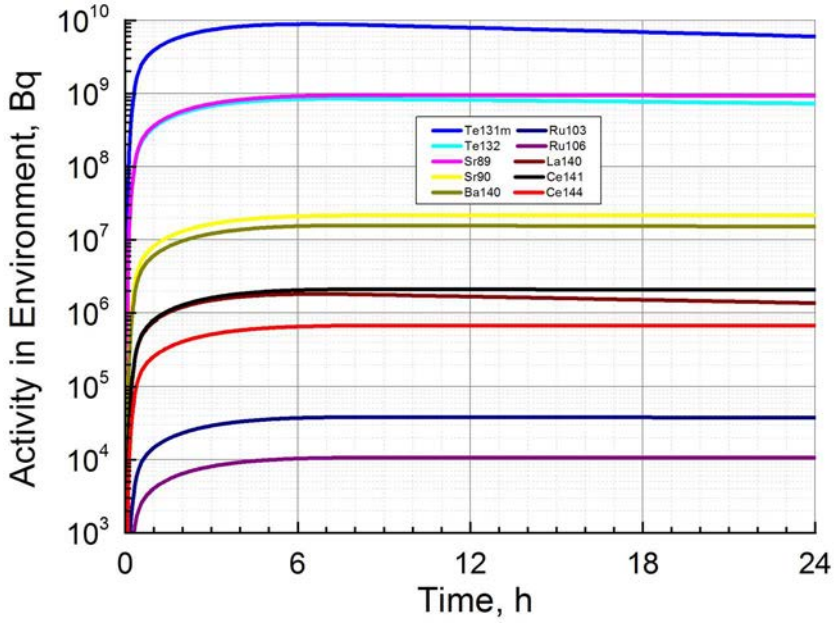

FIG. 256. FP in environment. Integral calculation, case 2, pool fire, realistic.

6.5.3. Summary

FP activity in RCB

Initial activity of fission products in the RCB is determined by their release from primary contour. Next, aerosol deposition halves activity of aerosol FP every 2.4 days (conservative simulation with monodisperse 1.3 μm aerosols) or every 6 hours (realistic simulation with polydisperse coagulating aerosols; in fact, law of activity fall is not exactly exponential). For nuclides with shorter half-lives this decrease is faster due to spontaneous decay. Therefore, it is easy to obtain correct activities of FPs with half-lives shorter than several hours. It is easy to obtain correct activities of gaseous FPs. For example, Kr-85 will be almost constant due to long its half-life. Most complicated is to calculate the correct amounts of FPs which form aerosols and have long half-lives, like Sr-89. As shown in FIG. 234, after 24 hours of calculation activity of such elements in RCB may differ by an order of magnitude; the result mainly depends on the size of aerosols.

In realistic calculations, all fission products except noble gases deposit slightly faster in calculations with spray fire due to larger aerosol particles. This occurs because in the spray fire case there is more airborne sodium (100%) than in the pool fire case (<50%). Aerosols coagulate faster in the spray fire case.

FP activity in environment

Fission products are released into environment due to overpressure in the RCB. This overpressure appears because gas temperature temporarily increases due to sodium fire. All sodium in the RCB is burnt in 1.5 hours or less because there is no oxygen starvation in the calculations. Then RCB gas pressure falls due to heat exchange with walls. Most of FP release to environment occurs in first 2 hours. After 8 hours it ends completely. Activity of FP in environment is approximately 3 orders lower than that in RCB.

The most important factor for FP release into environment is the gas temperature in containment. It depends strongly on the fraction of burning energy transferred to the gas and the heat exchange factor between gas and walls. These are user-defined parameters which affect

the result. It can be seen that in conservative simulation Sr-89 release into environment is 3 times higher than in realistic simulation. The same is true for other fission products.

Enclosure does not significantly affect the total amount of FP released into environment. It mainly changes the dynamics, for example, pool fire in enclosure lasts longer than without enclosure. In case of pool fire in enclosure, FP release to environment is not as intense but lasts longer.

Aerosol deposition on leak paths from the RCB into environment are not considered in this calculation. Deposition processes do not have time to decrease RCB activity strongly during the first couple of hours when the release peaks. Thereforem complicated aerosol effects have only weak effect on FP release into environment. The size of aerosol particles may be important for further calculation of FP behavior in environment, however.

6.6. SIMULATION EXERCISE USING ASTEC-NA CODE (CIEMAT, SPAIN)

6.6.1. **Description of the Methods and Model**

Calculations have been carried out with the ASTEC-Na code according to the benchmark specifications. Two cases have been simulated, named as reference case (case 1) and realistic case (case 2). Both simulations are based on the conditions derived after an energetic CDA which implies the release of 350 kg of Na into the containment.

In case 1, the ejected sodium into the containment exothermically reacts with the air of the reactor containment building (74000 m^3). In case 2 ,the Na spill takes place inside an enclosure volume (616 m^3). In the former, a Na spray fire is modelled by using the Na pool fire model and setting an equivalent pool surface equal to the total Na droplets surface (a mean droplet diameter of 1 mm has been assumed [50]). In the latter, a Na pool fire has been modelled.

6.6.1.1. *Nodalization and heat structures*

The containment building nodalization in case 1 (FIG. 257) consists of a single cell (RCB) of 74000 m3 volume (the containment volumes below deck structure are not considered in the calculation). Six heat structures have been defined for heat transfer and aerosol deposition calculations (FIG. 257): the top head (ceiling) and the deck structure (bottom), the wall (wall) and the internal components, i.e., the cells housing the cover gas system (cells) and the cover above roof slab (cover). In CPA*, the sodium spray fire is modelled as a heat structure facing up to properly account for the heat transfer from the pool.

Case 2 (FIG. 258) shares the same containment building nodalization, i.e., 1 single cell (RCB). Besides, a new volume is added for the enclosure modelling (ENCL). A top vent area (3.5 m^2) and a side vent area (1.5 m^2) are defined as openings at the top and wall of the enclosure, respectively. The sodium pool is modelled also as a heat structure inside the enclosure volume.

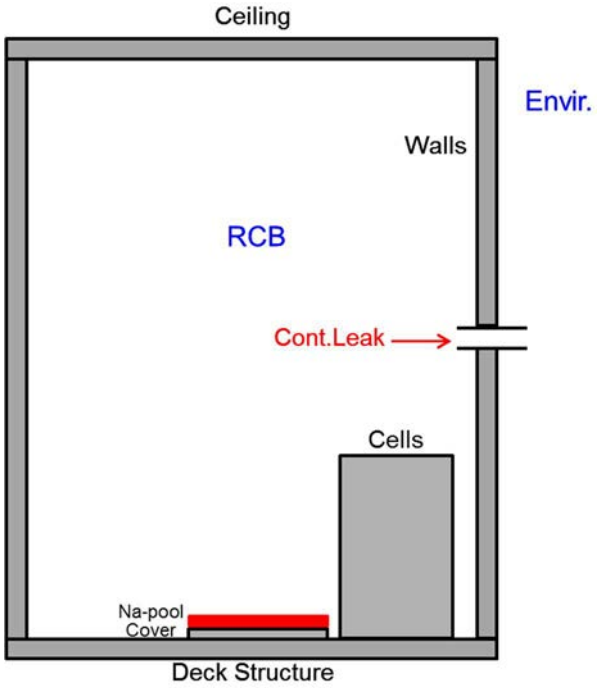

FIG. 257. Case 1 (Reference case).

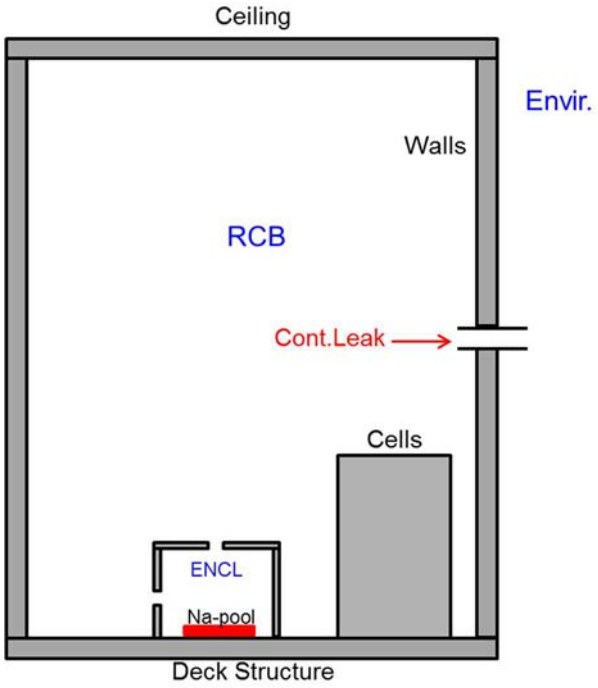

FIG. 258. Case 2 (Realistic case).

The surface areas characteristics are given in TABLE 62.

TABLE 62. HEAT STRUCTURES

Heat structures	**Area (m^2)**	**Orientation**	**Material**	**Thickness (m)**
Case 1				
Top_RCB	1400	Horizontal	Concrete	1.0
Bottom_RCB	1400	Horizontal	Concrete	1.0
Wall_RCB	7929	Vertical	Concrete	1.0
Cells	1226	Vertical	Concrete	0.20
Cover	329.8	Horizontal	Carbon steel	1.0
Pool	2608.7*	Horizontal	Sodium	1.0**
Case 2				
Top_RCB	1400	Horizontal	Concrete	1.0
Bottom_RCB	1246	Horizontal	Concrete	1.0
Wall_RCB	7929	Vertical	Concrete	1.0
Cells	1226	Vertical	Concrete	0.20
Top_ENCL	154.0	Horizontal	Carbon steel	0.030
Bottom_ENCL	154.0	Horizontal	Carbon steel	0.030
Wall_ENCL	176.0	Vertical	Carbon steel	0.030
Pool	153.9*	Horizontal	Sodium	0.5**

*See Section 6.6.1.3. for more details of sodium pool size definition.

**Minimum thickness necessary to avoid code crush.

6.6.1.2. *Initial boundary conditions*

In TABLE 63, the initial conditions for both simulations are defined. The RCB is at around normal conditions with a humidity of 60% in both cases. The enclosure in case 2 (ENCL) is at 393.15 K with a relative humidity of 15%. The initial temperature and relative humidity in RCB and ENCL differ. An initial sodium pool temperature of 873.15 K was set.

In both simulations, sodium fires started at the beginning of the calculation (t = 0s). CPA* requires setting the end time of the fire by the user. This time is set when all the sodium released (350kg) is burned out.

TABLE 63. INITIAL CONTAINMENT BOUNDARY CONDITIONS

	Case 1	Case 2
Initial containment atmosphere		
Oxygen concentration (%)	21	21
Temperature (K)	305.15	305.15
Relative humidity (%)	60	60
Pressure (Pa)	1.006E+5	1.006E+5
Initial enclosure atmosphere		
Oxygen concentration (%)	-	21
Temperature (K)	-	393.15
Relative humidity (%)	-	15
Pressure (Pa)	-	1.006E+5
Sodium spill		
Sodium mass delivered (kg)	350	350
Initial sodium temperature (K)	873.15	873.15
Pool fire burning area (m^2)	2608.7	153.9
End of calculation time (s)	13.9	9535.0

6.6.1.3. *Major hypothesis and approximations*

The major hypothesis and approximations are summarized in TABLE 64.

TABLE 64. MAJOR HYPOTHESIS AND APPROXIMATIONS FOR BOTH CASES

Phenomenon	**Case 1**	**Case 2**
Amount of primary sodium ejected into the containment	350 kg	
Modelled type of fire	Na-spray fire modelled as a Na pool fire by an equivalent pool surface.	Na-pool fire.
Pool dimensions	Pool surface assumed to be equivalent to the total surface of the sodium droplets generated during the sodium spray fire (total fragmentation of the jet supposed – conservative assumption). A mean droplet	Pool dimensions defined according to the reactor vault dimensions (7 m radius).

	diameter of 1 mm [50] is considered.	
Gas-surface heat exchanges	The containment vessel atmosphere and the contacting surfaces of the vessel walls are initially set at room conditions. Natural convection heat transfer has been activated in the simulation and radiation heat transfer between sodium pool and vessel walls has been also considered.	
Sodium-concrete interaction	Currently, CPA* does not include a sodium-concrete interaction model.	
Leakage rate from containment	A leakage rate of 0.1% volume per hour at 1.25E+5 Pa overpressure has been modelled in the containment vessel. No leaks for lower overpressure have been modelled.	
Sodium oxides formation	In CPA*, the fraction of oxygen producing sodium oxide (Na_2O) is defined through the input parameter f_1 (ranging from 0.0 to 1.0; the rest of O_2 not producing Na_2O, forms sodium peroxide (Na_2O_2)). A value of 0.3 is given by assuming both Na-oxide and peroxide formation reactions infinitely fast	
Heat transfer from Na pool and combustion energy	Heat transfer from sodium pool is modelled through a rigid wall (sodium pool surface) with an initial temperature of 873.15 K. There is no restriction in heat transfer other than an emissivity setting for Na thermal radiation (0.65 according to [51]). The energy released during the pool fire is modelled in CPA* using the SOFIRE-II approach [41]: the fraction of the chemical energy absorbed by the pool is defined through the user input parameter f_2 (the complement is released in the atmosphere). A value of 0.5 is used supported by a rough estimation* of the ratio between the heat flux by radiation from the flame to the pool surface and the heat flux by convection from the flame to the ambient.	
Aerosolization of sodium combustion products	CPA* estimates the amount that eventually enters the atmosphere of each species (Na_2O and Na_2O_2) through the f_3 (fraction of Na_2O released in the atmosphere, complement is released to the pool) and f_4 (fraction of Na_2O_2 released in the atmosphere, complement is released to the pool) parameters in the input deck. It has been assumed that all Na_2O get instantaneously depleted on sodium pool surface ($f_3 = 0.0$) based on experimental observations concerning Na aerosol composition [52], and 80% of Na_2O_2 is aerosolized ($f_4 = 0.8$) by taking into account that only 40% of sodium burnt leads to aerosol production in a sodium pool fire [53].	
Aerosol modelling	The aerosol density is assumed to be the Na_2O_2 density (2800 kg/m^3). Particles have been assumed to be spherical [54].	

* Traditional correlations for natural convection and radiation have been used for the estimation.

6.6.2. **Results**

6.6.2.1. *Thermal-hydraulics*

Atmosphere temperature and pressure versus time up to 1E5 s are shown for both cases in the next figures. From FIG. 259, gas temperature evolution in case 1 may be described in two phases: a noticeable heat up phase from the beginning of the calculation and until the end of the fire (13.9 s) due to the energy released by the sodium-oxygen chemical reactions (approx. 2/3 of the total energy delivered to the vessel) and the hot sodium pool surface temperature; and then, a progressive cooldown phase due to the heat removal from the containment atmosphere to the RCB containment walls. Note that this simulation entails a drastic approximation concerning Na-bearing particles: they are assumed not to play any role in containment heat transfer. However, given their high temperature and the large surface area they may. As it can be observed, the combustion energy released during the sodium fire phase did not result in a significant gas temperature increase (approximately 30 K) due to the huge containment volume. According to the modelling, the hot sodium fire surface is off once the fire is ended.

In short, even if the global thermal description above might give good insights into a real CDA scenario, it is likely that the temperature rise during the fire phase is somewhat higher and the cooling down after the fire end is even slower. Nevertheless, given other hypotheses involved it does not make any sense to intend a quantitative analysis of both anticipated deviations.

FIG. 261 shows the gas temperature evolution in case 2 for the modelled volumes: the enclosure (ENCL) and the containment (RCB). At the enclosure, during the first 70s of the calculation there is an increase of the temperature due to the chemical energy released from the combustion; then, a decrease of the temperature can be observed that corresponds to a quench of the combustion reactions due to the reduction in the oxygen available for combustion. As expected, given the reduced enclosure volume the temperature rise is much larger than the one in case 1 and its increase rate is about one order of magnitude faster. The damping of the temperature drop from 1700s on is due to the much lower O_2 concentration at the time (<1%), which makes oxidation a much weaker energy source. At the time of fire end, a sharp temperature rise is predicted. This clearly unphysical trend is due to an artefact introduced by the heat transfer modelling during the sodium fire. For some unknown and unjustified reason, heat transfer from the sodium pool surface and enclosure walls into the atmosphere is hindered; this would not affect the first 70s of the transient when an intense fire is the mean heating-up mechanism of the atmosphere, but when it weakens due to O_2 lean gas composition in the enclosure, those other heat sources become more relevant and should be considered in the model. As a result, if the modelling had properly considered all the energy transfers in the system, in-enclosure temperature from 70s would have decreased at a slower pace and no temperature jump would have happened once the sodium fire eventually extinguishes.

Consistent with gas temperature, pressure evolution for both cases is shown in FIG. 260 and FIG. 262. As it can be seen from the figures, the needed overpressure for a leak in the containment is not reached (25 kPa according to the working material document) in any of the cases.

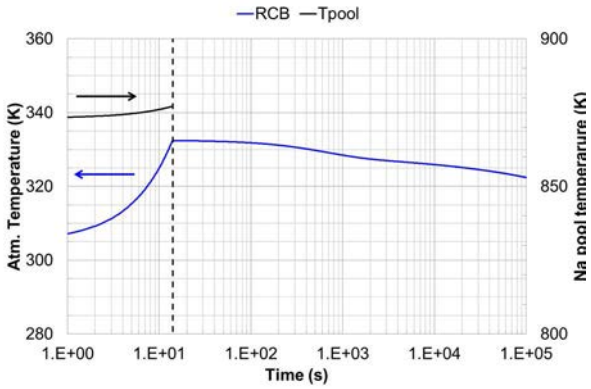

FIG. 259. Atmosphere temperature (Case 1).

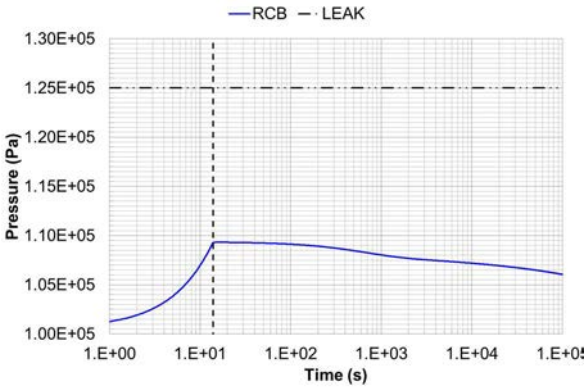

FIG. 260. Pressure (Case 1).

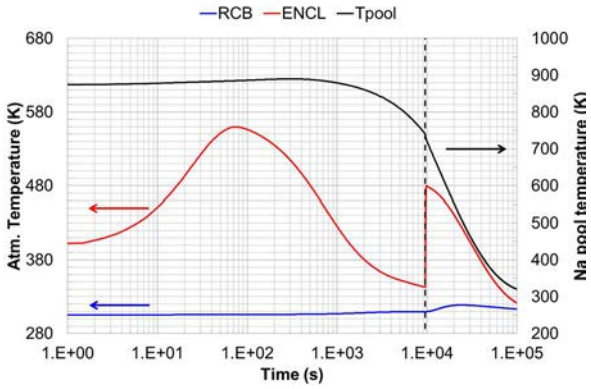

FIG. 261. Atmosphere temperature (Case 2).

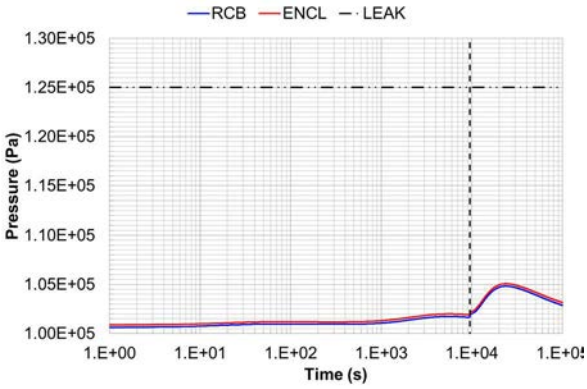

FIG. 262. Pressure (Case 2).

6.6.2.2. *Aerosol behavior*

Aerosol behaviour is described through three variables: suspended mass concentration, Aerodynamic Mass Median Diameter (AMMD) and final mass distribution.

FIG. 263 shows the evolution of the aerosol concentration in case 1. After reaching the concentration maximum (~3.4E-3 $kg \cdot m^{-3}$) during sodium burning, a gentle decreasing trend is observed as a pseudo steady state resulting from slow gravitational settling until the tendency speeds up after around 3000 s; as shown in FIG. 264. Between the end of the fire and 3000 s, a net particle growth resulting from the dominance of Brownian agglomeration over settling is predicted, which became more accentuated between about 3000 s and 17000 s. Note that the log-scale in the y axis of the plot maximizes such a change in the growth rate slope. At 17000s the AMMD reached its maximum value (6.8 μm). The particle depletion rate is in the order of 1E-7 $kg/m^3 \cdot s$ until around 20000 s and from then on, once the concentration is lower than 1E-3 kg/m^3, it slowed down. As a final outcome of the transient, most of aerosol mass ends on horizontal surfaces, and a minor fraction (less than 8%) is deposited on vertical walls mostly by thermophoresis (FIG. 265).

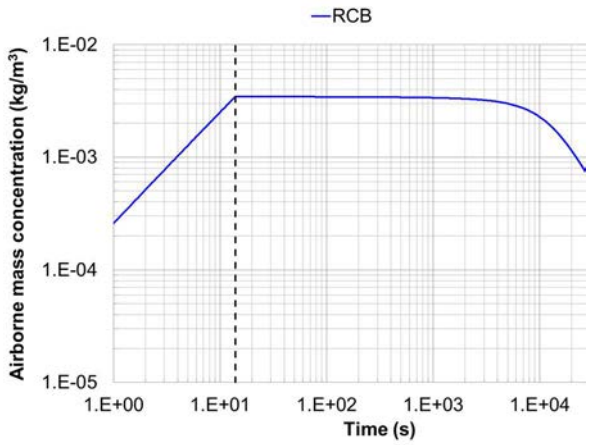

FIG. 263. Airborne concentration (Case 1).

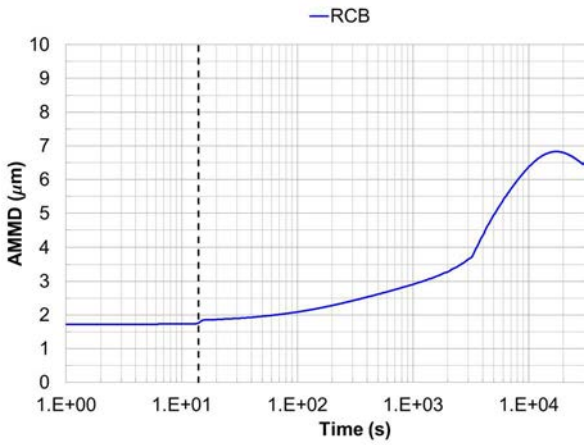

FIG. 264. AMMD (Case 1).

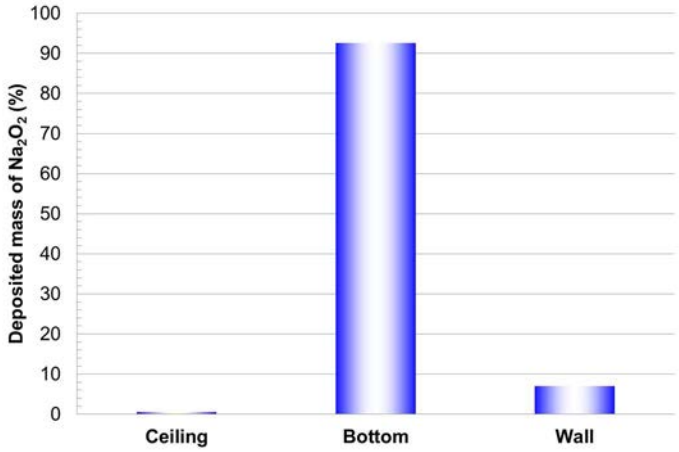

FIG. 265. Aerosol mass distribution (Case 1).

In case 2 (FIG. 266), it must be highlighted that more than 99% of the aerosolized Na_2O_2 (all the Na_2O has been assumed not to be aerosolized) aerosol generated remained in the enclosure volume and is there deposited. The airborne concentration in the enclosure volume increased with time until reaching the maximum value at 440 s (~ 0.1 kg/m^3), then it progressively decreased until the end of the fire due to both the lower aerosol generation from Na combustion and the enhancement of gravitational settling at such big particle diameters (~5.5 μm at the time of peak concentration, FIG. 267). It is worth noting that the decreasing trend slows down with time, being of the order of 1E-4 kg/m^3·s right after the maximum and falling nearly 2 orders of magnitude (1E-6 kg/m^3-s), once the fire is fully over. Note that particle size (FIG. 267) continued growing for around 300 s after the concentration maximum despite the deposition of the bigger particles by sedimentation due to agglomeration and less particle generation (which size is smaller than the aged particles remaining airborne). At the time the fire is entirely extinguished, the small AMMD increase was due to the total elimination of any particles at the lower bound of the size distribution generated by the fire.

In the RCB, as foreseen, up to 3 orders of magnitude lower airborne concentrations were predicted (2 of which are the result of the volume ratio between both compartments). In this compartment the maximum was reached at 60 s, notably still during the sodium pool fire in the enclosure. Then, it remained almost constant until at the end of the fire when the pressure balance between compartments drove some outflow from the enclosure into the containment and a slight concentration increase was noted. As the particles carried from the enclosure are

bigger a sharp increase in AMMD was also observed. As for the final mass distribution, despite how it appears in FIG. 268, the RCB analysis can be neglected since the total mass deposited there was about 1% of that deposited onto the enclosure surfaces. The relative mass distribution is rather similar to the one discussed in case 1. The enclosure, though, showed a notably different distribution than the one in case 1. Sedimentation was still the main depletion mechanism, but just about 61% of the mass was driven to horizontal surfaces. Significant fractions of the Na mass is estimated to be deposited onto vertical walls and ceiling (~28% and 11%, respectively). As discussed in the thermal analysis, the high temperatures reached in the atmosphere might have given rise to huge temperature gradients and so that thermophoresis was the competing mechanism with sedimentation in the enclosure.

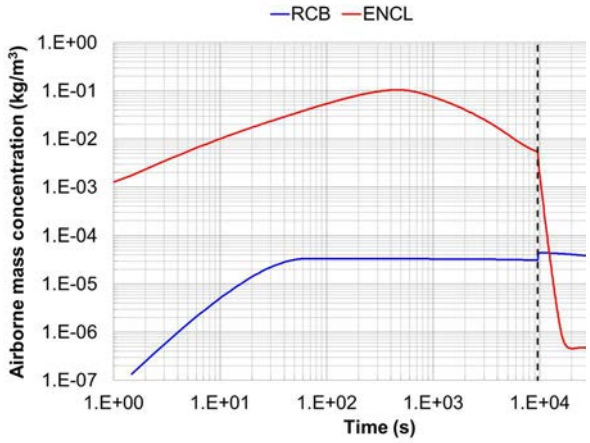

FIG. 266. Airborne concentration (Case 2).

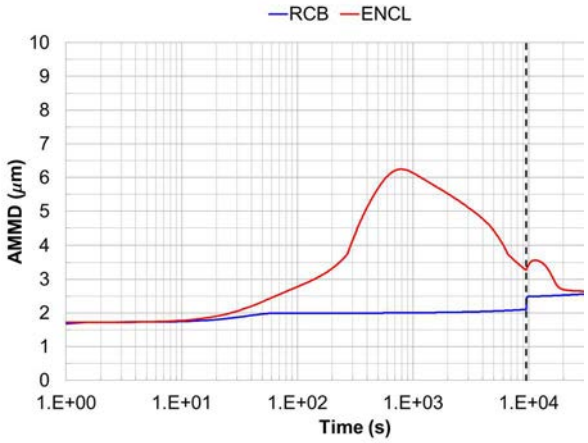

FIG. 267. AMMD (Case 2).

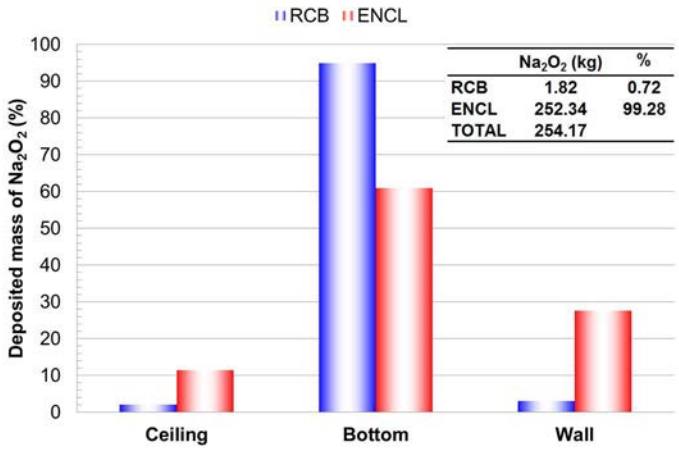

FIG. 268. Aerosol mass distribution (Case 2).

6.6.2.3. *FPs behavior*

Fission Products (FPs) transport in ASTEC-Na CPA is based on the concept of a host (i.e., FPs are carried by hosts). Five hosts are foreseen: gas, aerosol and water as mobile hosts and gas phase surfaces and water phase surfaces as immobile hosts. This approach entails a number of assumptions and limitations [55]: they do not contribute to the heat capacity of the host, do not transmute, do not chemically react and do not condense on surfaces. However, they may release thermal energy.

From the radionuclide inventory at the 100 GWd/t burnup case given in the technical specifications report, the FPs masses entering the containment have been calculated through the law of radioactive disintegration and applying the settled release fraction for each FPs group, as shown in TABLE 65. The amount of FPs estimated has been injected for each case during the intensive phase of aerosol generation (10s in Case 1, 460s in Case 2).

TABLE 65. FISSION PRODUCTS INVENTORY

FP	Mass (kg)	Release fraction	FPs release (kg)
I	4.07E-1	1.0E-1	4.07E-2
Cs	3.31E+1	1.0E-1	3.31
Rb	1.17E-4	1.0E-1	1.17E-5
Ru	1.07E+1	1.0E-4	1.07E-3
Sr	6.30	1.0E-1	6.30E-1
Ce	1.09E+1	1.0E-4	1.09E-3
Te	1.70E-1	1.0E-4	1.70E-5
Ba	7.13E-1	1.0E-1	7.13E-2
Zr	2.22	1.0E-4	2.22E-4
La	9.54E-2	1.0E-4	9.54E-6
Kr	3.24E-1	1.0	3.24E-1
Xe	3.96E-1	1.0	3.96E-1

As expected from the above description of FP modelling in CPA*, FIG. 285 to FIG. 288 clearly indicate that the evolution of airborne FPs is determined by the aerosol (FIG. 287 and FIG. 288) and their deposition too (FIG. 289 and FIG. 290).

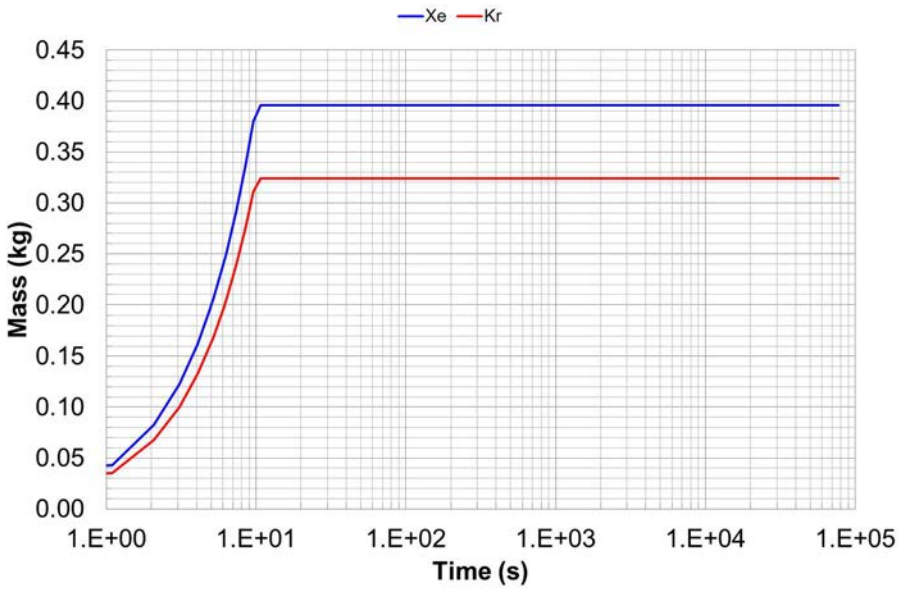

FIG. 269. Noble gases mass (Case 1).

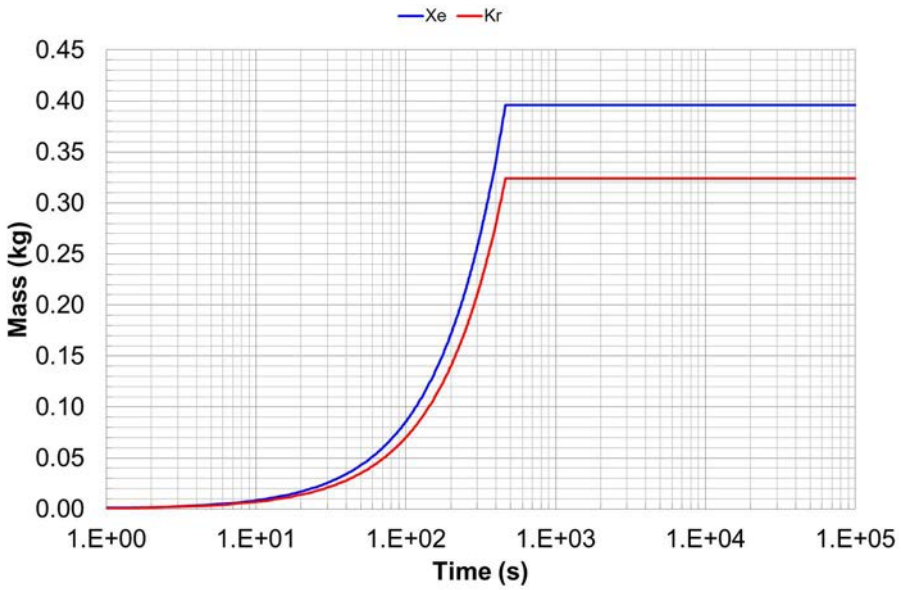

FIG. 270. Noble gases mass (Case 2, RCB).

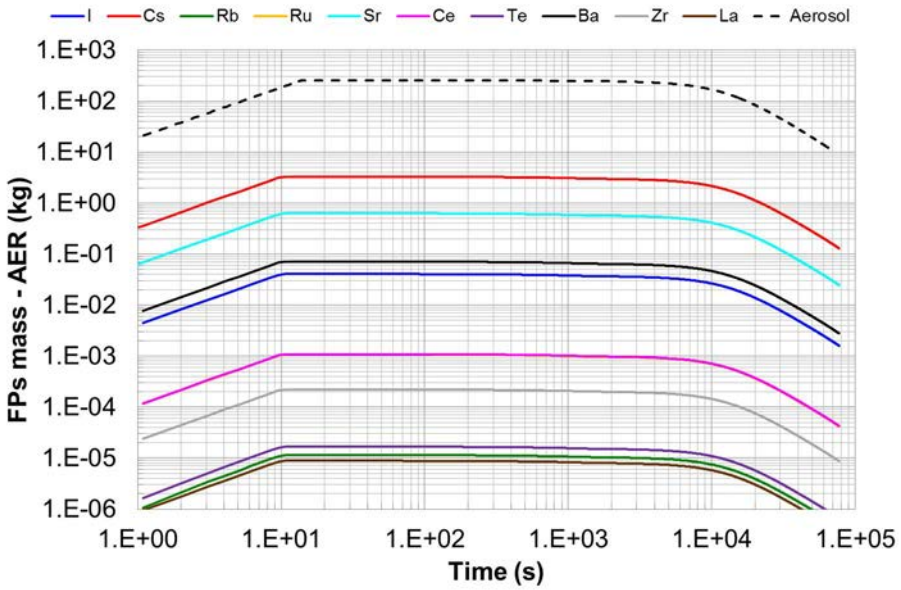

FIG. 271. FPs airborne mass (Case 1).

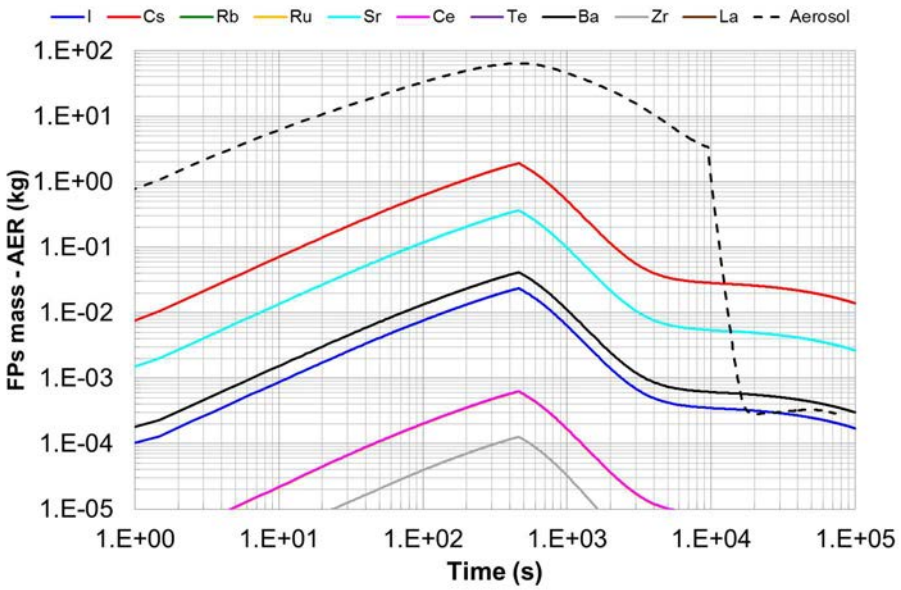

FIG. 272. FPs airborne mass (Case 2, RCB).

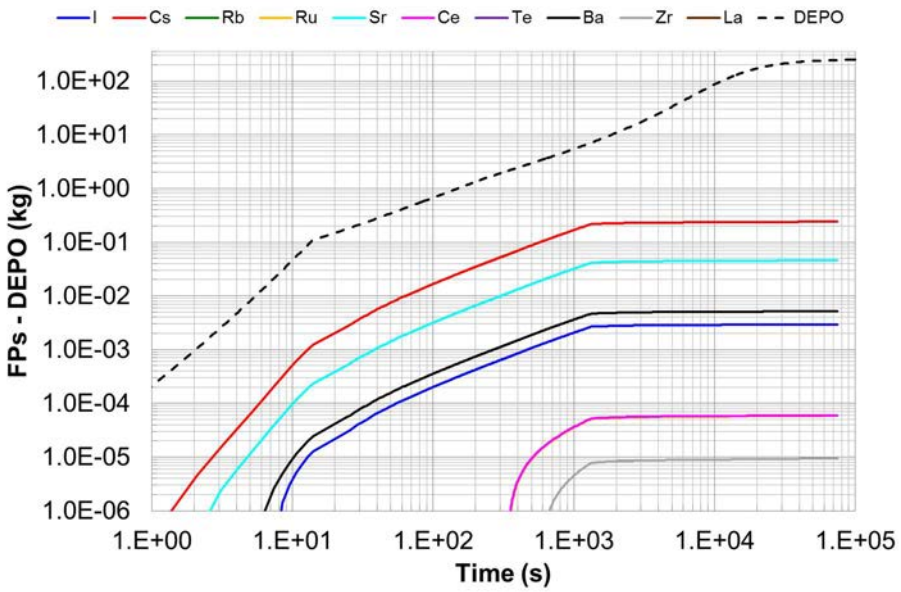

FIG. 273. FPs deposition (Case 1).

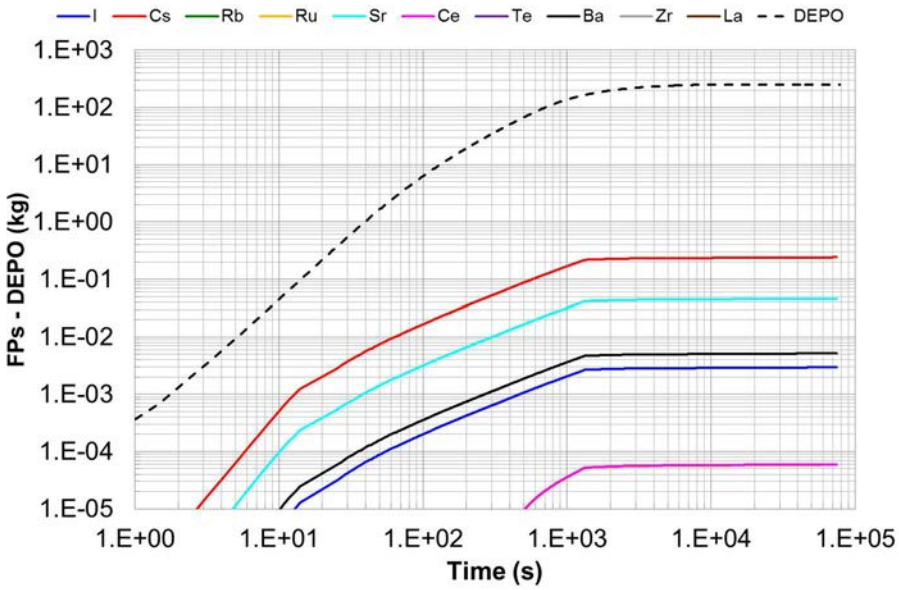

FIG. 274. FPs deposition (Case 2, RCB).

6.6.3. **Summary**

A numerical model of a postulated reactor containment building of a typical medium to large sized pool type SFR during a hypothetical CDA was developed in the frame of the IAEA CRP project. The simulation was based on the conditions derived after an energetic CDA which implies the release of 350 kg into the containment. The code used is ASTEC-Na. The material released within the project plus a number of hypothesis and assumptions have been the basis of the modelling.

The in-containment phenomenology analysis reveals maximum pressures during sodium spray and pool fires far away from the overpressure containment threshold. As for aerosol behaviour, a huge aerosol production in the order of hundreds of kilos is estimated. An exponential decrease of airborne aerosol as a consequence of particles natural depletion mechanisms, among which gravitational sedimentation dominates is predicted in the sodium spray fire. In the case with enclosure, however, the final aerosol mass distribution suggests that thermophoresis might play a key role when large temperature gradients are established.

6.7. SIMULATION EXERCISE USING CONTAIN-LMR CODE (TERRAPOWER, USA)

6.7.1. **Description of Methods and Model**

6.7.1.1. *Model Options, Nodalization, and Conditions Used*

TerraPower performed both cases in WP-3 as defined in Section 3:

— Case 1: sodium spray fire in the reactor containment building
— Case 2: sodium pool fire in the small enclosure space

Case 1 provided a baseline comparison among the WP-3 participants. Since the ejected sodium was sprayed in a large space with sufficient oxygen, the sodium chemical reaction occurs instantaneously. FIG. 275 shows the CONTAIN-LMR noding scheme including the control volumes, sodium spray fire location, and heat structure options. The containment leak was not

assumed so it would result in the limiting containment responses in terms of pressure and temperature.

Case 2 was a more realistic simulation as the ejected sodium is initially confined within the small enclosure volume above the reactor roof slab. Additionally, the containment heating, ventilating, and air-conditioning (HVAC) system was also included and was isolated within 10 seconds during the event. As shown in FIG. 276, a few more volumes were added in the CONTAIN-LMR model (i.e., volume nos. 4 and 5) in order to simulate proper natural circulation between the enclosure volume (volume no. 1) and the containment volume (volume no. 2).

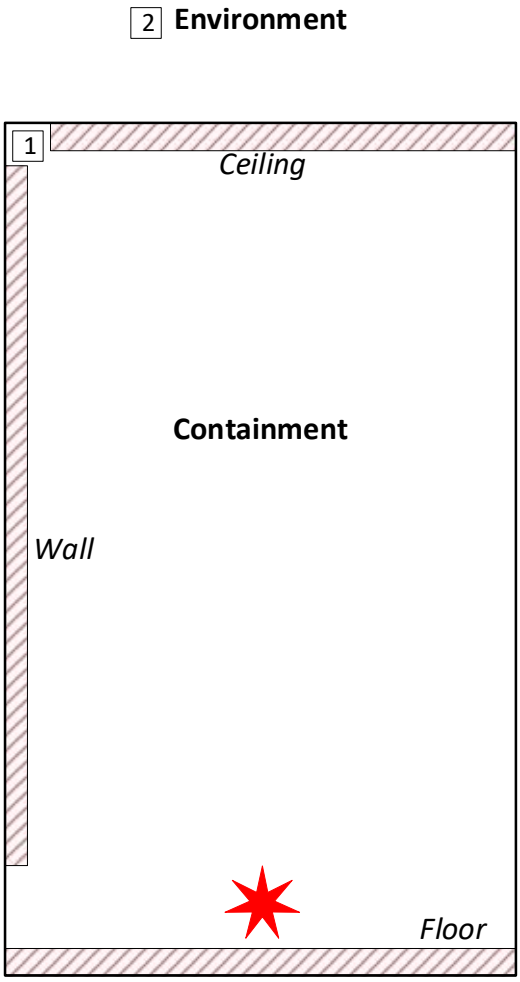

FIG. 275. CONTAIN-LMR noding scheme for sodium spray fire (case 1).

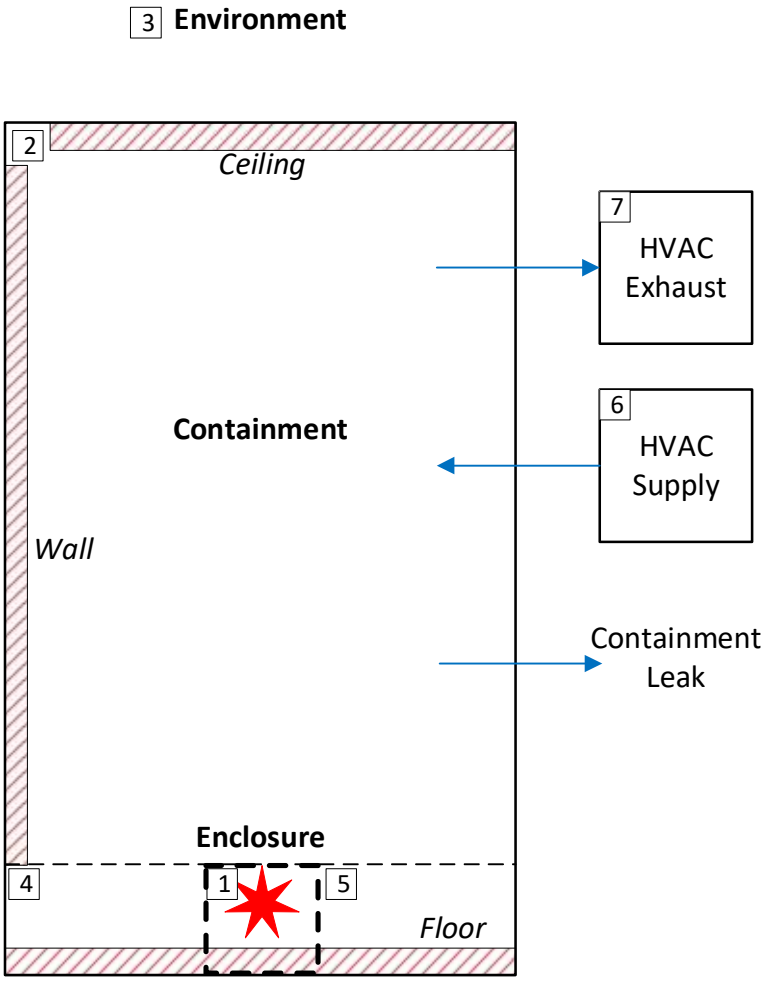

FIG. 276. CONTAIN-LMR noding Scheme for Sodium Pool Fire (Case 2).

The conditions used for the reactor containment building are shown in TABLE 66 and TABLE 67. As discussed above, a single volume was used for the sodium spray fire case and four volumes were used for the sodium pool fire in the reactor containment building. The natural circulation behavior between the enclosure volume and the containment volume is a very complicated but crucial phenomenon that needs to be modelled carefully. It is coupled to the sodium pool fire such that more circulation enhances the oxygen supply to the enclosure space, increases the sodium fire, and further promotes the air circulation. Currently CONTAIN-LMR is not capable of simulating detailed flow distribution. More sophisticated tools relying on porous media approach or computational fluid dynamics could be used to confirm the natural circulation and mixing behavior.

The heat structure noding in CONTAIN-LMR is a manual input and requires some insights. Depending on the anticipated heat transfer rate and material composition, the noding size should be adjusted appropriately to develop a suitable temperature profile within the nodes. Typically, this can be done by limiting the node size to meet a smaller Biot number.

TABLE 66. REACTOR CONTAINMENT BUILDING INPUTS FOR SODIUM SPRAY FIRE (CASE 1)

Input Parameters	Value	Note
RCB net free volume [m^3]	74,000	-
RCB height [m]	54.0	-
Initial temperature [°C]	30.0	303.15 [K]
Initial pressure [Pa]	100,600	-0.7 kPa

TABLE 67. REACTOR CONTAINMENT BUILDING INPUTS FOR SODIUM POOL FIRE (CASE 2)

Input Parameters	Value	Note
Enclosure volume (vol. no. 1) [m^3]	617.75	-
Enclosure height [m]	4.0	-
Enclosure ceiling area [m^2]	153.94	-
Enclosure wall area [m^2]	175.93	-
RCB volume (vol. no. 2) [m^3]	70,103.8	-
RCB height [m]	54.0	-
RCB ceiling area [m^2]	1,254.0	-
RCB wall area [m^2]	8,626.0	-
RCB floor area [m^2]	974.0	-
RCB internal wall area [m^2]	1,100.0	-
RCB horizontal surface area [m^2]	126.0	-
Volume no. 4 [m^3]	1,948.1	Left connection
Height of vol. no. 4 [m]	4.0	-
Volume no. 5 [m^3]	1,948.1	Right connection
Height of vol. no. 5 [m]	4.0 [m]	-

6.7.1.2. *Sodium Fire Model Options*

The sodium spray fire inputs to CONTAIN-LMR are rather simple from TABLE 68 as long as they capture appropriate sodium drop diameter distributions. Currently the sodium spray fire model based on the NACOM model in CONTAIN-LMR considers only the vertical downward injection and estimates the terminal velocity based on the sodium fall height. In this case the full height of the containment was used to completely burn the sodium along with a small drop diameter. Since all the oxygen in the containment is available to react, sodium peroxide was chosen as the sodium burn product, which also results in higher energy release than sodium monoxide.

TABLE 68. SODIUM SPRAY FIRE OPTIONS

Input Parameter	Value	Note
Sodium Amount [kg]	350.0	-

Sodium Mass Flow Rate [kg/s]	700.0	Linear function
Sodium Ejection Duration [s]	0.5	From 0.03 s to 0.53 s
Sodium Temperature [°C]	600.0	-
Sodium Fall Height [m]	54.0	-
Sodium Drop Diameter [mm]	1.0	Fine droplets
Sodium Burn Product	Na_2O_2	100%

There are many ways to simulate the sodium pool fire using CONTAIN-LMR. Typically, the initial pool conditions are given such that the pool surface is exposed to ambient conditions. However, in order to capture the initial sodium reaction dynamics during the sodium ejection period, the sodium spray fire model in CONTAIN-LMR was utilised to simulate this behavior. An arbitrary large drop diameter was introduced to limit the sodium drop burn and to achieve the sodium fill process into the enclosure volume. Although it takes very short time to fill up the sodium pool, the peak burn rate will start from the high sodium spray fire rate and then transit to the sodium pool fire rate. Therefore, the sodium will burn quicker than the pure sodium pool fire. TABLE 69 represents the sodium pool fire inputs.

TABLE 69. SODIUM POOL FIRE INPUTS

Input Parameter	**Value**	**Note**
Pool Surface Area [m^2]	150.0	Area of the enclosure floor
f_1	0.0	Fraction of total O_2 consumed that reacts to form monoxide
f_2	0.9	Fraction of sensible heat from the reaction to the pool
f_3	0.0	Fraction of Na_2O products that enters the pool after the fire
f_4	0.0	Fraction of Na_2O_2 products that enters the pool after the fire
Initial Sodium Amount [kg]	0.0	No sodium initially
Initial Sodium Temperature [K]	303.15	Maintain the initial structure temperature
Thickness of Roof Slab [m]	1.8	-

6.7.1.3. *Aerosol Dynamics Options*

During the hypothetical core disruptive accident (HCDA), noble gases, volatile elements, semi-volatile elements, as well as solid particles come out through the reactor core and leak through the gaps of the reactor vessel head seals via large core bubbles. The mass median diameter (MMD) of aerosols was varied from 0.1 micrometer (μm) to 10.0 μm for spray fire. Aerosols with larger MMD tend to settle sooner. However, once the larger MMD aerosols settle down, the suspended aerosol concentration converges regardless of the initial MMD. Mainly fine aerosols will be coagulated by Brownian motion and larger aerosols will be deposited due to gravitational settling. It is worth noting that during a sodium fire, a typical size of aerosols is an order of micrometres whereas that of fission products can be much smaller, i.e., submicron.

The MAEROS module in CONTAIN-LMR is a sectional-based aerosol tracking model. 20 sections (so-called 'bins') were used to cover very fine aerosols from the fission products to large aerosols that were agglomerated due to various interaction mechanisms. These 20 sections are ranged from 1E-7 m to 1E-4 m to cover the wide ranges of fission products as well as sodium chemical products. The default values in CONTAIN-LMR are both 1.0 for dynamic shape factor and agglomeration shape factor, which are used in MAEROS. Larger dynamic shape factor (χ) results in less deposition/removal of suspended aerosol whereas larger agglomeration shape factor (γ) results in more deposition/removal of suspended aerosols. Based on the previous test and CONTAIN-LMR simulations [56] the suggested ranges of dynamic shape and agglomeration shape factor for sodium peroxide (Na_2O_2) are 1.2 and 1.1 – 1.3, respectively. However, it should be noted that these values are slightly different when a mixture of other species such as CeO_2 exists. TABLE 70 presents the key aerosol dynamics inputs.

TABLE 70. KEY AEROSOL DYNAMICS INPUTS

Input Parameter	Value	Note
Dynamic shape factor (χ)	1.2	Different from the default value of 1.0
Agglomeration shape factor (γ)	1.2	Different from the default value of 1.0
Diffusion boundary layer thickness (deldif)	1E-5	Default
Thermal conductivity ratio (tkgop)	0.05	Default
Turbulent dissipation coefficient (turbds)	0.001	Default

6.7.1.4. *Fission Product Releases*

The inventory of the fission products is given as activity in Section 3. The radionuclide activities have been converted to mass, which is a direct input to CONTAIN-LMR. TABLE 71 shows the noble gas inventory and 100% of the noble gases are released during the event. The noble gases are released immediately to the containment or the enclosure space when they are ejected along with sodium.

TABLE 71. NOBLE GASES AND THEIR RELEASE FRACTIONS

Radionuclide	Activity in Fuel [Bq]	Mass in Fuel [Kg]	Release Fraction	Released Mass [Kg]
Kr-83m*	2.36E+15	3.09E-06	1.0	3.09E-06
Kr-85	2.24E+17	1.54E+01	1.0	1.54E+01
Kr-85m	4.04E+17	1.33E-03	1.0	1.33E-03
Kr-87	4.89E+17	4.67E-04	1.0	4.67E-04
Kr-88	2.52E+18	5.43E-03	1.0	5.43E-03
Kr-89*	2.63E+18	1.06E-04	1.0	1.06E-04
Xe-131m	1.46E+18	4.71E-01	1.0	4.71E-01
Xe-133	2.52E+18	3.64E-01	1.0	3.64E-01
Xe-133m	2.51E+18	1.51E-01	1.0	1.51E-01

Radionuclide	Activity in Fuel [Bq]	Mass in Fuel [Kg]	Release Fraction	Released Mass [Kg]
Xe-135	2.63E+18	2.80E-02	1.0	2.80E-02
Xe-135m*	2.21E+18	3.93E-02	1.0	3.93E-02
Xe-137*	5.19E+16	3.90E-06	1.0	3.90E-06
Xe-138*	4.98E+16	1.40E-05	1.0	1.40E-05

* These radionuclides were not included in the fission product transport model.

The following noble gases were modelled with decay chains in CONTAIN-LMR:

Kr-85m (4.48 hours) → Kr-85 (10.72 years) → Rb-85 (stable)

Kr-87 (76.3 minutes) → Rb-87 (4.7E+10 years; near stable)

Kr-88 (2.84 hours) → Rb-88 (17.8 minutes) → Sr-88 (stable)

Xe-131m (11.9 days) → Xe-131 (stable)

Xe-133m (2.188 days) → Xe-133 (5.245 days) → Cs-133 (stable)

Xe-135 (9.09 hours) → Cs-135 (2.3E+6 years; near stable)

The modelled radionuclides of noble gases cover more than 99.7% of those of the technical specifications in TABLE 71. Therefore, the decay chains would provide sufficient details of noble gas releases to the containment during the event.

The rest of fission products are modelled as aerosols. Condensation and entrainment are the key phenomena that form fine aerosols of fission products. The detailed aerosol transport mechanism from the fuel to the cover gas is not part of the WP-3 scope and the chemical forms are supposed to come from the WP-2 results. However, in this work, all the fission products except the noble gases are assumed to be aerosols. TABLE 72 shows the aerosol radionuclides and their release fractions from Section 3.

TABLE 72. RADIONUCLIDES AND THEIR RELEASE FRACTIONS

Radionuclide	Activity in Fuel [Bq]	Mass in Fuel [Kg]	Release Fraction	Released Mass [Kg]
I-131	1.46E+18	3.18E-01	0.1	3.18E-02
I-132	1.94E+18	5.08E-03	0.1	5.08E-04
I-133	2.51E+18	5.99E-02	0.1	5.99E-03
I-134	2.50E+18	2.53E-03	0.1	2.53E-04
I-135	2.21E+18	1.69E-02	0.1	1.69E-03
Rb-88	5.17E+17	1.16E-04	0.1	1.16E-05
Cs-134	5.19E+16	1.09E+00	0.1	1.09E-01
Cs-137	4.98E+16	1.55E+01	0.1	1.55E+00
Te-131m	1.61E+17	5.46E-03	0.0001	5.46E-07
Te-132	1.86E+18	1.63E-01	0.0001	1.63E-05

Radionuclide	Activity in Fuel [Bq]	Mass in Fuel [Kg]	Release Fraction	Released Mass [Kg]
Sr-89	6.31E+17	5.87E-01	0.1	5.87E-02
Sr-90	1.43E+16	2.80E+00	0.1	2.80E-01
Ba-140	1.91E+18	7.06E-01	0.1	7.06E-02
Ru-103	2.22E+18	1.86E+00	0.0001	1.86E-04
Ru-106	6.16E+17	5.05E+00	0.0001	5.05E-04
La-140	1.94E+18	9.44E-02	0.0001	9.44E-06
Zr-95	1.49E+18	1.88E+00	0.0001	1.88E-04
Cm-242	3.51E+16	2.86E-01	0.0001	2.86E-05
Cm-243	8.74E+12	4.58E-03	0.0001	4.58E-07
Cm-244	9.4E+14	3.14E-01	0.0001	3.14E-05
Ce-141	1.98E+18	1.88E+00	0.0001	1.88E-04
Ce-144	6.37E+17	5.41E+00	0.0001	5.41E-04
U-237	1.37E+17	4.54E-02	0.0001	4.54E-06
U-239	2.34E+19	1.89E-02	0.0001	1.89E-06
Np-238	2.8E+16	2.92E-03	0.0001	2.92E-07
Np-239	2.53E+19	2.94E+00	0.0001	2.94E-04
Pu-239	2.38E+15	1.05E+03	0.0001	1.05E-01
Pu-240	3.68E+15	4.38E+02	0.0001	4.38E-02
Pu-241	3.08E+17	8.04E+01	0.0001	8.04E-03
Pu-242	4.61E+12	3.17E+01	0.0001	3.17E-03

Since many of elements behave similar and there are also limitations on number of components that can be tracked at the same time, the radionuclides were grouped as shown in TABLE 73. This grouping is consistent with typical light water reactor applications.

TABLE 73. RADIONUCLIDE GROUPS MODELLED

No.	Group Name	Elements	Radionuclides
1	Noble Gases	Kr, Xe	Kr-85m, Kr-85, Kr-87, Kr-88, Xe-131m, Xe-133m, Xe-133, Xe-135
2	Halogens	I	I-131, I-132, I-133, I-134, I-135
3	Alkali Metals	Cs, Rb	Rb-88, Cs-134, Cs-137
4	Tellurium	Te	Te-131m, Te-132
5	Barium and Strontium	Ba, Sr	Sr-89, Sr-90, Ba-140
6	Noble Metals	Ru	Ru-103, Ru-106
7	Lanthanides	La, Zr, Cm	La-140, Zr-95, Cm-242, Cm-243, Cm-244
8	Cerium	Ce, U, Np, Pu	Ce-141, Ce-144, U-237, U-239, Np-238, Np-239, Pu-239, Pu-240, Pu-241, Pu-242
9	Sodium	Na	Na-24*

* Na-24 was not specifically tacked in the CONTAIN-LMR model but rather the sodium chemical products ($Na_2O_2$and Na_2O) were used as a surrogate to track sodium in the containment.

Each group of aerosols has the same size distributions such that it will have the same natural deposition rate. The aerosol size can be vary depending on the event and the transport

phenomena. Typically, a distribution of fission products is submicron in diameter. In the analysis, between 0.1 μm and 1.0 μm was assumed. As shown in the previous sensitivity study, smaller aerosols take more time to deposit on the containment surface.

The release rates of the aerosols are controlled by the sodium burn rate. During the sodium spray fire, the aerosols are released during the sodium injection period since the injected sodium reacts instantaneously within the containment. While the sodium spray fire lasts much longer, the aerosol release profile mimics the sodium burn profile.

Due to the limitation of CONTAIN-LMR the decay processes of the rest of radionuclides were not explicitly modelled. This would impact the concentrations of the relatively short-lived radionuclides compared with the duration of interest, i.e., 24 hours. It is noted that the decay process will suppress the natural deposition process, as it will reduce the radionuclide concentration – less probability of agglomeration. Overall, it is believed that ignoring the radionuclide decay may not have significant impact. It should be noted that the decay heat was not modelled in this study.

The reactor core inventory carries a large amount of plutonium compared with other elements. Applying a release fraction that is based on the radionuclide group would results in a very large release of plutonium to the containment and eventually to the environment. A more mechanistic simulation from WP-1 and WP-2 would be very beneficial to estimate appropriate heavy elements including plutonium, uranium, neptunium, etc.

6.7.2. **Results**

6.7.2.1. *Sodium Spray Fire Results (WP-3 Case 1)*

350 kg of sodium was ejected into the reactor containment building for 0.5 second, as shown in FIG. 277. The sodium mass flow rate is assumed to be a step function instead of the detailed profile function that was calculated from IGCAR. Since it's a very short duration and the sodium spray fire occurs instantaneously, this would have little to no impact on the overall result.

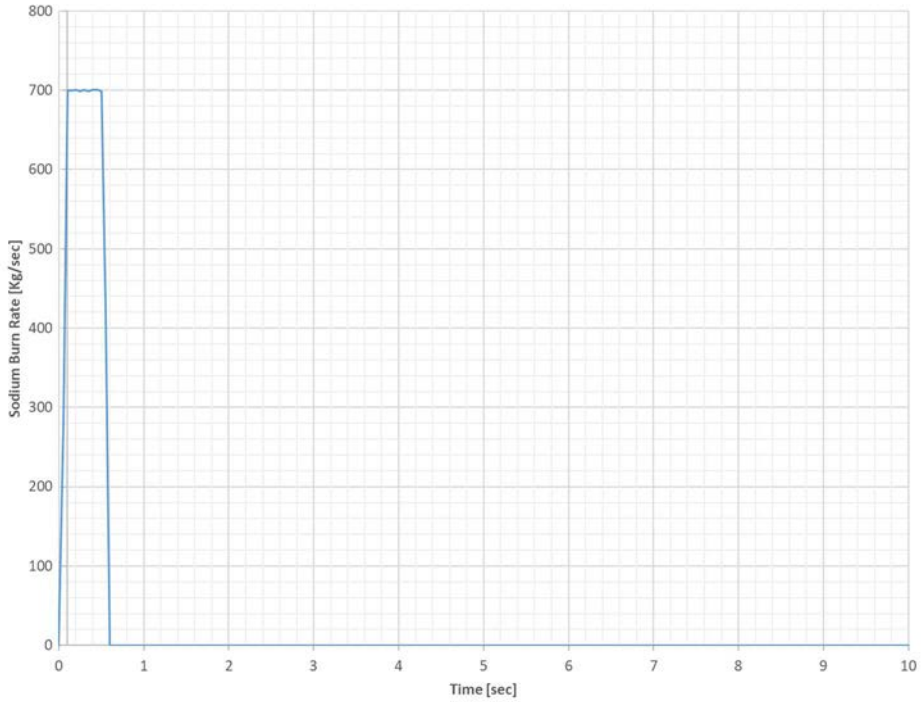

FIG. 277. Sodium Burn Rate during Sodium Spray Fire.

The ejected sodium reacted with oxygen in the containment and quickly exhausted when the sodium ejection terminated, as shown in FIG. 278. The containment provides sufficient oxygen with a large fall height so the major product of sodium chemical reaction would be Na_2O_2 rather than Na_2O.

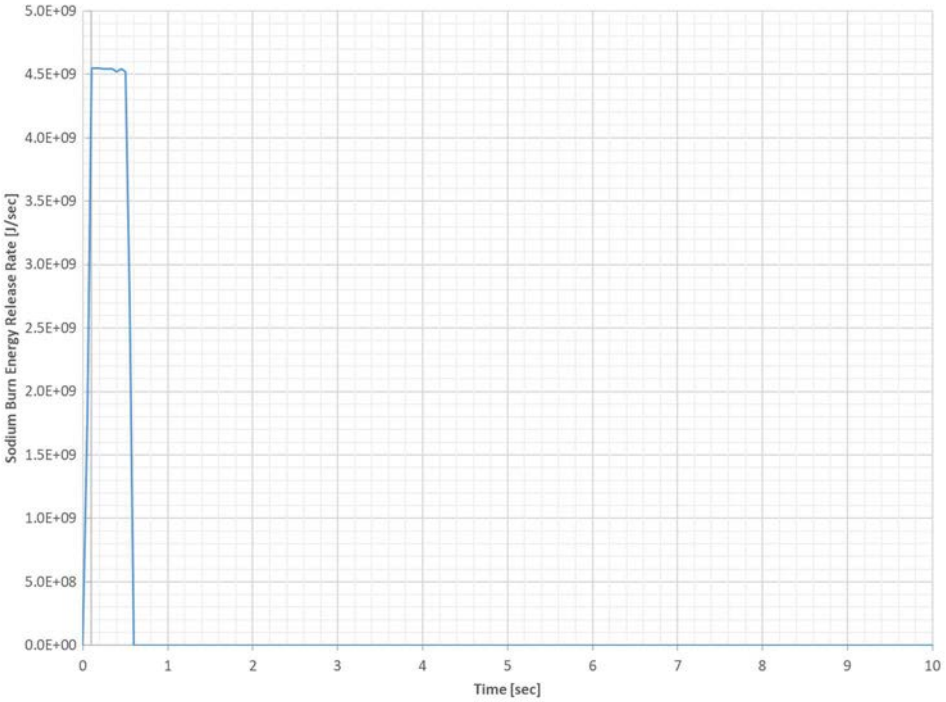

FIG. 278. Sodium Burn Energy Release Rate during Sodium Spray Fire.

The sodium reaction energy drove the reactor containment building pressure and temperature immediately, as shown in FIG. 279 and FIG. 280. Since no containment leakage is assumed to the environment during the event, this case resulted in the peak containment pressure during the postulated sodium fire, which may inform the containment design. The peak containment pressure was 122,500 Pa [or 11.9 kPa increase]. The peak containment temperature was 339.9 K [or 36.75 K increase]

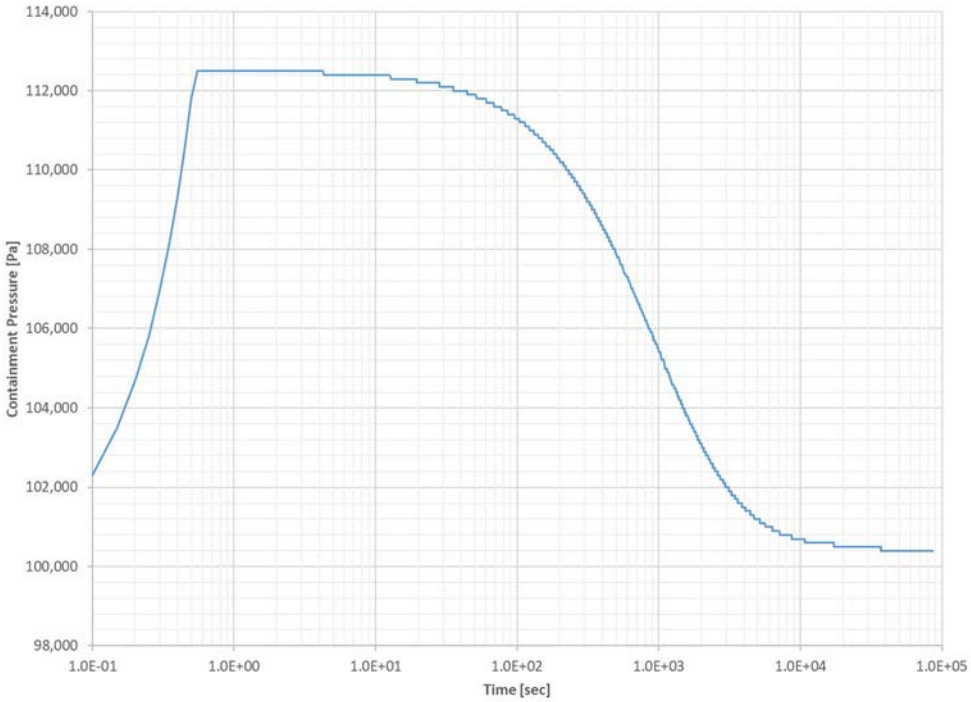

FIG. 279. Containment pressure response during sodium spray fire.

The containment pressure and temperature gradually decreased as the energy in the containment atmosphere transfers to the structures in the reactor containment building. Especially, the containment walls were dominant heat sinks due to the higher heat transfer rates compared with horizontal surfaces.

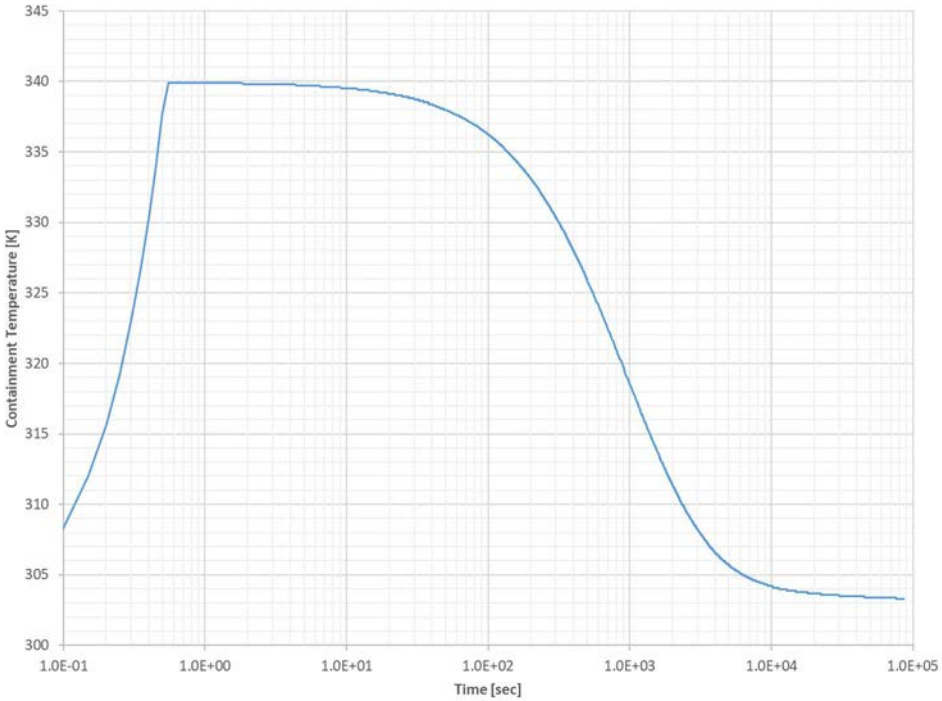

FIG. 280. Containment Temperature Response during sodium Spray Fire.

The aerosols from both the sodium chemical reaction and the fission products were released within the sodium ejection/reaction period, shown in FIG. 281. The aerosols remain in the containment atmosphere for a relatively longer period, which is believed due to the fine aerosols agglomerating to become larger aerosols and finally falling and depositing on the surfaces.

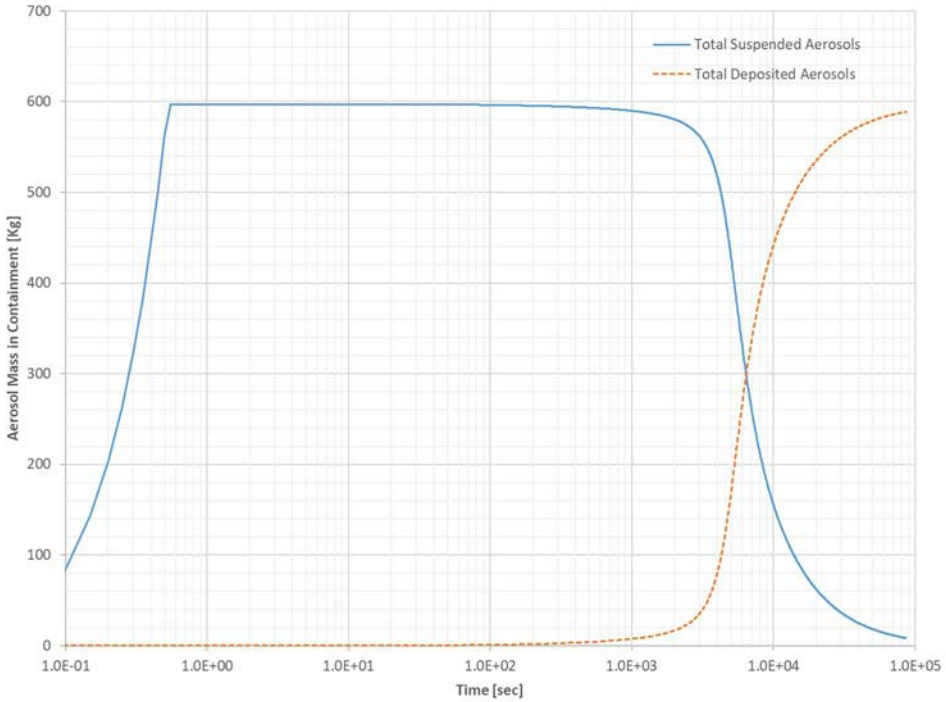

FIG. 281. Total Suspended and deposited Aerosol Mass in Containment during Sodium Spray Fire.

The noble gases, i.e., krypton and xenon, are also released during the sodium ejection period and remain in the containment during the entire duration, as shown in FIG. 282. It is noted that a small portion of noble gases were reduced due to decay.

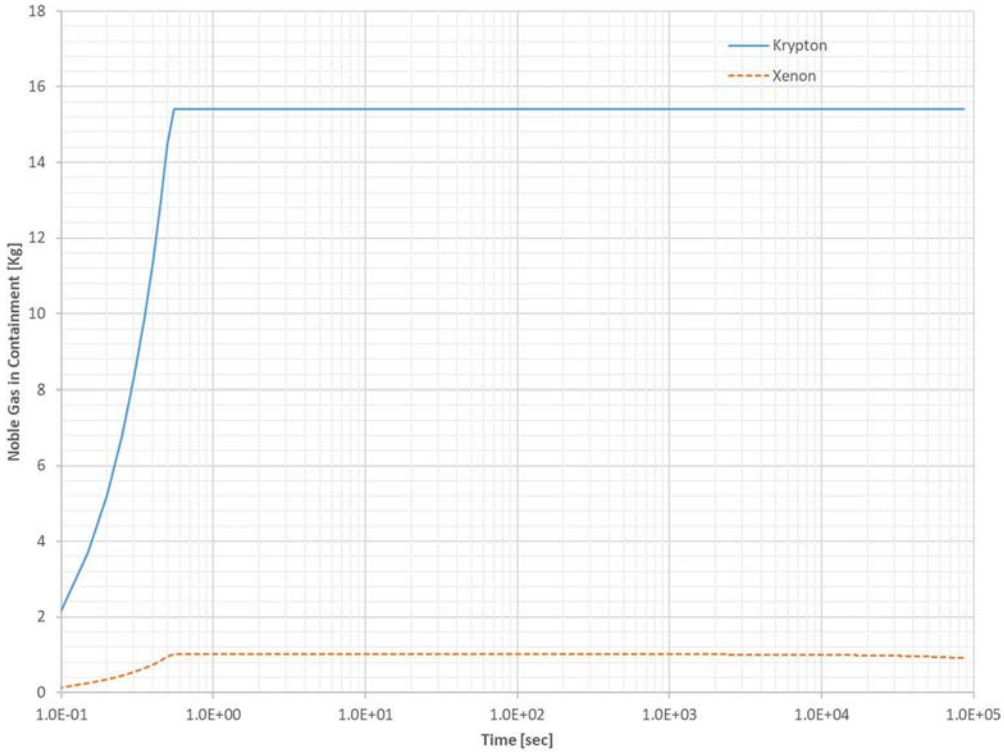

FIG. 282. Noble Gas Mass in Containment during Sodium Spray Fire.

FIG. 283 represents the suspended aerosol mass in the containment. Typical containment tools like CONTAIN-LMR may not track individual radionuclides or elements in some cases, so the radionuclide groups are often used. Their quantities are plotted in FIG. 283. Later these radionuclide groups can be decomposed to elements or radionuclides based on their original mass fraction while accounting for decay, removal, in-growth, etc.

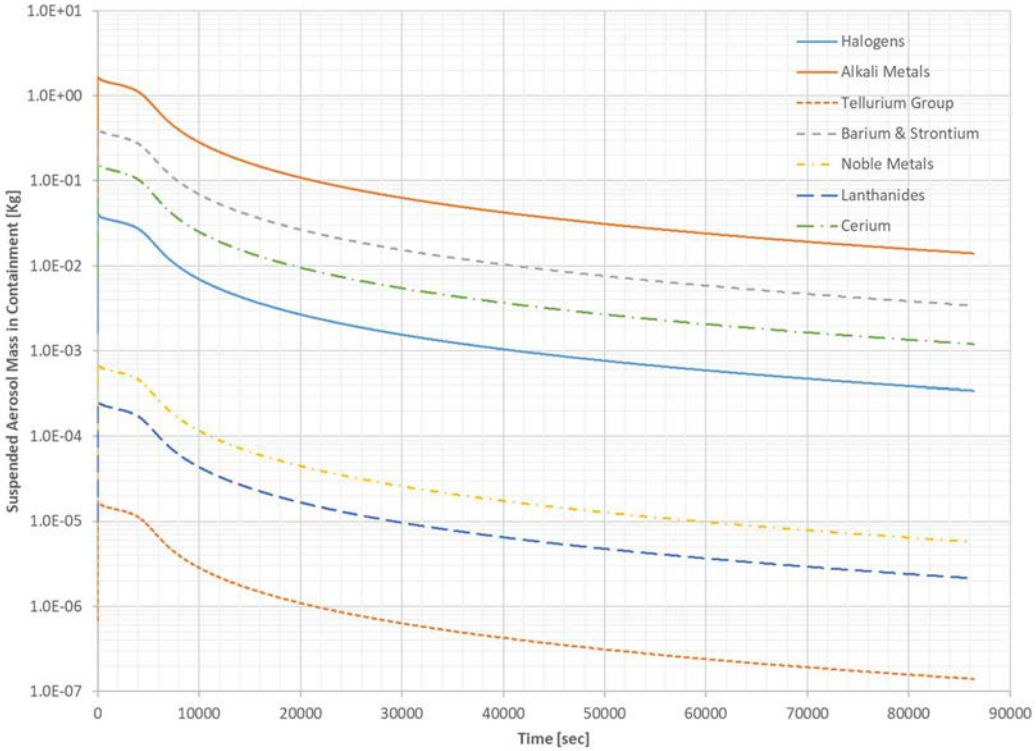

FIG. 283. Suspended Aerosol Mass in Containment during Sodium Spray Fire.

FIG. 284 shows the deposited aerosol mass in the containment. Similar to the previous figure, only radionuclide groups were plotted.

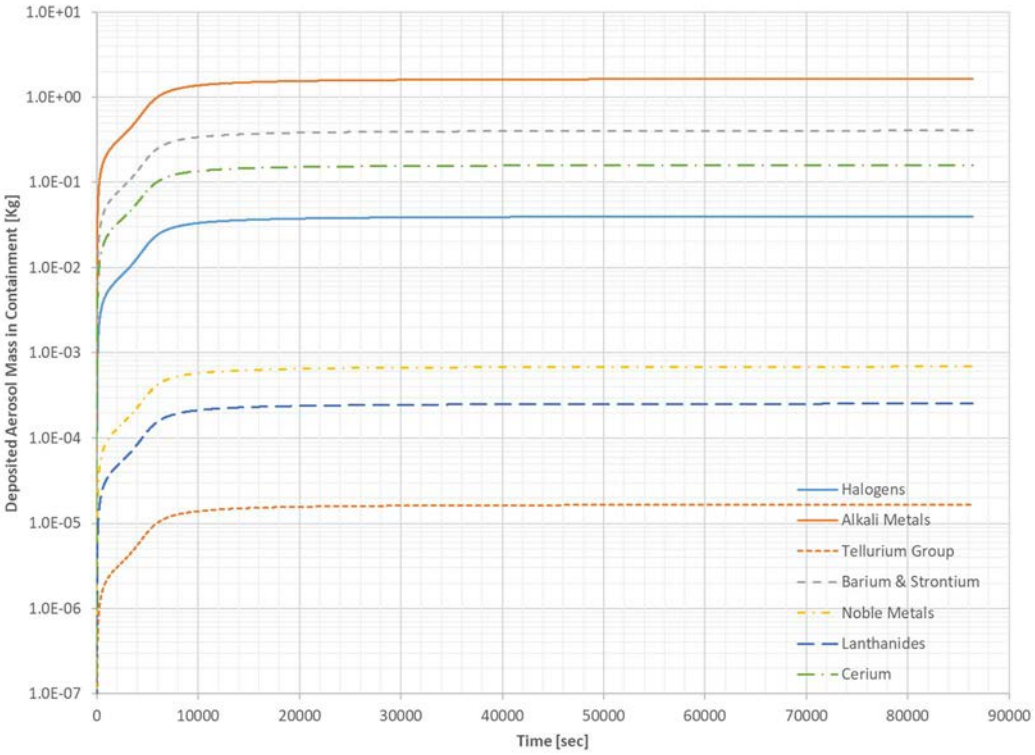

FIG. 284. Deposited Aerosol Mass in Containment during Sodium Spray Fire.

6.7.2.2. *Sodium Pool Fire Results (WP-3 Case 2)*

The sodium pool fire lasted much longer, till almost 280 seconds as shown in FIG. 285 compared with 0.5 second for the sodium spray fire in the previous section (i.e., Case 1). When the sodium is initially ejected, the atmosphere within the enclosure started reacting, but the overall sodium burn rate was maintained by the sodium pool surface area as well as the air exchange between the enclosure and the rest of the compartments in the reactor containment building.

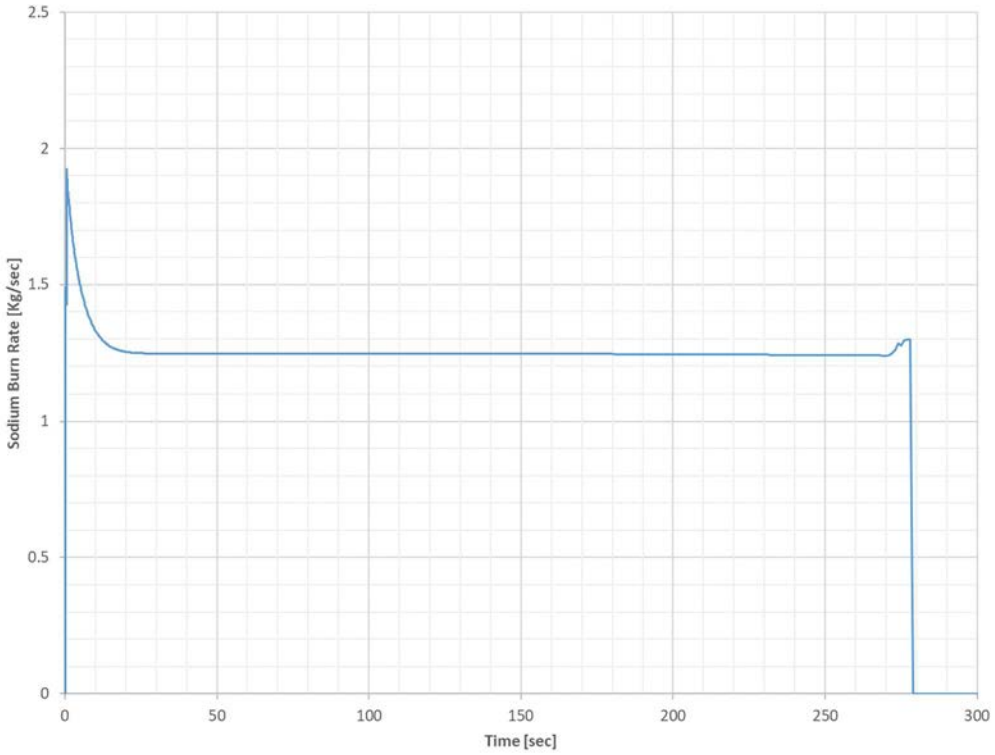

FIG. 285. Sodium Burn Rate during Sodium Pool Fire.

The energy release rate also depicts the sodium burn rate in FIG. 286. It should be noted that the initial peak of 8.2E-8 J/sec is due to the instant and complete burn of the sodium that was ejected at the beginning that did not yet form the sodium pool.

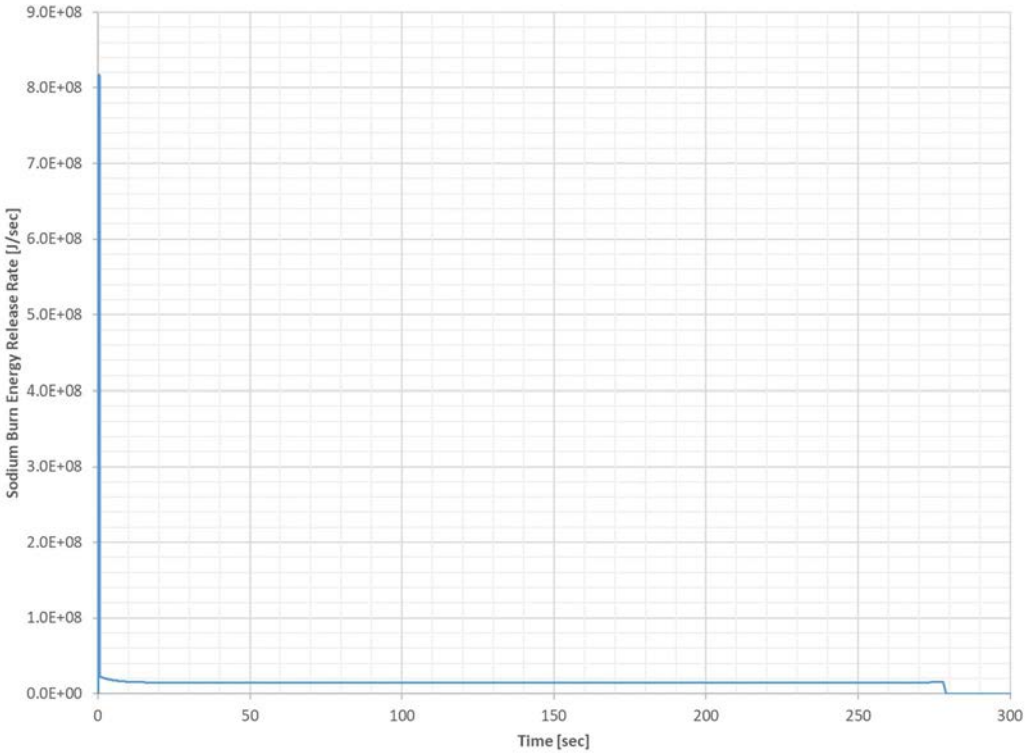

FIG. 286. Sodium Burn Energy Release Rate during Sodium Pool Fire.

From FIG. 287, the benefit of the enclosure structure is shown such that the peak containment pressure was dramatically reduced while delaying the sodium chemical reaction. The peak containment pressure was 105700 Pa [or 5.1 kPa increase]. This would further reduce and mitigate the radionuclide release to the containment and eventually to the environment.

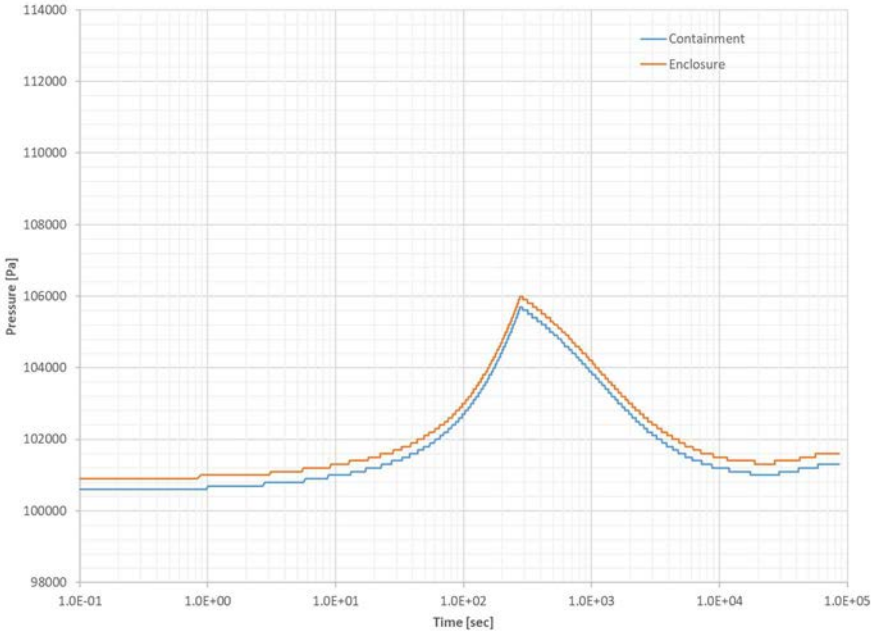

FIG. 287. Containment and Enclosure Pressure Responses during Sodium Pool Fire.

A similar impact is also shown in FIG. 288; the containment temperature was much lower here too. The peak containment temperature was 318.8 K [or 15.65 K increase]. Since the enclosure space temperature gets very high, i.e., 420.3 K, it is worth noting that a review of environmental qualification in the enclosure space may be necessary. Although it is a severe accident, potential

adverse impact on any important equipment or post-accident monitoring systems should be reviewed if applicable.

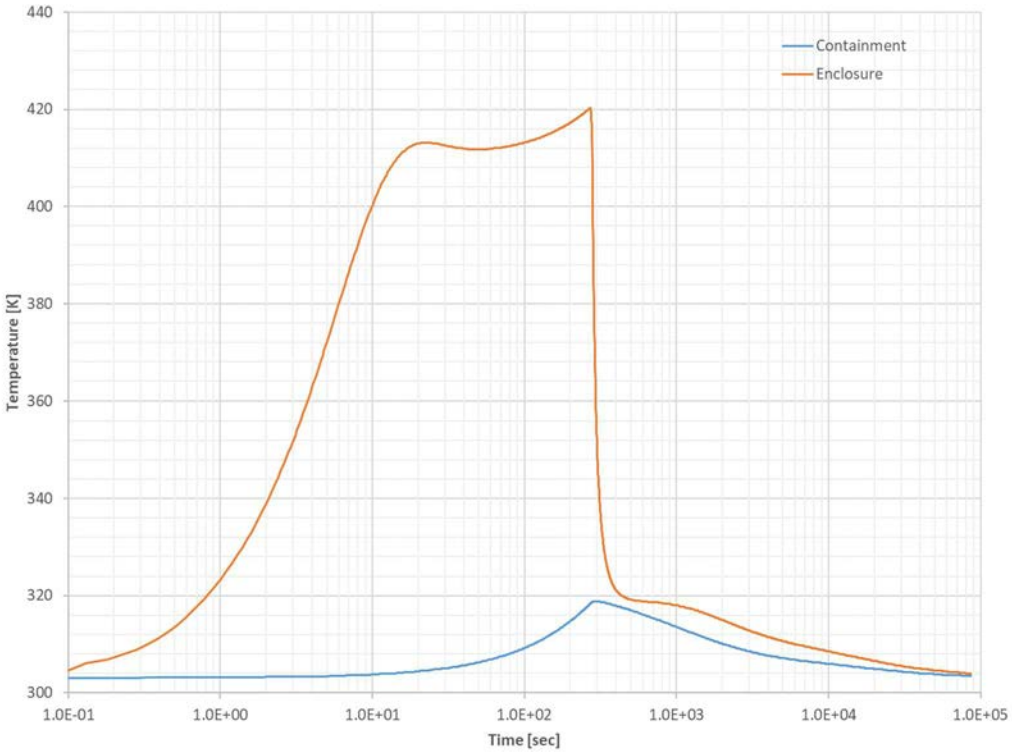

FIG. 288. Containment and Enclosure Temperature Responses during Sodium Pool Fire.

The aerosols ejected fission products were modelled proportional to the sodium chemical reaction rate. However, the fission products may come out quicker and spread out in the containment slightly earlier than the sodium chemical reaction profile. If the fission products are released earlier, the behavior would be closer to the sodium spray fire (i.e., Case 1). The mass of the fission products is much smaller than the sodium chemical products and the mass mean diameters are very different so their interactions may take a longer and overall impact may not be significant. However, if the containment isolation is delayed and its heating, ventilating, air-conditioning (HVAC) system is operating prolong time, the environmental consequences should be carefully reviewed due to this release timing difference. The suspended and deposited aerosol profile is similar to the previous case except the slight shift of the timing in FIG. 289.

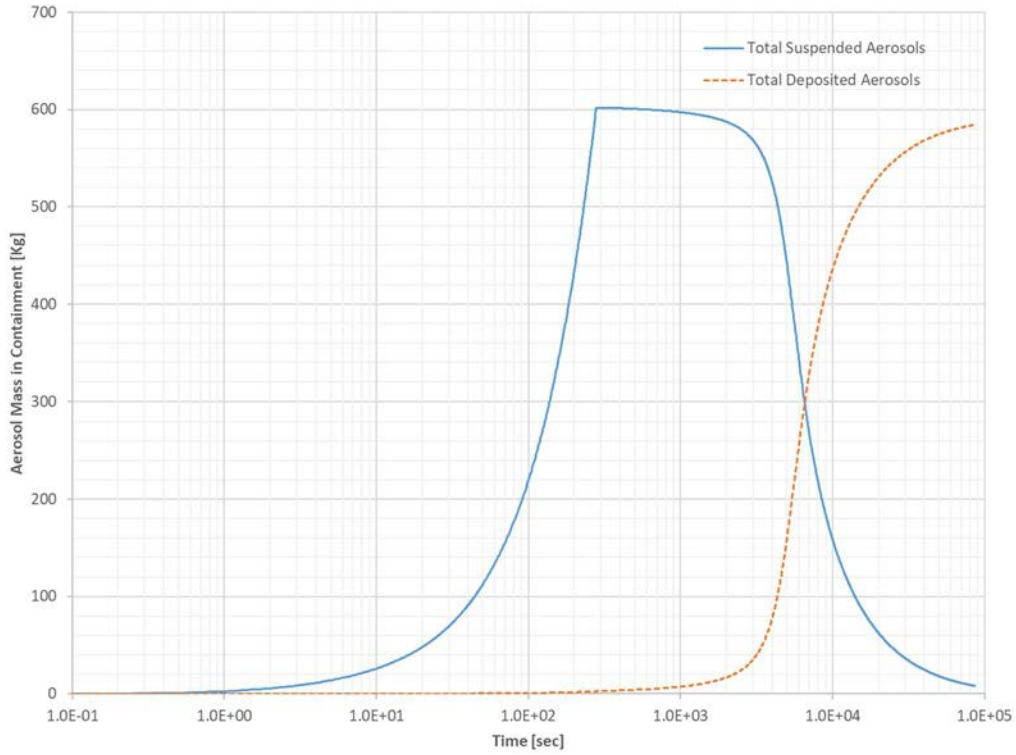

FIG. 289. Total Suspended and Deposited Aerosol Mass in Containment during Sodium Pool Fire.

Unlike fission product aerosols the noble gases were ejected with the sodium so the behavior is similar to Case 1 as shown in FIG. 290.

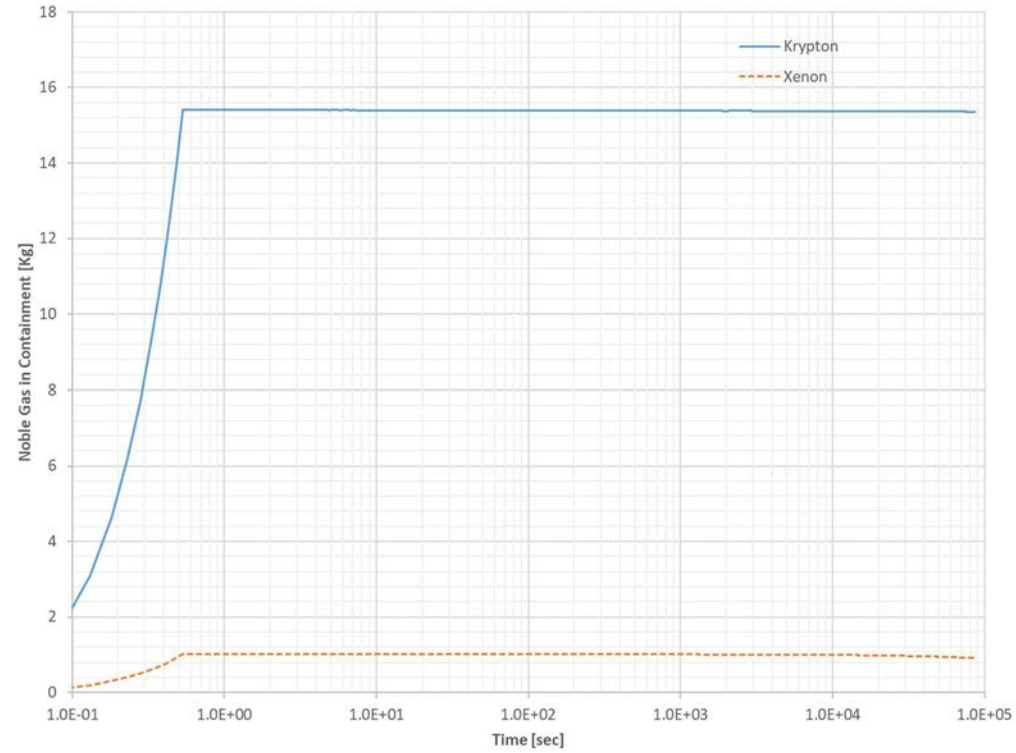

FIG. 290. Noble Gas Mass in Containment during Sodium Pool Fire.

Although the fission product aerosols were released slowly in accordance with the sodium chemical reaction, the overall behavior was very similar to the sodium spray fire as shown in FIG. 291. The containment leakage was modelled during the sodium pool fire and some aerosols were released with the containment leak to the environment. It is noted that the aerosol deposition through the microstructures of the containment concrete wall during the leak is beyond the scope of the CRP and was not modelled here.

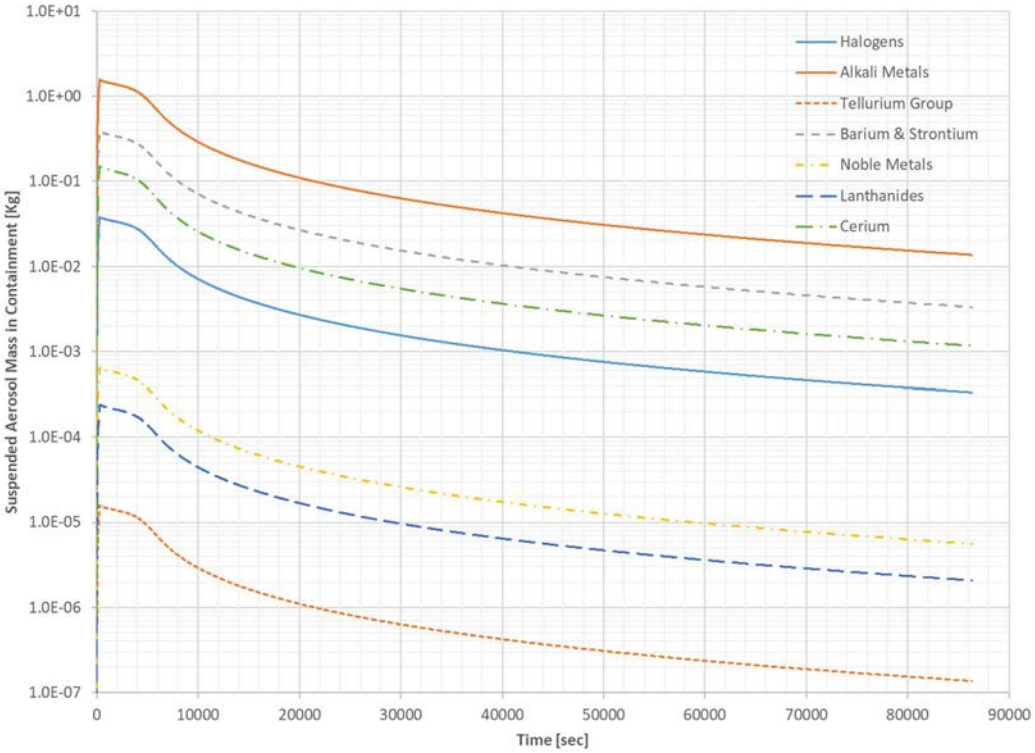

FIG. 291. Suspended Aerosol Mass in Containment during Sodium Pool Fire.

FIG. 292 represents the deposited aerosol mass in the containment during the sodium pool fire.

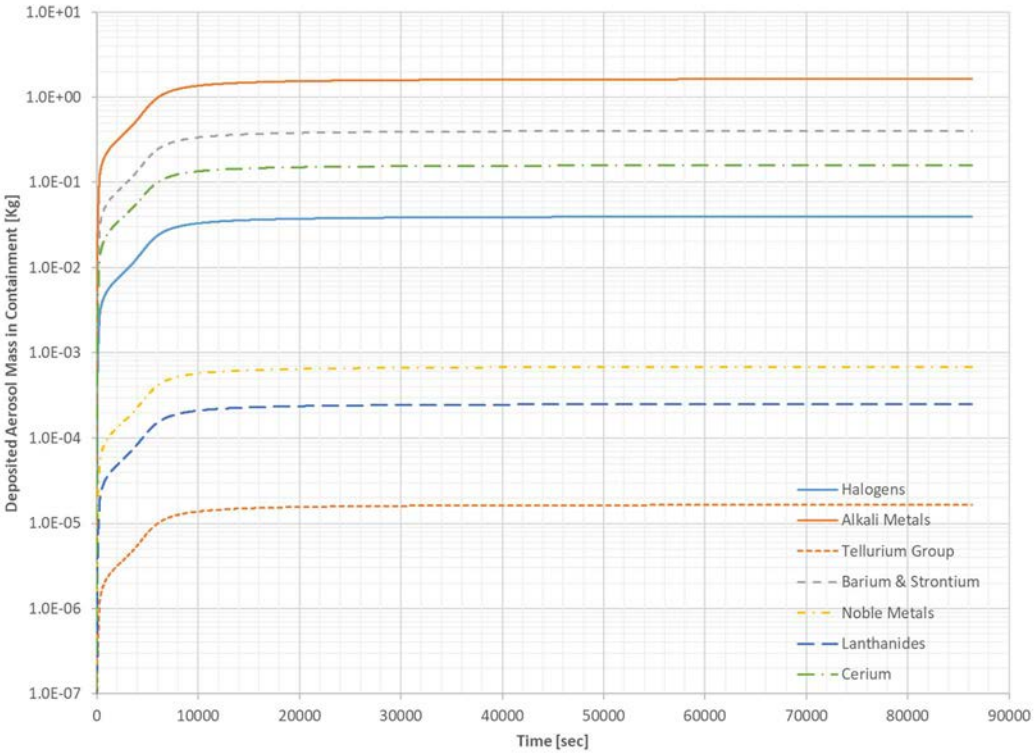

FIG. 292. Deposited Aerosol Mass in Containment during Sodium Pool Fire.

6.7.3. Summary

The sodium pool fire modelling is relatively complex and thus requires more empirical or semi-empirical input parameters that must be supplied by a user. Additionally, those inputs need to be justified for the particular conditions. Typically, this results in a validation of the evaluation models relying on prototype experiments. Furthermore, the initial formation of the sodium pools is also difficult to model, which should simulate both the sodium burn and the sodium ejection and/or fill.

During the CRP the participants discussed on the aerosol deposition phenomenon through very fine concrete structures like small pores, micro cracks, and torturous paths in the containment wall. This is necessary to determine a realistic activity release to the environment. However, this work scope may stretch too much the participants, given the CRP schedule, so it was not pursued as part of this CRP. Typically, no credit has taken during the design basis events since it is a complex matter. It is worth noting that the U.S. Nuclear Regulatory Commission (USNRC) sponsored code, RADTRAD [57], has the Brockmann model [58] that estimates the aerosol deposition through piping bends, but this option was never formally reviewed for licensing applications.

7. COMPARISON OF SIMULATION RESULTS

This section provides comparison of results as obtained by each participating organization in respective work packages.

7.1. WORK PACKAGE 1: COMPARISON OF IN-VESSEL SOURCE TERM SIMULATIONS

Three organizations provided calculation results for work package 1: IGCAR, IBRAE RAN and JAEA. IGCAR and IBRAE RAN calculated RN fractions in cover gas starting from the input data on CDA as given in the benchmark. IBRAE RAN used EUCLID/V2 with SAFR/V1 which has mechanistic models for fission product transport (without chemical reactions) and IGCAR used thermo-chemical equilibrium calculations to determine the release fractions. However, JAEA conducted calculations of PDE phase of PSFR severe accident condition. Therefore, it is difficult to compare JAEA results with the other two.

The release fractions of xenon and krypton are 100% for both organizations IBRAE RAN and IGCAR. JAEA has reported that it takes about 10s from the initiation of the core expansion for the fission gases to arrive at the cover gas region based on SIMMER IV calculations. The comparison of caesium, iodine, strontium and tellurium release fractions are shown in FIG. 293 to FIG. 296 as calculated by IBRAE RAN and IGCAR

For caesium fractions in cover gas, there is good agreement between IBRAE RAN and IGCAR calculations with ideal and real mixture cases. The no-mixture case release fractions are very conservative as evident from the comparison, as expected. The agreement is likely due to the fact that most caesium is available in elemental form. Mechanistic models in this case are more likely to agree even though chemical reactions are not treated.

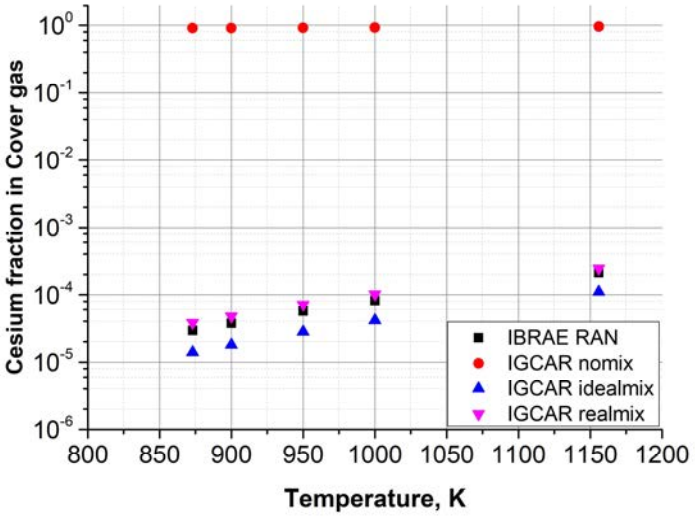

FIG. 293. Comparison of Caesium release fractions in cover gas.

For iodine the release fractions estimated by IGCAR with ideal/real mixture assumption is lower by at least an order of magnitude compared to IBRAE RAN estimates. The estimates diverge further at higher temperatures. However, the no-mixture case results are conservative compared to the IBRAE/RAN results. Since most of the iodine reacts with sodium, the model which considers the chemical reactions is likely to result in lower release fractions.

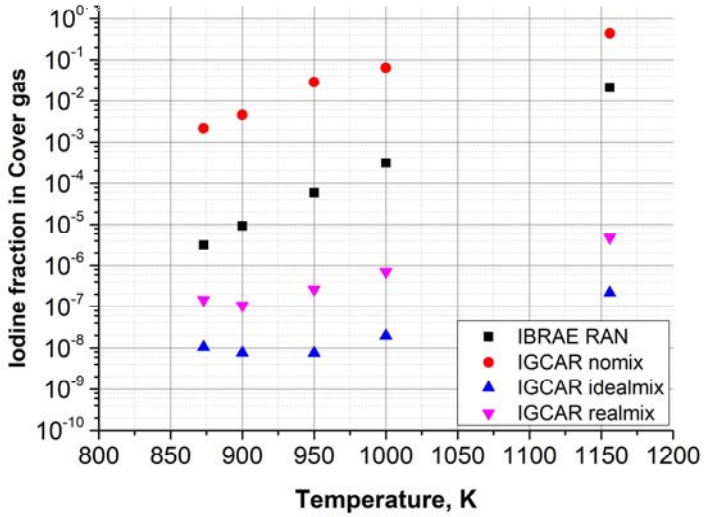

FIG. 294. Comparison of iodine release fractions in cover gas.

For strontium release fractions, IGCAR and IBRAE RAN predictions do not agree well. IBRAE RAN's values show a decreasing fraction with increase in sodium temperature. Whereas IGCAR's values increase with increasing temperature. Since vapor pressures generally increase with temperature, the increasing RF with temperature is expected from general considerations.

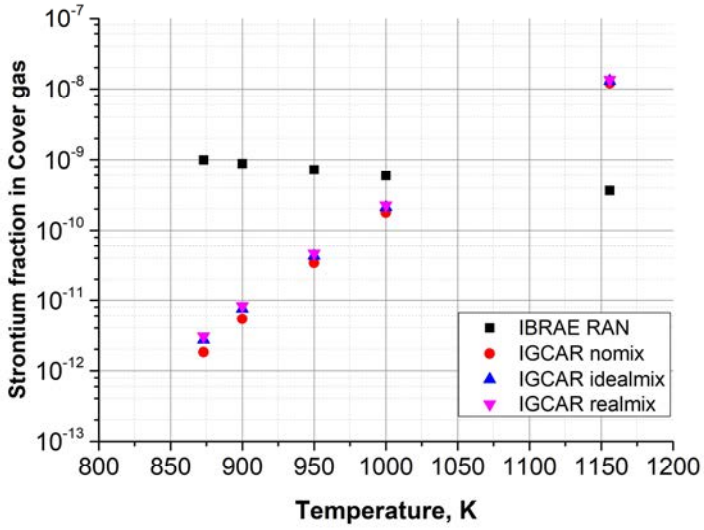

FIG. 295. Comparison of strontium release fractions in cover gas.

For tellurium release fractions, IGCAR and IBRAE RAN predictions are very low less than 1.0E-9, though the numbers are still many orders less for IGCAR.

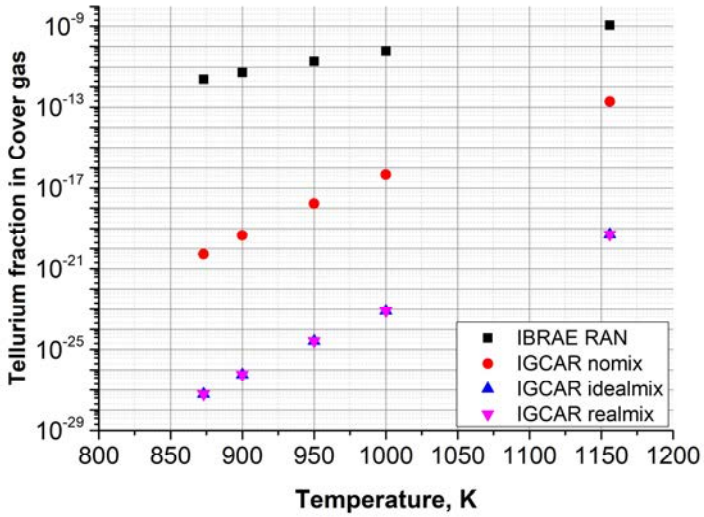

FIG. 296. Comparison of tellurium release fractions in cover gas.

7.1.1. Conclusions

The simulations of WP-1 were performed by IBRAE RAN using Russian EUCLID/V2 integral code, and by IGCAR using MINICHEM code. Both organizations showed 100% release of Xe and Kr into cover gas. The release fractions obtained by IGCAR and IBRAE RAN calculations generally agree with each other satisfactorily for fission gases, caesium and strontium (only near 1000K for strontium). For iodine and tellurium there is significant difference.

Possible reasons of differences in RN fractions in cover gas are:

- IGCAR and IBRAE RAN used two different approaches to calculate RN release. IGCAR used thermo-chemical approach to calculate chemical form and phase of RN to decide release behaviour. IBRAE RAN used interphase mass transfer mechanistic model;
- Differences in initial FP activity in coolant. For the calculations IGCAR assumes that all RN are initially effectively in coolant. Whereas IBRAE RAN calculates release from melted fuel to coolant and then coolant to cover gas;
- Thermodynamic parameters that were used for calculations
- Chemical reactions are not considered in IBRAE/RAN calculations.
- Transport and diffusion related retentions are not modelled in the IGCAR calculations.

Though IBRAE/RAN provided time dependent release fractions IGCAR has not reported time dependent release fractions due to the limitation of chemical equilibrium calculations. The chemical equilibrium model needs to be combined with a particle transport model in the future.

The results of SIMMER-IV calculation, mass, temperature and pressure distribution of fuel, steel, sodium and fission gas in reactor vessel have potential to be used in calculating RN transportation from fuel to cover gas through coolant sodium considering bubble transportation and diffusion of RN. Whether the RN diffusion and transportation model are implemented into the SIMMER code is one of the important issues to be discussed in further work.

7.2. WORK PACKAGE 2: COMPARISON OF SOURCE TERM SIMULATIONS FOR PRIMARY SYSTEM/CONTAINMENT SYSTEM INTERFACE

Overall, the calculation results of IGCAR, IBRAE, NCEPU, and JAEA as given in TABLE 74 are similar. The calculation results show only minor differences in specific values The comparison between the calculation results of IGCAR, IBRAE, NCEPU and JAEA is also shown in FIG. 297 through FIG. 313.

As shown in FIG. 297, the leakage of liquid sodium first increases and then stabilized. The spraying process of liquid sodium lasted for about 0.5 s and then stabilized, indicating that the leakage of liquid sodium has stopped.

In the process of liquid sodium passing through the top cover of the reactor, there are several main leak channels: RS-LRP, LRP-SRP, RS-IHX/pump and RS-DHX. FIG. 301 through FIG. 313 show different mass rate of sodium leakage in the leak path.

TABLE 74. COMPARISION OF LEAKED SODIUM FROM VARIOUS TOP SHIELD LEAK PATHS

Leak Paths	**NCEPU**	**IBRAE RAN**	**IGCAR**	**JAEA**
RS-LRP	149.82	150.6	150.54	141.1
LRP-SRP	93.34	108.0	103.73	95.9
RS-IHX/Pump (4/2)*	33.84	41.0	36.15	44.0
SRP-CP	14.28	15.6	14.47	19.7
SRP-OSP	--	11.5	8.57	12.1
RS-DHX (4)*	6.46	7.6	6.84	8.8
Others	10.00	10.95	9.28	13.38
Total:	307.7	345.13	329.58	334.9

* Value in the bracket corresponds to the number of the component.

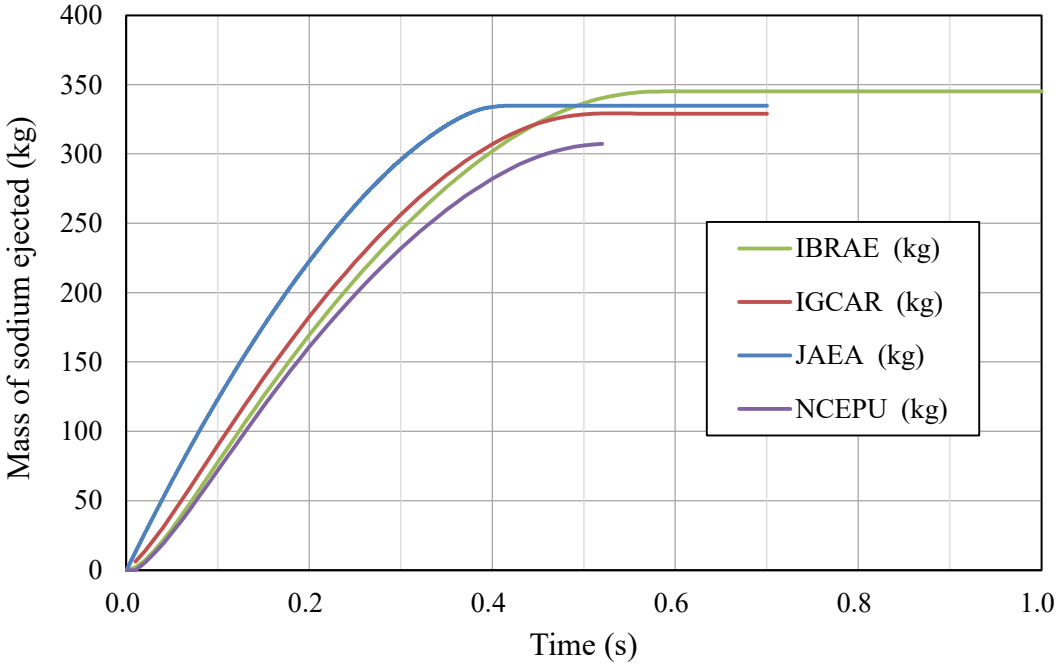

FIG. 297. Results of total liquid sodium leakage.

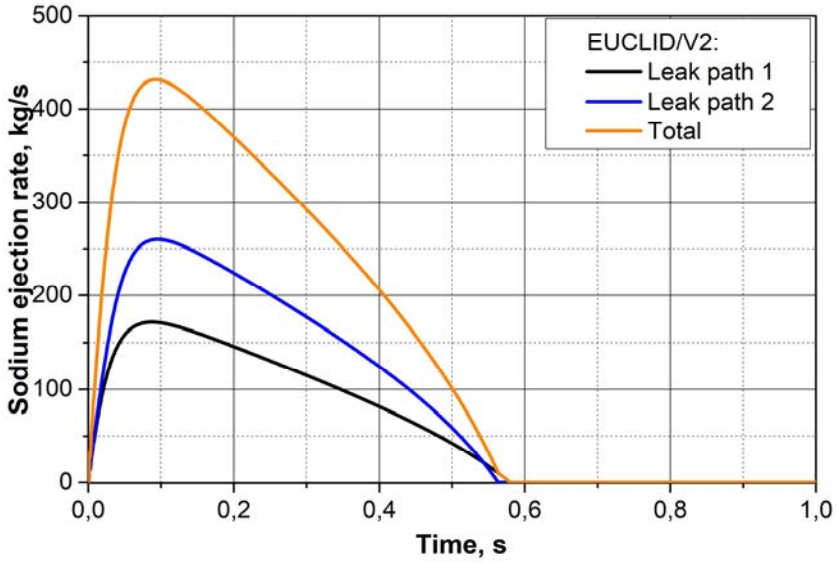

FIG. 298. Results of liquid sodium leakage rate for RS-LRP (IBRAE)

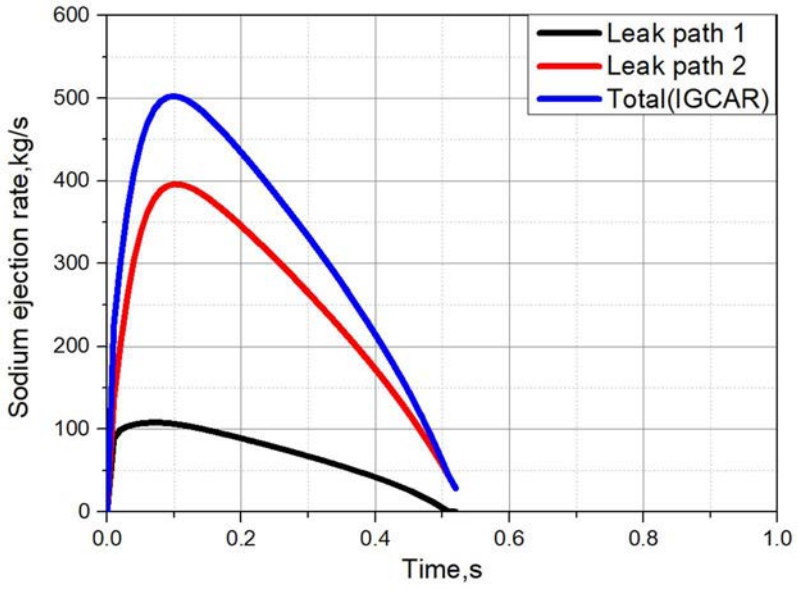

Fig. 299. Results of liquid sodium leakage rate for RS-LRP (IGCAR)

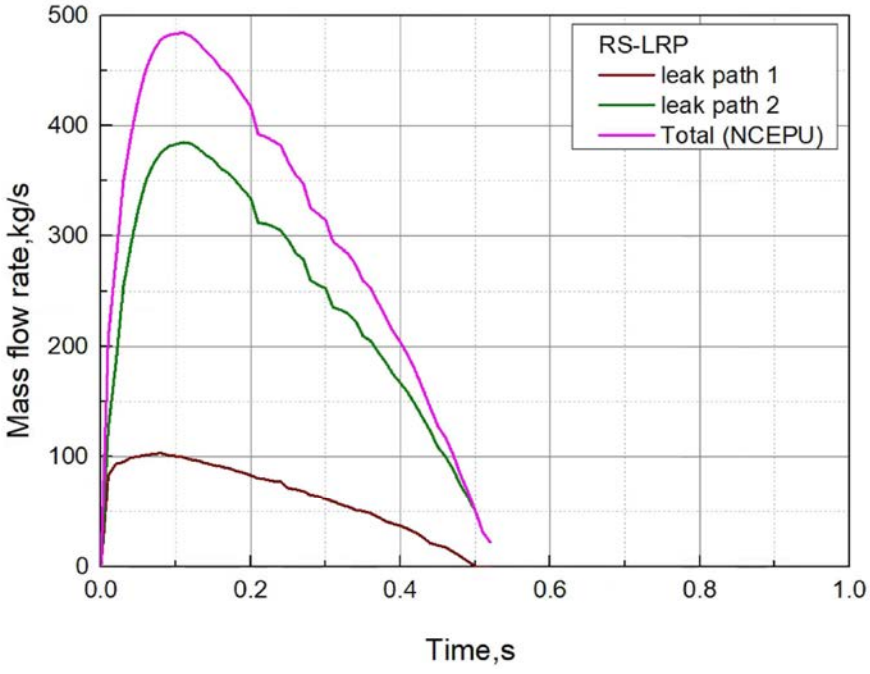

9

Fig. 300. Results of liquid sodium leakage rate for RS-LRP (NCEPU)

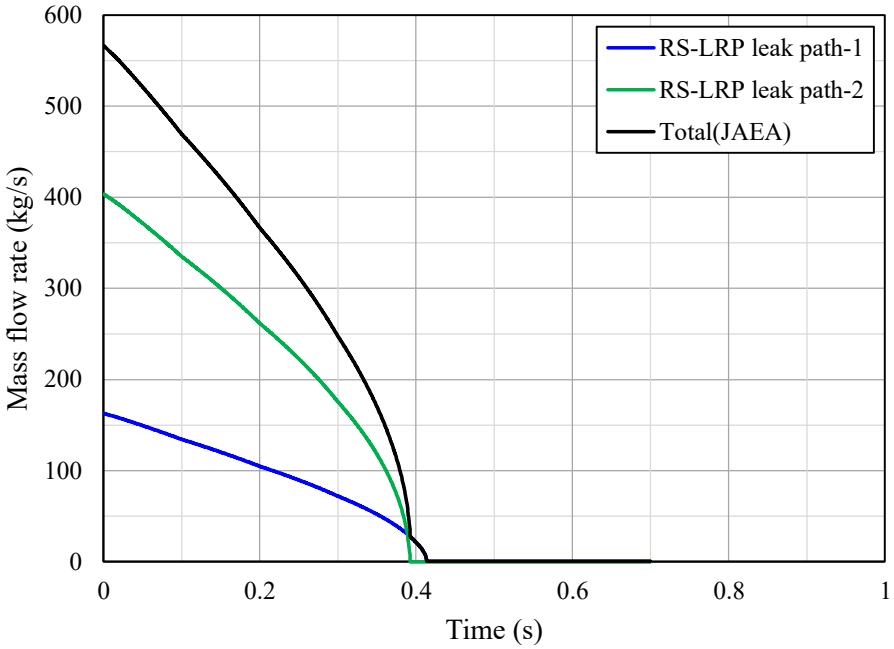

FIG. 301. Results of liquid sodium leakage rate for RS-LRP (JAEA).

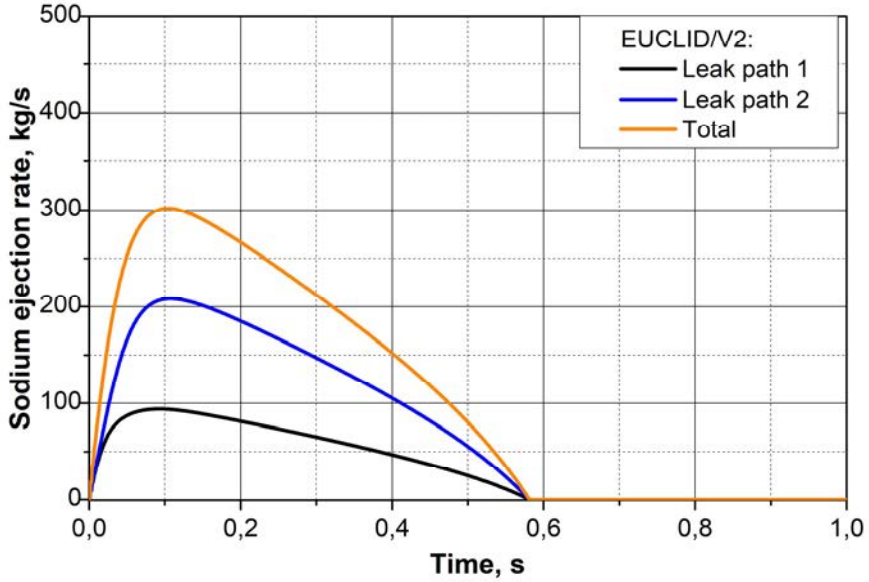

Fig. 302. Results of liquid sodium leakage rate for LRP-SRP (IBRAE)

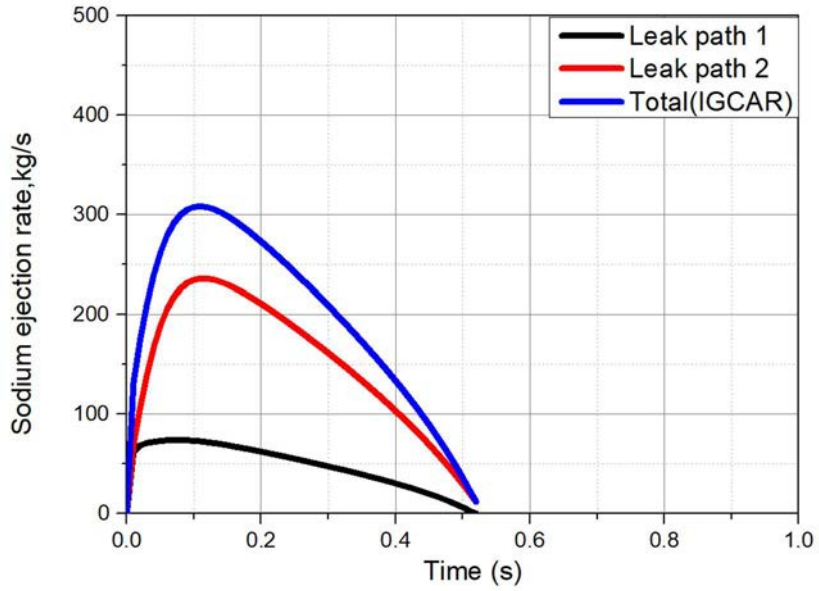

Fig. 303. Results of liquid sodium leakage rate for LRP-SRP (IGCAR)

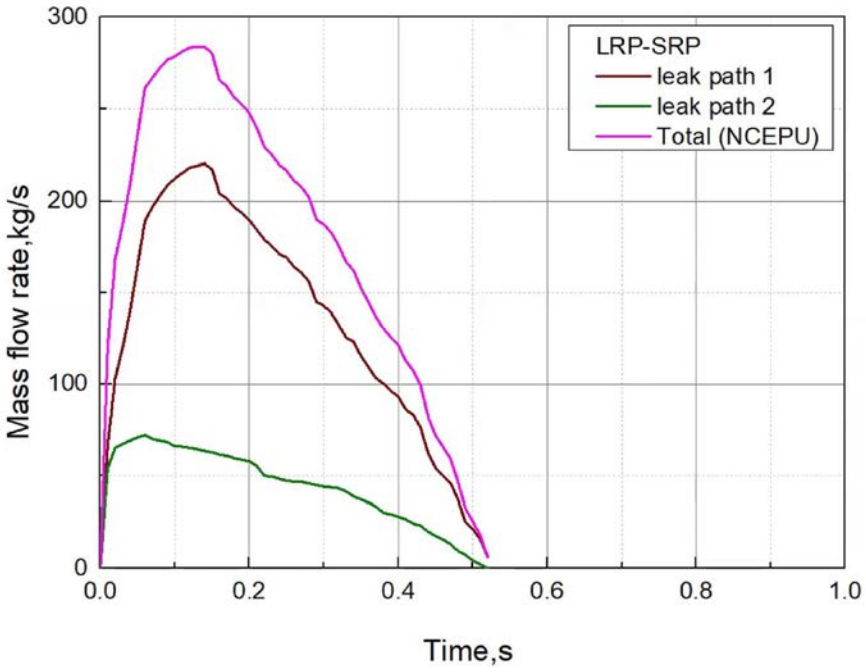

Fig. 304 Results of liquid sodium leakage rate for LRP-SRP (NCEPU).

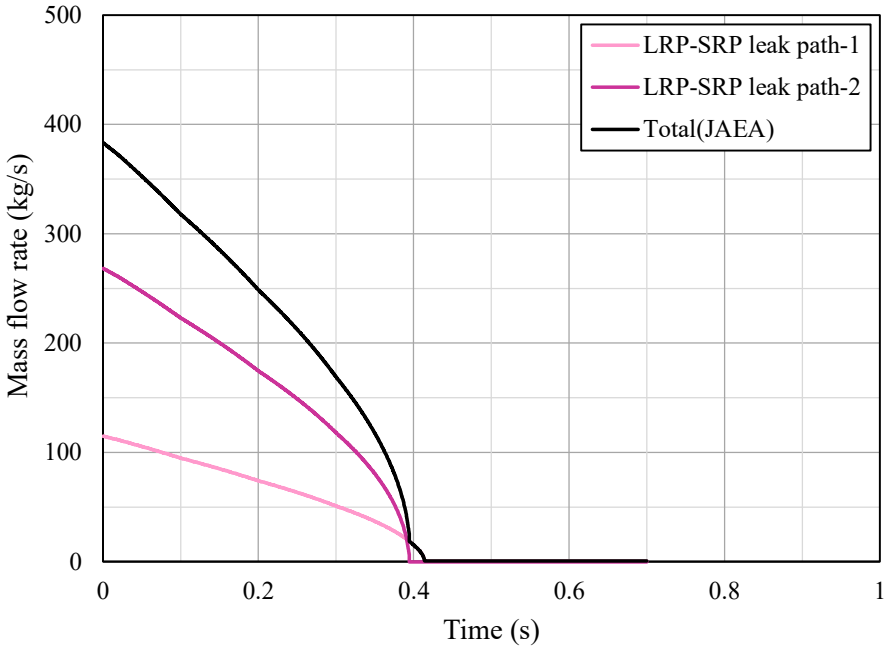

FIG. 305. Results of liquid sodium leakage rate for LRP-SRP (JAEA).

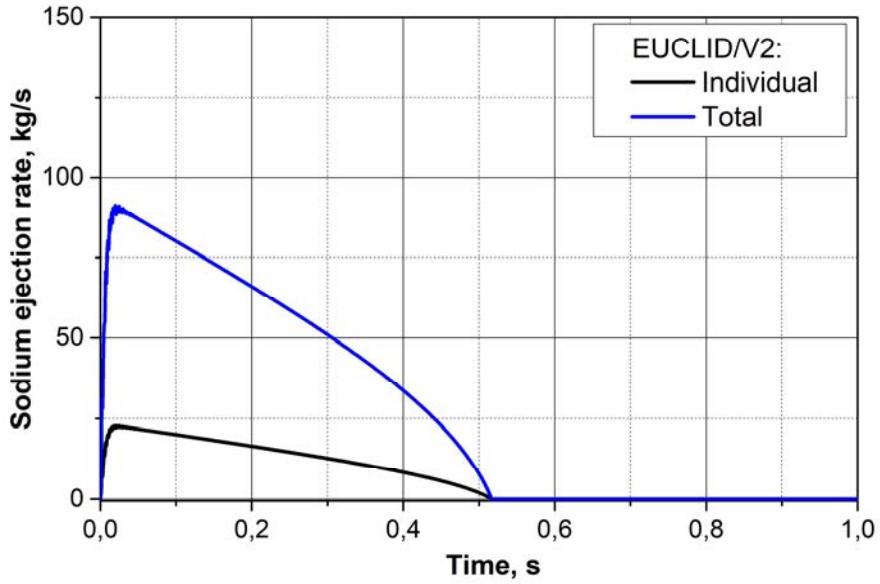

Fig. 306. Results of liquid sodium leakage rate for RS-IHX(Pump) (IBRAE).

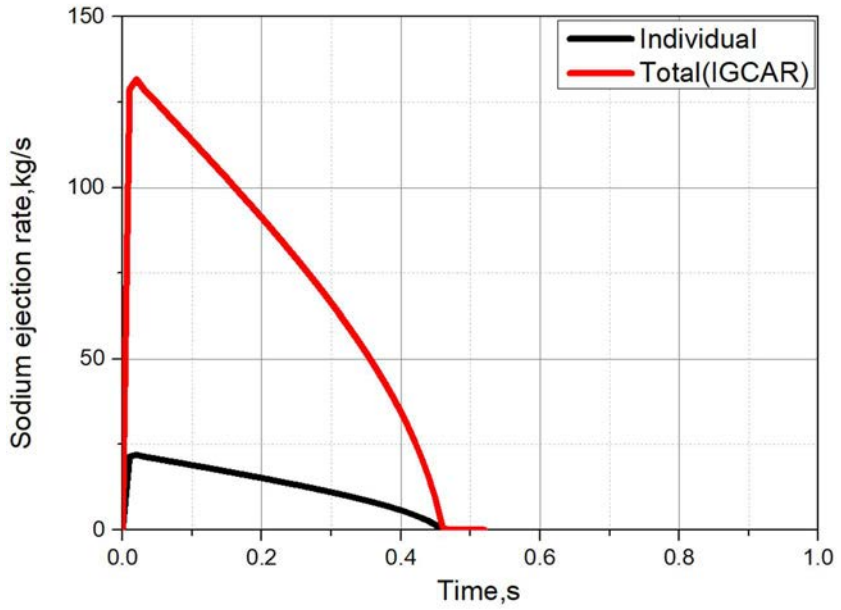

Fig. 307. Results of liquid sodium leakage rate for RS-IHX(Pump) (IGCAR).

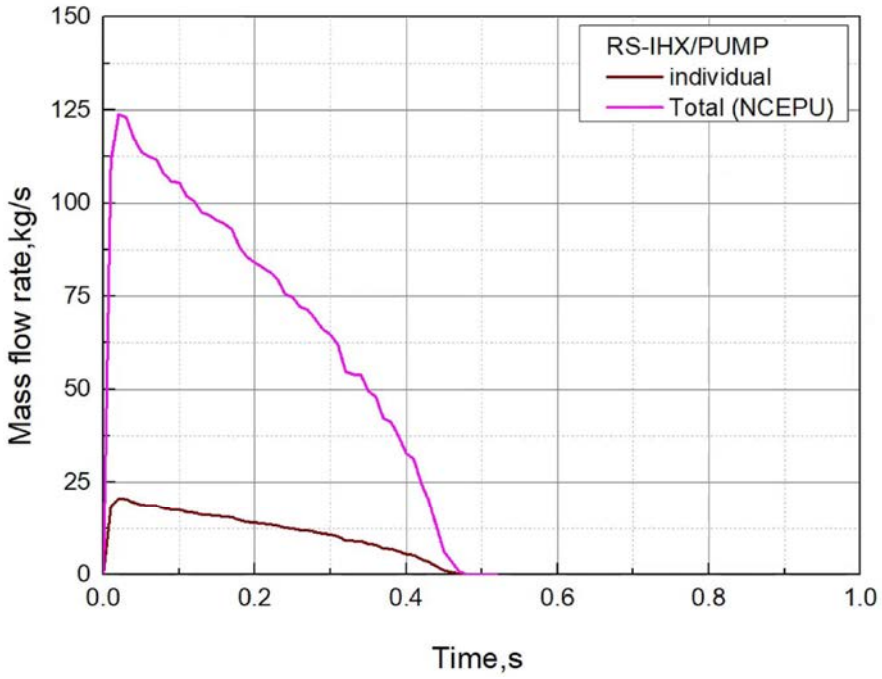

Fig. 308 Results of liquid sodium leakage rate for RS-IHX(Pump) (NCEPU).

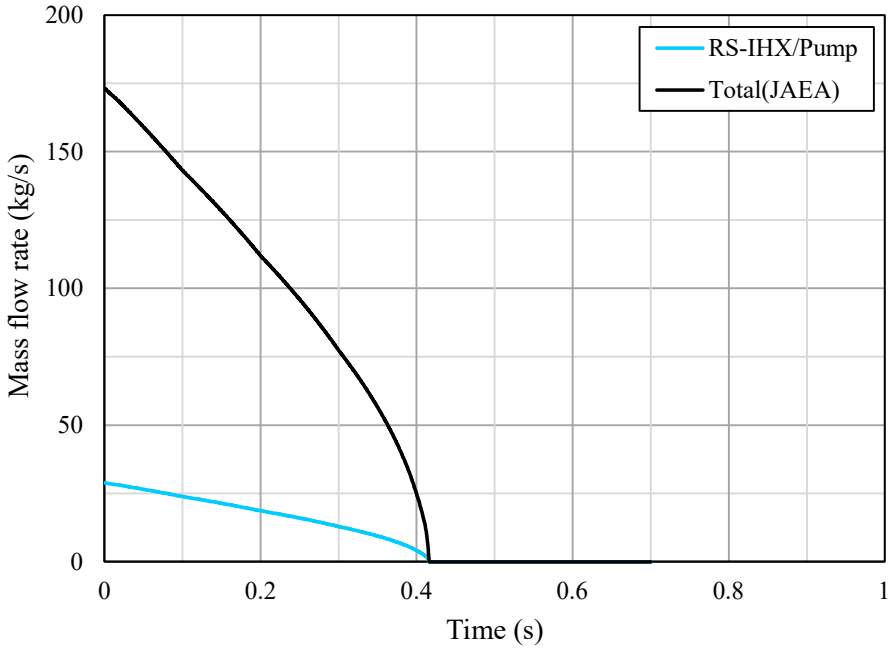

FIG. 309. Results of liquid sodium leakage rate for RS-IHX(Pump) (JAEA).

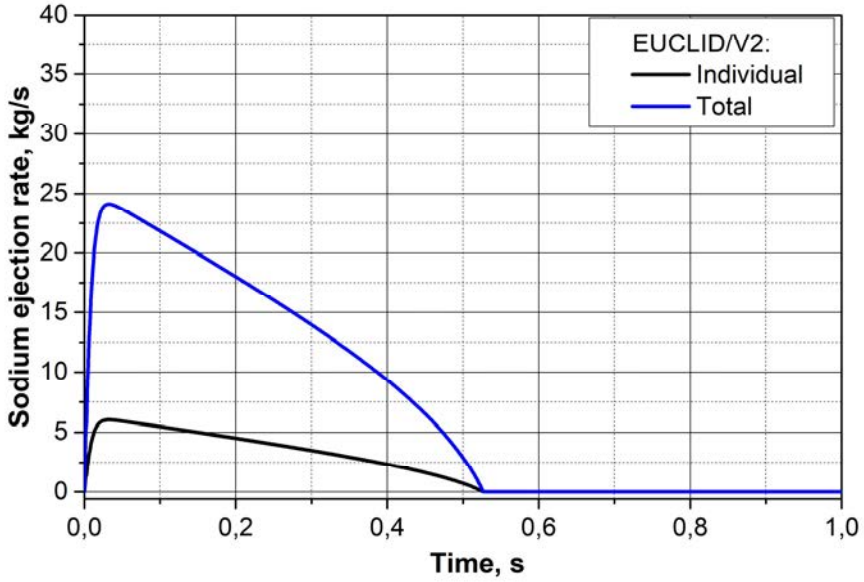

Fig. 310. Results of liquid sodium leakage rate for RS-DHX (IBRAE).

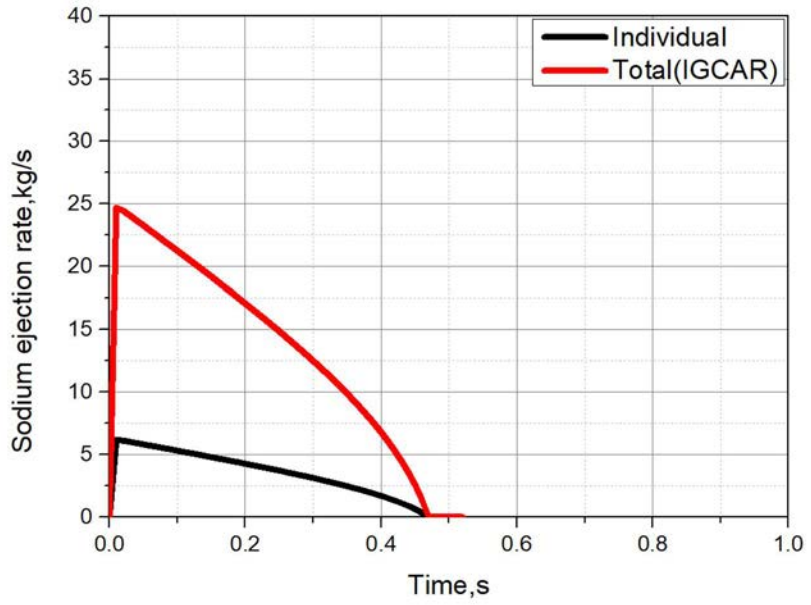

Fig. 311. Results of liquid sodium leakage rate for RS-DHX (IGCAR).

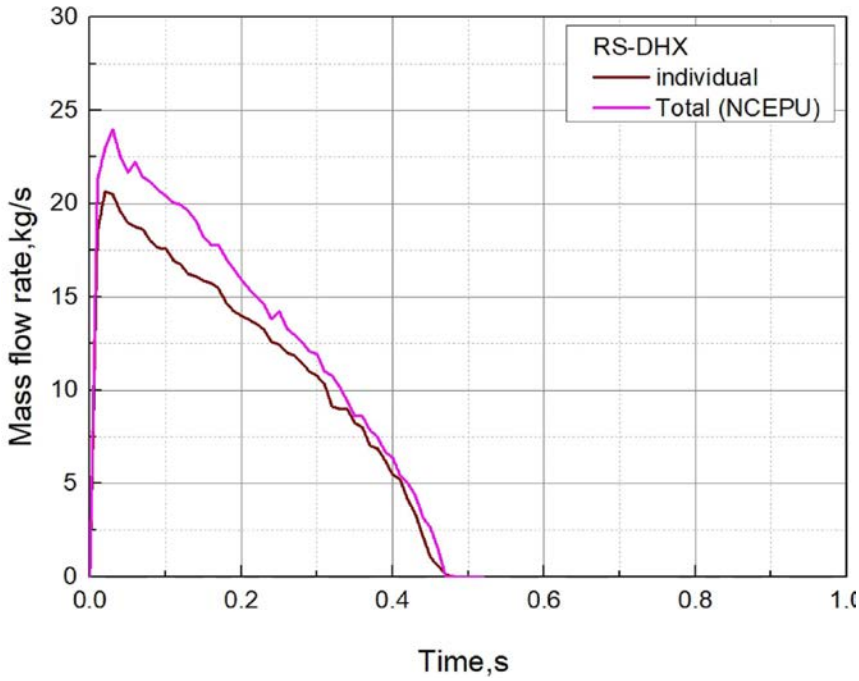

Fig. 312. Results of liquid sodium leakage rate for RS-DHX (NCEPU).

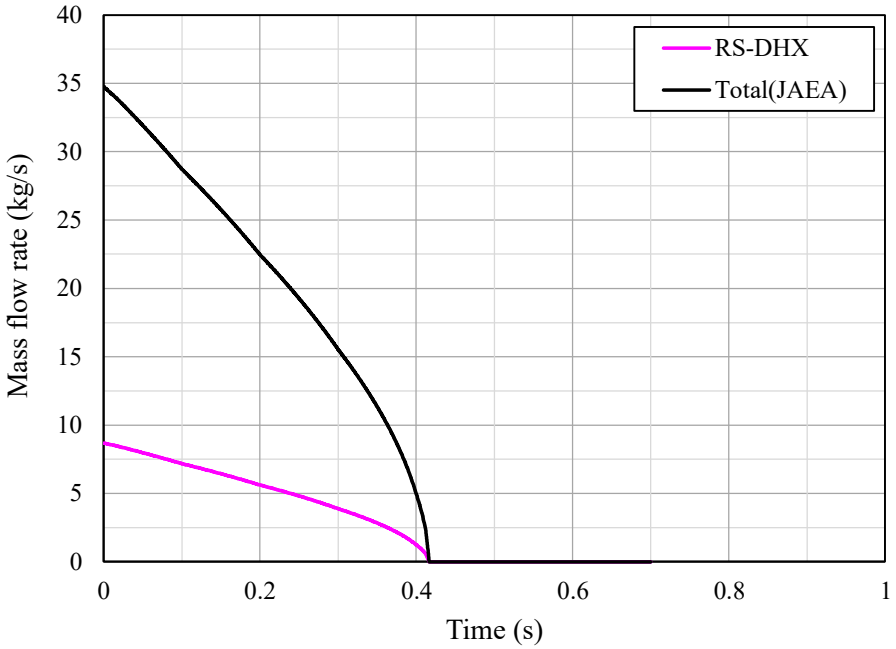

FIG. 313. Results of liquid sodium leakage rate for RS-DHX (JAEA).

From FIG. 301 through FIG. 313, it is shown that the variation rate of sodium leakage rate in the main leakage channel is very similiar. Within 0.1 s of the start of the leak, the rate of leakage of liquid sodium quickly reached a maximum and then gradually decreased until it was zero, indicating that the leak completely stopped. However, NCEPU, IGCAR and IBRAE have some differences in the calculation of the leak stop time. From the simulation results of each sub-channel, NCEPU and IGCAR predicted that the leak will end within about 0.5s, and IBRAE's simulation results suggested that this time is longer.

The results of JAEA calculation can be compared with those of others. In calculations carried out by NCEPU, IBRAE, and IGCAR, time derivative is considered in the basic equation so that the inertia of the fluid is appropriately taken into account. However it is not taken into account in the calculation by JAEA. Because input pressure is the same and friction and singular loss of the flow paths are not so different in each calculation, the effect of inertia of the fluid can be highlighted by comparison. JAEA calculations predicted 335 kg of sodium ejected, similar to that of others. This result can be explained as the beginning of the leak, mass flow rate is greater in JAEA calculation, whereas at the end of the leak, mass flow rate decreases rapidly in JAEA calculation due to no inertia effect As a result, the total leaked mass became comparable in all the calculations.

TABLE 75 shows the results of the parametric analyses. Parametric analyses of IBRAE RAN concluded that the leaked mass was largest in the following combinations, of which the effect of input pressure was most pronounced: sodium temperature / reference (900K) -50K, inlet pressure / reference +5%, outlet pressure / reference -10kPa, cross-section area / reference +3%. IGCAR conducted a parameter analysis in which the loss coefficient at the bend was changed from 1.0 to 0.3, and this results in the leaked mass increased from 330 kg to 409 kg. In NCEPU leak mass calculation, +10KPa has been added to reference pressure as the conservative boundary conditions. NCEPU conducted parameter analysis of pressure, if pressure conservative was removed, leak mass will be reduced to 87% of the reference value. These results indicate that the change of parameters regarding uncertainty, such as input pressure, outlet pressure, cross-sectional area, and loss coefficient, bring about the change of

leaked mass in the range of several tens of %. JAEA conducted an analysis using the input pressure as a parameter (pressure obtained by the analysis using SIMMER code), and the leaked mass increased from 335 kg to 1840 kg. This calculation is placed as a different calculation case, because the input pressure is significantly different from that of reference case.

TABLE 75. RESULTS OF THE PARAMETRIC CALCULATIONS

	IBRAE RAN	**NCEPU**	**IGCAR**	**JAEA**
Released mass of sodium (relative to reference case)	370 kg (107 %)	267.6 kg (87%)	409 kg (124 %)	1840 kg (549 %)

In this benchmark analysis, all instituitions assumed that the leak path is filled with sodium as the initial condition. This ignores the transients that sodium flows into the leak path. In reality, the sodium enters into the gaps between the plugs after the sodium slug impacts on the lower surface of the top shield, and after the gap capacity being filled with the sodium, it outflows onto the top shield. The approximate capacity of the gaps between the plugs is shown in TABLE 76. Since the leaked mass obtained by the reference case calculation, even by the parameter case calculation other than JAEA parameter case, is less than this gap capacity, the sodium does not outflow onto the top shield if this gap capacity is taken into consideration. The amount of sodium outflows onto the top shield in JAEA parameter case only amounts to 75 kg if the gap capacity is taken into account (leaked mass through the paths LRP-SRP and SRP-OSP exceeds the gap capacity).

TABLE 76. CAPACITY OF THE LEAK PATH

Leak Paths	Capacity* (in kg of sodium)
RS-LRP	908
LRP-SRP	460
RS-IHX/Pump	1214 (6x205)
SRP-CP	213
SRP-OSP	34
RS-DHX	108 (4x27)
Others	256
Total:	3223

* Liquid sodium density is assumed here to 820 kg/m^3 (~550 degree C).

In this benchmark analysis, each of the leak paths being opened at a certain width in advance was assumed as the calculation condition, and the amount of sodium ejected onto the top shield was compared. In reality, ordinary plugs including roof slab are fixed with bolts, and rotating plugs are often fixed with freeze seals and then prevention measures for the missile are taken. Therefore even if the pressure increases in the reactor vessel, the plug will not move upward nor open the leak path onto the top shield unless the pressure exceeds the weight of the plug and the force of the bolt. In order to evaluate this effect, it is necessary to analyze the dynamic response of the plugs.

7.2.1. Conclusions

Four institutions conducted benchmark analyses of sodium ejection. In the analysis using a common pressure history, the results of the analysis of each institution were in good agreement. This indicates that the variation in modelling for this task is small, and that the analysis accuracy

of the analysis method of each institution is almost the same. The amount of sodium ejected onto the top shield calculated in reference case is approximated to be 350 kg and will be utilized in WP-3 as input for sodium combustion calculation.

According to the results of the parametric analyses performed here, the change of parameters regarding uncertainty, such as input pressure, outlet pressure, cross-sectional area, and loss coefficient bring about the change of leaked mass in the range of several tens of %.

It is assumed in this benchmark analysis that the leak path is filled with sodium as the initial condition in all institutions. This ignores the transients that sodium flows into the leak path. Considering the volume of the leak path, sodium was not ejected under common pressure conditions, and the ejection amount was about 75 kg even in the case of the JAEA pressure parameter case.

Ordinary plugs including roof slab are fixed with bolts, and rotating plugs are often fixed with freeze seals and then prevention measures for them being missile are taken. Therefore, even if the pressure increases in the reactor vessel, the plug will not move upward nor open the leak path onto the top shield unless the pressure exceeds the weight of the plug and the force of the bolt. In order to evaluate this effect, it is necessary to analyse the dynamic response of the plugs.

7.3. WORK PACKAGE 3: COMPARATIVE PHENOMENOLOGY ANALYSIS OF IN-CONTAINMENT SIMULATIONS

Based on the above two work packages, WP-3 simulated the sodium fire, the containment responses after the sodium ejection, and the aerosol dynamics from the sodium chemical reactions and the released fission product with sodium. Largely, two comparison cases were performed and compared in this section based on the sodium fire modelling options: sodium spray fire and sodium pool fire.

Two participants, IGCAR and IBRAE, performed all the work pages. In addition to the given simulation conditions, they used inputs to WP-3 from more realistic values from their WP-1 and WP-2 simulation results. In this section these cases are referred to as integral cases. The purpose of this effort is to demonstrate the conservatism built in the work package inputs, for example, release fractions, chemical forms, sodium ejection amounts, etc.

7.3.1. Sodium Spray Fire Simulation Comparison

The sodium ejection amount and duration was specified as an input to WP-3. The individual participants assumed or calculated the sodium ejection profile (i.e., the time depended sodium mass flow rate). FIG. 314 and FIG. 315 show the sodium mass flow rate. Although the sodium amount and duration are fixed, the flow profile may be different based on participants' assumptions. However, since the sodium spray fire burns instantaneously all the sodium in the containment, the overall impact to the containment response would be negligible due to these small differences in the ejection profile.

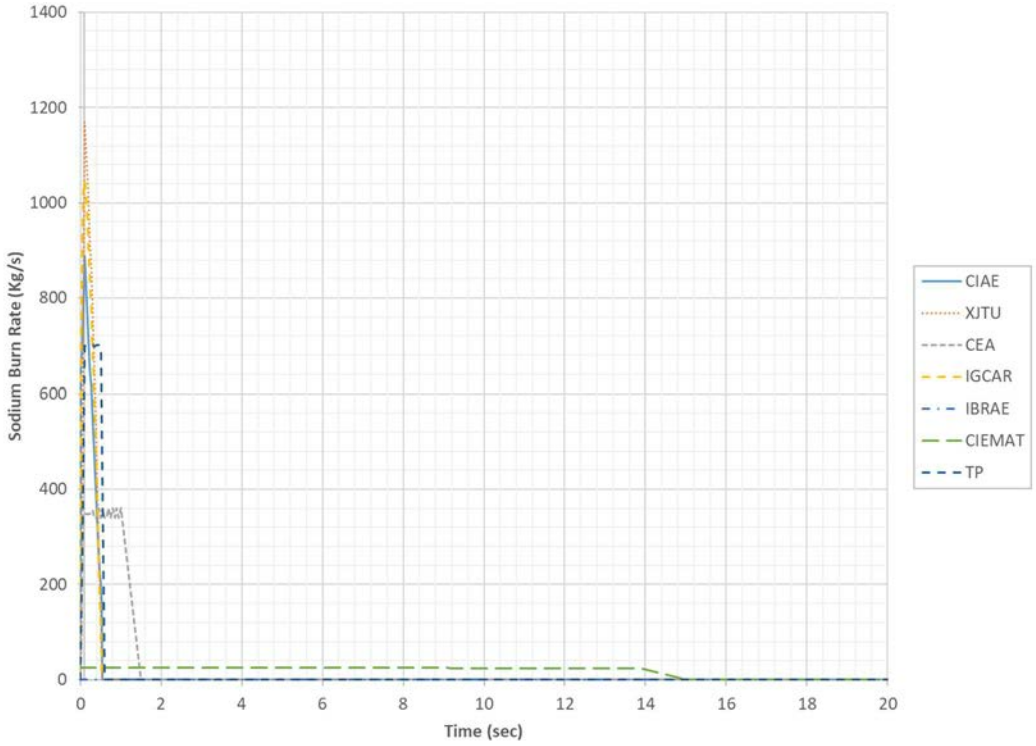

FIG. 314. Sodium spray fire: sodium burn rate (linear scale).

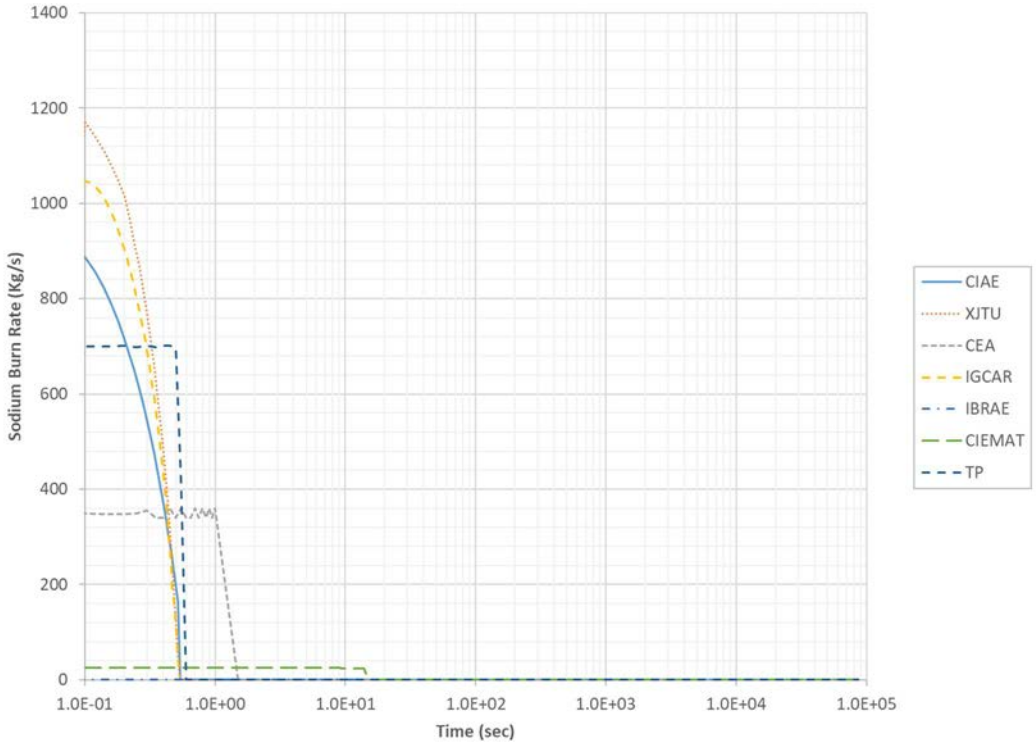

FIG. 315. sodium spray fire: sodium burn rate (semi log scale).

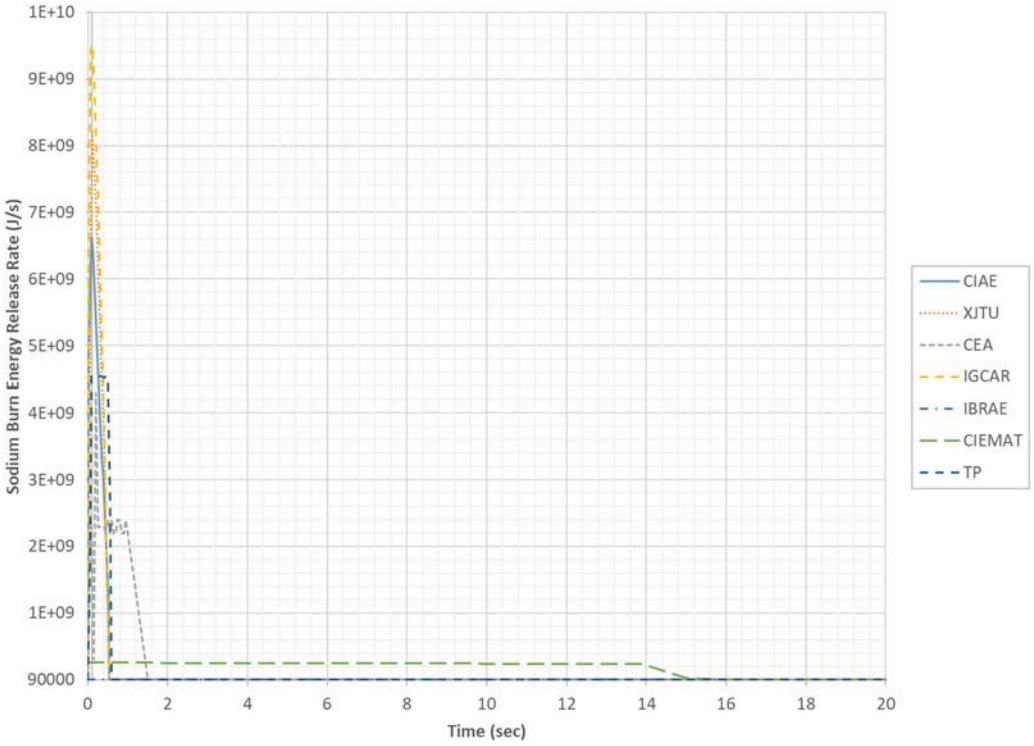

FIG. 316. Sodium spray fire: sodium burn energy release rate (linear scale).

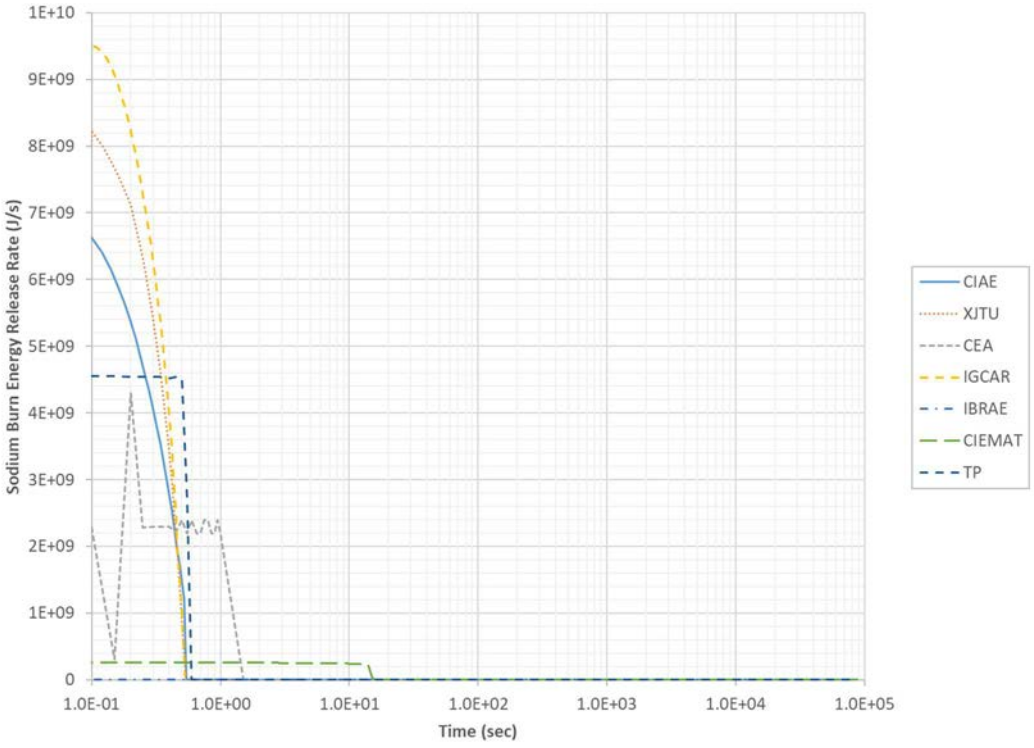

FIG. 317. Sodium spray fire: sodium burn energy release rate (semi log scale).

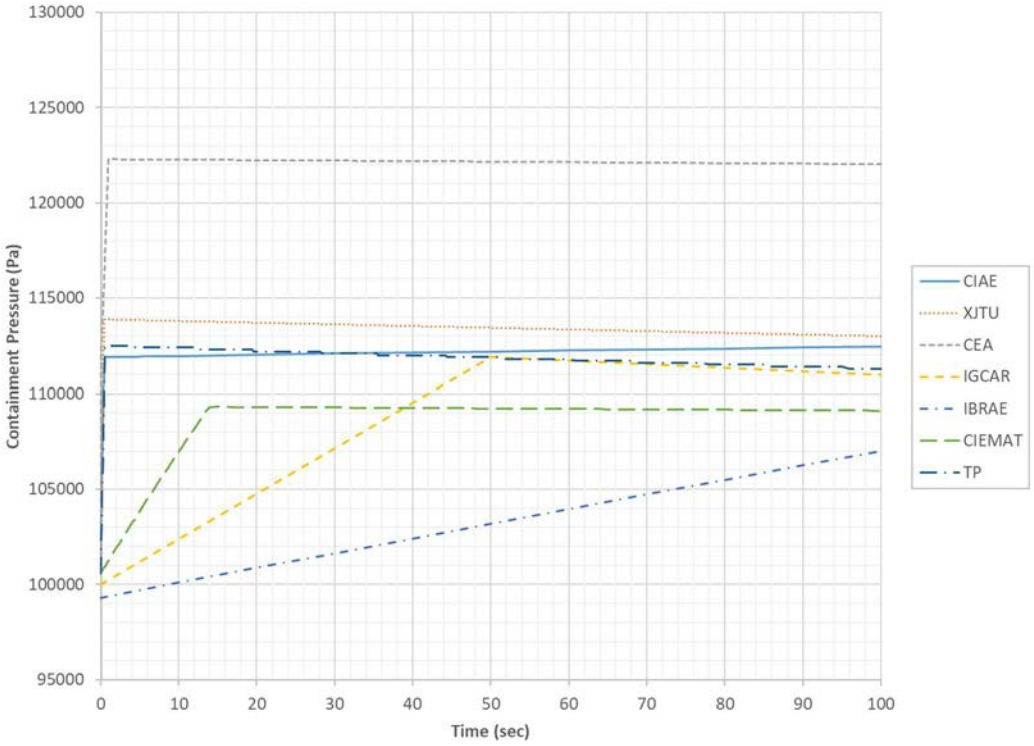

FIG. 318. Sodium spray fire: containment pressure (linear scale).

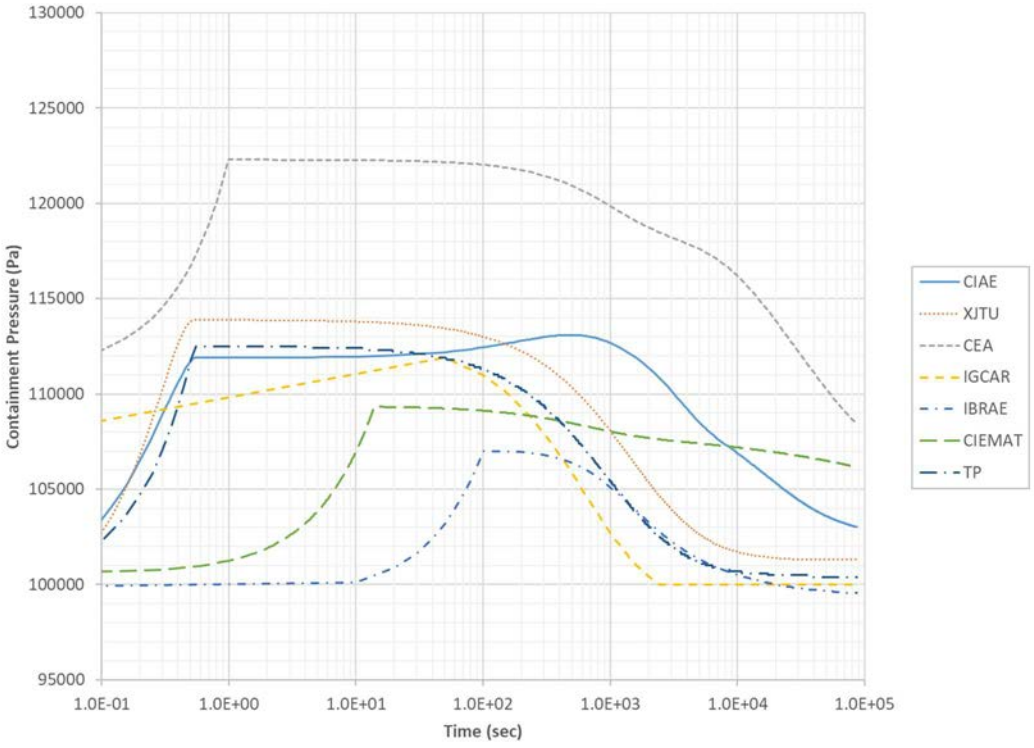

FIG. 319. Sodium spray fire: containment pressure (semi log scale).

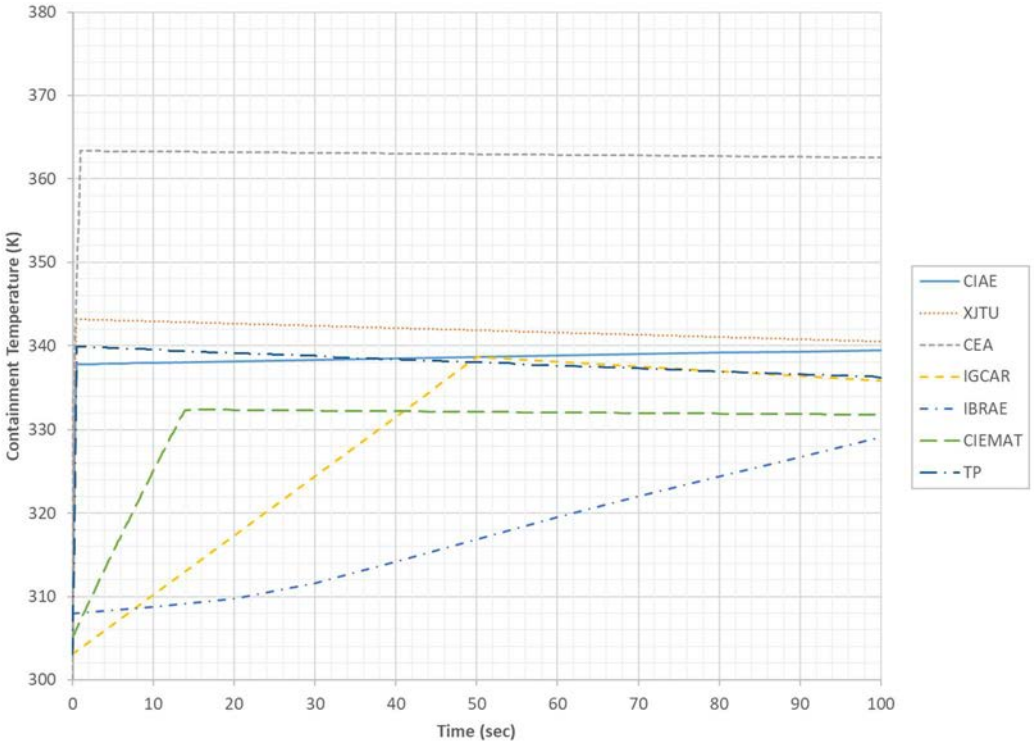

FIG. 320. Sodium spray fire: containment temperature (linear scale).

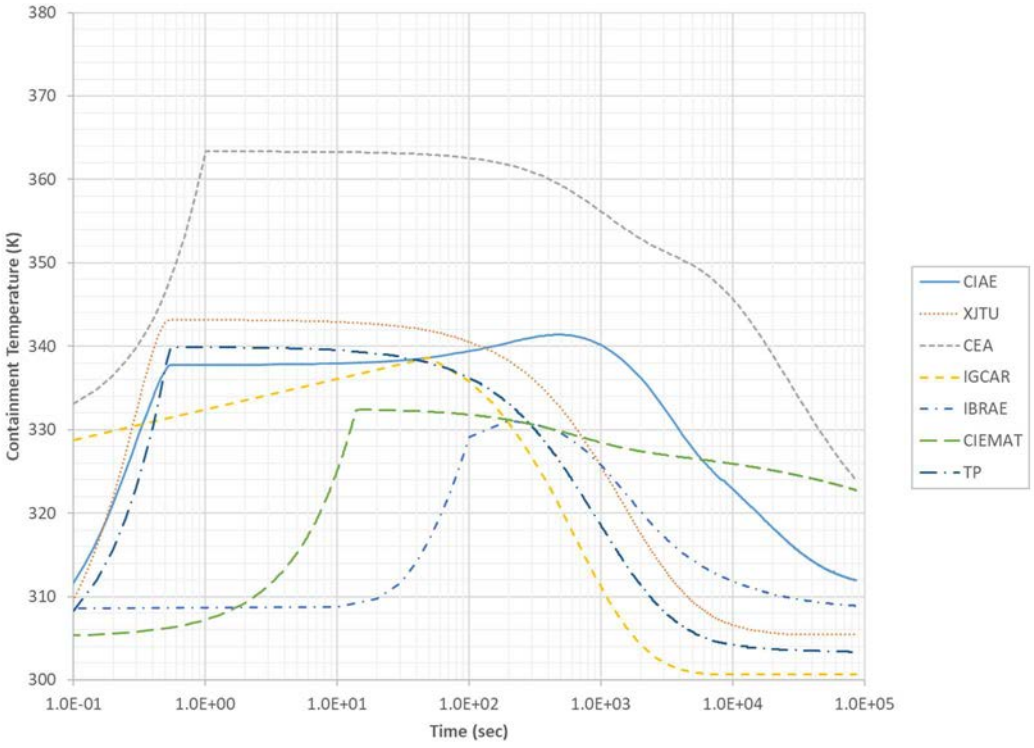

FIG. 321. Sodium spray fire: containment temperature (semi log scale).

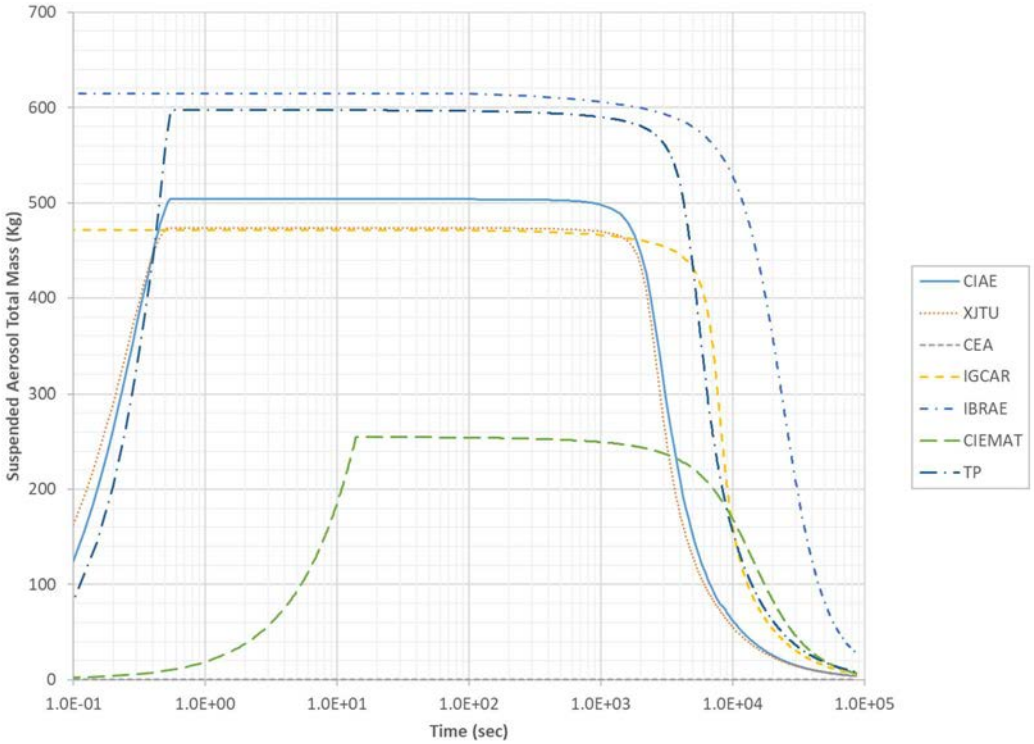

FIG. 322. Sodium spray fire: suspended aerosol total mass in containment (semi log scale).

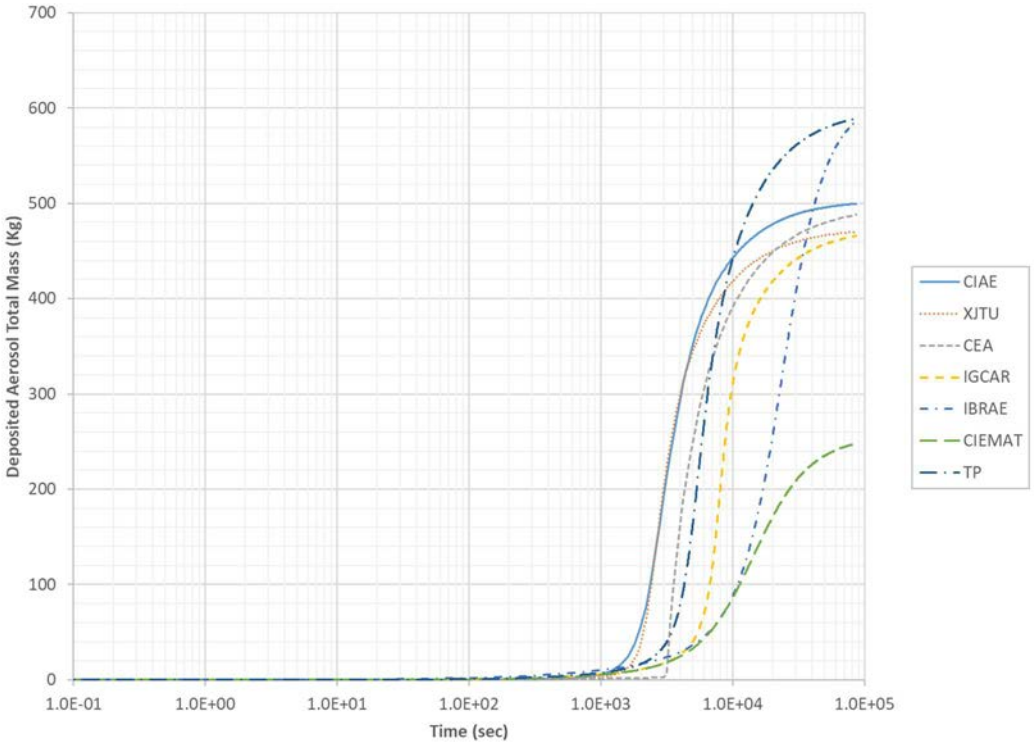

FIG. 323. Sodium spray fire: deposited aerosol total mass in containment (semi log scale).

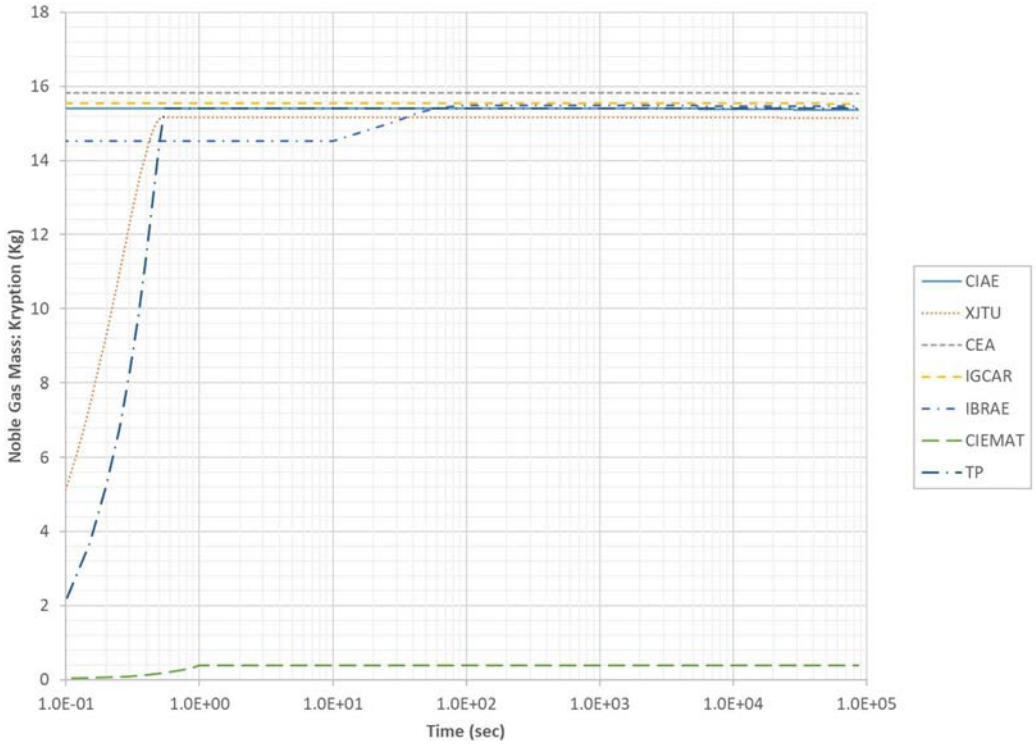

FIG. 324. Sodium spray fire: noble gas mass in containment – krypton (semi log scale).

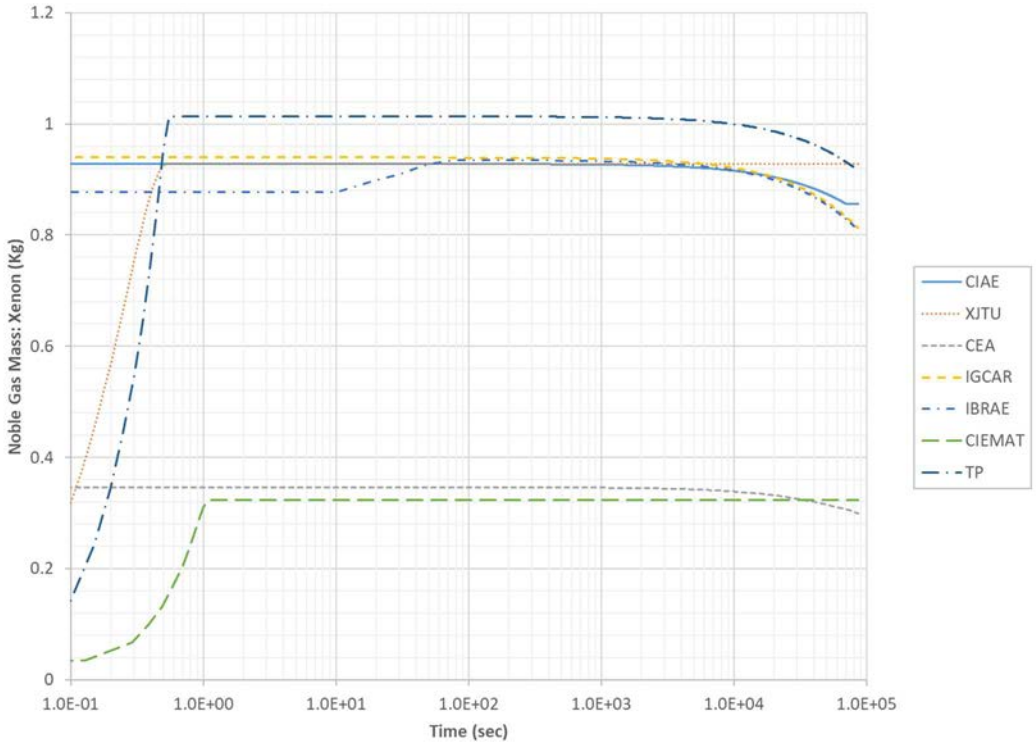

FIG. 325. Sodium spray fire: noble gas mass in containment – xenon (semi log scale).

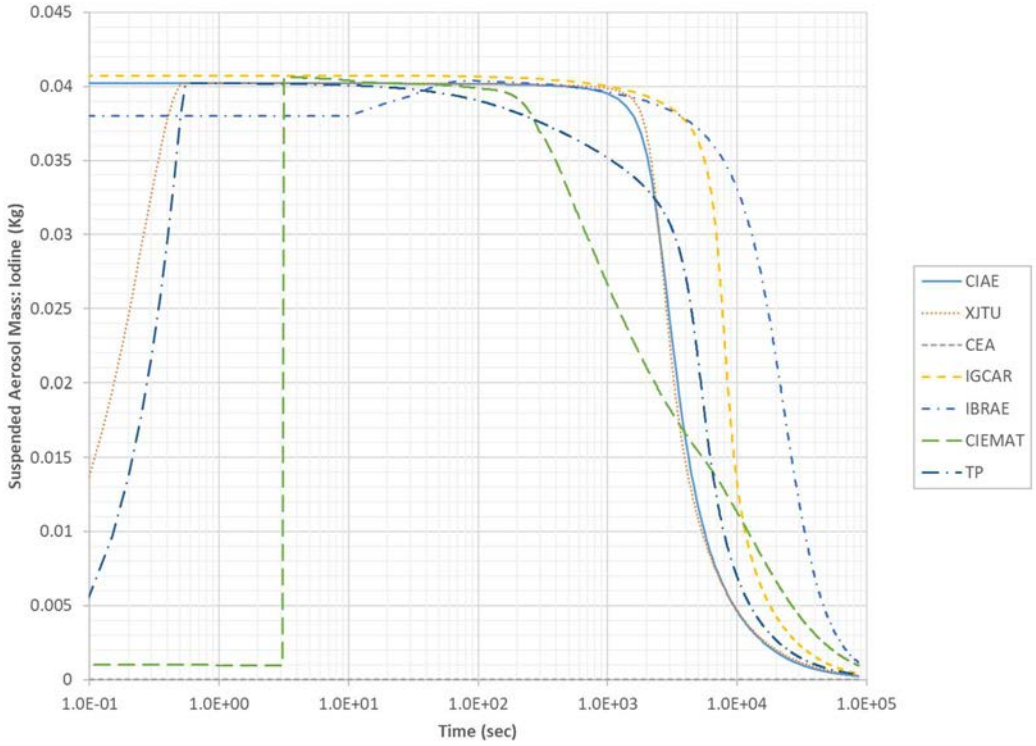

FIG. 326. Sodium spray fire: suspended aerosol mass in containment – iodine (semi log scale).

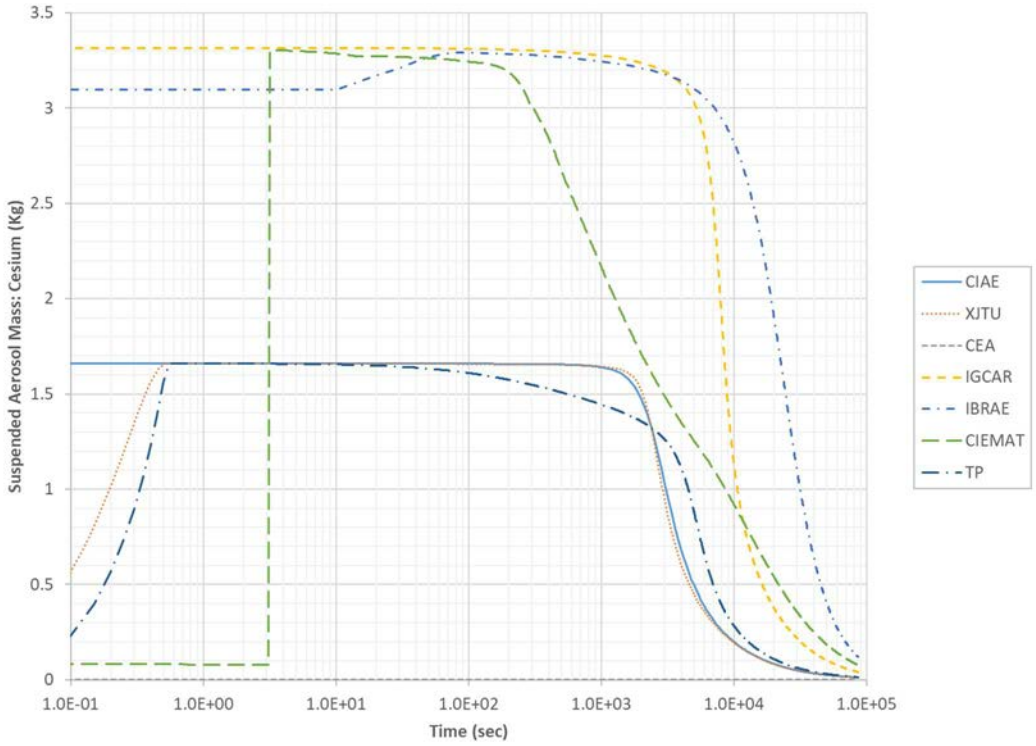

FIG. 327. Sodium spray fire: suspended aerosol mass in containment – caesium (semi log scale).

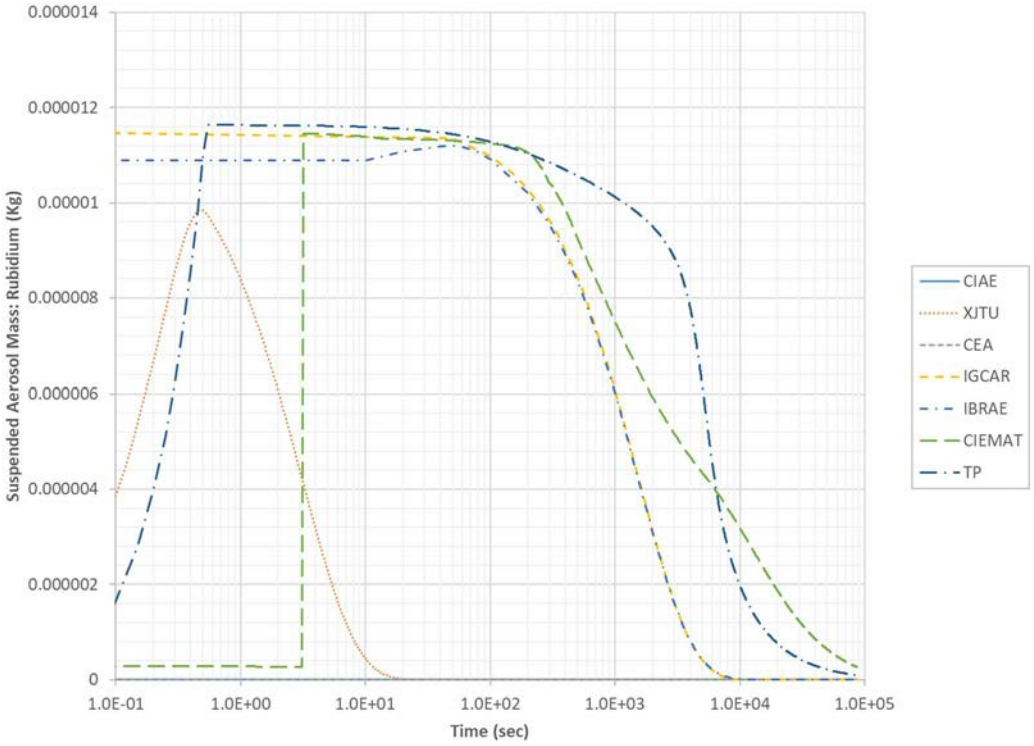

FIG. 328. Sodium spray fire: suspended aerosol mass in containment – rubidium (semi log scale).

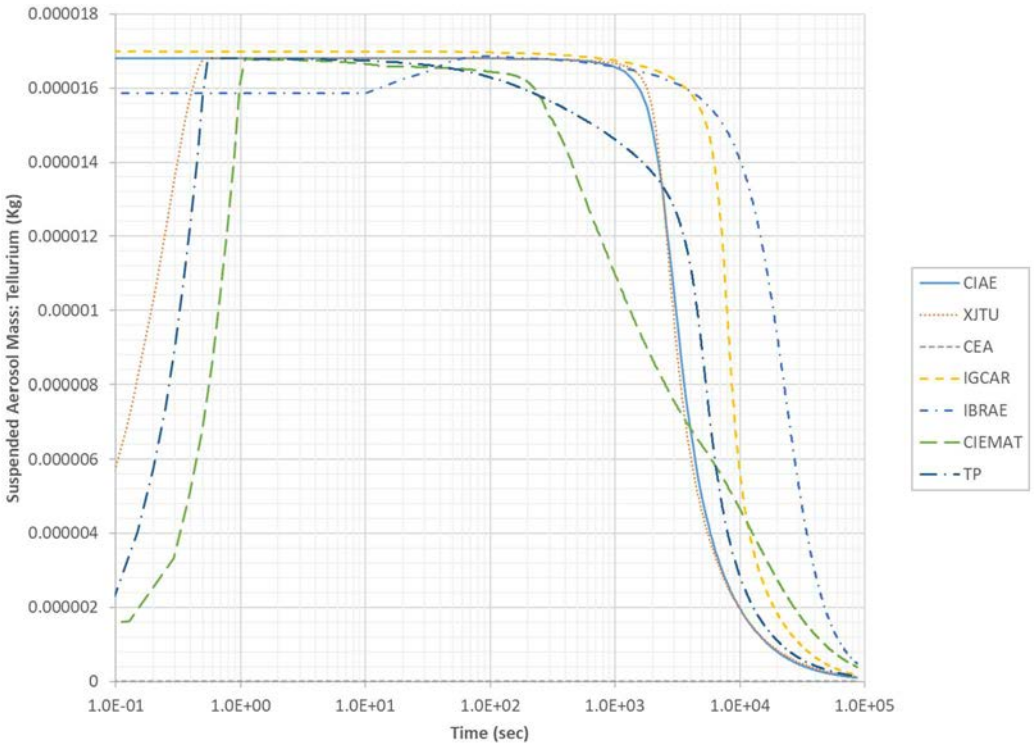

FIG. 329. Sodium spray fire: suspended aerosol mass in containment – tellurium (semi log scale).

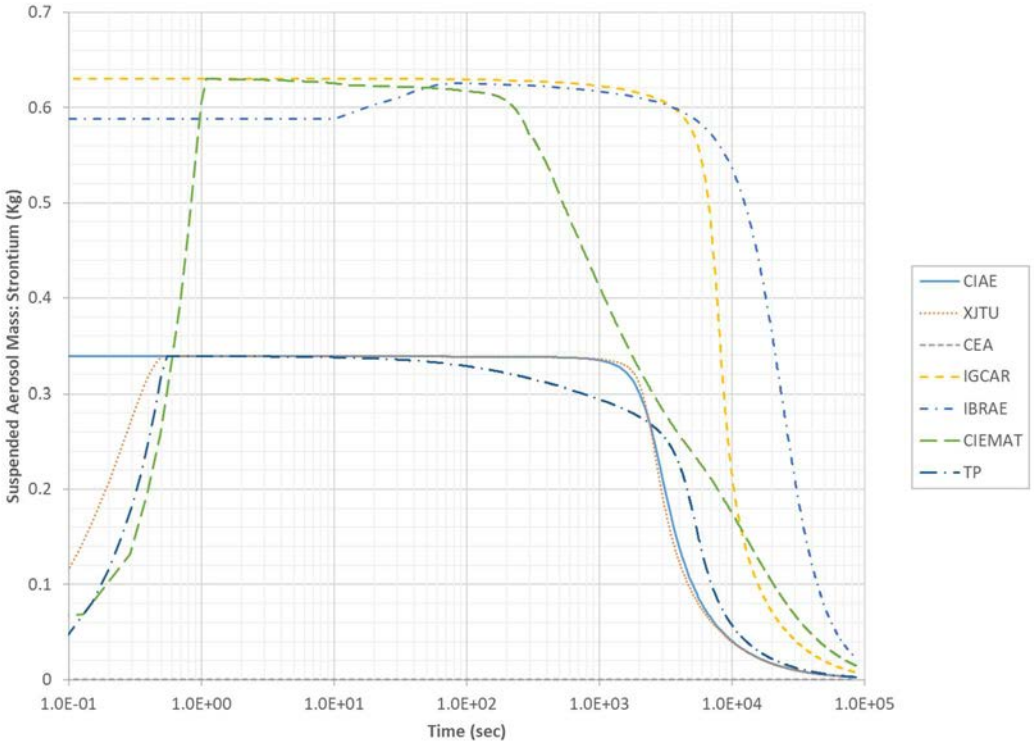

FIG. 330. Sodium spray fire: suspended aerosol mass in containment – strontium (semi log scale).

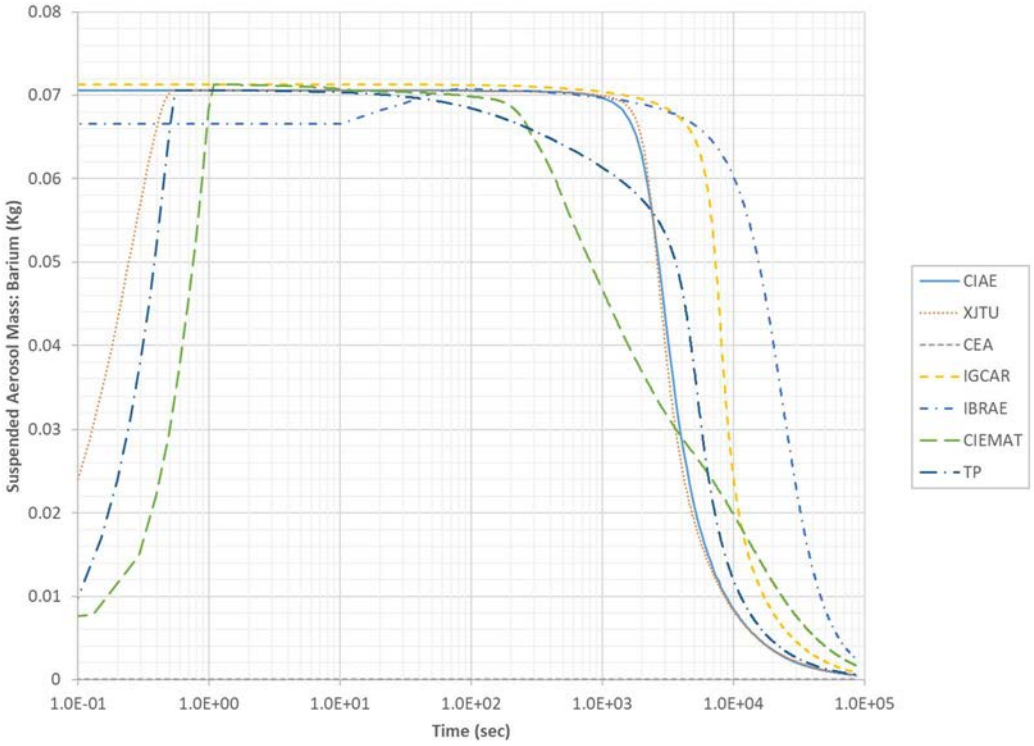

FIG. 331. Sodium spray fire: suspended aerosol mass in containment – barium (semi log scale).

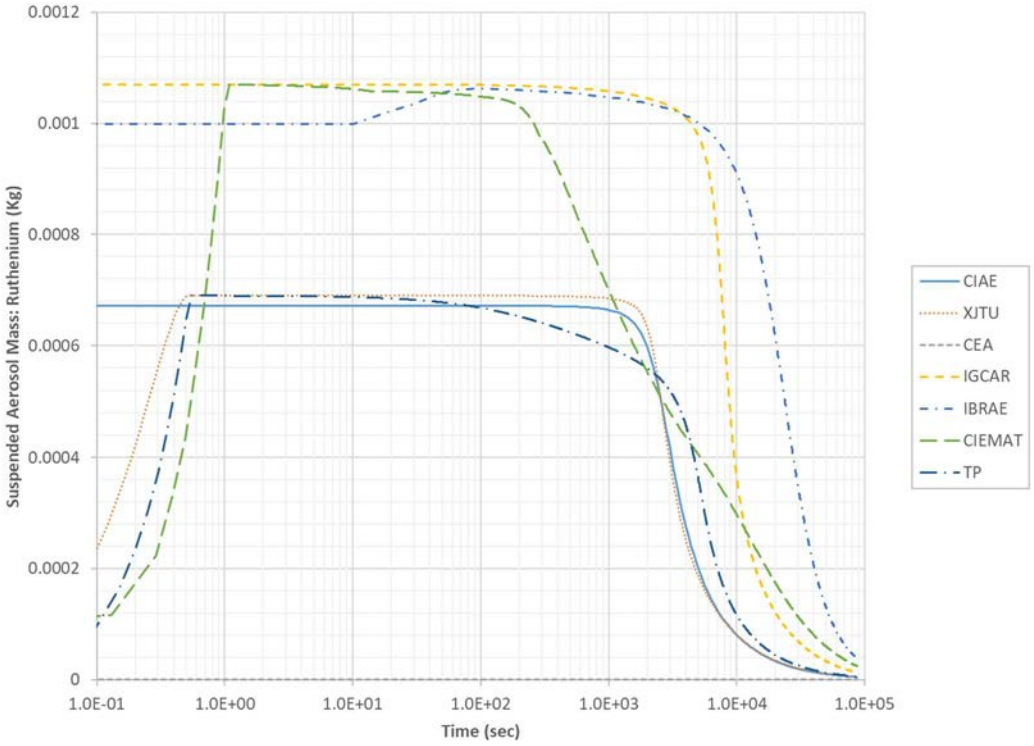

FIG. 332. Sodium spray fire: suspended aerosol mass in containment – ruthenium (semi log scale).

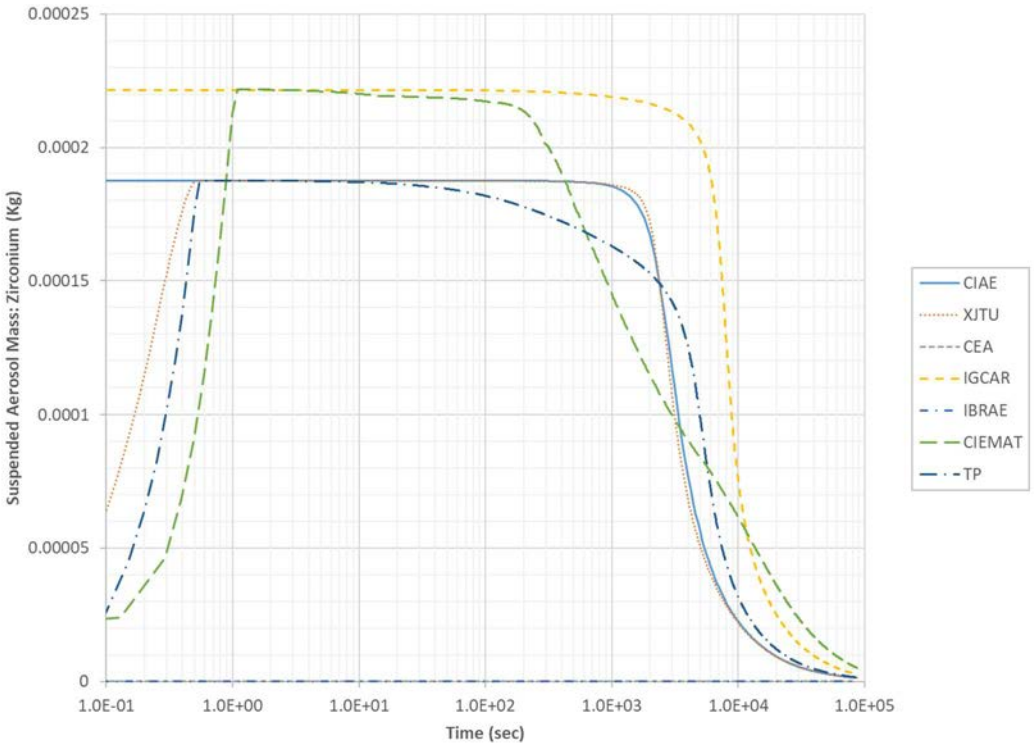

FIG. 333. Sodium spray fire: suspended aerosol mass in containment – zirconium (semi log scale).

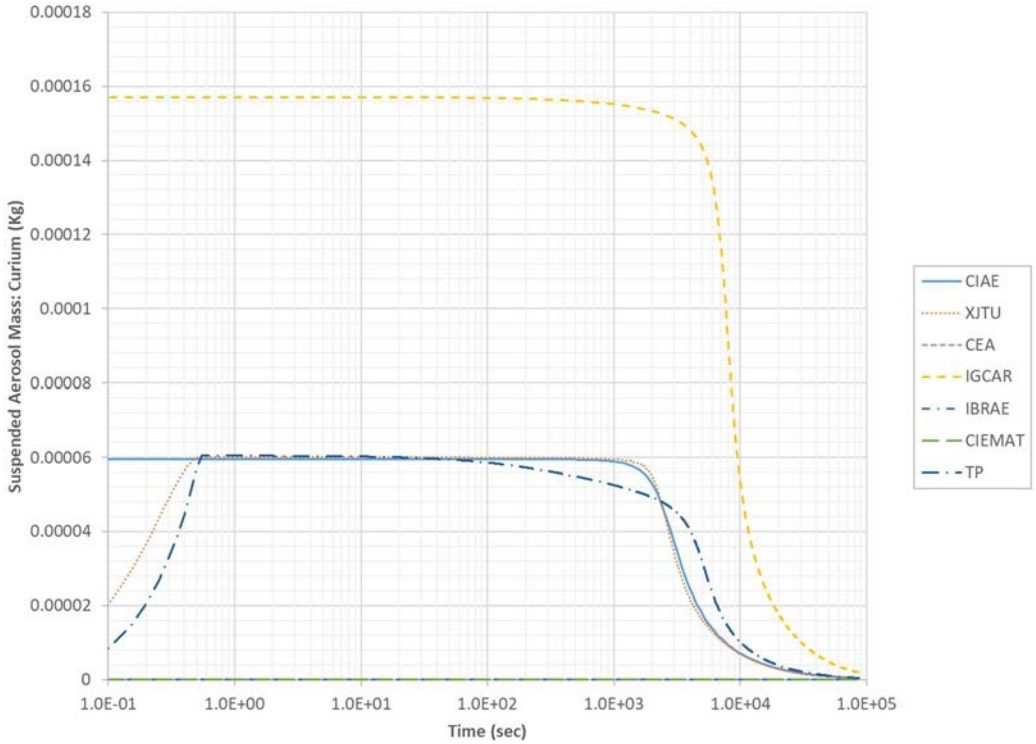

FIG. 334. Sodium spray fire: suspended aerosol mass in containment – curium (semi log scale).

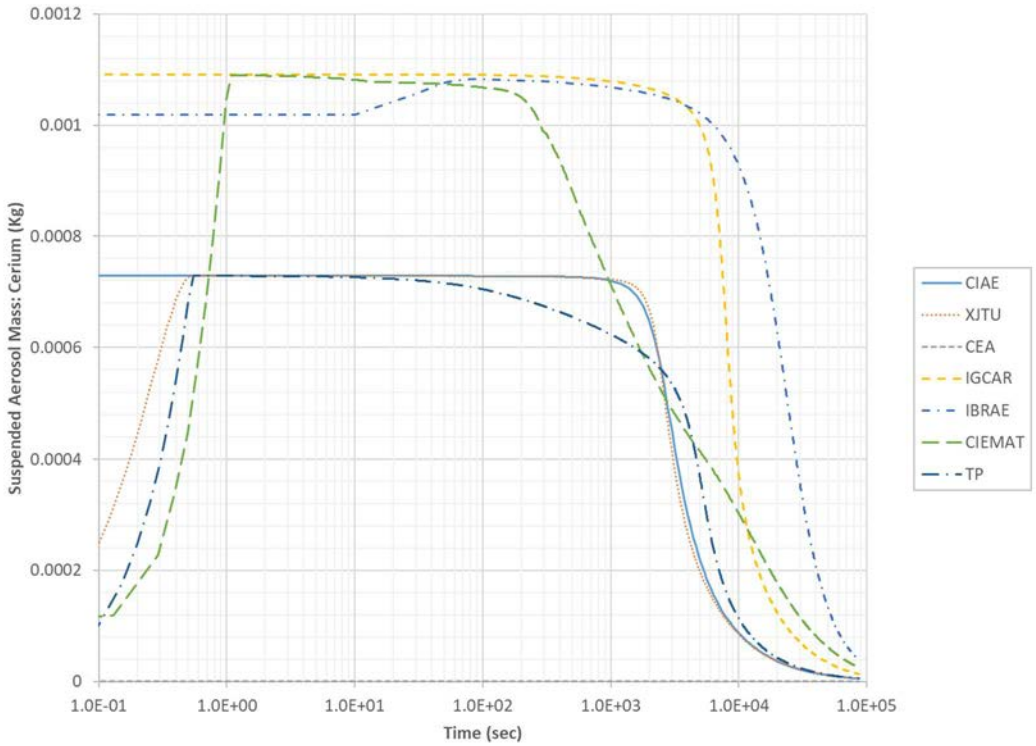

FIG. 335. Sodium spray fire: suspended aerosol mass in containment – cerium (semi log scale).

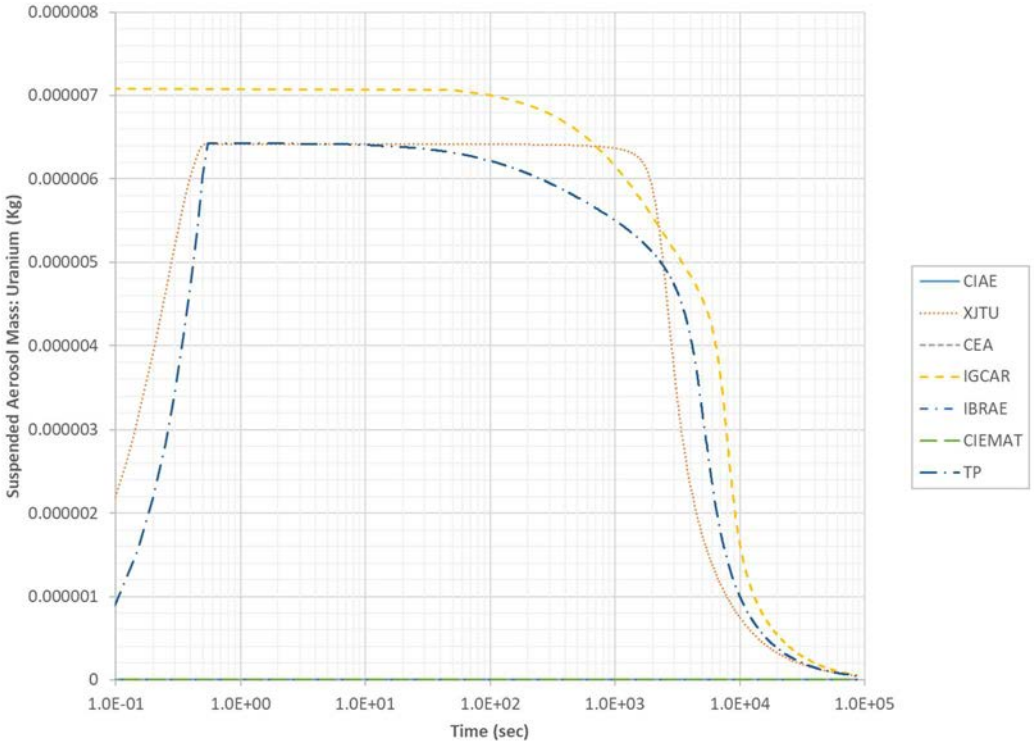

FIG. 336. Sodium spray fire: suspended aerosol mass in containment – uranium (semi log scale).

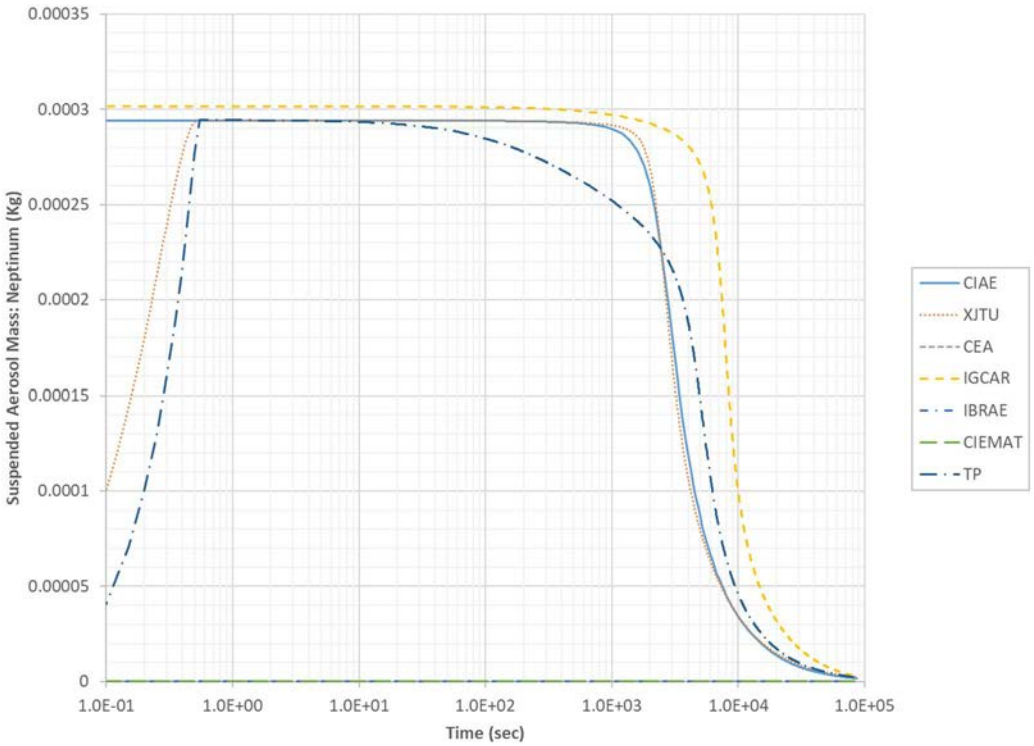

FIG. 337. Sodium spray fire: suspended aerosol mass in containment – neptunium (semi log scale).

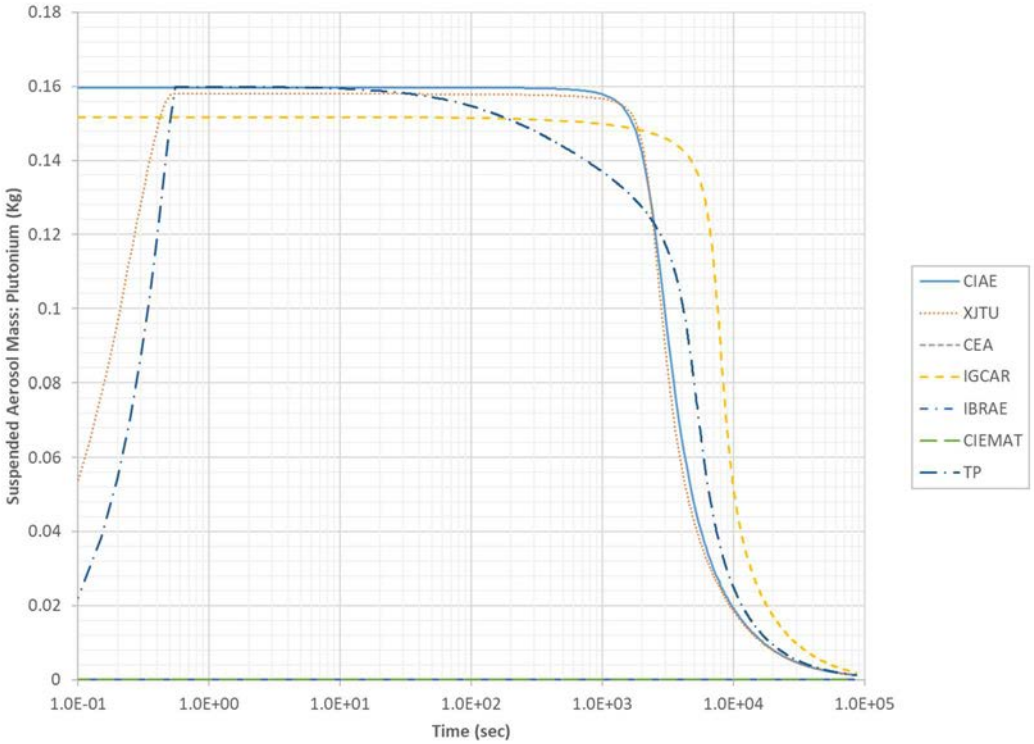

FIG. 338. Sodium spray fire: suspended aerosol mass in containment – plutonium (semi log scale).

7.3.2. Sodium Pool Fire Simulation Comparison

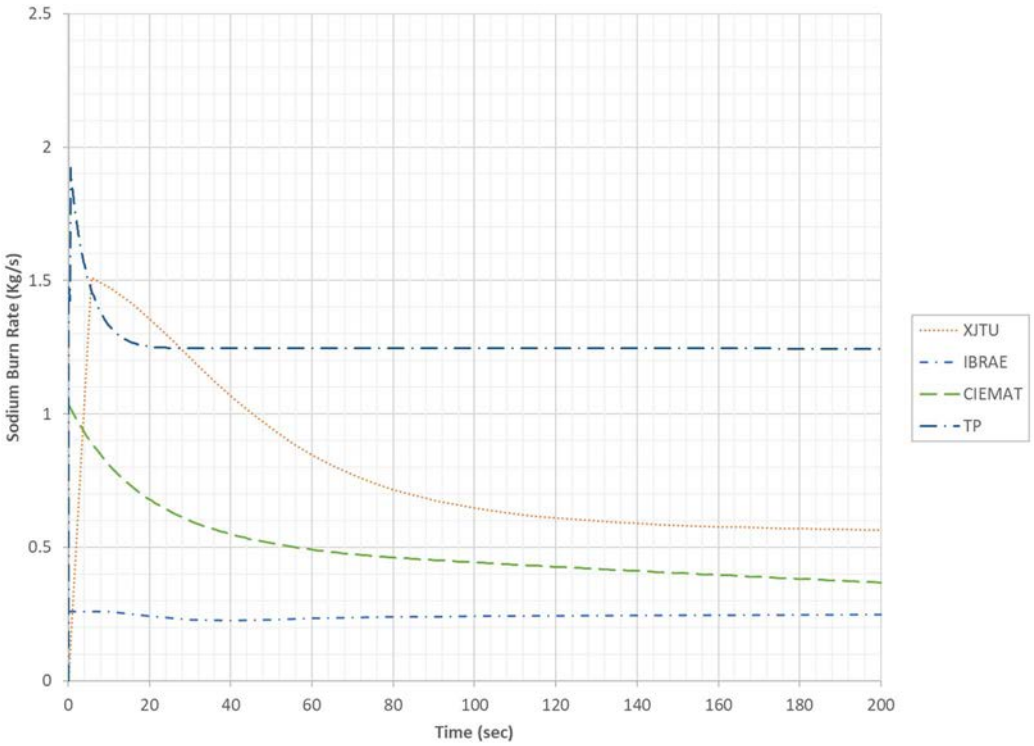

FIG. 339. Sodium pool fire: sodium burn rate (linear scale).

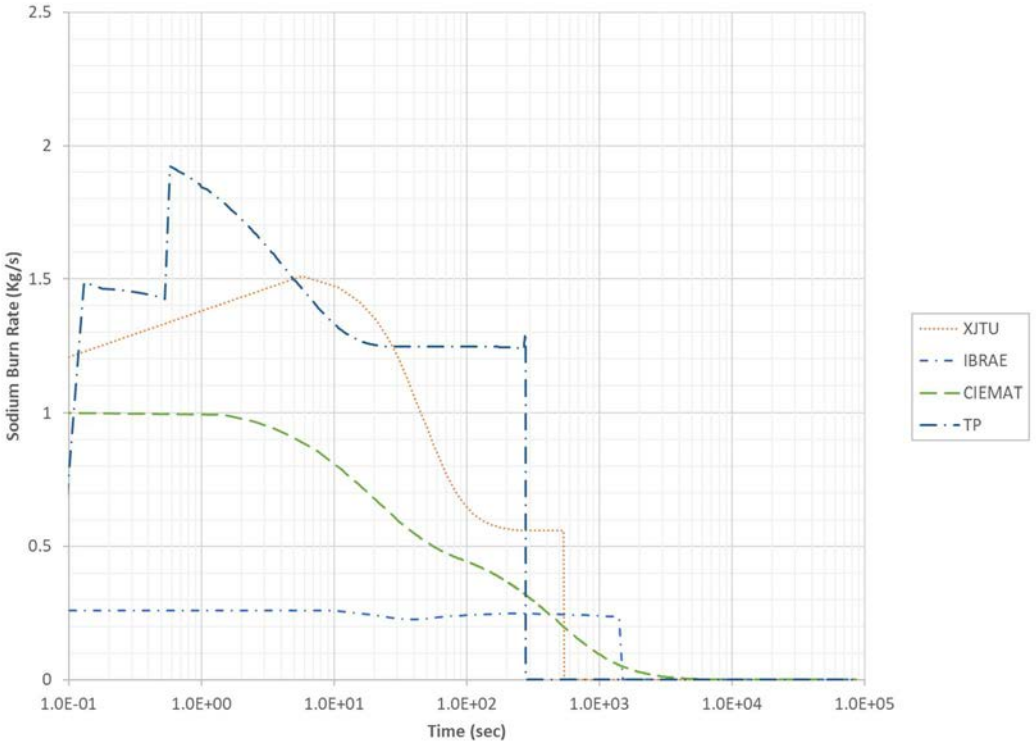

FIG. 340. Sodium pool fire: sodium burn mass (semi log scale).

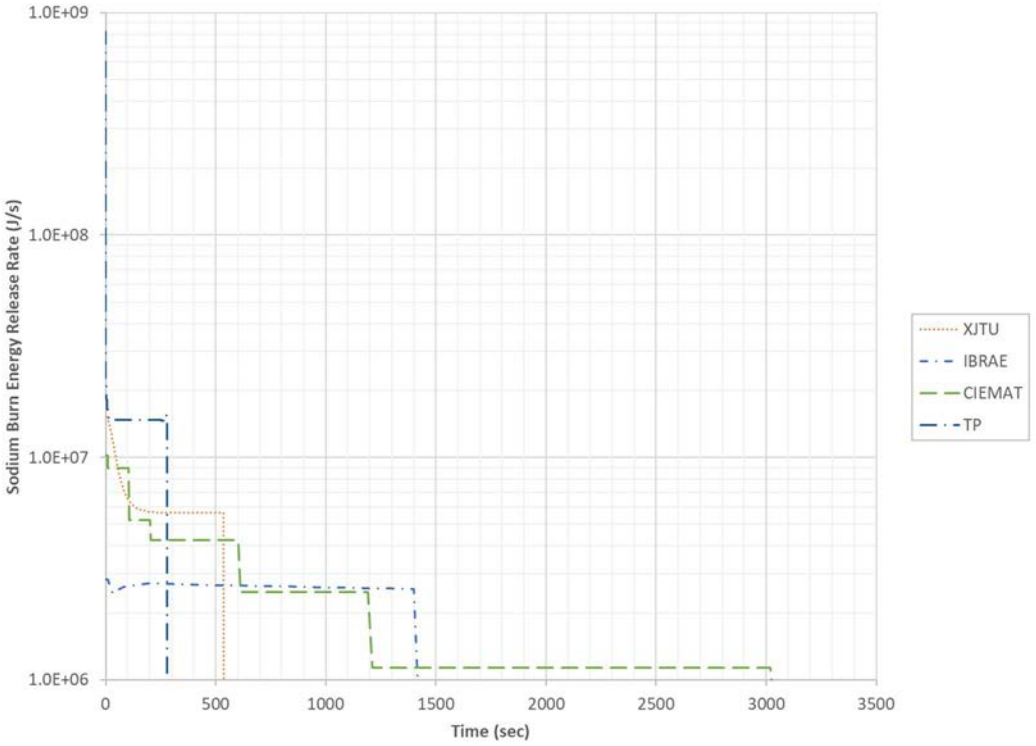

FIG. 341. Sodium pool fire: sodium burn energy release rate (semi log scale).

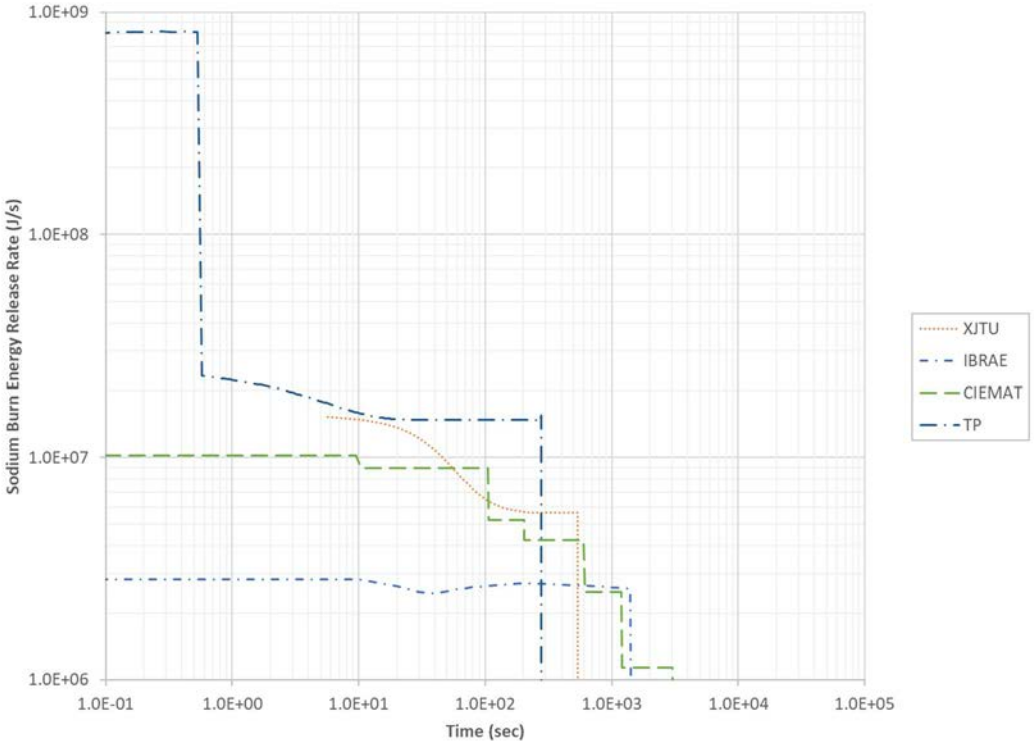

FIG. 342. Sodium pool fire: sodium burn energy release rate (loglog scale).

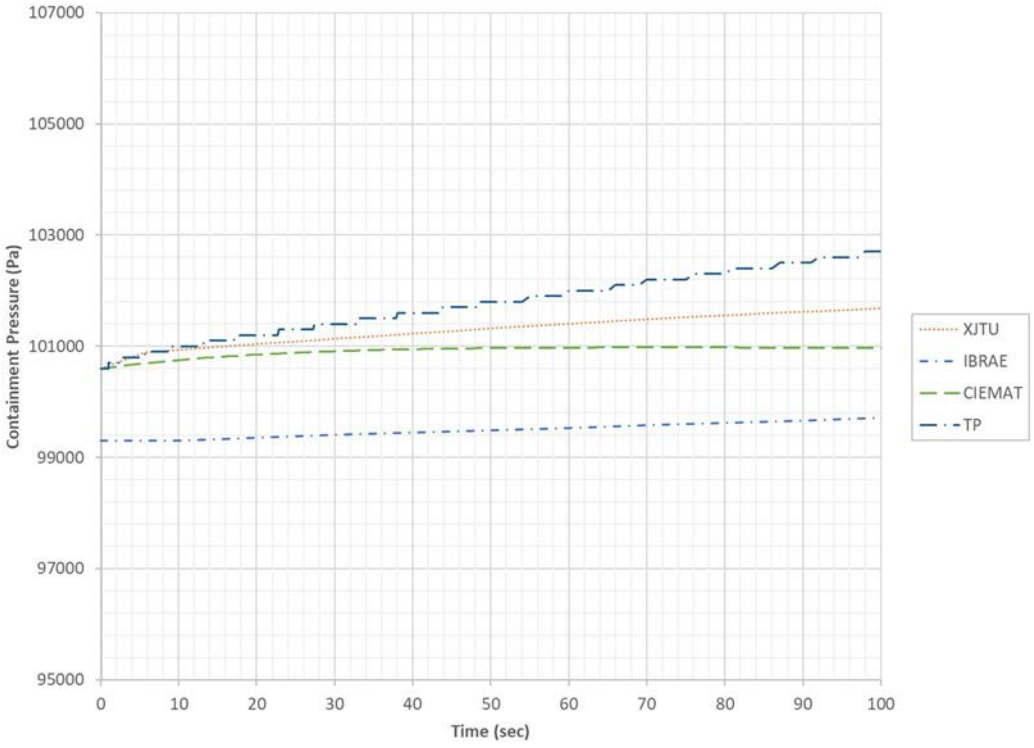

FIG. 343. Sodium pool fire: containment pressure (linear Scale).

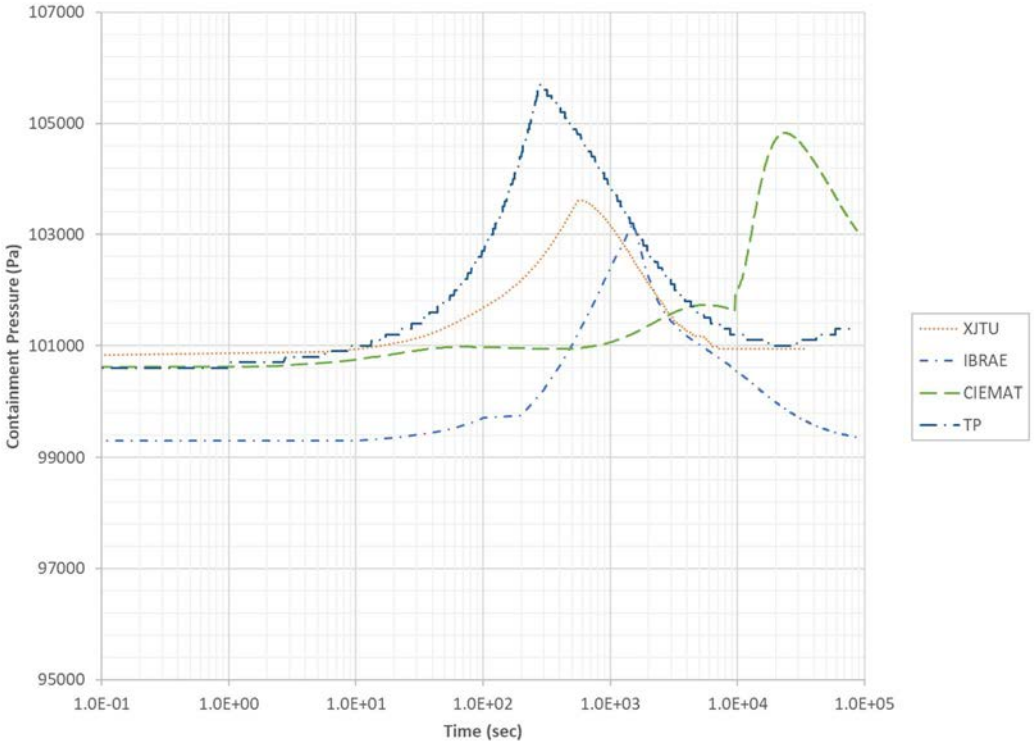

FIG. 344. Sodium pool fire: containment pressure (semi log scale).

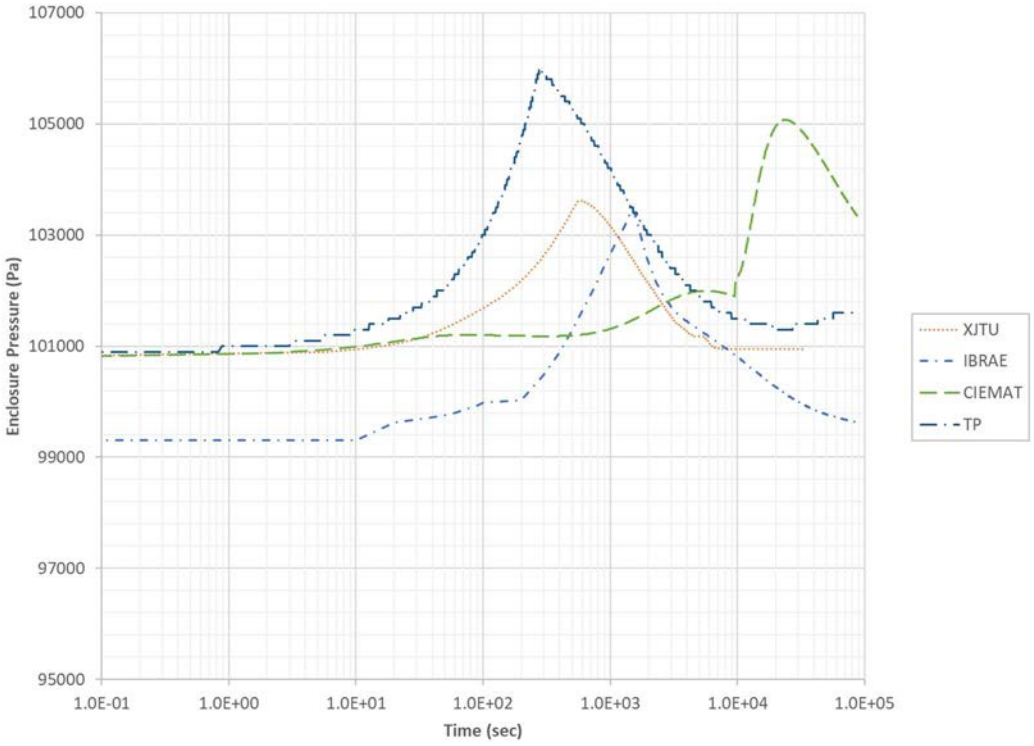

FIG. 345. Sodium pool fire: enclosure pressure (semi log scale).

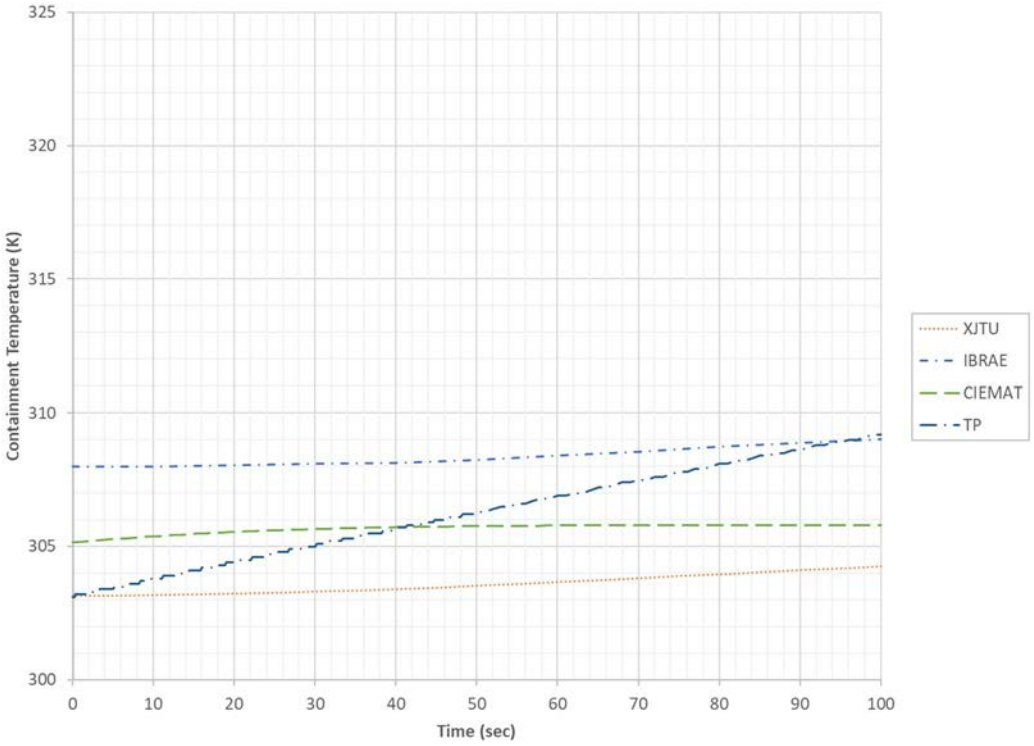

FIG. 346. Sodium pool fire: containment temperature (linear scale).

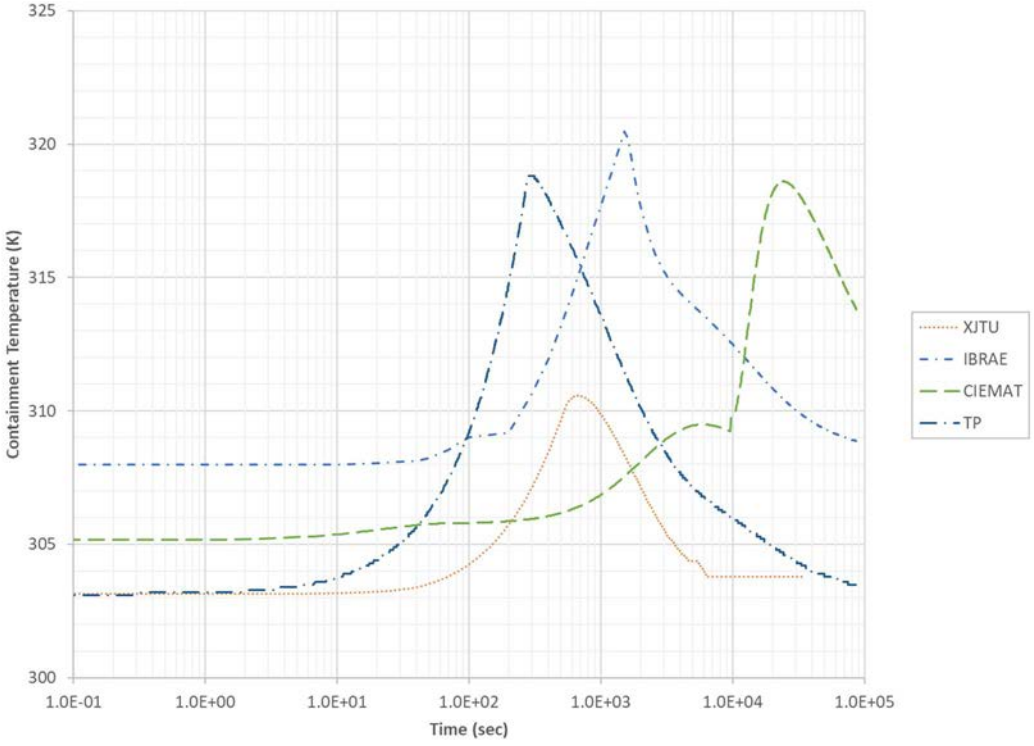

FIG. 347. Sodium pool fire: containment temperature (semi log scale).

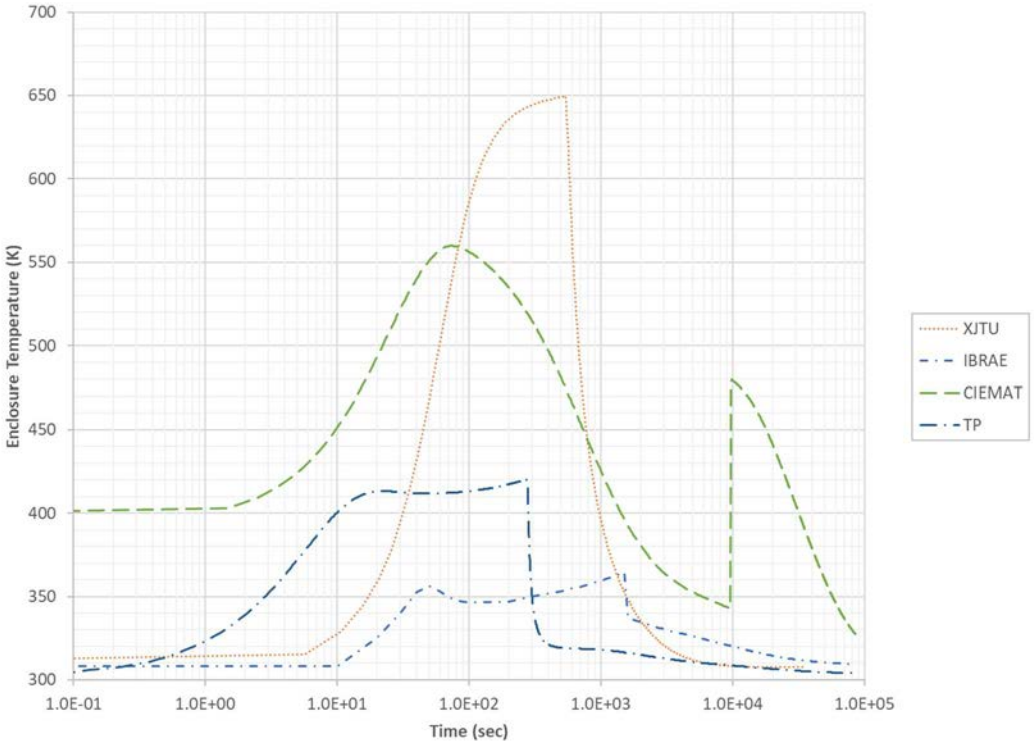

FIG. 348. Sodium pool fire: enclosure temperature (semi log scale).

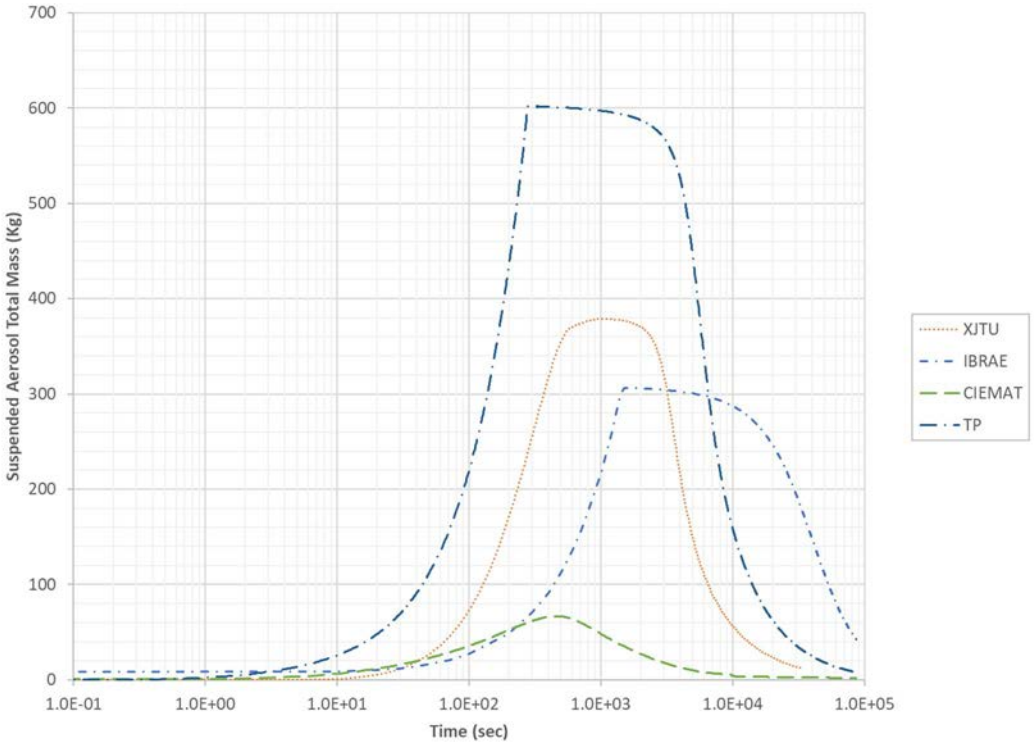

FIG. 349. Sodium pool fire: suspended aerosol total mass in containment (semi log scale).

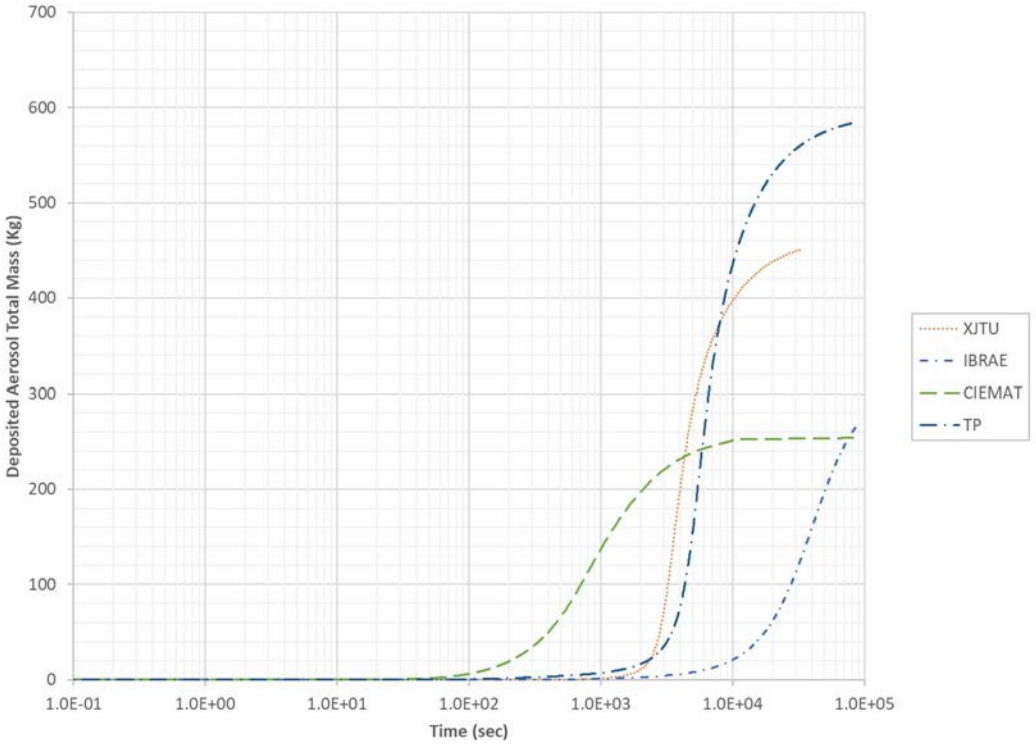

FIG. 350. Sodium Pool fire: deposited aerosol total mass in containment (semi log scale).

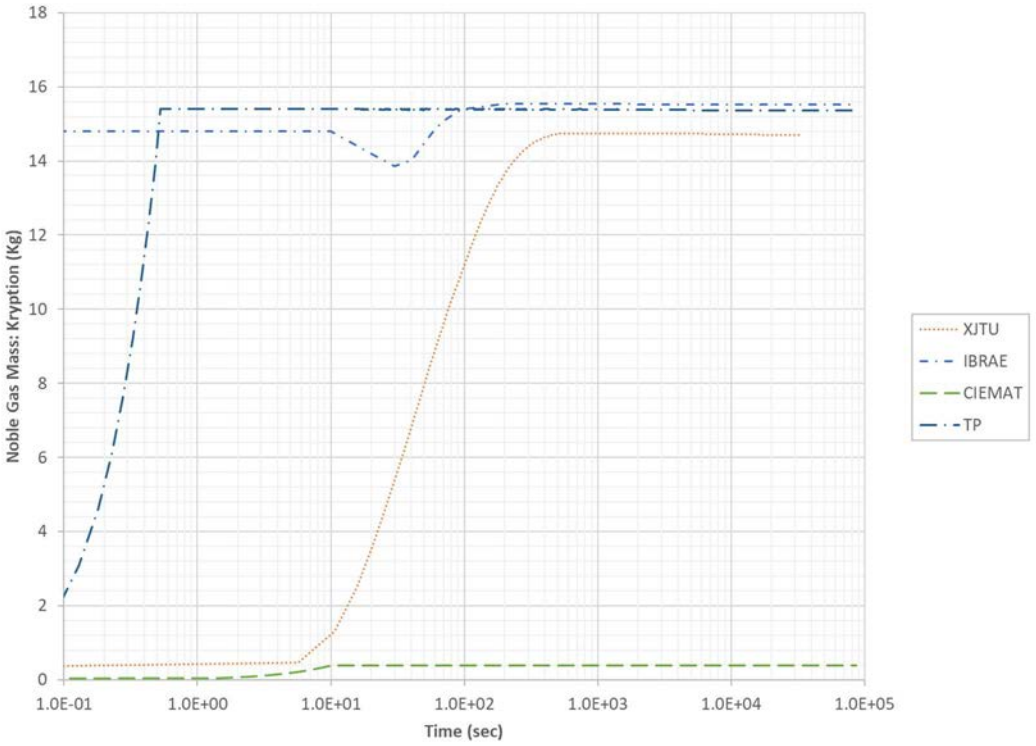

FIG. 351. Sodium pool fire: noble gas mass in containment – krypton (semi log scale).

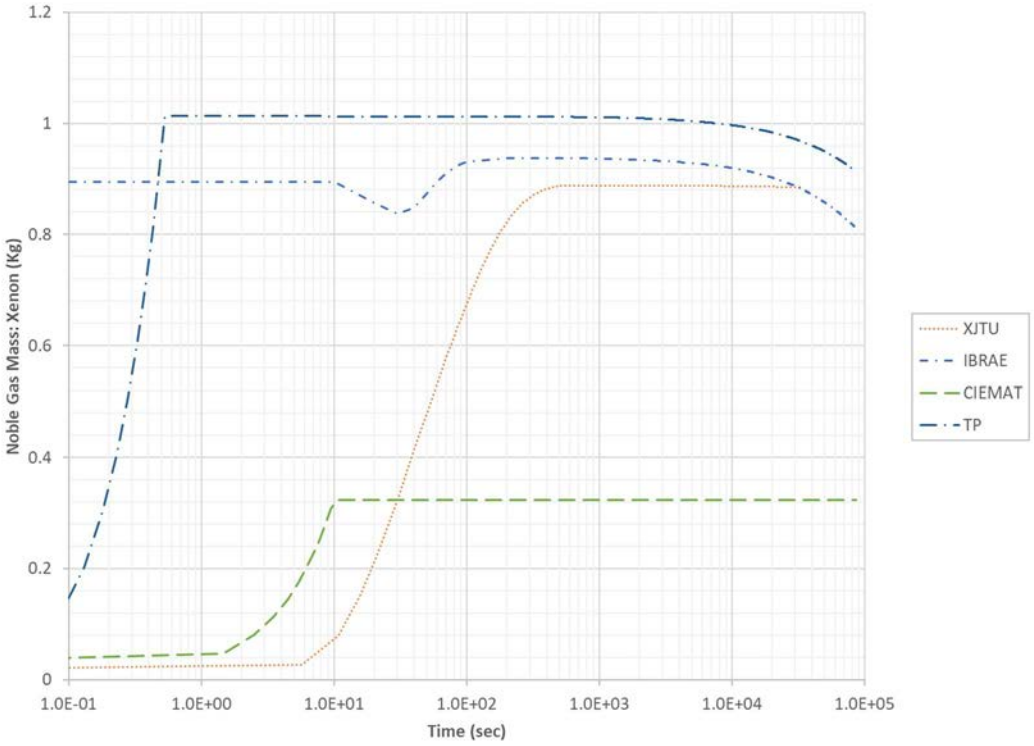

FIG. 352. Sodium pool fire: noble gas mass in containment – xenon (semi log scale).

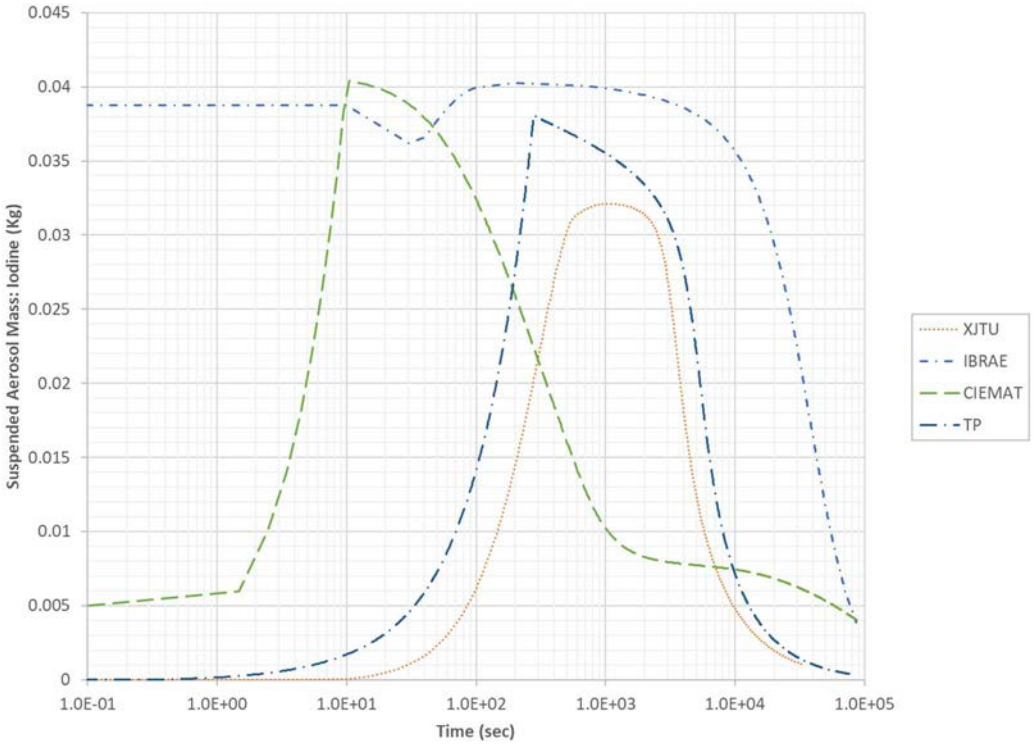

FIG. 353. Sodium pool fire: suspended aerosol mass in containment – iodine (semi log scale).

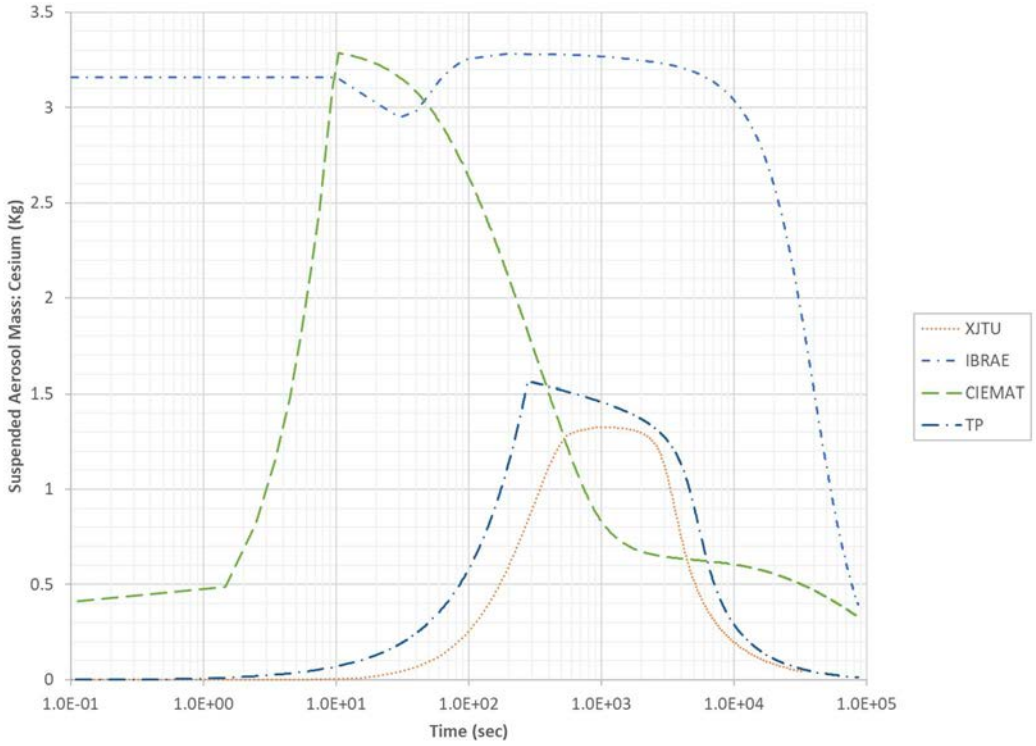

FIG. 354. Sodium pool fire: suspended aerosol mass in containment – caesium (semi log scale).

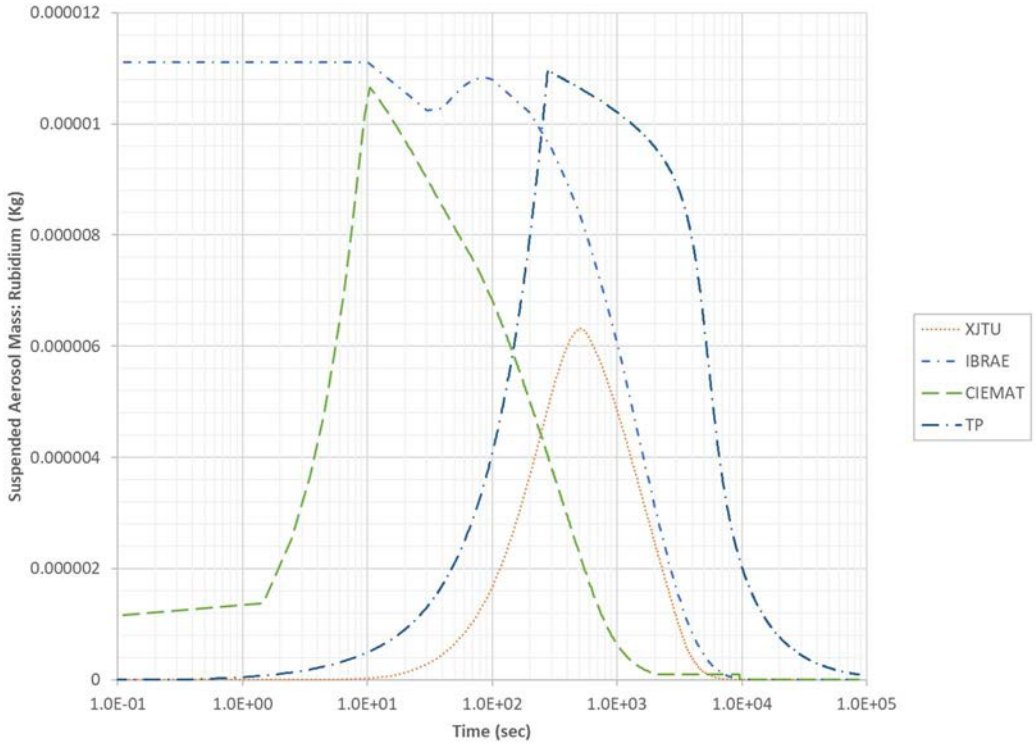

FIG. 355. Sodium pool fire: suspended aerosol mass in containment – rubidium (semi log scale).

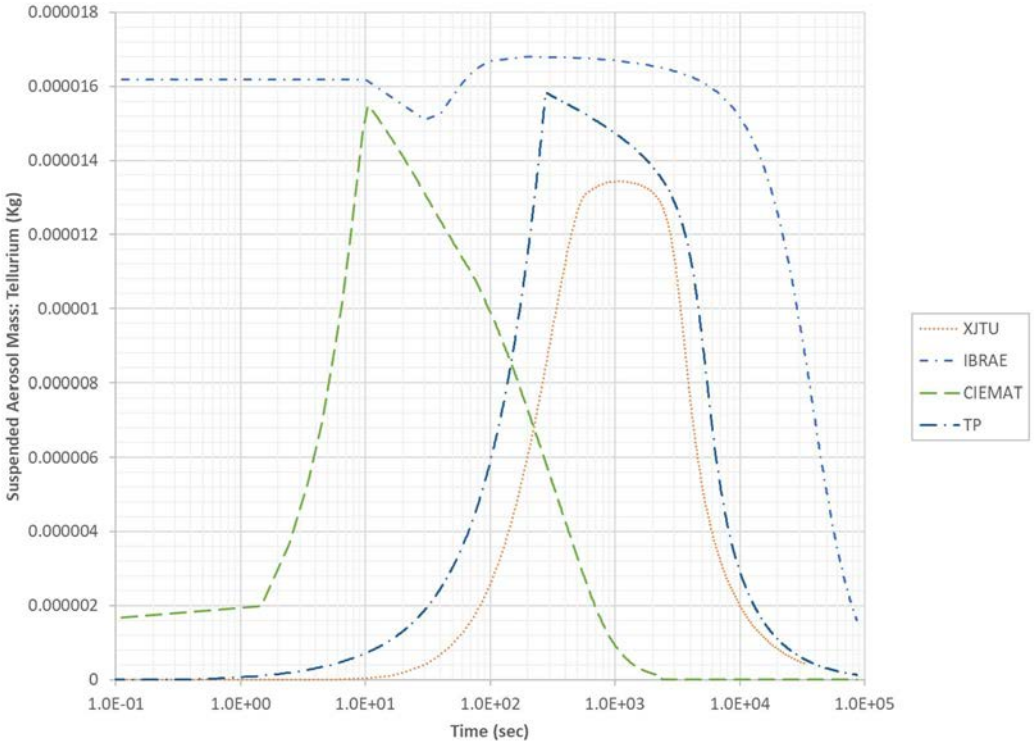

FIG. 356. Sodium pool fire: suspended aerosol mass in containment – tellurium (semi log scale).

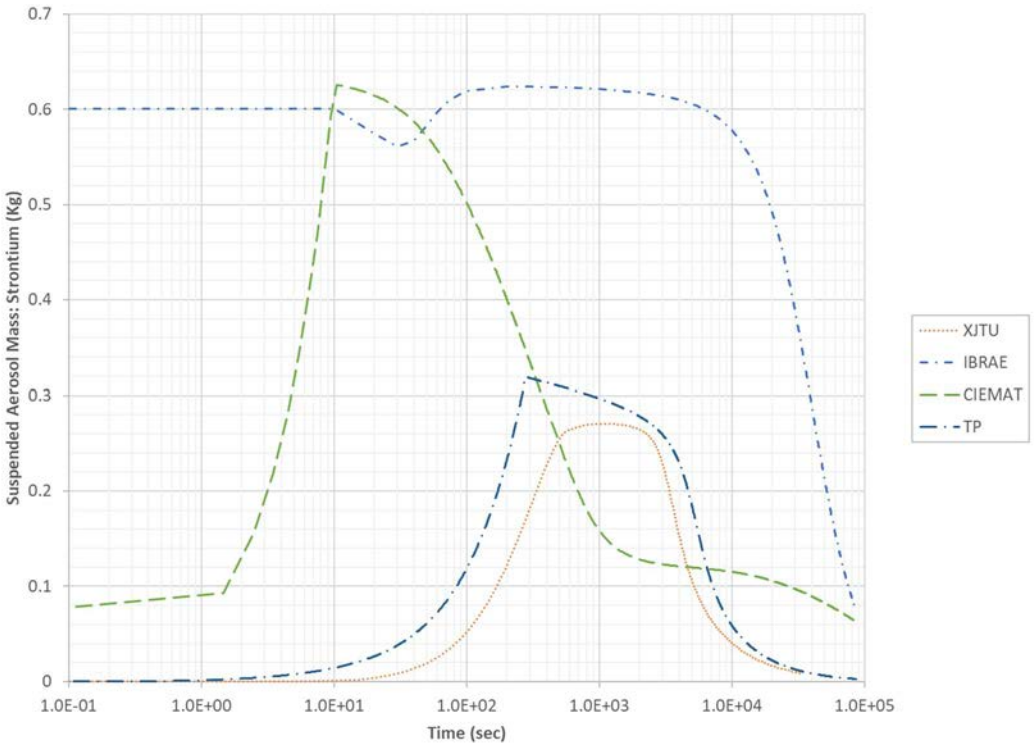

FIG. 357. Sodium pool fire: suspended aerosol mass in containment – strontium (semi log scale).

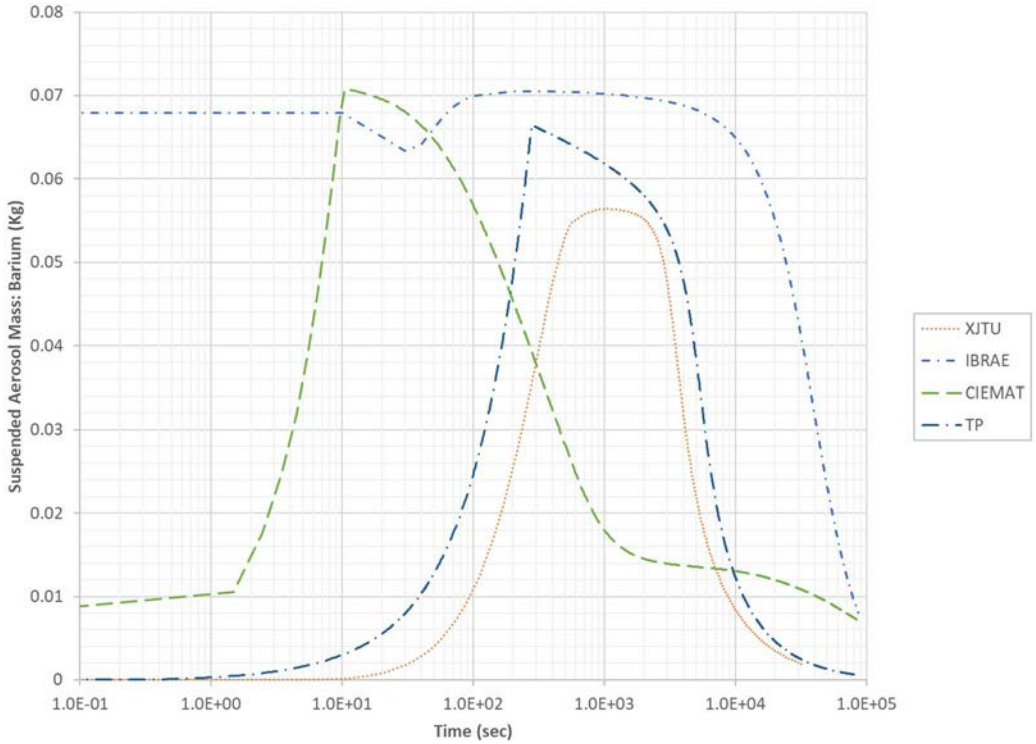

FIG. 358. Sodium pool fire: suspended aerosol mass in containment – barium (semi log scale).

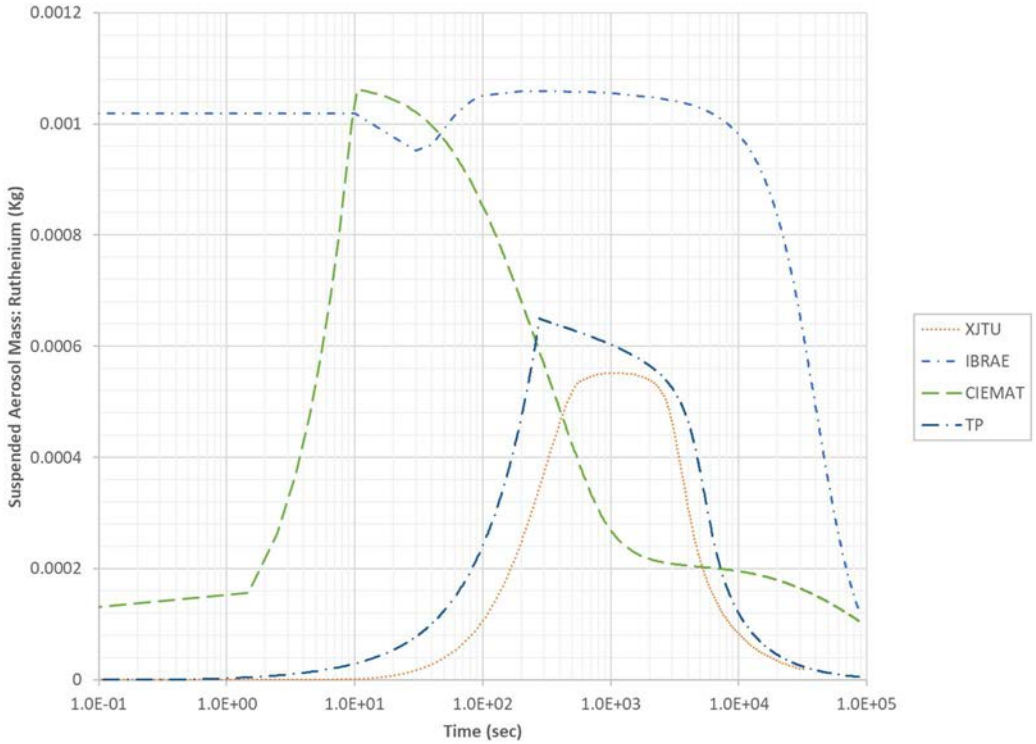

FIG. 359. Sodium pool fire: suspended aerosol mass in containment – ruthenium (semi log scale).

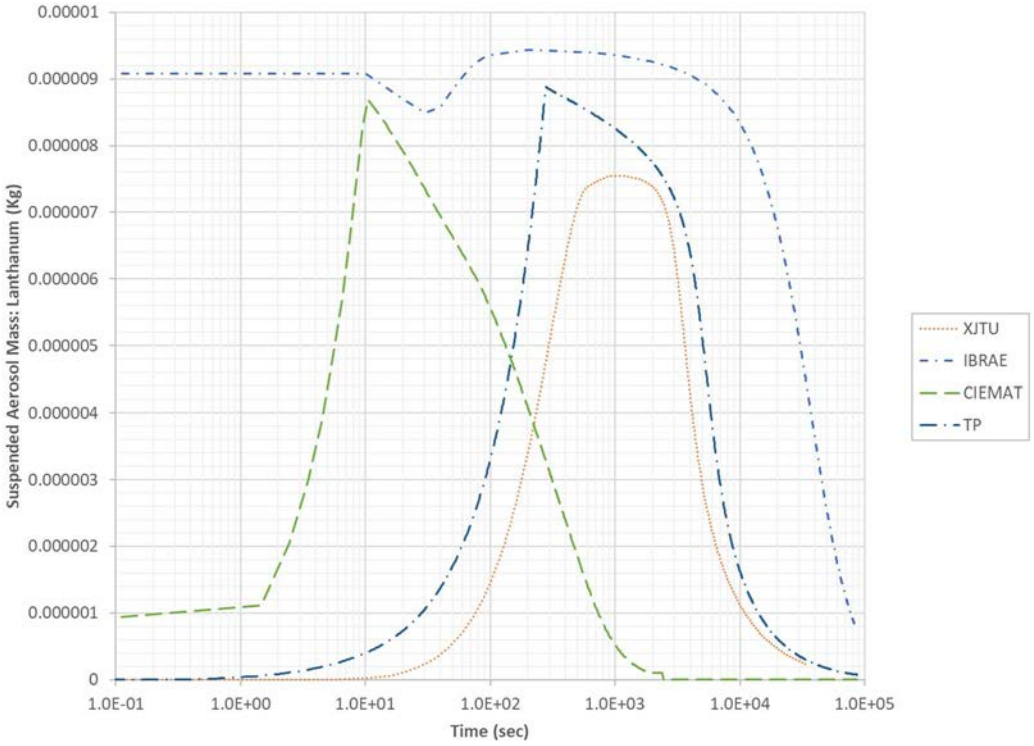

FIG. 360. Sodium pool fire: suspended aerosol mass in containment – lanthanum (semi log scale).

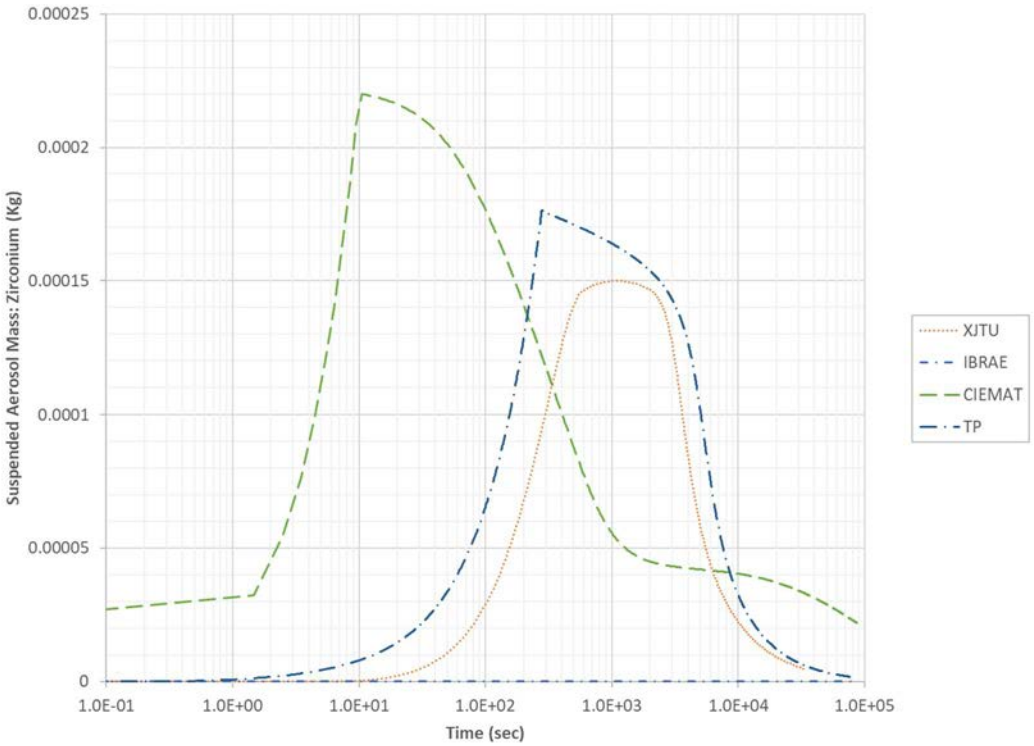

FIG. 361. Sodium pool fire: suspended aerosol mass in containment – zirconium (semi log scale).

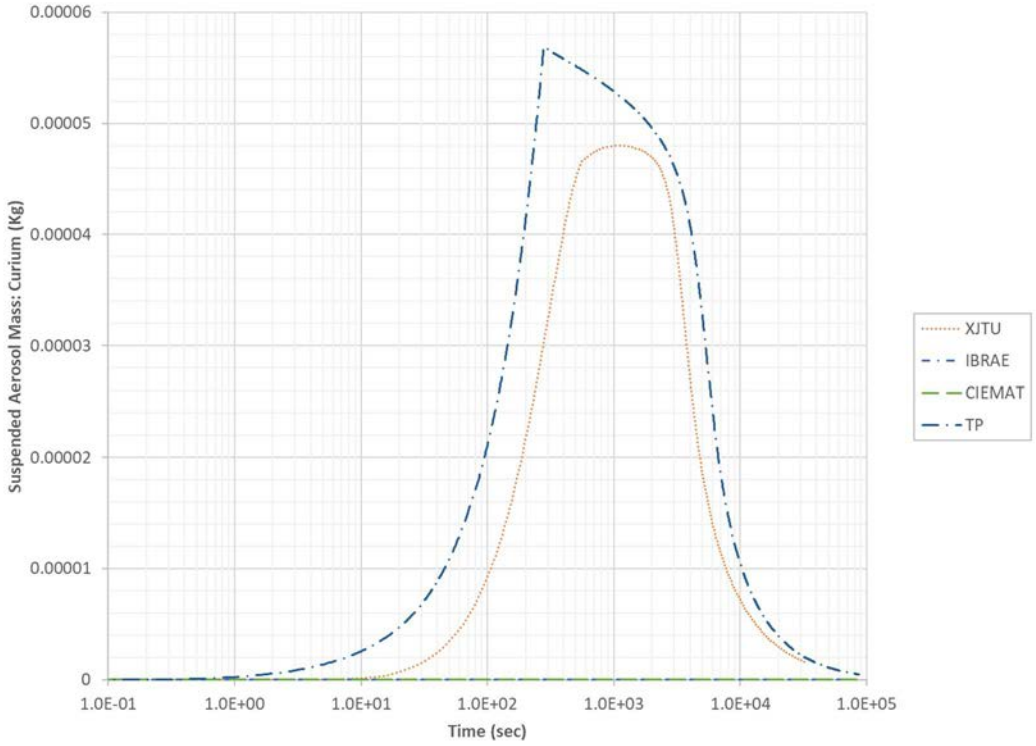

FIG. 362. Sodium pool fire: suspended aerosol mass in containment – curium (semi log scale).

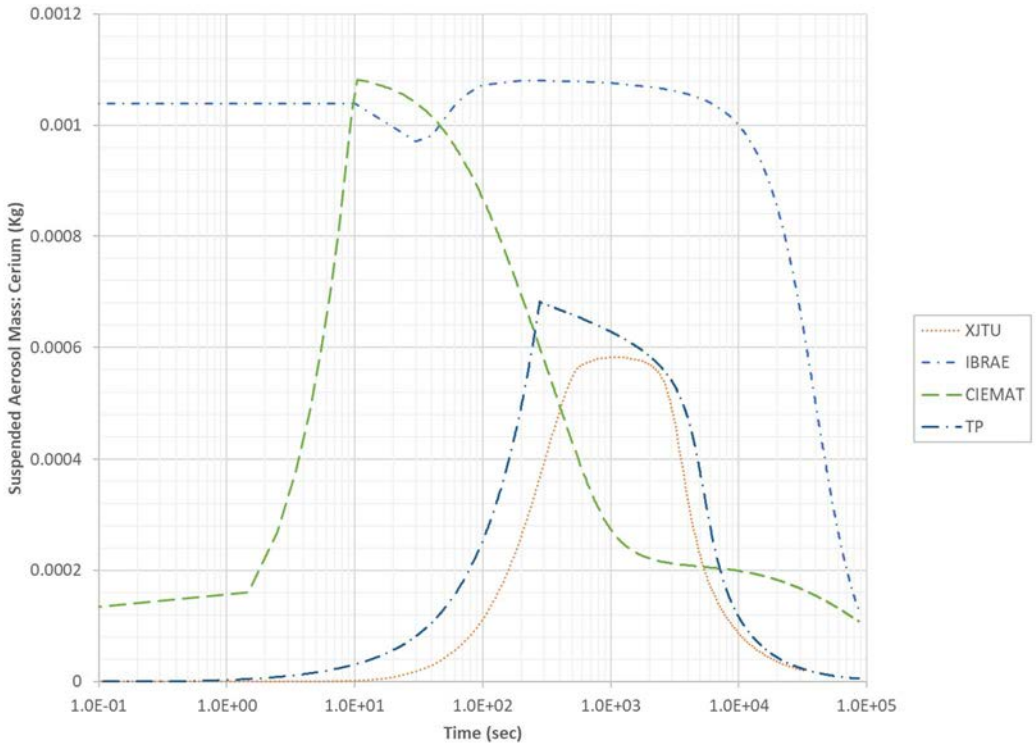

FIG. 363. Sodium pool fire: suspended aerosol mass in containment – cerium (semi log scale).

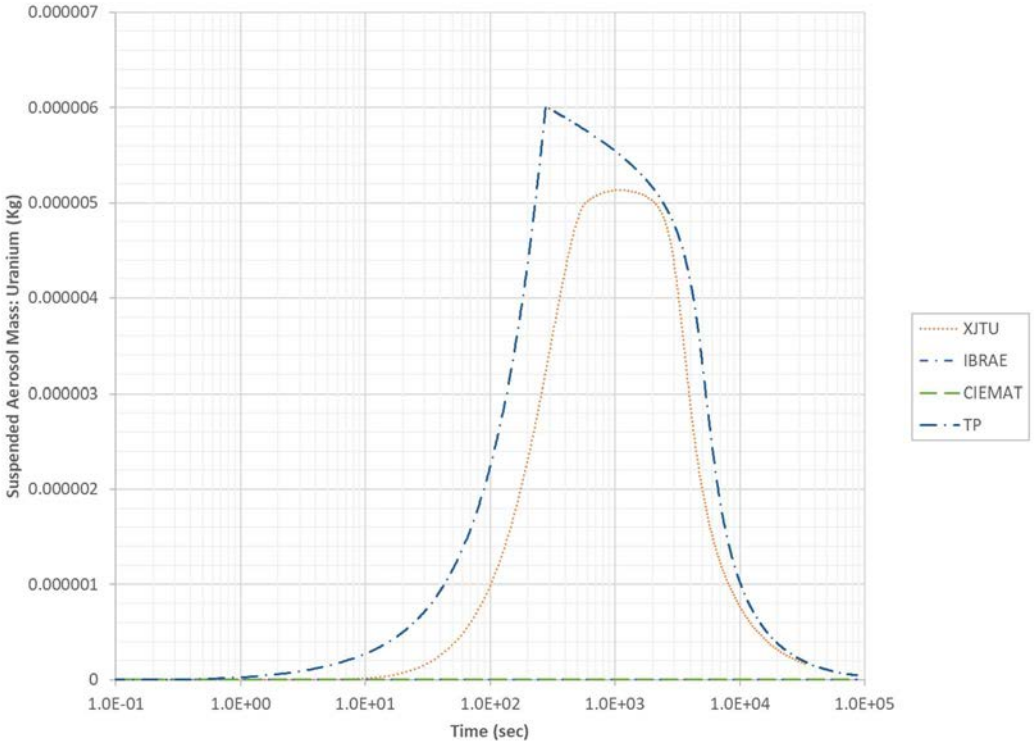

FIG. 364. Sodium pool fire: suspended aerosol mass in containment – uranium (semi log scale).

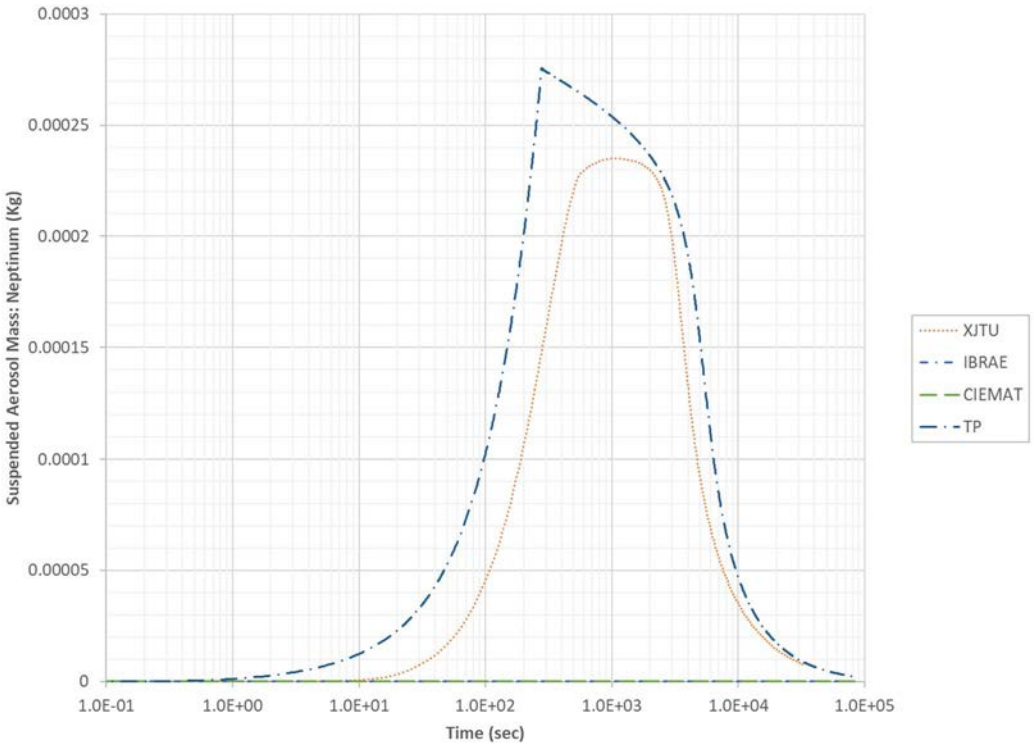

FIG. 365. Sodium pool fire: suspended aerosol mass in containment – neptunium (semi log scale).

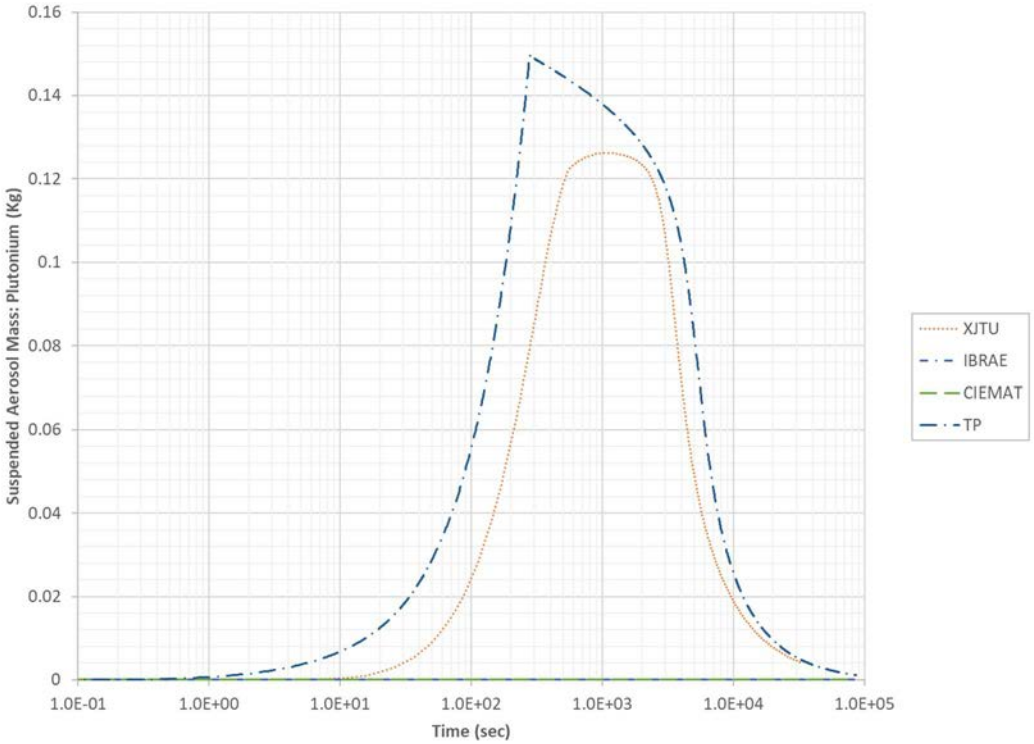

FIG. 366. Sodium pool fire: suspended aerosol mass in containment – plutonium (semi log scale).

7.3.3. Integral case Simulation Comparison

The participants simulating all work packages, IGCAR and IBRAE, were given an option to simulate an additional case where, for simulation of the WP-3, the inputs from the WP-1 & 2 were used instead of the reference RN release fraction input prescribed for WP-3. The comparison of the IBRAE and IGCAR release fractions at the end of WP-2 calculations are shown in FIG. 367.

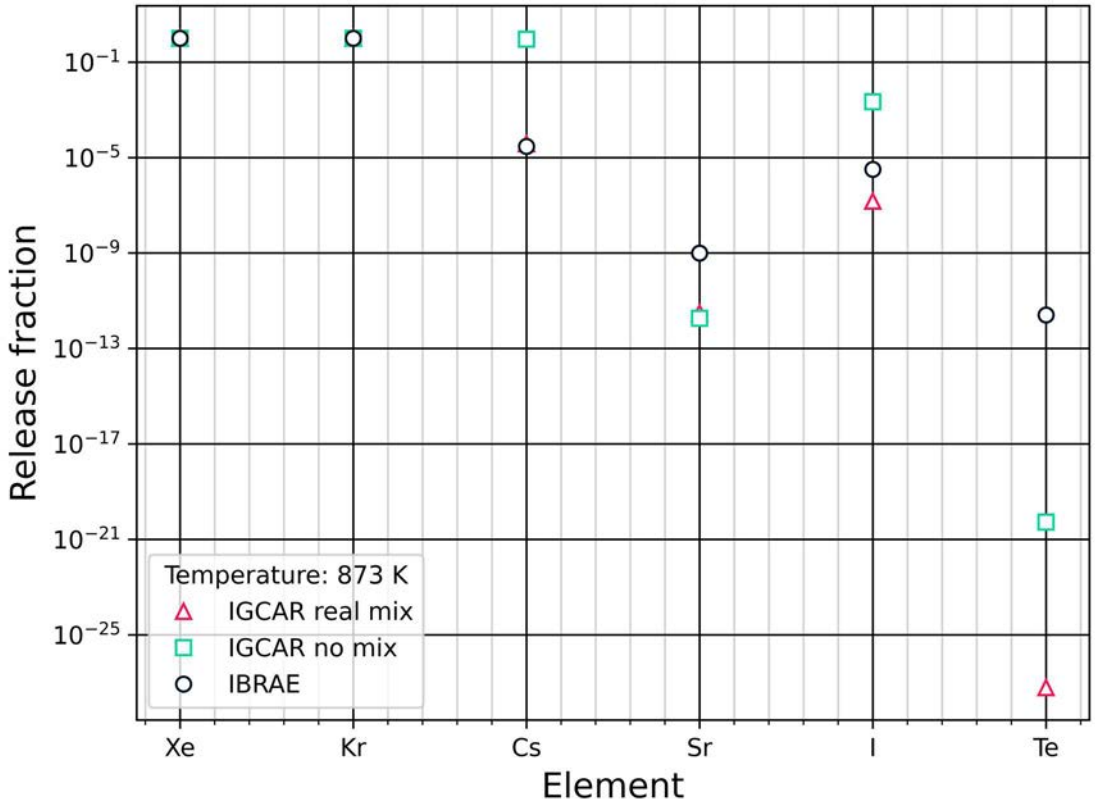

FIG. 367. Comparison of release fractions calculated from WP-1 & 2.

It was assumed that all the cover gas would be expelled into RCB following the CDA. Therefore, the radionuclides release fractions at the end of WP-1 are used in WP-2. This is conservative as scrubbing or deposition of RN aerosols in the leak paths are not modelled at this stage. The discussion on the comparison of the release fractions in section 7.1 is applicable.

The in-containment mass and activity evolution results from IGCAR and IBRAE calculations are shown in FIG. 368 to FIG. 375.

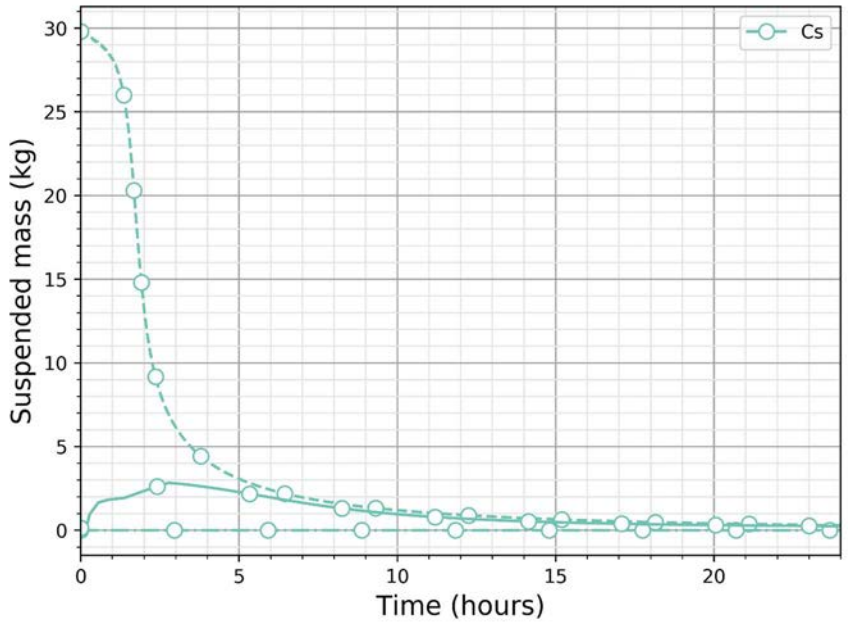

FIG. 368. Suspended Cs mass in the containment (dashed line is no mix-IGCAR, dash-dot is real mix-IGCAR, solid line-IBRAE).

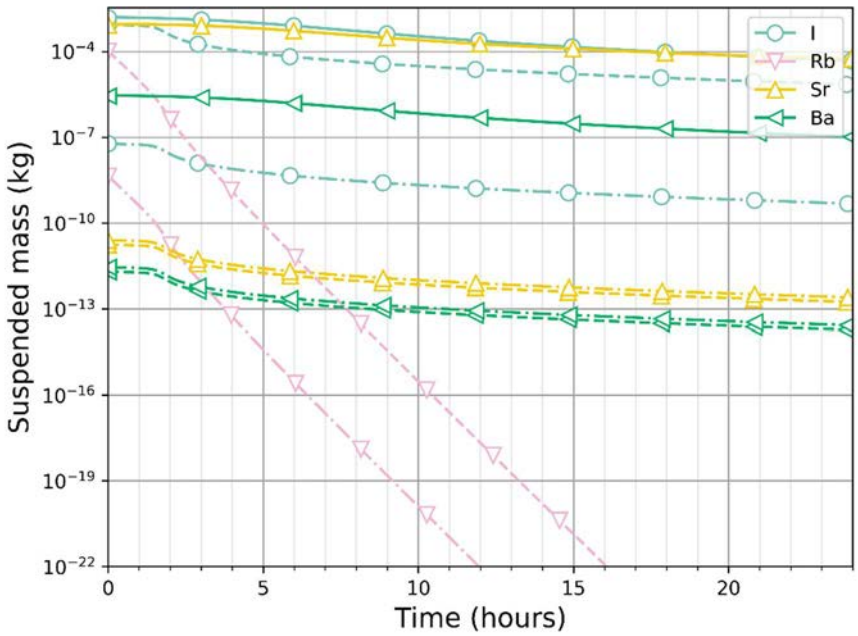

FIG. 369. Suspended volatile RN in the containment (dashed line is no mix-IGCAR, dash-dot is real mix-IGCAR, solid line-IBRAE).

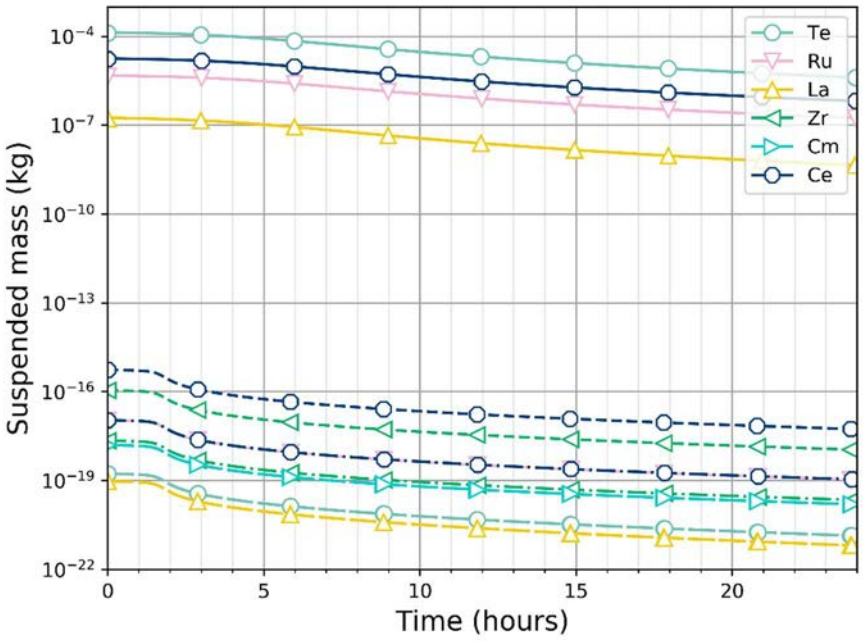

FIG. 370. Suspended RN in the containment (dashed line is no mix-IGCAR, dash-dot is real mix-IGCAR, solid line-IBRAE).

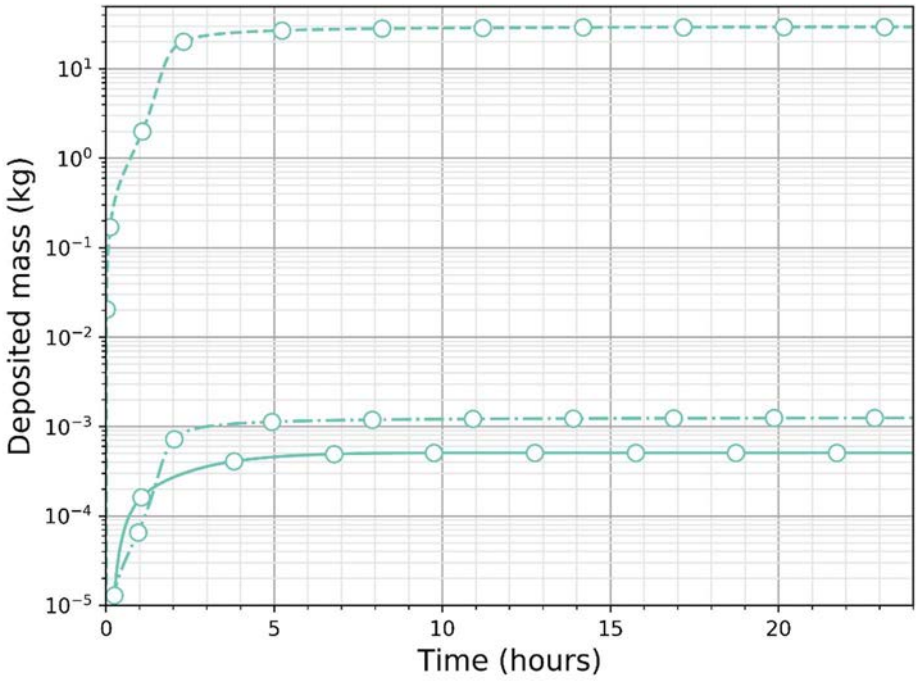

FIG. 371. Deposited Cs in the containment with time (dashed line is no mix-IGCAR, dash-dot is real mix-IGCAR, solid line-IBRAE).

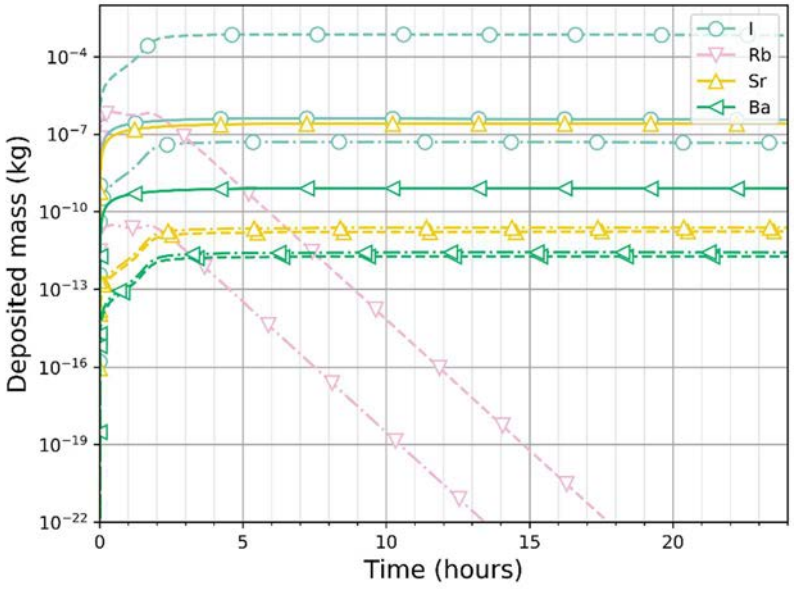

FIG. 372. Deposited volatile RN in the containment (dashed line is no mix-IGCAR, dash-dot is real mix-IGCAR, solid line-IBRAE).

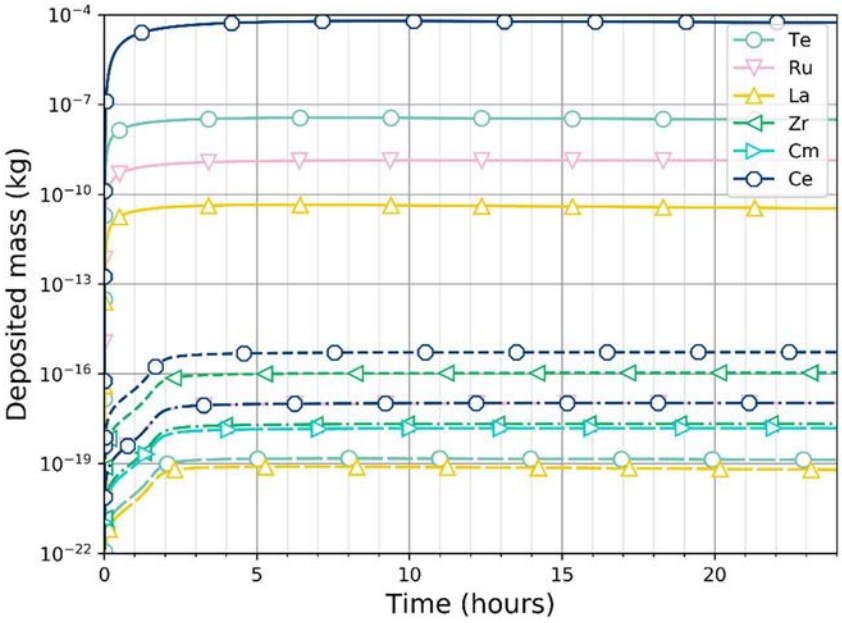

FIG. 373. Deposited RN in the containment (dashed line is no mix-IGCAR, dash-dot is real mix-IGCAR, solid line-IBRAE).

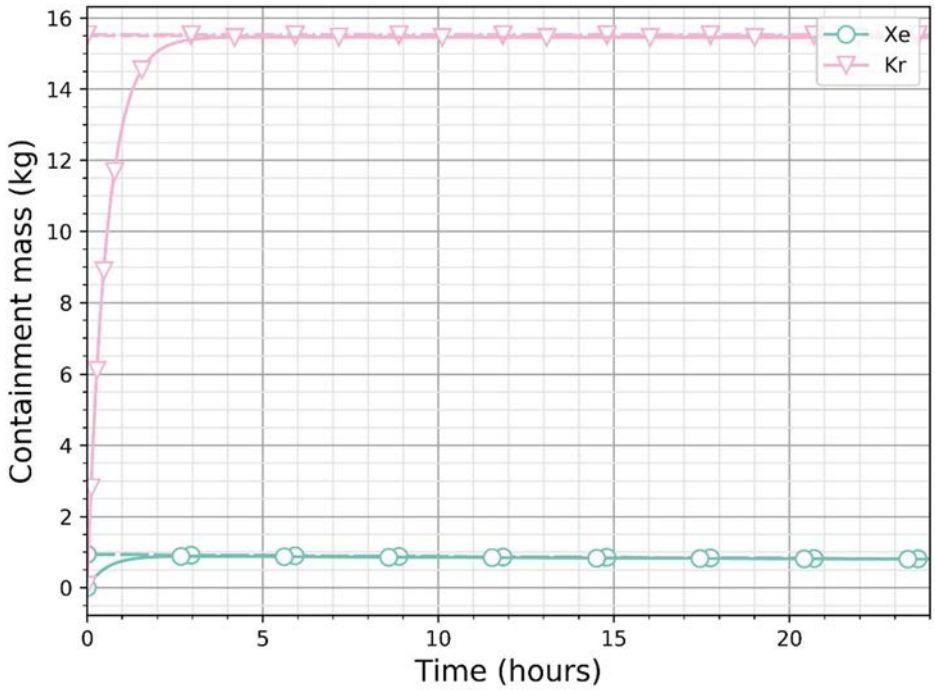

FIG. 374. Total Xe and Kr mass in the containment (dashed line is no mix-IGCAR, dash-dot is real mix-IGCAR, solid line-IBRAE).

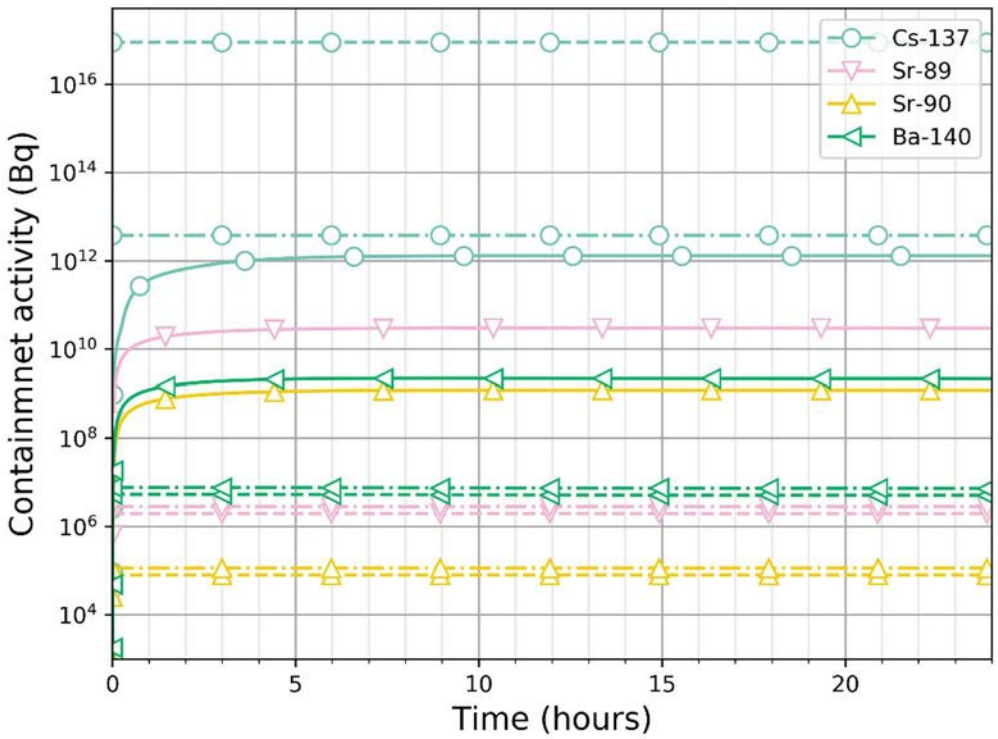

FIG. 375. Total containment activity of few radiologically important RN (dashed line is no mix-IGCAR, dash-dot is real mix-IGCAR, solid line-IBRAE).

—

— The quantity of Cs (Cs137 and Cs134), as shown in FIG. 368, matches only after about 5h. The initial amount reported by IGCAR is more for the no-mixture case as Cs solubility is ignored, whereas for the real mixture case the release is much less than that reported by IBRAE.
— The sharp decrease of Rb in FIG. 369 is due to its short half-life of 17 minutes. The Rb plot for IBRAE is not shown.
— For Sr and Ba, as shown in FIG. 369, IGCAR simulations predict only trace amounts, as Sr forms oxide condensate in sodium. For IBRAE suspended Sr is about 0.1 grams and Ba is shown in milligrams.
— Large difference in predicted suspended mass of Te, Ru, La, Zr, Cm, Ce, Ba, as shown in FIG. 370, is due to differences in the in-vessel release models and very different release fraction estimates of IBRAE and IGCAR.
— For the calculation, IGCAR assumed no leak through containment, which will give the maximum containment activity in the containment; whereas IBRAE has performed their calculation with 1% peak leak/vol. For example, deposited mass of Cs reported by IBRAE is much less than the initial suspended mass.
— There is a good agreement between IBRAE and IGCAR on total mass in the containment of Xe and Kr, shown in FIG. 374.
— The difference in the total containment activity, shown in FIG. 375, is due to differences in the in-containment release fraction.

8. SUMMARY AND CONCLUSIONS

The IAEA coordinated research project (CRP) on “Radioactive Release from the Prototype Sodium Cooled Fast Reactor under Severe Accident Conditions” was devoted to the realistic numerical simulations of fission products and fuel particles inventory inside the reference sodium cooled fast reactor (SFR) volumes under severe accident conditions at different time scales, from few initial seconds for the instantaneous source terms to several days for the long-term source term. The scope of analysis was divided into three parts, defined as three work packages: (1) in-vessel source term estimation; (2) primary system/containment system interface source term estimation; and (3) in-containment phenomenology analysis. It was assumed that the work packages would be used sequentially, with outputs from one work package serving as the inputs to the next work package. However, estimating the complexity of the project, some initial boundary conditions for work package 2 and 3 were predefined to allow for stand-alone calculations for each work package. Nine organizations from seven Member States have participated in the CRP while every participant had a choice to contribute to one or more work packages.

Three organizations have contributed to work package 1 starting with IBRAE/RAN Russia and IGCAR. Subsequently in 2019, JAEA also joined. IBRAE used the EUCLID/V2 code to model the radioactivity transport from the molten core to the coolant and from the coolant to the cover gas. The release fractions and the quantity of the released radionuclides are reported. The modelling by IBRAE involves mass transfer correlations validated by experiments. IGCAR used MINICHEM thermo-chemical equilibrium code to calculate release fractions from the molten core coolant mixture to the cover gas. The release fractions and released quantity are also reported. Using the SIMMER-IV code, JAEA simulated the transient flow and temperature fields that can be used to calculate the transport of radionuclides. Comparison of the results obtained by three participating organizations indicates that the release fractions of noble gases, and caesium radionuclides are in a good agreement. However, significant difference is observed in the release fractions of strontium, tellurium and other radionuclides. Despite completely different modelling approaches by IBRAE and IGCAR, the agreement in the predicted fractions of radionuclides released to the cover gas is reasonably good. However, for more accurate analysis, it would be beneficial to combine mass transfer and chemical equilibrium models. The results of SIMMER-IV calculation, mass, temperature and pressure distribution of fuel, steel, sodium and fission gas in reactor vessel have potential to be used in calculating RN transportation from fuel to cover gas through coolant sodium considering bubble transportation and diffusion of RN.

Four organizations participated in work package 2. IBRAE/RAN did the simulations with EUCLID/V2. IGCAR used FUSTIN/BLVDYN and NETFLOW codes for simulations. NCEPU used ANSYS FLUENT to calculate sodium ejection onto the top shield and performed experiments on modelling of particle transport in the primary system, however, due to the technical problems in the experiment, the final experimental results have not been obtained. In 2019, JAEA joined the CRP and used PLUG code for the calculations. In the analysis using a common pressure history, the results of the analysis of each institution were in good agreement. This indicates that the variation in modelling for this task is small, and that the analysis accuracy of the analysis method of each institution is almost the same. The amount of sodium ejected onto the top shield calculated in reference case is approximated to be 350 kg and will be utilized in WP-3 as input for sodium combustion calculation. According to the results of the parametric analyses performed here, the change of parameters regarding uncertainty, such as input

pressure, outlet pressure, cross-sectional area, and loss coefficient bring about the change of leaked mass in the range of several tens of %.

In work package 3, seven organizations participated and contributed. IBRAE used EUCLID/V2, XJTU used REBAC-SFR, and CIEMAT used ASTEC-Na. IGCAR used SOFIRE based fire simulation code PFIRE and PANDICA for in-containment aerosol evolution. All other organizations used CONTAIN-LMR. To decouple this part of analysis from previous packages, an additional standalone calculation was defined for the package, which uses a set of pre-defined release fractions. In the coupled case, the release fractions of radionuclides computed at the previous work packages were used as initial conditions. The standalone case is appropriate for inter-comparison with respect to assessing the tools of WP-3 calculations. In conclusion, there is broad consensus among the predicted results in this package with respect to the stand-alone case. However, the CEA calculation results are substantially different. The reason could be due to the different initial conditions used in the calculations.

After intensive discussions of the WP-1 results, participants have agreed that it is necessary to include chemical reaction aspects in IBRAE/RAN approach and mechanical transport models in IGCAR simulations. Experimental activity for compilation of chemical potentials of important fission product compounds, minor actinide compounds and compilation of excess functions of these in sodium is very important for the calculation of in-vessel release fractions of radionuclides.

In WP-2, applying CFD codes or correlations adopted from CFD codes would add an additional valuable dimension to improved simulation of aerosol transport and leak path deposition. In order to evaluate movement of the top shields considering their restriction by connecting bolts and resultant sodium ejection, it is necessary to analyse the dynamic response of the top shields.

It has been discovered that current modelling and simulation tools applied to WP-3 calculations lack important physical models, such as aerosol initial size distribution generation models for sodium and radionuclides from sodium fire, and therefore needs to be improved.

APPENDIX

Participating Organizations and Simulation Tools

A.1. CHINA INSTITUTE OF ATOMIC ENERGY (CIAE), CHINA

A.1.1. Research Activities and Capabilities on SFR Severe Accident Simulation at CIAE

CIAE SFR severe accident analysis research is divided into independent steps with different simulation tools. A comprehensive SFR severe accident analysis tool is not available now. CIAE research focuses on five key areas in the severe accident analysis:

- **Simulation of Unprotected Accidents** CIAE developed a computer code named CODA for the analysis of unprotected accidents. It is a sodium cooled fast reactor severe accident analysis program used to calculate the sodium boiling and melting behavior caused by ULOF, UTOP and TIB. CODA contains three modules: fluid dynamics module, structural module, and neutron dynamics module.
- **Energy Release Evaluation during HCDA** To evaluate the energy release during a hypothetical core disruptive accident, a code based on modified Bethe-Tait model with mechanical analysis was developed
- **Reactor Vessel Mechanical Response during HCDA** Reactor vessel mechanical response during HCDA was analysed for China's demonstration fast reactor. A method was developed to assess the amount of liquid sodium leakage.
- **Sodium fire Accident Analysis in Containment** Three computer codes are used in CIAE for sodium fire accident analysis, FEUMIX, BOX and CONTAIN-LMR. FEUMIX is used specially for sodium spray fire analysis. BOX is used for sodium pool fire analysis. CONTAIN-LMR is an integrated analysis tool for predicting the physical, chemical, and radiological conditions inside the containment. This program can be used for sodium pool fire analysis, sodium spray fire analysis and radionuclide transportation analysis in the containment. In this publication, CONTAIN-LMR is used for the analysis of WP3.
- **Post-accident Natural Circulation** CFD numerical simulation is used to model natural circulation following a severe accident using a simplified internal structure of the reactor. In-vessel core catcher design is based on the simulation results to preserve natural circulation.

A.1.2. CONTAIN-LMR code introduction and application

The CONTAIN code is the US NRC's best-estimate tool for predicting the physical and radiological conditions that may exist in reactor containment buildings in the event of a severe accident. It can also be used to predict release to the environment in the event of containment failure. CONTAIN simultaneously analyses thermal-hydraulic, aerosol, and fission product behavior. The basic phenomenological areas in CONTAIN and some couplings and feedback loops are illustrated in FIG. 376. CONTAIN offers a broad variety of models to the analyst in a system-level computational structure, which allows for the complex interactions and feedback among the diverse phenomena to be studied. Among models available are those for:

- Intercell gas flow, including natural circulation effects,
- Two-phase atmospheric thermodynamics,
- Conduction in structures,

— Convective and radiant heat transfer,
— Condensation/evaporation at structure and pool surfaces,
— Hydrogen combustion,
— Multicomponent aerosol processes,
— The transport and decay heating effects of fission products,
— Ablation of concrete by core debris.

CONTAIN-LMR is a special version of the CONTAIN computer code that has been provided with extra capabilities to model LMR applications. The code is produced by applying LMR-specific updates to an official light water reactor (LWR) version of the CONTAIN code. This official LWR version is referred to as the base version. The version used in the project is CONTAIN LMR/1B-Mod.1, the base version of which is CONTAIN 1.11.

Some of the sodium specific features are part of the standard version of CONTAIN. Their presence in the code dates back to the original versions, which provided both LMR and LWR analysis capability. This dual capability of standard CONTAIN has been maintained, and modifications to these LMR-specific models developed in the course of LMR applications have been incorporated into the standard code when this could be done easily. CONTAIN-LMR includes models for sodium chemistry, sodium-concrete interactions, debris bed phenomena and other LMR-specific models in an integrated manner.

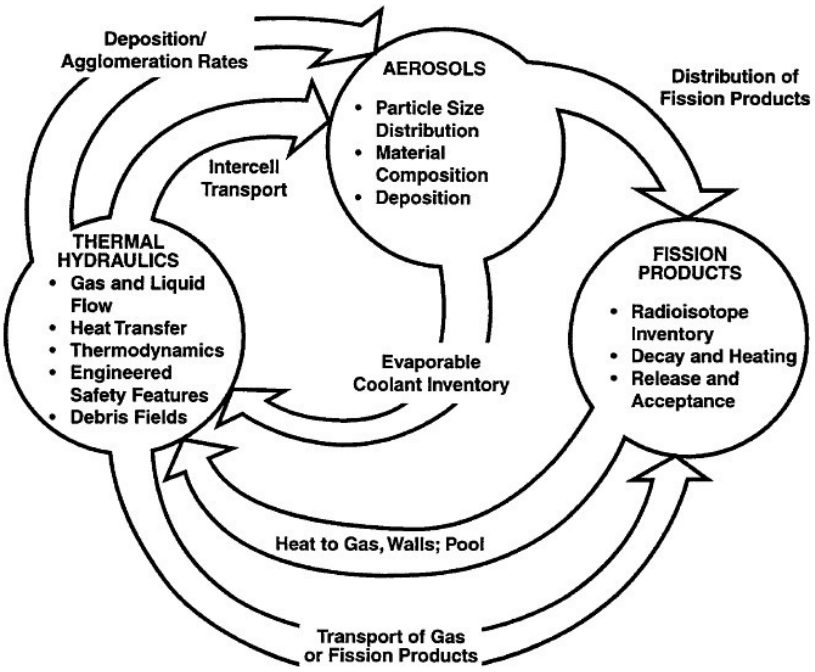

FIG. 376 Three basic phenomenological areas treated in CONTAIN and some coupling and feedback loops among them.

The integrated nature and the wide spectrum of models available make CONTAIN-LMR well suited for analysis of accidents, ranging from relatively benign scenarios to severe core melt accidents involving release of radioactive materials to the environment. It may also be useful for applications in which there is no conventional containment building, because the phenomena of sodium fires, aerosol transport and deposition, and natural convection may be important in determining the source term whenever the pathway to the environment is indirect.

For example, in many cases, best-estimate analyses with CONTAIN-LMR have shown that even after the containment has failed, deposition processes in the containment and connected buildings can have large contributions to reduction of the source term. Experience with CONTAIN on LWR accident analysis has shown that the synergism among the phenomena can lead to results that would be difficult to predict with non-integrated analysis tools.

A.2. NORTH CHINA ELECTRIC POWER UNIVERSITY (NCEPU), CHINA

A.2.1. **Research Activities and Capabilities on SFR Severe Accident Simulation at NCEPU**

China Electric Power University (NCEPU) has been conducting theoretical researches and experimental researches in the fields of thermal hydraulics and flow-induced vibration. The school's thermal engineering topics include: advanced nuclear reactor thermal fluid design; thermal fluid problems in nuclear power plant operation, maintenance and accidents; experimental and theoretical studies of boiling heat transfer and multiphase flow; heat transfer experiments and theoretical studies of single-phase fluids Computational fluid dynamics and numerical simulation of complex systems; natural circulation and passive safety cooling systems; reactor thermal hydraulic experimental testing techniques. Among them, the hardware foundation involves conventional thermal hydraulic measuring instruments and advanced flow field measuring systems, such as high performance Charge Coupled Device Camera (CCD) and laser particle image velocity field instrument (PIV); software foundation involves international general computational fluid dynamics software and results Software that has conversions. Relevant thermal engineering platforms, equipment and measuring instruments provide strong support for the implementation of the project. In addition, North China Electric Power University has experience in participating in the National Major Science and Technology Projects of China. It provides basic engineering verification for the CFR600 (Chinese Fast Reactor) that China is currently developing independently, including key technologies such as core flow distribution, flow-induced vibration, hydraulic characteristics of throttle components and Class B components, and is the CFR600 experimental fast reactor. Provide technical support and services for R&D and construction.

In the WP2, the main task of the NCEPU is to calculate the amount of leakage and leakage rate of sodium from the top shield assembly gap at the time of the accident. NCEPU aims to model and calculate the ICEM CFD software to derive the amount of liquid sodium leakage in each sub-channel, which will provide input data for the third working group.

A.2.2. **Introduction and application of ANSYS simulation software**

ANSYS software has long been used in computational fluid dynamics related simulations. The NCEPU builds a model based on the geometric parameters of the leaky flow path, and uses the ICEM CFD to mesh the mode, and then uses FLUENT to calculate. More details are explained in Section 5.1.

A.3. XI'AN JIAOTONG UNIVERSITY (XJTU), CHINA

A.3.1. **Introduction of the XJTU-NuTHeL**

The Nuclear Thermal-hydraulic Laboratory of Xi'an Jiaotong University (XJTU-NuTHeL) is mainly devoted to the frontier research of nuclear reactor thermal-hydraulic safety and severe accident analysis. The laboratory is engaged in thermal-hydraulic experiments of vapor-liquid two-phase flow, boiling thermal-hydraulic experiments of liquid sodium metal, CFD and application of advanced numerical algorithm (particle method), mechanism of severe accident

phenomena, Development of system analysis and phenomenological programs, and thermal-hydraulic design and safety analysis of new type reactor.

The laboratory has an advanced reactor thermo-hydraulic simulation test circuit, liquid sodium boiling test circuit, AP1000 ADS-4 pressure relief injection test bench, hydrogen explosion test bench, lower head melt behavior test bench under severe accidents, ECC injection test bench of nuclear power plant and T-tube entrainment test bench, etc. The laboratory has a system analysis programs, sub-channel analysis programs, CFD programs, fuel performance analysis programs, containment analysis programs, severe accident analysis programs, coupled physical and thermal design analysis programs, steam explosion analysis programs, sodium cooled fast reactor system analysis program, supercritical water cooled reactor system analysis programs, 3-D two-phase flow field simulation and analysis program for secondary side of steam generator.

A.3.2. **Capabilities on SFR Severe Accident Simulation at XJTU-NuTHeL**

XJTU-NuTHeL has been engaged in basic experimental and theoretical research of sodium cooled fast reactor for a long time. A large number of basic experiments have been carried out on the characteristics of sodium two-phase boiling flow and heat transfer involved in severe accident of sodium-cooled fast reactor. The laboratory has set up the international leading sodium boiling test bench. The mechanism models of liquid metal boiling initial superheat, critical heat flux and multi-bubble two-phase flow were constructed, and the theoretical system of liquid metal two-phase flow and heat transfer was improved.

An experimental bench COSA for studying the fragmentation characteristics of molten materials was set up. Copper and other high temperature metal materials are selected as core substitutes, and liquid metal sodium is used as coolant. The fragment morphology and size distribution of core melt after fragmentation in liquid metal sodium were studied, and the mass and size distribution characteristics of copper melt fragments under different experimental parameters were obtained. In numerical simulation, the laboratory independently developed a severe accident analysis program of physical-thermal coupling in pressure vessel of fast reactor. The program is based on general physical model, energy transfer model, hydraulic model, fuel failure model, molten fuel movement model, molten fuel/coolant interaction model, neutron model and so on to analyze reactor core performance under severe accidents.

IAEA has started up the project of Radioactive release from the Prototype Fast Sodium-cooled Reactor (PFSR) under severe accident conditions. The scope of the project is to perform realistic estimations of fission product and fuel particle inventory inside some specific SFR reactor areas (i.e. in-primary vessel, cover gas system and in-containment building) at different time scales, under severe accident conditions. XJTU joined this group in 2016 and undertook the task of WP3, whose main purpose is to analyze the diffusion behavior of fission products in the containment under sodium fire. In order to complete WP3 simulation, the laboratory independently developed radioactive Release Analysis Code for Sodium Fast Reactor (REBAC-SFR).

A.3.3. **Introduction and application of REBAC-SFR code**

This project mainly studies the leakage of radioactive fission products into the top area of pressure vessel through sealed channels in severe accidents. There are mainly two kinds of calculation, one is the release of radioactive fission products in the sodium pool formed; the two is the release of radioactive fission products in the form of sodium spray. The release of

fission products is usually accompanied by the release of coolant sodium into the containment. Therefore, the sodium fire during the release of sodium will affect the diffusion of fission products aerosols in the containment. The main function of REBAC-SFR program is to simulate the diffusion and migration of sodium pool fire, sodium spray fire, oxide, and fission product aerosol in compartment. The code includes several modules: thermal hydraulic module, sodium pool fire module, sodium spray fire module, fission product aerosol module, nuclides decay module. These modules are coupled together by relevant numerical algorithms.

— **Thermal hydraulic module**- used for calculating temperature, pressure, gas flow, and heat transfer in compartments.
— Temperature and pressure calculation model
— Natural convection model(vertical and horizontal openings) [59] [60]
— Radiation, conduction, and convection heat transfer model
— Heat balance model
— **Sodium pool fire module**- used to calculate the surface combustion and evaporative combustion of sodium pool. The diagram of sodium pool combustion is shown in the FIG. 377. The combustion model mainly comes from reference [61].
— Surface combustion model
— Sodium vapor combustion model

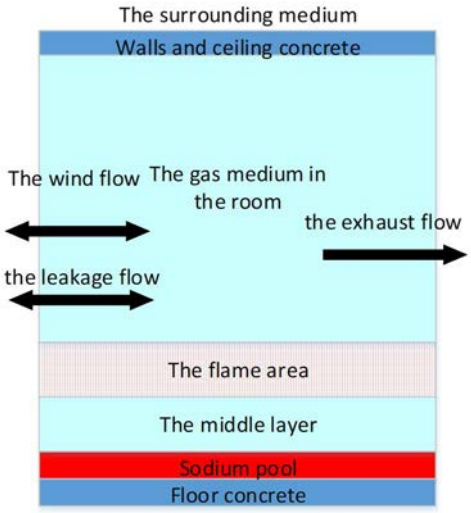

FIG. 377. Schematic diagram of sodium pool combustion model.

— **Sodium spray fire module**- It is mainly used to calculate the burning rate of sodium under spray condition. The models mainly come from [62].
— Combustion model for a spherical, stationary droplet
— Combustion model for a free-falling droplet (as shown in FIG. 378)
— Droplets motion model
— Droplet size distribution model
— Spray combustion model

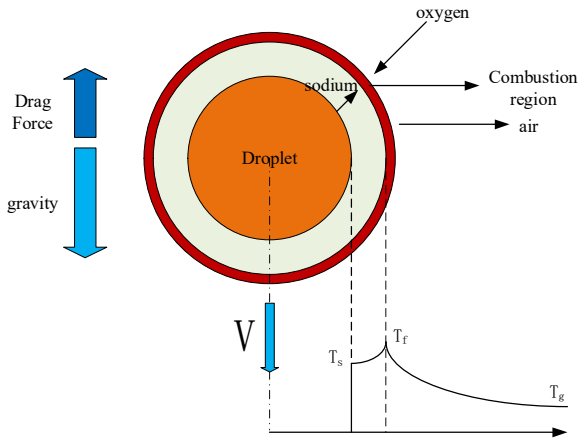

FIG. 378. Sodium droplet combustion model.

— **Fission product aerosol module**- It is mainly used to calculate the kinetic behavior of fission product aerosols in compartments. The models mainly come from [61].
— Source term release model
— Aerosol mass distributions model
— Aerosol size distributions model
— Aerosol agglomeration model
— Aerosol deposition model
— **Nuclides decay module**- It is mainly used to calculate the conversion of fission product mass to radioactivity. Simplified calculations are used in this module, without considering the decay heat of nuclides and the effect of products of nuclide decay on existing nuclides.
— Radioisotope inventory calculation model
— Nuclide decay conversion model

A.4. FRENCH ALTERNATIVE ENERGIES AND ATOMIC ENERGY COMMISSION (CEA), FRANCE

A.4.1. **CEA research on SFR**

Created in 1945, the Commissariat à l'ÉnergieAtomique et aux ÉnergiesAlternatives (formerly Commissariat à l'ÉnergieAtomique) is a key player in French research related to energy, and particularly in the nuclear research. France and CEA were engaged in late fifties in a natural uranium, graphite-moderated and carbonic gas-cooled (UNGG) reactor program; the fast reactor program appears as an excellent complement thanks to its breeding option. Nowadays, CEA is an innovation leader, particularly for Pressurized Water Reactors (PWR) and Sodium Fast Reactors (SFR).

The first experimental Sodium Fast Reactor built by the CEA is RAPSODIE, located in Cadarache. It achieved criticality in 1967 and was used to validate the different design choices such as the fuel and the reactor materials.

PHENIX was built on the site of Marcoule from 1968 and achieved criticality in 1973. Phénix is a pool-type SFR prototype. PHENIX was in operation until 2008 and was used to gain experience on SFR before building the full-size industrial SFR prototype SUPERPHENIX. PHENIX's operation allowed to address problems met on the main components such as the pumps. It served to increase the performance of the fuel and the fuel cycles too. PHENIX dismantling is now in progress.

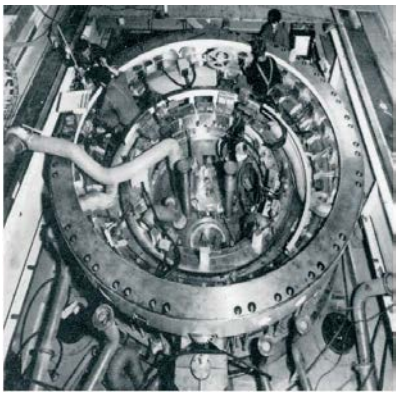

FIG. 379: Top view of RAPSODIE.

FIG. 380: PHENIX building.

FIG. 381: ASTRID reactor.

SUPERPHENIX is the last of the SFR reactors built in France. It was an industrial SFR that produced 1200 MW(e) operated by utilities from France (EDF), Italy (ENEL) and Germany (RWE). During the 53 months operation (1985-1997), only 3 incidents were met (storage drum Sodium leak, primary Sodium pollution due to air ingress, an argon leak on the inlet pipe of the IHX bell) and, one significant non-nuclear issue occurred with the collapse of the turbine hall due to exceptional snowfall). However, the civil opposition to this reactor led to its closing in 1997.

Development and operation of these SFRs were supported by large R&D programs at CEA, including Severe Accident Code developments and associated Experimental Programs such as CABRI and SCARABEE in-pile programs.

France (CEA, Électricité de France, AREVA) resumed its SFR R&D programs in 2006, in the frame of the French 2006 law relative to management of nuclear materials and wastes. In 2010, a new SFR project of an Advanced Sodium Technological Reactor of Industrial Demonstration (ASTRID, 600 MW(e)) was started. However, changes in the French energetic policy led, in 2019, to end the ASTRID project: there are no need to build a commercial SFR for Pu management before next half of this century. However, a large SFR R&D program must be carried out in the CEA to address identified technological locks and to lower the SFR cost.

In the frame of the ASTRID program, the Severe Accident R&D program include code developments, associated experimental programs, mitigation devices studies and Severe Accident Transient calculations on ASTRID reactor to support its safety file.

Regarding the Severe Accident, a new version of SIMMER (called SIMMER-V) is developed by JAEA and CEA which allow calculation of core degradation from the initial phase of the accident till the long-term phase. A Severe Accident platform named SEASON allow to chain or couple SIMMER-V with fuel codes such as GERMINAL (to get the initial state of the irradiated fuel), with neutronic codes (including in the close future APOLLO-3) and with a thermal hydraulics codes (such as CATHARE) to get the fluid conditions at the boundary of the SIMMER calculations.

For Fuel Coolant Interactions simulations, the SCONE code is developed, and the mechanical consequences on the reactor structures are calculated with EUROPLEXUS.

Evaluation of fission product transport towards the environment is performed with CONTAIN-LMR (see 0).

Associated experimental programs are carried out: study of material mixture at high temperatures, study of corium/Na interactions, study of corium impingement on core catcher materials, and a new in-pile program is being carried-out, under CEA funding in the IGR reactor operated by NNC-RK (Kazakhstan), to study corium discharges from the core region thanks to a dedicated Transfer Tube.

ASTRID program and associated R&D programs was carried-out with industrial partners (Framatome, Électricité de France, Mitsubishi Heavy Industries, Mitsubishi FBR, Bouygues, General Electric …) and with research organizations (mainly Japan Atomic Energy Agency and KarlsruherInstitutfürTechnologie for Severe Accident Issues).

A.4.2. **Radionuclide transport and release modelling using CONTAIN-LMR**

CONTAIN was a code developed by Sandia National Laboratories to calculate the radiological releases in case of a severe accident for water reactors. Derived versions of the code were developed by Forschungszentrum Karlsruhe (FZK, now KarlsruherInstitutfürTechnologie) with the capability to calculate radiological releases for Light Metal Reactor (named CONTAIN-LMR) and containing aerosols models in Sodium environment, Sodium fire models, Sodium boiling model, Na chemistry, debris bed models, and Sodium-concrete and corium concrete interaction models. In 1998, the CEA released a new CONTAIN-LMR version « CONTAIN-LMR/1B – MOD1 CEA 1.01 » with the capability to model complex gas circuits with filters, blowers, and hydraulics safety valves.

The nodalization used in a CONTAIN-LMR input deck in order to describe a reactor is divided into cells. Each cell is 0-dimension and represents a different part of the reactor. FIG. 382 shows how CONTAIN-LMR performs simulations for each cell before simulating the global behavior and the different fluxes between the cells [50]. This calculation is performed for each time step.

CONTAIN-LMR physics is divided into 3 major blocks: aerosol physics, fission products (including their decay) and thermal-hydraulics (including chemical reactions related to sodium fire and sodium vapor recombination with oxygen and water). For each cell, the 3 blocks are calculated and interact between each other.

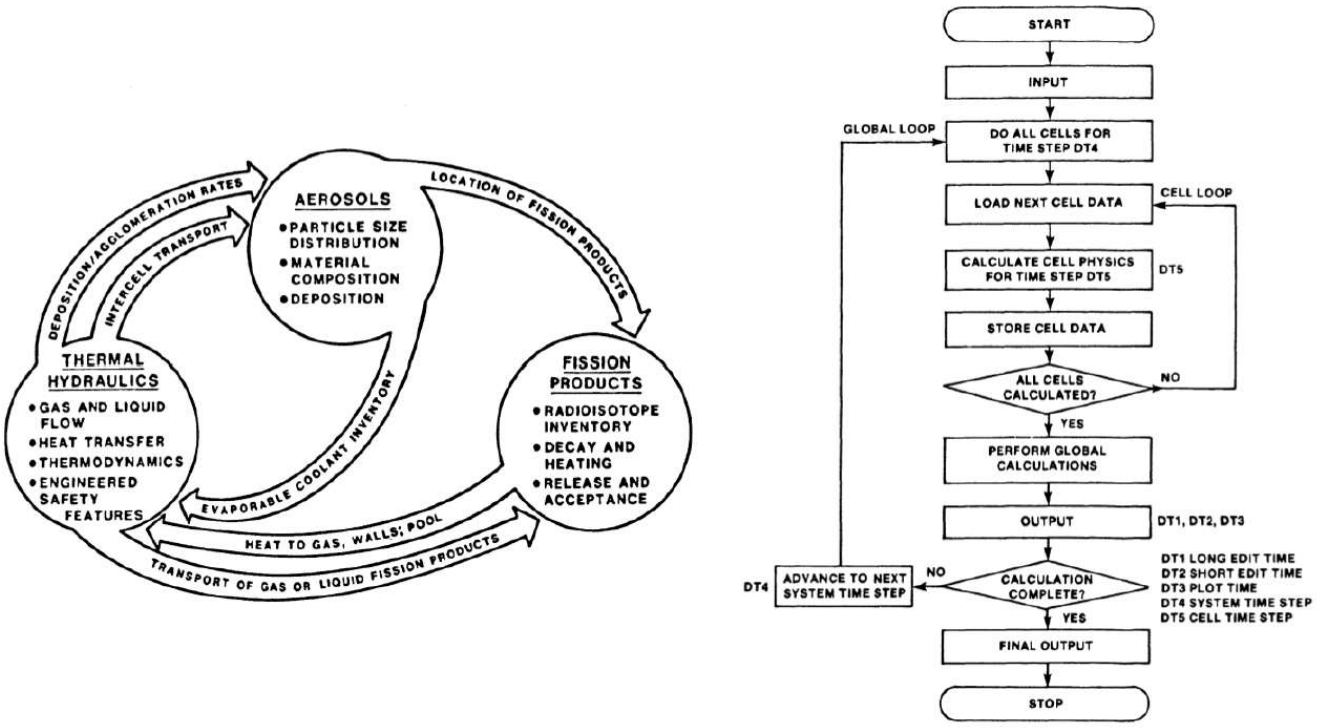

FIG. 382. CONTAIN-LMR global calculation scheme.

A.5. INDIRA GANDHI CENTER OF ATOMIC RESEARCH, INDIA

A.5.1. **IGCAR numerical codes for simulation of the severe accidents**

Indira Gandhi Centre for Atomic Research was established in the year 1971, under the Department of Atomic Energy, Government of India. The centre is engaged in broad based multidisciplinary programme of advanced scientific research and engineering directed towards the development of fast breeder reactor technology. The centre houses Fast Breeder Test Reactor fuelled by unique mixed Plutonium/Uranium Carbide core, is being successfully operated and utilized for various experiments supporting the FBR programme. The centre has also designed the 500 MW(e) Prototype Fast Breeder Reactor whose construction and commissioning is in progress. The centre has testing facilities for FBR components, metallurgical and materials development programme, and laboratories for performing safety related experiments. A number of advanced code systems are used for the analysis and design of the reactor. For severe accident analysis, the in house developed codes such as KALDIS for pre disassembly and disassembly calculations, the finite element arbitrary Lagrangian-Eulerian coordinate-based code FUSTIN to calculate post CDA fluid motion and structural deformations. In addition, LANL codes NACOM, SOFIRE-II had been used to model sodium fire.

For use in the CRP the following additional codes were developed.

— MINICHEM: A system of computer codes for assessing and performing thermo-chemical equilibrium calculations. The code uses quadratic gradient descent (QGD) and sequential least squares programming (SLSQP) algorithms for free energy optimization. The code has been validated with known basic chemical/phase equilibrium results and fission product release data available in literature for ALMR.

— NETFLOW: A flow network thermal hydraulics computer code to calculate flow through top shield leak paths.
— PFIRE: Computer code for calculation of the temperature and pressure evolution in the containment is based on modified SOFIRE-II one cell code. The code considers sodium pool fire, decay heat and solar radiation input to calculate temperature evolution. The model has been validated with the FAUNA 5, 6 and LTV test 4 experiments and the estimates are well within bounds.
— PANDICA: A computer code for simulating polydisperse aerosol agglomeration and removal process in the containment. The code uses a finite difference implicit scheme to solve the aerosol dynamic equation.

All the above codes were written in Python. Though efforts have been made to validate the above codes based on physics of the process and inter-comparison with experimental and theoretical results available in the literature further validation is in progress. Further details of the codes are provided in the respective sections where they are used.

A.6. JAPAN ATOMIC ENERGY AGENCY (JAEA), JAPAN

A.6.1. **Introduction of JAEA**

JAEA, Japan Atomic Energy Agency, was established in 2005 by integrating JAERI (Japan Atomic Energy Research Institute) which mainly conducted basic nuclear research, and JNC (Japan Nuclear Cycle Development Institute) which focused on developing Sodium cooled Fast Reactors (SFRs) and nuclear fuel cycles. JAEA has 23 offices and research centres throughout Japan and is currently focusing on efforts following the Fukushima Dai-ichi Nuclear Power Plant accident, as well as research on improving nuclear safety, basic research of nuclear power, and research and development of nuclear fuel cycle.

Research and development of SFRs is being carried out in the “Sector of Fast Reactor and Advanced Reactor Research and Development” together with High Temperature Gas cooled Reactor (HTGR) and fuel cycle technology. In this sector, analysis codes for the design and safety evaluation of SFRs are developed as well as experimental studies are also conducted using out-of-pile experimental facilities. The following experimental studies are being conducted in this sector:

— Decay heat removal in reactor vessel,
— Safety of reactor core and mechanical properties of the structures,
— Suppression of chemical reactivity of sodium, and
— Ex-vessel events.

Joyo is an experimental fast reactor built by JAEA in Oarai, Ibaraki Prefecture. It is the first fast breeder reactor in Japan designed to produce 100 MW(th). It has two primary coolant loops and was used as a neutron irradiation test facility for fuel and materials necessary for the development of a new SFR using Japan’s own technology. After receiving a national reactor installation license in February 1970, construction began in March of the same year. The first criticality was achieved on April 24, 1977. Joyo has contributed much to the LMFBR development program through design, construction, testing, operation, and maintenance experience. Many kinds of irradiation tests have been conducted for the development of fuels and materials under the conditions of higher fast neutron flux and temperature than those in light water reactors. Joyo is currently suspended but is undergoing licensing procedures for restart.

Monju is a prototype breeder fast reactor built by JAEA in Tsuruga City, Fukui Prefecture. It is a sodium cooled, MOX-fueled, loop-type reactor with three primary coolant loops, designed to produce 280 MW(e) from 714 MW(th). Monju achieved initial criticality in April 1994. The first transmission was completed in August 1995. With 40% rated power operation, confirmation of the industrial technology such as large equipment manufacturing that can be used for the future reactor can be performed in addition to the design and handling technology of the core, fuel, equipment, system, and Na handling of the power generation SFR. During the performance test in December 1995, Na leakage occurred in the secondary main cooling system, and operation was stopped. The renovation work was carried out and the reactor restarted in May 2010. However, the In-Vessel Transfer Machine (IVTM) fell into the reactor vessel when being removed after a scheduled fuel replacement operation, and operation of the reactor was stopped again. At the Nuclear Ministerial Meeting in December 2016, it was decided to decommission.

A.6.2. **Introduction and application of SIMMER-IV and PLUG**

ULOF accident sequence was divided into several accident phases as shown in FIG. 383. JAEA developed methods to calculate accident progression for each accident phases. JAEA focused the scope of study in this CRP on the analysis of event progression during Post-Disassembly Expansion phase (PDE phase).

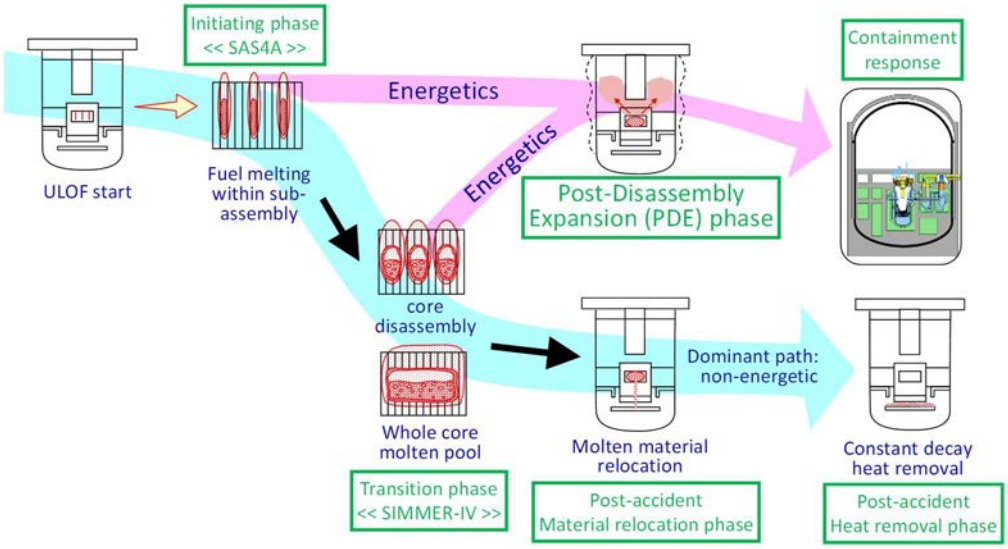

FIG. 383. Typical event progression of ULOF accident and accident phases.

Methods to calculate reactor vessel response and sodium ejection in PDE phase is shown in FIG. 384. SIMMER-IV code can evaluate the thermal energy in transition phase and the results, namely mass, temperature, velocity and pressure distribution of materials concerned are utilized as input in PDE phase analysis. Pressure history under the shield plugs and P-V relation of CDA bubble, which is a mixture of gas (fuel, steel vapor and fission gas) and molten core material, is obtained by mechanical energy evaluation in the PDE phase analysis using SIMMER-IV, and the former is used for the evaluation of sodium ejection with PLUG code, and the latter is used for reactor vessel response evaluation with AUTODYN code. For WP-1, SIMMER-IV code is used to calculate material distribution within the reactor vessel and energy conversion ratio. For WP-2, PLUG code is used to calculate the amount of sodium ejected to the reactor containment through the gaps between roof slab and its embarkation equipment.

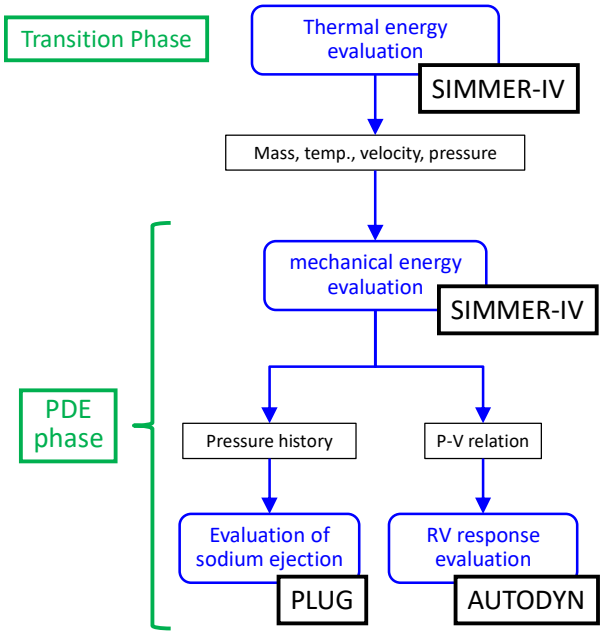

FIG. 384. Method to calculate reactor vessel response and sodium ejection in PDE phase.

A.7. NUCLEAR SAFETY INSTITUTE OF THE RUSSIAN ACADEMY OF SCIENCES (IBRAE RAN), RUSSIAN FEDERATION

A.7.1. **Research Activities and Capabilities on SFR Severe Accident Simulation at IBRAE RAN**

Nuclear Safety Institute of the Russian Academy of Sciences (IBRAE RAN) was established on November 3, 1988 with the aim to perform advanced R&D and independent assessment of nuclear and radiation safety. Fundamental R&D and applied R&D are successfully combined in IBRAE RAN. Institute constantly spread its' field of work which includes models and code development, safety assessment of NPP and spent fuel storages, research on socio-economic aspects of operation of nuclear power facilities, etc.

Since 2010 IBRAE RAN is involved in the "Codes of New Generation" subproject of "PRORYV" project (in frame of Federal Target Program "New generation of nuclear power technologies for 2010-2015 and up to 2020"). IBRAE RAN was designated as "Responsibility centre" for "Codes of New Generation" subproject. It means that on IBRAE RAN basis the funds and human resource are concentrated. The notion "New generation codes" refer to software with the following characteristics:

— Based on the state-of-the-art theoretical knowledge and experimental data on physical processes and phenomena;
— Employs efficient numerical algorithms;
— Developed in accordance with up-to-date requirements of programming language standards and adapted to modern computing technology;
— Has a user-friendly interface;
— Supplied with a full package of documentation (users' guide, reference manual, programmers guide);
— Employs automated work with CAD models.

24 different codes of new generation are under development, 9 of them are already certified in Rostechnadzor to ensure the possibility of using the developed codes in materials justifying the

safety of nuclear facilities. Most of the codes are already used according to their fields of application by the users.

Among those 24 codes there are two integral codes that can be used for SFR severe accidents modelling: SOCRAT-BN/V2 and EUCLID/V2. SOCRAT-BN/V2 code was developed based on integral SOCRAT code applied for safety assessment of reactors with water coolant. SOCRAT-BN/V2 includes approaches and models similar to those used in SOCRAT. EUCLID/V2 code [63] [64] contains more comprehensive models. Besides it allows modelling both sodium and lead (lead-bismuth) cooled reactor units.

In the current CRP the EUCLID/V2 code was used to simulate all work packages.

A.7.2. **Integral EUCLID/V2 code**

The Russian EUCLID/V2 code allows simulating the behaviour of fast reactors with liquid metal coolant in different modes of operation including severe accidents. The integral code consists of the following modules:

— The thermohydraulics module (HYDRA-IBRAE/LM), which allows modelling of thermohydraulic processes both in circulation circuits and a reactor containment building;
— The neutronics module (DN3D);
— The fuel rod module (BERKUT);
— The module of fission, activation and corrosion products transport in the primary loop and gas system of a reactor facility (AEROSOL-LM);
— The module of solid phase impurities transport in the primary loop of a reactor facility with heavy liquid metal coolant (OXID);
— The tritium migration module (TRITIUM);
— The module of fission product source calculation taking into account physicochemical interaction between the fuel and the coolant (is a part of the BERKUT module), the fuel rod and core disruption module (SAFR);
— The module of simulation of radiation situation beyond an industrial site of a NPP (ROM).

Coupled, self-consistent calculations are provided by the SMART_LM integrating shell. Furthermore, the integrated code includes the material and coolant properties database (SmartDB) and the module of instrumentation and control systems simulation (CFunc).

In the current CRP only HYDRA-IBRAE/LM, BERKUT, SAFR and AEROSOL/LM modules were used. That's why those modules are described in more details below.

A.7.3. **HYDRA-IBRAE/LM system thermohydraulic module**

The main parameters calculated by the thermal– hydraulic code HYDRA-IBRAE/LM include the velocity, temperature, and pressure fields of the coolant and working fluid and also the void fraction values in the calculation cells.

The following processes are modelled:

— Heat and mass transfer in the reactor circuits;
— Boiling of sodium coolant;
— Flow with gaseous phase inclusions;
— Heat and mass transfer when steam–water mixture enters into heavy liquid metal coolant;

— Heat and mass transfer in cover gas (argon) taking into account its dissolving in and transfer by liquid metal coolant, and in the air-cooled normal and emergency reactor cooling down systems.

A.7.4. **BERKUT fuel rod module**

The BERKUT fuel rod module of the EUCLID/V2 integrated code is used to model the processes occurring in fuel rods of fast reactors with nitride, mixed nitride, dioxide and mixed oxide uranium–plutonium fuel and claddings made of austenitic or ferrite-martensite steels.

The BERKUT fuel rod module allows to simulate the following processes:

— Temperature distribution in a fuel rod;
— Stress-strain state of a fuel rod with the open gap and in the case of the pellet-cladding mechanical interaction (PCMI);
— Cladding integrity analysis according to the performance criteria (margins for melting, ultimate strength, long-term strength, etc.);
— Fission gas release (FGR) under the cladding;
— Degradation of the gas gap conductivity due to FGR.

The simulation is performed taking into account dependencies of thermophysical and mechanical material properties on fuel rod fabrication parameters and irradiation conditions.

A.7.5. **SAFR/V1 severe accident module**

The module SAFR/V1 allows simulating the following processes:

— The melting of a fuel rod and solidification of the formed melt;
— The movement of the melt along the surface of the fuel element under the influence of gravitational force and friction of the melt with fuel pin surface and coolant flow;
— The blockage of the cross sectional area of the fuel pin bundle due to solidification of the melt on the surface of fuel pins;
— The entrainment of the melt into the coolant flow and deposition of the melt on fuel pin surface;
— The formation of melting pool;
— The fission products release from melting pool;

The more detailed description of models is presented in [16] [17] [18].

A.7.6. **AEROSOL/LM fission products module**

The aerosol module AEROSOL/LM allows simulating the following processes:

— The nucleation of different vapors;
— The coagulation of multicomponent polydisperse aerosol particles;
— The condensation of various (multicomponent) vapors on particles;
— The condensation and sorption of vapors on surfaces;
— The deposition of aerosols on surfaces due to different mechanisms;
— The formation of multicomponent deposits on surfaces;
— The absorption of water vapor by hygroscopic aerosol (equilibrium and kinetic approach);
— The transfer of aerosols and various vapors through the compartments.

A.8. CENTRE FOR ENERGY, ENVIRONMENT AND TECHNOLOGY (CIEMAT), SPAIN

A.8.1. **Research activities and capabilities on SFR severe accident simulation at CIEMAT**

CIEMAT is a public research centre depending on the Spanish Ministry of Science, Innovation and Universities. It is supported mostly by national and European funds but also gets resources from project agreements with other public or private companies. The areas of research of CIEMAT are mainly the energy and the environment as well as in many vanguard technologies and in various areas of fundamental research. CIEMAT is technically and geographically diversifying to better care for the R&D needs of Spain.

Concerning nuclear energy, the CIEMAT activities cover very many aspects from materials to innovation, with nuclear safety research being a major subject of its portfolio. Under the frame of the Unit for Nuclear Safety Research, CIEMAT investigates safety aspects of in-reactor and interim dry storage of fuel behavior, severe accidents and innovative reactor designs. In the last decade, the research conducted in the latter has been focused on High Temperature Gas Cooled Reactors and Sodium Fast Reactors. Aside a collaboration agreement signed with PBMR Ltd. at the start of the present decade, the experience in dealing with beyond design basis accidents in innovative reactors has been gained through participation in the European Framework Programmes, under which projects like RAPHAEL, CP-ESFR, JASMIN and ESFR-SMART, have been developed. In those projects both model development and analytical simulations of accident scenarios have been carried out. Specifically related to the current CRP on "Radioactive Release from the Prototype Fast Breeder Reactor (PFBR) under Severe Accident Conditions", is the CIEMAT experience on complex aerosol scenarios [65] [41]], the development of ad-hoc models [55] [66] the validation of the ASTEC-Na code [67] and the analysis of prototypical SFR accident scenarios that has been collected in a number of scientific contributions in journals and conferences.

The objective of the developed research in the CRP has been to assess the ASTEC-Na code capability [68] to estimate the in-containment source term evolution. Numerical simulations of a reference pool type Sodium-cooled Fast Reactor (SFR) under CDA conditions has been conducted with the focus placed on in-containment transport. By doing so some insights concerning key phenomena that might affect fission product and aerosol behavior have been gained and modelling aspects that visibly influence predictions have been identified. In addition, through sensitivity analyses some weaknesses in the current modelling capabilities have been either found or confirmed. As a result, some opportunities for improvement concerning analytical needs have been identified.

A.8.2. **ASTEC-Na code**

ASTEC-Na [68] [69] is being developed to simulate any sort of postulated accidents in Na-cooled fast reactors, particularly severe accidents. A significant progress has been made in the development of source term models, their implementation in the code and the specific validation of the code module ASTEC-Na CPA, hereafter named CPA*, under the auspices of the JASMIN project [67].

The most important addition to CPA* has been the pool fire combustion model, which is based on the SOFIRE-II model [48] that is present in CONTAIN-LMR [70]. In addition, developments took place to filling some of the gaps previously identified by Herranz et al [71].

In particular, a model for particle generation during pool fires [55] [66] and the subsequent chemical reactions of airborne particles with steam and carbon monoxide [13] have been implemented in CPA*.

Beyond any model development and implementation, qualification of CPA* requires validation against a reliable and representative database. The major results obtained in a benchmark set between CPA* and a number of experiments chosen from the open literature is summarized in this section. A thorough description of the model bases formulation and CPA* validation has been reported by Herranz et al [72] [67].

A.8.3. **Validation of ASTEC-Na/CPA***

Based on a number of criteria like their scale, completeness and accuracy of data reported, two large-scale experiments from the U.S. ABCOVE program [73] [74] [75] (AB1 and AB2 tests) and one middle-scale experiment from FAUNA program [76] [52] [77] [53] (F2 test) were chosen for the assessment of the CPA* code. In all of them, the aim was to understand the sodium burning process and to study the sodium compound aerosols behavior and their chemical composition during a sodium pool fire. In all the tests, the experimental procedure consisted on producing a sodium pool fire inside a containment vessel in a circular burn pan by the release of a given amount of hot liquid sodium.

In the next table an overview of the simulated experiments is shown (TABLE 77).

TABLE 77. CPA VERIFICATION EXPERIMENTS OVERVIEW

	AB1	**AB2**	**F2**
Geometry			
Type	Cylindrical	Cylindrical	Cylindrical
Volume (m^3)	852	852	220
Initial Conditions			
O2 (%)	19.8	20.9	17-25
Temperature (K)	299.65	293.65	298.15
RH (%)	35.5	43.3	-
Steam Addition	NO	YES	YES
Sodium Spill			
Initial Na Temp. (K)	873.15	873.15	773.15
Burning Area (m^2)	4.4	4.4	2
Fire duration (s)	3600	3600	12600

The comparison of the code predictions with the experimental data have shown that the anticipated thermal evolution in SFR containment during a sodium pool fire might be captured whenever models parameters are adequately set and containment is meshed properly (i.e., the single-node approach used during the assessment might not be suitable under fast transient conditions resulting in temporarily non-uniform atmospheres). As an illustration of that the AB2 results are shown below. In general, AB2 calculations follow the experimental trends. Consistently with major experimental observations, the calculations roughly follow the same thermal trends by describing a heat-up phase, in which Na oxidation is taking place, and a cooling phase, in which Na fire finishes and a fast cool-down phase period right after the fire is over, is followed by moderate cooling governed by natural convection.

Similarly, aerosol models show a promising response in terms of order of magnitude of airborne concentration, dominant depletion mechanism (i.e., sedimentation) and particle size variation. Quantitative deviations from data, though, have been observed both in the airborne aerosol concentration and aerosol size along time. To depict the later, airborne concentration of aerosols for AB2 test is shown in FIG. 386.

By observing the evolution of the aerosol concentration in FIG. 386, although the CPA* results fall within experimental uncertainties during the observed quasi-steady state period (from approximately 700 s to 1800 s) they do not follow the observed trend before the sodium pool fire ending (3600 s). Besides, the experimental depletion phase is about twice higher than the predictions, indicating a too efficient particle removal by the aerosol depletion mechanisms, likely associated to the particle size overprediction (FIG. 387) since the dominant particle depletion process (i.e., sedimentation) is proportional to the diameter squared.

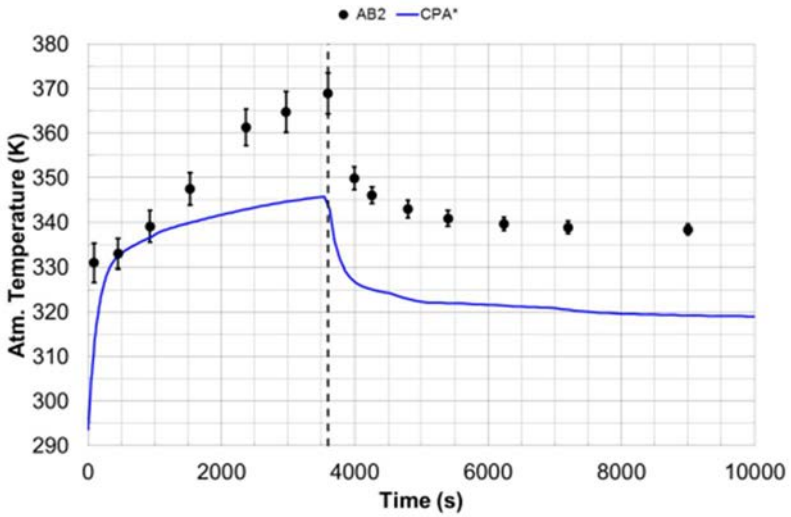

FIG. 385 Atmosphere temperature.

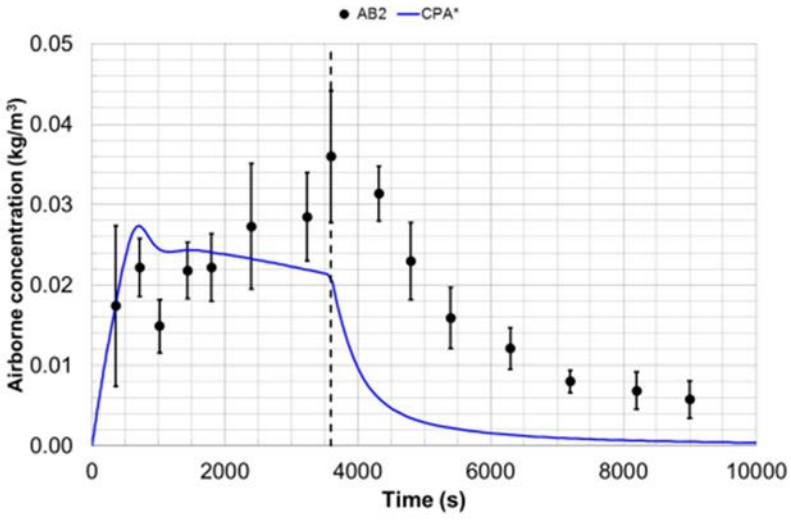

FIG. 386 Airborne concentration.

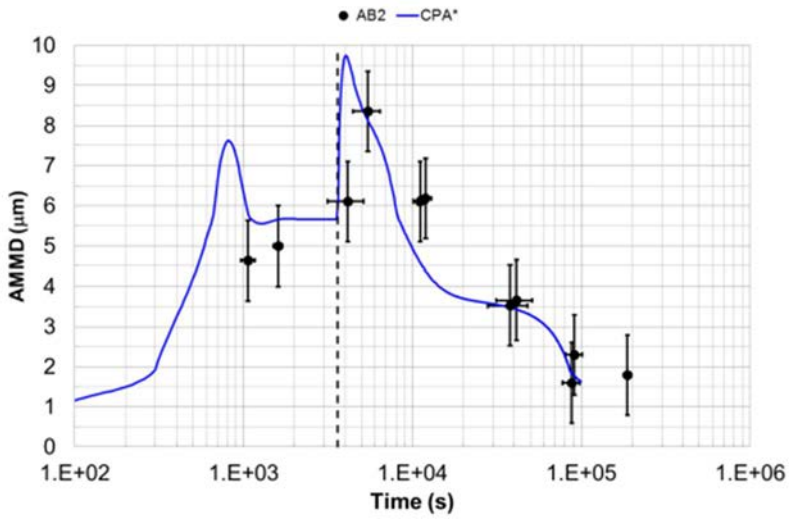

FIG. 387. Aerodynamic Mass Median Diameter (AMMD).

A.9. TERRAPOWER, USA

A.9.1. **TerraPower, LLC (USA)**

TerraPower, LLC (TerraPower) is a leading nuclear innovation company that strives to improve the world through nuclear energy and science based on Bellevue, Washington. TerraPower has emerged as an incubator and developer of ideas and technologies that offer energy independence, environmental sustainability, medical advancement, and other cutting-edge opportunities. TerraPower actively works to bring together the strengths and experiences of the world's public and private nuclear research and energy sectors. This approach takes root in the original impetus; TerraPower was founded when Bill Gates and a group of like-minded visionaries decided that the private sector needed to take action in developing advanced nuclear answers for pressing global needs.

A.9.2. **Nuclear Safety Analysis of Sodium-Cooled Fast Reactors**

The safety analysis of the Traveling Wave Reactor (TWR®) program includes methods development, model development, code verification and validation (V&V). The development of the safety analysis has focused on areas of primary importance for establishing the conceptual design of the core and nuclear island systems. Models of the core and nuclear island have been developed using SAS4A/SASSYS-1 [78], and a full plant model including the balance of plant has been developed in RELAP5-3D® [79]. Additionally, detailed models of the core and nuclear island have been developed using GOTHIC to support the conceptual design and development of safety analysis methods. For sodium fire analysis, CONTAIN-LMR has been used to calculate the peak pressure in containment and radiological analyses have been performed to demonstrate the potential for a reduced emergency planning zone. For radiological dose consequences, RADTRAD has been used to assess the on-site and off-site projected doses during transients and accidents.

These codes, models, and methodologies have been used to assess the safety of a variety of design basis and beyond design basis events together referred to as Licensing Basis Events (LBEs). These models and methods were used to compare benchmarking of the modelling technique to the EBR-II SHRT-45 experiment to add to the national experimental experience enhancing the credibility of SAS4A/SASSYS-1 for SFR safety analysis [80]. Other safety analysis work includes:

- Containment response to sodium fires,
- Core mechanical response to seismic events, including reactivity impacts of geometry changes,
- Developing a three-dimensional (3-D) kinetics model to validate the point reactor physics in system codes,
- Sodium water reaction and mitigation in the steam generator,
- Sensitivity analyses to determine appropriate scram set points for DBEs, and
- Methods for determining the emergency planning zones (EPZs) for advanced reactor designs.

A.9.3. **Introduction and application of CONTAIN-LMR**

CONTAIN-LMR, developed by the Sandia National Laboratory (SNL) [50] was used for the sodium fire and aerosol dynamics modelling. The sodium spray fire model in CONTAIN-LMR is largely based on the sodium combustion model, NACOM, developed by Brookhaven National Laboratory (BNL) [42]. Some input parameters were adjusted from the default values based on the similar sodium spray fire test, ABCOVE AB5, performed by Hanford Engineering Development Laboratory (HEDL) [81].

The sodium pool fire model in CONTAIN-LMR is based on SOFIRE II, developed by Atomic International Division under Rockwell International [41]. Although the model is very flexible to simulate various sodium pool fire conditions, it requires some insights from the actual configuration and appropriate inputs from similar experiments and/or events. Test 4 of the large test vessel (LTV) was used to adjust the sodium pool fire input parameters.

The aerosol dynamics model in CONTAIN-LMR is from MAEROS, developed by SNL [62]. MAEROS uses sectional methods that divides aerosol size distributions in log-normal basis and calculates aerosol interactions among the size groups (so called 'bin'). This model has been very successfully used for system analysis tools as part of aerosol dynamics modules.

A.10. SUMMARY

TABLE 78. SUMMARY OF PARTICIPANTS CONTRIBUTION IN WORK PACKAGES

Country	**Organization**	**Computer Code(s)**	**Work Package 1 Participation**	**Work Package 2 Participation**	**Work Package 3 Participation**
China	CIAE	CONTAIN-LMR			X
China	NCEPU	ANSYS(FLUENT)		X	
China	XJTU	REBAC-SFR			X
France	CEA	CONTAIN-LMR			X
Japan	JAEA	SIMMER	X	X	
India	IGCAR	MINICHEM, NETFLOW, PFIRE, PANDICA	X	X	X
Russia	IBRAE	EUCLID/V2	X	X	X
Spain	CIEMAT	ASTEC-Na			X
USA	TerraPower	CONTAIN-LMR			X

REFERENCES

[1] INTERNATIONAL ATOMIC ENERGY AGENCY, IAEA Safety Glossary: 2018 Edition, Non-serial Publications, IAEA, Vienna, Austria 2018.

[2] PATEL, P., JOHN ARUL, A., In-vessel source term calculation using chemical equilibrium approach for a medium sized sodium cooled fast reactor, Nuclear Engineering and Design, **362** (2020) 110583.

[3] SCHRAM, R., CORDFUNKE, E., HUNTELAAR, M., Source term calculations of the ALMR, Netherlands Energy Research Foundation (ECN-R--95-021), 1995.

[4] MCBRIDE, B., GORDON, S., Computer Program for Calculation of Complex Chemical Equilibrium Compositions and Applications-I: Analysis, NASA, Cleveland, OH 1996.

[5] WHITE, W., JOHNSON, S., DANTZIG, G., Chemical Equilibrium in Complex Mixtures, J. Chem. Phys., **28** (1958) 751–755.

[6] CASTLEMAN, A., TANG, I., MACKAY, R., Fission Product Behavior in Sodium Systems, Brookhaven National Lab, Upton, N. Y. 1966.

[7] WICHNER, R., JOLLEY, R., L. GAT, U., RODGERS, B., R. Chemical factors affecting fission product transport in severe LMFBR accidents, Oak Ridge National Lab., Oak Ridge, Tennessee 1984.

[8] ALIPCHENKOV, V., et al., Fundamentals, current state of the development of, and prospects for further improvement of the new-generation thermal-hydraulic computational HYDRA-IBRAE/LM code for simulation of fast reactor systems, Thermal Engineering, **63** 2 (2016) 130-139.

[9] MOSUNOVA, N. The EUCLID/V1 Integrated Code for Safety Assessment of Liquid Metal Cooled Fast Reactors. Part 1: Basic Models, Thermal Engineering, **65** 5 (2018) 304-316.

[10] FILIPPOV, M., KOLOBAEVA, P., SOROKIN, A., MOSUNOVA, N., The modeling of the formation and transport of fission product aerosols in the first circuit of fast reactors in the AEROSOL/LM/Na module, Atomic Energy, **124** 4 (2018) 266-271.

[11] SOROKIN, A. Modeling of the dynamics of aerosols of fission products in the first loop, Atomic Energy, **118** 3 (2015) 208-214.

[12] SOROKIN, A. Modeling the coagulation of aerosols of fission products, Atomic Energy, **118** 4 (2015) 290-295.

[13] HERRANZ, L., GARCIA, M., KISSANE, M., In-containment source term in accident conditions in sodium-cooled fast reactors: Data needs and model capabilities., Progress in Nuclear Energy, **54** (2012) 138-149.

[14] SEINFELD, J., Y. PANDIS, S., Atmospheric Chemistry and Physics, Wiley, New York 1998.

[15] COUSIN, F., DIESCHBOURG, K., JACQ, F., New capabilities of simulating fission product transport in circuits with ASTEC/SOPHAEROS v. 1.3, Nuclear Engineering and Design, **238** (2008) .

[16] USOV, E., et al., Features of the numerical solution of thermal destruction fuel pins problems in the fast reactor, J. Phys.: Conf. Ser, **891** (2017) 012171.

[17] USOV, E., et al., Fuel pin melting in a fast reactor and melt solidification: simulation using the SAFR/V1 module of the EUCLID/V2 integral code, Atomic Energy, **124** 3 (2018) 123-126.

[18] USOV, E., et al., SAFR/V1 (EUCLID/V2 integral code module) aided simulation of melt movement along the surface of a fuel element in a fast reactor during a serious accident, Atomic Energy, **124** 4 (2018) 232-237.

[19] YAMANO, H., FUJITA, S., TOBITA, Y., SATO, I., NIWA, H., Development of a three-dimensional CDA analysis code: SIMMER-IV and its first application to reactor case, Nucl. Eng. and Des., **238** (2008) 66-73.

[20] VAN LEER, B. Towards the Ultimate Conservative Difference Scheme. IV. A New Approach to Numerical Convection, J. Computational Physics, **23** (1977) 276-299.

[21] BOHL, W., R. et al., AFDM: An Advanced Fluid-Dynamics Model, Volume I: Scope, Approach, and Summary (LA-11692-MS, Vol. I), Los Alamos National Laboratory, Los Alamos, 1990.

[22] PIGNY, S., COSTE, P., "Two-phase flow averaged codes: criteria for numerical methods," in Proc. of Trends in Numerical and Physical Modeling for Industrial Multiphase Flows, Cargese, France, (2001).

[23] TOBITA, Y., et al., "Interfacial Area Modeling for a Multiphase, Multicomponent Fluid-Dynamics Code," in Proc. Int. Conf. Multiphase Flows '91-TSUKUBA, Tsukuba, Japan, (1991).

[24] MORITA, K., FISCHER, E., A. Thermodynamic properties and equations of state for fast reactor safety analysis, Part I: Analytic equation-of-state model, Nucl. Eng. Des., **183** (1998) 177-191.

[25] MORITA, K., FISCHER, E., A. THURNAY, K., Thermodynamic properties and equations of state for fast reactor safety analysis, Part II: Properties of fast reactor materials, Nucl. Eng. and Des., **183** 3 (1998) 193-211.

[26] FISCHER, E. A. Fuel Equation of State Data for Use in Fast Reactor Accident Analysis Codes, Kernforschungszentrum Karlsruhe report, 1992.

[27] BUCKEL, G., HESSELSCHWERDT, E., al., e., A new SIMMER-III version with improved neutronics solution algorithms, FZKA, (1999) .

[28] MASCHEK, W., RINEISKI, A., SUZUKI, T., CHEN, X.-N. SIMMER-III, a Code for Analyzing Transients and Accidents in ADS, Washington D.C., USA 2000.

[29] ANL/NE-12/4, Nuclear Engineering Division, The SAS4A/SASSYS-1 Analysis Code System, Chapter 8: DEFORM-4: Steady-State and Transient Pre-Failure Pin Behavior, Argonne National Laboratory, 2012.

[30] ONODA, Y., MATSUBA, K.-I. TOBITA, Y., SUZUKI, T., Preliminary analysis of the post-disassembly expansion phase and structural response under unprotected loss of flow accident in prototype sodium cooled fast reactor, Mechanical Engineering Journal, **4** 3 (2017) .

[31] USOV, E., et al., A step in the verification of the HYDRA-IBRAE/LM/V1 thermohydraulic code for calculating sodium coolant flow in fuel-rod assemblies, At. Energy, **118** (2015) 382–388.

[32] USOV, E., et al., System of closing relations of a two-fluid model for the HYDRA-IBRAE/LM/V1 code for calculation of sodium boiling in channels of power equipment, Thermal Engineering, **64** (2017) 504-510.

[33] I. IDEL`CHIK, Handbook of hydraulic resistance. Coefficients of local resistance and of friction, GosudarstvennoeEnergeticheskoeIzdatel'stvo, Moskva-Leningrad 1960.

[34] BOL'SHOV, L., MOSUNOVA, N., STRIZHOV, V., O.V., S., Dedicated to the 60th anniversary of the journal AtomnayaEnergiya: Next generation design codes for a new technological platform for nuclear power, Atomic Energy, **120** 6 (2016) 369-379.

[35] STEPNEWSKI, D., FOX, G., PEAK, R., MERCKX, K., Mechanical Consequences of Hypothetical Core Disruptive Accidents, Hanford Engineering Development Lab., Richland, Wash. 1971.

[36] TODREAS, N., KAZIMI, M., Nuclear Systems 1: Thermal Hydraulic Fundamentals, Hemisphere Publication Corporation, New York, New York, USA 1993.

[37] CHELLAPANDI, P., et al., "Analysis for Mechanical Consequences of a Core Disruptive Accident in Prototype Fast Breeder Reactor," in Conf. Proc. SMIRT 17, International conference on structural mechanics in reactor technology, Prague, Czech Republic, (2003).

[38] THE JAPAN SOCIETY OF MECHANICAL ENGINEERS, Hydraulic Losses in Pipes and Ducts, The Japan Society of Mechanical Engineers, Tokyo 1979.

[39] THE JAPAN SOCIETY OF MECHANICAL ENGINEERS, JSME Mechnical Engineers' Handbook, The Japan Society of Mechanical Engineers, Tokyo 2014.

[40] VELUSAMY, K., et al., A fundamental approach to specify thermal and pressure loadings on containment buildings of sodium cooled fast reactors during a core disruptive accident, Ann. Nucl. Energy, **38** (2011) .

[41] BEIRIGER, P., et al., SOFIRE II User Report, Atomics International, Canoga Park, California, 1973.

[42] S. TSAI, NACOM code for analysis of postulated sodium spray fires in LMFBRs, Brookhaven National Lab., Upton, NY 1980.

[43] SMOLUCHOWSKI, M. V. VersucheinermathematischenTheorie der KoagulationskinetikkolloiderLösungen, Z. Für Phys. Chem., **92** (1918) .

[44] M. JACOBSON, Fundamentals of Atmospheric Modeling, 2nd edition, Cambridge University Press, Stanford University, California 2005.

[45] U.S. NUCLEAR REGULATORY COMMISION, Technical Bases for Estimating Fission Product Behavior During LWR Accidents Technical Report, U.S. Nuclear Regulatory Commission, Washington, DC, 1981.

[46] ALLELEIN, H.-J. et al., State of the art report on nuclear aerosols, Organization for Economic Cooperation and development. Nuclear Energy Agency. Committee on the safety of nuclear installations, 2009.

[47] BERTHOUD, G., LONGEST, A., WRIGHT, A., SCHÜTZ, W., Experiments on liquid-metal fast breeder reactor aerosol source terms after severe accidents, Nucl. Technol., **81** (1988) 257–277.

[48] GARCIA, M., HERRANZ, L., KISSANE, M., Theoretical assessment of particle generation from sodium pool fires, Nuclear Engineering and Design, **310** (2016) 461-475.

[49] INTERNATIONAL ATOMIC ENERGY AGENCY, Technical Specification for WP-3 of IAEA-CRP on “Radioactivity Release from Sodium Cooled Fast Reactor Under Severe Accident Condition”, IAEA, Vienna, Austria, 2018.

[50] MURATA, K., CARROLL, D., BERGERON, K., VALDEZ, G., CONTAIN LMR/1B-Mod.1, A Computer Code for Containment Analysis of Accidents in Liquid-Metal Cooled Nuclear Reactors (No. SAND91-1490), Sandia National Laboratory, Albuquerque, NM (United States) 1993.

[51] YAMAGUCHI, A., TAJIMA, Y., A numerical study of radiation heat transfer in sodium pool combustion and response surface modeling of luminous flame emissivity., Nuclear Engineering and Design, **236** (2006) .

[52] HILLIARD, R., MCCORMACK, D., POSTMA, A., Aerosol behavior during sodium pool fires in a large vessel - CSTF tests AB1 and AB2 (No. HEDL-TME 79-28), Hanford Engineering Development Lab, Hanford, WA, USA, 1979.

[53] JORDAN, S., CHERDRON, W., MALET, J., RZEKIECKI, R., HIMENO, Y., Sodium aerosol behavior in liquid-metal fast breeder reactor containments, Nuclear Technology, **81** (1988) 183-192.

[54] PUJALA, U., SUBRAMANIAN, V., KUMAR, A., SUJATHA, P., BASKARAN, R., "Determination of Sodium Combustion Aerosol Density And Shape Factor," in IASTA 2016 Conference of Indian Aerosol Science and Technology Association, Navrangpura, Ahmedabad, India, (2016).

[55] BESTELE, J., KLEIN-HESSLING, W., ASTEC V0 CPA Module, Containment Thermalhydraulics and Aerosol and Fission Product Behaviour, User Guidelines, Institut de Protection et de Sureté Nucléaire, France and Gesellschaft für Anlagen- und Reaktorsicherheit (GRS)mbH, Germany, 2000.

[56] GORDEEV, S., HERING, W., SCHIKORR, M., STIEGLITZ, R., "Sensitivity analysis of contain-LMR calculations to the aerosol shape factors," in Conf. Proc. of ICAPP 2013: Nuclear Power - A Safe and Sustainable Choice for Green Future, Held with the 28th KAIF/KNS Annual Conference 2013, Jeju Island, South Korea, (2013).

[57] U.S. NUCLEAR REGULATORY COMMISSION, SNAP/RADTRAD 4.0: Description of Models and Methods, 2016.

[58] J. BROCKMANN, "Sampling and Transport of Aerosols," in *Aerosol Measurement: Principles, Techniques, and Applications*, Hoboken, New Jersey, USA, John Wiley & Sons, 2011.

[59] BROWN, W., G. SOLVASON, K., R. Natural convection through rectangular openings in partitions-1 vertical partitions, International Journal of Heat and Mass Transfer, **5** 9 (1962) 859-862.

[60] BROWN, W. G. Natural convection through rectangular openings in partitions-2 horizontal partitions, International Journal of Heat and Mass Transfer, **5** 9 (1962) 869-881.

[61] LEE, Y., B. CHOI, S., K. A Study on the Development of Advanced Model to Predict the Sodium Pool Fire, Journal of the Korean Nuclear Society, **29** 3 (1997) 240-250.

[62] F. GELBARD, MAEROS User Manual, Sandia National Laboratories, Albuquerque, NM, USA 1982.

[63] USOV, E., et al., Verification of the EUCLID/V2 Code Based on Experiments Involving Destruction of a Liquid Metal Cooled Reactor’s Core Components., Thermal Engineering, **66** 5 (2019) 302-309.

[64] USOV, E., V. et al., The EUCLID/V2 Code Physical Models for Calculating Fuel Rod and Core Failures in a Liquid Metal Cooled Reactor, Thermal Engineering, **66** 5 (2019) 293-301.

[65] JOHN ARUL, A., et al., "International Conference on Fast Reactors and Related Fuel Cycles: Next Generation Nuclear Systems for Sustainable Development (FR17)," in Conf. Proc. of International Conference on Fast Reactors and Related Fuel Cycles, Yekaterinburg, Russian Federation, (2017).

[66] CHERDRON, W., CHARPENEL, J., Thermodynamic consequences of sodium spray fires in closed containments. Pt. 2 (No. KFK--3831), Kernforschungszentrum Karlsruhe G.m.b.H., Germany, 1985.

[67] CHERDRON, W. J. S. Die Natrium-Brandversuche in der FAUNA-Anlage auf Brandflächen bis 12m2 (No. KfK 3041), Kernforschungszentrum Karlsruhe G.m.b.H., Germany, 1983.

[68] CHERDRON, W., JORDAN, S., Determination of sodium fire aerosol process coefficients from FAUNA-experiments, in: NUREG/CR-1724, Gatlingburg, Tennessee, USA, 1980.

[69] CHERDRON, W., JORDAN, S., LINDNER, W., Die Natriumbrand-Untersuchungen in der FAUNA: Poolbrände und Aerosolverhalten, Kernforschungszentrum Karlsruhe G.m.b.H., Germany, 1990.

[70] GIRAULT, N., et al., "On-going activities in the European JASMIN project for the development and validation of ASTEC-Na SFR safety simulation code," in International Congress on Advances in Nuclear Power Plants (ICAPP 2015), Nice, France, (2015).

[71] GIRAULT, N., CLOAREC, L., LEBEL, L., "Main outcomes from the JASMIN project: development of ASTEC-Na for severe accident simulation in Na cooled fast reactors," in Conf. Proc. of Fast Reactors and Related Fuel Cycles: Next Generation Nuclear Systems for Sustainable Development (FR17), Yekaterinburg, Russia, (2017).

[72] HERRANZ, L., GARCIA, M., KISSANE, M., SPENGLER, C., A lumped parameter modelling of particle generation from Na-pool fires in SFR containments, Progress in Nuclear Energy, **109** (109) 223-232.

[73] HERRANZ, L., GARCIA, M., LEBEL, L., MASCARI, F., SPENGLER, C., In-containment source term predictability of ASTEC-Na: Major insights from data-predictions benchmarking, Nuclear Engineering and Design, **320** 15 (2017) 269-281.

[74] HERRANZ, L. G. M. M. S. Benchmarking LWR codes capability to model radionuclide deposition within SFR containments: An analysis of the Na ABCOVE tests, Nuclear Engineering and Design, **265** (2013) 772–784.

[75] HERRANZ, L., KISSANE, M., GARCIA, M., Comparison of LWR and SFR in-containment source term: Similarities and differences, Progress in Nuclear Energy, **66** (2013) 52-60.

[76] HERRANZ, L., LEBEL, L., MASCARI, F., SPENGLER, C., Progress in modeling in-containment source term with ASTEC-Na, Annals of Nuclear Energy, **112** (2018) 84-93.

[77] HILLIARD, R., MCCORMACK, J., HASSBERGER, J., MUHLESTEIN, L., Preliminary results of CSTF aerosol behavior test, Hanford Engineering Development Lab., Richland, Wash. (USA), 1977.

[78] KWON, Y.-M. TRUONG, B., "Effect of Pump Transient Characteristic Model on Safety Analysis of Sodium-Cooled Fast Reactor," in Conf. Proc. of 26th International Conference on Nuclear Engineering (ICONE), London, United Kingdom, (2018).

[79] HASHMI, A., A. BATES, E., TRUONG, B., "GRS Uncertainty and Sensitivity Evaluation of an Unprotected Transient Overpower (UTOP) in a TWR Design," in ANS Best Estimate Plus Uncertainty International Conference (BEPU), Lucca, Italy, (2018).

[80] BATES, E., et al., "Conclusions of a Benchmark Study on the EBR-II SHRT-45R Experiment," in Conf. Proc. of Fast Reactor and Related Fuel Cycles: Next Generation Nuclear Systems for Sustainable Development (FR-17), Yekaterinburg, Russia, (2017).

[81] HILLIARD, R., K. MCCORMACK, J., D. POSTMA, A., K. Results and Code Predictions for ABCOVE Aerosol Code Validation – Test AB5 (HEDL-TME 83-16), Hanford Engineering Development Laboratory, Hanford, Washington, USA, 1983.

[82] Mathé, E., Kissane, M., Petitprez, D., "Improved Modelling of Sodium-Spray Fires and Sodium-Combustion Aerosol Chemical Evolution," in International Congress on Advances in Nuclear Power Plants (ICAPP 2015), Nice, France, (2015).

[83] MCCORMACK, J., HILLIARD, R., POSTMA, A., Recent Aerosol Tests in the Containment Systems Test Facility (No. HEDL-SA-1686), Hanford Engineering Development Lab., Richland, WA., USA, 1978.

[84] CLARK, A., DENMAN, M., Sodium Spray Fire Simulations using CONTAIN-LMR, Sandia National Laboratories, Albuquerque, NM, 2016.

[85] INTERNATIONAL ATOMIC ENERGY AGENCY, First Research Coordination Meeting of the IAEA Coordinated Research Project on “Radioactive Release from the Prototype Fast Breeder Reactor under Severe Accident Conditions", IAEA, Vienna, Austria, 2016.

ABBREVIATIONS

CDA	core disruptive accident
CPLD	cold pool level detector
CP	control plug
CRP	coordinated research project
CSRDM	control and safety rod drive mechanisms
DHX	decay heat exchanger
DND	delayed neutron detector
DSRDM	diverse safety rod drive mechanisms
EL	elevation level
FSA	fuel subassembly
FBR	fast breeder reactor
FFIM	failed fuel identification module
HPLD	hot pool level detector
IFTM	inclined fuel transfer machine
IHX	intermediate heat exchangers
IWF	inter-wrapper flow
IV	inner vessel
IVTP	vessel transfer post cum periscope access
LOCA	loss-of-coolant accident
LRP	large rotating plug
LWR	light water reactor
MOEC	middle of equilibrium core
MV	main vessel
OD	outer diameter
OSP	oval shield plug of transfer arm
PFBR	prototype fast breeder reactor
RCM	research coordination meeting
RF	release fractions
RN	radionuclides
RS	roof slab
SA	subassembly
SFR	sodium-cooled fast reactor
SGDHRS	safety grade decay heat removal system
SRP	small rotating plug
ULOFA	unprotected loss-of-flow accident
UTOPA	unprotected transient overpower accident

CONTRIBUTORS TO DRAFTING AND REVIEW

Arokiaswamy, J. A.	Indira Gandhi Center for Atomic Research (IGCAR), India
Batra, C.	International Atomic Energy Agency (IAEA)
Chang, J. E.	TerraPower, LLC, United States of America (USA)
Garcia, M.	Centro de InvestigacionesEnergéticas, Medioambientales y Tecnológicas (CIEMAT), Spain
Herranz, L. E.	Centro de InvestigacionesEnergéticas, Medioambientales y Tecnológicas (CIEMAT), Spain
Klimonov, I.A.	Nuclear Safety Institute of The Russian Academy Of Sciences, Russia
Kriventsev V.	International Atomic Energy Agency (IAEA)
Li, S.	China Institute of Atomic Energy (CIAE), China
Liegeard, C.	French Alternative Energies and Atomic Energy Commission (CEA), France
Mahanes, J.	International Atomic Energy Agency (IAEA)
Monti, S.	International Atomic Energy Agency (IAEA)
Mosunova, N.A.	Nuclear Safety Institute of The Russian Academy Of Sciences, Russia
Onoda, Y.	Japan Atomic Energy Agency (JAEA), Japan
Ren, L.	China Institute of Atomic Energy (CIAE), China
Ruggieri, J. M.	French Alternative Energies and Atomic Energy Commission (CEA), France
Serre, F.	French Alternative Energies and Atomic Energy Commission (CEA), France
Sui, D.	North China Electric Power University (NCEPU), China
Sun, H. P.	Xi'an Jiaotong University (XJTU), China
Tarasov, O.V.	Nuclear Safety Institute of The Russian Academy of Sciences, Russia
Zhang, D. L.	Xi'an Jiaotong University (XJTU), China
Zhang, Y. P.	Xi'an Jiaotong University (XJTU), China

Research Coordination Meetings

Vienna, Austria: 3-6 May 2016
Kalpakkam, India: 13- 17 November 2017
Vienna, Austria: 8-11 April 2019
Vienna, Austria: 10-13 February 2020

IAEA
International Atomic Energy Agency

No. 26

ORDERING LOCALLY

IAEA priced publications may be purchased from the sources listed below or from major local booksellers.

Orders for unpriced publications should be made directly to the IAEA. The contact details are given at the end of this list.

NORTH AMERICA

Bernan / Rowman & Littlefield

15250 NBN Way, Blue Ridge Summit, PA 17214, USA
Telephone: +1 800 462 6420 • Fax: +1 800 338 4550

Email: orders@rowman.com • Web site: www.rowman.com/bernan

REST OF WORLD

Please contact your preferred local supplier, or our lead distributor:

Eurospan Group

Gray's Inn House
127 Clerkenwell Road
London EC1R 5DB
United Kingdom

Trade orders and enquiries:

Telephone: +44 (0)176 760 4972 • Fax: +44 (0)176 760 1640
Email: eurospan@turpin-distribution.com

Individual orders:

www.eurospanbookstore.com/iaea

For further information:

Telephone: +44 (0)207 240 0856 • Fax: +44 (0)207 379 0609
Email: info@eurospangroup.com • Web site: www.eurospangroup.com

Orders for both priced and unpriced publications may be addressed directly to:

Marketing and Sales Unit
International Atomic Energy Agency
Vienna International Centre, PO Box 100, 1400 Vienna, Austria
Telephone: +43 1 2600 22529 or 22530 • Fax: +43 1 26007 22529
Email: sales.publications@iaea.org • Web site: www.iaea.org/publications

22-03254E

International Atomic Energy Agency
Vienna